

Green And Versatile: Catalytic Production Of Recyclable Co-Polymers From Epoxides And Anhydrides

Matthew Shaw



**A thesis submitted to Cardiff University in accordance with the requirements
for the degree of Doctor of Philosophy**

School of Chemistry, Cardiff University

September 2023

Acknowledgements

It goes without saying that a PhD project is not a solo endeavour, and for that reason I'd like to thank all of those who have shared 1.124 with me over the duration of my project. To Taylor Young, Eve Tarring, Rob Amesbury, Owaen Guppy, Dom Ward, Halimah Alahmari, Sahar Al-Fayez, Mark Sullivan, Ibtisam Mousa, Siôn Edwards, Bria Thomas, Ben Wellburn, Adam Day, Ash Steer, Ibrahim Shoetan, Allie Ibbot, Maddy Thorne and Dan Clements, it has been a pleasure. And a big thank you to Dr. Ben Ward, for all of the advice, guidance, teaching and discussions over the last few years that have made this project possible.

Thank you to Sophie Fitzgerald and Prof. Simon Pope for their collaboration with the iridium-doped polymers, Dr. Emma Richards for EPR analysis of the copper doped polymer, Dr. Mark Eaton for the training and use of DSC, and Prof. Paul Joseph, Dr Svetlana Tretsiakova-McNally, and Dr Malavika Arun for kindly offering their time and expertise for PCFC analyses and more general discussions of flame retardancy. I'd also like to acknowledge the analytical services team at Cardiff University, including Dr Rob Jenkins for assistance with DOSY experiments and Simon Waller and Pete Iafrate for mass spectrometry analyses.

Finally, thank you to Mum, Dad and Kirsty, for a lifetime of support for which I could never be thankful enough. And to Eve, thank you for all of your support and encouragement both during my time in the lab and since – it certainly wouldn't have been the same without it!

Abstract

The Ring-Opening Copolymerisation (ROCOP) of epoxides and cyclic anhydrides is a versatile, atom economical and controllable way of synthesising a broad range of chemically recyclable polyesters. Throughout this work, the synthesis and material properties of ROCOP polyesters will be investigated, including the development of metal catalysts and their coordination chemistry, experimental and theoretical mechanistic investigations into both the initiation and propagation cycles of the polymerisation, and analysis of the resultant novel polymers. The following is a summary of the research undertaken in each of the following chapters:

Chapter 1: Introduces Ring-Opening Copolymerisation and describes some of its core concepts as well as key achievements within the field. Experimental techniques pertaining to polymers which are used in the subsequent chapters are also introduced.

Chapter 2: Features the synthesis and full characterisation of a series of novel aluminium complexes based on the “Salpy” ligand framework. These complexes will then be investigated for use as catalysts in ROCOP both experimentally and computationally.

Chapter 3: Features the catalytic screening of a series of Group 4 metallocene complexes as pre-catalysts for ROCOP, including the synthesis of partially bio-derived poly(LO-*alt*-PA) and its subsequent scale up to produce over 200 g of polymer. The mechanism of action for the Group 4 complexes, which are underrepresented in the ROCOP literature, will be examined using a variety of approaches.

Chapter 4: Details the material properties of the poly(LO-*alt*-PA) made on a large scale in chapter 3, and its subsequent post-polymerisation modification by the thiol-ene click reaction. This modification also includes cross-linking, performed both post-polymerisation and *in situ*, and how it can influence a polymer’s properties. Modification by phosphorylation will be performed to examine the effect of binding chemical functionality possessing flame retardant behaviour has on the resulting polymer,

Chapter 5: Details investigations into the doping of an epoxide containing a bipyridine-like unit into ROCOP reactions, meaning the resultant polymer is able to chelate metals. Metal-doped polymers of Ir, Ru, Cu, Fe and Zn will be synthesised and extensively characterised, including examination of the photophysical properties of the iridium polymer with a view to its use in electronic devices.

Chapter 6: Features a summary of the above and avenues for further investigations.

Chapter 7: Provides details of experimental procedures.

Contents

Chapter 1 - Introduction: Plastics, Polyesters and Ring-Opening Copolymerisation.....	1
1.1: Plastics and Polymers.....	1
1.2: Polyesters: Chemical Recyclability and Step-Growth vs. Chain-Growth Polymerisation.....	5
1.3: Ring-Opening Copolymerisation (ROCOP).....	13
1.4: ROCOP: The Current Literature.....	17
1.5: ROCOP: Mechanistic Considerations.....	23
1.6: Characterisation and Analysis of Polymers.....	30
1.6.1: Characterisation and Analysis of Polymers.....	30
1.6.2 : Gel Permeation Chromatography (GPC).....	30
1.6.3 : MALDI-ToF Mass Spectrometry.....	32
1.6.4 : Diffusion Ordered (NMR) Spectroscopy (DOSY).....	33
1.6.5 : Thermal Properties of Polymers and Differential Scanning Calorimetry (DSC).....	34
1.7: Summary.....	36
1.8: References for Chapter 1.....	37
Chapter 2 - Aluminium “Salpy” Complexes: Synthesis, Characterisation, and ROCOP Catalysis.....	42
2.1: Aluminium Catalysts in ROCOP.....	42
2.2: Aluminium “Salpy” Complexes – Synthesis and Characterisation.....	49
2.3: Catalytic Performance of Salpy Complexes in ROCOP.....	53
2.3.1: Initial ROCOP Experiments – Two Equivalent [PPN]Cl.....	53
2.3.2: Further ROCOP Experiments – One Equivalent DMAP.....	55
2.3.3: Expanding Anhydride Scope.....	60
2.4: Mechanistic Investigations: Stoichiometric Reactions.....	61
2.5: Mechanistic Investigations: DFT Calculations.....	64
2.6: Summary.....	73
2.7: References for Chapter 2.....	74
Chapter 3 - Group 4 Metallocene Complexes as ROCOP Pre-Catalysts.....	78
3.1: Group 4 Metallocene Complexes.....	78
3.2: The Group 4 Metals in ROP and ROCOP.....	79

3.3: Catalytic Performance of [Cp ₂ MCl ₂] Complexes in Epoxide-Anhydride ROCOP.....	83
3.4: MALDI-ToF, DOSY NMR and GPC Analysis of Polymers.....	89
3.5: Mechanistic Studies.....	92
3.6: Density Functional Theory Calculations.....	100
3.7: Copolymerisation of Limonene Oxide.....	105
3.8: <i>ansa</i> -Zirconocenes as Pre-Catalysts.....	110
3.9: Summary.....	113
3.10: References for Chapter 3.....	114

Chapter 4 - Post-Polymerisation Modification Reactions of Poly(LO-*alt*-PA) and Investigations into Polymer Flame Retardancy.....119

4.1: Post-Polymerisation Modification Reactions.....	119
4.2: Literature Modifications of ROCOP Polymers.....	119
4.3: Thiol-ene Click Modification of Poly(LO- <i>alt</i> -PA).....	125
4.4: 1,6-Hexanedithiol Crosslinking of Poly(LO- <i>alt</i> -PA).....	130
4.5: <i>In Situ</i> Diepoxide Cross-linking of Poly(LO- <i>alt</i> -PA).....	132
4.6: Flame Retardant Behaviour of Polymers.....	135
4.7: Reactive Type Phosphate Flame Retardants and Polyesters.....	137
4.8: Synthesis and Characterisation of Phosphorylated Poly(LO- <i>alt</i> -PA).....	140
4.9: Thermal Stability of the Phosphorylated Polymers.....	145
4.10: Flame Retardancy (PCFC) of the Phosphorylated Polymers.....	147
4.11: Summary.....	152
4.12: References for Chapter 4.....	153

Chapter 5 - Metal Complex Incorporation into ROCOP Polyesters.....156

5.1: Cyclometallated Iridium Complexes and their Luminescence.....	156
5.2: Iridium Doped Polymers.....	158
5.3: Incorporation of Bipyridine-like Units into Polyesters.....	162
5.4: Synthesis and Characterisation of Iridium Containing Polyesters.....	167
5.5: Photophysical Properties of the Iridium Containing Polyesters.....	170
5.6: Synthesis of Low <i>T_g</i> Bipyridine-containing Polyesters.....	177
5.7: Ruthenium Doped Polyesters.....	181

5.8: Synthesis and Characterisation of 1 st Row Transition Metal Containing Polyesters.....	185
5.9: Summary.....	195
5.10: References for Chapter 5.....	196
Chapter 6 - Conclusions and Future Work.....	201
6.1: Summary of Completed Work.....	201
6.2: Future Work.....	202
6.3: References for Chapter 6.....	205
Chapter 7 - Experimental.....	206
7.1: Instrumentation, General Considerations and Polymerisations.....	206
7.2: Synthesis and Characterisation of Salpy Ligands.....	207
7.3: Synthesis and Characterisation of [Al(Salpy)Cl] Complexes.....	211
7.4: Synthesis and Characterisation of ansa-Zirconocene Complexes.....	214
7.5: Thiol-ene Click Post-Polymerisation Modification.....	216
7.5.1: Synthetic Procedure for Thiol-ene Click Modification.....	216
7.5.2: NMR Spectra of Thiol-ene Click Modified Polymers.....	217
7.6: Hydroboration-Oxidation and Phosphorylation of poly(LO-alt-PA).....	221
7.7: NMR Spectra of EDHP-doped Polymers.....	224
7.8: Synthesis of Ruthenium Doped poly(EDHP-CHO-PA).....	225
7.9: Synthesis of 1st Row Transition Metal Doped Polyesters.....	226
7.10: References for Chapter 7.....	226
Appendix - X-Ray Crystallographic Data of [Salpy-Al-Cl] Complexes.....	227
A.1: [3,5-di-tert-butylsalpy-Al-Cl] (Al-2).....	227
A.2: [5-nitrosalpy-Al-Cl] (Al-3).....	246

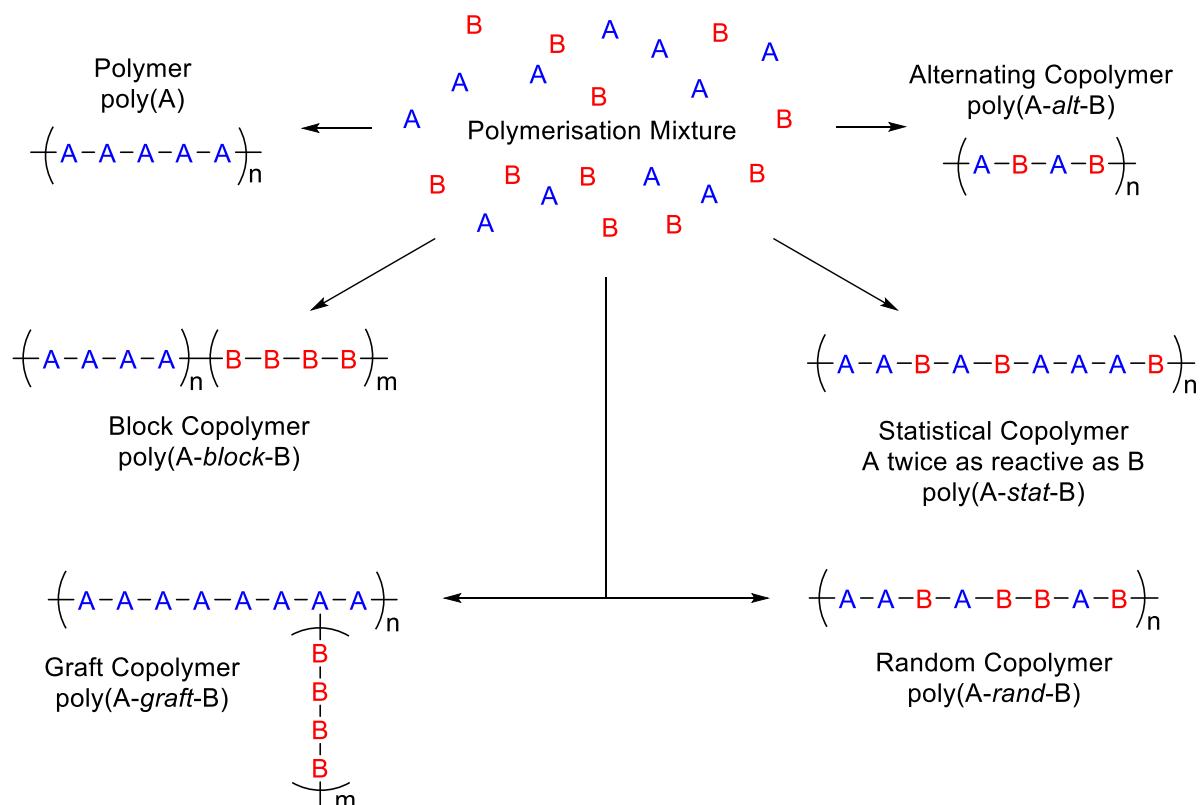
Introduction: Plastics, Polyesters and Ring-Opening Copolymerisation

1.1: Plastics and Polymers

Plastics are ubiquitous in everyday life, and demand for them has been consistently increasing since their invention, with a global production of 359 megatonnes in 2018 alone.¹ Plastics have found widespread use due to their unique blend of properties, including (but certainly not limited to) high mechanical strength, thermal and chemical resistance and excellent barrier properties.^{2,3}

Plastics are composite materials primarily composed of polymers, and it is largely the use of these polymers which imparts the desirable material properties to plastics.³ Polymers themselves are large molecules comprised of relatively small (*approx.* 50 – 1000 g mol⁻¹) repeat units covalently bound together, which are known as monomers. Polymers can range from a few (*c.a.* 10) of these units joined together, to uninterrupted chains of tens of thousands of monomers, meaning the molecular mass of a polymer chain can range from hundreds to millions of Daltons. This vast mass range has a profound influence on the material properties of the resultant polymer.³ To turn polymers into the consumer product plastic, polymers are blended with additives, such as dyes, flame retardants, and plasticisers, which are added reduce the brittleness of polymers, as well as lubricants which may aide material processing.³⁻⁵ In the solid state, polymer chains can either pack in a highly ordered, crystalline structure, in a randomly orientated amorphous structure, or in a semi-crystalline fashion, where there are both amorphous and crystalline regions.³

Polymers can be comprised of more than one monomer; if two monomers are used then the polymer is termed a copolymer; for three monomers, a terpolymer and so on. Taking a copolymer as an example, the two different monomers can be arranged in several different ways within copolymer chains (**Scheme 1.1**): in large distinct blocks (a block copolymer), in a perfectly alternating sequence (an alternating copolymer), dispersed apparently randomly but with a bias according to their relative reactivity (a statistical copolymer) or completely randomly interspersed (a random copolymer).³ Polymers chains can also contain branches, rather than being purely linear, and if these branches feature a different monomer to the main polymer chain then it is termed a graft copolymer. **Scheme 1.1** also details the common nomenclature used to describe the copolymers for example monomers A and B. The subscripts n and m potentially represent large numbers depending on the molecular weight of the polymer.



Scheme 1.1: Common types of copolymer that can result from reaction of generic monomers A and B, and their associated nomenclature.³ n and m represent potentially large numbers depending on the molecular weight of the polymer.

One of the key reasons why polymers are used to make plastics is their resistance to degradation, although this also means that plastic is a highly persistent environmental pollutant. Indeed, the extensive mismanagement of plastic waste has been well documented, and it estimated that between 5 and 13 megatonnes of plastic entered the oceans in 2010.⁶ This is deeply concerning, as not only does this lead to the immediate threat of the entanglement of wildlife, but plastics can be broken apart into smaller pieces by mechanical forces and weathering, to the extent they can be ingested by organisms.^{6,7} Furthermore, in a process known as bio-accumulation, the concentration of ingested plastics can increase up the food chain, potentially compounding their toxicological effects.⁸ Therefore, it is of vital importance that polymers are designed with in-built solutions for their end-of-life stage.

One such way of minimising the long-term impact that plastic waste has on the environment is to make plastics from polymers which are broken down chemically in the environment, in a process called biodegradation.⁹ In this case, the bonds between monomer units must be susceptible to some

form of scission, which for plastics in the natural environment typically represents either hydrolysis or degradation by enzymes in bacteria, or a combination of the two.⁷ A series of biodegradable polymers are shown in **Figure 1.1**, with these examples all showing ester linkages. These ester linkages are important, as the O-C bond is susceptible to (relatively slow) chemical hydrolysis under (mildly) acidic or basic conditions, as well as (relatively fast) degradation by enzymes.¹⁰ These enzymes include lipases, whose natural function is to degrade the same ester linkages found in fats, or cutinases, which degrade cutin, a naturally occurring polyester in plant leaves.⁷ Some polymers, such as poly(ethylene glycol) (PEG), do not feature ester linkages but are degraded by bacteria, yet, from the perspective of plastic manufacture, polyesters represent the most important class of biodegradable polymers.^{4,11}

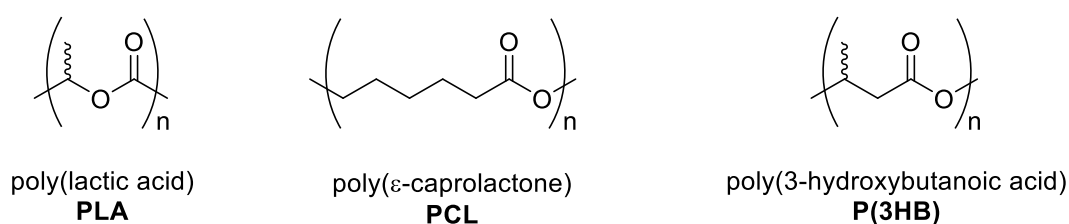


Figure 1.1: Examples of some biodegradable polyesters, with biodegradability in the natural environment increasing from left to right.^{4,7}

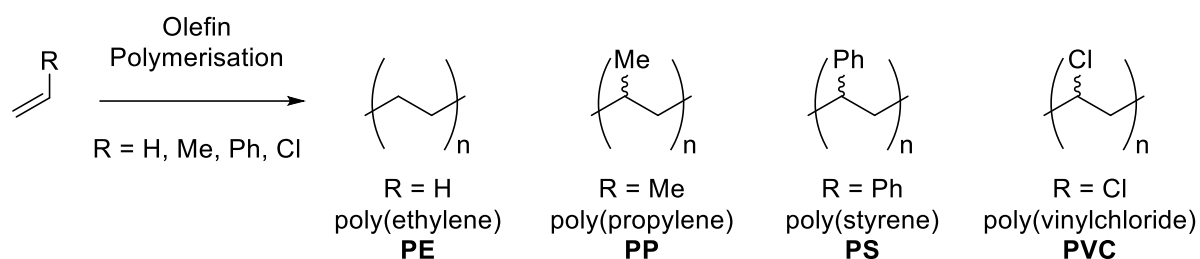
However, “biodegradable” is something of an umbrella term, and a selection of biodegradable polymers can exhibit wildly different degradation behaviour. For many, the term biodegradable represents how a material degrades in the natural environment, but some biodegradable polymers are incredibly robust to “natural” degradation. The most notable example of this is poly(lactic acid) (PLA, **Figure 1.1**), which under “natural” conditions such as in a landfill or in the ocean does not readily degrade.⁴ For PLA, its biodegradation requires the use of an industrial composter and carefully controlled, unnatural, conditions, meaning if plastic waste made from PLA is released into the environment, it will still persist for long periods. Whilst poly(ϵ -caprolactone) (PCL) and poly(3-hydroxybutanoic acid) are more biodegradable in natural environments, there are still several questions relating to the impact these materials have on the environment.¹² For example, what do the polymers biodegrade to? It could be argued that if complete mineralisation to CO₂ occurs, then there is no long term impact, yet in marine or freshwater environments this release of CO₂ will acidify water, with this having knock-on effects for other organisms.⁹ Methane may be another product of biodegradation, yet this is a highly potent greenhouse gas. Furthermore, if biodegradation is incomplete, what are the toxicological effects of the remaining small molecules, including if the contaminated water is a source of drinking water?⁹

Another question facing biodegradable polymers is that if the material is composted at end-of-life, is this really the most efficient way to use resources? This still represents linear use, in that a material is made with fresh feedstock, but then once its purpose has been served it is destroyed.⁵ This can still be considered somewhat wasteful, as although the waste has been managed, it has not been eliminated or reduced significantly, as to make more polymer, new feedstock would have to be grown and/or manufactured. This could be ameliorated with the use of bio-derived feedstocks, where waste products from agriculture are refined and used in a sustainable and renewable process.¹³ However, just because a polymer is bio-derived, it does not mean it is biodegradable; PLA is manufactured from renewable resources yet is far less biodegradable in the natural environment than PCL, which is made from non-renewable petroleum-based feedstocks.^{4,12,13} In short, simply using plastics based on biodegradable polymers is not an all-encompassing solution to the issue of plastic waste

To try to transition from this linear to circular usage, the reprocessing, or recycling of waste plastics into new plastics has been widely implemented.⁵ Most plastics are mechanically recycled, which involves grinding, melting, and re-extruding plastics into material that can be used to remake plastic items.¹⁴ Although this is preferable from a diminished creation of waste standpoint, there are still several problems with mechanical recycling. Firstly, many different plastics are present in waste streams, all of which are based on different polymers and must be separated. However, this separation can be challenging, particularly if there are different plastics (or indeed non-plastics like metals) used for different parts of any one object. This means the reformed material is often contaminated with a mixture of polymers, with this having a deleterious effect on the material properties of the recycled plastic.¹⁴ To add to this, plastics contain additives like dyes and plasticisers as well as polymers, all of which will contaminate the recycled plastic. The amounts of these contaminants will be inconsistent and largely unknown, and again will almost certainly not be at the proportions optimal for material use.⁴ Furthermore, older waste material may contain legacy additives such as brominated flame retardants (see section 4.6), which have been phased out of modern plastics due to toxicity concerns. However, in a mechanical recycling process, these additives can remain in new product made from recycled material.¹⁵ Finally, mechanical recycling process can degrade the polymer, again diminishing the material properties of the recycled polymer compared to its freshly synthesised, or virgin, polymer.¹⁴ This means that mechanically recycled plastics have a reduced lifetime and utility compared to virgin plastic, and so it cannot be infinitely recycled in a practical sense, meaning there is still waste generated and cannot be termed a fully “circular” process in the strictest sense. It is for this reason that mechanical recycling processes can be termed “downcycling”, and the large amount

of infrastructure required to collect, separate and process plastics for recycling is often economically prohibitive for developing economies, and is often found wanting in developed nations.^{4,5,16}

Despite this, mechanical recycling is a key method of reducing plastic waste. This is particularly true for polymers based on carbon-carbon bonds, with these linkages largely resistant to chemical scission.¹⁷ The majority of plastics in use today are based upon polymers made through the polymerisation of olefins (**Scheme 1.2**), with two-thirds of global plastic production in 2015 comprised of poly(ethylene) (PE) and poly(propylene) (PP).⁴ This represents a major concern from a sustainability perspective, as the ethylene and propylene monomers are derived from non-renewable petroleum sources, whilst the challenging separation of PE and PP means mechanical recycling only returns a brittle, low value blend of the two.¹⁰ This means waste poly(olefins) are often pyrolysed to at least extract some energy, albeit at the cost of increased greenhouse gas emissions.⁵



Scheme 1.2: Examples of common poly(olefins).

1.2: Polyesters: Chemical Recyclability and Step-Growth vs. Chain-Growth Polymerisation

A more enticing alternative is to synthesise polymers which can be chemically degraded back into their monomers, or precursors to monomers, so that when a material reaches the end of its useful life, it can (in theory) be completely converted back to the materials from which it was made. Not only does this help eliminate waste, but also, if the monomers are obtained in sufficient purity, then the remade polymers will have identical material properties as the virgin polymer. This is termed chemical recycling, and although there are challenges related to the cost and infrastructure required, clearly represents the optimum solution from a sustainability and waste reduction perspective.² Furthermore, as the recycled polymer is of the same quality as the virgin polymer, there is no reduction of value as is often seen for mechanical recycling.

Given the kinetic inertness and thermodynamic stability of carbon-carbon bonds, poly(olefins) are not generally suitable for chemical recycling, despite research efforts being made to change this.¹⁰ Conversely, polymers containing carbon-heteroatom bonds can be susceptible to nucleophilic attack, with a key example of this being aforementioned polyesters.⁴ The most common polyester used in plastic manufacture is poly(ethylene terephthalate), PET (**Figure 1.2**), which represents around 10% of annual global plastic production, and is used for plastic bottle manufacture and as fibres in textiles.⁴ PET is chemically recyclable and can be depolymerised under acidic or alkaline conditions,¹⁸ as well as through use of organocatalysts,¹⁹ metal catalysts,²⁰ or by glycolysis or aminolysis.¹⁰

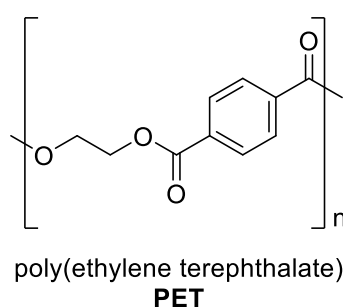
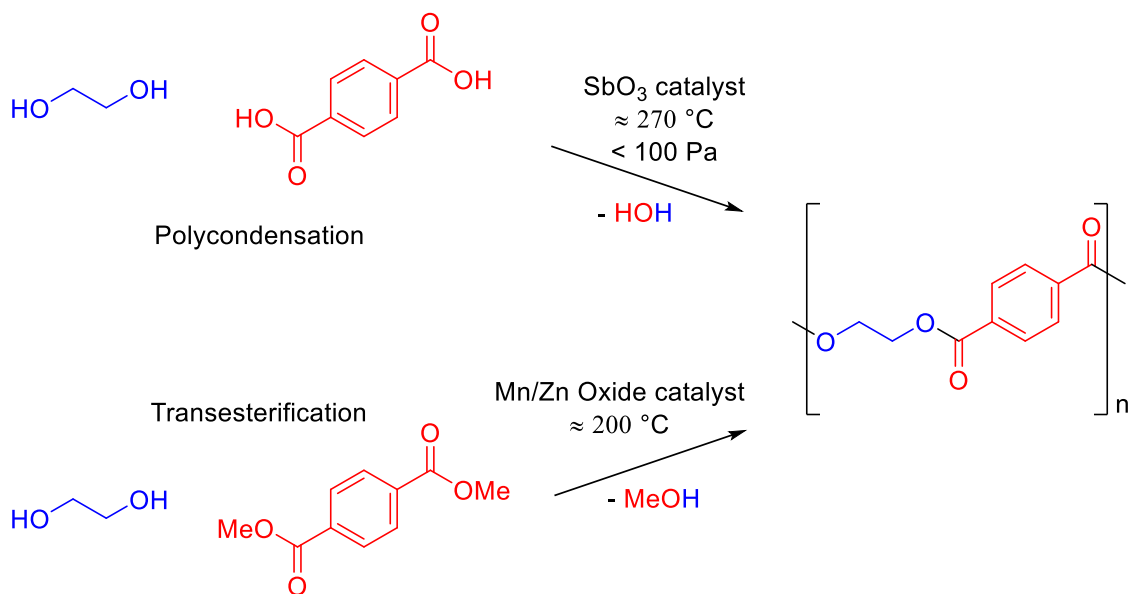


Figure 1.2: Structure of poly(ethylene terephthalate), PET, the most commonly manufactured polyester.⁴

Even though it can be chemically recycled, the vast majority of PET is mechanically recycled. Although PET is one of the most recycled plastics in terms of volume, the material properties of mechanically recycled PET pale in comparison to virgin PET: for example, virgin PET is ductile and requires 200% elongation to break, with this figure at only 10% for brittle mechanically recycled PET.¹⁰ As a result of this, most mechanically recycled PET is used as lower-grade material in the textile industry.⁴

PET is synthesised in two main ways, in a reaction of ethylene glycol with either terephthalic acid in a polycondensation reaction, or with dimethyl terephthalate in a transesterification reaction (**Scheme 1.3**).^{21,22} In both cases, a volatile by-product in water (polycondensation) or methanol (transesterification) are produced, which necessitates the use of low pressures for them to be continuously removed. As the reactions are equilibria, efficient removal of the by-product is crucial to ensure high conversions and yields of PET, as are the high temperatures and catalysts.²¹



Scheme 1.3: The two main synthetic pathways and conditions for PET production; polycondensation of ethylene glycol and terephthalic acid, and transesterification of ethylene glycol and dimethyl phthalate.^{21,22}

Both the polycondensation and transesterification pathways are examples of step-growth polymerisations.³ This is because both monomers are bifunctional and can react at either end, yet the reactivity at both ends is preserved post-reaction. This means that at any time, a growing polymer chain could react with a monomer, or a dimer, or a trimer, or any length polymer chain, and given that the chemical reactivity of all of these species is identical, the polymerisation outcomes are largely driven by statistical probability.³ As the relative concentration of monomer remains high until very high conversions, step-growth polymerisations must usually be run to high monomer conversion to produce high molecular weights, as only when the monomer concentration becomes low does the concentrations of higher oligomers become dominant, with the coupling of these fragments predominantly responsible for the formation of polymer chains. This is described mathematically by the Carothers Equation in **Figure 1.3**, which shows the reciprocal relationship between degree of polymerisation, P_n , or the number of monomer units in a polymer chain, and the fractional conversion of monomer, p .³

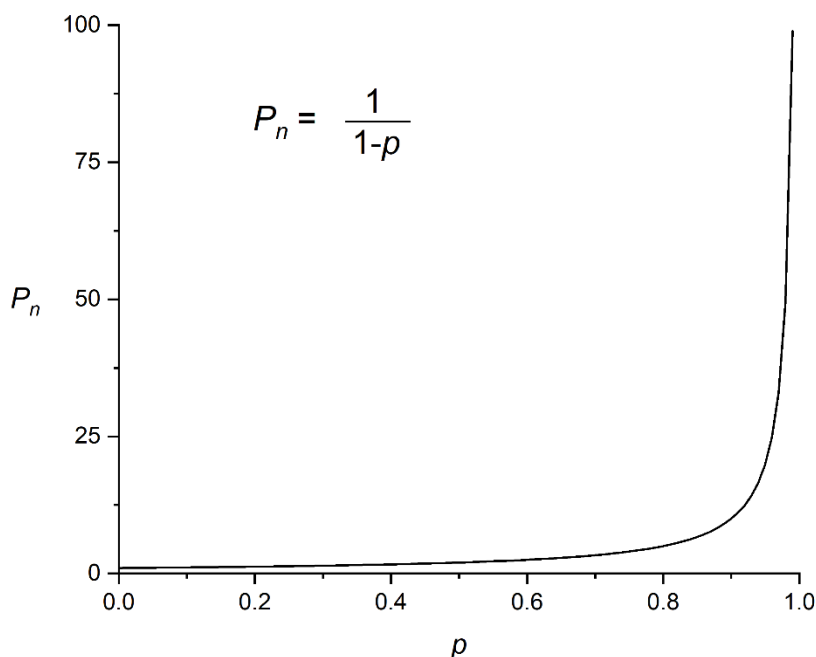


Figure 1.3: Relationship between number average degree of polymerisation, P_n , or the average number of monomers in a polymer chain and monomer conversion, p , for a bifunctional step-growth polymerisation with two monomers in a 1:1 stoichiometry.³

The Carothers Equation indicates that a monomer conversion of 90% would still, on average, only produce polymers with 10 monomer units. However, conversion of a further 5% of monomer would lead to a doubling of the degree of polymerisation, which explains why PET syntheses must be run to high monomer conversion to produce useful polymer. Another characteristic feature of step-growth polymerisations is that the polymers chains typically have a large variation in chain length, or molecular weight. So far, the length of a polymer chain has only been considering in terms of the average number of monomers in it. When one considers the formula mass of the monomer, m_1 , the mass of any one polymer chain, M , is calculated (neglecting for the mass of additional end groups) by

Equation 1.1:

$$\text{Equation 1.1:} \quad M = m_1 \times P_n$$

However, in real life polymer samples, where polymer chains of similar length will be both present and largely indistinguishable (a 20-mer will have near identical properties to a 21-mer, for example), an average molecular weight across a sample must be determined. This can be done by calculating the average of the mass of all polymer chains. This is known as the number average molecular weight, M_n , and is calculated according to **Equation 1.2:**³

$$\text{Equation 1.2:} \quad M_n = \frac{\sum_i n_i \cdot M_i}{\sum_i n_i}$$

Where n_i represents the number of chains of mass M_i , whilst the denominator represents the total number of polymer chains. In a trivial example, if a sample contains two polymer chains with a mass of $10,000 \text{ g mol}^{-1}$, and one other polymer chain of mass $20,000 \text{ g mol}^{-1}$, the M_n is equal to $13,333 \text{ g mol}^{-1}$, as calculated below:

$$M_n = \frac{(2 \times 10000) + (1 \times 20000)}{3} = 13,333 \text{ g mol}^{-1}$$

However, an alternative measure of molecular weight is to consider not the average number of monomers in the chain, but the average mass of each polymer chain. This is known as the weight average molecular weight, M_w , and can be calculated by replacing the number of chains of mass i (n_i) with the total mass of the chains of mass i , m_i , as in **Equation 1.3**:³

$$\text{Equation 1.3:} \quad M_w = \frac{\sum_i m_i \cdot M_i}{\sum_i m_i}$$

As the total mass of chains of mass i (m_i) is equal to the number of chains of mass i multiplied by M_i , **Equation 1.3** can be re-written as **Equation 1.4**:

$$\text{Equation 1.4:} \quad M_w = \frac{\sum_i (n_i \cdot M_i) \cdot M_i}{\sum_i (n_i \cdot M_i)}$$

Which is in-turn simplified to **Equation 1.5**, the most commonly encountered form of M_w :³

$$\text{Equation 1.5:} \quad M_w = \frac{\sum_i n_i \cdot M_i^2}{\sum_i n_i \cdot M_i}$$

In the trivial example mentioned above, the M_w is now equal to $15,000 \text{ g mol}^{-1}$, on account of the higher contribution that longer polymer chains make towards the total mass of the sample. Indeed, the value of M_w can only be equal to or exceed the value of M_n .

$$M_w = \frac{(2 \times 10000 \times 10000) + (1 \times 20000 \times 20000)}{(2 \times 10000) + (1 \times 20000)} = 15,000 \text{ g mol}^{-1}$$

These are not the only two measures of molecular weight, but are by far the most common. Only if a sample is completely monodisperse, meaning that every single polymer chain has exactly the same mass, would $M_w = M_n$. In practice, polymer samples will contain a range of different chain lengths; some samples will have a small range of chain lengths, some will have a vast range of chain lengths. The array of chain lengths in a sample is referred to as the molecular weight distribution. A simple measure of the breadth of a molecular weight distribution is called the polydispersity index, PDI, or \mathfrak{D} , and is calculated by a simple ratio of M_w and M_n in **Equation 1.6**:³

$$\text{Equation 1.6:} \quad \mathfrak{D} = \frac{M_w}{M_n}$$

Taking the M_w and M_n values calculated in the trivial example mentioned previously, the polydispersity of the sample is 1.13, with a dispersity of 1 representing a sample with completely uniform chain lengths. If in the above example, the chain at 20,000 g mol⁻¹ is changed to 30,000 g mol⁻¹, the PDI increases to 1.32 ($M_n = 16,667$ g mol⁻¹, $M_w = 22,000$ g mol⁻¹), reflecting the increased range of masses seen for the polymer chains. Therefore, the closer PDI is to 1, the more monodisperse a sample is, whilst as PDI increases, the sample becomes more polydisperse. Again, PDI is not the only measure of the breadth of molecular weight distributions, but it is the most common.²³

Returning to the step-growth synthesis of PET, the weight average degree of polymerisation, P_w (in contrast to the number average degree of polymerisation, P_n , as described previously) can also be described after a lengthy derivation by **Equation 1.7**:³

$$\text{Equation 1.7:} \quad P_w = \frac{1+p}{1-p}$$

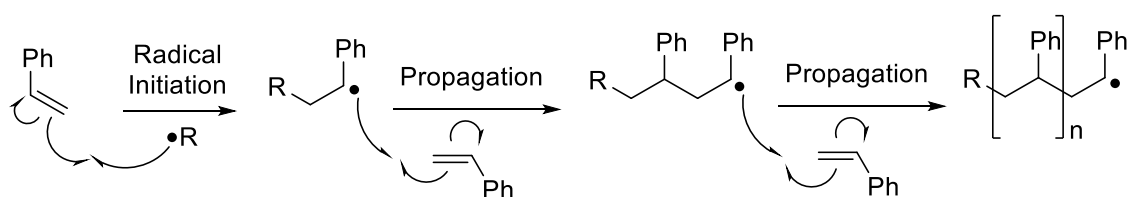
It follows from **Equation 1.6** that PDI will equal to the ratio of P_w to P_n , and so the PDI for a step-growth polymerisation (conducted with 1:1 ratio of monomers) can be described by **Equation 1.8**:³

$$\text{Equation 1.8:} \quad \mathfrak{D} = \frac{P_w}{P_n} = \left[\frac{1+p/1-p}{1-p} \right] = 1+p$$

Therefore, it follows that as monomer conversion p increases, the polymer sample necessarily becomes more polydisperse, and tends towards 2. In practice, polydispersities greater than 2 can be seen if there is an imbalance in monomer concentrations, which may be required to increase reactivity, if there are impurities in the monomer feedstock, or if there are side-reactions occurring.^{3,24}

This means that not only is the synthesis of PET energy intensive to remove the by-products, but the PET produced is by its nature polydisperse. Furthermore, PET is made from monomers which are typically petroleum-derived, whilst PET also shows limited biodegradability compared to other polyesters.^{13,25} This is mainly due to the aromaticity of the terephthalate constituents, which increases the crystallinity and rigidity of PET, meaning biodegradation enzymes are less able access the vulnerable C-O bonds.²⁵ However, PET does retain ester linkages which can be harnessed for relatively straightforward chemical degradation and recycling. Therefore, alternative methods of polyester synthesis represent an important research objective.

In contrast to the step-growth polymerisation used to manufacture PET, polymers can also be synthesised in a chain-growth manner. Rather than bifunctional monomers, chain-growth polymerisations rely on the propagation of a highly reactive species, such as an anion, cation or radical, to extend polymer chains.³ This species is generated by an initiator, which then reacts with a monomer. Crucially, the reactive species is then transferred to the opposite end of the newly incorporated monomer, meaning that the chain end of the polymer retains the reactivity, and so can continue to propagate by sequential reaction with other monomers. The key contrast to step-growth polymerisations is that monomer can only react with propagating polymer chains, rather than with other monomers. Typically, the ratio of initiator: monomer is low, and so at any one time the number of propagating chains is also low. This means that chain-growth polymers tend to produce higher molecular weights at lower conversions when compared to step-growth polymers.³ An example of chain-growth polymerisation is the radical polymerisation of styrene (**Scheme 1.4**), where reaction of styrene leads to a radical species at the chain end, which can in turn react with more styrene.



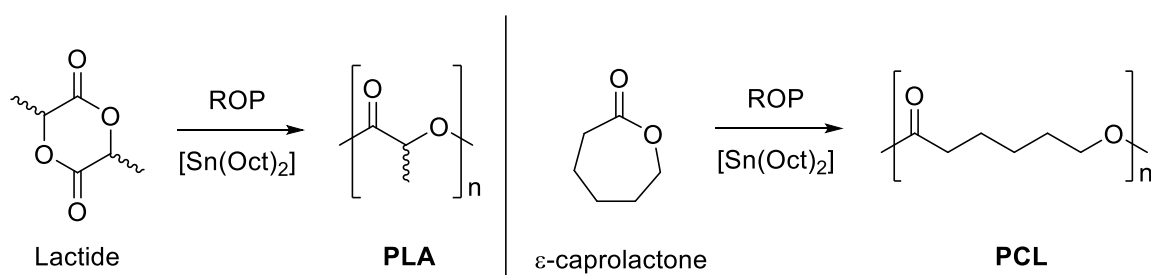
Scheme 1.4: An example chain-growth polymerisation, the radical polymerisation of styrene.³

In theory, chain-growth polymerisations can continue indefinitely if there is monomer remaining for the polymer chains to react with. However, reactive polymer chains may stop growing through chain termination reactions, such as the coupling of two radicals, or chain transfer reactions, where the reactive species become inactive, for example if an anionic species becomes protonated, in the process transferring the anion to another molecule.³ The relative rates of these reactions compared

to the rate of chain propagation is primarily what governs the molecular weight and molecular weight distributions of the product polymers. This contrasts with the largely statistical and probability based relationships for step-growth polymerisations.

Chain-growth polymerisations can be highly controlled if the rates of chain termination and chain transfer can be limited. If these reactions can be prevented entirely, and the rate of initiation is also significantly faster than propagation, then there will be a well-defined (according to the concentration of initiator) number of polymer chains all growing at a constant rate. In this case, the polymerisation is termed a living polymerisation, which are characterised by linear increases in M_n against conversion of monomer. This control is reflected in the polydispersity index, with values < 1.1 reflecting a narrow molecular weight distribution and hence excellent control of the molecular weight of the polymer.³ Although there is no strict boundary (in terms of PDI) between a living and non-living polymerisation, chain-growth polymerisations have the potential to produce far more monodisperse polymers than their step-growth alternatives, and are required to access some polymer architectures such as block copolymers.²⁶

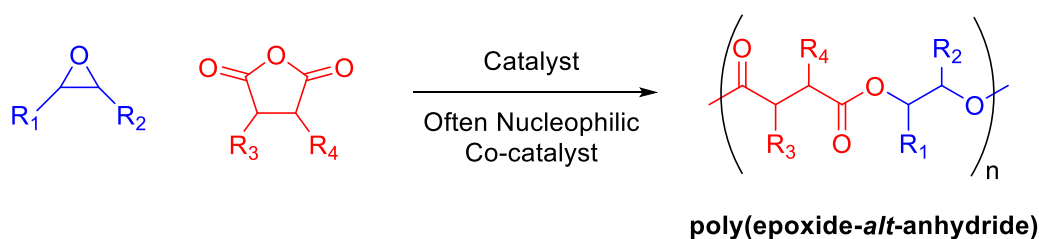
There have already been extensive efforts to produce chemically recyclable polyesters by chain-growth polymerisation. Chiefly among these is the ring-opening polymerisation (ROP) of cyclic esters, or lactones.²⁷ Both PCL and PLA can be synthesised by ROP (**Scheme 1.5**), most commonly using homogeneous metal catalysts such as $[\text{Sn}(\text{Oct})_2]$ (Oct = 2-ethylhexanoate).^{28,29} Although PLA presents some advantages over PET in that it is manufactured from a renewable monomer, far less than 1% of the global plastics market is currently occupied by PLA.⁴ PLA and PCL have many desirable attributes, yet there are only a relatively small number of readily synthetically accessible cyclic esters that can be polymerised by ROP.³⁰ This means that the resulting polymers are somewhat limited in terms of the material properties they can have, and so for many applications they have been unable to dislodge the incumbent petroleum-derived polymers like PET, PE and PP.



Scheme 1.5: ROP of lactide and ϵ -caprolactone with $[\text{Sn}(\text{Oct})_2]$ as a catalyst to give PLA and PCL respectively.^{28,29}

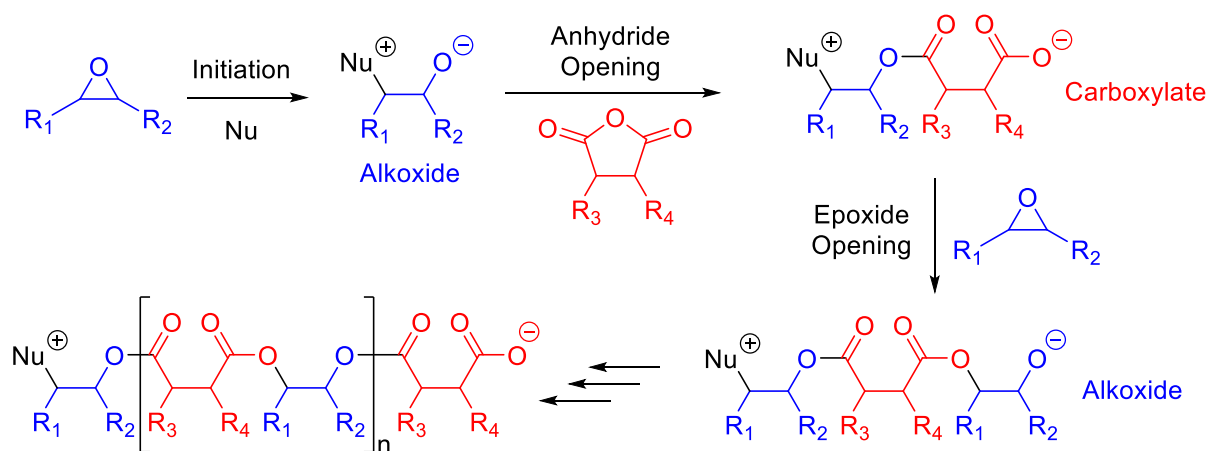
1.3: Ring-Opening Copolymerisation (ROCOP)

Given the limitations of lactone ROP, an alternative method for the chain-growth synthesis of a wider range of polyesters is an important objective. One method which shows promise is the ring-opening copolymerisation (ROCOP) of epoxides and cyclic anhydrides, a type of alternating anionic polymerisation. (**Scheme 1.6**).³¹ Throughout this work, the alternating structure of ROCOP-made polymers will be described as poly(epoxide-*alt*-anhydride).



Scheme 1.6: Top: ROCOP of generic epoxides and cyclic anhydrides, to give a polyester.

ROCOP is most often performed using a metal catalyst and nucleophilic co-catalyst, which can serve as an initiator.³¹ However, there are some catalyst systems which only require a single catalyst/initiator, whether that be a metal complex^{32,33} or organic nucleophile.³⁴ A simplified ROCOP mechanism is shown in **Scheme 1.7**, which details how initiation by a nucleophile (Nu) ring-opens an epoxide to give an alkoxide, before ring-opening of an anhydride gives an ester linkage and a carboxylate chain terminus.³¹ This continues until chain transfer or chain termination to give an alternating polyester. Although in this example a neutral nucleophile is used, Nu could be an ion-paired species, meaning the Nu-C unit would be neutral, and charge balance is achieved by association of the counter-cation to the chain terminus.³¹



Scheme 1.7: A simplified mechanism featuring alternating ring-opening of an epoxide to give an alkoxide and a cyclic anhydride to give a carboxylate.³¹ Note, if an ion-paired initiator is used, then Nu-C will be neutral and the counter-cation will be ion-paired to the anionic chain terminus.

One of the major advantages of ROCOP over ROP is the vast array of potential polyesters that can be synthesised simply by exchanging the monomers, potentially giving access to a far wider range of material properties. Furthermore, if either the epoxide or anhydride (or both) feature additional reactive functional groups such as alkenes or halides, then the polymer can be further altered through post-polymerisation modification. This again expands the potential material properties which can be achieved through ROCOP, whereas the lactones used for ROP rarely have such reactive groups present.³¹

When compared to the step-growth synthesis of PET, ROCOP has a 100% atom economy, meaning there are no by-products which must be removed from the reaction to produce high conversions, whilst its chain-growth nature also allows for narrower molecular weight distributions.³¹ As previously discussed, PET is synthesised from non-renewable petroleum derived monomers, yet for ROCOP, the broader scope of potential monomers means it is readily possible to introduce renewable bio-derived monomers. A selection of commonly used monomers in the ROCOP literature is detailed in **Figure 1.4**, with some bio-derived monomers indicated in green. This selection includes limonene oxide, α -pinene oxide and eugenyl glycidyl ether for the epoxides, and the Diels-Alder product of α -phellandrene and citraconic anhydride for the anhydrides.^{31,35} Synthesising Diels-Alder adducts using terpenes and maleic anhydride has also been investigated for producing partially renewably sourced anhydrides.³⁶

Perhaps the most commonly used anhydride in ROCOP is phthalic anhydride (PA), which is currently produced from petroleum sources, although it can be synthesised from bio-derived furfural *via* the Diels-Alder reaction of maleic anhydride and furan, before dehydration to PA.³⁷ Both maleic anhydride (MA) and its unsaturated derivative succinic anhydride (SA) both also fall into this category, in that they *can* be synthesised from renewable resources, but industrially are not currently. The monomer selection features a large range of structures, including aromaticity which may help increase the crystallinity of the resultant polyesters, as well as 5- or 6-membered anhydrides, with the extra methylene group in the latter conversely increasing the flexibility of polymer chains.³⁸ Also featured are tricyclic anhydrides, and monomers containing double bonds, which makes them amenable to post-polymerisation modification.³¹ This is by no means a complete list of monomers, and there are ongoing efforts in the field to synthesise new bio-derived monomers to help expand the scope of ROCOP.^{13,39}

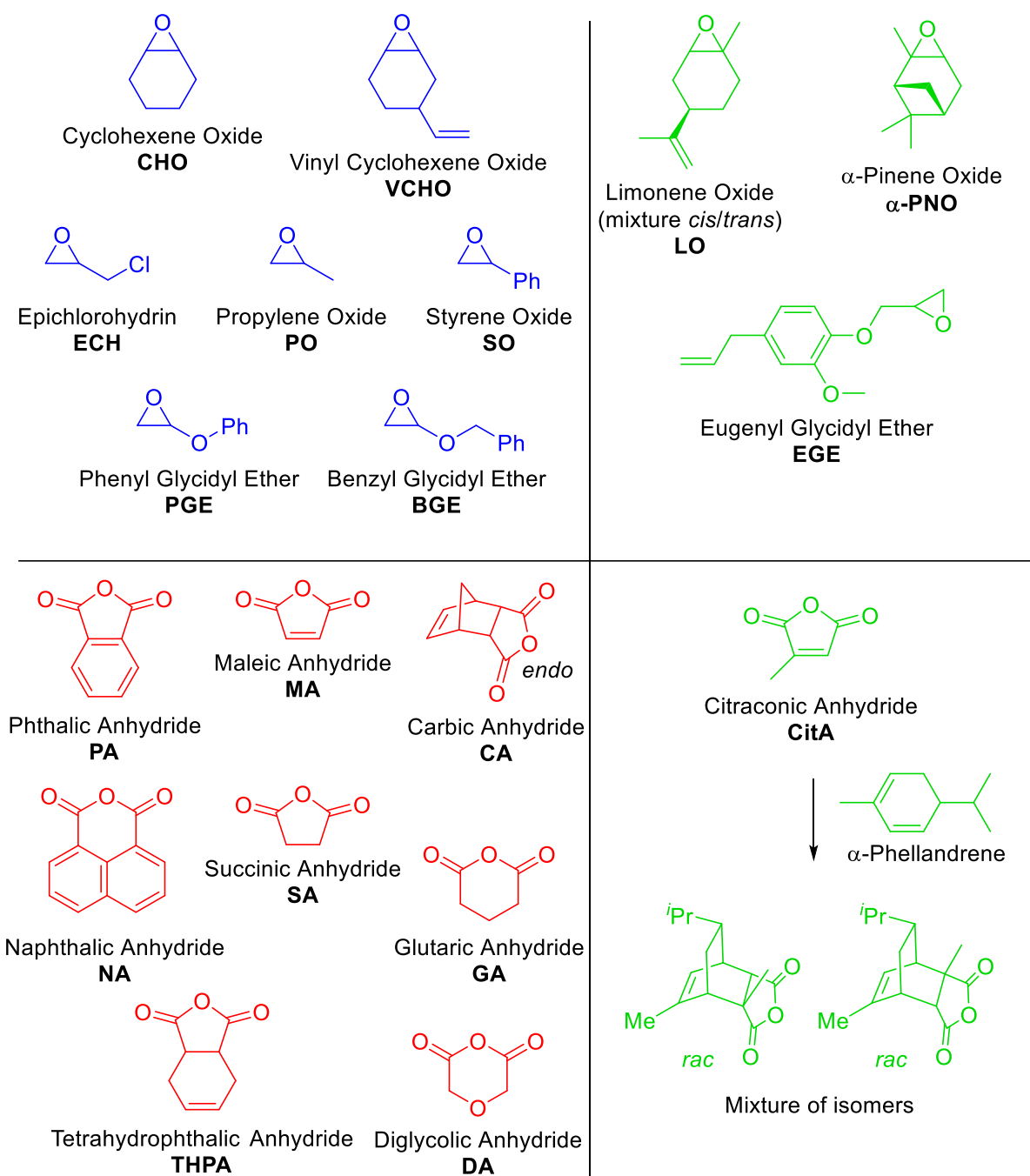


Figure 1.4: Non-exhaustive selection of monomers commonly used in ROCOP, with bio-derived monomers shown in green.^{31,35} A synthetic pathway to phthalic anhydride (PA), has also been reported from furfural, which proceeds *via* maleic anhydride, another anhydride on this list.³⁷ Carbic anhydride = *cis*-5-Norbornene-endo-2,3-dicarboxylic anhydride.

Many different metals have been investigated as catalysts for ROCOP, a selection of which will be discussed in section 1.4. This includes catalysts based upon Al,⁴⁰ Cr,⁴¹ Co,⁴² Fe,³⁶ Mg,³⁶ Mn,⁴³ Y,⁴⁴ Ti,⁴⁵ Zr,⁴⁶ Zn,⁴⁷ In,⁴⁸ Ga,⁴⁹ and Sn,⁵⁰ although there are far more examples than those referenced here. ROCOP is usually conducted in three ways: a) using excess neat epoxide as the only solvent, b) using a

stoichiometric ratio of epoxide to anhydride with additional solvent (typically but not exclusively toluene), or c) a smaller excess of epoxide with added solvent.³¹ In most cases, a nucleophilic co-catalyst (typically 0.9 to 2 equivalents to metal catalyst) is used to improve catalyst performance. A selection of co-catalysts are shown in **Figure 1.5**, which have the general function of initiating polymer chains, meaning the alkoxides and carboxylates which form as a result can coordinate to metal catalysts, facilitating further reaction. However, in the absence of metal catalysts, these nucleophiles are ROCOP catalysts in their own right, albeit at a generally far slower rate when compared to the catalyst/co-catalyst pair. This means that any discussion about catalytic activity must be carefully considered and compared to this “background” control reaction. Of the examples shown in **Figure 1.5**, DMAP and [PPN]Cl are by far the most widely used. It should also be noted that in many cases, a labile bond of a metal catalyst, such as a Metal-Cl or Metal-OAc can themselves be nucleophilic and initiate polymer chains bound to the metal centre.⁵¹

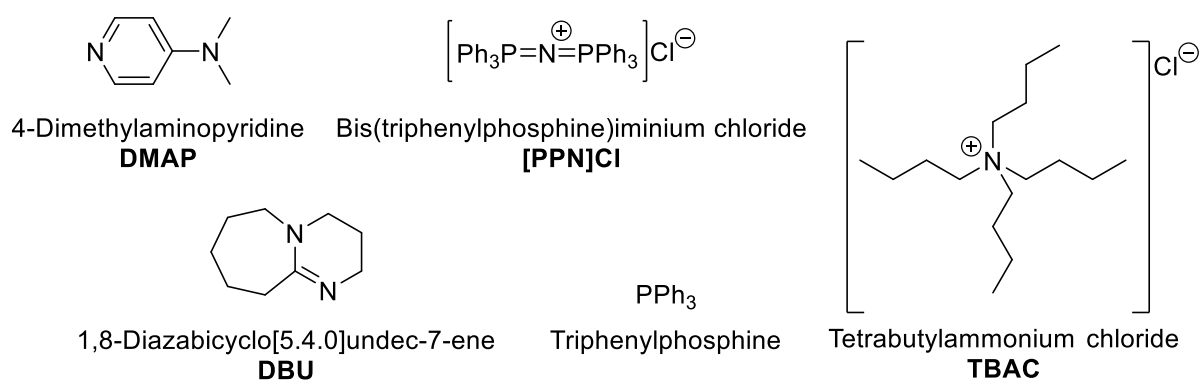
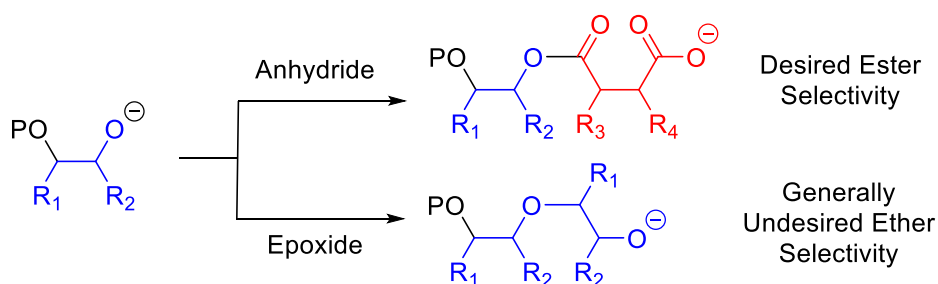


Figure 1.5: Selection of nucleophilic co-catalysts often used in ROCOP, with DMAP and [PPN]Cl being by far the most common.^{31,52}

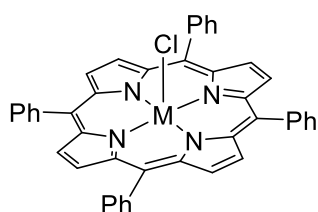
As well as increasing the rate of polymerisation by initiating polymer chains, co-catalysts generally increase the selectivity of the polymerisation.⁵¹ For ROCOP, the alternative selectivity is to the homopolymerisation of epoxide, to give generally unwanted polyether units (**Scheme 1.8**). These units do not feature the same chemically recyclable ester bonds, and can increase the flexibility of polymer chains and lower T_g (although naturally in some cases this will be desirable).⁴⁶



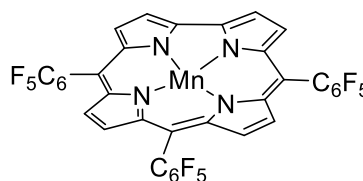
Scheme 1.8: Representation of ester *versus* ether selectivity, caused by the homopolymerisation of epoxide.

1.4: ROCOP: The Current Literature

The first report of a controlled epoxide anhydride ROCOP reaction was published in 1985 by Inoue and Aida, where phthalic anhydride (PA) and propylene oxide (PO) were successfully copolymerised using the aluminium porphyrin complex **1.1** (Figure 1.6).⁵³ This then led to the development of other porphyrin systems, namely the analogous chromium complex **1.2** reported by the Duchateau group in 2011, or the related Mn-corrole complex **1.3**.^{54,55} Both the Al and Cr complexes **1.1** and **1.2** do not selectively produce polyester without a co-catalyst, yet can still initiate polymer chains through reaction of the M-Cl bond.^{54,56} However, the use of Mn(II) in **1.3** means that there is no labile ligand which can initiate chains, meaning co-catalyst was required to see any reactivity whatsoever.⁵⁵



1.1: M = Al (Inoue 1985, Coates 2011)
1.2: M = Cr (Duchateau 2011)



1.3: Nozaki 2014

Figure 1.6: Series of porphyrin or corrole based complexes reported as catalysts for ROCOP, all of which required nucleophilic co-catalyst to achieve >50% ester selectivity. Also indicated is the year and lead author of the report.⁵³⁻⁵⁶

A key feature of complexes **1.1-1.3** is the planar ligand set, which means that once initiation at the M-Cl bond (for **1.1** and **1.2**) has occurred, there are two *trans* active sites for chains to propagate at. This theme has been continued with the use of the Salph (**1.4-1.6**) and Salcy (**1.7-1.9**) complexes shown in **Figure 1.7**, as first reported by the Duchateau and Coates groups respectively.^{52,54,56,57} These simple to synthesise and versatile ligands have proved popular catalysts since, and a significant proportion of the ROCOP literature is focussed on the three metals used here, in Al, Cr, and Co. For the Salph complexes **1.4-1.6**, the rate of polymerisation of cyclohexene oxide (CHO) and PA was slowest for Al and fastest for Cr.⁵² Furthermore, copolymerisations conducted using a 1:1 ratio of epoxide to anhydride produce polymer with a higher ester selectivity than copolymerisation performed with excess epoxide as solvent. This is because the rate of epoxide homopolymerisation will be greatly reduced when the concentration of epoxide in the reaction mixture is decreased, meaning ester linkages will be more abundant. Interestingly, the [Cr(Salcy)Cl] complex **1.7** has been reported to be perfectly ester selective for the copolymerisation of PO and maleic anhydride (MA) without the need of a co-catalyst.⁵⁶ This contrasts to findings where CHO and MA were copolymerised, where a co-catalyst was required for any conversion at all.⁵²

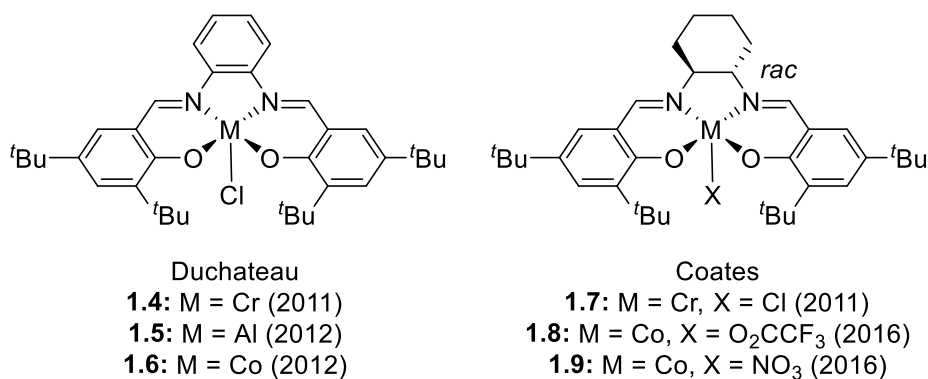
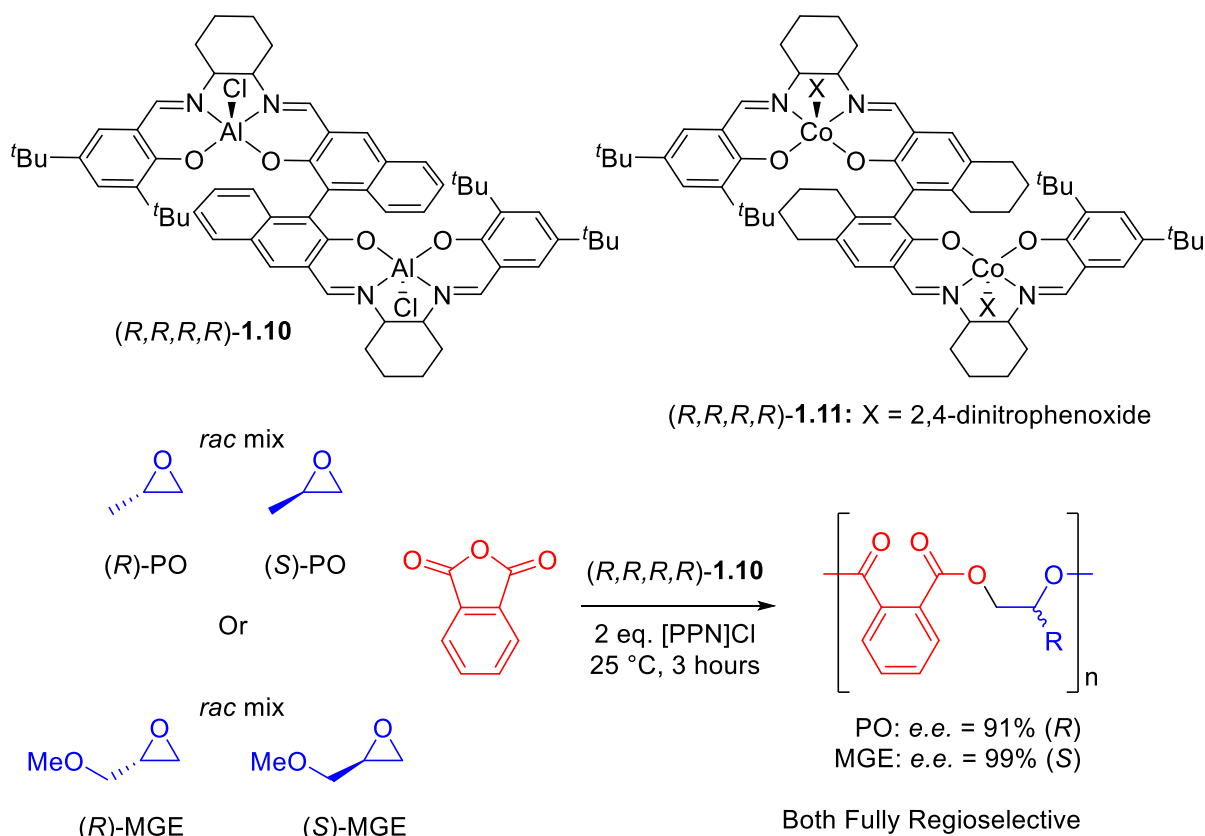


Figure 1.7: Commonly employed Salph and Salcy complexes, as reported by the Duchateau and Coates groups.^{52,54,56,57}

Furthermore, for the [Co(Salcy)X] complexes **1.8-1.9**, the use of non-chloride initiating groups of the metal led to hugely contrasting polymerisation behaviour, with **1.9** leading to double the amount of anhydride conversion than **1.8**, when each complex was used alongside a corresponding [PPN]X (X = O₂CCF₃ or NO₃) co-catalyst.⁵⁷ Clearly, this demonstrates that the overall polymerisation performance is sensitive not only to the ligand environment of the metal catalyst, but also to the initiating groups.

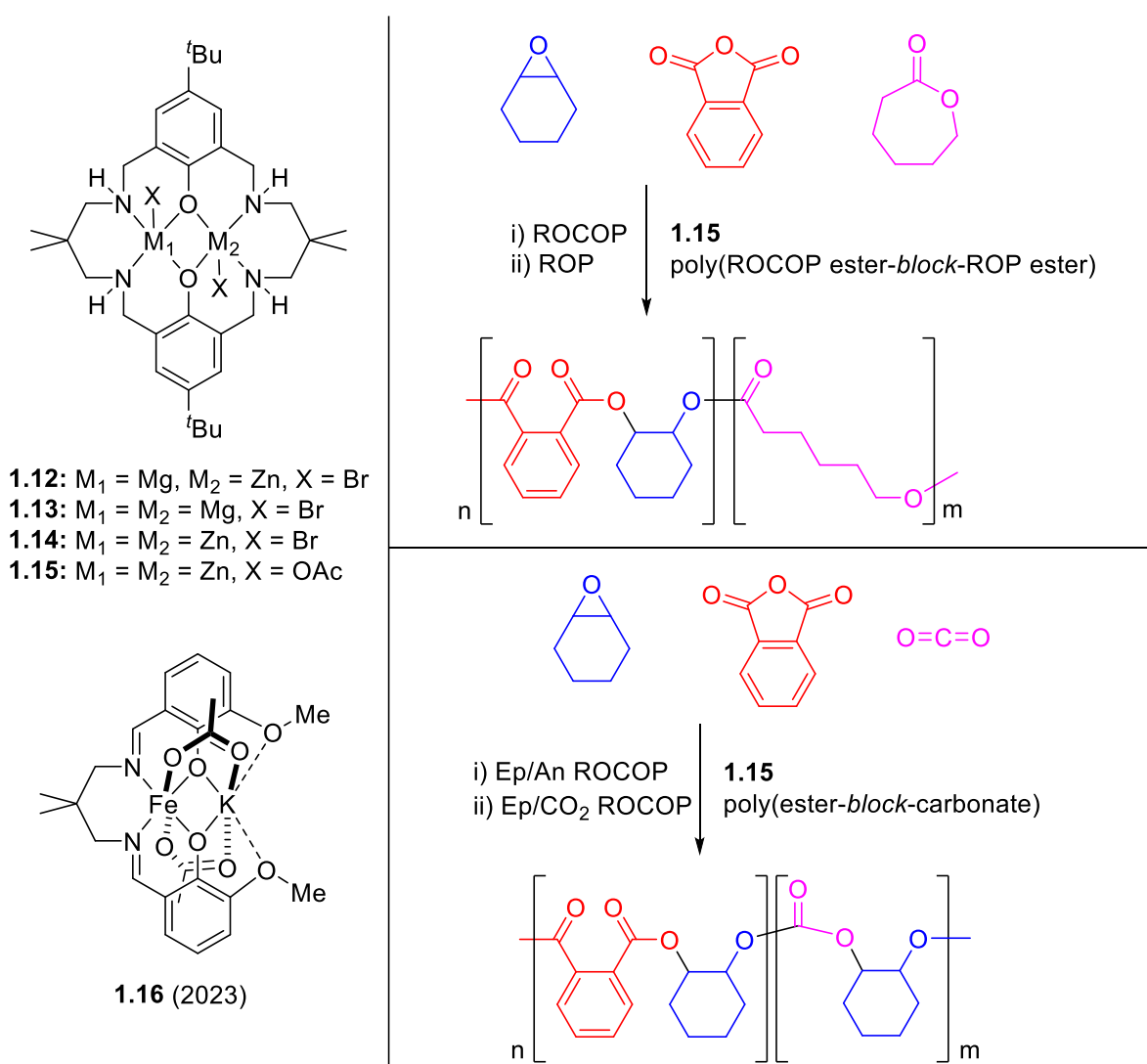
In an extreme example of above complexes featuring a planar ligand set (about the metal centre), a 2019 report by Lu and colleagues featured bimetallic Al (**1.10**) and Co (**1.11**) complexes, which could be synthesised in an enantiopure manner in an (*R,R,R,R*) configuration (**Scheme 1.9**).⁵⁸ These catalyst systems demonstrate two other forms of selectivity to consider in ROCOP on top of the chemoselectivity, namely regio- and enantio-selectivity. For the Al complex **1.10**, the copolymerisation of a racemic mixture of either PO or methyl glycidyl ether (MGE) with PA led in both cases to a highly regioselective ring-opening of the epoxide at their unhindered methylene carbons. This regioselectivity allowed the enantiomeric excess of the resulting polyester to be determined, with **1.10** preferentially reacting with (*R*)-PO and (*S*)-MGE with over 90% *e.e.* in both cases. Although the *e.e.* of the polymer could not be determined directly, the chemical degradation of the ester units using NaOH to diols before analysis by either chiral phase GC or using derivatised compounds in HPLC did allow the *e.e.* to be determined. Polymer enantioselectivity has profound implications for the behaviour of the polymer in the solid state, as crystallinity can be drastically increased and therefore dramatically alter the polymer's response to heat. Whilst **1.10** showed excellent enantioselectivity, the related Co complex **1.11** produced polyester with only a modest *e.e.* of 11%.⁵⁸



Scheme 1.9: Synthesis of enantiomerically enriched polyesters using the enantiopure Al complex **1.10**, as reported by Lu *et. al.*⁵⁸

Other examples of bimetallic ROCOP catalysts have been reported by the Williams group, where a macrocyclic tetrakis(amine)bis(phenoxy) ligand has been employed in conjunction with Zn and Mg (**Scheme 1.10**).⁵⁹ In this case, the authors found that the heterobimetallic complex **1.12**, which features one Zn and one Mg centre, was far more active than the homobimetallic complexes **1.13** and **1.14** in the copolymerisation of CHO and PA. These findings were attributed to the Zn centre being predominantly responsible for the binding the epoxide in close proximity to the magnesium centre, which features a more labile and therefore more nucleophilic Mg-carboxylate bond, with this carboxylate responsible for the ring-opening and chain propagation. Furthermore, in a follow up report in 2016 by Williams, Romain and co-workers, the bis(acetate) dizinc complex **1.15** was investigated for copolymerising mixtures of CHO, PA and ϵ -caprolactone, with this producing poly({CHO-*alt*-PA}-*block*-CL) copolymers.⁶⁰ Interestingly the ROCOP pathway occurs first, before ϵ -CL ROP occurs only once PA is largely consumed. A similar phenomenon was observed for copolymerisations of CHO, PA and CO₂, where epoxide/anhydride ROCOP was seen in preference to epoxide/CO₂ ROCOP to give a polycarbonate block. Again, the co-operativity between the two metal centres was a key feature of the DFT explored mechanism, which in both cases reinforced the

experimental observations that PA ring-opening is thermodynamically preferable to both ϵ -CL and CO₂ ring-opening. Research into this type of bimetallic ligand and has continued, with a recent example featuring a bis(imine)bis(phenoxy)bis(methyl ether) mixed Fe/K complex in **1.16** (Scheme 1.10).³³ Complex **1.16** showed much higher activities and selectivities when compared to using the equivalent complex with no K coordination, and also proved effective at copolymerising a number of tricyclic anhydrides.



Scheme 1.10: Selection of homo- and hetero-bimetallic catalysts reported by the Williams group (left).^{33,59} Also shown is the formation of block copolymers when mixtures of PA, CHO and either CO₂ or ϵ -CL are copolymerised, as reported by Romain, Williams and colleagues.⁶⁰

Although ligand sets with *trans* vacant sites are popular in ROCOP catalysis, they are not ubiquitous, with the Kleij group having developed the Al, Fe, Mn, Co and Cr tris(phenolate) complexes **1.17-1.21** (Figure 1.8).^{36,38,61} Both the Al and Fe complexes are effective at producing copolymers of limonene oxide (LO), a key bio-derived epoxide, and PA when used alongside one equivalent of [PPN]Cl as a co-

catalyst, with the Fe complex **1.17** proving to be significantly faster.³⁸ The semi-aromatic nature of poly(LO-*alt*-PA) leads to the development of interesting material properties, which were explored further using a series of other terpene derived epoxides, such as carene oxide (CNO) and menthene oxide (MNO). In another interesting finding, the molecular weight of the poly(LO-*alt*-PA) produced when only *cis*-LO was more than 50% higher than when a mixture of *cis*- and *trans*-LO was used, when THF was used as the solvent and **1.17** and [PPN]Cl were used as the catalyst/co-catalyst pair. However, for Cr-complex **1.19**, no external co-catalyst was required to give highly selective polyester, as de-coordination of the DMAP ligands would lead to both vacant sites for catalysis and an external nucleophile to initiate polymer chains.⁶¹ Conversely, however, the Mn and Co complexes **1.20-1.21** showed only trace levels of activity.

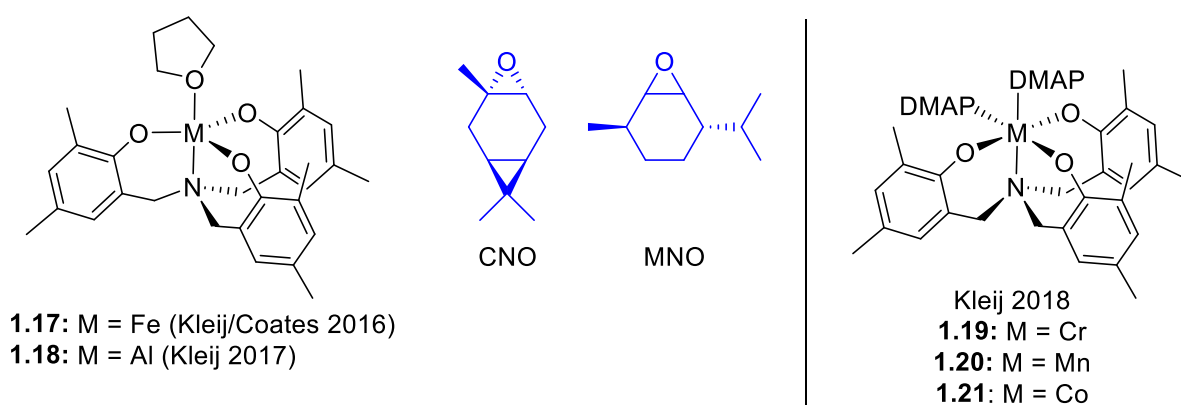
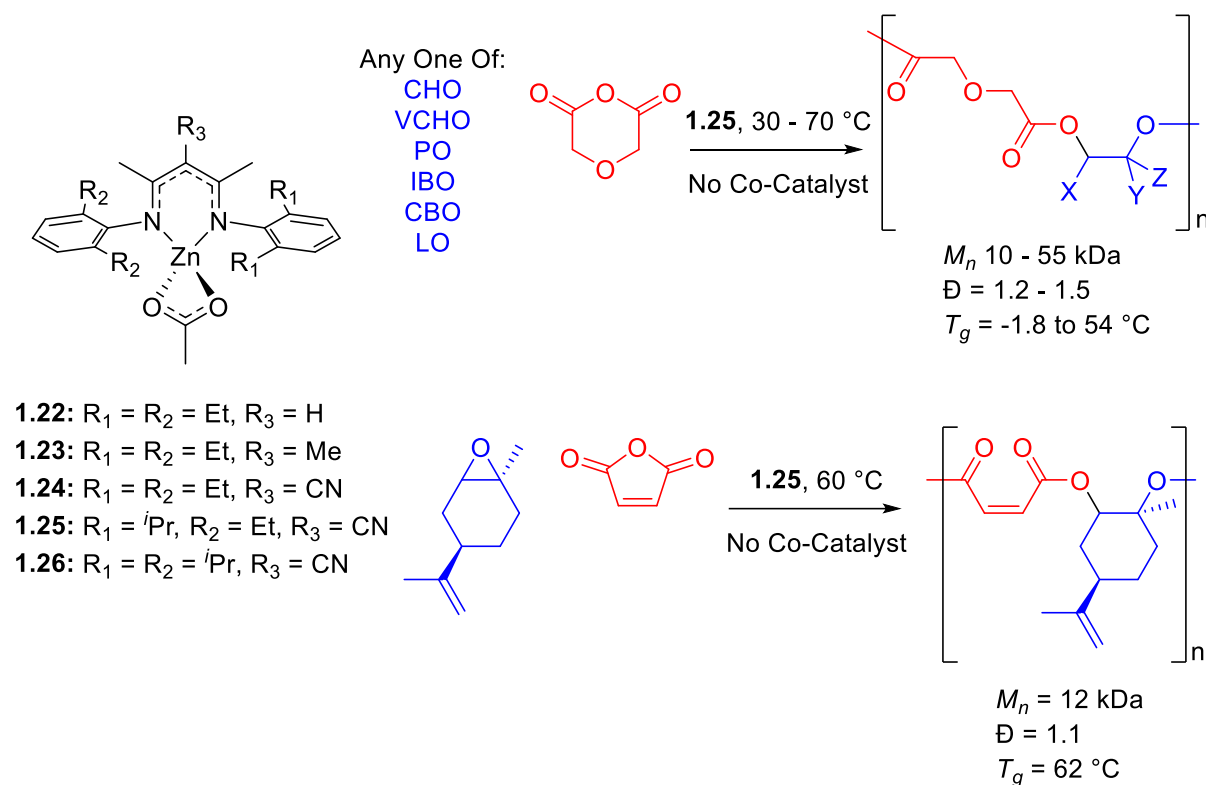


Figure 1.8: Series of tris(phenolate) ligands pioneered by the Kleij group used in Fe, Al, Cr, Mn and Co complexes, as well as the structure of two terpene based epoxides, carene oxide (CNO) and menthene oxide (MNO) which has been used to produce semi-aromatic polyesters with PA, with **1.17** as a catalyst.^{36,38,61}

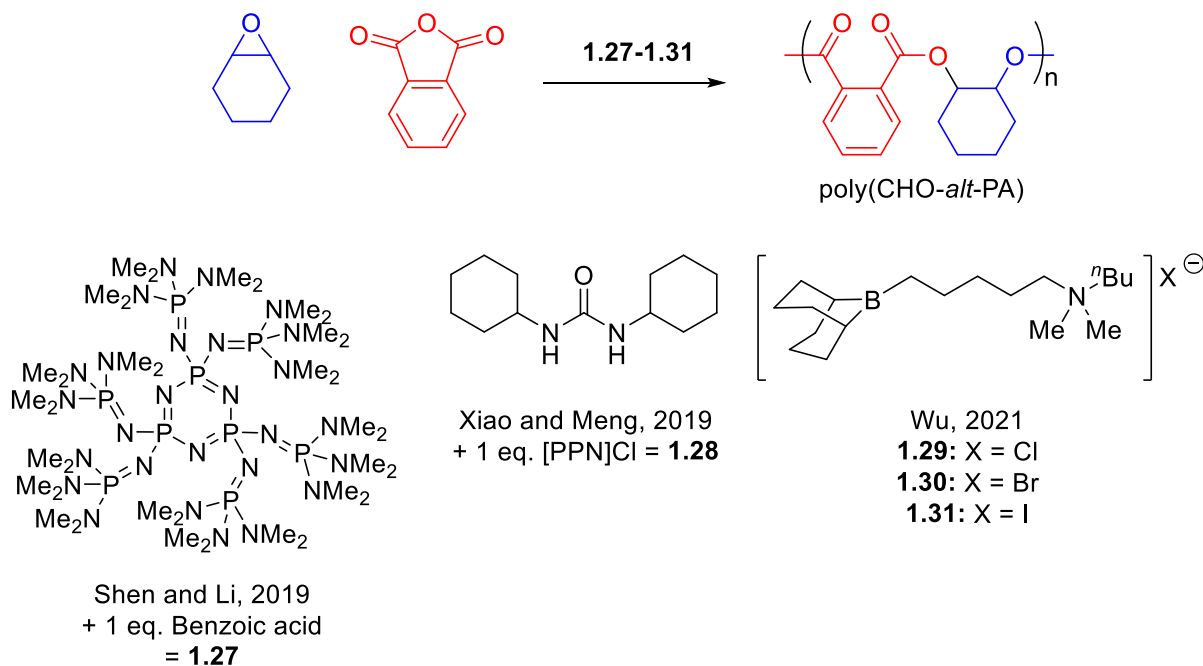
Another complex with known utility without additional co-catalysts is the [Zn(β -diiminate)(acetate)] complex **1.25**, which was reported by the Coates group in 2007 alongside a number of ligand analogues (**Scheme 1.11**).³² Interestingly, catalytic activity increased markedly when an electron withdrawing nitrile group was incorporated into the ligand backbone, with the protio and methyl substituted complexes **1.22** and **1.23** proving far less effective. Furthermore, the heterogeneity between the substituents on each flanking phenyl ring also proved advantageous compared to the fully ethyl substituted **1.24** and the fully *iso*-propyl substituted **1.26**. Complex **1.25** proved capable of copolymerising diglycolic anhydride (DGA) with several epoxides, including CHO, vinyl cyclohexene oxide (VCHO), PO, *iso*-butylene oxide (IBO) and *cis*-butene oxide (CBO). Although only mild reaction conditions were used, the rate of reaction is exceptionally high for reactions conducted in solution and with no additional co-catalyst present. Furthermore, *trans*-LO and maleic anhydride (MA) were successfully copolymerised under similarly mild conditions to give poly(LO-*alt*-MA) with a narrow

polydispersity and (in the context of other reports of LO copolymerisation) a competitive molecular weight of 12 kDa, with poly(LO-*alt*-DGA) even exceeding this at 36 kDa. Although it was a less effective epoxide/anhydride ROCOP catalyst, the ethyl substituted complex **1.24** shows excellent activity and control in the ROCOP of epoxides and CO₂ to give poly(limonene carbonate).⁶²



Scheme 1.11: [Zn(β -diimine)(acetate)] complexes reported as catalysts for ROCOP, including for the synthesis of poly(LO-*alt*-MA) with narrow polydispersity and competitive M_n . As reported by Jeske, DiCiccio and Coates.³²

A number of organocatalysts have also been reported for ROCOP, with a selection of notable examples shown for the copolymerisation of CHO and PA in **Scheme 1.12**. This includes the phosphazene derived **1.27**, as well as the urea **1.28** which was used alongside [PPN]Cl as a co-catalyst, with both producing modest molecular weights of highly ester selective poly(CHO-*alt*-PA).^{63,64} The organoboranes **1.29-1.31** have also been used for high temperature (up to 180 °C) ROCOP for CHO and PA, with the chloride compound **1.29** proving particularly effective, yielding M_n values approaching 100 kDa whilst retaining narrow PDIs of around 1.2.⁶⁵ In this report, catalyst loading was decreased to extremely low levels (1:20,000:10,000 ratio of **1.29**:CHO:PA), whilst a copolymerisation conducted at a 1:1000:1000 ratio of **1.29**:CHO:PA produced poly(CHO-*alt*-PA) of 95 kDa with a catalytic efficiency of over 7000 g of polymer per g of catalyst, with this exceeding the productivity of all of the previously discussed metal-based catalysts, albeit at a far elevated temperature of 150 °C.



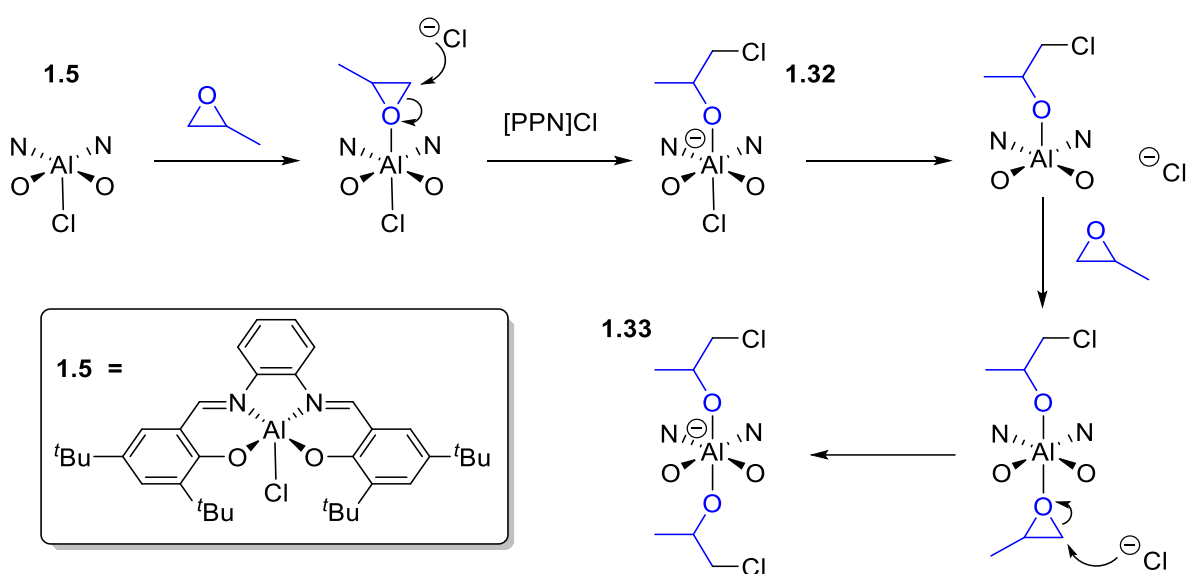
Scheme 1.12: Organocatalysts reported for the ROCOP of CHO and PA, with lead author(s) and year of publication indicated.^{63–65}

Although the examples discussed above are by no means exhaustive, they feature some of the key examples across the entirety of ROCOP catalysis. In chapters 2 and 3 where aluminium and the Group 4 metals are considered as catalysts, then further examples relevant to those metals will be discussed further.

1.5: ROCOP: Mechanistic Considerations

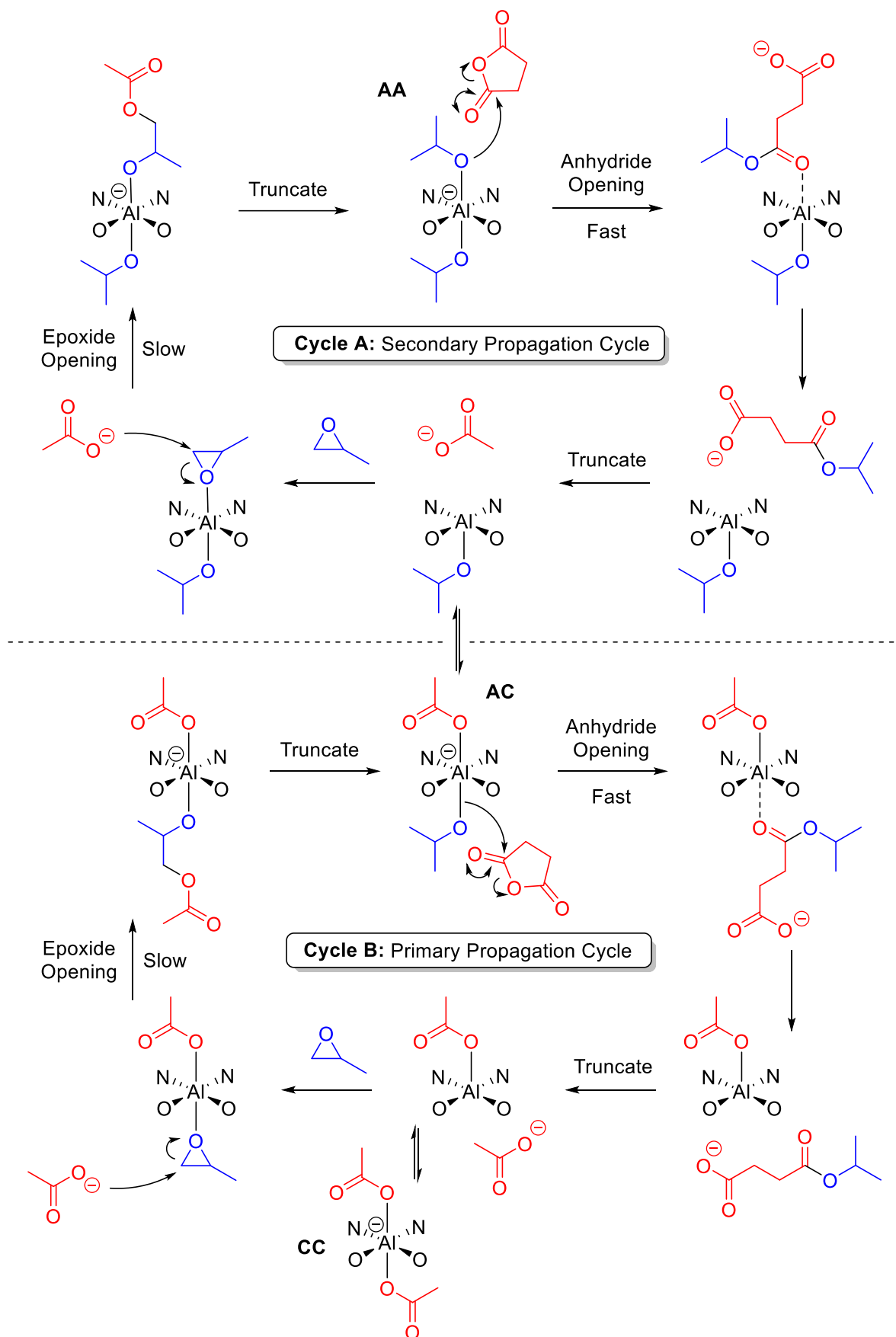
As with all polymerisation catalysis, and indeed catalysis more generally, mechanistic discussion often begins with understanding how a reaction works and the molecular level, with a view to using this knowledge to iteratively improve reaction efficiency, and ROCOP is no exception to this. In the context of ROCOP, the broad term “initiation” can be considered in both a catalytic and polymerisation context. For the former, this entails understanding how the (more properly titled) pre-catalyst reacts to become a catalytically active, on-cycle species, whilst in the latter sense, initiation reflects the first step in the growing of nascent polymer chains prior to propagation steps which reflect the bulk of the catalysis. As for metal pre-catalyst initiation, a general pathway to initiation features the ring-opening of an epoxide at the pre-catalyst, with the nucleophile in this case being from the co-catalyst, from insertion into a metal-X bond (usually labile “X” type ligands such as chloride, bromide, or acetate), or from a combination of the two. This concept has been studied in detail by the Cramer, Coates, Tolman

and colleagues for the [Al(Salph)Cl] pre-catalyst **1.5** in its reaction with propylene oxide (PO) and [PPN]Cl co-catalyst, whereby initial PO opening by an external, co-catalyst derived chloride produces the anionic mono(alkoxide), mono(chloride) complex **1.32** (**Scheme 1.13**).⁵¹ Complex **1.32** then undergoes another PO ring-opening using chloride which has de-coordinated from the pre-catalyst to give the bis(alkoxide) complex **1.33** (**Scheme 1.13**). Interestingly, reaction of **1.5** with PO in the absence of [PPN]Cl also leads to mono(alkoxide) formation, yet an additional source of nucleophiles in [PPN]Cl is needed to access the bis(alkoxide) complex, highlighting the important role of the co-catalyst. Analogous experiments with butylene oxide also showed this initiation occurred with high (97:3) regioselectivity with ring-opening occurring at the least hindered carbon of butylene oxide (this regiochemical outcome is also shown for PO in **Scheme 1.13**).



Scheme 1.13: Initiation pathway of [Al(Salph)Cl] complex **1.5** in the presence of PO and one equivalent of [PPN]Cl. PPN⁺ cations are omitted. As investigated by Cramer, Coates and Tolman.⁵¹

The propagation mechanism was also studied by the same authors, who showed experimentally with **1.5** and computationally with a close analogue that there are two possible propagation cycles, both of which as shown in **Scheme 1.14**. In the first instance, **AA** (top-middle, read clockwise), a bis(alkoxide) complex as seen forming in the final step in initiation described previously, inserts into a non-coordinated anhydride (modelled theoretically as succinic anhydride), to form an ester linkage and produce a weakly coordinated polymer chain. De-coordination and truncation (for computational cost) then means there is an equilibrium between a neutral mono(alkoxide) complex and external anionic polymer chain (modelled as acetate), and an anionic (mono)alkoxide, mono(carboxylate complex) **AC**.



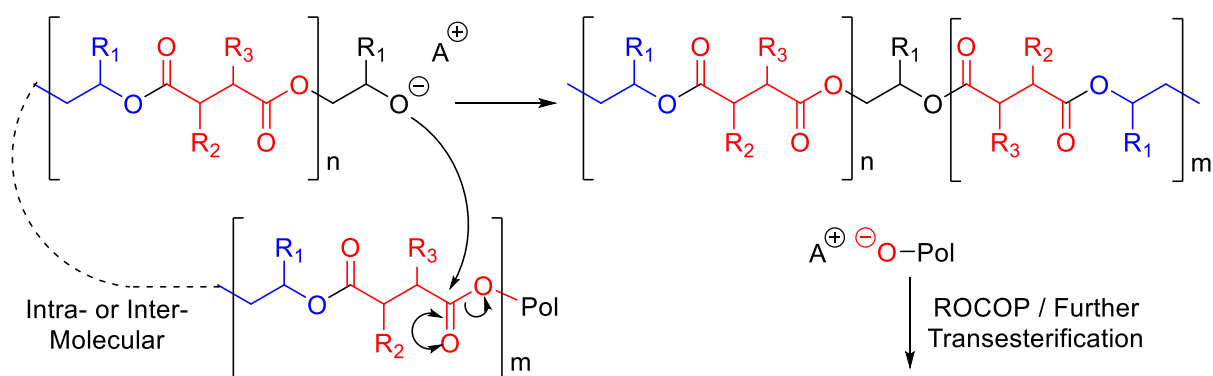
Scheme 1.14: Propagation cycle studied experimentally and theoretically by Cramer, Coates, Tolman and co-workers, using complex **1.5** (full ligands and [PPN]⁺ cations omitted for clarity). Computational studies were performed on an analogue of **1.5** with no ^tBu groups *para* to the phenoxide oxygens.⁵¹

From **AC** there is a choice of pathways; either a de-coordinated polymer chains ring-opens a newly bound epoxide (Cycle 1, top), or, the polymer chain remains bound to the aluminium centre and another molecule of anhydride is ring-opened (Cycle 2, bottom). In what is a general feature of ROCOP catalysis, anhydride opening is energetically far more favourable than epoxide opening, meaning Cycle 2 is preferred, and another ester linkage is produced. The product of this is another equilibrium, between a neutral mono(carboxylate) complex and de-coordinated anionic polymer chain (again modelled as acetate), and an anionic bis(carboxylate) complex **CC**. DFT calculations have shown that for this system, complex **CC** is favoured in the equilibrium by 10.4 kcal mol⁻¹, yet for the cycle to continue, one of the carboxylate-terminated polymer chains must de-coordinate to allow a new molecule of epoxide to coordinate and be ring-opened, which reforms **AC** at the interface of both cycles.

Whilst the DFT calculations showed epoxide opening to be the highest energy barrier in the cycle (and thereby rate-limiting), this was corroborated experimentally by performing ROCOP reactions in neat, excess epoxide as the solvent. In this case, the concentration of anhydride decreases throughout the reaction as it is consumed, yet epoxide concentration remains high and in excess. However, under these conditions, conversion of anhydride (a measure of rate of reaction) increases linearly with time. In other words, the decreasing concentration of anhydride has no effect on the rate of reaction. These *pseudo-zero-order* conditions are widely used in the literature, as it leads to significantly higher TOFs than when a stoichiometric ratio of epoxide and anhydride are used with a separate solvent, where a first order dependence of rate on epoxide concentration is seen. This helps to explain why Cycle 2 is energetically preferred, and only once anhydride is fully consumed and there is only epoxide left to react with, will Cycle 1 again be preferred, leading to the formation of **AA**.

Another interesting feature of this catalytic cycle is the dependence on the de-coordination of polymer chains to allow for subsequent reaction. The relative energetic favourability of the several coordination and de-coordination steps required in the catalysis will clearly be dependent on the lability of the metal centre, which for a main group element in aluminium would be expected to be facile. However, there have been few mechanistic investigations into other metals using the same ligand set, such as Co and Cr. This is particularly relevant for Cr and Co, with their low spin, M(III), d³ and d⁶ configurations respectively expected to be kinetically inert, and thereby perhaps not particularly amenable to this type of mechanism, despite the fact experimentally [Cr(Salph)Cl] complexes have shown faster rates of reaction than their Al congeners.⁵²

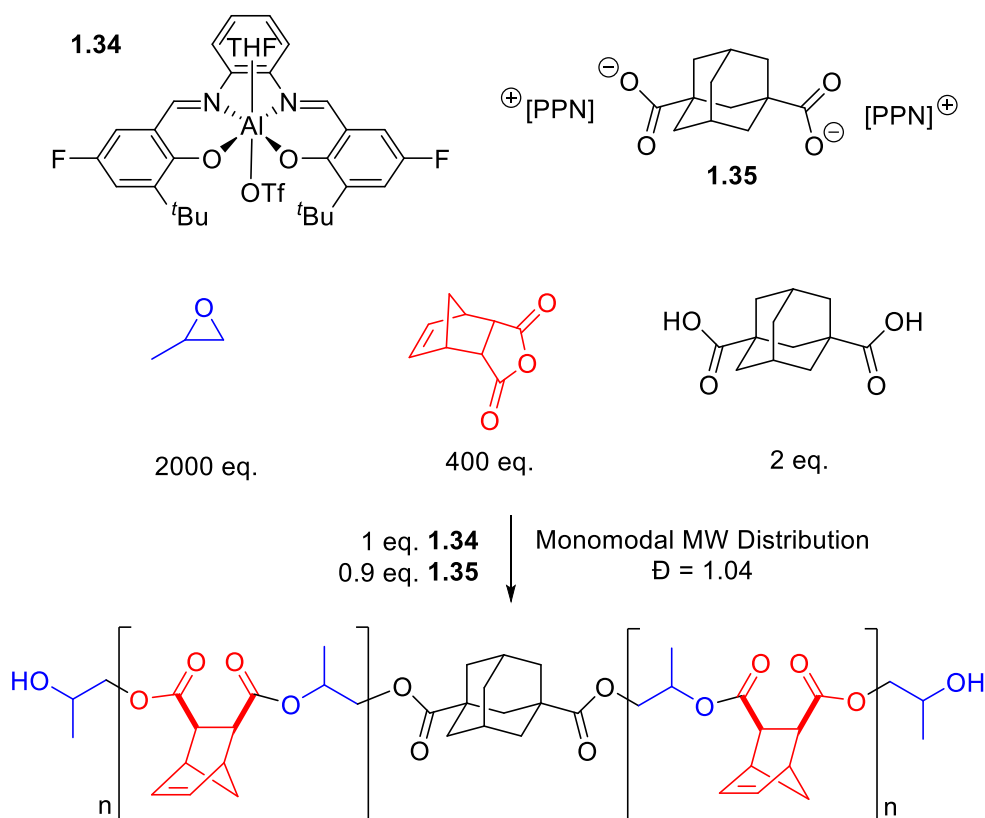
In addition to the desired ROCOP propagation steps, there is potential for additional side reactions to occur which can impact the polymers produced. The main example of this is transesterification (**Scheme 1.15**), where a nucleophile can attack an ester linkage within a polymer chain, producing a new nucleophile and ester.⁶⁶ Although transesterification is an example of a chain transfer, rather than chain termination reaction, it can significantly broaden molecular weight distributions, modify polymer end groups and scramble head-head, head-tail or tail-tail linkages, all of which can have a deleterious effect on the resultant material properties of the polymer.⁶⁶ In the context of ROCOP, metal-alkoxides or [PPN]-alkoxides are nucleophiles capable of inducing transesterification, and represent the cation A in **Scheme 1.15**. When considering this in the context of the ROCOP catalytic cycle seen previously, Cycle A leads to the formation of a bis(alkoxide) **AA**, which is associated with additional transesterification and epimerisation reactions occurring at the end of the reaction once anhydride is consumed. Transesterification can occur either intermolecularly or intramolecularly, the latter of which leads to the formation of cyclic polymers.



Scheme 1.15: Transesterification reaction at a generic ROCOP-made polyester, producing a new alkoxide species able to propagate, and an ester with a head-head linkage of anhydrides. A⁺ = counter-cation either from a metal complex or from a co-catalyst like [PPN]⁺.⁶⁶

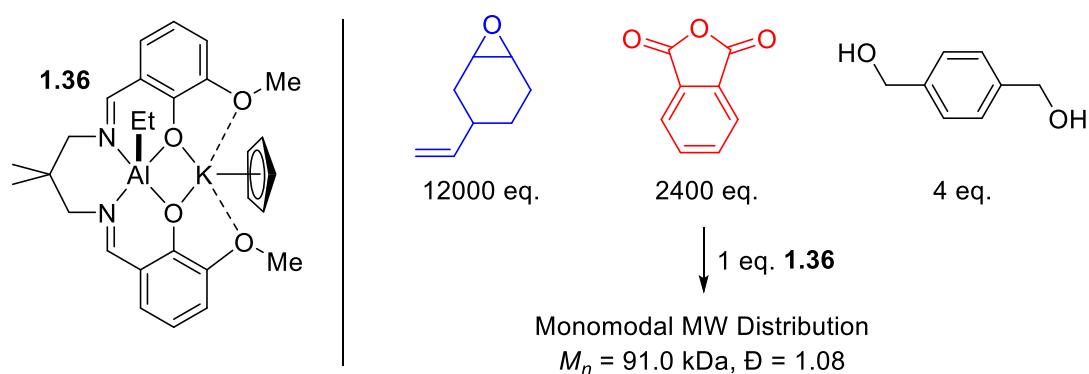
Another common feature of ROCOP polyesters is a bimodal molecular weight distribution, in that within the polyester produced there are two distinct molecular weight ranges, rather than a single broad distribution. This is generally attributed to the presence of hydrolysed impurities in the monomer feedstock, such as diols or diacids, which can initiate polymer chains in two directions, leading to there being a majority of the polymer at one molecular weight, with a smaller proportion of polymer having a molecular weight approximately double that.⁶⁷ Not only does this bimodality broaden the molecular weight distribution, but it limits the ability to synthesise well-defined block copolymers. Even when highly rigorous purification techniques are used on the monomers this bimodality is observed, and so separate efforts have been made to try to limit bimodality. One such method is through the deliberate addition of protic chain transfer agents (CTAs) such as diols, where

usually about 2-10 equivalents are added (with respect to pre-catalyst). This contrasts to the trace presence of CTAs in the monomer feedstock, with the key difference being that the extra source of protons means that when the polymer chain reacts, the resultant alkoxide or carboxylate will become protonated, and thereby inactive. Naturally, this protonation will be reversible, and so at any one time the reverse deprotonation yields an on-cycle species, which quickly reacts. This shuttling between inactive and active forms has been termed “reversible-deactivation anionic ROCOP”, and is somewhat analogous to radical polymerisations performed by RAFT.⁶⁷ This is also often termed as an “immortal polymerisation”, with a key example of this shown in **Scheme 1.16**, where Coates and co-workers used the non-initiating triflate complex **1.34**, an adamantane-derived bis([PPN]) salt **1.35** as the co-catalyst, and a series of diols and diacids, with a diacid based on the adamantane framework giving optimum results.⁶⁷ In this case, addition of two equivalents of CTA led to a polydispersity as low as 1.04, with this having the desired monomodal distribution. Another advantage of this method is the excellent control of end groups, as the dormant protonated chains are not nucleophilic enough for transesterification reactions, and so this method lends itself to the sequential additional of further monomer to synthesise block copolymers.



Scheme 1.16: Reversible-deactivation anionic ROCOP, as described by Coates *et. al.*, through use of a non-initiating aluminium pre-catalyst, and bis([PPN]) salt as a co-catalyst, and two equivalents of CTA to produce extremely narrow monomodal molecular weight distributions.⁶⁷

Similarly, the Williams group have reported another non-initiating aluminium complex in **1.36**, where in this case an organometallic ethyl group is used in combination with a $K-(\eta^5-C_5H_5^-)$ unit in a bimetallic complex, alongside a diol CTA (**Scheme 1.17**).⁶⁸ Not only were extremely narrow molecular weight distributions obtained, but the control of end groups allowed for block copolymer synthesis using ϵ -decalactone as an additional monomer in subsequent ROP catalysis. Furthermore, molecular weights of poly(VCHO-*alt*-PA) approaching 100 kDa could also be achieved, with this increased molecular weight polyester showing significantly improved material properties compared to its lower molecular weight forms.



Scheme 1.17: Example of a non-initiating Al/K complex **1.36** used in combination with a diol CTA agent to give high molecular weight and low polydispersity poly(VCHO-*alt*-PA). As reported by Diment and Williams.⁶⁸

Despite the popularity of epoxide-anhydride ROCOP, alternative substrates have been reported which operate under similar conditions, such as the shift from a 3-membered cyclic ether in an epoxide to a 4-membered cyclic ether in oxetanes,^{69–71} or a 5-membered ring in THF or methyl-THF.⁴⁶ In more radical departures, epoxides and anhydrides can be replaced by episulfides⁷² and thioanhydrides⁷³ respectively, or the anhydride can be replaced by phenyl isocyanate in a copolymerisation with cyclohexene oxide as a method of synthesising poly(urethanes).⁷⁴ All of these modifications are in addition to the widely studied ROP of lactones, ROCOP of epoxides and CO_2 to give poly(carbonates), and the ROP of epoxides to give poly(ethers), all which can (but not necessarily in all cases) operate in a form of anionic ring-opening polymerisation.

1.6.1: Characterisation and Analysis of Polymers

In this section, the key properties of polymers, and the way in which they will be measured throughout this work will be discussed, including methods to determine their molecular weight such as Gel Permeation Chromatography (GPC), Diffusion Ordered (NMR) Spectroscopy (DOSY) and Matrix Assisted Laser Desorption Ionisation Time of Flight (MALDI-ToF) mass spectrometry, which can also help identify polymer end groups. These techniques will be used alongside more general analytical techniques used throughout chemistry which can also be applied to polymers, such as conventional NMR experiments, FT-IR and UV-Vis, but these will not be discussed here. The ways in which polymers respond to heat, and how this differs from small molecules will also be discussed, alongside Differential Scanning Calorimetry, a technique used to ascertain the glass transition temperature (T_g) of amorphous polymers.

1.6.2: Gel Permeation Chromatography (GPC)

Like other chromatographic techniques, Gel Permeation Chromatography (GPC, also known as Size-Exclusion Chromatography, SEC) involves the separation of components dissolved in a mobile phase through interaction with a stationary phase. What separates GPC from similar techniques (from an apparatus perspective) like HPLC is that the separation is based on the hydrodynamic volume, or size of a polymer, rather than intermolecular interactions with a stationary phase.³ The stationary phase used in GPC is typically a swollen, cross-linked polymer gel (often poly(styrene-divinylbenzene)) packed into a column, with this producing a porous structure containing a range of pore sizes.⁷⁵ This size range is crucial, as the size of any one pore determines what size of polymer can enter: large polymers will only be able to enter a very small number of pores across the column, whereas small polymers will be able to enter a much higher proportion of pores.³ As polymers enter and leave pores and travel through the column, those that enter more pores will travel further and take longer to elute. Therefore, polymers of large size elute quickly in GPC experiments, with small polymers having longer retention times. A concentration-sensitive detector such as a refractive index (RI) or UV detector is then required to produce a concentration of polymer *versus* retention time chromatogram. In terms of the mobile phase, THF, DMF, toluene and hexafluoro-2-propanol are often used for organic soluble samples, whilst aqueous phase GPC can be used for water soluble polymers such as poly(ethylene glycol).

So far, only size, rather than molecular weight has been measured, meaning calibration with well-defined molecular weight standards is required to correlate the former to the latter. In the simplest sense, measuring standards of the same polymer of different (known) molecular weights can yield a calibration. But, different polymers will fold differently in any one mobile phase (and thereby have different hydrodynamic volume even if they are the same molecular weight), and so the calibration would be limited to the specific polymer used in the calibration. To counter this, modern GPC systems are often fitted with multiple detectors to translate from a “conventional” calibration to a “universal” calibration. A universal calibration means only one set of standards (usually polystyrene) is required to obtain accurate molecular weights for a whole range of different polymers.⁷⁵ This is achieved by adding a viscometry detector (VS), which can measure the intrinsic viscosity (*i.e.* the contribution the polymer makes to the overall viscosity of the solution it is dissolved in, $[\eta]$) of the polymer solution, which is related to this molecular weight (M) *via* the Mark-Houwink equation:³

$$[\eta] = KM^a$$

Where K is a constant related to the specific polymer and solution and a represents interactions between solvent and solute ($a = 0.5$ for a theta solvent for example). Together, K and a are termed the Mark-Houwink parameters for a given polymer and solvent. These parameters are generally unknown, yet by extrapolating a double logarithmic plot of $[\eta]$ vs. M can be calculated for (in principle) any polymer sample.³ This can then be equated to the known Mark-Houwink parameters for the polymer used in the calibration, thereby providing a relation between the measured intrinsic viscosity of the sample and the known molecular weight of the calibrant. Therefore, it is possible to accurately determine molecular weight independent of the polymer used.

Light Scattering (LS) detectors are also often employed in modern GPC systems, which measure the Rayleigh scattering at multiple angles, and is an absolute method, meaning no column calibration is necessary.⁷⁵ Together with the RI detector, VS and LS can be combined in so-called “triple detection analysis”; the RI detector measures concentration, the VS detector measures size and conformational data, whilst the LS detector provides further molecular weight information.⁷⁵ Together, they represent a powerful tool in the analysis of novel polymers where well-defined polymer standards are not available. In terms of the specific analysis in this work, all GPC experiments were performed in THF using Agilent PL-Gel columns against a universal calibration using polystyrene standards and use triple detection wherever possible.

1.6.3: MALDI-ToF Mass Spectrometry

Mass spectrometry is a well-established method to determine the molecular mass (more properly m/z) of molecules within a sample. Matrix Assisted Laser Desorption Ionisation Time of Flight (MALDI-ToF) mass spectrometry is a technique pioneered for use on macromolecules like polymers and proteins which retains the broader principles of mass spectrometry, in that ions are accelerated and reflected towards a detector, which is calibrated to determine mass the charge ratio (m/z), which for singly charge ions simply equals the (monoisotopic) mass. The main difference with MALDI-ToF is the method of sample preparation and ionisation: the polymer solution is mixed with a separate solution of matrix, a small organic molecule which is usually conjugated to efficiently absorb laser light (λ typically 337 nm), as well as an ion source, often NaOAc or F_3CCO_2Na .³ This solution is then “spotted” on a metal plate, before evaporation leading to matrix crystallisation, and in the process the separation of polymer chains from each other, and its encirclement by matrix molecules. A selection of these matrices is shown in **Figure 1.9**, with trans-2-[3-(4-tert-Butylphenyl)-2-methyl-2-propenyldene]malononitrile, **DCTB**, being used throughout this work.

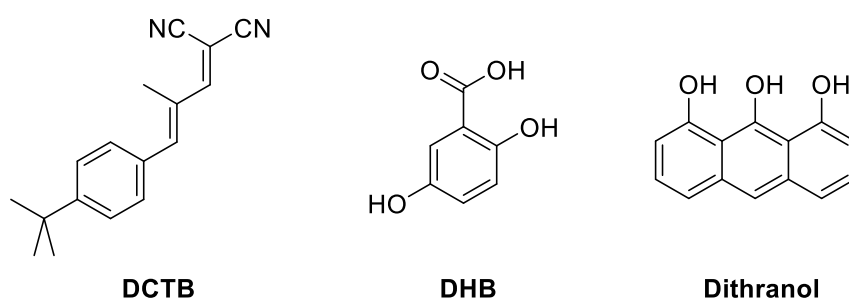


Figure 1.9: Selection of some commonly employed MALDI matrices, including DCTB, that will be used throughout this work.³

Once the sample spot is dry, under a high vacuum a laser will irradiate the sample, with the large amounts of energy absorbed by the matrix leading to vaporisation of the sample, including polymer and ion source. This combination alongside the residual energy from the laser light helps to ionise the polymers, which are then analysed through a conventional time-of-flight mass spectrometer. Generally, singly charged ions will result, meaning a MALDI-ToF mass spectrum will show the exact masses of each polymer chain. In contrast to small molecules with well-defined masses, a polymer sample will contain a range of different molecular weights, and therefore peaks in the mass spectrum. These peaks will be separated by the repeat unit of the polymer in question, meaning the chemical identity of the polymer can be determined (unlike in GPC). More succinctly, by knowing the exact mass of any one polymer chain, the identity of its end groups can be found by subtracting the mass of the repeat unit n times (where n is the degree of polymerisation) to give a residual mass corresponding to

the end groups (as well as any ionic adduct from the ion source). MALDI-ToF can be conducted in both positive and negative mode.

Although a MALDI-ToF spectrum gives quantitative m/z values, the M_n of the entire sample cannot be determined accurately as what peaks appear in the spectrum is dependant not only on their relative abundance in the sample but also to what extent they are successfully vaporised and ionised. This ability can depend on the molecular weight of the polymer chain, and so the MALDI-ToF spectrum may not quantitatively represent the entire composition of the sample, with higher molecular weight peaks being particularly susceptible to broadening, poor resolution and limited ionisation.³ Despite this limitation, MALDI-ToF is a crucial tool in the characterisation of novel polymers, with the ability to identify end groups particularly pertinent to mechanistic studies.

1.6.4: Diffusion Ordered (NMR) Spectroscopy (DOSY)

Diffusion Ordered Spectroscopy is a 2D NMR technique where the chemical shift of individual resonances (typically ^1H) can be correlated to diffusion coefficient, a measure of the speed at which a molecule diffuses in a solution. This diffusion coefficient is related to hydrodynamic volume, and can therefore be calibrated to determine molecular weight.⁷⁶ DOSY works by applying two pulses to the sample which can align and then re-align the direction of the magnetisation of molecules in the sample. The first pulse produces a corkscrew pattern of magnetisation, whilst the second aims to align all the magnetisation parallel to each other. However, in the time delay between the two pulses, molecules will diffuse vertically, and so the magnetisation is somewhat scrambled. The more powerful the first pulse, the stronger the corkscrew effect will be, which transpires leads to faster scrambling of magnetisation by diffusion. By performing experiments multiple times at different pulse strengths and measuring the degree of magnetisation that can be recovered by the second pulse, the diffusion coefficient can be determined, as smaller molecules will diffuse faster and therefore less magnetisation will be recovered by the second pulse.

To translate to molecular weight, the logarithm of measured diffusion coefficient can be plotted against the logarithm of (known by using standards) molecular weight to yield a linear calibration. This calibration can be corrected for solvent viscosity, whilst in one study there was little difference in the calibration lines for poly(ethylene glycol) and poly(styrene), indicating the near universal like nature of the calibration.⁷⁷ Despite this utility, DOSY is still principally used not for molecular weight

determination, but to determine to what extent different resonances in the ^1H NMR spectrum of a polymer are within the same polymer chain. For example, in a block copolymer, the resonances of A and B in poly(A-*block*-B) will be distinct in a ^1H NMR spectrum, yet the same spectrum could be obtained by mixing two separate samples of poly(A) and poly(B). In this case, it would be difficult to tell from conventional ^1H NMR spectroscopy whether the sample was a block copolymer or a mixture of separate polymers. Therefore, DOSY experiments can obtain a diffusion coefficient for each resonance: if the diffusion coefficients for A and B differ, they will have different molecular size and therefore be separate polymers; whereas if the diffusion coefficients are identical, there is a high probability (unless the molecular weights happen to be identical) that both A and B are part of the same polymer chains, *i.e.* in a block copolymer. Therefore, DOSY is a powerful tool to determine whether multiple different monomers are incorporated into the same or different polymer chains, and it is within this context that DOSY will be used in this work.

1.6.5: Thermal Properties of Polymers and Differential Scanning Calorimetry (DSC)

Polymers are categorised into two main groups depending on their response to heat: thermoplastics and thermosets. Thermoplastics respond to heat in much the same way that small organic molecules do, in that they can be melted and solidified repeatedly, and this can be used to access different shapes each time, depending on the mould used.³ Contrastingly, when exposed to elevated temperatures, thermosets do not melt, but eventually degrade. This is because the polymer chains within thermosetting plastics are heavily cross-linked to one another, meaning that the movement of individual polymer chains is far more restricted than for thermoplastics. Cross-linking in thermosets generally features strong covalent bonds between adjacent polymer chains, whereas only weaker non-covalent interactions like van der Waals forces or hydrogen bonds must be overcome to induce the movement of chains past one another, and subsequently material flow, in thermoplastics.⁷⁸ This means thermosets can only be moulded into shape once, and are then permanent set, or cured.

When considering a polymer's response to heat, there are two key parameters which are often discussed, the melting temperature (T_m) and the glass transition temperature (T_g). For polymers which pack amorphyously in the solid state, the T_g is a kinetic, or second-order transition (as opposed to a first-order, thermodynamic transition such as the boiling point of an organic molecule, which has a specific ΔG , ΔH and ΔS associated with it), and is the temperature where a polymer changes from a rigid, brittle, glassy state below the T_g to a rubbery state where there is sufficient thermal energy for

polymer chains to move past one another above the T_g .^{3,79} The T_g is distinct from the melting temperature, T_m , which is observed for semi-crystalline or crystalline polymers, as there is no distinct enthalpy change by going from the glassy to rubbery state, unlike for the transition from solid to liquid. Above and below the T_g , the polymer chains are still arranged amorphously, and if a freeze-frame of a polymer above and below its T_g was taken there would be no discernible difference between the two. This contrasts to T_m , where there is a distinct transition from an ordered crystalline state to an amorphous state, with this transition associated with overcoming the material's lattice enthalpy.³ Polymers which pack amorphously in the solid state only exhibit a T_g , whilst fully crystalline polymers only exhibit a T_m . Semi-crystalline polymers, where there are both amorphous and crystalline regions present in the solid state, can exhibit both a T_g and a T_m .³ Somewhat confusingly, if amorphous thermoplastics are heated sufficiently above their T_g , the movement of polymer chains past one another can become so facile that the polymer will flow much like a liquid. This state is often referred to as a polymer melt, despite the fact the material itself does not have a distinct T_m .

As well as thermosets and thermoplastics, a third class of polymer, elastomers, are partially cross-linked polymers with a low glass transition temperature (T_g), generally well below its desired operating temperature.³ Elastomers show increased flexibility and reduced brittleness above their T_g , allowing them to bend rather than break. To add to this, the presence of cross-links induces elasticity as the cross-links allow elastomers to rebound to their original shape after stress is applied, with vulcanised rubber an archetypal example of this.

As for measuring the T_g of amorphous or semi-crystalline polymers, Differential Scanning Calorimetry (DSC) is a commonly used technique which relies on observing the difference in heat capacity above and below the T_g .³ In DSC, a small amount of solid sample is heated at a constant rate ($20\text{ }^\circ\text{C min}^{-1}$, for example) and the heat flow required to achieve this heating rate is measured and compared to a reference sample with known heat capacity. At the T_g there is a distinct jump in heat flow as there is an increase in heat capacity, meaning to maintain the constant heating rate a higher heat flow is required. T_g peaks are sometime termed endothermic for this reason, yet there is no enthalpy change associated with T_g . To obtain accurate results, multiple heating and cooling cycles are performed on the polymer before measurement on the third cycle, to ensure any hysteresis within the material is suppressed. DSC can also be used to observe thermodynamic transitions such as the T_m in semi-crystalline or crystalline polymers, and on cooling cycles can also observe the equivalent T_c , the crystallisation temperature.³

1.7: Summary

The ROCOP of epoxides and cyclic anhydrides is a versatile, atom economical and controllable way of synthesising a broad range of chemically recyclable polyesters. Furthermore, ROCOP does not feature some of the drawbacks associated with the step-growth synthesis of PET, including a reliance on petroleum-based monomers, energy intensive synthetic conditions, and characteristically broad molecular weight distributions. Throughout this work, the synthesis and material properties of ROCOP polyesters will be investigated, including the development of metal catalysts and their coordination chemistry, experimental and theoretical mechanistic investigations into both the initiation and propagation cycles of the polymerisation, and analysis of the resultant novel polymers. The following is a summary of the research undertaken in each of the following chapters:

Chapter 2: Features the synthesis and full characterisation of a series of novel aluminium complexes based on the “Salpy” ligand framework. These complexes will then be investigated for use as catalysts in ROCOP both experimentally and theoretically, and the bimodality of the molecular weight distributions produced will be deconvoluted.

Chapter 3: Features the catalytic screening of a series of Group 4 metallocene complexes as pre-catalysts for ROCOP, including the synthesis of partially bio-derived poly(LO-*alt*-PA) and its subsequent scale up to produce over 200 g of polymer. Again, the mechanism of action for the Group 4 complexes, which are underrepresented in the ROCOP literature, will be examined using a variety of approaches.

Chapter 4: Details the material properties of the poly(LO-*alt*-PA) made on a large scale in chapter 3, and its subsequent post-polymerisation modification by the thiol-ene click reaction. This modification also includes cross-linking, performed both post-polymerisation and *in situ*, and how it can influence a polymer's properties. Modification by phosphorylation will be performed to examine the effect of binding chemical functionality possessing flame retardant behaviour has on the resulting polymer,

Chapter 5: Details investigations into the doping of an epoxide containing a bipyridine-like unit into ROCOP reactions, meaning the resultant polymer is able to chelate metals. Metal-doped polymers of Ir, Ru, Cu, Fe and Zn will be synthesised and extensively characterised, including examination of the photophysical properties of the iridium polymer with a view to its use in electronic devices.

1.8: References for Chapter 1

- 1 C. Wang, Y. Liu, W. Q. Chen, B. Zhu, S. Qu and M. Xu, *J. Ind. Ecol.*, 2021, **25**, 1300–1317.
- 2 A. L. Merchan, T. Fischöder, J. Hee, M. S. Lehnertz, O. Osterthun, S. Pielsticker, J. Schleier, T. Tiso, L. M. Blank, J. Klankermayer, R. Kneer, P. Quicker, G. Walther and R. Palkovits, *Green Chem.*, 2022, **24**, 9428–9449.
- 3 S. Koltzenburg, M. Maskos and O. Nuyken, *Polymer Chemistry*, Springer, Berlin, English Ed., 2017.
- 4 J. C. Worch and A. P. Dove, *ACS Macro Lett.*, 2020, 1494–1506.
- 5 Z. O. G Schyns and M. P. Shaver, *Macromol. Rapid Commun.*, 2021, **42**, 2000415.
- 6 J. R. Jambeck, R. Geyer, C. Wilcox, T. R. Siegler, M. Perryman, A. Andrady, R. Narayan and K. L. Law, *Science (80-.)*, 2015, **347**, 768–771.
- 7 M. Suzuki, Y. Tachibana and K. Kasuya, *Polym. J.*, 2021, **53**, 47–66.
- 8 J. M. D. Souza, F. M. Windsor, D. Santillo and S. J. Ormerod, *Glob. Chang. Biol.*, 2020, **26**, 3846–3857.
- 9 C. I. Arias La Fuente, B. Chierigato Maniglia and C. Cecília Tadini, *Packag. Technol. Sci.*, 2023, **36**, 81–95.
- 10 M. Hong and E. Y. X. Chen, *Green Chem.*, 2017, **19**, 3692–3706.
- 11 G. K. Watson and N. Jones, *Water Res.*, 1977, **11**, 95–100.
- 12 F. De Falco, R. Avolio, M. E. Errico, E. Di Pace, M. Avella, M. Cocca and G. Gentile, *J. Hazard. Mater.*, 2021, **416**, 126231.
- 13 Y. Zhu, C. Romain and C. K. Williams, *Nature*, 2016, 540, 354–362.
- 14 G. Faraca and T. Astrup, *Waste Manag.*, 2019, **95**, 388–398.
- 15 Y. Wu, G. Z. Miller, J. Gearhart, K. Romanak, V. Lopez-Avila and M. Venier, *Environ. Sci. Technol. Lett.*, 2019, **6**, 14–20.
- 16 B. A. Abel, R. L. Snyder and G. W. Coates, *Science (80-.)*, 2021, **373**, 783–789.
- 17 M. Häußler, M. Eck, D. Rothauer and S. Mecking, *Nature*, 2021, **590**, 423–427.
- 18 A. Barredo, A. Asueta, I. Amundarian, J. Leivar, R. Miguel-Fernández, S. Arnaiz, E. Epelde, R.

- López-Fonseca and J. I. Gutiérrez-Ortiz, *J. Environ. Chem. Eng.*, 2023, **11**, 109823.
- 19 S. Kaiho, A. A. R. Hmayed, K. R. Delle Chiaie, J. C. Worch and A. P. Dove, *Macromolecules*, 2022, **55**, 10628–10639.
- 20 A. Khan, M. Naveed, Z. Aayanifard and M. Rabnawaz, *Resour. Conserv. Recycl.*, 2022, **187**, 106639.
- 21 E. Gubbels, T. Heitz, M. Yamamoto, V. Chilekar, S. Zarbakhsh, M. Gepraegs, H. Köpnick, M. Schmidt, W. Brüggling, J. Rüter and W. Kaminsky, in *Ullmann's Encyclopedia of Industrial Chemistry*, Wiley-VCH Verlag GmbH & Co. KGaA, Weinheim, Germany, 2018, pp. 1–30.
- 22 W. A. MacDonald, *Polym. Int.*, 2002, **51**, 923–930.
- 23 S. Harrisson, *Polym. Chem.*, 2018, **9**, 1366–1370.
- 24 M. R. Thomsett, J. C. Moore, A. Buchard, R. A. Stockman and S. M. Howdle, *Green Chem.*, 2019, **21**, 149–156.
- 25 I. Taniguchi, S. Yoshida, K. Hiraga, K. Mayamoto, Y. Kimura and K. Oda, *ACS Catal.*, 2019, **9**, 4089–4105.
- 26 C. Romain and C. K. Williams, *Angew. Chemie Int. Ed.*, 2014, **53**, 1607–1610.
- 27 M. D. Jones, L. Brady, P. McKeown, A. Buchard, P. M. Schäfer, L. H. Thomas, M. F. Mahon, T. J. Woodman and J. P. Lowe, *Chem. Sci.*, 2015, **6**, 5034–5039.
- 28 M. Labet and W. Thielemans, *Chem. Soc. Rev.*, 2009, **38**, 3484–3504.
- 29 E. Balla, V. Daniilidis, G. Karlioti, T. Kalamas, M. Stefanidou, N. D. Bikiarais, A. Vlachopoulos, I. Koumentakou and D. N. Bikiaris, *Polymers (Basel)*, 2021, **13**, 1822.
- 30 F. Della Monica and A. W. Kleij, *ACS Sustain. Chem. Eng.*, 2021, **12**, 17.
- 31 J. M. Longo, M. J. Sanford and G. W. Coates, *Chem. Rev.*, 2016, **116**, 15167–15197.
- 32 R. C. Jeske, A. M. DiCiccio and G. W. Coates, *J. Am. Chem. Soc.*, 2007, **129**, 11330–11331.
- 33 W. T. Diment, G. Rosetto, N. Ezaz-Nikpay, R. W. F. Kerr and C. K. Williams, *Green Chem.*, 2023, **25**, 2262–2267.
- 34 H.-Y. Ji, X.-L. Chen, B. Wang, L. Pan and Y.-S. Li, *Green Chem.*, 2018, **20**, 3963–3973.
- 35 B. Liu, J. Chen, N. Liu, H. Ding, X. Wu, B. Dai and I. Kim, *Green Chem.*, 2020, **22**, 5742–5750.

- 36 M. J. Sanford, L. Peña Carrodegua, N. J. Van Zee, A. W. Kleij and G. W. Coates, *Macromolecules*, 2016, **49**, 6394–6400.
- 37 E. Mahmoud, D. A. Watson and R. F. Lobo, *Green Chem.*, 2014, **16**, 167–175.
- 38 L. Peña Carrodegua, C. Martín and A. W. Kleij, *Macromolecules*, 2017, **50**, 5337–5345.
- 39 F. Della Monica and A. W. Kleij, *Polym. Chem.*, 2020, **11**, 5109–5127.
- 40 F. Isnard, F. Santulli, M. Cozzolino, M. Lamberti, C. Pellicchia and M. Mazzeo, *Catal. Sci. Technol.*, 2019, **9**, 3090–3098.
- 41 H. K. Ryu, J. Cha, N. Yu, E. Lee and K. sun Son, *Inorg. Chem. Commun.*, 2020, **122**, 108278.
- 42 M. Hatazawa, R. Takahashi, J. Deng, H. Houjou and K. Nozaki, *Macromolecules*, 2017, **50**, 7895–7900.
- 43 D. F. Liu, L. Q. Zhu, J. Wu, L. Y. Wu and X. Q. Lü, *RSC Adv.*, 2015, **5**, 3854–3859.
- 44 Y.-C. Su, W.-L. Liu, C.-Y. Li and B.-T. Ko, *Polymer (Guildf.)*, 2019, **167**, 21–30.
- 45 Y. Jeong, M. K. Cho, S. Seo, H. Cho, K. Son and H. Kim, *ChemCatChem*, 2023, e202201086.
- 46 R. W. F. Kerr and C. K. Williams, *J. Am. Chem. Soc.*, 2022, **144**, 6882–6893.
- 47 F. De La Cruz-Martínez, M. Martínez De Sarasa Buchaca, J. Martínez, J. Martínez, J. Tejada, J. Fernández-Baeza, C. Alonso-Moreno, A. M. Rodríguez, J. A. Castro-Osma and A. Lara-Sánchez, *Inorg. Chem.*, 2020, **59**, 8412–8423.
- 48 Carlos Diaz, Tannaz Ebrahimi and Parisa Mehrkhodavandi, *Chem. Commun.*, 2019, **55**, 3347–3350.
- 49 S. Ghosh, E. Glöckler, C. Wölper, A. Tjaberings, A. H. Gröschel and S. Schulz, *Dalt. Trans.*, 2020, **49**, 13475–13486.
- 50 T. Ungpittagul, T. Jaenjaj, T. Roongcharoen, S. Namuangruk and K. Phomphrai, *Macromolecules*, 2020, **53**, 9869–9877.
- 51 M. E. Fieser, M. J. Sanford, L. A. Mitchell, C. R. Dunbar, M. Mandal, N. J. Van Zee, D. M. Urness, C. J. Cramer, G. W. Coates and W. B. Tolman, *J. Am. Chem. Soc.*, 2017, **139**, 15222–15231.
- 52 E. Hosseini Nejad, C. G. W. Van Melis, T. J. Vermeer, C. E. Koning and R. Duchateau, *Macromolecules*, 2012, **45**, 1770–1776.
- 53 T. Aida and S. Inoue, *J. Am. Chem. Soc.*, 1985, **107**, 1358–1364.

- 54 S. Huijser, E. Hosseinienejad, R. Sablong, C. De Jong, C. E. Koning and R. Duchateau, *Macromolecules*, 2011, **44**, 1132–1139.
- 55 C. Robert, T. Ohkawara and K. Nozaki, *Chem. - A Eur. J.*, 2014, **20**, 4789–4795.
- 56 A. M. Diccio and G. W. Coates, *J. Am. Chem. Soc.*, 2011, **133**, 10724–10727.
- 57 A. M. Diccio, J. M. Longo, G. G. Rodríguez-Calero and G. W. Coates, *J. Am. Chem. Soc.*, 2016, **138**, 7107–7113.
- 58 J. Li, B.-H. Ren, Z.-Q. Wan, S.-Y. Chen, Y. Liu, W.-M. Ren and X.-B. Lu, *J. Am. Chem. Soc.*, 2019, **141**, 8937–8942.
- 59 J. A. Garden, P. K. Saini and C. K. Williams, *J. Am. Chem. Soc.*, 2015, **137**, 15078–15081.
- 60 C. Romain, Y. Zhu, P. Dingwall, S. Paul, H. S. Rzepa, A. Buchard and C. K. Williams, *J. Am. Chem. Soc.*, 2016, **138**, 4120–4131.
- 61 C. Martín, A. Pizzolante, E. C. Escudero-Adán and A. W. Kleij, *Eur. J. Inorg. Chem.*, 2018, **2018**, 1921–1927.
- 62 C. M. Byrne, S. D. Allen, E. B. Lobkovsky and G. W. Coates, *J. Am. Chem. Soc.*, 2004, **126**, 11404–11405.
- 63 X. Kou, Y. Li, Y. Shen and Z. Li, *Macromol. Chem. Phys.*, 2019, **220**, 1900416.
- 64 L. Lin, J. Liang, Y. Xu, S. Wang, M. Xiao, L. Sun and Y. Meng, *Green Chem.*, 2019, **21**, 2469–2477.
- 65 R. Xie, Y.-Y. Zhang, G.-W. Yang, X.-F. Zhu, B. Li and G.-P. Wu, *Angew. Chemie Int. Ed.*, 2021, **60**, 19253–19261.
- 66 N. J. Van Zee, M. J. Sanford and G. W. Coates, *J. Am. Chem. Soc.*, 2016, **138**, 2755–2761.
- 67 M. J. Sanford, N. J. Van Zee and G. W. Coates, *Chem. Sci.*, 2018, **9**, 134–142.
- 68 W. T. Diment and C. K. Williams, *Chem. Sci.*, 2022, **13**, 8543–8549.
- 69 T. M. McGuire, E. F. Clark and A. Buchard, *Macromolecules*, 2021, **54**, 5094–5105.
- 70 L. Zheng, J. Feng, H. Xie and Z. Xu, *J. Polym. Sci.*, 2023, **61**, 1–9.
- 71 D. Takeuchi, T. Aida and T. Endo, *Macromol. Rapid Commun.*, 1999, **20**, 646–649.
- 72 T.-J. Yue, M.-C. Zhang, G.-G. Gu, L.-W. Wang, W.-M. Ren and X.-B. Lu, *Angew. Chemie - Int. Ed.*, 2018, **131**, 628–633.

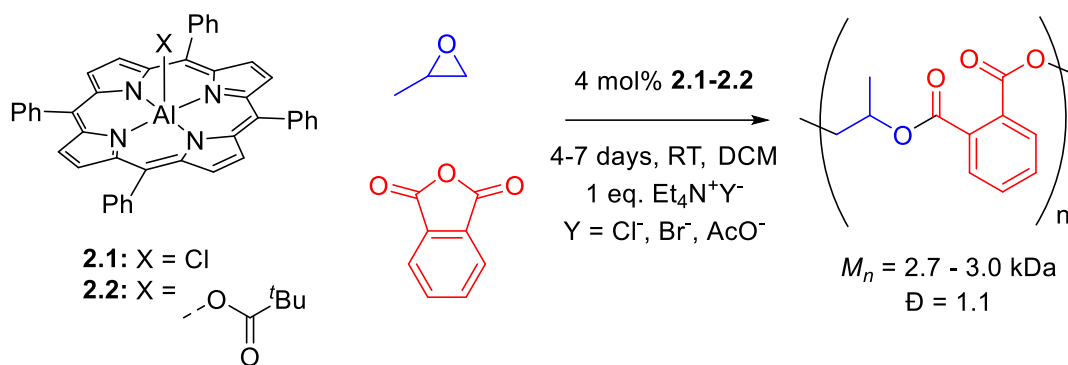
- 73 L. Y. Wang, G. G. Gu, T. J. Yue, W. M. Ren and X. B. Lu, *Macromolecules*, 2019, **52**, 2439–2445.
- 74 M. Jurrat, B. J. Pointer-Gleadhill, L. T. Ball, A. Chapman and L. Adriaenssens, *J. Am. Chem. Soc.*, 2020, **142**, 8136–8141.
- 75 A. Grice and B. MacCreath, *Expanding the GPC/SEC Experiment Beyond Conventional Limits using Viscometry and Light Scattering Detection - Application Note*, Warwick Polymer Group and Agilent Technologies, 2016.
- 76 P. Groves, *Polym. Chem.*, 2017, **8**, 6700–6708.
- 77 P. J. Voorter, A. McKay, J. Dai, O. Paravagna, N. R. Cameron and T. Junkers, *Angew. Chemie Int. Ed.*, 2022, **61**, e202114536.
- 78 M. A. Rashid, W. Liu, Y. Wei and Q. Jiang, *J. Appl. Polym. Sci.*, 2022, e52493.
- 79 K. Balani, V. Verma, A. Agarwal and R. Narayan, *Biosurfaces*, 2015, 329–344.

Chapter 2: Aluminium “Salpy” Complexes: Synthesis, Characterisation, and ROCOP Catalysis

2.1: Aluminium Catalysts in ROCOP

Aluminium based ROCOP catalysis has proven a popular research objective for polymer chemists, with aluminium’s combination of high earth abundance, low cost, biocompatibility, generally low toxicity, and the lack of colour imparted on the polymer by catalyst residues all major advantages over other transition metal catalysts, particularly chromium.¹ Furthermore, from the perspective of a catalytic chemist, the diamagnetism of Al(III) allows for easy study by NMR spectroscopy, whilst its high (and tuneable through ligand modification) Lewis acidity means aluminium containing catalysts have been successful in synthesising new polyesters in a highly controlled manner.^{2,3}

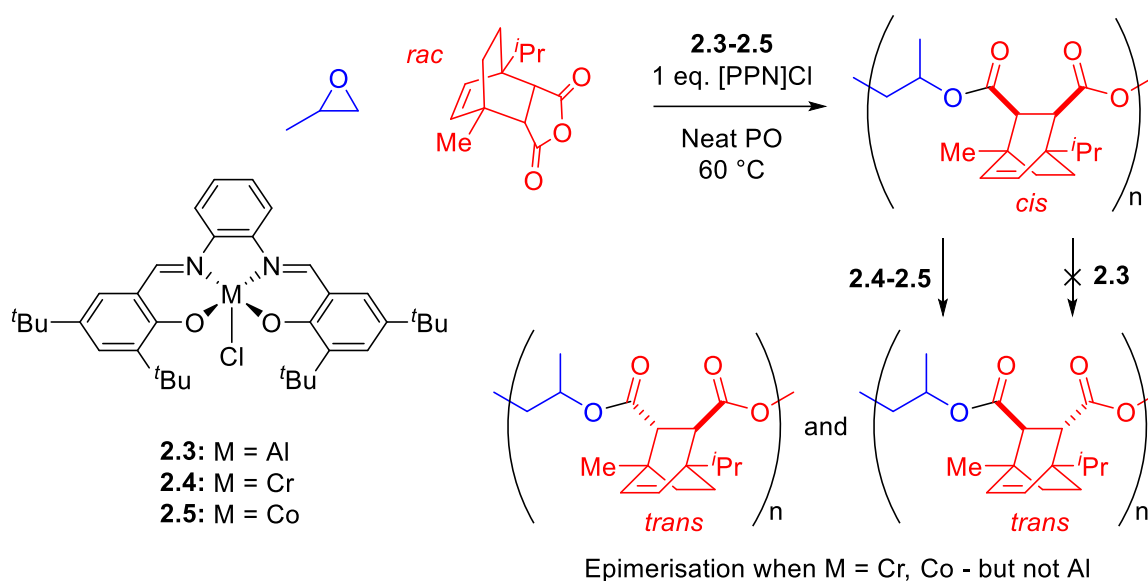
The first report of catalysed ROCOP was published in 1985 by Aida and Inoue, which detailed how Al(III) porphyrin complexes could copolymerise propylene oxide and phthalic anhydride, when employed alongside an ammonium or phosphonium salt (**Scheme 2.1**).⁴ The most effective of these salts proved to be tetraethyl ammonium salts, which in combination with complexes **2.1-2.2** produced a polyester with a polydispersity as low as 1.1, albeit under incredibly mild reaction conditions, which concurrently led to an extremely long reaction time.



Scheme 2.1: Aluminium porphyrin complexes used alongside a Et₄N⁺Y⁻ co-catalyst, as described by Aida and Inoue for the ROCOP of propylene oxide and phthalic anhydride.⁴

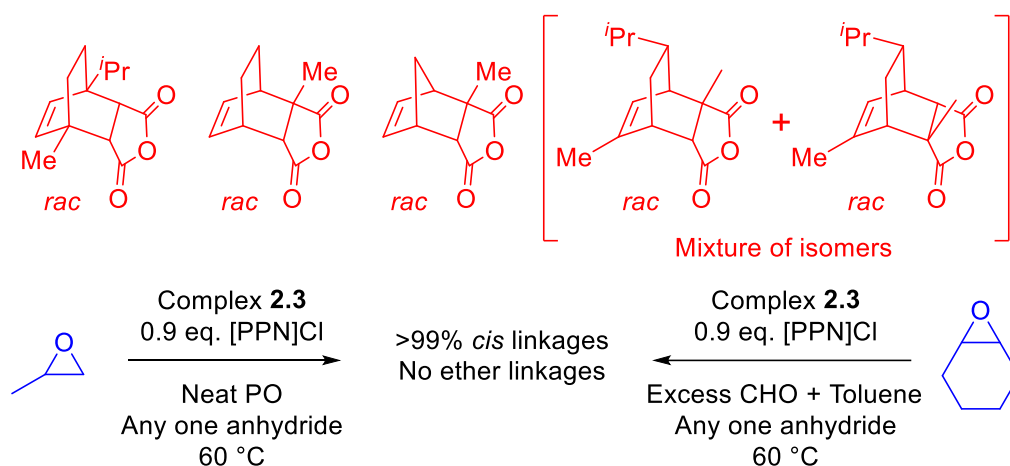
In Aida and Inoue’s report, one of the key mechanistic tenets of aluminium ROCOP, that the propagating species is a six-coordinate anionic complex with two propagating polymer chains mutually *trans* above and below the porphyrin plane, was described for the first time. This principle remains relevant to contemporary reports, with full mechanistic investigations into the [Al(Salph)Cl] complex **2.3** (**Scheme 2.2**), which employs a planar, dianionic ligand isolobal to a porphyrin, also invoking similar intermediates and a resting state of a bis(carboxylate) complex in the catalytic cycle (see Chapter 1

for a full discussion).² This ligand motif has been investigated by several groups, with the ease of synthesis and tuneability of the aromatic substituents or the metal centre a key selling point. Indeed, the chromium analogue of complex **2.3** (as well as its close relative made with 1,2-diaminocyclohexane, as opposed to 1,2-phenylenediamine) **2.4**⁵⁻⁹ and the cobalt congener **2.5**¹⁰⁻¹² (and its ligand derivatives) have both been studied as catalysts for ROCOP. Direct comparisons between complexes **2.3-2.5** in the copolymerisation of propylene oxide and an unsaturated tricyclic anhydride made by the Diels-Alder reaction of maleic anhydride and α -terpinene were reported by the Coates group in 2015 (**Scheme 2.2**).¹³ Interestingly, when the reaction reached high levels of conversion, the α -methine protons in the ring-opened anhydride were seen to epimerise from their *cis* to *trans* form when **2.4** and **2.5** were used as catalysts, but only in trace amounts for the aluminium catalysed reaction. This isomerisation is important as the resulting T_g of the polyesters was decreased where isomerisation was detected. Also, the use of complex **2.3** reduced transesterification reactions, producing polyesters with narrower molecular weight distributions and higher molecular weights.



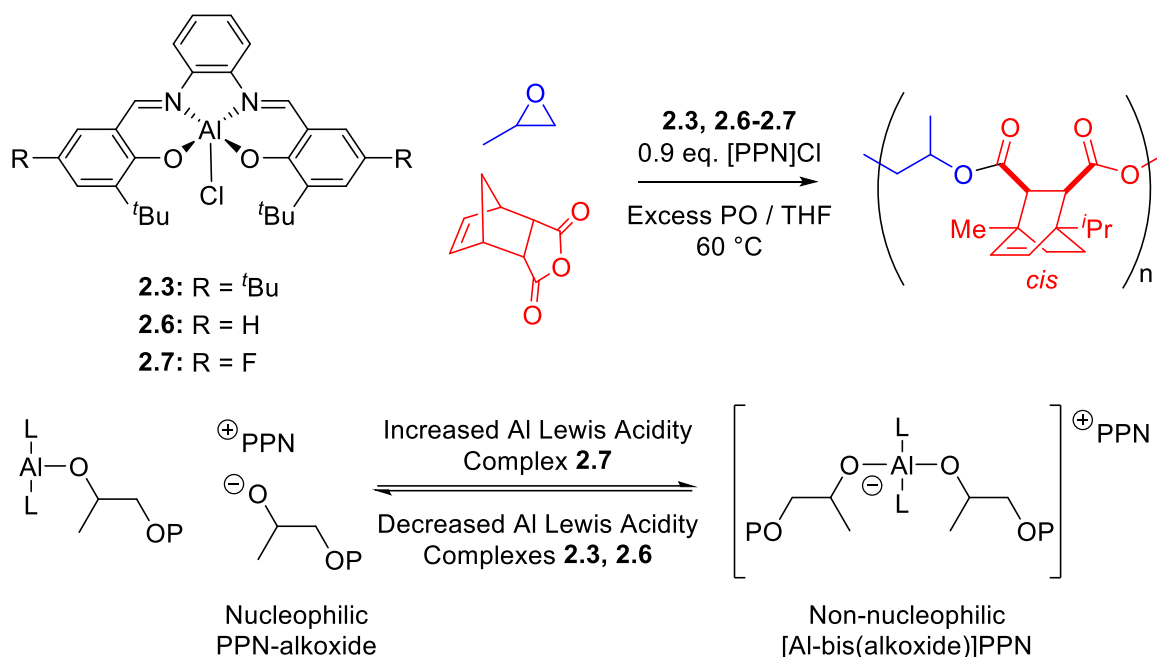
Scheme 2.2: [M(Salph)Cl] complexes as catalysts for the ROCOP of propylene oxide and a terpene-derived tricyclic anhydride. The presence of α -protons to the ester linkages led to *cis* to *trans* isomerisation when Cr and Co catalysts were used, but not for Al.¹³

The substrate scope for complex **2.3** was expanded to include a wider range of terpene-derived (and thereby partially renewable) anhydrides as well as cyclohexene oxide in 2016 (**Scheme 2.3**).¹⁴ Swapping propylene oxide for cyclohexene oxide increased the T_g to as high as 184 °C (from 108 °C for the same anhydride used with propylene oxide), whilst there remained no evidence of epimerisation in the ¹³C NMR spectra of the polymers, or transesterification in MALDI-ToF mass spectra, as only series corresponding to chloride initiated, OH terminated (α -Cl, ω -OH) polymers could be seen.



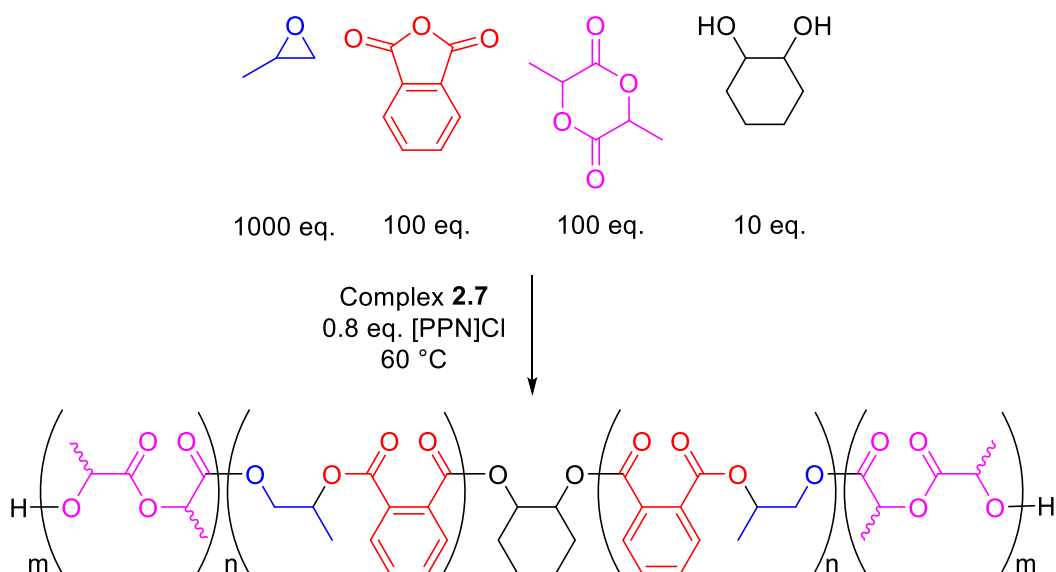
Scheme 2.3: ROCOP of either propylene oxide or cyclohexene oxide with a series of terpene derived anhydrides using the [Al(Salph)Cl] complex **2.3** alongside [PPN]Cl as a co-catalyst. The use of this catalyst system meant no epimerisation of the *cis* diester units of the polymer was observed.¹⁴

As well as modification of the metal centre, changing the aromatic substituents of the ligands has a profound effect on the polymerisation performance. For example, the protio- and fluoro-substituted complexes **2.6** and **2.7** have also been investigated for ROCOP, with the fluoro complex **2.7** showing that even after full anhydride conversion, and in the presence of excess epoxide, that there is no evidence of any epimerisation or transesterification occurring (**Scheme 2.4**).³ This is in contrast to **2.3** and **2.6**, which show no epimerisation and transesterification during the reaction, but do once anhydride is consumed. The authors hypothesised that this is because when using [PPN]Cl as a co-catalyst alongside excess epoxide, there will be [PPN]-alkoxides present at the end of the reaction, even when sub-stoichiometric amounts are used. PPN-alkoxides are good nucleophiles (as evidenced by the fact that [PPN]Cl catalyses ROCOP by itself), meaning that when there is no anhydride to react with to convert the alkoxides to far less nucleophilic carboxylates, the alkoxides instead slowly attack the ester units, causing transesterification and broadening the molecular weight distribution. Concurrently, the aluminium centre is assumed to reside as a neutral mono(alkoxide) complex once anhydride is consumed, existing in an equilibrium with the [PPN]-alkoxides (**Scheme 2.4**). Interestingly, the introduction of electron withdrawing fluorine atoms into the ligand produced a more Lewis acidic metal centre, which is believed to push this equilibrium towards an anionic bis(alkoxide) complex, with a [PPN] counterion. By pushing this equilibrium away from the free [PPN]-alkoxides, the transesterification and epimerisation pathways are prevented, meaning there was no observed deleterious effect on molecular weight or polydispersity even several hours after full anhydride consumption when complex **2.7** was used.



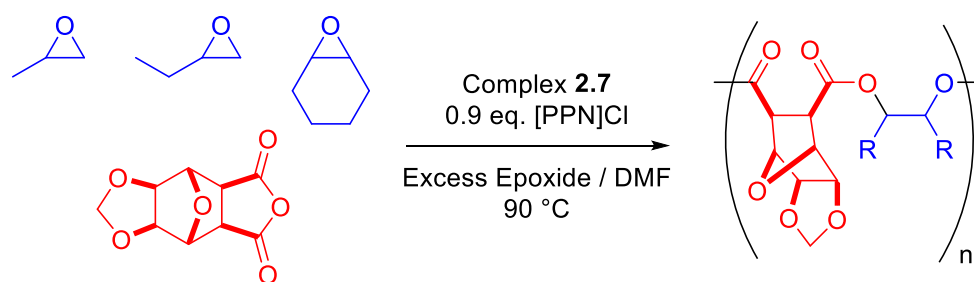
Scheme 2.4: Series of substituted [Al(Salph)Cl] complexes investigated for ROCOP, with the fluoro-substituted complex **2.7** shown to not cause epimerisation or transesterification for long periods after full anhydride consumption. The authors hypothesised this was due to the increased Lewis acidity induced by employing a more electron withdrawing ligand, causing the equilibrium presented at the bottom to lie further to the right.³

Given its proven ability to efficiently catalyse ROCOP whilst minimising transesterification, it is no surprise that complex **2.7** has been investigated for a wider range of substrates. This includes a report by the Williams group of the terpolymerisation of propylene oxide, phthalic anhydride and lactide to produce highly controlled block copolymers (**Scheme 2.5**) by complex **2.7** alongside a sub-stoichiometric amount of [PPN]Cl as a co-catalyst.¹⁵ These blocks consisted of epoxide/anhydride ROCOP blocks, which are formed first, before the catalyst “switches” to producing poly(lactic acid) blocks once anhydride is consumed. As cyclohexane-1,2-diol was used as a bifunctional initiator, the initial ROCOP block propagated in two directions, with the latter ROP block also growing from each end, producing an ABA triblock copolymer (A being ROP, B being ROCOP). The authors described how sequential addition of mixtures of the epoxide/anhydride/lactide monomers into an ongoing polymerisation in the ROP stage could switch the catalysis from ROP back to ROCOP. This process could be repeated up to 9 times, to producing a polyester with up to 27 distinct blocks. Interestingly, an excess of propylene oxide was required to form an alkoxide terminated polymer chain in the ROCOP block before ROP could occur, as the equivalent bis(carboxylate) complex was inactive for ROP.



Scheme 2.5: Block copolymers formed by the switchable catalysis from epoxide/anhydride ROCOP and cyclic ester ROP, as catalysed by complex **2.7**, and using cyclohexane-1,2-diol as a bifunctional initiator. Monomer mixtures could be re-added up to 9 times to switch from ROP back to ROCOP.¹⁵

Another possible incentive for the use of a particular catalyst may be that it allows for an enhanced substrate scope when compared to the co-catalyst only system. This was demonstrated by Wang *et al.*, who used complex **2.7** alongside [PPN]Cl to copolymerise a biomass-derived tetracyclic anhydride with propylene oxide, butylene oxide and cyclohexene oxide (**Scheme 2.6**).¹⁶ None of these copolymerisations were possible using [PPN]Cl alone, whilst the polymers themselves possessed far lower gas permeabilities than aliphatic polyesters, largely due to the use of the highly rigid anhydride.



Scheme 2.6: ROCOP of a series of epoxides and a highly rigid tetracyclic anhydride, which proved to have excellent gas barrier properties when compared to aliphatic polyesters.¹⁶

A common feature of the reports detailing catalysis using complex **2.7** is the use of [PPN]Cl as a co-catalyst. However, in 2019 the Coates group reported a modified ligand set, where a cyclopropenium moiety was included into the phenylene backbone, effectively providing an in-built source of chloride ions to act as a co-catalyst in an analogous way to [PPN]Cl.¹⁷ This series of complexes **2.8-2.12** are shown in **Figure 2.1**, where the tethering of the co-catalyst system was seen to both suppress

transesterification and epimerisation by eliminating [PPN]-alkoxides from the reaction, but also proved to be highly active catalysts at far lower loadings than usual. Indeed, for the copolymerisation of propylene oxide and carbic anhydride, the TOF of the polymerisation for complex **2.8** remained constant at between 85-90 hr⁻¹ down to a 0.025 mol% loading of catalyst to anhydride. This contrasts to the analogous pairing of complex **2.3** and one equivalent of [PPN]Cl, where TOF reduced by an order of magnitude as catalyst loading decreased from 0.25 mol% to 0.025 mol% (from 115 hr⁻¹ to 10 hr⁻¹).

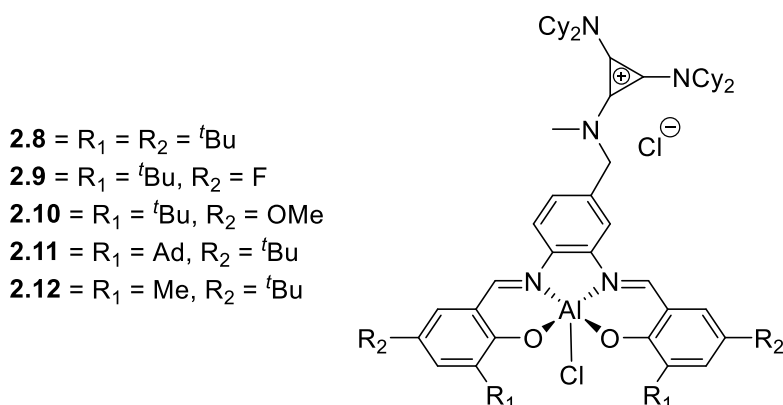
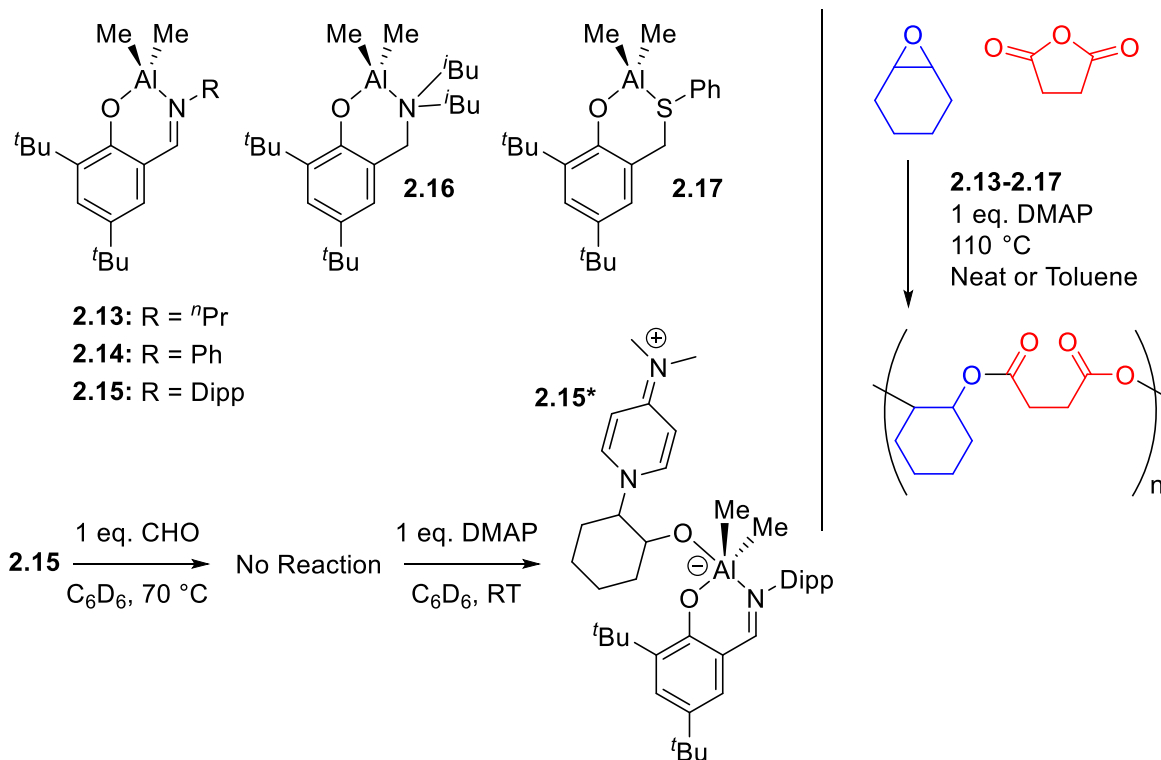


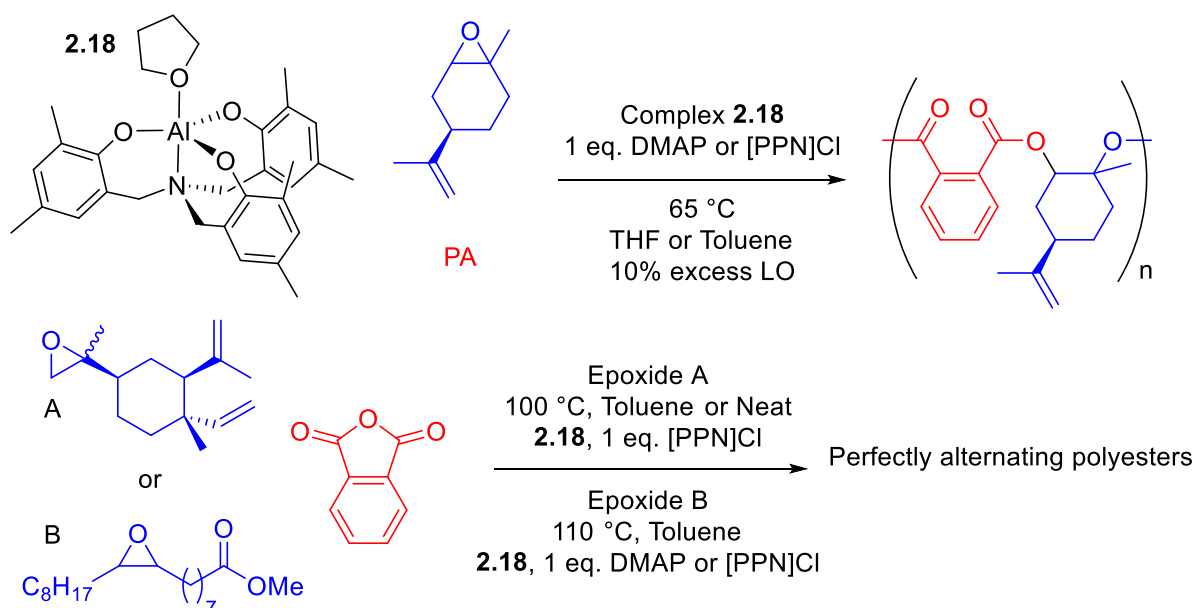
Figure 2.1: Series of cyclopropenium containing aluminium catalysts, effectively tethering the nucleophilic co-catalyst to the metal catalyst, leading to high TOFs at low catalyst loadings.¹⁷

In a deviation from the salen/salph ligand structure, Mazzeo and co-workers have reported a series of bis(methyl) aluminium complexes featuring only one phenoxy-imine (complexes **2.13-2.15**), phenoxy-amine (**2.16**) or phenoxy-thioether (**2.17**) moiety (**Scheme 2.7**).¹⁸ All complexes proved effective catalysts for the copolymerisation of cyclohexene oxide and succinic anhydride either neat or in toluene solution when used with one equivalent of DMAP as a co-catalyst. Interestingly, detailed initiation studies on complex **2.15** showed how only after the addition of DMAP would cyclohexene oxide ring open to give the zwitterionic species **2.15***, with this species fully characterised by NMR spectroscopy, including by DOSY, which allowed for the distinction of **2.15** and the slightly higher molecular weight **2.15*** in solution. Complexes **2.13-2.17** also showed efficacy in the ROCOP of limonene oxide and phthalic anhydride, with the phenoxy-imine complexes proving most effective.



Scheme 2.7: Series of bis(methyl) aluminium complexes reported for cyclohexene oxide/succinic anhydride ROCOP. The authors found DMAP was essential to initiate polymerisation, as evidenced by the lack of reaction of **2.15** with cyclohexene oxide (CHO) until DMAP was added to give **2.15***.¹⁸

Moving away from Schiff base ligands, the Kleij group have pioneered the use of the tris(phenolate) complex **2.18**, which has been shown to copolymerise limonene oxide and phthalic anhydride under mild conditions (65 °C), albeit at a slower rate than its iron analogue (**Scheme 2.8**).¹⁹

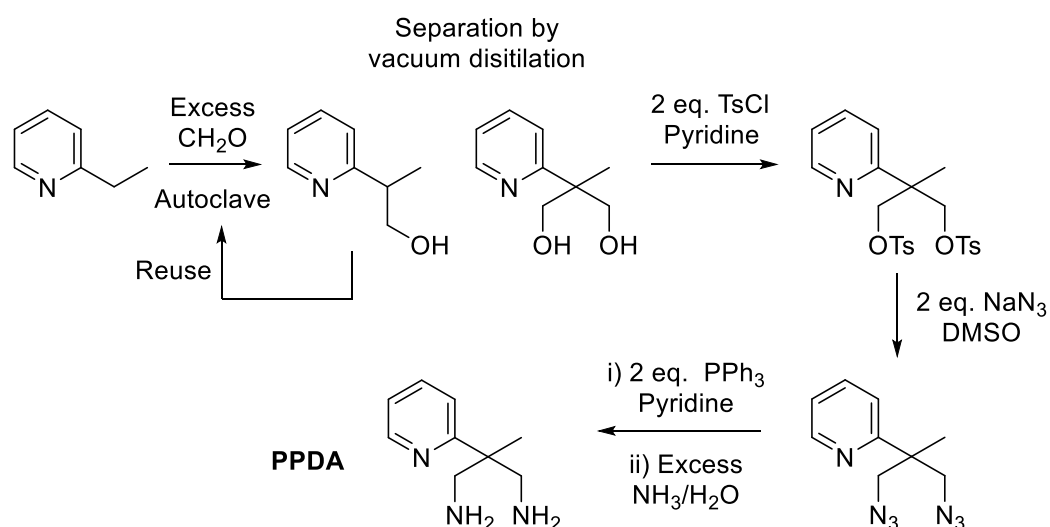


Scheme 2.8: Tris(phenolate) complex **2.18** reported for the ROCOP of PA with three biomass derived epoxides; limonene oxide, epoxide A (derived from β -elemene) and epoxide B (derived from oleic acid).¹⁹⁻²¹

As well as limonene oxide, further investigations into the β -elemene derived epoxide A and oleic acid derived epoxide B showed that complex **2.18** could produce an array of partially bio-derived polyesters when used in conjunction with DMAP or [PPN]Cl.^{20,21} The long-chain fatty acid nature of epoxide B meant its copolymer with PA had a T_g as low as $-20\text{ }^\circ\text{C}$, highlighting the highly versatile nature of ROCOP, in that one process can be used to synthesise polymers with incredibly diverse properties. In addition to the reports discussed in detail in this section, additional literature can be found here.^{22–29}

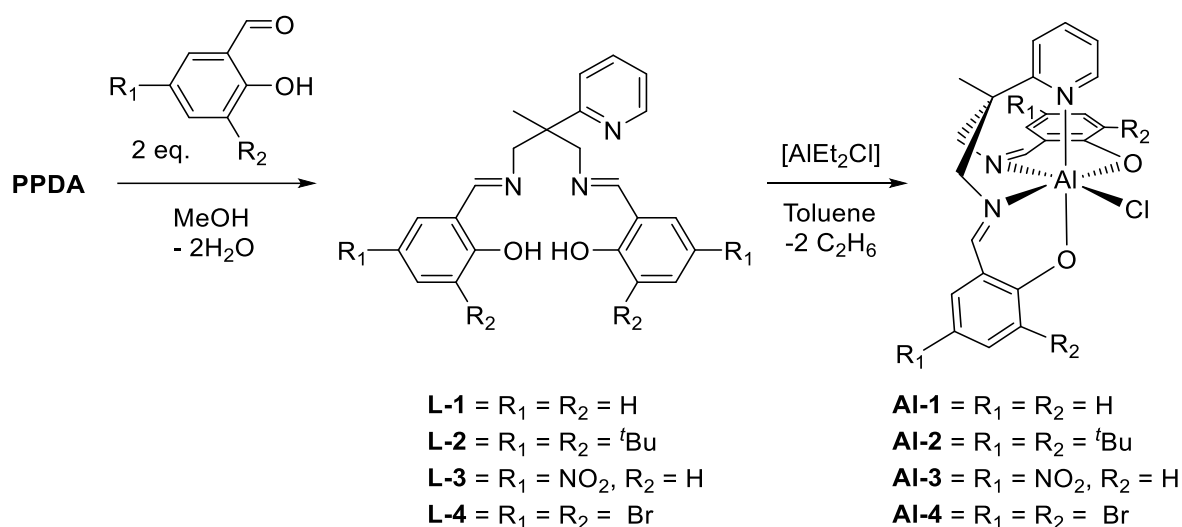
2.2: Aluminium “Salpy” Complexes – Synthesis and Characterisation

Previous mechanistic studies using complex **2.3** have identified anionic, bis(carboxylate) 6-coordinate aluminium complexes as the resting state of the catalyst during polymerisation, and that this is in equilibrium with a number of 5 and 6 coordinate (both neutral and anionic) species during the catalytic cycle (see Chapter 1 for full discussion).² Therefore, it was hypothesised that ligand design to help facilitate the de-coordination of a carboxylate ligand (*i.e.* a growing polymer chain) would in turn help increase the rate of polymerisation. To achieve this, analogues of the Salph ligands used widely in the field were synthesised, albeit using 2-methyl-2-(pyridin-2-yl)propane-1,3-diamine in place of 1,2-phenylenediamine. Indeed, work within the group has shown that this hemi-labile pyridine donor helps facilitate the de-coordination steps in the catalytic trimerisation of isocyanates.³⁰ PPDA was synthesised from 2-ethylpyridine and formaldehyde according to a literature procedure, which is detailed in **Scheme 2.9**.³⁰



Scheme 2.9: Synthesis of 2-methyl-2-(pyridin-2-yl)propane-1,3-diamine, PPDA.³⁰

Once PPDA was synthesised and purified by distillation, Schiff base condensation reactions were performed with a series of salicylaldehyde derivatives to produce a set of phenol-imine based proligands, **L-1 – L-4** (**Scheme 2.10**, see section 7.2 for experimental procedures), termed “Salpy” ligands. These Salpy derivatives were then reacted with the organometallic precursor $[AlEt_2Cl]$ to yield four $[Al(\text{Salpy})Cl]$ complexes **Al-1 – Al-4** (see section 7.3).



Scheme 2.10: Synthesis of “Salpy” ligands by Schiff base condensations, followed by complexation with $[AlEt_2Cl]$ to give four $[Al(\text{Salpy})Cl]$ complexes. Note the β -cis geometry of **Al-1 – Al-4**.

Complexations occurred cleanly given the only by-product of the reaction was ethane. Phenolic protons (δ_H 13.2 – 14.4 ppm) in the pro-ligands were no longer observed post-complexation, whilst distinct 1H NMR chemical shift differences between the pro-ligands and complexes were also observed. There is a downfield shift of the proton *ortho* to the pyridine nitrogen (labelled H^6 , albeit this change is small for **Al-4**, and in a different solvent) upon complexation. These differences are summarised in **Table 2.1**, which also detail the changing nature of the $N=CH$ imine proton, which becomes broadened and/or split into two distinct peaks for **Al-3** and **Al-4**.

Table 2.1: 1H NMR chemical shifts for both the imine protons ($N=CH$) and H^6 (*ortho* to the pyridine nitrogen) pre and post-complexation for the Salpy ligands. All chemical shifts are reported in $CDCl_3$ at 500 MHz and room temperature apart from those marked with an asterisk (CD_2Cl_2) or dagger ($DMSO-d^6$).

Pro-ligand / Complex	δ_H $N=CH$ (Pro-ligand)	δ_H $N=CH$ (Complex)	δ_H H^6 (Pro-ligand)	δ_H H^6 (Complex)
1	8.31	Very broadened *	8.63	9.32
2	8.35	7.56-8.16 (br) *	8.63	9.68 *
3	8.32	8.26, 7.88 *	8.66	9.30 *
4	8.12	8.61, 8.19 †	8.59	8.65 †

This is clear evidence that the symmetry of the pro-ligands and complexes are different, and means a complex of *trans* symmetry is not likely. Indeed, upon complexation, the aromatic protons of the phenoxy-imine rings show inequivalence, as do the two CH₂ groups on the ligand backbone, which become broad and magnetically inequivalent. Previous work in the group has shown it is possible through variable temperature NMR to sharpen individual signals of these CH₂ protons (and other signals), yet this was not done in this case.³¹ The broadness of certain resonances could also be inferred as evidence of fluxionality within the molecule, suggesting that the pyridine donor is indeed hemi-labile to an extent in solution, and that there is switching between two (or more) conformations.

The single crystal X-ray structures of **Al-1** – **Al-3** all showed a β -cis configuration of a κ^5 donor, with a chloride ligand *trans* to one of the imine donors, completing the octahedral geometry of the complex (for refinement details and full tables of structural data, see the Appendix). A representative example of **Al-3** is shown in **Figure 2.2**. Unfortunately, attempts to crystallise **Al-4** were unsuccessful, with this largely due to its poor solubility in several solvents (NMR analysis required DMSO-d₆ for samples of adequate solubility).

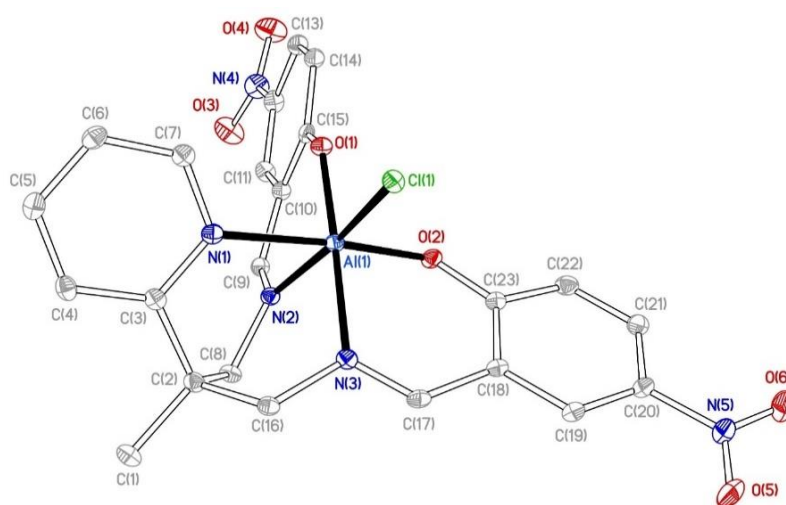


Figure 2.2: X-ray crystal structure of **Al-3**, showing the κ^5 unit of the nitro-substituted Salpy ligand in a β -cis geometry. Ellipsoids drawn at 30% probability; hydrogen atoms omitted for clarity.

By searching the Cambridge Structural Database (CSD) (v5.43, March 2022) of single crystal X-ray structures, it is possible to compare the observed bond lengths about the aluminium centre to those previously reported. For these purposes, all bond lengths to aluminium from the O and N donors of phenoxy-imine-based ligands, the nitrogen of pyridine-based ligands, and from chlorides in octahedral complexes were searched for and analysed. These searches are shown visually in **Figure 2.3** (shown in red) and include subsets and derivatives of the structures searched for (*i.e.* any pyridine-based donor would appear, as well as distinct pyridine ligands).

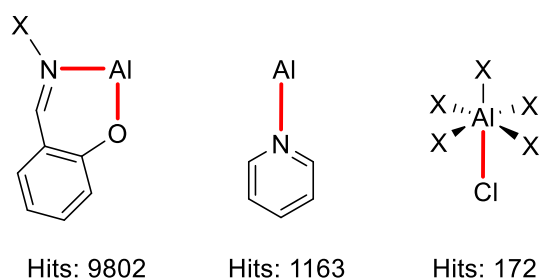


Figure 2.3: CSD (v 5.43, March 22) searches for relevant bond length information for comparative purposes to the [Al(Salpy)Cl] complexes. Bonds lengths shown in red were exported for analysis. The number of bond length results for each search (including multiple hits from the same structure) are also indicated. X = any atom.

The relevant bond lengths for complexes **Al-1** – **Al-3** are listed in **Table 2.2**, as are the percentile rank within the CSD data set in parentheses. All bond lengths to aluminium were in the expected range for single bonding, with values ranging from the 61st to 89th percentile when compared to the previously outlined search criteria. Interestingly however, despite being in an expected range, all 18 bond lengths across three complexes were above the median value compared to previous CSD entries. There were noticeable differences between bonds of the same type when *trans* to different substituents (*e.g.* O-Al bonds were longer when *trans* to the pyridyl donor than an imine donor for **Al-1** and **Al-3**, and marginally shorter for **Al-2**). Analysis of the bond angles about the aluminium centre showed the three mutually *trans* angles totalled 517.7 °, 517.0 ° and 519.3 ° for **Al-1**, **Al-2**, and **Al-3** respectively (the angle <180 ° was taken in all cases), showing the slight distortion of the octahedral structure from the idealised value of 540 °. For full ¹H and ¹³C{¹H} NMR spectral assignments, high resolution mass spectrometry data, X-ray crystal refinement and structural data, and characterisation by FT-IR and elemental analysis, see section 7.3.

Table 2.2: Selected X-ray crystal structure bond lengths about the aluminium centres for **Al-1**, **Al-2** and **Al-3**, alongside its rank amongst comparable bond lengths from the CSD in parentheses.

Complex	PhO – Al / Å		C=N – Al / Å		Py – Al / Å	Cl – Al / Å
	<i>trans</i> N=C	<i>trans</i> py	<i>trans</i> Cl	<i>trans</i> O		
Al-1 ^a	1.829 (76)	1.840 (85)	2.035 (77)	2.013 (62)	2.119 (89)	2.275 (63)
Al-2 ^b	1.821 (68)	1.816 (61)	2.015 (63)	2.021 (67)	2.102 (85)	2.300 (80)
Al-3	1.823 (70)	1.844 (89)	2.012 (61)	2.020 (66)	2.080 (78)	2.275 (63)

^a Crystal structure previously reported by Mohammad Bahili³¹ in the Ward group. ^b The asymmetric unit contained two molecules of **Al-2**, and so an average of the two matching bond lengths is listed.

2.3: Catalytic Performance of Salpy Complexes in ROCOP

As well as possibly facilitating the de-coordination of polymer chains during polymerisation, the addition of the pyridyl donor in the Salpy complexes has another mechanistic implication, in that the switch from *trans* to β -*cis* geometry allows for interaction between the two labile sites (Cl and pyridyl). This contrasts with the majority of the aluminium catalysed ROCOP literature discussed in section 2.1, where two polymer chains propagate *trans* to one another above and below a ligand plane. This not only potentially allows for intramolecular reaction between the two sites (as will be investigated computationally in section 2.5), but also could have wider implications for the steric encumbrance about the metal centre. For comparative purposes and to examine the impact of both the pyridyl donor and the change in geometry, a close analogue of the Salpy complexes was synthesised using 2,2-dimethyl-1,3-diaminopropane and 3,5-ditertbutylsalicylaldehyde. This “Salpn” complex, **Al-5**, is shown in **Figure 2.4**, and was prepared in an identical manner to the Salpy complexes. ^1H and $^{13}\text{C}\{^1\text{H}\}$ NMR spectra and X-ray crystallographic data showed it formed as the expected *trans* isomer. For full details of its synthesis and characterisation, see section 7.3.

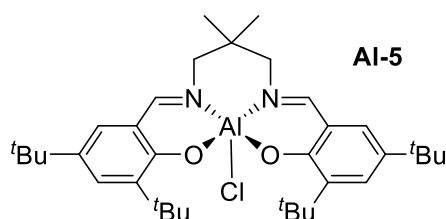
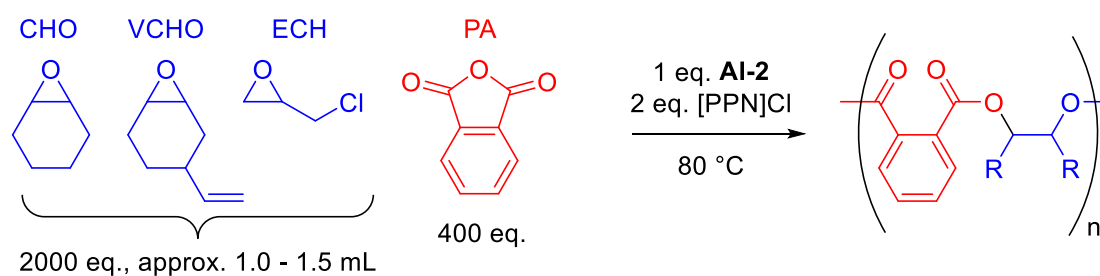


Figure 2.4: Aluminium “Salpn” complex **Al-5**, synthesised for comparative purposes to investigate the impact of the change of geometry seen for the Salpy complexes.

2.3.1: Initial ROCOP Experiments – Two Equivalents [PPN]Cl

Following on from previous work within the group, reactions were conducted using excess epoxide as solvent, at 80 °C, with molar ratios of [Al]:[PPN]Cl:[Anhydride]:[Epoxide] being 1:2:400:2000, with one equivalent equal to 6.4 μmol .³² Initial work would use phthalic anhydride (PA) and three epoxides, cyclohexene oxide (CHO), vinyl cyclohexene oxide (VCHO) and epichlorohydrin (ECH), and focus on the *tert*-butyl derivative **Al-2** as a pre-catalyst. These conditions are summarised in **Scheme 2.11**.



Scheme 2.11: Initial conditions for ROCOP experiments using **Al-2** as the pre-catalyst. 1 eq. = 6.4 μmol .

The kinetic data for the copolymerisations are presented in **Figure 2.5**. As expected, given ROCOP is generally zero order in anhydride and first order in epoxide, the conversion *versus* time graphs take a linear form (although the fit is poorer for ECH) for all three epoxides. Under these *pseudo-zero-order* conditions, where an excess of epoxide is maintained throughout the reaction, the decreasing concentration of PA has no effect on the rate. The linear fits allow for observed rate constants, k_{obs} , to be extracted, showing that conversion is fastest with ECH, followed by CHO and then VCHO, with this trend consistent with the increased steric encumbrance about the epoxide in each case, although the electron withdrawing chlorine atom in ECH may also impact its rate of reaction. Despite the uncertainties associated with each rate constant meaning there is little statistical difference between the epoxides, the time taken to reach 100% conversion is markedly different, and so much of this difference may be because of different rates of initiation, which are not measured in this analysis, rather than rates of propagation. Also noteworthy is that taking aliquots to determine the conversion of PA (see below) by ^1H NMR requires exposing the polymerisation to air, and so each data point in **Figure 2.5** is derived from one reaction run for a given time. This is repeated several times, but with an aliquot (and polymer work up) done after varying lengths of time to complete the data set.

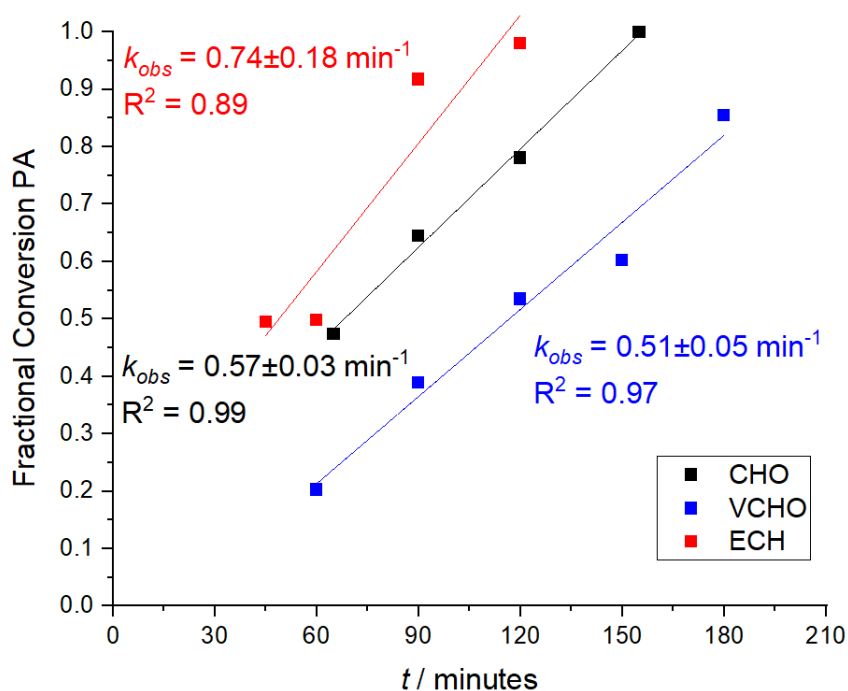


Figure 2.5: Conversion PA vs. time for CHO, ECH and VCHO, with R^2 and the *pseudo-zero-order* rate constant k_{obs} indicated for each (along with associated uncertainty, one standard deviation in the gradient). Conditions: 1 eq. (6.4 μmol) **AI-2**, 2 eq. [PPN]Cl, 400 eq. PA, 2000 eq. epoxide at 80 °C. Each data point is a distinct reaction, rather than consecutive aliquots of one reaction.

PA is a convenient anhydride for initial study in ROCOP, as ^1H NMR analysis of its reaction aliquots is straightforward. PA produces distinct peaks corresponding to unreacted and reacted anhydride, which

are themselves separate from any epoxide peaks (either reacted or unreacted), the solvent peak of CDCl_3 , or toluene if conducting polymerisations in solution. These peaks can be integrated to easily calculate the conversion of anhydride, with a representative example, showing a conversion of 64% (calculated by $(1 / (1 + 0.57)) * 100$) shown in **Figure 2.6**. The sharp, downfield resonances correspond to phthalic anhydride, which upon ring-opening shift upfield and show a broadened shape characteristic of polymers. This example has CHO as the epoxide, but a similar pattern of peaks is seen regardless of which epoxide is used.

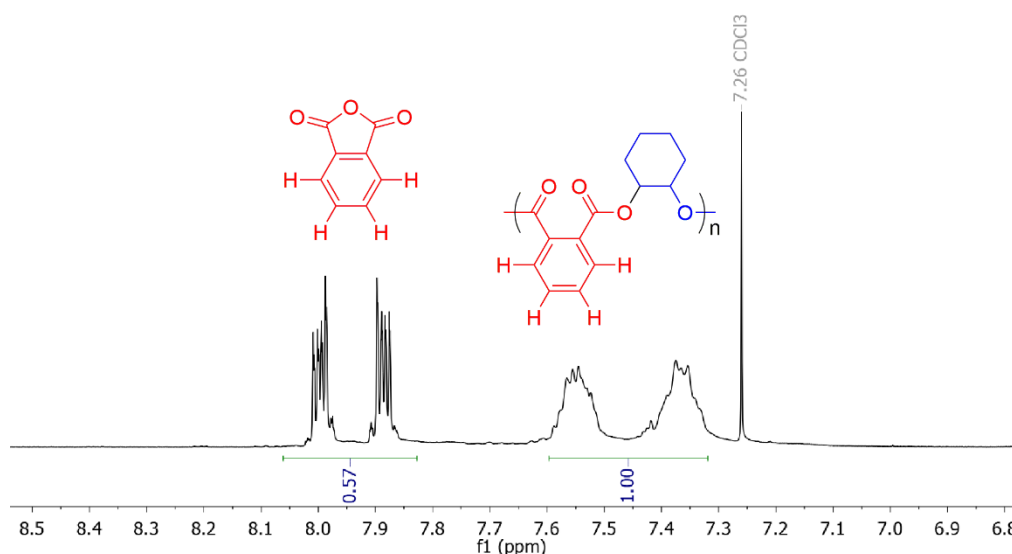


Figure 2.6: ^1H NMR spectrum (CDCl_3 , 300 MHz) of a reaction aliquot taken from a copolymerisation of CHO and PA, showing a PA conversion of 64%, with peaks corresponding to polymer and unreacted anhydride indicated.

Although the kinetic data show reasonable rates of reaction and the polymers produced had high ester selectivity, control reactions, where [PPN]Cl alone were used, are required to see what (if any) effect the aluminium pre-catalyst has on the rate of conversion. Interestingly, these control reactions showed near identical rates to reactions performed with **Al-2** across the three epoxides investigated above. This is likely due to the relatively forcing conditions originally investigated, with two equivalents of [PPN]Cl rather than a more typical value of 1 or 0.9 equivalents used. This coupled with the known efficacy of [PPN]Cl in ROCOP means future work would focus on reducing this co-catalyst loading, as well as changing the identity of the co-catalyst.³³

2.3.2: Further ROCOP Experiments – One Equivalent DMAP

Across the ROCOP literature, several different nucleophilic co-catalysts have been reported, including [PPN]Cl, ammonium salts, phosphines and imidazoles.^{33–37} However, 4-dimethylaminopyridine (DMAP) is a popular alternative to [PPN]Cl, given that on a per mole basis, DMAP is around 30 times

cheaper than [PPN]Cl.³⁸ This price difference may still be small for sub-gram scale syntheses, but producing significant quantities of polymer at a reasonable cost would be far more challenging using [PPN]Cl. Furthermore, whilst DMAP is an active catalyst for ROCOP, it is slower than [PPN]Cl, and so the influence of the metal catalyst may be easier to observe against a slower background reaction, albeit at the expense of the rate of reaction generally.³³ To compensate for this, an slightly elevated temperature of 90 °C was used, whilst the ratios of reactants remained the same. **AI-1 – AI-5** were screened for catalytic activity under these conditions for the copolymerisations of CHO and PA, and compared to the control reaction when only DMAP was used. The conversion *versus* time data is plotted in **Figure 2.7**, which again displays a *pseudo-zero-order* linear relationship, albeit with no significant distinction between all the aluminium pre-catalysts and the control reaction.

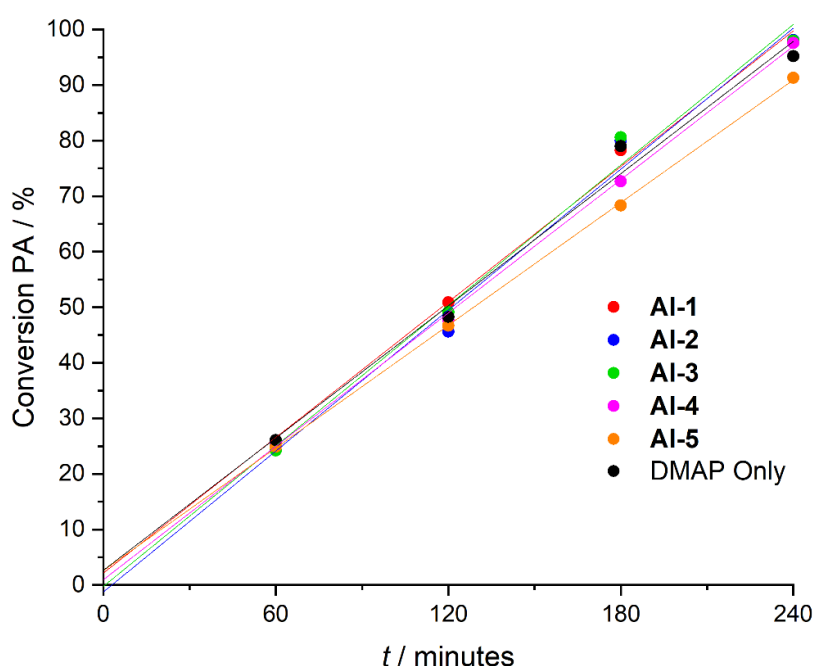


Figure 2.7: Conversion PA vs. time for the five aluminium pre-catalysts and the DMAP only control reaction for the ROCOP of PA and CHO. Conditions: 1 eq. (6.4 μ mol) aluminium pre-catalyst, 1 eq. DMAP, 400 eq. PA, 2000 eq. CHO at 90 °C. Each data point is a distinct reaction, rather than consecutive aliquots of one reaction.

Clearly, there is no significant rate enhancement when the [Al(Salpy)Cl] complexes are used compared to the DMAP only reaction. Perhaps surprisingly, the *trans* complex **AI-5**, which is very similar to the Salph complexes used widely in the literature, also produced no rate enhancement. However, this does not necessarily mean that the complexes are completely inert during the polymerisation, as there could be a significant influence upon the resulting polymers, such as on the molecular weight or breadth of the molecular weight distribution, or the ester vs. ether selectivity. On this final point, ester selectivity remained between 85-90% for all the polymers produced (including the DMAP only reaction), which was independent of both conversion and molecular weight. Selectivity can be readily

determined though ^1H NMR analysis of the polymers, which show distinct peaks for ester units (4.7 – 5.4 ppm for CHO-PA) and ether units (3.3 – 3.6 ppm for CHO) which can be integrated and compared. A representative example of poly(CHO-*alt*-PA) with an ester selectivity of 90% is shown in **Figure 2.8**, which is calculated by dividing the integral of the ester peak by the sum of the ester and ether peaks, before multiplying by 100 to give the selectivity in percentage form. Given the broad and low intensity nature of the ether peak, it is important to measure spectra on concentrated samples and with increased scan numbers, as failing to do this gave artificially high selectivities as the ether peak can suffer from poor signal to noise ratio. At very high selectivities, this issue is compounded by the fact that any part of the baseline could be integrated, yet return a selectivity of less than 100%, even when taking a region which is typically vacant (*e.g.* 12-15 ppm, for example). This could be ameliorated by applying a baseline correction, although this in turn can significantly deflate the relative size of the ether peak compared to the ester peak, and again produce an artificially high selectivity. Therefore, baseline corrections were not applied to polymer spectra when calculating selectivity.

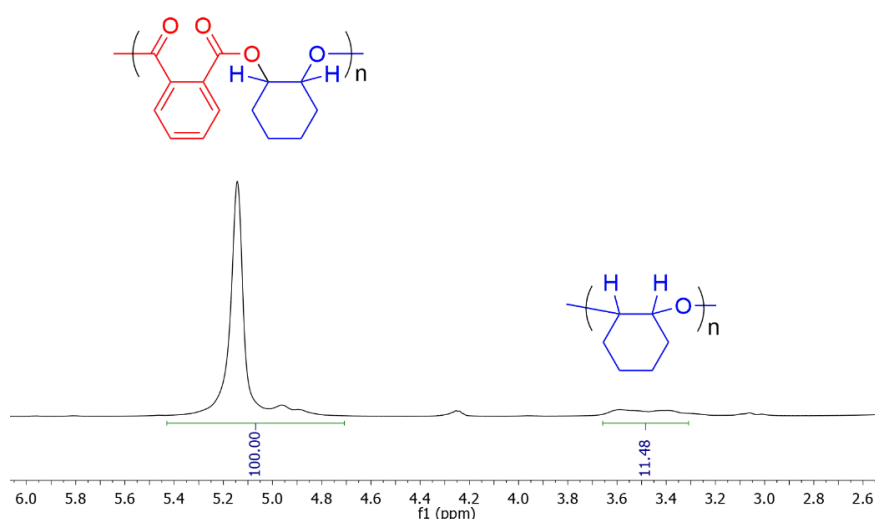


Figure 2.8: ^1H NMR spectrum (500 MHz, CDCl_3) of poly(CHO-*alt*-PA), showing an ester selectivity of 90%.

In terms of the molecular weight, **Figure 2.9** shows the relationship between number average molecular weight, M_n , and both reaction time and conversion. Interestingly, there is a steady increase in molecular weight throughout the reaction for all six scenarios, highlighting that the polymerisation is well controlled. This is further evidenced by the narrow molecular weight distributions seen, with dispersities constant at between 1.1 and 1.2 regardless of conversion. These findings show a degree of similarity to true living polymerisations that one would expect in a chain growth mechanism, which are characterised by a linear relationship between increasing degree of polymerisation of molecular weight. When **AI-1** – **AI-5** are used, the molecular weights are decreased from when DMAP alone is used, which suggests that although they do not provide a rate enhancement, that **AI-1** – **AI-5** are most

likely acting as chain transfer agents under these conditions, and at least have some interaction with the substrate, rather than being completely inert throughout.

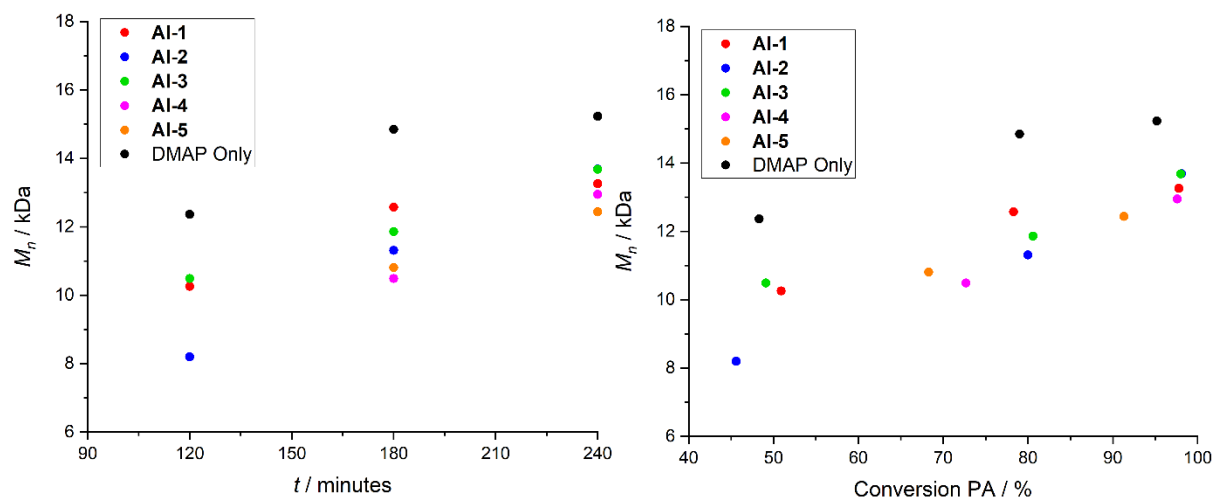


Figure 2.9: Number average molecular weight, M_n , vs. reaction time (left) and conversion PA (right) for the copolymerisation of CHO and PA with the aluminium pre-catalysts and the DMAP only reaction. Conditions: 1 eq. ($6.4\mu\text{mol}$) aluminium pre-catalyst, 1 eq. DMAP, 400 eq. PA, 2000 eq. CHO at 90°C . Molecular weights were obtained by GPC in THF, against polystyrene standards.

Despite all the polymers above showing dispersities between 1.1 and 1.2, every GPC trace was bimodal and contained two overlapping peaks. This is a common feature of copolymers made by ROCOP, and is caused by traces of hydrolysed substrate, in this case diacids or diols, which can persist despite extensive efforts to remove them.^{14,21} However, by exporting the raw data and fitting an exponentially modified Gaussian curve to each peak, it is possible to deconvolute the peaks and calculate molecular weight data for both component peaks. Exponentially modified Gaussian curves are often used to fit chromatographic peaks,³⁹ with this fitting performed in the Fityk peak fitting software (v1.3.1).⁴⁰ An example of this peak fitting can be seen in **Figure 2.10**, with this particular example taken from poly(CHO-*alt*-PA) obtained after 2 hours of reaction with **Al-1**. Clearly, following the black trace of experimental data, the higher molecular weight peak is lower in intensity, which is modelled as the blue trace. The green trace corresponds to the major, lower molecular weight peak. To ensure an adequate fit, the sum of the two fitted peaks is also shown as the red trace, which is an excellent match for the experimental data. This analysis was repeated for all five aluminium complexes and the control reactions, with the high conversion (4 hour reaction time) data presented in **Table 2.3**. This shows that the molecular weight of the sample was largely determined by the lower molecular weight peak, which was the largest in all cases. Also, the higher molecular weight peak is close to double that of the lower molecular weight peak, which is consistent with the previously discussed cause of small amounts of bifunctional initiator being present. This contrasts to another possible explanation, in that there are two different active catalysts present, each producing polymer with distinct molecular weights.

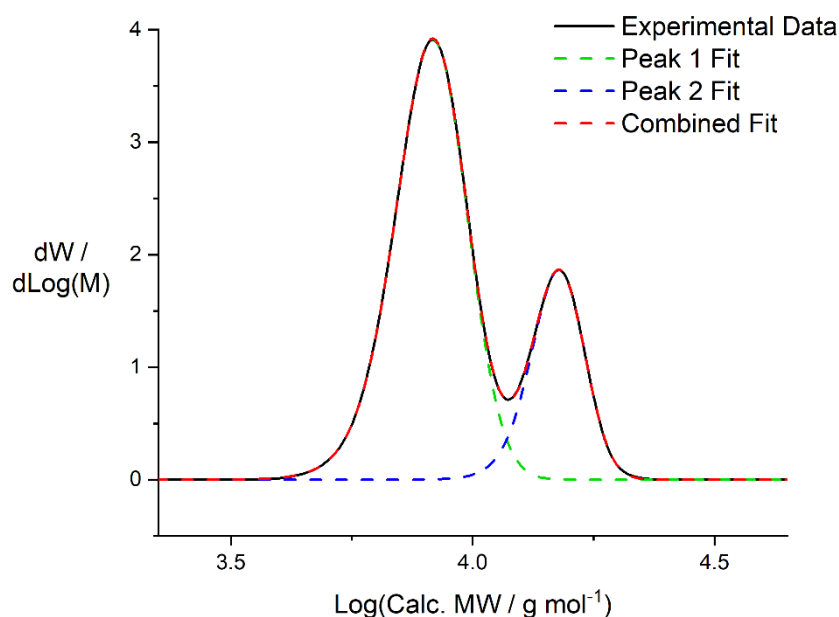


Figure 2.10: GPC chromatogram of a sample of poly(CHO-*alt*-PA) produced by **AI-1** after 2 hours reaction time, showing a bimodal trace. The two peaks were deconvoluted and modelled as exponentially modified Gaussian curves (green and blue) using the Fityk software package.⁴⁰

Table 2.3: Molecular weight data of polymers produced after 4 hour reaction times for **AI-1** – **AI-5** and with DMAP alone, as well as the individual molecular weights and polydispersities of each individual peak extracted post-deconvolution.

Catalyst	Entire Sample		Fitted Peak 1		Fitted Peak 2	
	M_n / kDa	\bar{D}	M_n / kDa	\bar{D}	M_n / kDa	\bar{D}
AI-1	13.3	1.11	12.2	1.03	20.0	1.03
AI-2	13.7	1.09	12.0	1.03	19.2	1.04
AI-3	13.7	1.13	12.4	1.04	20.9	1.02
AI-4	12.9	1.10	10.9	1.03	19.0	1.03
AI-5	12.4	1.09	10.3	1.04	18.3	1.03
DMAP	15.2	1.09	14.1	1.03	21.7	1.02

In all cases, the individual peaks showed remarkably narrow dispersities as low as 1.02, demonstrating that if traces of diacid and diol could be eliminated, that an extremely well controlled polymerisation would result. An alternative way to produce unimodal molecular weight distributions was reported in 2018 by Coates *et. al.*, and features the use of a non-initiating, non-nucleophilic analogue of complex **2.7**, where the chloride ligand is replaced with triflate.⁴¹ This, and the addition of ten equivalents of various diacids or diols as deliberate chain transfer agents did indeed produce unimodal distributions with dispersities as low as 1.04, even when a different anhydride was added after the consumption of the first to produce a block copolymer.

2.3.3: Expanding Anhydride Scope

With, at least under the conditions probed so far, little impact on either the rate of polymerisation or on molecular weight distributions, there is little to justify the use of the [Al(Salpy)Cl] complexes as pre-catalysts. However, it is possible that given there is a degree of interaction between the aluminium complexes and the substrate as chain transfer agents, that the substrate scope of the reaction could be expanded from what can be achieved using DMAP alone. An example of this was discussed in section 2.1 (**Scheme 2.6**), and so copolymerisation of anhydrides which have proved difficult were attempted.¹⁶ This includes maleic anhydride (MA) and carbic anhydride (*cis*-5-norbornene-endo-2,3-dicarboxylic anhydride, CA), itself a product of a Diels-Alder reaction of MA and cyclopentadiene, both of which are unsaturated and contain protons α - to the anhydride, albeit in sp^2 and sp^3 hybridisation respectively (**Figure 2.11**). Unfortunately, both anhydrides failed to produce polyester when copolymerisations with CHO were attempted at 90 °C using **Al-2** with one equivalent of [PPN]Cl.

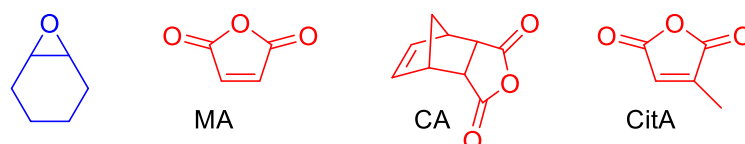


Figure 2.11: Alternative anhydrides in attempted copolymerisations with CHO. MA = maleic anhydride, CA = carbic anhydride, *cis*-5-norbornene-endo-2,3-dicarboxylic anhydride, CitA = citraconic anhydride.

Finally, citraconic anhydride (CitA, **Figure 2.11**) was attempted in copolymerisations. CitA is made from dehydrating itaconic acid, which being derived from biomass, could have potential to comprise part of a renewably sourced polyester.⁴² However, reports of its successful copolymerisation are very limited, with examples producing either broad molecular weight distributions with ambiguous selectivity and a poorly assigned polymer spectrum when copolymerised with styrene oxide,³⁷ or low levels of conversion to oligomers in a copolymerisation with a biomass-derived oxetane.⁴³ In a screening of **Al-2** and 0.9 eq. [PPN]Cl, only small amounts of polymeric material were produced after 4 hours at 80 °C. This material contained a high ether content, but tentatively appeared to have an anhydride conversion of 26.5% and a broad, polyester-like resonance at 4.3-5.1 ppm. However, MA and CitA are both susceptible to dimerisation, cross-linking, and Michael addition and so these ester-like peaks could be as a result of unwanted side reactions, as well as minor incorporation into poly(CHO).^{43,44} However, the polymers are readily soluble, and cross-linking would transform the sp^2 centres to sp^3 , yet a further resonance at 5.7-6.3 ppm remains, both of which are consistent with at least some alkene functionality surviving, as widespread cross-linking renders polymers highly insoluble. Increasing the quantity of **Al-2** fivefold moderately increased CitA conversion yet did not modify a tentatively calculated selectivity of around 30% from when one equivalent was used. [PPN]Cl

alone did not produce polymeric material at all, meaning, at least under these conditions, **AI-2** is an active catalyst, albeit in poor ester selectivity. **Figure 2.12** is a tentative assignment for poly(CHO-*alt*-CitA), with a lack of sensitivity due to low ester selectivity limiting the utility of $^{13}\text{C}\{^1\text{H}\}$ NMR and 2D experiments.

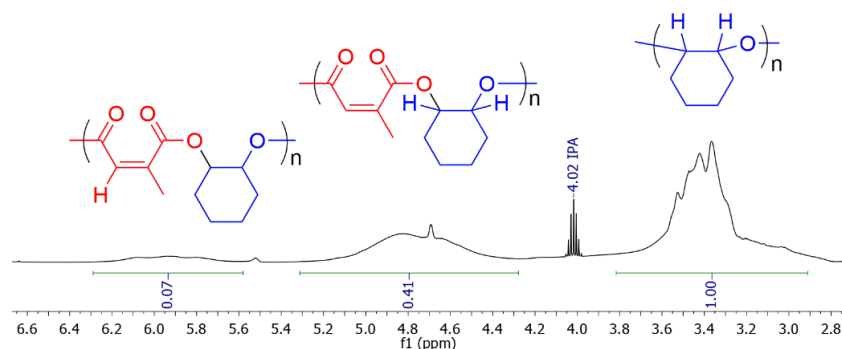


Figure 2.12: Tentative assignment of the polymeric resonances in a sample of poly(CHO-*alt*-CitA) with a high (71%) ether content.

2.4: Mechanistic Investigations: Stoichiometric Reactions

To try to understand the reasons for the poor catalytic performance of the Salpy complexes, stoichiometric reactions between **AI-2** (chosen due to its high solubility in CDCl_3) and ROCOP substrates were performed. Firstly, the regioselectivity of epoxide insertion into the Al-Cl bond of **AI-2** was investigated using epichlorohydrin (ECH), with both regiochemical possibilities for alkoxide formation indicated in **Figure 2.13**. This includes attack at the least hindered carbon to give **AI-2***, or at the most hindered for **AI-2'**. After addition of one equivalent (32 μmol) of ECH to **AI-2** in CDCl_3 solution with overnight heating to 60 $^\circ\text{C}$, the distinctive signal for the H^6 proton (*ortho* to the pyridyl nitrogen, $\delta_{\text{H}} = 9.61$ ppm) had been split into two resonances; one unchanged from that of **AI-2**, and another, with the same line shape and multiplicity, shifted downfield to $\delta_{\text{H}} = 9.25$ ppm. These two peaks presented in a 1:1 ratio, meaning 50% of **AI-2** had reacted with ECH to form an alkoxide product. Addition of excess ECH and further heating led to the complete disappearance of the H^6 signal for **AI-2**, with the new downfield signal at 9.25 ppm now dominant. Alongside this shift in the H^6 proton, the CH_2 resonances on the ligand backbone became far sharper, whilst there are also two new resonances, in a 4:1 ratio, in the alkoxide region of the ^1H NMR spectrum, with the less intense peak being in a 1:1 ratio with the shifted H^6 peak, suggesting a 1:1 reaction. This is consistent with the formation of **AI-2*** as the major regioisomer. Interestingly, there is another species present in about 5% abundance compared to **AI-2***. This species shows a similar pattern of resonances, albeit with a H^6 proton shifted further downfield to 8.59 ppm. This chemical shift is far more similar to the pro-ligand ($\delta_{\text{H}} = 8.35$ ppm), raising the possibility that this species could be the five coordinate, pyridyl decoordinated complex **AI-**

2**. However, these resonances could also be caused by the minor regioisomer of insertion, **AI-2'**, which, at an observed regioselectivity of 95%, is consistent with literature reports involving propylene oxide inserting at **2c**.² The three spectra are displayed in **Figure 2.14**, which detail how **AI-2** is completely consumed after addition of excess ECH.

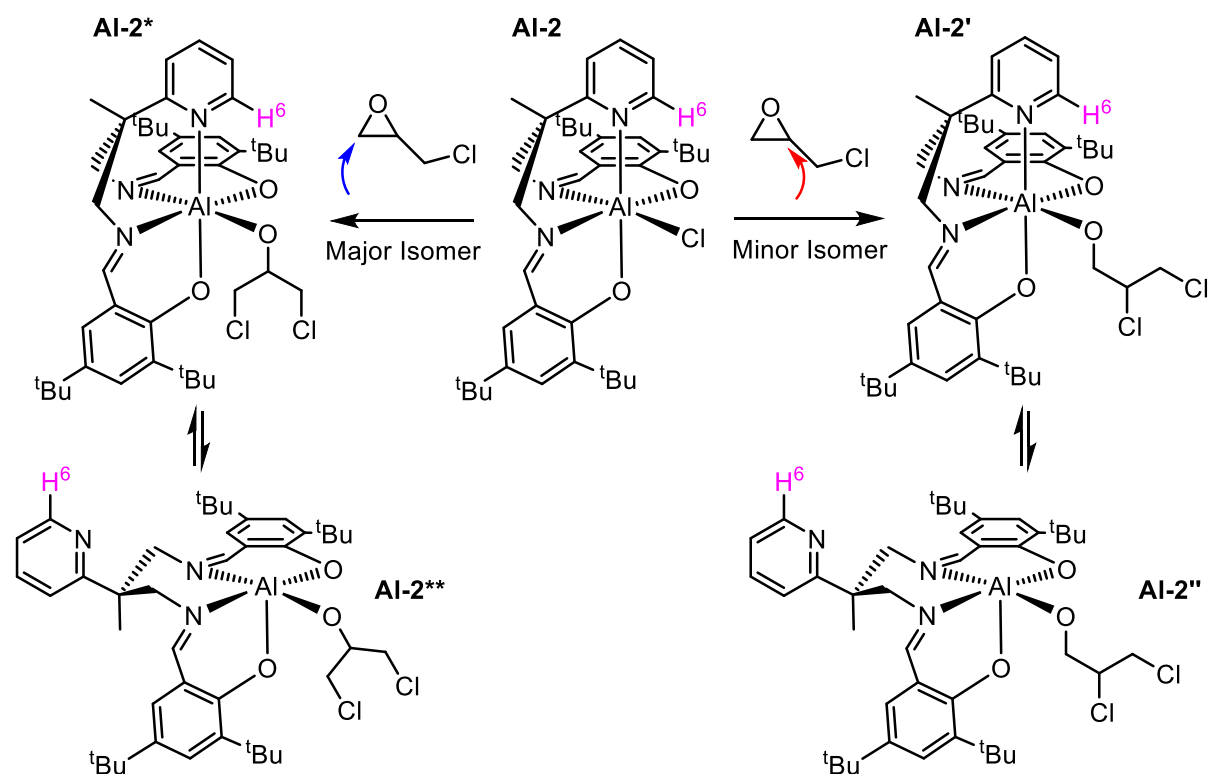


Figure 2.13: The two regiochemical possibilities for chloride opening of epichlorohydrin at **AI-2**. Also indicated are the equivalent five-coordinate complexes with the pyridyl donor de-coordinated.

Reaction of this sample with one equivalent of [PPN]Cl and two equivalents of PA shifted both H^6 signals (for both the major and minor isomer), and the previously vacant ester region (5.0- 5.5 ppm) of the spectrum became populated, indicating the likely formation of an aluminium carboxylate complex. This is clear evidence that **AI-2** (and thereby most likely to other Salpy complexes) are reactive towards epoxides and anhydrides, and can facilitate their ring-opening. Indeed, analogous experiments were performed using CHO in place of ECH, which, upon work up (addition of MeOH) and analysis by electrospray ionisation mass spectrometry (EI-MS) showed oligomers of CHO-*alt*-PA. The ions detected are shown in **Figure 2.15**, and include epoxide terminated chains in positive mode (along with unreacted PA, [PPN]⁺, and [AI-2(-Cl)]⁺), and a more extensive series of oligomers in negative mode, alongside an anionic mono(methoxy), mono(acetate) aluminium complex. These ligands are most likely a result of reaction during the work up and with the NaOAc ion source respectively. No oligomers bound to aluminium were detected, with this either due to cleavage during work up or in the mass spectrometer, or that propagating chains are not present at the aluminium centre at all.

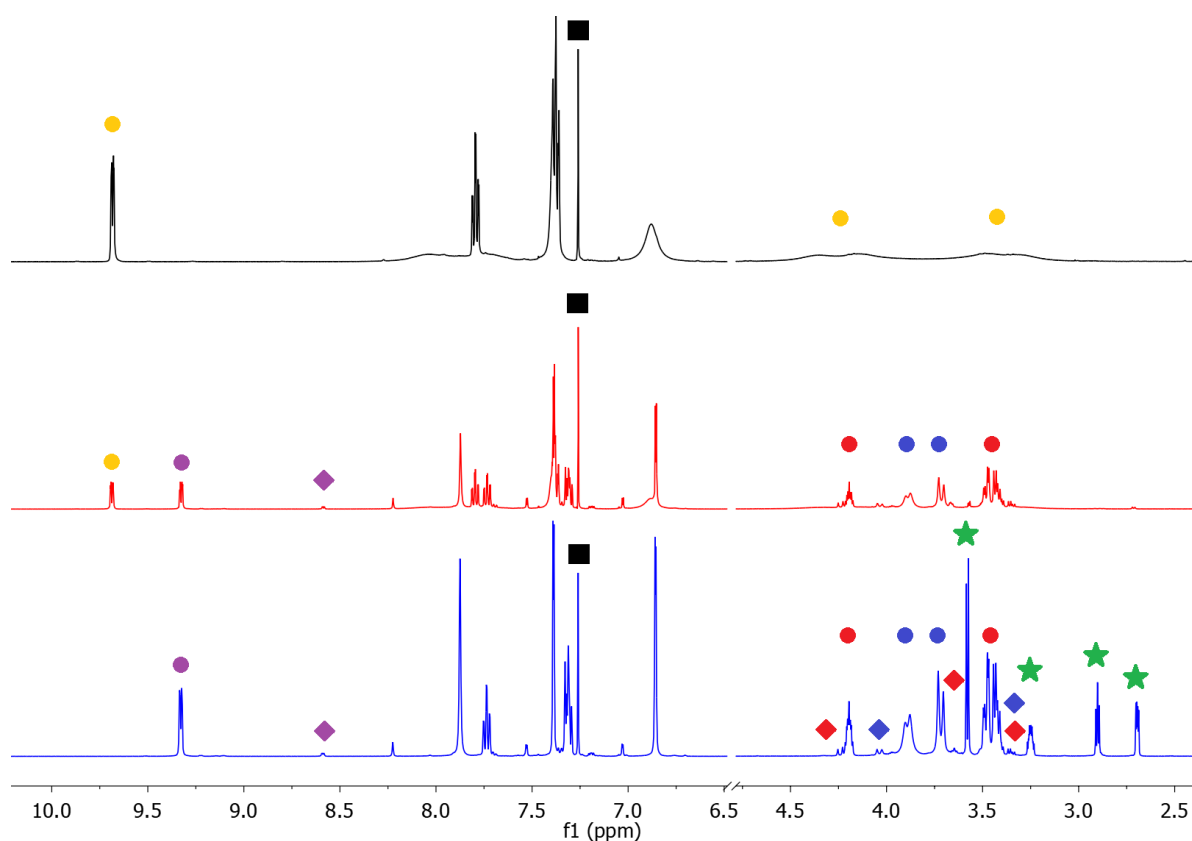


Figure 2.14: Stacked ^1H NMR spectra (CDCl_3 , 500 MHz) of top (black): **Al-2**, middle (red): reaction of **Al-2** with one equivalent ECH heated to 60°C , bottom (blue): as above with excess ECH. Yellow = unreacted **Al-2** (H^6 proton at 9.61 ppm, CH_2s of ligand backbone 3.4 – 4.5 ppm). Purple circles = H^6 proton of product alkoxide, red circles = ring-opened ECH, blue circles = CH_2s of the ligand backbone after ring-opening. Diamonds of a given colour indicate equivalent peaks in minor isomer. Green stars = unreacted ECH. Black square = CDCl_3 .

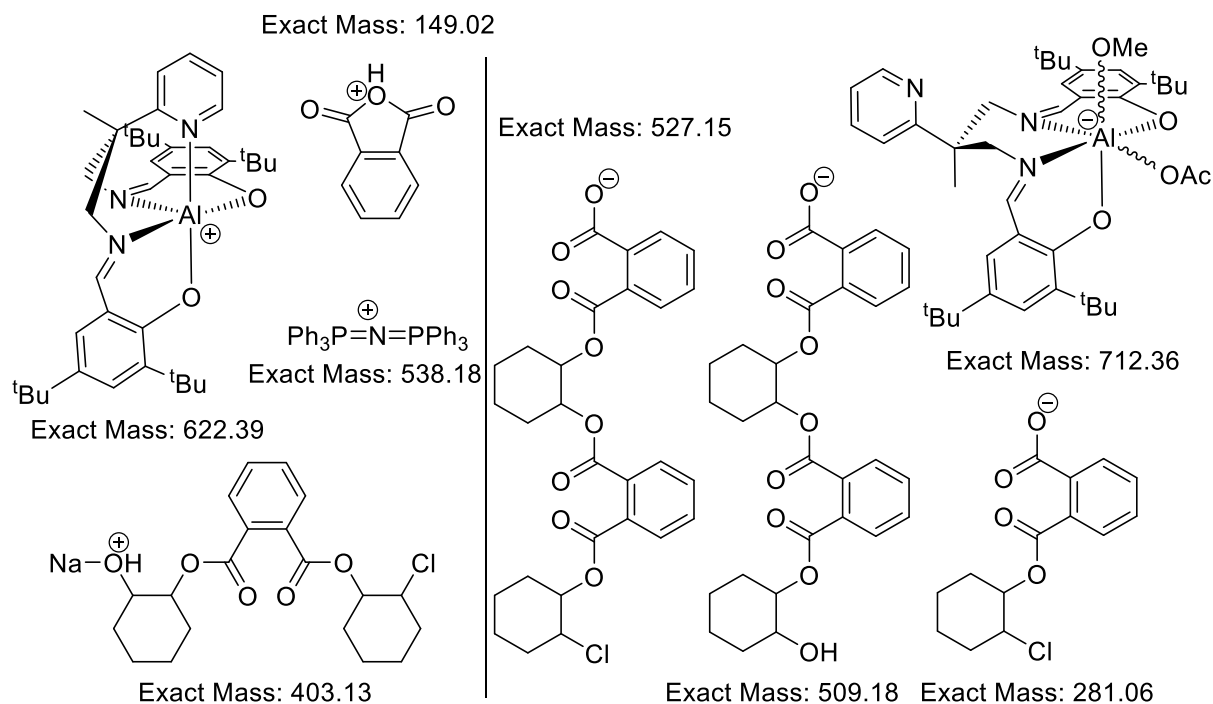


Figure 2.15: Fragments detected by EI-MS post MeOH work up from a reaction of **Al-2** (1 eq.), [PPN]Cl (1 eq.), CHO (4 eq.) and PA (2 eq.) in CDCl_3 . Both positive (left) and negative (right) modes were employed.

2.5: Mechanistic Investigations: DFT Calculations

To try to understand potential reasons for the lack of catalytic activity shown by the [Al(Salpy)Cl] complexes under the conditions tested so far, a series of DFT calculations were performed. Calculations were performed using the M06-2X density functional given its previous use in the field within the Gaussian 09 suite.^{2,45,46} The cc-pVDZ and cc-pVTZ double and triple- ζ basis sets were both used, with diffuse functions added to aluminium in both cases.⁴⁷⁻⁴⁹ Implicit THF solvent was also modelled in each calculation, as a close mimic to the excess CHO present under experimental conditions.⁵⁰ Structures were allowed to relax unconstrained except in the case of transition states, where bond lengths relevant to the reaction coordinate were scanned at small intervals to approximate the saddle point, before submission to a transition state calculation. All minima and saddle points were confirmed as such by performing frequency calculations, returning zero or one (which upon animation resembled the reaction coordinate) imaginary frequency respectively. This also allowed thermochemical data (enthalpy, free energy) to be computed for each structure within the catalytic cycle. For reasons of computational simplicity, the unsubstituted complex **Al-1** was modelled as the aluminium centre.

Calculations into the propagation cycle would take the previously modelled mechanism reported by Coates *et. al.* as a starting point, but with the use of CHO and PA (rather than propylene oxide and succinic anhydride) as more relevant substrates.² Further considerations made included modelling intermediates with the pyridyl of the Salpy ligand coordinated and decoordinated, and to the change in geometry in the aluminium complex. In the Coates mechanism, two polymer chains propagate *trans* to one another, with anhydride opening occurring in a single step by metal-alkoxide insertion into a non-metal bound anhydride. However, despite extensive searching, in this study, no transition states of this type could be found. Instead, a viable two step intramolecular anhydride insertion pathway whereby a metal-alkoxide undergoes migratory insertion into a metal-bound anhydride, before subsequent ring-opening produces a carboxylate complex, was found. This pathway is analogous to that invoked in the ROP of lactones⁵¹⁻⁵⁴, and in a recent ROCOP report also featuring a catalyst of *cis* symmetry.⁵⁵ The full array of structures modelled in this study is shown in **Figure 2.16**, with **Int0**, an anionic bis(carboxylate) complex, set as 0.0 kcal mol⁻¹, analogously to Coates *et. al.*² However, in-keeping with the use of PA as a substrate, the carboxylate ligands of **Int0** and all subsequent structures were modelled as methyl phthalate (OP in **Figure 2.16**), rather than acetate.

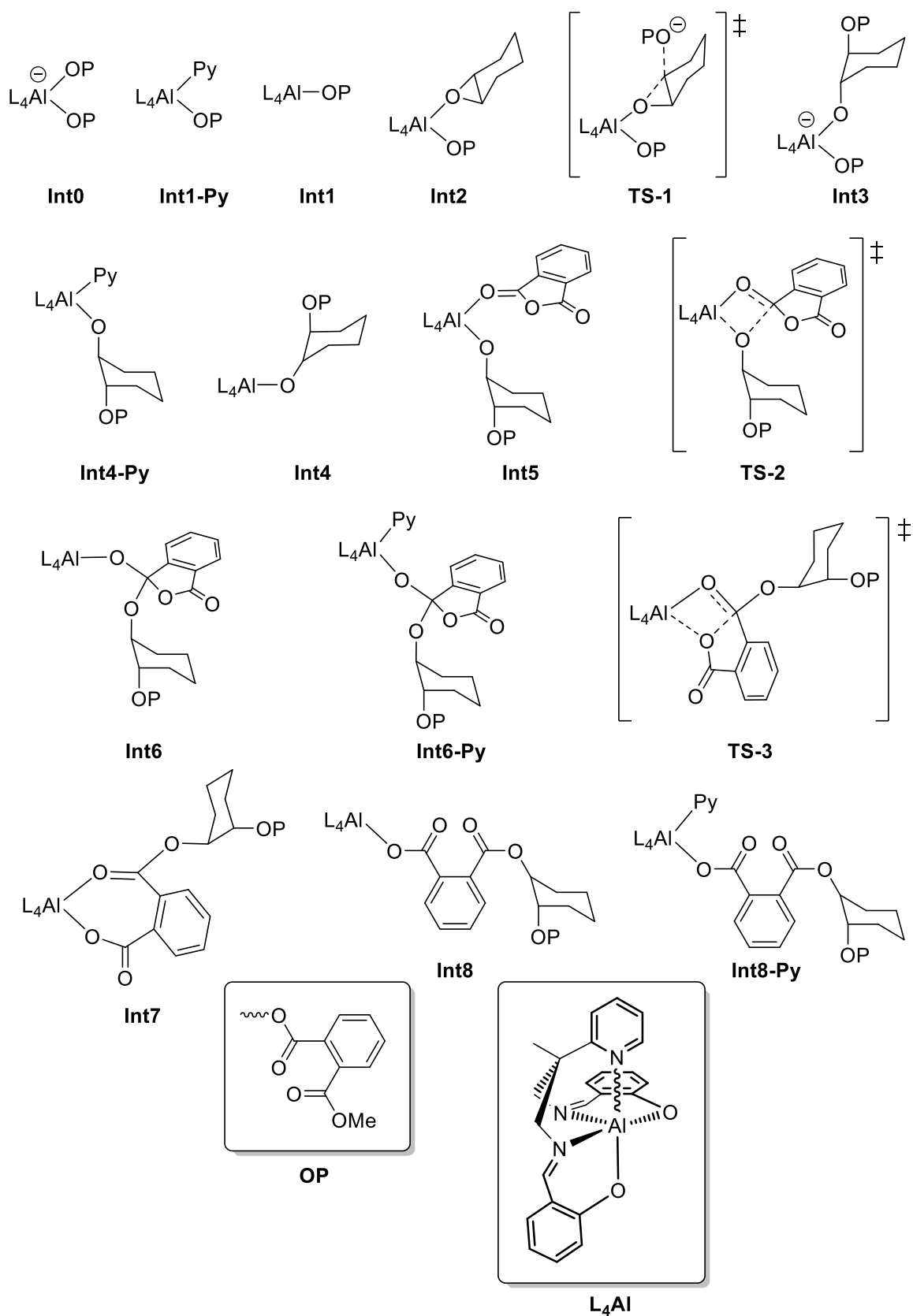


Figure 2.16: Structures modelled by DFT calculations (M06-2X/cc-pV(D+d(Al))Z and cc-pV(T+d(Al))Z) in this study. Py= pyridyl donor of the Salpy ligand of **Al-1**, with intermediates with it pendant and bound indicated.

Structures were originally relaxed in a double- ζ basis set prior to submission at a triple- ζ level of theory to minimise computational cost. The energy profile of the reaction at double- ζ level is shown in **Figure 2.17**, with the labels of each structure taken from **Figure 2.16**. As expected from experimental reactions which were zero order in anhydride, epoxide opening (**TS1**) represents the highest energy barrier in the cycle, at +25.1 kcal mol⁻¹ compared to **Int0**, and 18.8 kcal mol⁻¹ higher than the proceeding **Int2**, where CHO is bound to the aluminium centre. This step features an external carboxylate acting as a nucleophile, rather than a migratory insertion from the *cis* carboxylate ligand, in contrast to a recent report investigating titanium-catalysed ROCOP.⁵⁵ Epoxide opening leads to the formation of **Int3** in a highly favourable process, before on-metal anhydride insertion (**TS2**) and ring-opening (**TS3**) produces the mono(κ^2 -carboxylate) complex **Int7**. Pyridyl coordination in **Int8-Py** then gives a complex analogous to **Int1-Py**, with this energy difference of -14.8 kcal mol⁻¹ showing that the process is spontaneous ($\Delta G < 0$). Analysis of the reaction enthalpy also indicates the reaction is exothermic by -41.3 kcal mol⁻¹, with these enthalpies shown alongside free energies in **Scheme 2.12** for all structures.

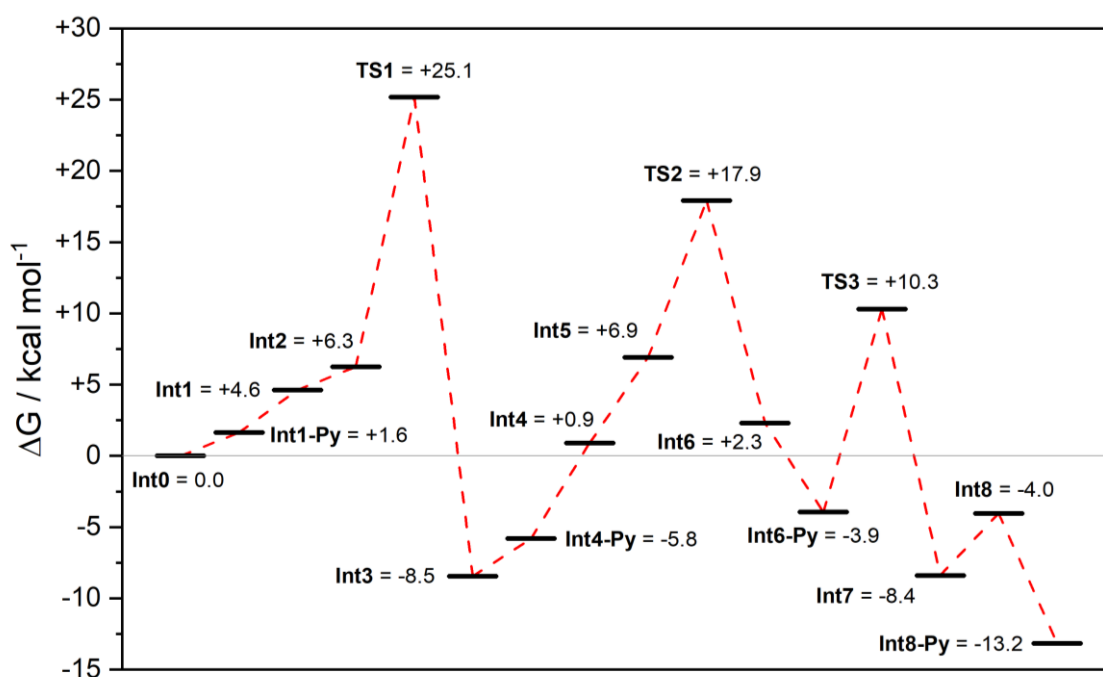
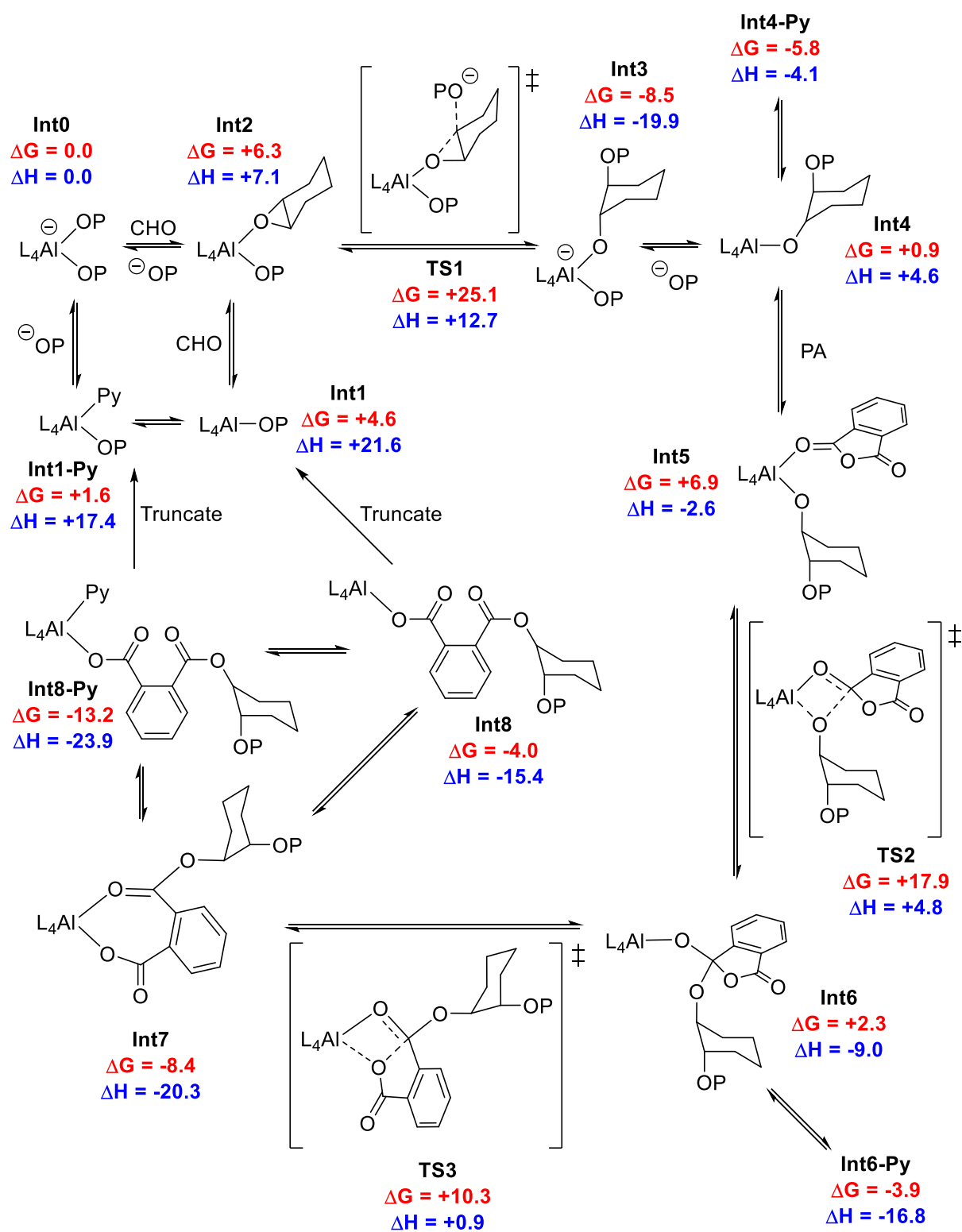


Figure 2.17: Free energies of an energetically feasible catalytic cycle for the ring opening of CHO and PA at **Al-1**. As calculated in Gaussian 09 at the M06-2X/cc-pV(D+d)Z level of theory. All values are quoted in kcal mol⁻¹.

The structures obtained in the feasible cycle in **Scheme 2.12** were then recalculated at a higher level of theory, using the cc-pV(T+d)Z triple- ζ basis set. This increases the number of functions used to describe each atomic orbital by two to three, which means each orbital is more accurately represented, albeit at a higher computational cost.^{47,56} Therefore, it is convenient to first calculate structures at double- ζ , and then triple- ζ , rather than immediately in triple- ζ .



Scheme 2.12: Free energies and enthalpies (in kcal mol⁻¹) of an energetically realistic ring-opening of CHO and PA at Al-1, at the M06-2X(cc-pVDZ(+d for Al)) level of theory, in implicit THF solvent, as calculated in Gaussian 09. The structures of **Int4-Py** and **Int6-Py** are not shown but are drawn in **Figure 2.16**, as are the structures of L₄Al and OP (methyl phthalate).

The same energy profile for the ring-opening of CHO and PA at **AI-1** is presented in **Figure 2.18**, with the energies at both double and triple- ζ indicated. Unfortunately, **TS2** failed to converge at triple- ζ level, likely because of a very shallow potential energy surface meaning conversion criteria could not be met. However, the lowest energy structure still only returned on imaginary frequency which resembled the reaction coordinate, and so the energy quoted is likely to be similar to the true energy. Interestingly, **Int1-Py** and **Int1** are both lower in energy (by 4.3 and 4.9 kcal mol⁻¹ respectively) at triple- ζ level than at double- ζ . However, **TS1** is also higher in energy at triple- ζ , whilst also having a higher free energy of activation ($\Delta G^\ddagger = 23.4$ and 18.9 kcal mol⁻¹ for triple and double- ζ respectively) than in double- ζ . The product of epoxide opening (**Int3**) is also significantly (6.5 kcal mol⁻¹) higher in energy at triple- ζ . Interestingly, the bis(carboxylate) complex **Int0** is marginally (+4.0 kcal mol⁻¹) higher in energy than **Int1-Py**, meaning this would be expected to be the predominant resting state of the catalyst given it is the lowest energy intermediate before the rate limiting **TS1**. However, the energy differences to both **Int0** and **Int1** are both small, and so there is presumably a fairly even equilibrium between the three.

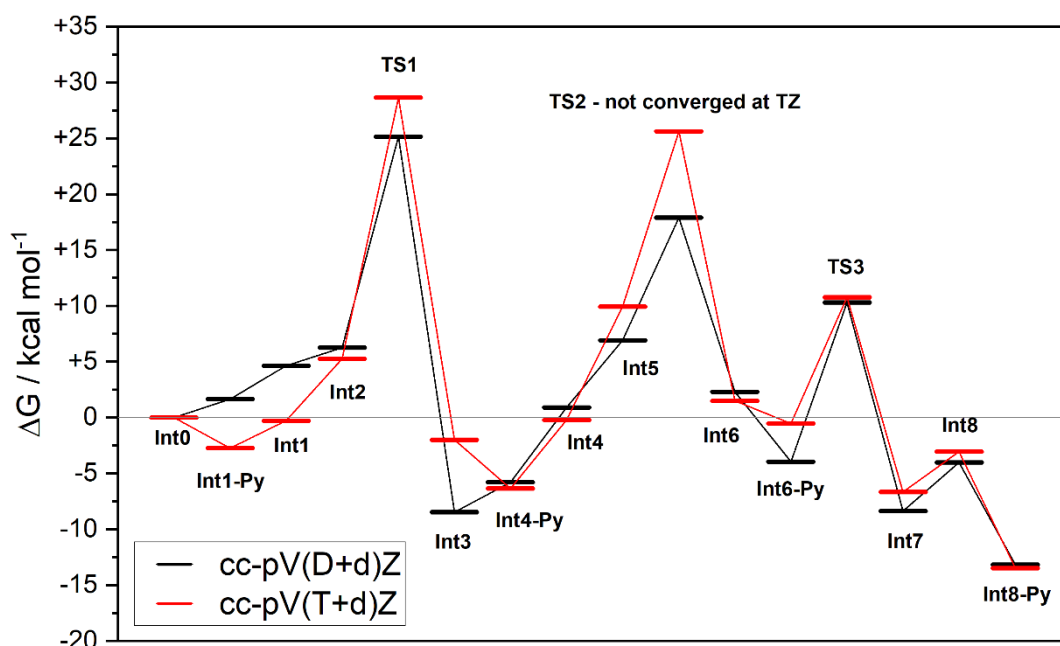


Figure 2.18: Comparison of free energies for the ring-opening of CHO and PA at **AI-1** for the M06-2X density functional using both double and triple- ζ basis sets.

Despite the increased energy and activation energy of **TS2** (G increased by 7.7 kcal mol⁻¹, ΔG^\ddagger increased by 4.7 kcal mol⁻¹) epoxide opening (**TS1**) remains the highest energy structure and highest energy barrier in the catalytic cycle at triple- ζ level. The energies in the rest of the cycle are largely similar, in both magnitude and their relative ordering. Again, the cycle is both spontaneous ($\Delta G = -10.7$ kcal mol⁻¹ from **Int1-Py** to **Int8-Py**) and exothermic ($\Delta H = -35.8$ kcal mol⁻¹ from **Int1-Py** to **Int8-Py**).

As well as calculating a catalytic cycle for poly(CHO-*alt*-PA), two anhydrides which experimentally failed to polymerise in maleic anhydride (MA) and carbic anhydride (CA, *cis*-5-norbornene-endo-2,3-dicarboxylic anhydride) were also investigated, to try to rationalise experimental findings. An additional stereochemical consideration must be made for CA, as, unlike PA and MA, CA is not flat and can coordinate through the carbonyl group α to either its *R* or *S* stereocentre. The relevant intermediates and transition states are depicted in **Figure 2.19**, with both pathways indicated (some intermediates are not shown, but were calculated regardless). In these examples, the structures are drawn in the same orientation apart from which face of the anhydride is coordinated, but are free to rotate when relaxed to minimise energy (*i.e.* in the (*SR*) pathway, the methylene bridge is always pointing upwards out of the plane, but in reality can also point downwards with a simple rotation of the Al-O=C axis). A further complication comes from the nomenclature of each pathway, as insertion α to the *R* stereocentre leads to a product with the *S* stereocentre at the aluminium-bound end of the polymer chain. Both pathways, the (*RS*) and (*SR*), are named as such to describe the distribution of stereocentres reading outwards from the aluminium after ring-opening has occurred.

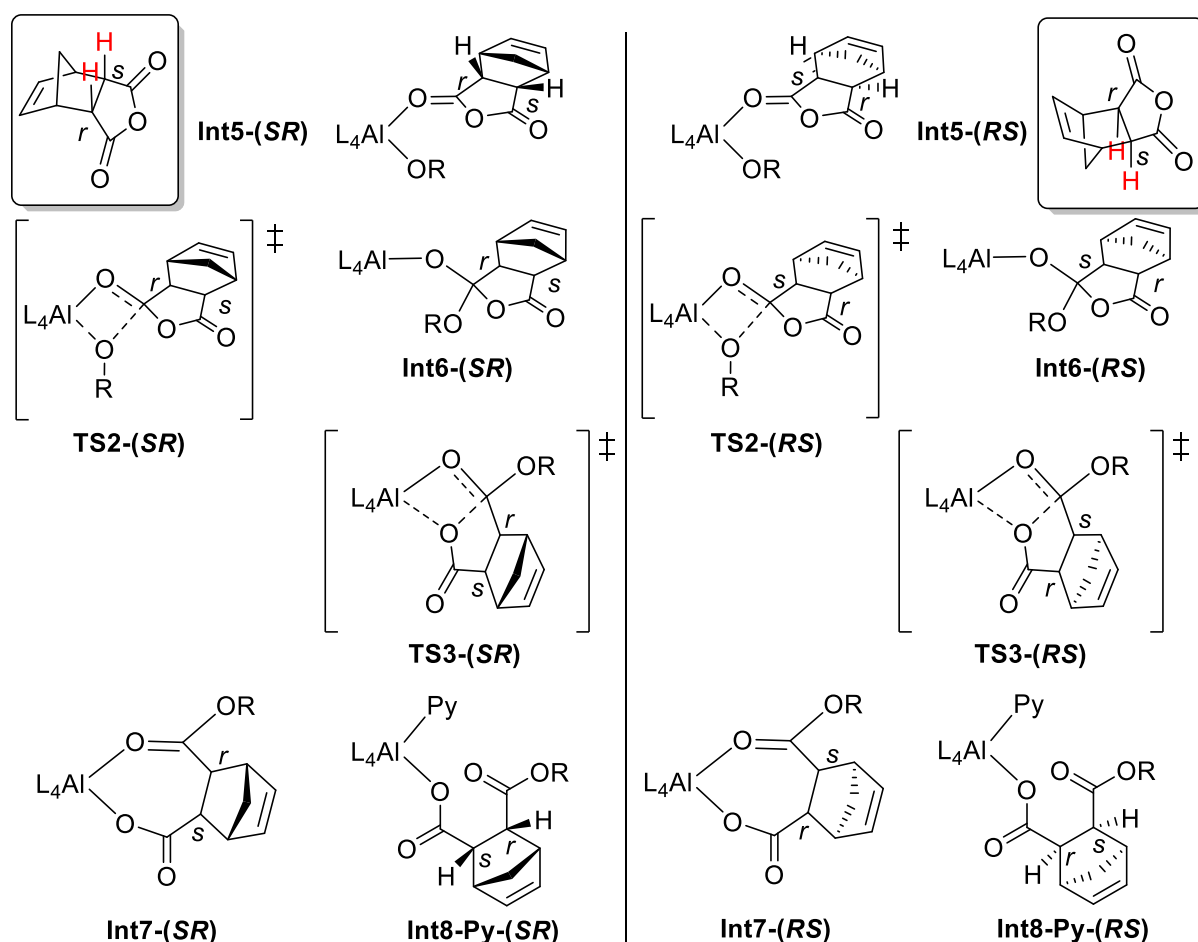


Figure 2.19: Selection of intermediates and transition states for the ring-opening of carbic anhydride at Al-1, showing both stereochemical outcomes, where reading from aluminium outwards, the product contains a (*SR*) (left) or (*RS*) (right) orientation of stereocentres. OR = ring-opened CHO-methyl ester of CA. M06-2X(cc-pVDZ(+d for Al)) level of theory.

Cycles were calculated in an analogous way to PA, but with replacement of the anhydride and the carboxylate ligands and nucleophile, which were modelled as the methyl ester of the ring-opened anhydride in question. All calculations in this instance were performed at the M06-2X/cc-pV(D+d)Z level of theory. The results of all four cycles (PA, MA, CA-(RS), CA-(SR), both CA pathways are identical until Int5, before which only CA(RS) is plotted)) are shown in **Figure 2.20**, and tabulated in **Table 2.4**.

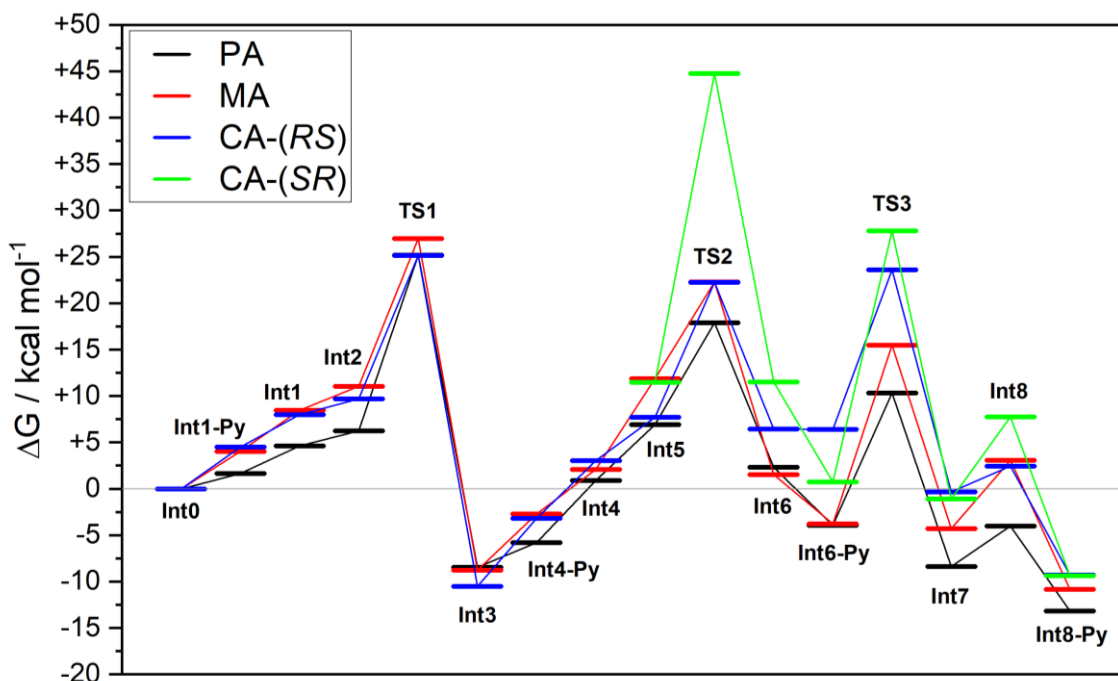


Figure 2.20: Free energies of the ring opening of CHO and either PA, MA or CA (both stereochemical outcomes) at **Al-1**. As calculated in Gaussian 09 at the M06-2X/cc-pV(D+d)Z level of theory.

Table 2.4: Free energies of ring opening of CHO and each anhydride at **Al-1**, in kcal mol⁻¹. All calculations were performed at the M06-2X/cc-pV(D+d)Z level of theory, with implicit THF solvent in Gaussian 09.

Structure	G / kcal mol ⁻¹			
	PA	MA	CA-(RS)	CA-(SR)
Int0	0.0	0.0		0.0
Int1-Py	+1.6	+4.0		+5
Int1	+4.6	+8.5		+8.0
Int2	+6.3	+11.0		+9.7
TS1	+25.2	+27.0		+25.1
Int3	-8.5	-8.8		-10.5
Int4-Py	-5.8	-2.7		-3.2
Int4	+0.9	+2.1		+3.0
Int5	+6.9	+11.9	+7.7	+11.5
TS2	+17.9	+22.3	+22.2	+44.8
Int6	+2.3	+1.5	+6.4	+11.5
Int6-Py	-3.9	-3.8	+6.4	+0.7
TS3	+10.3	+15.5	+23.6	+27.8
Int7	-8.4	-4.3	-0.3	-1.1
Int8	-4.0	+3.1	+2.4	+7.7
Int8-Py	-13.2	-10.8	-9.3	-9.4

The start of the cycles between **Int0** and **Int3** are largely similar, with the energies of **TS1** all within 1.8 kcal mol⁻¹ of each other, with MA the highest of the three. Again, the energies are comparable until **Int5**, where anhydride coordination occurs, where there is a small gap between PA and MA coordination, as well as a gap between coordination in the (*RS*) and (*SR*) pathway for CA. This difference is multiplied for **TS2**, where PA is the lowest in energy at +17.9 kcal mol⁻¹, MA and CA-(*RS*) are similar at 22.3 and 22.2 kcal mol⁻¹ respectively, and CA-(*SR*) is far higher in energy at 44.8 kcal mol⁻¹. The reasons for this enormous discrepancy is unclear, but could be due to the very specific steric demands placed on the substrate by the chiral ligand scaffold of **Al-1**. Indeed, one might expect that if the enantiomer of **Al-1** was calculated, then the energies of both CA pathways may be reversed. Also, the use of real substrates means the conformational space to be explored by each calculation is huge, and there is little way of knowing whether each minimum is a local minimum or a true minimum (for a given structure). This complexity is one of the reasons why simplified substrates are often employed, as there is far less conformational ambiguity in smaller molecules, meaning one can be more satisfied that a given structure is indeed a true minimum. Conversely however, the energies of the intermediates after **TS2** are much more alike for both CA pathways (albeit (*SR*) is generally higher in energy), and so it also possible that the conformational space has been adequately explored, and that the **TS2** is simply unfavourable when CA coordinates in the (*SR*) pathway. This can be seen when examining the simplified structures as shown in **Figure 2.21**, where the (*RS*) pathway (top) has the bulk of the CA ring, including the C₂H₂ bridge pointing upwards, away from the inserting alkoxide. This contrasts with the (*SR*) pathway (bottom), where the CA ring is bent downwards, increasing the steric congestion and the energy as a result.

For both MA and CA, anhydride insertion and opening (**TS2**, **TS3**) is higher in energy than for PA. However, this increase in energy seems unlikely to be the reasons why experimentally these substrates fail to polymerise, as in all cases the magnitude of the energies do not preclude reaction, especially at 80 °C. Even when considering energies of activation when going from **Int5** to **TS2**, and **Int6** to **TS3**, the energies of activation for MA (10.4 and 19.3 kcal mol⁻¹ respectively) and CA-(*RS*) (14.5 and 17.2 kcal mol⁻¹) when compared to PA (11.0 and 14.2 kcal mol⁻¹) do not represent differences to the extent that one would expect such extreme differences in experimental reactivity. Therefore, it is likely that a separate process is responsible for this difference. One explanation for this could be that, given both the non-existent rate enhancement seen experimentally in section 2.3.2 and the observed opening of epoxides in stoichiometric reactions in section 2.4, that the catalytic cycle does not extend past the favourable formation of epoxide at to reach **Int5**. In order to ring-open an anhydride, there is a significant increase in energy to reach **Int5**, which also relies on the pyridyl donor being de-

coordinated. Given that both **Int3** and **Int4-Py** are in all cases significantly lower in energy than **Int5**, the equilibrium between the three would lie towards **Int3** and **Int4-Py**, thereby limiting anhydride coordination and reaction, especially when there is another energy barrier to insertion at **TS2**. This could be an example where the system is under a thermodynamic control, rather than kinetic control where one would expect the relatively small barriers at **TS1-3** to be readily overcome. Herein lies a major difference to the previous mechanistic work described by Coates *et. al.*, where a transition state to anhydride opening was found where pre coordination was not necessary, meaning there is no such competition for metal binding and the system may be under kinetic control.²

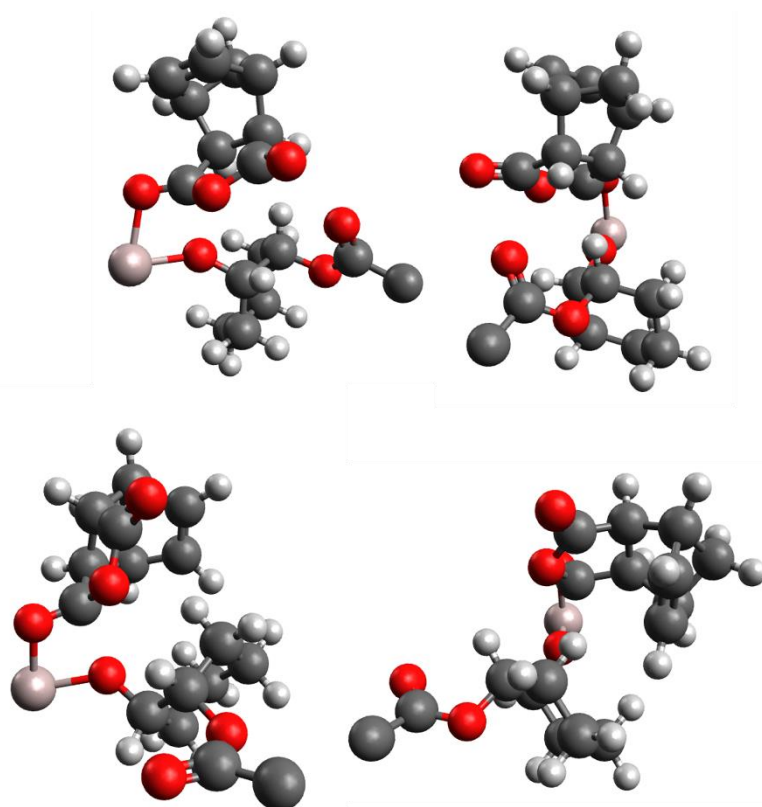


Figure 2.21: Simplified (ligands omitted, polymer chain truncated as opened-CHO-CO₂C for clarity) structures of top: **TS2-CA-(RS)** and bottom: **TS2-CA-(SR)**. Pink = aluminium, red = oxygen, grey = carbon, white = hydrogen.

This apparent competition between the pyridyl donor and anhydride coordination may be the reason for poor catalytic performance, as, rather than assist in the de-coordination of carboxylates to aid epoxide coordination as was originally hypothesised, the pyridyl may be out competing anhydride and limiting turnover. The difference in experimental reactivity between PA, MA and CA would then be determined by the properties of the DMAP-only control reaction, which were not studied here. Interestingly, [PPN]Cl has been reported to catalyse the copolymerisation of CHO and CA under conditions where DMAP appeared inactive, meaning the lack of conversion observed in section 2.3.2 is not surprising.³³

2.6: Summary

Four novel [Al(Salpy)Cl] complexes, **AI-1** – **AI-4**, were synthesised and characterised, with the ONNO unit of the two phenoxy-imine units bound in a β -*cis* arrangement, as evidenced by the change in symmetry from pro-ligand to complex observed by NMR, and X-ray crystallography. This geometry contrasts to the widely studied planar Salph ligands, as well as **AI-5**, which was synthesised for comparative purposes. Analysis of the single crystal X-ray structures showed bond lengths within the expected range for each bond about the aluminium centre.

In terms of catalytic activity, **AI-2** alongside two equivalents of [PPN]Cl produced a linear relationship between anhydride conversion and time, indicating the reaction was zero-order in anhydride and that epoxide opening was rate limiting. Under these conditions, as well as when one equivalent of DMAP was used in place of [PPN]Cl, there was no observable rate increase with or without a [Al(Salpy)Cl] complex (including for the *trans* orientated **AI-5**). Molecular weight distributions were bimodal in each case, likely due to traces of diacid or diol in the reaction mixture. Bimodal distributions were deconvoluted into separate peaks, the individual polydispersities of which were as low as 1.02, indicating a highly controlled polymerisation. The addition of **AI-2** to reaction mixtures of CHO and either MA or CA failed to produce polymer, and a high ether content polymer was produced for the biomass derived anhydride CitA.

Stoichiometric reactions of **AI-2** showed it regioselectively ring-opened epichlorohydrin at its least hindered carbon in the absence of co-catalyst. A minor isomer in the reaction mixture was identified as either a five-coordinate pyridyl de-coordinated isomer, or the minor regioisomer of insertion. Analogous reactions with CHO produced chloride initiated oligomers in the EI-MS spectrum of the concentrated reaction mixture.

DFT calculations aimed to rationalise the reasons for the poor activity of the complexes. An energetically feasible cycle for the ring opening of CHO and PA was presented at both double and triple- ζ level, whilst two more anhydrides, MA and CA, were calculated at double- ζ level only. Despite differences in energy, there appeared nothing to preclude the reaction of these substrates in terms of the height of the energy barriers to be overcome. Instead, it seems likely that, coupled with the lack of rate enhancement seen experimentally, that the catalytic cycle is equilibrium limited, and that the high favourability of pyridyl coordination over anhydride coordination limits further reactivity.

2.7 References for Chapter 2

- 1 K. A. Andrea, H. Plommer and F. M. Kerton, *Eur. Polym. J.*, 2019, **120**, 109202.
- 2 M. E. Fieser, M. J. Sanford, L. A. Mitchell, C. R. Dunbar, M. Mandal, N. J. Van Zee, D. M. Urness, C. J. Cramer, G. W. Coates and W. B. Tolman, *J. Am. Chem. Soc.*, 2017, **139**, 15222–15231.
- 3 N. J. Van Zee, M. J. Sanford and G. W. Coates, *J. Am. Chem. Soc.*, 2016, **138**, 2755–2761.
- 4 T. Aida and S. Inoue, *J. Am. Chem. Soc.*, 1985, **107**, 1358–1364.
- 5 R. Baumgartner, Z. Song, Y. Zhang and J. Cheng, *Polym. Chem.*, 2015, **6**, 3586–3590.
- 6 Y. Liu, J.-Z. Guo, H.-W. Lu, H.-B. Wang and X.-B. Lu, *Macromolecules*, 2018, **51**, 771–778.
- 7 T. Stößer and C. K. Williams, *Angew. Chemie Int. Ed.*, 2018, **57**, 6337–6341.
- 8 D. J. Darensbourg, R. R. Poland and C. Escobedo, *Macromolecules*, 2012, **45**, 2242–2248.
- 9 C. Chatterjee and M. H. Chisholm, *Inorg. Chem.*, 2012, **51**, 12041–12052.
- 10 A. M. Diccio, J. M. Longo, G. G. Rodríguez-Calero and G. W. Coates, *J. Am. Chem. Soc.*, 2016, **138**, 7107–7113.
- 11 M. Hatazawa, R. Takahashi, J. Deng, H. Houjou and K. Nozaki, *Macromolecules*, 2017, **50**, 7895–7900.
- 12 Y. Hiranoi and K. Nakano, *Beilstein J. Org. Chem.*, 2018, **14**, 2779–2788.
- 13 N. J. Van Zee and G. W. Coates, *Angew. Chemie - Int. Ed.*, 2015, **54**, 2665–2668.
- 14 M. J. Sanford, L. Peña Carrodeguas, N. J. Van Zee, A. W. Kleij and G. W. Coates, *Macromolecules*, 2016, **49**, 6394–6400.
- 15 T. Stößer, D. Mulryan and C. K. Williams, *Angew. Chemie - Int. Ed.*, 2018, **57**, 16893–16897.
- 16 H. Zhang, G. Zhou, M. Jiang, H. Zhang, H. Wang, Y. Wu and R. Wang, *Macromolecules*, 2020, **53**, 5475–5486.
- 17 B. A. Abel, C. A. L. Lidston and G. W. Coates, *J. Am. Chem. Soc.*, 2019, **141**, 12760–12769.
- 18 F. Isnard, F. Santulli, M. Cozzolino, M. Lamberti, C. Pellicchia and M. Mazzeo, *Catal. Sci. Technol.*, 2019, **9**, 3090–3098.
- 19 L. Peña Carrodeguas, C. Martín and A. W. Kleij, *Macromolecules*, 2017, **50**, 5337–5345.
- 20 F. Della Monica and A. W. Kleij, *ACS Sustain. Chem. Eng.*, 2021, **12**, 17.

- 21 A. Brandolese, F. Della Monica, M. À. Pericàs and A. W. Kleij, *Macromolecules*, 2022, **55**, 2566–2573.
- 22 J. Li, Y. Liu, W. M. Ren and X. B. Lu, *Proc. Natl. Acad. Sci. U. S. A.*, 2020, **117**, 15429–15436.
- 23 J. Li, B.-H. Ren, S.-Y. Chen, G.-H. He, Y. Liu, W.-M. Ren, H. Zhou and X.-B. Lu, *ACS Catal.*, 2019, **9**, 1915–1922.
- 24 M. J. Sanford, N. J. Van Zee and G. W. Coates, *Chem. Sci.*, 2018, **9**, 134–142.
- 25 F. Isnard, M. Lamberti, C. Pellicchia and M. Mazzeo, *ChemCatChem*, 2017, **9**, 2972–2979.
- 26 F. Isnard, M. Carratù, M. Lamberti, V. Venditto and M. Mazzeo, *Catal. Sci. Technol.*, 2018, **8**, 5034–5043.
- 27 C. A. L. Lidston, B. A. Abel and G. W. Coates, *J. Am. Chem. Soc.*, 2020, **142**, 20161–20169.
- 28 Y. Zhou, C. Hu, T. Zhang, X. Xu, R. Duan, Y. Luo, Z. Sun, X. Pang and X. Chen, *Macromolecules*, 2019, **52**, 3462–3470.
- 29 J. Li, B.-H. Ren, Z.-Q. Wan, S.-Y. Chen, Y. Liu, W.-M. Ren and X.-B. Lu, *J. Am. Chem. Soc.*, 2019, **141**, 8937–8942.
- 30 S. Friedrich, M. Schubart, L. H. Gade, I. J. Scowen, A. J. Edwards and M. McPartlin, *Chem. Ber./Recueil*, 1997, **130**, 1751–1759.
- 31 M. A. Bahili, PhD Thesis, Cardiff University, 2017.
- 32 M. Sullivan, PhD Thesis, Cardiff University, 2020.
- 33 B. Han, L. Zhang, B. Liu, X. Dong, I. Kim, Z. Duan and P. Theato, *Macromolecules*, 2015, **48**, 3431–3437.
- 34 L. F. Hu, C. J. Zhang, H. L. Wu, J. L. Yang, B. Liu, H. Y. Duan and X. H. Zhang, *Macromolecules*, 2018, **51**, 3126–3134.
- 35 K. A. Andrea, M. D. Wheeler and F. M. Kerton, *Chem. Commun.*, 2021, **57**, 7320–7322.
- 36 R. Xie, Y.-Y. Zhang, G.-W. Yang, X.-F. Zhu, B. Li and G.-P. Wu, *Angew. Chemie Int. Ed.*, 2021, **60**, 19253–19261.
- 37 E. Hosseini Nejad, A. Paoniasari, C. E. Koning and R. Duchateau, *Polym. Chem.*, 2012, **3**, 1308–1313.
- 38 Sigma Aldrich, Comparison of price of DMAP and [PPN]Cl, made 07-4-23 on

- sigmaaldrich.com/GB. 10g [PPN]Cl = £104 = £5970 per mole. 25g DMAP = £37 = £181 per mole.,
<https://www.sigmaaldrich.com/GB/en/product/aldrich/107700>
<https://www.sigmaaldrich.com/GB/en/product/aldrich/223832>.
- 39 Y. Kalambet, Y. Kozmin, K. Mikhailova, I. Nagaev and P. Tikhonov, *J. Chemom.*, 2011, **25**, 352–356.
- 40 M. Wojdyr, *J. Appl. Cryst.*, 2010, **43**, 1126–1128.
- 41 M. J. Sanford, N. J. Van Zee and G. W. Coates, *Chem. Sci.*, 2018, **9**, 134–142.
- 42 J. M. Longo, M. J. Sanford and G. W. Coates, *Chem. Rev.*, 2016, **116**, 15167–15197.
- 43 T. M. McGuire, E. F. Clark and A. Buchard, *Macromolecules*, 2021, **54**, 5094–5105.
- 44 A. M. Diccio and W. Coates, *J. Am. Chem. Soc.*, 2011, **133**, 10724–10727.
- 45 Y. Zhao and D. G. Truhlar, *Theor. Chem. Acc.*, 2008, **120**, 215–241.
- 46 M. J. Frisch, G. W. Trucks, H. B. Schlegel, G. E. Scuseria, M. A. Robb, J. R. Cheeseman, G. Scalmani, V. Barone, G. Petersson, H. Nakatsuji, X. Li, M. Caricato, A. Marenich, J. Bloino, B. G. Janesko, R. Gomperts, B. Mennucci, H. P. Hratchian, J. V. Ortiz, A. F. Izmaylov, J. L. Sonnenberg, D. Williams-Young, F. Ding, F. Lipparini, F. Egidi, J. Goings, B. Peng, A. Petrone, T. Henderson, D. Ranasinghe, V. G. Zakrzewski, J. Gao, N. Rega, G. Zheng, W. Liang, M. Hada, M. Ehara, K. Toyota, R. Fukuda, J. Hasegawa, M. Ishida, T. Nakajima, Y. Honda, O. Kitao, H. Nakai, T. Vreven, K. Throssell, J. A. J. Montgomery, J. E. Peralta, F. Ogliaro, M. Bearpark, J. J. Heyd, E. Brothers, K. N. Kudin, V. N. Staroverov, T. Keith, R. Kobayashi, J. Normand, K. Raghavachari, A. Rendell, J. C. Burant, S. S. Iyengar, J. Tomasi, M. Cossi, J. M. Millam, M. Klene, C. Adamo, R. Cammi, J. W. Ochterski, R. L. Martin, K. Morokuma, O. Farkas, J. B. Foresman and D. J. Fox, *Gaussian 09, Revision D.01*, Gaussian Inc., Wallingford, CT, 2016.
- 47 T. H. Dunning, *J. Chem. Phys.*, 1989, **90**, 1007–1023.
- 48 R. A. Kendall and T. H. Dunning, *J. Chem. Phys.*, 1992, **96**, 6796–6806.
- 49 T. H. Dunning, K. A. Peterson and A. K. Wilson, *J. Chem. Phys.*, 2001, **114**, 9244–9253.
- 50 J. Tomasi, B. Mennucci and R. Cammi, *Chem. Rev.*, 2005, **105**, 2999–3094.
- 51 R. Lapenta, A. Buonerba, A. De Nisi, M. Monari, A. Grassi, S. Milione and C. Capacchione, *Inorg. Chem.*, 2017, **56**, 3447–3458.
- 52 A. Meduri, M. Mazzeo, M. Lamberti, C. Capacchione and S. Milione, *Mol. Catal.*, 2019, **471**, 54–

- 59.
- 53 J. Wei, M. N. Riffel and P. L. Diaconescu, *Macromolecules*, 2017, **50**, 1847–1861.
- 54 C. Romain, Y. Zhu, P. Dingwall, S. Paul, H. S. Rzepa, A. Buchard and C. K. Williams, *J. Am. Chem. Soc.*, 2016, **138**, 4120–4131.
- 55 Y. Jeong, M. K. Cho, S. Seo, H. Cho, K. Son and H. Kim, *ChemCatChem*, 2023, e202201086.
- 56 B. P. Prascher, D. E. Woon, K. A. Peterson, T. H. Dunning and A. K. Wilson, *Theor. Chem. Acc.*, 2011, **128**, 69–82.

Chapter 3: Group 4 Metallocene Complexes as ROCOP Pre-Catalysts

3.1: Group 4 Metallocene Complexes

The Group 4 metals (Ti, Zr, Hf) are synonymous with olefin polymerisation and the pioneering work of Karl Ziegler and Giulio Natta, who were both awarded the Nobel Prize in 1963 for their study of heterogeneous olefin polymerisation catalysis.^{1,2} However, in terms of homogeneous systems, it wasn't until the 1970s and 80s that "metallocene" pre-catalysts employing the cyclopentadienyl ($\eta^5\text{-C}_5\text{H}_5^-$, Cp) ligand and its derivatives (*e.g.* indenyl ($\eta^5\text{-C}_9\text{H}_7^-$), Cp* ($\eta^5\text{-C}_5\text{Me}_5^-$)) were developed.³⁻⁷ Crucially, using discrete molecular catalysts, with well-defined active sites, can increase both the rate and control of the polymerisation, when compared to analogous heterogeneous systems.⁸ This includes control of tacticity, molecular weight, the molecular weight distribution, and co-monomer incorporation of the polymer produced. This in turn influences the material's bulk properties, and, ultimately, its usefulness.^{4,9}

There are several sub-classifications used for Group 4 Cp containing complexes (**Figure 3.1**): Metallocenes containing two Cp-based ligands (*e.g.* complex **3.1**, hafnocene dichloride); *ansa*-metallocenes, which also have two Cp-based ligands but are linked together, typically through a silyl (*e.g.* complex **3.2**) or alkylene bridge (*e.g.* complex **3.3**); half-metallocenes contain only one Cp based ligand, with a subsection of this being so-called "constrained geometry catalysts", where the lone Cp-based ligand is tethered to a non-Cp donor, usually a nitrogen amide (*e.g.* complex **3.5**).

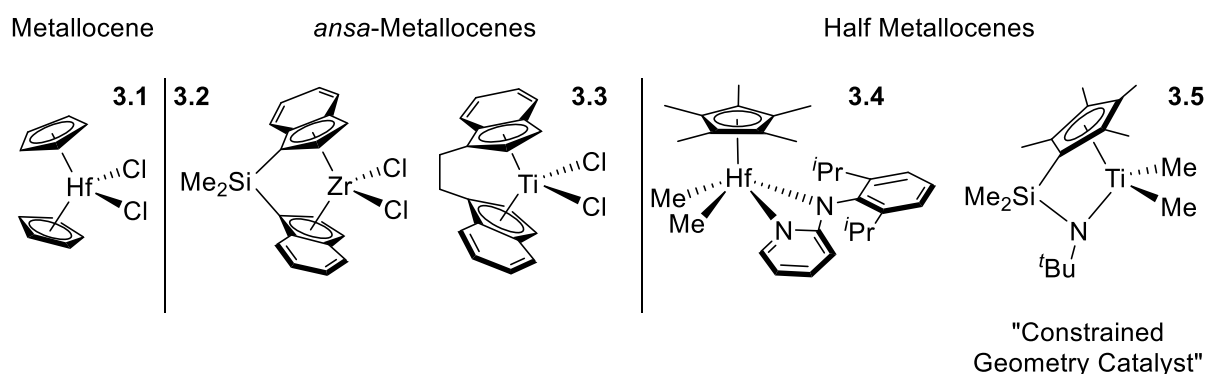


Figure 3.1: Nomenclature of Group 4 metallocene, *ansa*-metallocene and half metallocene complexes.

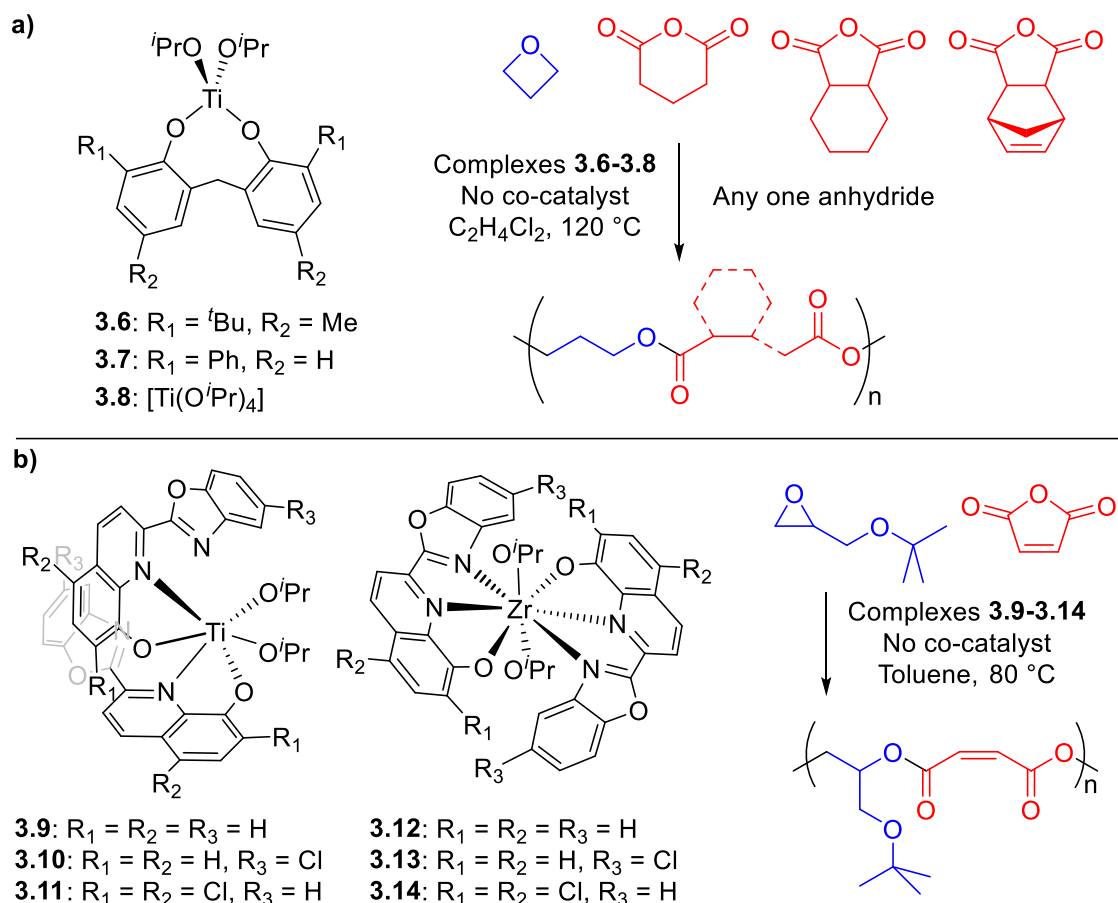
Despite the vast number of reports into metallocene-catalysed olefin polymerisation, this remains an active research field.¹⁰ These investigations include developing catalysts that can tolerate

heteroatoms in the monomer, such as methyl methacrylate (MMA) and amino-alkenes, which have been successfully catalysed by complexes **3.5** and **3.2** respectively.^{11,12} Using oxygen and nitrogen containing monomers can be challenging, as these Lewis bases have the potential to bind strongly to Lewis acidic and oxyphilic metals, as is the case with Group 4 d^0 complexes. This is particularly pertinent in the context of epoxide-anhydride ROCOP, where highly oxygenated substrates are necessarily present, and so any successful ROCOP catalyst must have this functional group tolerance.

3.2: The Group 4 Metals in ROP and ROCOP

The Group 4 metals have also shown efficacy in the ROP of cyclic esters,^{13–17} epoxide-CO₂ ROCOP,^{18–23} and, to a limited extent, cyclic ether-anhydride ROCOP.^{24–27} This is a step beyond the previously discussed tolerance of oxygenated monomers; given that metal alkoxides are invoked as key intermediates in the catalytic cycles of ROP and ROCOP, it is crucial that these M-O bonds are not so thermodynamically strong or kinetically inert as to prevent catalyst turnover.^{28–30} However, a certain Lewis acidity is required in order to bind epoxide substrate, so any successful catalyst must straddle these two regimes.²⁵

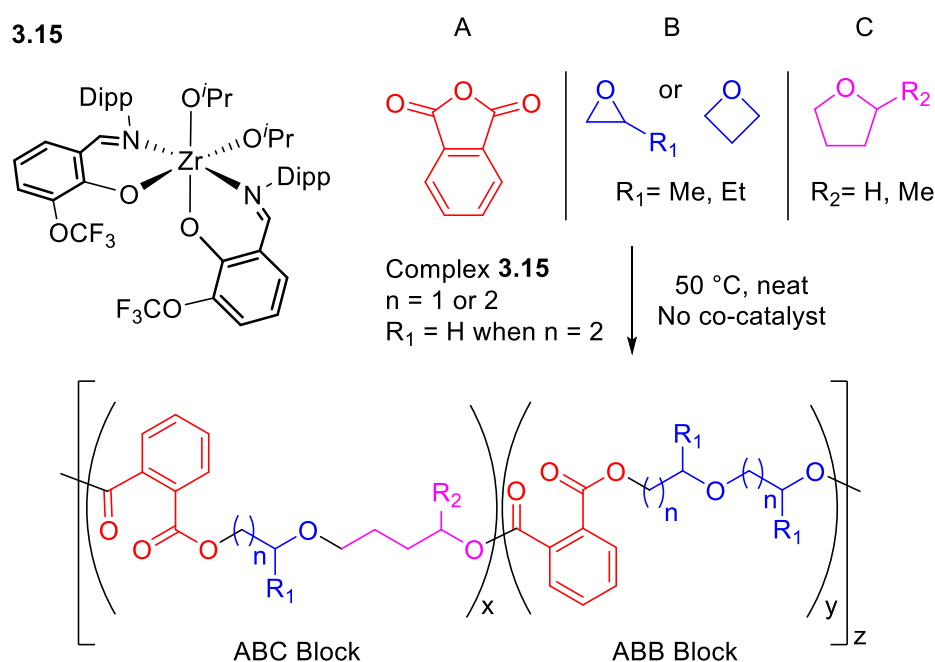
The first example of cyclic ether-anhydride ROCOP using a Group 4 catalyst was reported in 1999 by Endo and colleagues, who employed titanium bis(phenolate) complexes in the ROCOP of oxetane and a series of anhydrides in the absence of co-catalyst (**Scheme 3.1**).²⁶ Although the ester selectivities were generally low (between 40 – 80%), the use of bulky bis(phenolate) ligands was seen to significantly narrow the molecular weight distribution compared to using [Ti(O^{*i*}Pr)₄]. Barring heterogeneous examples,^{31–33} the next example of Group 4 catalysed ROCOP was not reported until 2017, when Chakraborty and Chand detailed the use of Ti and Zr bound by benzoxazole-substituted 8-hydroxyquinolate ligands for the ROP of *L*-lactide and the ROCOP of *tert*-butyl glycidyl ether and maleic anhydride (**Scheme 3.1**).²⁴ Again, no co-catalyst was used in this polymerisation, yet perfect ester selectivities were still seen for the zirconium complex **3.14**, producing polyester with an M_n of up to 40.5 kDa with a Đ of 1.44.



Scheme 3.1: Examples of Group 4 catalysed cyclic ether-anhydride ROCOP, as reported by Endo *et. al.* (top) and Chakraborty and Chand (bottom).^{24,26}

Recently, the Williams group reported a bis(isopropoxide) Zr(IV) complex (**Scheme 3.2**) used in the terpolymerisations of phthalic anhydride, a furan and either an epoxide or oxetane.²⁵ This produces a copolymer of poly(ester-*alt*-ether) in a selective ABB block, as opposed to the random incorporation of ether units seen in non-selective epoxide-anhydride ROCOP. The key distinction between the two scenarios is the active propagation species: In the latter example where there is random incorporation of any ether linkages, the anhydride opening step is usually far faster than epoxide insertion, meaning anhydride insertion would likely take place regardless of what step(s) preceded it, as long as there was an active metal-alkoxide intermediate to react. This metal alkoxide reacts in an identical manner if there is a metal-epoxide-anhydride unit or metal-epoxide-epoxide unit, giving rise to random ether incorporation. Conversely, in the case presented here (**Scheme 3.2**), the epoxide or oxetane insertion into a Zr-carboxylate species is slow and rate-limiting, but, rather than react with anhydride, an insertion of either another epoxide/oxetane or furan is observed to give an ether linkage before rapid anhydride insertion to produce an ester linkage. The reason why only after a second insertion of cyclic

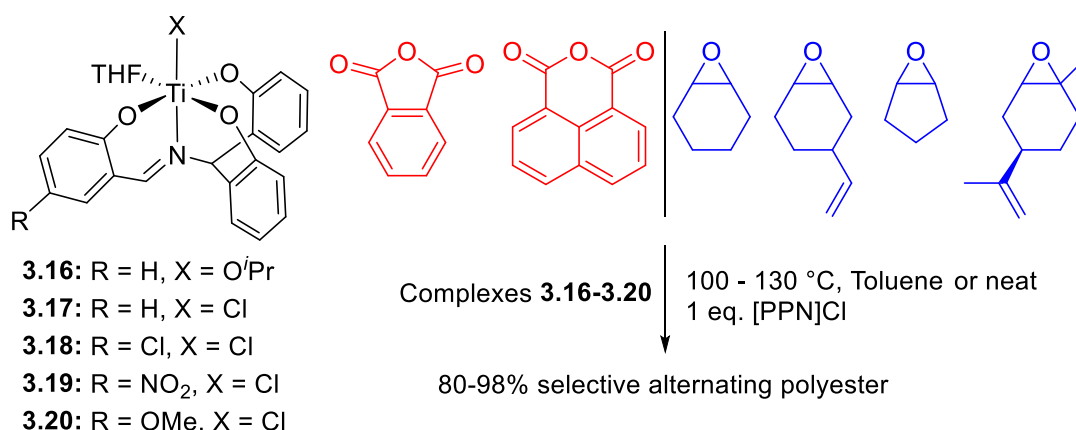
ether is anhydride insertion rapid is unclear, yet the authors hypothesised that both the large ionic radius of zirconium and its ability to accommodate expanded coordination numbers may allow for polymer back-coordination to the metal, meaning the metal-alkoxide intermediates preceding cyclic ether and anhydride insertion are distinct and thereby have different reactivity. This reactivity could be modified through adjusting the reaction stoichiometry, to either increase the concentration of furan to give a higher proportion of ABC links (Scheme 3.2, $x > y$), or increase the concentration of epoxide/oxetane to yield more ABB links (Scheme 3.2, $y > x$). This unusual yet regular and controlled selectivity gives rise to polymers with flexible ether linkages dispersed evenly throughout the polymer chain, contributing to low T_g polymers with “soft” blocks (analogous to hexene insertion into poly(ethylene)), which can lead to phase separation and interesting material properties.



Scheme 3.2: Zr bis(isopropoxide) catalyst (Dipp = 2,6-diisopropylphenyl) showing unusual poly(ester-*alt*-ether) selectivity in terpolymerisations with phthalic anhydride (A), either an epoxide or oxetane (B) and a furan (C). Modification of the reaction stoichiometry influences the relative prevalence of ABB ($y > x$) linkages or ABC ($x > y$) linkages.²⁵

Most recently in 2023, Son, Kim and co-workers reported a series of iminotriphenolate titanium complexes (**Scheme 3.3**) employing either an isopropoxide or chloride co-ligand for use in the ROCOP of phthalic or naphthalic anhydride with a series of bicyclic epoxides.²⁷ Interestingly, in contrast to [Al(Salen)X] complexes widely used in ROCOP where the ligand occupies four equatorial sites, forming complexes of *trans* symmetry, the tetradentate ligands here produce complexes with two mutually *cis* vacant sites (once the THF and either chloride or isopropoxide have reacted).³⁰ This means there is potential for migratory insertions to occur between propagating polymer chains on the same catalyst

molecule. Indeed, DFT calculations suggest that a titanium-alkoxide undergoing migratory insertion into a C=O bond of a metal-bound anhydride is a viable route for the anhydride opening step of the propagation. But, in a departure from the majority of the literature on the mechanism of ROCOP, the authors showed by DFT calculations that intramolecular titanium-carboxylate insertion into a C-O bond of a titanium-bound epoxide is an energetically feasible pathway for epoxide opening.

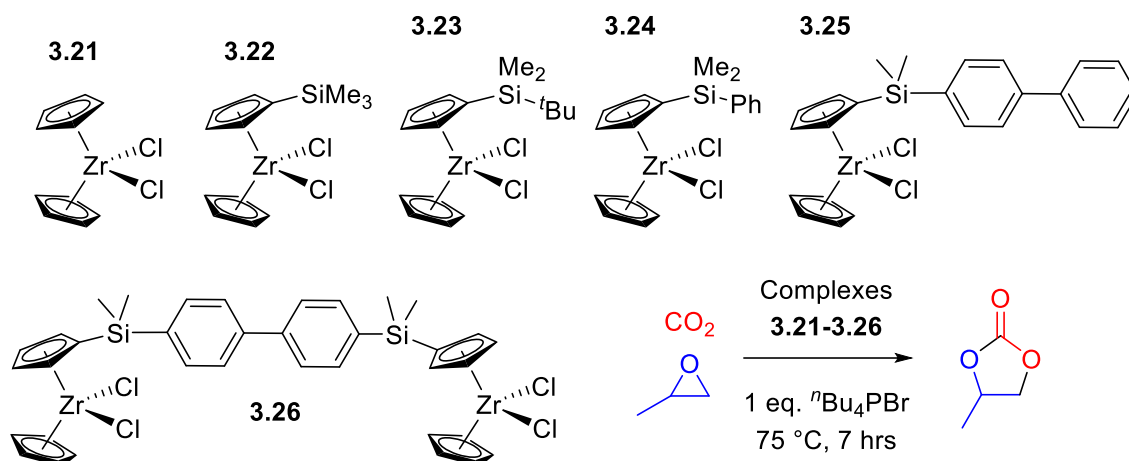


Scheme 3.3: Titanium mono(isopropoxide) and mono(chloride) complexes used as pre-catalysts alongside [PPN]Cl for the ROCOP of a range of epoxides and anhydrides with good selectivity.²⁷

After screening complexes **3.16-3.20** for catalytic performance, the mono(chloride), chloride substituted complex **3.18** gave the fastest epoxide conversion. Also, complex **3.18** produced polymer with high ester (up to 98%) selectivities when one equivalent of [PPN]Cl was used as a co-catalyst, with dispersities as narrow as 1.11 for a copolymer of cyclopentene oxide and phthalic anhydride. However, the ester selectivity dropped to only 80% when limonene oxide was used, with the forcing conditions (130 °C, neat limonene oxide) perhaps a reason for this loss of selectivity. Furthermore, a low M_n of 3.8 kDa was produced, most likely due to the increased rate of chain transfer, back-biting and transesterification reactions at said higher temperature.

As well as epoxide-anhydride ROCOP, there have been several reports detailing the use of Group 4 catalysts for epoxide-CO₂ ROCOP to give cyclic carbonates (that can later undergo ROP to yield identical polycarbonates).²³ Most interestingly though in the context of Cp-based complexes, [Cp₂TiCl₂] has been shown to produce cyclic carbonate from a wide range of epoxides such as styrene oxide, cyclohexene oxide, epichlorohydrin and propylene oxide when used alongside a Lewis base such as DMAP or tetrabutylammonium salts, or the inorganic additive KI.^{34,35} To add to this, a series of (bis)chloride zirconocene complexes (**3.21-3.26**) have been shown to efficiently produce cyclic

carbonate from propylene oxide and CO₂, again whilst employing an additive in ⁿBu₄PBr (**Scheme 3.4**).³⁶ Given their clearly demonstrated ability to activate and ring-open epoxides, and yet not irreversibly bind intermediate metal-alkoxides and thereby preventing catalyst turnover, under the appropriate reaction conditions it was hypothesised that Group 4 metallocenes may prove effective catalysts for epoxide-anhydride ROCOP.



Scheme 3.4: A series of bis(chloride) zirconocene complexes used as catalysts for producing cyclic carbonate from propylene oxide and CO₂.³⁶

3.3: Catalytic Performance of [Cp₂MCl₂] Complexes in Epoxide-Anhydride ROCOP

*The key findings of the work described in sections 3.3 - 3.7 has been published here.*³⁷

Starting from a simple 2x2 matrix of epoxides and cyclic anhydrides, the three metallocene dichloride complexes [Cp₂MCl₂] (M = Ti, Zr, Hf) were investigated for their use in ROCOP. DMAP was used as a co-catalyst to allow differentiation of initiation by external co-catalyst and chlorides present in the pre-catalyst, (see MALDI-ToF data, section 3.4). Substrates examined include cyclohexene oxide (CHO) and 4-vinylcyclohexene oxide (VCHO), as well as phthalic anhydride (PA) and tetrachlorophthalic anhydride (TCPA). VCHO is of interest as its vinyl functionality allows for post-polymerisation modification through hydroboration and thiol-ene reactions, whilst TCPA is used in the production of flame retardant materials.³⁸⁻⁴¹ The polymerisation data for PA are presented in **Table 3.1**. The addition of metallocene complex increases anhydride conversion significantly for both CHO (entries 1-3) and VCHO (entries 5-7), in comparison to when DMAP alone is used (entries 4, 8) over the same time period. This activity increase is most prominent for [Cp₂TiCl₂] (entries 1, 5), followed by [Cp₂ZrCl₂] (entries 2, 6) and [Cp₂HfCl₂] (entries 3, 7), respectively.

Table 3.1: Copolymerisation of PA with CHO and VCHO. ^a

Entry	Epoxide	M	Conv. PA / % ^b	Ester / % ^c	M_n^d / kDa	$\bar{D}^{d,e}$
1	CHO	Ti	74	89	16.8	1.24
2		Zr	61	83	17.7	1.39
3		Hf	55	66	14.4	1.61
4		None	32	>95	19.1	1.22
5	VCHO	Ti	74	85	37.0	1.20
6		Zr	66	80	31.4	1.47
7		Hf	57	52	17.7	1.44
8		None	35	94	60.2	1.33

^a Average of at least two runs. Conditions: 1 eq. = 6.4 μmol (1 eq.) metallocene (unless otherwise stated), 2 eq. DMAP, 400 eq. PA, 400 eq. epoxide, 1 mL toluene, 80 °C for 21 hours. ^b Determined by ^1H NMR spectroscopy of reaction mixture. ^c Determined by ^1H NMR spectroscopy of the resultant polymer. ^d Determined by GPC (viscometry detection against polystyrene standards). ^e $\bar{D} = M_w / M_n$.

Interestingly, an identical trend is seen for the selectivity towards alternating $(\text{AB})_n$ microstructure (determined from ester versus ether regions in the ^1H NMR spectra, see section 3.4), with $[\text{Cp}_2\text{TiCl}_2]$ slightly more selective than $[\text{Cp}_2\text{ZrCl}_2]$, which in turn is far more selective than $[\text{Cp}_2\text{HfCl}_2]$. Whilst the selectivities remain high for titanium and zirconium, copolymers with near perfect alternating selectivity were observed in the absence of metallocene; with the region of the ^1H NMR spectrum corresponding to ether linkages (arising from homopolymerisation of epoxide) often containing no discernible resonances. In terms of molecular weight, both $[\text{Cp}_2\text{TiCl}_2]$ and $[\text{Cp}_2\text{ZrCl}_2]$ produced polymers with a significantly higher molecular weight (far more than if one adjusts for the extra mass of the vinyl group and differences in conversion) for VCHO, indicating a reduced propensity for chain transfer processes when compared to CHO. This, however, does not extend to $[\text{Cp}_2\text{HfCl}_2]$, where the molecular weights were similar regardless of the epoxide used. The highest molecular weights were observed in the absence of metallic catalyst, reflecting the relatively small number of propagating chains, a result of the reduced number of initiating groups (chlorides and DMAP) in the reactions. The polyesters generally possessed relatively low dispersities (\bar{D}) and were similar across both epoxides;

aside from $[\text{Cp}_2\text{HfCl}_2]$, which gave the highest dispersities (1.61, entry 3) for the CHO-PA copolymer. In general, the conversions and molecular weights seen are of similar order to commonly employed Schiff-base-ligated metal complexes in toluene, albeit at different reaction temperatures and catalyst loadings.⁴² Polymerisations of CHO and PA conducted without DMAP using $[\text{Cp}_2\text{TiCl}_2]$ showed low (*c.a.* 30%) ester selectivity, highlighting the importance of the co-catalyst in this system.

Polymerisations were also conducted “in bulk” using neat CHO as the solvent (1:2:2000:400 $[\text{Cp}_2\text{TiCl}_2]:[\text{DMAP}]:[\text{CHO}]:[\text{PA}]$, 80 °C) which yielded the expected pseudo zero-order rate plot (**Figure 3.2**), albeit producing polymers with lower (75% vs. 89%) ester selectivity, which was independent of anhydride conversion. The rate of anhydride conversion is significantly faster when excess epoxide is the solvent, as noted by the near full (98%) conversion after 2.5 hours.

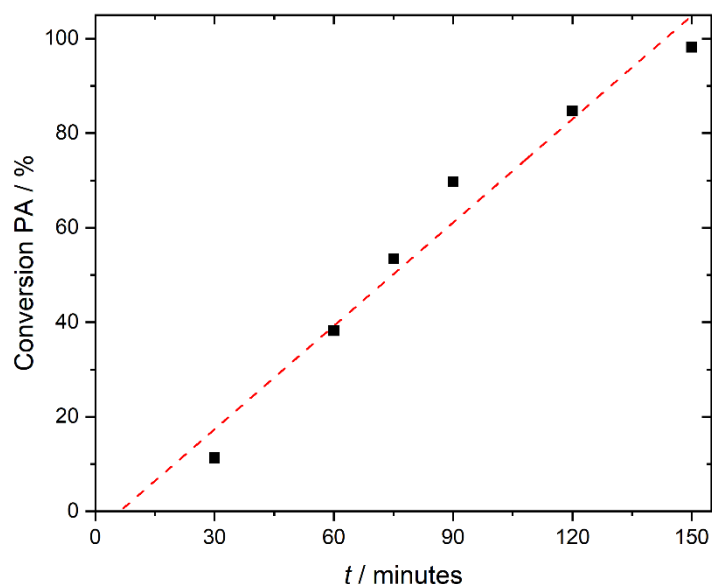


Figure 3.2: Conversion of PA against time for CHO-PA copolymerisations when a 5-fold excess of CHO was used as the solvent (1:2:2000:400 $[\text{Cp}_2\text{TiCl}_2]:[\text{DMAP}]:[\text{CHO}]:[\text{PA}]$) conducted at 80 °C. Note the short reaction times (2.5 hours vs. 21 hours with toluene) and the near linear relationship, denoting the reaction is zero-order in anhydride. Each data point is a different polymerisation that has been fully worked up, rather than from aliquots of the same reaction.

When the above reactions were worked up and polymer isolated, the resulting GPC data showed a gradual (although non-linear) increase in the M_n with the conversion of anhydride alongside only small oscillations in polydispersity (**Figure 3.3**). The exception to this comes once anhydride is fully consumed, upon which the M_n decreases and polydispersity increases, likely due to transesterifications or chain-end couplings which broaden the molecular weight distribution.⁴³

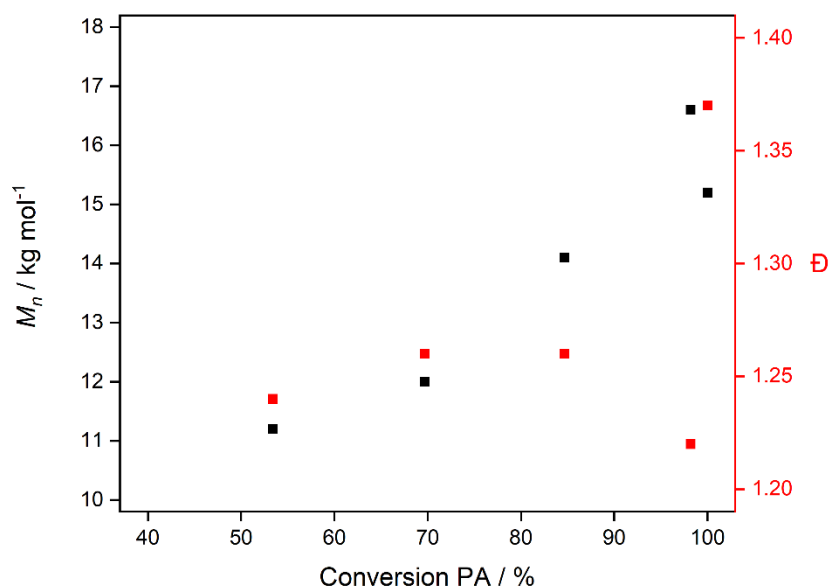


Figure 3.3: M_n (left, black) and polydispersity index (\bar{D} , M_w/M_n , right, red) against conversion of PA for neat copolymerisations of CHO-PA. Conditions: 1:2:2000:400 [Cp₂TiCl₂]:[DMAP]:[CHO]:[PA], conducted at 80 °C. GPC data is from viscometry measurements against polystyrene standards.

The analogous polymerisations using TCPA are described in **Table 3.2**. As the NMR handle to measure anhydride conversion (the aromatic protons of PA) are removed for TCPA, all conversions are measured by epoxide conversion. This calculation is complicated by the presence of ether linkages, meaning the conversion was calculated by:

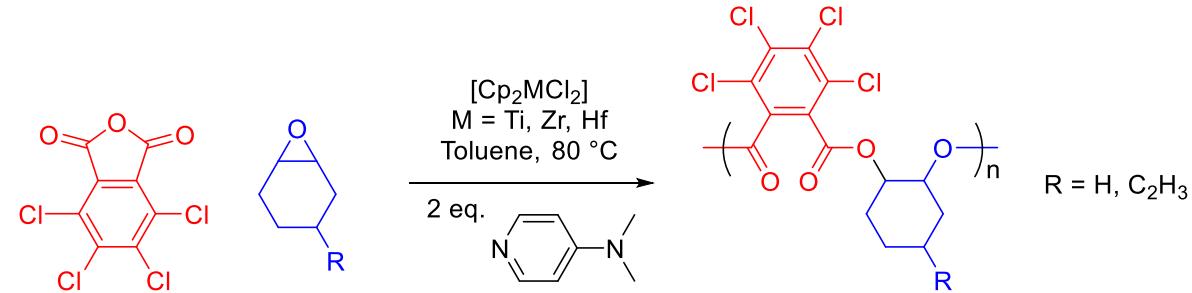
$$\text{Epoxide Conversion} / \% = \frac{[\delta_{\text{Ester}}^H + \delta_{\text{Ether}}^H]}{[\delta_{\text{Ester}}^H + \delta_{\text{Ether}}^H + \delta_{\text{Epoxide}}^H]} \times 100$$

Where δ^H represents the integration of the region of the ¹H NMR spectrum of a sample of the reaction mixture corresponding to ester linkages, ether linkages, or unreacted epoxide (δ^H ester = 5.20 – 5.00, ether = 3.60 – 3.40, epoxide = 3.10 ppm for CHO-TCPA) of the two chemically equivalent CH protons about the epoxide (or ring-opened epoxide) functionality. This is less sensitive than anhydride conversion given the broad nature and relative low intensity (particularly when analysing reaction aliquots) of ether peaks, which can suffer from a poor signal-noise ratio, and that unreacted epoxide can evaporate once the vial is opened to sample the reaction mixture.

Due to the reduced solubility of TCPA, the amounts of all reagents aside from the solvent were halved (molar ratios of [Metallocene]:[DMAP]:[Epoxide]:[Anhydride] remained 1:2:400:400). Despite this however, reaction times decreased dramatically, with near quantitative conversion of CHO observed after 14 hours using both [Cp₂ZrCl₂] and [Cp₂HfCl₂] (entries 2 and 3). Given that the rate determining

step of this reaction remains epoxide opening, this increase in activity could be attributed to the electron-withdrawing chloro substituents stabilising the carboxylate anion in non-polar media, better facilitating its de-coordination and subsequent reaction with metal-bound epoxide. In another departure from copolymerisations of PA discussed previously, runs using $[\text{Cp}_2\text{TiCl}_2]$ (entries 1 and 5) gave lower conversions than both the zirconium and hafnium congeners (entries 2-3, 6-7). This reversal in activity could be attributed to steric congestion around the metal centres, where the larger zirconium and hafnium can more easily accommodate the significant extra volume occupied by the chloro-substituted polymer chains.

Table 3.2: Copolymerisation of TCPA with CHO and VCHO. ^a



Entry	Epoxide	t / h	M	Conv. Epoxide / % ^b	Ester / % ^c	M_n ^d / kDa	\bar{D} ^{d,e}
1	CHO	14	Ti	88	94	11.2	1.23
2			Zr	99	89	20.3	1.10
3			Hf	98	81	15.3	1.39
4			None	77	95	11.8	1.30
5	VCHO	15	Ti	85	>95	18.5	1.15
6			Zr	>99	82	19.2	1.28
7			Hf	>99	65	27.8	1.39
8			None	76	90	28.5	1.21

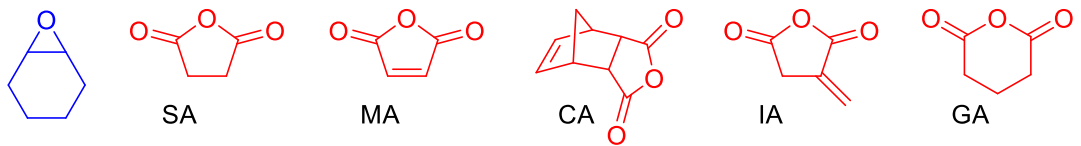
^a Average of at least three runs. Conditions: 1 eq. = 3.2 μmol (1 eq.) metallocene (unless otherwise stated), 2 eq. DMAP, 400 eq. TCPA, 400 eq. epoxide, 1 mL toluene, 80 °C. ^b Determined by ^1H NMR spectroscopy of reaction mixture. ^c Determined by ^1H NMR spectroscopy of the resultant polymer. ^d Determined by GPC (viscometry detection against polystyrene standards). ^e $\bar{D} = M_w / M_n$.

Concurrently, the selectivity of reactions involving $[\text{Cp}_2\text{HfCl}_2]$ and CHO-TCPA increased relative to CHO-PA (entry 3), although hafnium remained the least selective of the three metals. Also noteworthy is the detection of polyether resonances when no metallocene is added, in particular for VCHO where the addition of $[\text{Cp}_2\text{TiCl}_2]$ actually increased ester selectivity (entries 5, 8). Despite the molecular weights being similar for both TCPA and PA in absolute terms (with the exception of VCHO with

[Cp₂HfCl₂], entry 7), the increased mass of the monomer means this translates to fewer repeat units. This is likely due to chain transfer processes, specifically the increased favourability of transesterification at a more electrophilic ester carbonyl group.

To broaden the substrate scope, a series of alternative, non-phthalate derived anhydrides were screened in copolymerisations with CHO (**Table 3.3**). This includes the simplest cyclic anhydride, succinic anhydride (SA), its unsaturated congener maleic anhydride (MA), the tricyclic carbic anhydride (CA, *cis*-5-norbornene-endo-2,3-dicarboxylic anhydride), the citric acid derivative itaconic anhydride (IA), and the six-membered glutaric anhydride (GA).

Table 3.3: Copolymerisations of various anhydrides with CHO, using either [Cp₂TiCl₂] or [Cp₂ZrCl₂] as pre-catalysts. ^a



Anhydride	M	Conversion		<i>M_n</i> ^d / kDa	Đ ^{d,e}
		Anhydride / % ^b	Ester / % ^c		
SA	Ti	88	85	1.9	1.10
MA		0	-	-	-
CA		0	-	-	-
IA	Zr	38	36	13.3	1.52
GA		>99	84	1.2	1.10

^a Conditions: 1 eq. = 6.4 μmol (1 eq.) metallocene, 2 eq. DMAP, 400 eq. anhydride, 400 eq. epoxide, 1 mL toluene, 80 °C. ^b Determined by ¹H NMR spectroscopy of the reaction mixture. ^c Determined by ¹H NMR spectroscopy of the resultant polymer. ^d Determined by GPC (viscometry detection against polystyrene standards). ^e Đ = *M_w*/*M_n*.

Neither MA or CA copolymerised under these conditions, whilst IA showed some reactivity, albeit at high ether selectivity. SA and GA both polymerised quickly compared to PA (table 3.1, entries 1-2), yet produced polymers with low molecular weight. In fact, the product of GA-PA copolymerisation was only isolated as a viscous oil, highlighting its oligomeric character. The reason why these substrates either do not work, produce high ether content polymers, or oligomers is unclear, given that there are several literature examples of their effective copolymerisation (with the exception of IA⁴⁴).^{26,45} However, the high rates of reaction with SA and GA are consistent with their sterically unencumbered

nature. Furthermore, the ring-opening of GA or SA produces an unhindered $(\text{CH}_2)_n\text{-CO}_2^-$ unit ($n = 2$ or 3 for SA and GA respectively), with this potentially conducive to transesterification as well as deprotonation of the α -protons (which are not present in PA or TCPA) by alkoxide intermediates, both of which could be responsible for the depressed molecular weights.⁴³

3.4: MALDI-ToF, DOSY NMR and GPC Analysis of Polymers

MALDI-ToF mass spectrometry of the polymers was used to ascertain whether the observed polyether resonances in the ^1H NMR spectra of the polymers were incorporated into predominantly polyester chains, or into distinct polyether chains produced by a separate polymerisation process. A representative MALDI-ToF spectrum of the CHO-PA polymer produced by $[\text{Cp}_2\text{TiCl}_2]$ is displayed in **Figure 3.4**, with the repeating series corresponding to the CHO-PA unit of 246 Da indicated by different colours. All observed series in positive mode were initiated by DMAP, highlighting its importance as a nucleophilic co-catalyst, with these findings consistent with previously reported MALDI-ToF spectra for polyesters produced by an aluminium bis(methyl) pre-catalyst and DMAP.⁴⁶

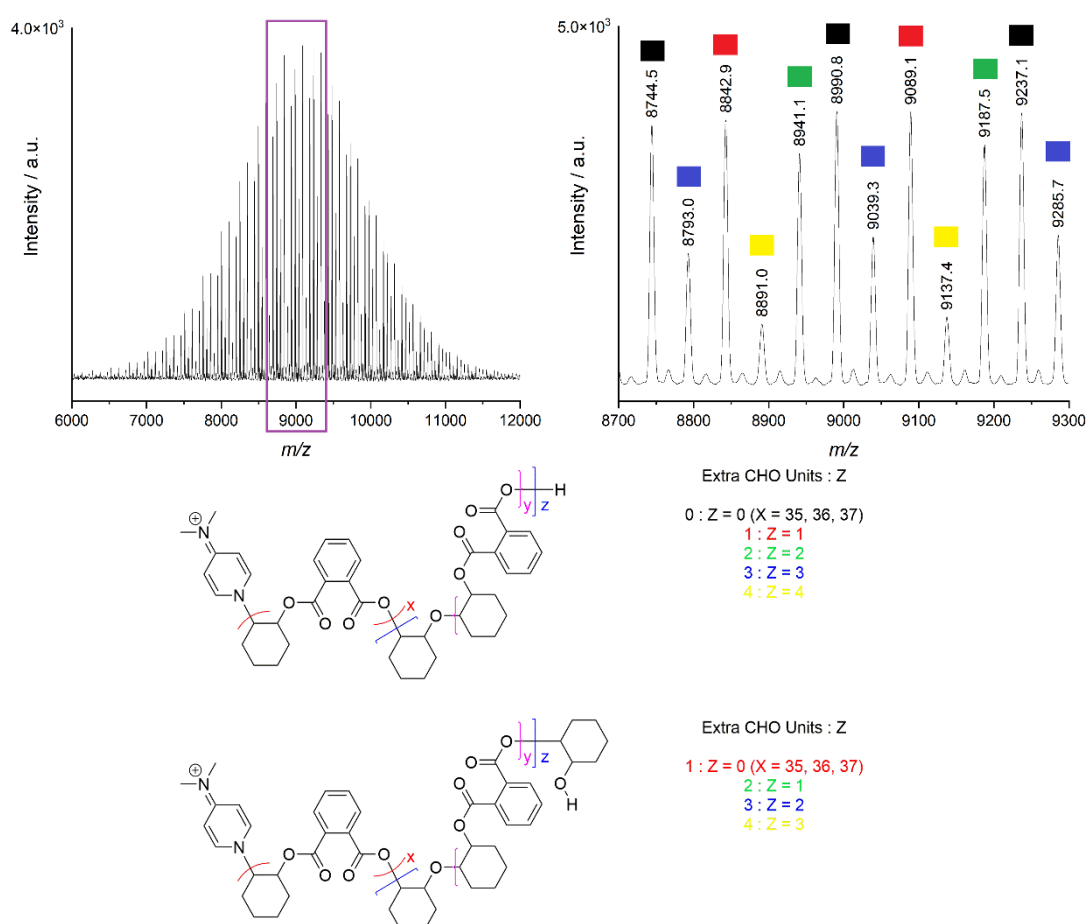


Figure 3.4: MALDI-ToF spectrum (positive mode) of poly(CHO-*alt*-PA) (table 3.1, entry 1). Also shown is a zoomed section with five series indicated, each with 0-4 (N) additional CHO units in the polymer chain, corresponding to either N polyether linkages or N-1 polyether linkages and a protonated epoxide end group.

The appearance of several series corresponding to various “extra” CHO units (up to 4 across the polymer chain) indicate that there are polyether linkages within the chains, as well as potentially as end groups. These possibilities are indistinguishable by mass and therefore both are shown in **Figure 3.4**. Similarly, MALDI series containing up to 8 extra epoxide units have been observed for a polymer containing a higher ether (20% vs. 11%) selectivity (**Figure 3.5**). These findings are consistent with previous mechanistic work where ester and ether producing catalytic cycles are thought to originate from a single catalytic species.²⁵ Despite this, under identical reaction conditions in the absence of anhydride, $[Cp_2ZrCl_2]$ only slowly produced oligomers of CHO, with this highlighting the intrinsic differences in rate of reaction between the monomers.

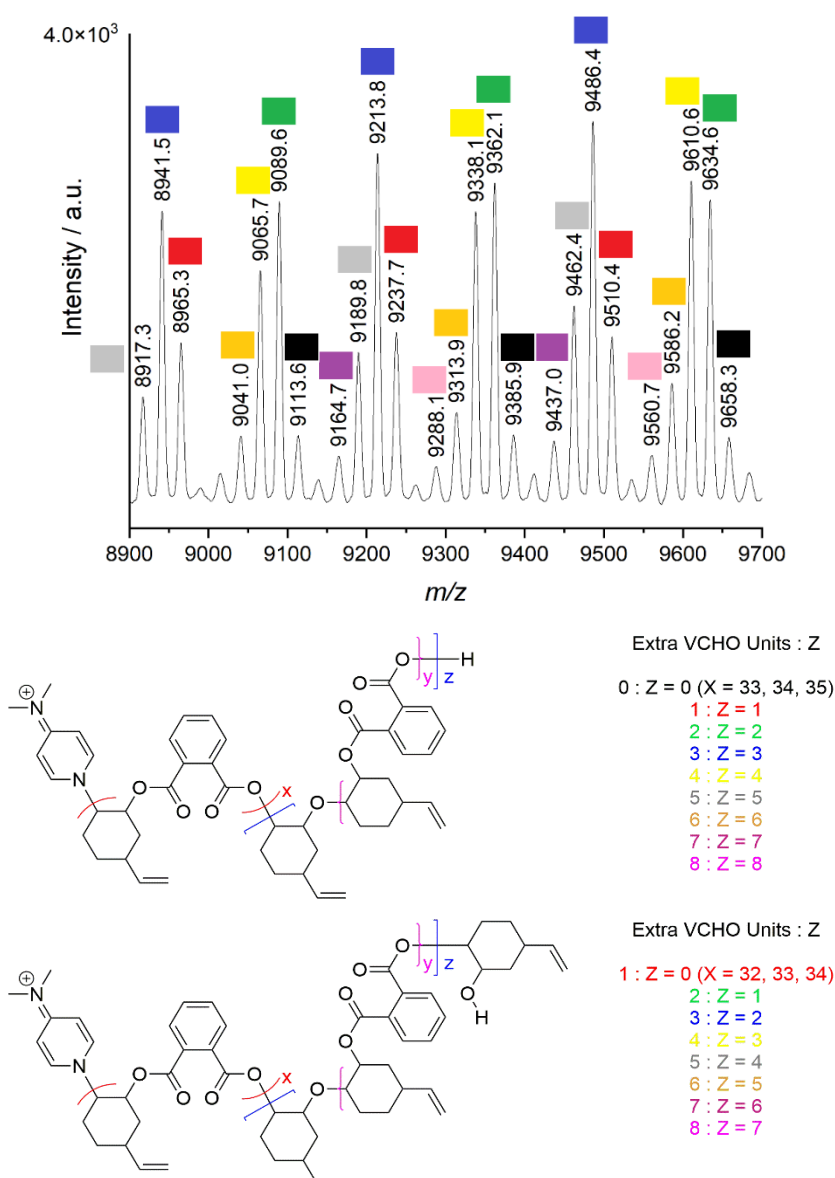


Figure 3.5: Part of the MALDI-ToF spectrum of poly(VCHO-*alt*-PA) (entry 6, table 3.1). Each series represents a different number of additional epoxide units either terminating the polymer chain, within the polyester chain, or both, given these possibilities are indistinguishable by MALDI-ToF. This sample has a relatively low (80%) ester selectivity, and so the appearance of series related to up to 8 additional VCHO units is to be expected.

To further illustrate that both ester and ether units coexist in the same polymer chains, Diffusion Ordered Spectroscopy (DOSY) experiments were performed on the high polyether content sample of poly(VCHO-*alt*-PA) as isolated when [Cp₂HfCl₂] was used as the pre-catalyst (table 3.1, entry 7). **Figure 3.6** shows its DOSY spectrum, where the ¹H NMR chemical shift is displayed on the x-axis and diffusion coefficient is read on the y-axis. All resonances, including the broad resonance between 3.9-3.7 ppm which represents ether linkages, have the same diffusion coefficient, meaning they have the same molecular size, and therefore that it is highly likely that they are part of the same polymer chains. When coupled to the MALDI data shown previously, the small possibility that the DOSY spectrum contains only one diffusion coefficient as separate polyester and polyether chains coincidentally have the same molecular weight can be ruled out, meaning this is further evidence of random incorporation of ether units within a wider polyester structure.

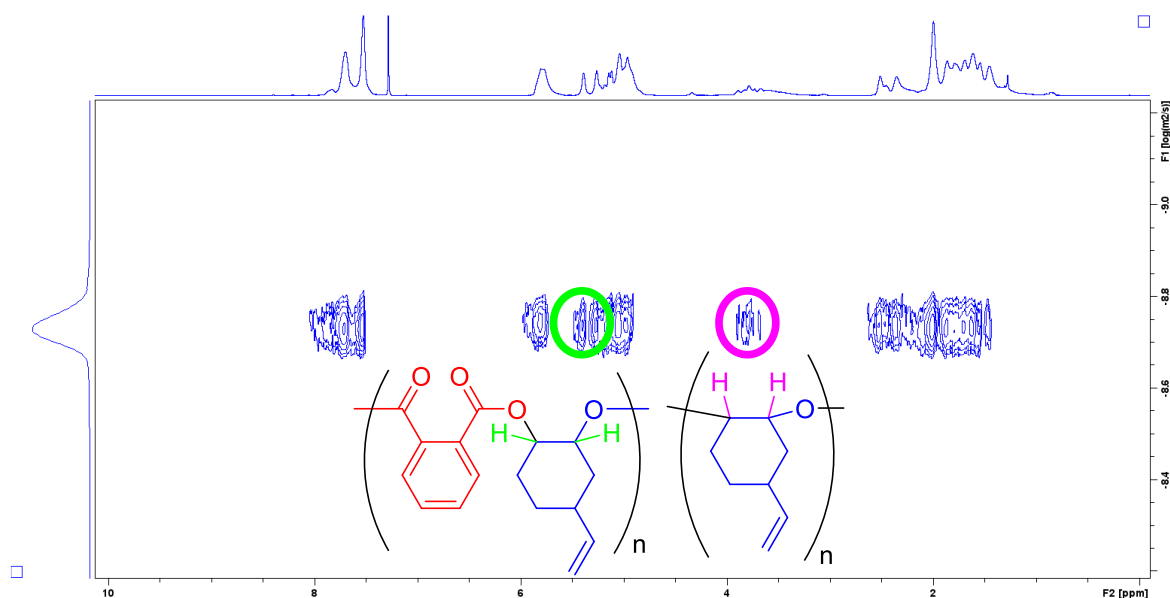


Figure 3.6: DOSY NMR spectrum (600 MHz, 298 K, CDCl₃) of a high ether content sample of poly(VCHO-*alt*-PA) (entry 7, table 3.1). Note the identical diffusion coefficient for ester (green) and ether (purple) resonances.

During GPC analysis of the polymers produced by the metallocene catalysts, there was a consistent discrepancy between the signals produced by the light scattering (LS) detector when compared to both the refractive index (RI) and viscometry (VS) detectors, which both produced comparable traces. A typical example of this behaviour can be seen in **Figure 3.7**, which represents the data obtained from poly(VCHO-*alt*-PA) as produced by [Cp₂ZrCl₂]. This discrepancy limited the method of analysis that could be used, as using triple detection (where all three detectors are used) gave inconsistent results that were not consistent with MALDI-ToF data. Therefore, all polymers analysed in this chapter, including for control reactions where no metallocene was present and where this effect was not observed, all rely on viscometry detection, which uses both the viscometer and the refractive index

detector (for concentration determination) in tandem. This gave results that were both reproducible and more consistent with MALDI-ToF than when triple detection, where the light scattering data was included did. As for why the addition of metallocene catalysts causes this behaviour, it is possible that as the light scattering detector is extremely sensitive to nanoscale aggregates, that the use of these catalysts could lead to the aggregation of either polymer or residual catalyst and abnormally trigger the detector separately from what would be expected for dispersed polymer particles in the eluent.⁴⁷ Given the tiny quantities of catalyst used however, and the dilution of the sample upon GPC analysis, it seems likely that any aggregation is predominantly of polymer, possibly surrounding catalyst particles, rather than from any metal nanoparticles which could form as the catalyst degrades.

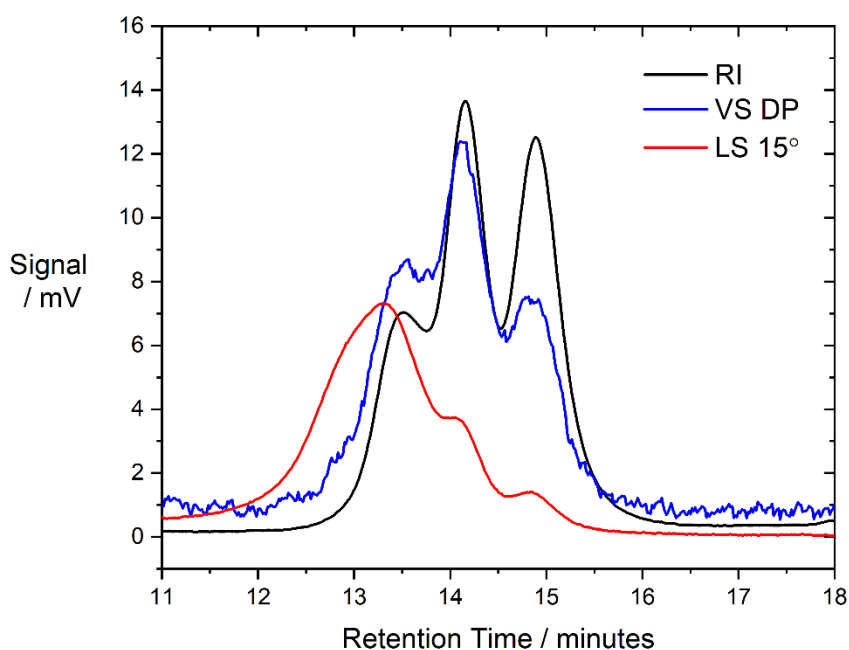
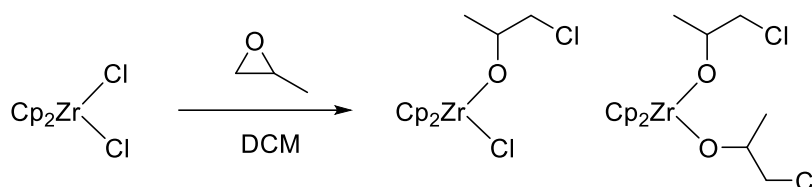


Figure 3.7: Normalised traces of the refractive index (RI, black), viscometry (differential pressure, VS DP, blue) and low angle light scattering (LS 15°C, red) detectors against retention time in the polymer-containing region of the GPC chromatogram produced by poly(VCHO-*alt*-PA) made using [Cp₂ZrCl₂] (table 3.1, entry 6). The apparent misalignment of the light scattering trace from both the viscometer and the refractive index detectors was a common feature in the analyses of polymers produced by metallocene catalysts, which was not observed either in Chapter 2 or in control reactions where no metallocene was present.

3.5: Mechanistic Studies

Although significant increases in conversion followed the introduction of all three metallocenes, there remained no direct evidence explaining how they initiate ROCOP. Therefore, experiments were performed to detect the generation of catalytic intermediates and follow the propagation of nascent polymer chains. It was hypothesised that [Cp₂ZrCl₂] would react with propylene oxide (PO) in the absence of co-catalyst to give two species, likely a mono- and bis(alkoxide) (**Scheme 3.5**).



Scheme 3.5: Synthesis of mono- and bis(alkoxide) complexes from $[\text{Cp}_2\text{ZrCl}_2]$ and propylene oxide. Note the regiochemistry of the ring-opening at the least hindered carbon of propylene oxide.

After addition of 20 equivalents of PO (20 mmol) to $[\text{Cp}_2\text{ZrCl}_2]$ in a DCM solution in a Schlenk flask, there was complete conversion of $[\text{Cp}_2\text{ZrCl}_2]$ to two complexes. This is illustrated in **Figure 3.8a-b**, where the $[\text{Cp}_2\text{ZrCl}_2]$ resonance at δ^{H} 6.48 ppm (red) is replaced by two species marked by yellow and green circles. Addition of another 20 equivalents of PO pushed conversion to a solitary major product marked by green circles in (**Figure 3.8c**). This species had ^1H NMR signals in a 10:2:4:6 integration ratio, whilst ^1H - ^1H COSY experiments confirmed the mutual coupling of the signal at δ^{H} = 4.15 (x) with the two resonances at δ^{H} = 3.34 (y) and 1.16 (z) (**Figure 3.8d**). This is consistent with a bis(alkoxide) complex and confirms the feasibility of reaction of the metallocene pre-catalysts with epoxides.

Whilst there is clear evidence of reaction to one major product, there remains two regiochemical possibilities for epoxide opening: either at the most or least hindered carbon, as the COSY spectrum displayed in **Figure 3.8d** cannot by itself distinguish between the two. Therefore, ^1H chemical shifts for the (bis)alkoxides that result from attack at either carbon atoms were predicted using DFT calculations in Gaussian 09 (M06 functional, def2-TZVP basis set, CHCl_3 implicit solvent).^{48,49} This was achieved by first optimising geometries for both regiochemical possibilities and ethanol (the reference molecule used here), before confirming they were true minima (no imaginary frequencies) and then calculating shielding tensors. Ethanol was chosen as a reference given its chemical similarity to the alkoxides, and that its chemical shifts (3.72, 1.25) span a similar region of the ^1H NMR spectrum.⁵⁰ Although shielding tensors are not the same as chemical shift, they scale linearly (analogously to degrees Celsius and Kelvin), and so interconversion can be achieved by comparing the simulated shielding tensors and known chemical shift for ethanol, and then applying the same conversion to both alkoxide complexes. In the case of the bis(alkoxide) resulting from attack at the least hindered carbon, this yielded predicted chemical shifts closely compatible (maximum deviation = 0.11 ppm) with those observed experimentally, suggesting the assigned regiochemistry in **Scheme 3.5** (*i.e.* chloride attack at the least hindered carbon of PO) is the major product [DFT predicted δ^{H} = 4.25 (2H), 3.35 (4H), 1.27 (6H), observed δ^{H} = 4.15 (2H), 3.34 (4H), 1.16 (6H)]. Indeed, a similar prediction on the isomer resulting from attack of the most hindered position gave δ^{H} = 4.24 (2H), 4.22 (4H), 1.45 (6H),

a far poorer match to the observed spectrum, as summarised in **Scheme 3.6**. This simulation is in agreement with the observed regioselectivity in [Al(Salph)Cl] reaction with PO.³⁰

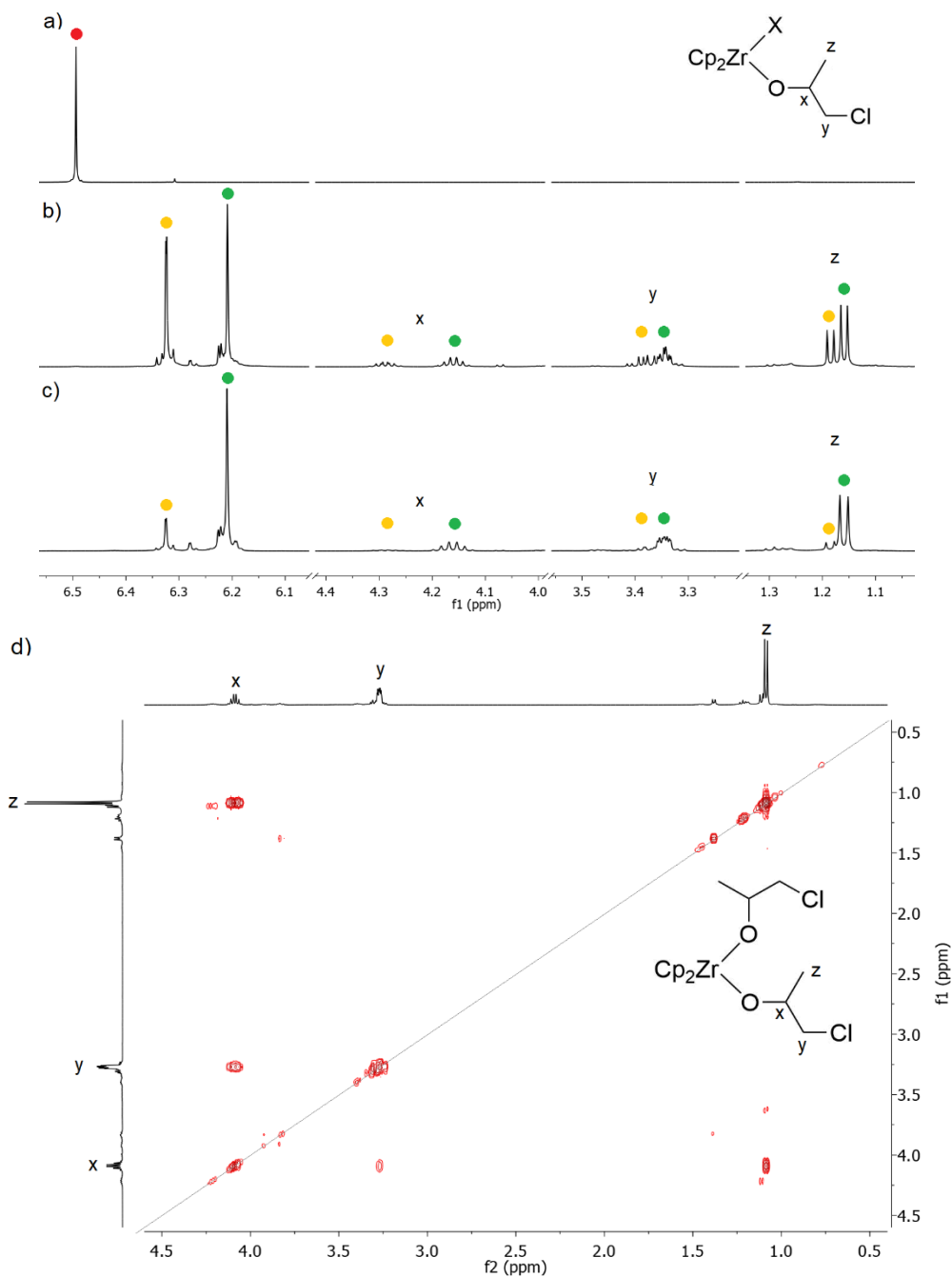
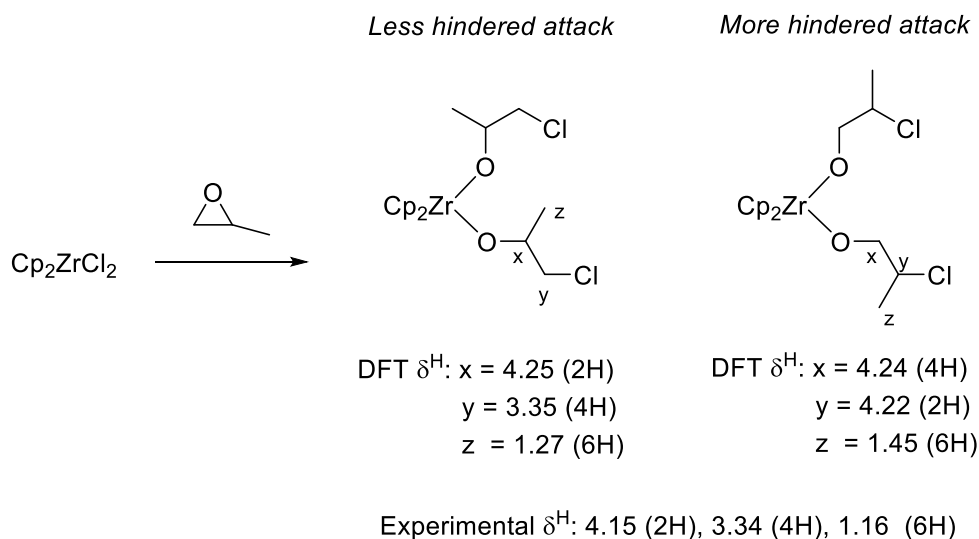
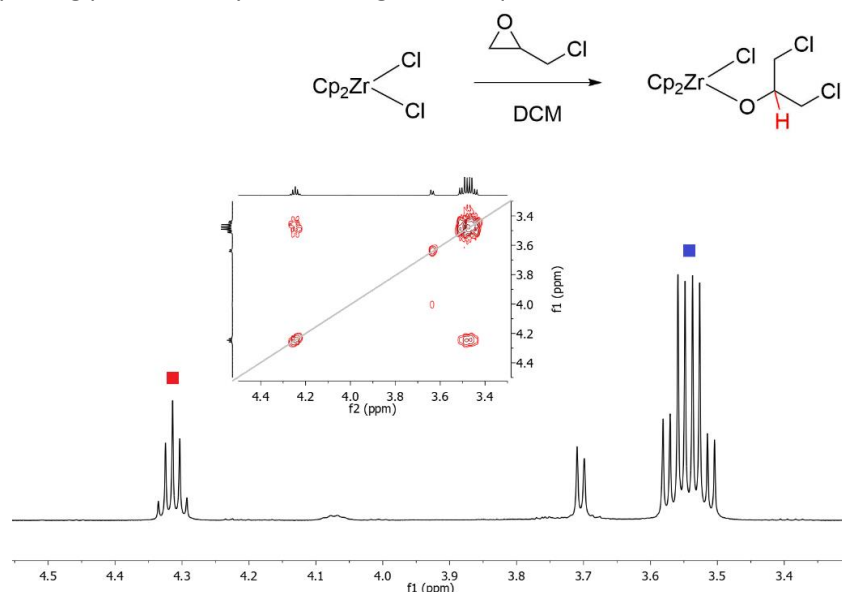


Figure 3.8a-d: Stacked ¹H NMR spectra (CDCl₃, 500 MHz) of top (a): Cp₂ZrCl₂ (red), middle (b): after reaction with 20 (20 mmol) equivalents of PO and bottom (c): after addition of a further 20 equivalents of PO (¹H-¹H COSY NMR below this (d)). Yellow resonances represent the mono(alkoxide) product (X = Cl) and green the bis(alkoxide) (X = OCH(Me)CH₂Cl). The COSY spectrum highlights the coupling of x-y and x-z (but not y-z).



Scheme 3.6: DFT predicted ^1H NMR chemical shifts for both regio-isomers of the bis(alkoxide) complex resulting from the reaction of $[\text{Cp}_2\text{ZrCl}_2]$ with excess PO. Note the far closer agreement with the experimental chemical shifts for the isomer resulting from chloride attack at the least hindered position of PO.

To experimentally confirm the regiochemistry, analogous reactions with epichlorohydrin were conducted, which gave two mutually coupled proton environments in a 4:1 ratio, the latter of which presents as a 1:4:6:4:1 quintet (red square, **Scheme 3.7**, $J = 5.3$ Hz). This coupling to four chemically equivalent protons is not possible if attack occurs at the most hindered carbon, where one would expect a triplet of triplets for the single proton environment. Puzzlingly, the methylene groups of the alkoxide appear as a 1:1:2:2:2:2:1:1 octet, despite only coupling to the methine proton in red, with this complex splitting pattern likely due to magnetic inequivalence between the methylene protons.



Scheme 3.7: Alkoxide region of the ^1H NMR spectrum (CDCl_3 , 500 MHz) reaction of $[\text{Cp}_2\text{ZrCl}_2]$ with epichlorohydrin, with ^1H - ^1H COSY insert. Red = 1:4:6:4:1 ($J = 5.3$ Hz) quintet resulting from coupling only to four chemically equivalent protons (blue), indicating reaction at the least hindered position.

As for the role of the co-catalyst in the polymerisation, similar experiments were performed using $[\text{Cp}_2\text{ZrCl}_2]$, but this time with two equivalents of DMAP (1 eq. = 34.2 μmol , in an NMR tube, 0.5 mL CDCl_3). This precise 1:2 ratio gave rise to new metallocene species once two equivalents of CHO were added (at room temperature, **Figure 3.9**). Given the previous experiments, these new metallocene species are likely zirconium-alkoxides, and are shown by orange circles in **Figure 3.9**, alongside $[\text{Cp}_2\text{ZrCl}_2]$ (red circle), DMAP (blue diamonds), and unreacted CHO (green triangles).

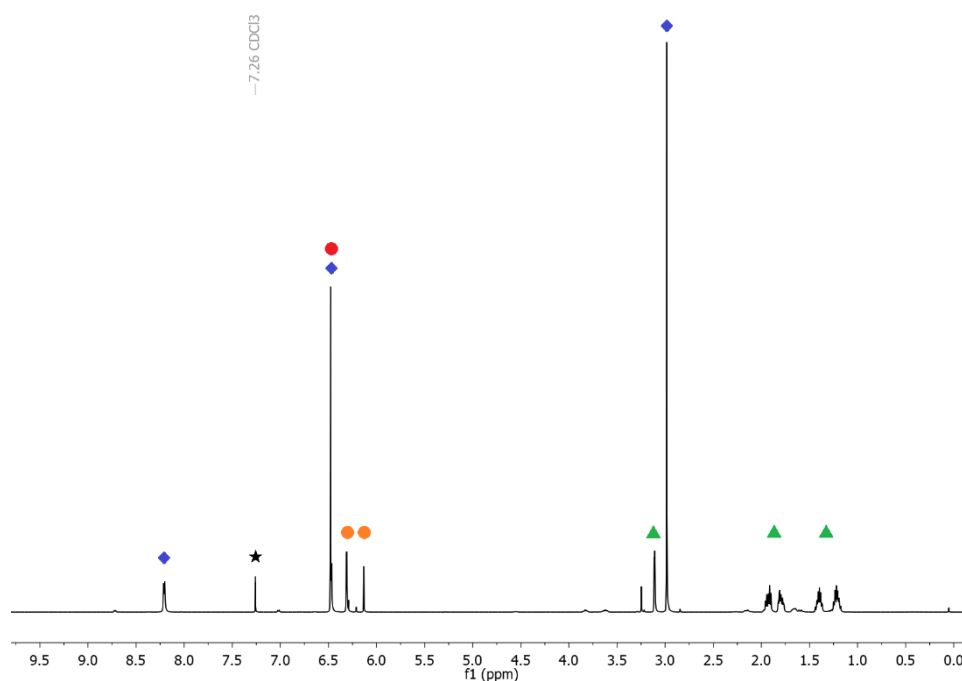


Figure 3.9: ^1H NMR spectrum (CDCl_3 , 500 MHz) of a 1:2:2 mixture of Cp_2ZrCl_2 : DMAP: CHO. Black star = CDCl_3 , blue diamonds = DMAP, red circle = Cp_2ZrCl_2 , green triangles = CHO, orange circles = new metallocene resonances.

After heating the NMR tube to 60°C for 4 hours (**Figure 3.10**), the new metallocene peaks became more intense, with signals beginning to appear in the ether region for CHO of the ^1H NMR spectrum, again likely attributed to metal alkoxide complexes resulting from the ring-opening of CHO (pink triangles, 3.5-4.0 ppm). More succinctly, resonances corresponding to DMAP-opened alkoxides (as indicated by COSY, **Figure 3.10**) highlight the feasibility of metal-free initiation, albeit the ratio of these signals (purple diamonds) to those of unreacted DMAP ($\delta^{\text{H}} = 8.21, 6.47, 2.98$, blue diamonds) is far lower than the equivalent ratio for metallocene species, where the original $[\text{Cp}_2\text{ZrCl}_2]$ is completely consumed. This mirrors the previously discussed experimental data, in that DMAP is an effective catalyst, but its initiation is slower than when used in combination with metallocenes, as reflected by the lower conversions in polymerisation reactions when only DMAP was used.

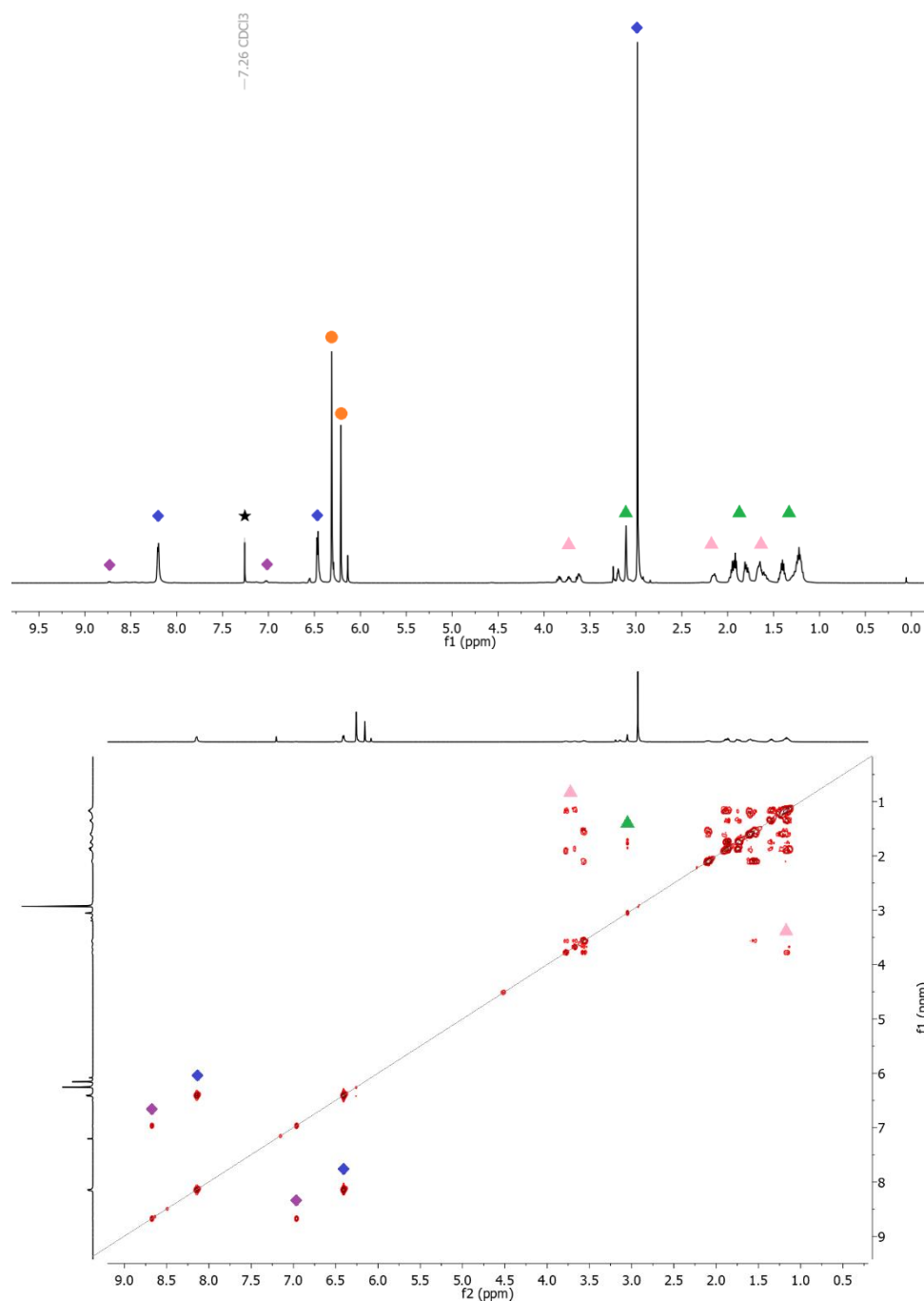


Figure S3.10: ^1H NMR spectrum (CDCl_3 , 500 MHz) (top) and ^1H - ^1H COSY spectrum (bottom) of a 1:2:2 mixture of Cp_2ZrCl_2 : DMAP: CHO after being heated to 60 °C. Black star = CDCl_3 , blue diamonds = DMAP, red circle = $[\text{Cp}_2\text{ZrCl}_2]$, green triangles = CHO, orange circles = new metallocene resonances, purple diamonds = reacted DMAP, pink triangles = ring-opened CHO.

Addition of two equivalents of PA led to new resonances comparable to signals in the spectrum of the CHO-PA copolymer, both in the ester and aromatic regions (**Figure 3.11**). No heating or any appreciable timeframe was required to see complete conversion of PA, showing the facile nature of anhydride opening compared to that of epoxide.

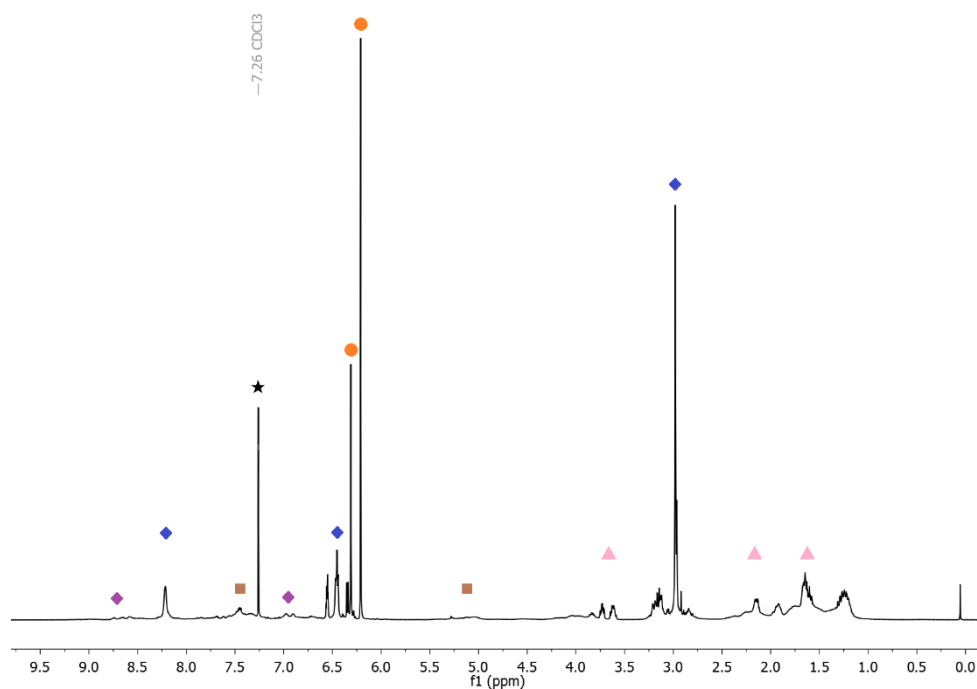


Figure 3.11: ^1H NMR spectrum (CDCl_3 , 500 MHz) of a 1:2:2 mixture of $[\text{Cp}_2\text{ZrCl}_2]$: DMAP: CHO: PA. Black star = CDCl_3 , blue diamonds = DMAP, red circle = Cp_2ZrCl_2 , green triangles = CHO, orange circles = new metallocene resonances, purple diamonds = reacted DMAP, pink triangles = ring-opened CHO. Brown squares = resonances associated with ring-opened PA-CHO units (“the ester region”).

Following the addition of two more equivalents of CHO, the reaction mixture was evacuated to dryness and analysed by electrospray ionisation mass spectrometry (ESI-MS), with ring-opened products initiated by DMAP apparent in positive mode (**Figure 3.12**). A chloride-initiated CHO-PA unit was seen in negative mode spectrum, alongside an unsaturated fragment of $m/z = 245.09$ Da, presumably forming within the mass spectrometer after a loss of HCl (**Figure 3.13**).

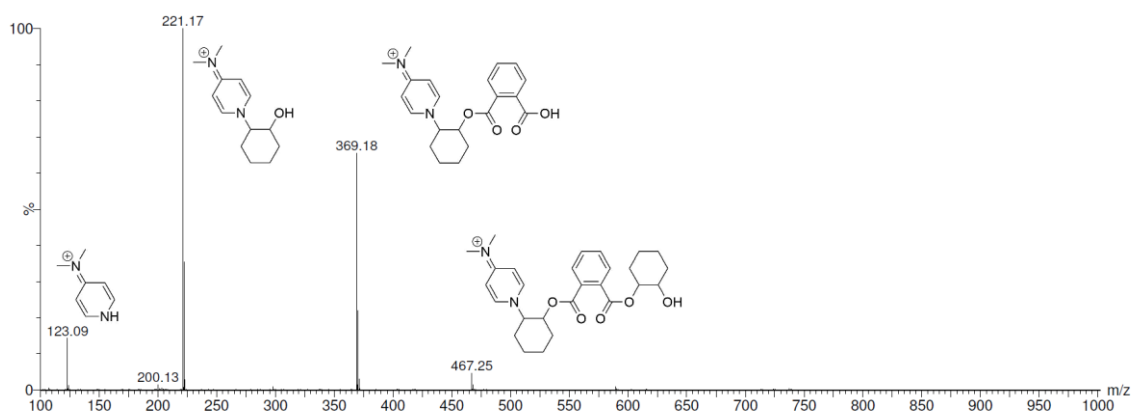


Figure 3.12: Positive mode electrospray ionisation mass spectrum of the products of a 1:2:4 reaction of $[\text{Cp}_2\text{ZrCl}_2]$: DMAP: CHO: PA conducted in CDCl_3 , with structures of characterisable cations indicated.

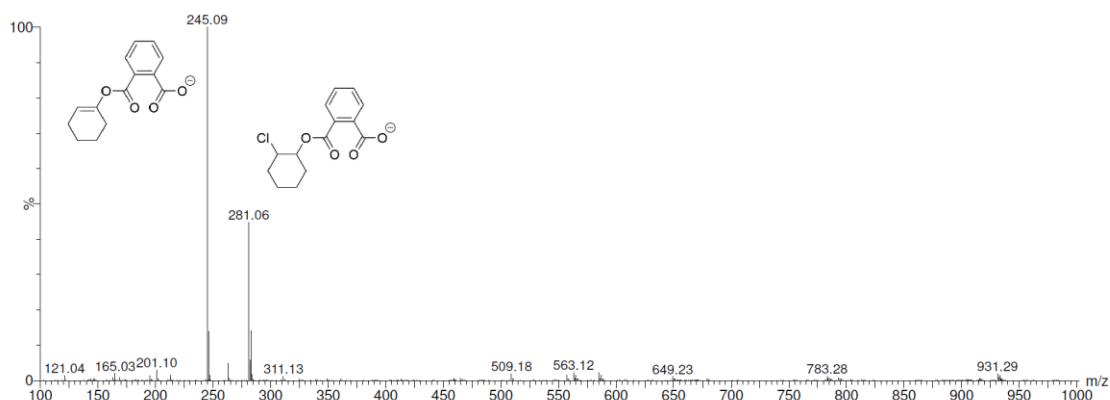
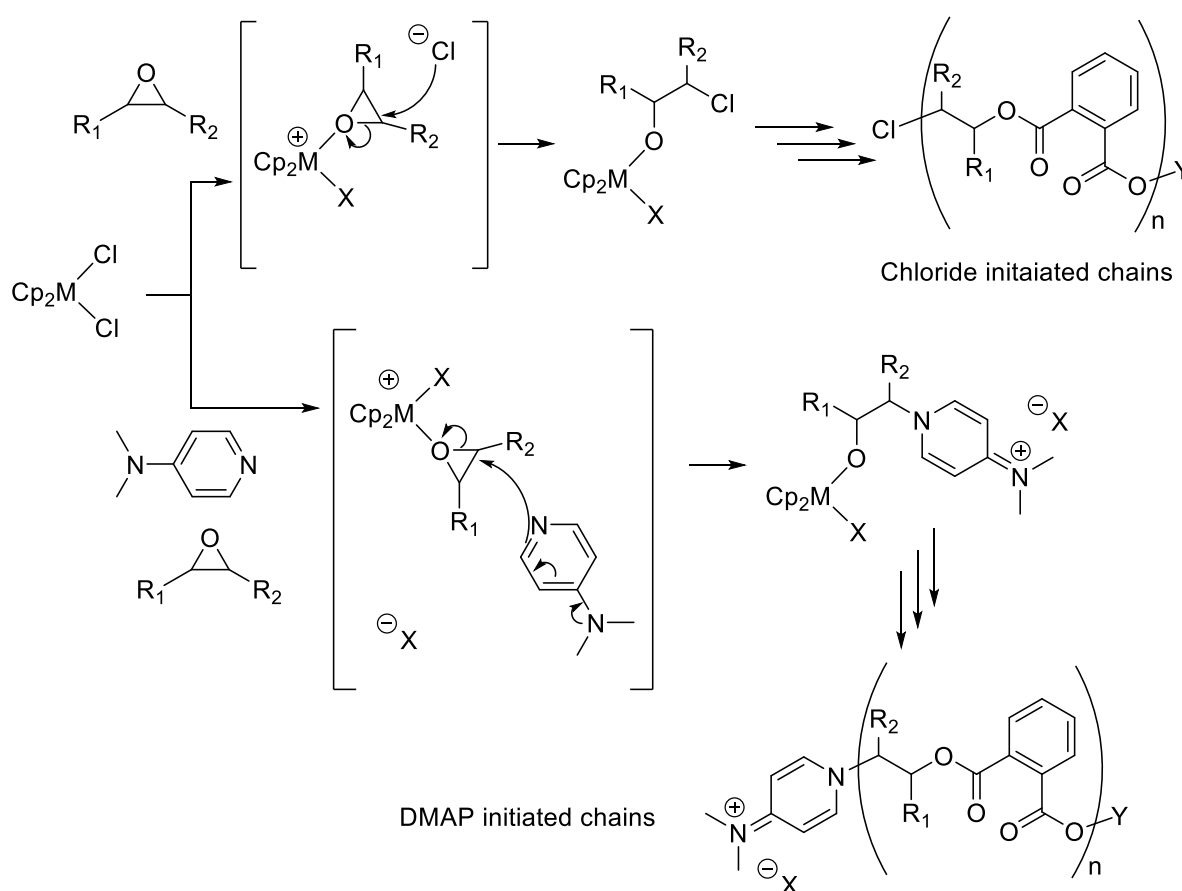


Figure 3.13: Negative mode electrospray ionisation mass spectrum of the products of a 1:2:4:2 reaction of $[\text{Cp}_2\text{ZrCl}_2]$: DMAP: CHO: PA conducted in CDCl_3 , with structures of characterisable anions indicated.

A summary of the proposed initiation modes is shown in **Scheme 3.8**, which details how both DMAP and chloride-initiated chains can arise, with the prevalence of both types of initiation consistent with both the stoichiometric reactions and MALDI-ToF spectra of the polymers as seen in section 3.4. This is not inclusive of DMAP initiated chains where no metal is involved, which will be present given the significant rate (as observed in section 3.3) of the DMAP-only control reaction.



Scheme 3.8 Proposed initiation routes to generate chloride initiated polymer chains (observed in stoichiometric studies) and DMAP initiated polymer chains (observed in stoichiometric studies and MALDI-ToF of polymers) for the ROCOP of a generic epoxide and PA. For reaction with the first chloride of the pre-catalyst, $\text{X} = \text{Cl}$. For reaction of the second chloride, $\text{X} = \text{carboxylate}$. Note that DMAP initiated chains are zwitterionic and so X may represent the carboxylate terminus of the same or different polymer chain, as well as chloride. $\text{Y} = \text{chain terminus}$.

3.6: Density Functional Theory Calculations

Further understanding of the propagation mechanism of the metallocene-mediated polymerisation was obtained using DFT calculations. Previous calculations performed by Cramer, Coates, Tolman and co-workers demonstrated a feasible propagation cycle for an aluminium Salph catalyst; and the previously discussed experimental observations are consistent with said mechanism. Therefore, this was used as the starting point for our calculations, examining $[\text{Cp}_2\text{Ti}(\text{OAc})_2]$ as an on-cycle catalyst for the copolymerisation of ethylene oxide (EO) and succinic anhydride (SA).³⁰ Since experimentally, the rate-limiting step is epoxide opening (affording an alkoxide) and anhydride addition (affording a carboxylate) is fast, the resting state of the catalyst is expected to contain two carboxylate-terminated polymer chains, which were truncated for computational simplicity and modelled as acetate ligands. The initiation steps (*i.e.* reaction of chloride pre-catalysts) examined by stoichiometric reactions were not studied here. EO and SA were initially chosen as substrates both for computational simplicity and to eliminate a large volume of conformational ambiguity leading to difficulty in isolating true minima for each intermediate. Therefore, the energies are expected to be attenuated by the steric and electronic parameters of the experimental substrates, as well as changeable ring strain.

In terms of establishing a feasible catalytic cycle, one must first consider the potential energy surface for any given reaction. This consists of relating energy against the $3N-6$ vibrational degrees of freedom that make up non-linear molecules, and which ultimately, dictate their structure. As all intermediates on the multi-step route are local minima, they are also mathematically speaking, stationary points on the potential energy surface, meaning the partial differential of energy with respect to these geometric parameters (bond lengths, angles *etc.*) will approach zero, with the second differential (in the case of a minimum) a positive value. Therefore, to find an intermediate, a structure is first allowed to relax towards a given convergence limit, which minimises the electronic energy of the system. Once this convergence is met, a frequency calculation determines vibrational frequency of all the bonds; positive values indicate “real” vibrations and therefore that the second differential is positive, whereas negative values indicate the inverse, either a local maximum, or not fully minimised structure. If no negative frequencies are found, a structure is considered a genuine local minimum.

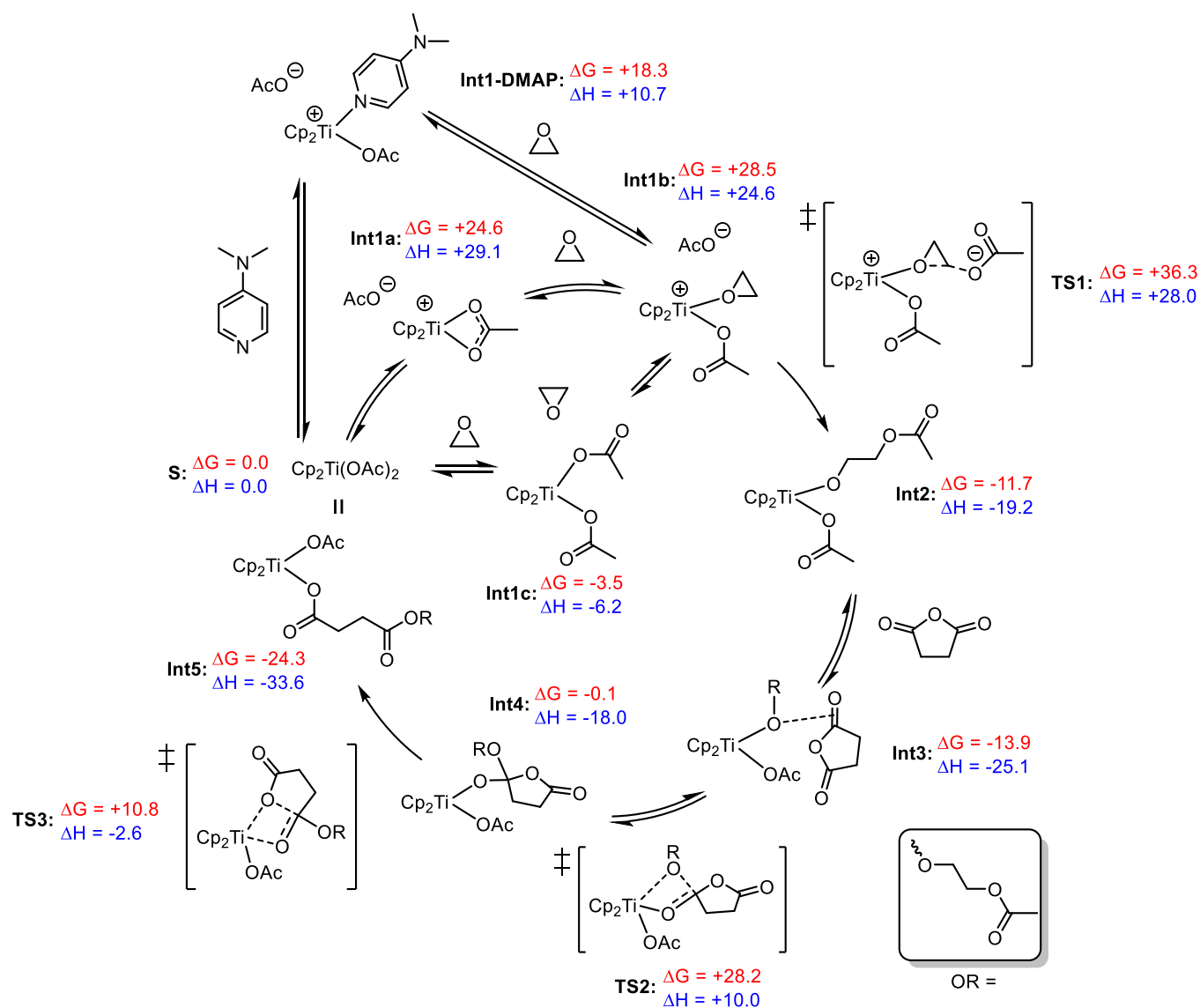
Conversely, transition states are saddle points on the potential energy surface, which means they are local minima with respect to all geometric parameters except one, the reaction coordinate, for which it is a local maximum. Therefore, finding transition states is different to intermediates; firstly, one can

perform a potential energy scan of a given bond (say a forming C-O bond when a hydroxide ion attacks a primary alkyl bromide *via* S_N2), whereby the structure is allowed to totally relax aside from this one parameter, which is adjusted by increments of a specified distance (say 0.1 Å). A sequence of these increments allows one to see the relationship between that bond distance and energy, with the maximum being closer to the transition state. This process can then be repeated for another aspect of the reaction coordinate (for example, the breaking C-Br bond of the above S_N2 example), with a similar downward facing curve expected. Repeated scans of smaller increments can be performed when the structure is close to that of the transition state. Once this has been achieved, a transition state calculation will run much like a geometry optimisation for a minimum, except that one degree of freedom will be maximised, not minimised. This returns a structure that once a frequency calculation is performed will have one negative, or imaginary, frequency, which once animated resembles the reaction coordinate (imagine a visual representation of hydroxide displacing a bromine atom during S_N2, the O-C bond will shorten whilst the C-Br bond simultaneously lengthens).

Frequency calculations also allows for the vibrational partition function to be calculated, which in turn allows for the computation of thermodynamic properties like free energies and enthalpies, rather than purely electronic energies. However, these thermodynamic properties are calculated at standard concentration, temperature, and pressure, which in the case of polymerisations (where the concentration of monomers far exceeds the concentration of catalyst) is not particularly relevant. Using the GoodVibes program can alter these concentrations and temperatures, allowing for a more accurate representation of experimental conditions.⁵¹ GoodVibes also corrects for low frequency vibrations which disproportionately inflate entropic parameters, and consequently free energy. The free energies and enthalpies between intermediates and transition states can then be compared, allowing one to construct a catalytic cycle.

Returning to the catalytic cycle of metallocene mediated ROCOP, the proximity of the two labile sites in the [Cp₂Ti] intermediates allows for two different routes for anhydride opening: a) insertion of a metal-alkoxide into a non-coordinating anhydride (as described by Cramer, Coates and Tolman) followed by spontaneous ring-opening or b) migratory insertion of a metal-alkoxide into a metal-bound anhydride, similar to a route often invoked in the ring-opening polymerisation (ROP) of lactones.⁵²⁻⁵⁴ This possibility was not considered in the Coates study as the [Al(Salph)Cl] catalyst used features a tetradentate ligand of *trans* symmetry, meaning migratory insertion is not possible between the two *trans* active sites. However, no minima corresponding to anhydride coordination could be

found for this system for EO/SA, and so the energetically feasible propagation cycle displayed in **Scheme 3.9** features an initial insertion step, followed by a distinct ring-opening step. The M06 functional was used in conjunction with the def2-TZVP basis set, alongside implicit toluene solvent.^{48,49,55–57}



Scheme 3.9: Energetically feasible propagation cycle for the polymerisation of ethylene oxide and succinic anhydride with a $[\text{Cp}_2\text{Ti}(\text{OAc})_2]$ on-cycle catalyst. As calculated in Gaussian 09 at the m06/def2tzvp level of theory (implicit toluene solvent).^{48,49,55–57} Free energies and enthalpies are quoted in kcal mol^{-1} , and have been temperature corrected (70 °C) and concentration corrected using the GoodVibes software package.⁵¹

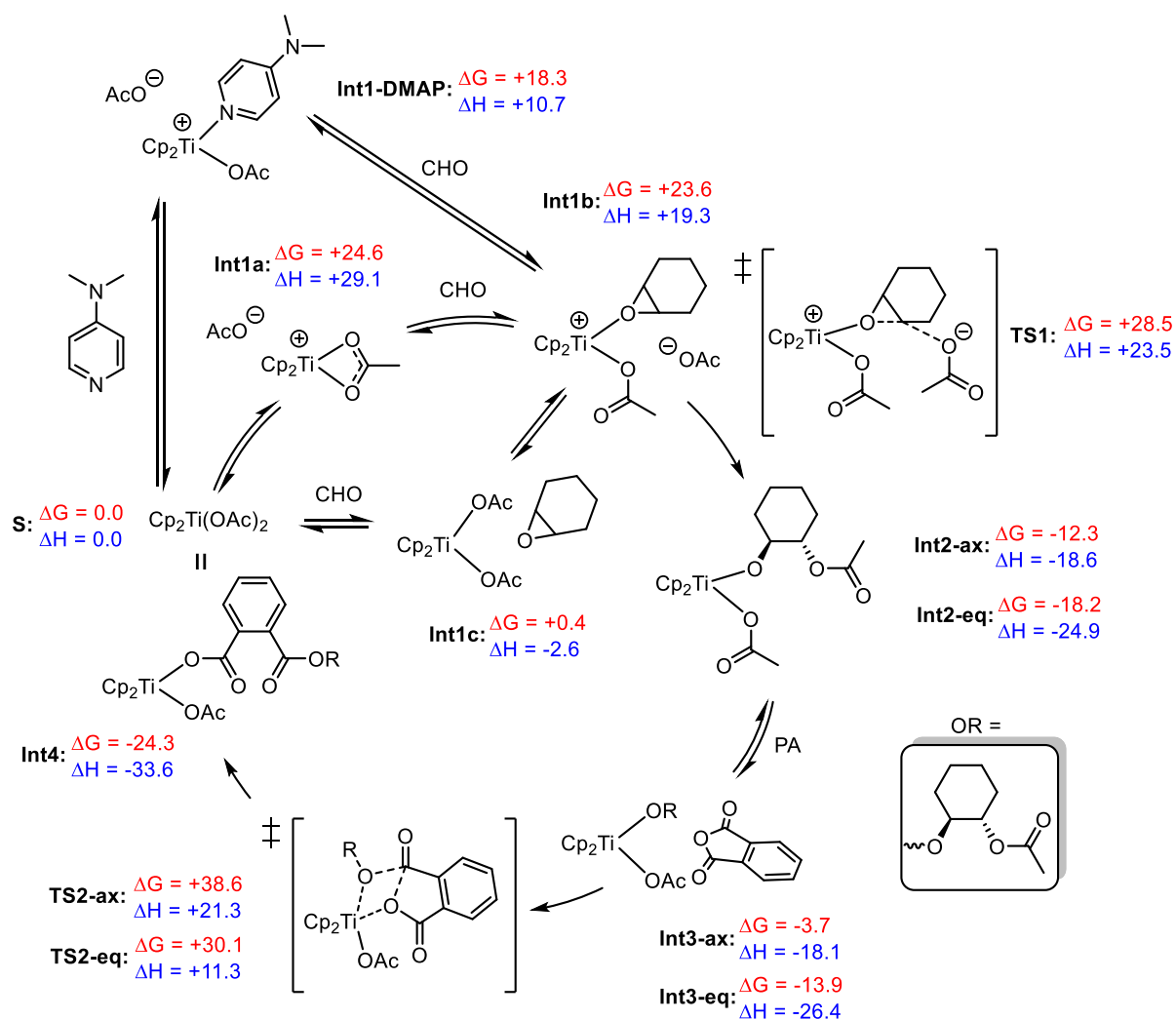
Starting from the resting state, **S**, there is a choice of pathways to **Int1b**, the precursor to epoxide opening. Either association of ethylene oxide (though not coordination, no such minima could be found) to $[\text{Cp}_2\text{Ti}(\text{OAc})_2]$ to give **Int1c**, or the formation of an ion pair resulting from the dissociation of one acetate ligand (**Int1a**). In addition to its role as a nucleophilic co-catalyst (as indicated by MALDI-ToF and stoichiometric reactions), it is possible to imagine a role for DMAP in the propagation cycle;

as a strong donor one may expect coordination to the metal centre, helping to facilitate the de-coordination of polymer chains necessary for the binding and reaction of addition substrate. Although **Int1-DMAP** is energetically accessible (+18.3 kcal mol⁻¹), attempts to observe metal-DMAP complexes by ¹H NMR spectroscopy proved fruitless, although this does not necessarily preclude a potentially transient existence.

The subsequent epoxide opening transition state (**TS1**) is significantly higher in energy than anhydride insertion (36.3 kcal mol⁻¹ vs. 28.2 kcal mol⁻¹), which corroborates experimental findings that epoxide opening is the rate limiting step. The product of this opening, **Int2**, is significantly lower in energy than **Int1b**. As with ethylene oxide, no minima corresponding to **Int2** with an additional coordinated anhydride could be found, and the equivalent complex with a decoordinated acetate was found to be significantly (≈ 40 kcal mol⁻¹) higher in free energy than **Int3**. Quantum Theory of Atoms in Molecules (QTAIM) and Natural Bonding Orbital (NBO) analyses highlighted weak interactions between the anhydride protons and acetate oxygens, as well as a bond critical point between the alkoxide oxygen and the C=O bond of the anhydride. Although weak, this interaction may be significant, as it mirrors the reaction coordinate in **TS2** for anhydride insertion. Finally, the ring-opening of the anhydride is completed with the relatively low energy **TS3**, remaking a bis(carboxylate) complex analogous to the starting point [Cp₂TiOAc₂].

As previously discussed in the context of the MALDI-ToF spectra of synthesised polymers, many of these carboxylate-terminated polymer chains will be DMAP initiated, and thereby zwitterionic. In this sense, DMAP may perform a role analogous to that described for [PPN]⁺ counterions in previous computational studies.³⁰ Overall, the cycle is both exothermic ($\Delta H < 0$) and spontaneous ($\Delta G < 0$), whilst the lower energy barriers to anhydride insertion/opening compared to epoxide opening are consistent with the lack of heating required for anhydride consumption in the stoichiometric reactions described previously.

Whilst modelling EO/SA as substrates allows for simpler computation a reduced conformational complexity, examination of “real” substrates more closely resembles experimental conditions. To that end, the cycle was re-calculated using CHO and PA as monomers, with the analogous catalytic cycle shown in **Scheme 3.10**.



Scheme 3.10: Energetically feasible propagation cycle for the polymerisation of cyclohexene oxide and phthalic anhydride with a $[\text{Cp}_2\text{Ti}(\text{OAc})_2]$ on-cycle catalyst. As calculated in Gaussian 09 at the m06/def2tzvp level of theory (implicit toluene solvent).^{48,49,55–57} Free energies and enthalpies are quoted in kcal mol^{-1} , and have been temperature corrected (70 °C) and concentration corrected using the GoodVibes software package.⁵¹

One of the major implications of modelling CHO rather than EO is the possibility for ring-flipped structures. The ring-opening of the epoxide immediately produces a 1,2-diaxial OCCO conformation (**Int2-ax**), but the ring-flipped diequatorial isomer **Int2-eq** is seen to be significantly ($5.9 \text{ kcal mol}^{-1}$) lower in free energy, with this diequatorial arrangement preferred through the rest of the cycle. In an interesting departure from the previously discussed cycle for EO/SA, no minimum could be found for insertion of a Ti-alkoxide into an off-metal anhydride, instead, **TS2** leads immediately to a fully ring-opened anhydride, **Int4**. This could be due to the larger steric demands of PA, as full ring opening allows for the growing polymer chain to “stretch”, placing the bulky aromatic ring of PA further from the metal. Alternatively, from an electronic standpoint, PA could be more susceptible to ring opening through a weaker C-O bond, meaning ring opening is essentially irreversible.

Perhaps the most important distinction between the two cycles is the re-ordering of the relative energies. The highest energy structure in the EO/SA is **TS1**, epoxide opening, which is consistent with experimental findings. However, for CHO-PA, both **TS2-eq** and **TS2-ax** are higher in energy than **TS1**, meaning anhydride opening *should* be rate limiting according to this model. Several attempts were made to find alternative structures for **TS2** (both axial and equatorial) which were significantly lower in energy, yet this could not be achieved. This either indicates a weakness of the computational method, or that an alternative, lower energy pathway for anhydride opening exists yet could not be found. This possibility is more likely in the case of PA and CHO, where there is a far larger area of conformational space to explore than for EO/SA. Also, the energy difference between **TS1** and **TS2-eq** is only 1.6 kcal mol⁻¹, and so is within computational error, meaning it is possible that **TS2-eq** is the lowest energy pathway to anhydride opening, but is energetically either identical to or slightly more favourable than epoxide opening. In reality, a combination of the above is likely responsible for this re-ordering.

3.7: Copolymerisation of Limonene Oxide

A key advantage of ROCOP is the wide variety of available substrates, meaning unsaturated natural products such as pinene or limonene can be epoxidated and used to produce partially renewable polyesters. Therefore, investigations were extended to (+)-limonene-1,2-epoxide (mixture of *cis/trans* isomers) (LO), which required harsher conditions to polymerise given the increased level of substitution about the epoxide functionality. The results of its copolymerisation with PA at 100 °C with all three Group 4 metallocenes are detailed in **Table 3.4**, where similarly to the results for TCPA both [Cp₂ZrCl₂] and [Cp₂HfCl₂] (entries 2 and 3) led to the largest increases in conversion in comparison to control reactions (entry 4). Again, this could be attributed to the greater ionic radii of zirconium and hafnium facilitating reaction with a sterically demanding monomer. Indeed, the slow rate of reaction with LO has in turn greatly reduced the rate of epoxide homopolymerisation, as seen through the complete absence of ether linkages detected in any of the polymers. Unsurprisingly, molecular weights are relatively high when only DMAP is used, and in general molecular weights are decreased compared to copolymers of CHO and VCHO with PA (**Table 3.1**), with this consistent with literature reports when using LO.^{27,46} In conjunction with this are the observed increases in \bar{M}_n (aside from CHO-PA [Cp₂HfCl₂], entry 3 **table 3.1**) which does not significantly change) when moving from CHO or VCHO to LO, suggesting that chain transfer is far more favourable with LO at higher reaction temperatures.

Table 3.4: Small scale copolymerisation of LO with PA. ^a

Entry	Cp ₂ MCl ₂	Conversion PA ^b / %	Ester ^c / %	M _n ^d / kDa	Đ ^{d,e}
1	Ti	58	>95	6.4	1.51
2	Zr	75	>95	5.8	1.52
3	Hf	78	>95	5.1	1.59
4	None	34	>95	14.6	1.27

^a Average of at least three runs. Conditions: 1 eq. = 6.4 μmol (1 eq.) metallocene (unless otherwise stated), 2 eq. DMAP, 400 eq. PA, 400 eq. epoxide, 1 mL toluene, 100 °C for 29 hours. ^b Determined by ¹H NMR spectroscopy of reaction mixture. ^c Determined by ¹H NMR spectroscopy of the resultant polymer. ^d Determined by GPC (viscometry detection against polystyrene standards). ^e Đ = M_w / M_n.

MALDI-ToF mass spectrometry was used to study the poly(LO-*alt*-PA) produced, with a representative example (taken from entry 2) displayed in **Figure 3.14**. Instead of the complex spectra seen in section 3.4 for non-perfectly alternative copolymers, only two series separated by *m/z* 300.3 were present.

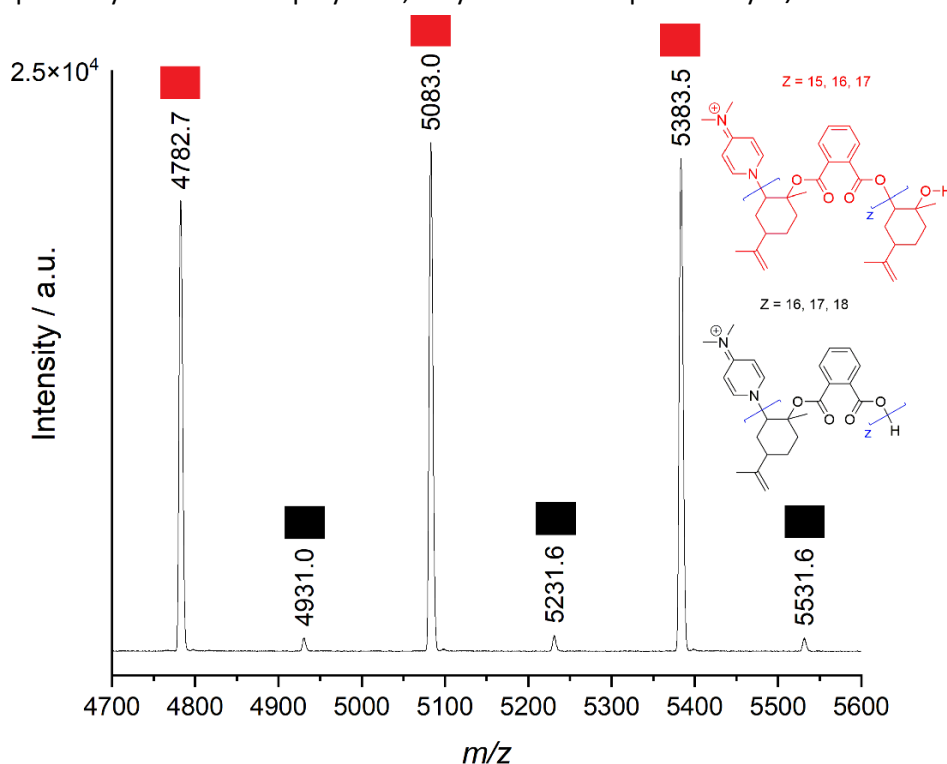


Figure 3.14: Portion of the MALDI-ToF spectrum of poly(LO-*alt*-PA) ([Cp₂ZrCl₂], entry 2, table 3.4), with labelled series. Given the lack of polyether resonances observed in the ¹H NMR spectrum, the position of the “extra” LO unit in the red series is assigned as an end group.

As there were no detectable ether linkages in the ^1H NMR spectra of the polymers, the series corresponding to an “extra” LO unit (red) is likely to represent an end group of a protonated LO.

Although comparisons to previously reported catalytic systems are tentative given significant differences in both reaction conditions and catalyst loading, the performance of $[\text{Cp}_2\text{ZrCl}_2]$ is somewhat comparable to known examples. For example, (salophan)Al-Cl and (salophan)Cr-Cl pre-catalysts have produced 24 and 28% conversion after 5 hours in toluene respectively at a higher catalyst loading and elevated temperature ($110\text{ }^\circ\text{C}$)⁵⁸, whilst an aminotriphenolate iron complex gave 46% conversion (84% in THF) in 24 hours at a higher concentration but far reduced ($65\text{ }^\circ\text{C}$) temperature with [PPN]Cl as a co-catalyst.⁵⁹ In terms of catalysis employing the Group 4 metals, a recent report of a iminotriphenolate titanium complex (section 3.2, **Scheme 3.3**, complex **3.18**) gave poly(LO-*alt*-PA) in neat LO at $130\text{ }^\circ\text{C}$, achieving 80% LO conversion in 1.5 hours using 1 equivalent of [PPN]Cl as a co-catalyst.²⁷ Although this is far faster, the catalyst loading is significantly higher (1:250 vs 1:400 as above) and the incredibly forcing conditions led to a polymer with 20% ether units. However, the performance of $[\text{Cp}_2\text{ZrCl}_2]$ is significantly poorer than one of the leading catalysts for this transformation, a $[(\beta\text{-diiminate})\text{Zn}(\text{OAc})]$ complex published by Coates.⁶⁰ Here, the authors reported a perfectly alternating copolymer of *trans*-LO and diglycolic anhydride of M_n 36 kDa ($\text{Đ} = 1.2$), produced under mild conditions ($70\text{ }^\circ\text{C}$) in toluene solution in the absence of co-catalyst. Although an excess of epoxide and higher catalyst loadings were used, this still represents a significantly faster (81% epoxide conversion in 16 hours) reaction given the colder temperature used. The authors also achieved a more moderate M_n of 12 kDa when copolymerising *trans*-LO and maleic anhydride.

Interestingly, in contrast to the high ether selectivity seen in the absence of DMAP for CHO and VCHO, polymerisations performed using $[\text{Cp}_2\text{ZrCl}_2]$ and LO-PA produced oligomers ($M_n = 950\text{ Da}$, $\text{PDI} = 1.5$, *c.a.* 3-4 LO-PA units) with no discernible ether linkages in the ^1H NMR spectrum. Although these reactions occurred with far lower activity (52% conversion of PA in 72 hrs) than those conducted employing DMAP as a co-catalyst, there is clearly potential for further catalyst development to produce a metallocene-like pre-catalyst which is both highly active and selective without the need for a co-catalyst. To this end, a series of polymerisations were conducted with varying ratios of DMAP: $[\text{Cp}_2\text{ZrCl}_2]$, with this compared to the rate of PA conversion. All polymerisations produced no detectable ether linkages. **Figure 3.15** shows the positive correlation between rate and DMAP concentration, which highlights the importance, yet not absolute reliance, of successful catalysis on the co-catalyst.

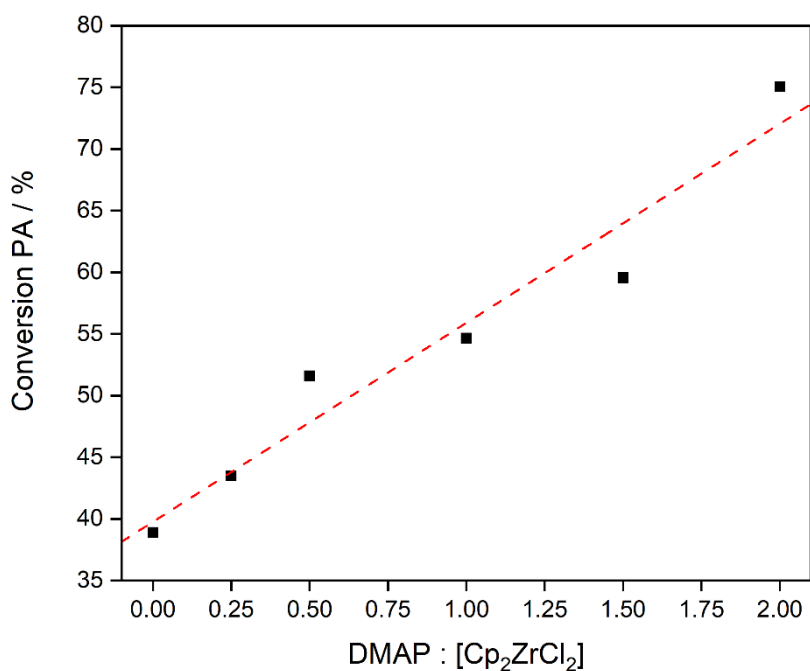
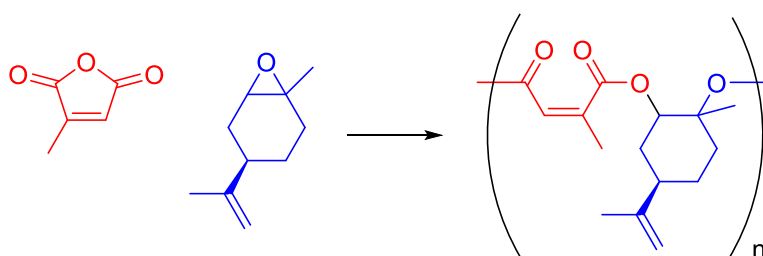


Figure 3.15: Conversion of PA against ratio of DMAP to [Cp₂ZrCl₂] used in the polymerisation of LO and PA. Conditions: 100 °C, 1 mL toluene, 6.4 μmol [Cp₂ZrCl₂], 400 eq. LO, 400 eq. PA, 29 hours.

Although there is a reported synthetic route to PA using renewable feedstocks, PA is typically made from petrochemicals, meaning poly(LO-*alt*-PA) is only partially bio-derived.⁶¹ Therefore, several attempts to copolymerise LO with citraconic anhydride, derived from the renewably sourced itaconic acid, (**Scheme 3.11**) were made.⁶² However, under the reaction conditions employed above, no polymerisation was observed. Indeed, using a range of solvents (including THF, xylene, diglyme and dioxane), both [Cp₂TiCl₂] and [Cp₂ZrCl₂], and indeed performing the polymerisation in neat citraconic anhydride also gave no reaction. Although this combination of monomers has never been reported, the lack of reactivity again highlights a substrate compatibility issue with the metallocene pre-catalysts.



Scheme 3.11: Attempted copolymerisation of two bio-derived monomers, citraconic anhydride and LO.

Despite extensive research in the field, epoxide-anhydride ROCOP is in its infancy as a technology, and as such there are few examples of multi-gram scale polymer syntheses using ROCOP. The ability to tolerate scale-up is clearly an important factor in process development, whilst also bridging the gap between catalytic chemistry and materials science. Therefore, given its favourable characteristics, a large-scale synthesis (500x scale, identical monomer feed ratios and temperature used, see section 7.1 for full details) of the LO-PA copolymer was performed with $[\text{Cp}_2\text{ZrCl}_2]$, yielding 218 g (57%) of perfectly alternating polyester when run to 81% anhydride conversion. An image of the reactor set up is shown in **Figure 3.16**, with a key difference being the fitting of an argon bubbler, rather than a sealed vial as used on the small scale, meaning the system is no longer closed.

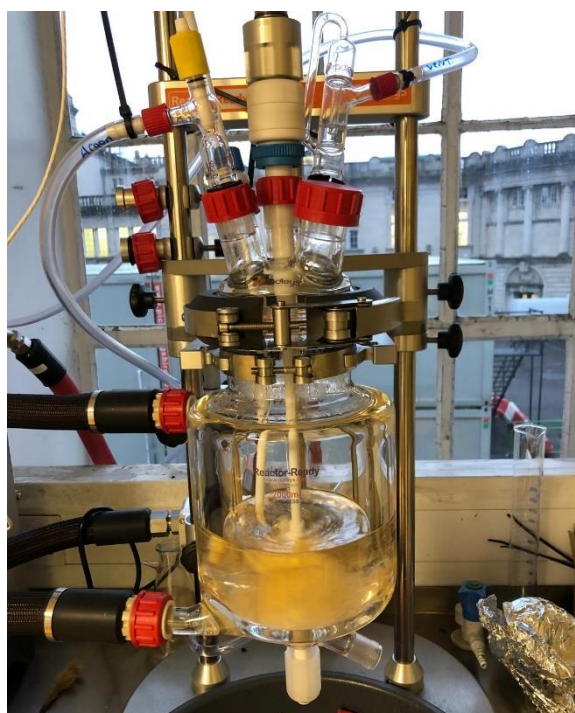


Figure 3.16: Image of large scale (x500) polymerisation of LO and PA using $[\text{Cp}_2\text{ZrCl}_2]$ and 2 equivalents of DMAP, with identical feed ratios to those used on the small scale. Note the internally controlled temperature using the thermocouple, the mechanical stirring and fitting of argon bubbler.

On this scale, distilling epoxides from CaH_2 and subliming anhydrides becomes impractical, and so a special consideration to whether the catalyst system is still effective under necessarily less stringently controlled reaction conditions is required. The observed drop in M_n from 5.8 to 4.1 kg mol^{-1} without using these techniques is unsurprising since trace amounts of water or phthalic acid can facilitate chain transfer. Pleasingly however, the PDI of the large-scale polymer decreased to 1.36 (vs. 1.52 on the small scale), meaning the reaction remains well controlled even without extensive purification of the monomers. This clearly demonstrates the utility of ROCOP in producing larger quantities of polymer, and investigations into the material properties and modification of this specific batch of poly(LO-*alt*-OA) are detailed fully in Chapter 4.

3.8: *ansa*-Zirconocenes as Pre-Catalysts

In many instances, *ansa*-metallocenes have proved more effective catalysts than their unbridged counterparts in olefin polymerisations. *ansa*-metallocenes were the first class of molecular catalysts to generate stereoregular polypropylene, and can also be used as one component of a catalyst mixture used to synthesise linear low density polyethylene.^{63,64} To add to this, the replacement of one Cp ring for an imido donor in a so-called “constrained geometry catalyst” has further expanded their use, including in the polymerisation of conjugated dienes such as 1,3-butadiene or isoprene.^{65,66} Given this precedent, and the promising activities seen for the unsubstituted metallocene complexes discussed previously, two silyl bridged *ansa*-metallocenes (**Zr-1**, **Zr-2**) and a constrained geometry catalyst **Zr-3** were targeted for use in ROCOP (**Figure 3.17**).

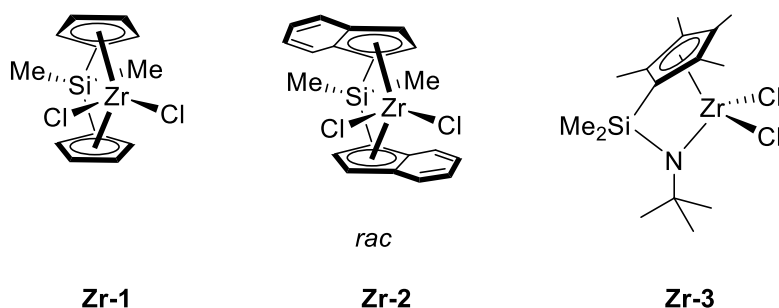
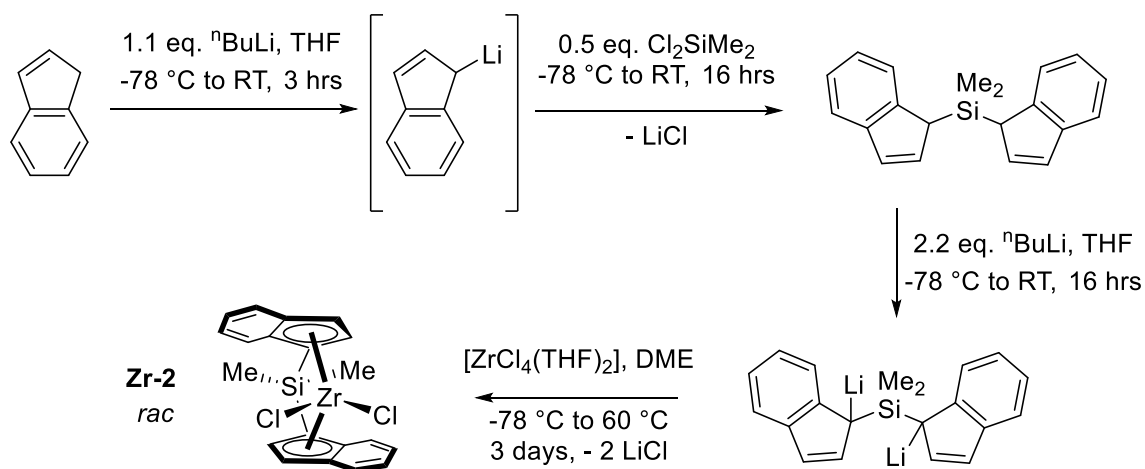


Figure 3.17: Three silyl bridged metallocenes and half-metallocene targeted for use in ROCOP.

Unfortunately, a single attempt to synthesise **Zr-3** failed to produce material of sufficient purity, with repeated recrystallisations yielding diminishing small quantities of complex. **Zr-2** was successfully synthesised according to the pathway in **Scheme 3.12**, whilst **Zr-1** was synthesised in an identical manner but starting from lithium cyclopentadienide as opposed to cracked dicyclopentadiene.



Scheme 3.12: Synthesis of **Zr-2** (**Zr-1** was made in an identical manner but starting from lithium cyclopentadienide, Li-C₅H₅). Square brackets indicate the intermediate was not isolated.

The *ansa*-indenyl complex **Zr-2** was screened as the C_2 symmetric *rac* isomer only, as the corresponding *meso* isomer could not be isolated cleanly. The isolation of a *rac* isomer only is commonplace for complexes of this type.⁶⁷ DME was used as a solvent as performing the reactions in toluene (as reported in the literature)⁶⁸ led to the formation of highly insoluble products, reminiscent of “ate-complex” formation, where elimination of LiCl is incomplete post-ligation.^{69,70} DME allowed for better de-coordination of LiCl in a more polar environment, and was preferred to other ethereal solvents like ether due to its higher boiling point, and THF given its tendency to ring-open at the Lewis acidic $[ZrCl_4(THF)_2]$ precursor. Full details of the syntheses can be found in section 7.4.

The catalytic ability of **Zr-1** and **Zr-2** was investigated by copolymerising CHO or LO with PA under identical conditions to those used in sections 3.3 and 3.7 respectively, thus allowing direct comparison to the simple metallocene pre-catalysts (**Table 3.5**). Interestingly, conversions and selectivities were rather similar for **Zr-1**, **Zr-2**, and $[Cp_2ZrCl_2]$ (entries 1-3 and 5-7), for both CHO and LO, although **Zr-2** produced the highest conversion of PA for CHO, and $[Cp_2ZrCl_2]$ had the highest PA conversion for LO. In terms of molecular weight, both *ansa*-zirconocenes produced polyesters of significantly reduced molecular weight compared to control reactions (entries 4, 8) and $[Cp_2ZrCl_2]$ (entries 3, 7). In spite of this dramatic decrease, polydispersities for **Zr-2** were comparable to $[Cp_2ZrCl_2]$, whereas significantly broader molecular weight distributions were observed when **Zr-1** was used as a pre-catalyst.

Table 3.5: Copolymerisations of CHO or LO with PA using **Zr-1** and **Zr-2** as pre-catalysts, as well as comparisons to $[Cp_2ZrCl_2]$ and the DMAP only control reaction. ^a

Entry	Epoxide	Zr Pre-Catalyst	Conversion PA ^b / %	Ester ^c / %	M_n ^d / kDa	\mathcal{D} ^{d,e}
1		Zr-1	68	82	4.9	1.73
2	CHO, $t = 21$	Zr-2	69	82	4.9	1.40
3	hours, 80 °C	$[Cp_2ZrCl_2]$	61	83	17.7	1.39
4		None	32	>95	19.1	1.22
5		Zr-1	67	>95	2.7	1.72
6	LO, $t = 29$	Zr-2	73	>95	2.9	1.48
7	hours, 100 °C	$[Cp_2ZrCl_2]$	75	>95	5.8	1.52
8		None	34	>95	14.6	1.27

^a Average of at least two runs. Conditions: 1 eq. = 6.4 μ mol (1 eq.) Zr complex (unless otherwise stated), 2 eq. DMAP, 400 eq. PA, 400 eq. epoxide, 1 mL toluene, for indicated time and reaction temperature. ^b Determined by ¹H NMR spectroscopy of reaction mixture. ^c Determined by ¹H NMR spectroscopy of the resultant polymer. ^d Determined by GPC (viscometry detection against polystyrene standards). ^e $\mathcal{D} = M_w / M_n$.

Another difference between **Zr-1** and **Zr-2** was observed in the size-exclusion chromatograms obtained from GPC analysis, where for CHO-PA (but not LO-PA) **Zr-2** showed an alignment between all three detectors, including the light scattering detector. This contrasts with **Zr-1**, where a misalignment of the light scattering trace was seen, in the same way as for the simple metallocene pre-catalysts as discussed in section 3.4. The reasons why **Zr-2** showed this behaviour is not clear, although the additional steric protection of the indenyl ligands may somehow hinder the formation of poly(CHO-*alt*-PA) aggregates that are likely responsible for the peculiar light scattering traces of the other polymers.⁴⁷ However for poly(LO-*alt*-PA), the typical misalignment of the light scattering detector was observed. Although the reason for this switch in behaviour from CHO to LO unclear, the enhanced reaction temperature for LO may open up additional reaction pathways that could increase the formation of aggregated. With the alignment of the light scattering detector, analysis of molecular weight by triple detection was possible for poly(CHO-*alt*-PA) for **Zr-2**, which produced an M_n of 17.4 kDa and a \mathcal{D} of 1.20. This molecular weight is far higher (and polydispersity somewhat narrower) than that seen by viscometry detection, suggesting that viscometry detection may be prone to underestimating polymer molecular weights.

To further probe the catalytic ability of **Zr-1** and **Zr-2**, copolymerisations of LO and PA were conducted with no co-catalyst (**Table 3.6**). Unfortunately, insufficient quantities of pure polymeric material could be isolated to be fully characterised by GPC. This likely indicates that much of the observed reactivity leads to oligomer formations, with these oligomers soluble in isopropanol. This precludes their isolation and separation from unreacted PA during work-up, and thereby prevents accurate GPC analysis. However, crude ¹H NMR analysis showed no detectable ether linkages as well as additional peaks in the ester region, likely corresponding to end groups and very short chain oligomers. In terms of comparisons to [Cp₂ZrCl₂], there is a marginal increase in PA conversion for both **Zr-1** and **Zr-2**, which produce near identical conversions.

Table 3.6: Copolymerisation of LO with PA in the absence of co-catalyst. ^a

Zr Pre-Catalyst	Conversion PA ^b / %	Ester ^c / %	M_n ^d / kDa	\mathcal{D} ^{d,e}
Zr-1	46	>95	-	-
Zr-2	47	>95	-	-
[Cp ₂ ZrCl ₂]	39	>95	-	-

^a Conditions: 1 eq. = 6.4 μ mol (1 eq.) [Zr], 400 eq. PA, 400 eq. epoxide, 1 mL toluene, 100 °C for 29 hours. ^b Determined by ¹H NMR spectroscopy of reaction mixture. ^c Determined by ¹H NMR spectroscopy of the resultant polymer. ^d Determined by GPC (viscometry detection against polystyrene standards). ^e $\mathcal{D} = M_w / M_n$.

Despite this modest improvement, these reactions again highlight the crucial role of the co-catalyst in this system, which clearly benefit from additional DMAP to act as an external nucleophile to initiate more polymer chains, thereby increasing conversion and molecular weight, as well as selectivity for epoxides other than LO.

3.9: Summary

Group 4 metallocene complexes were shown to be catalytically active in ROCOP, albeit with relatively modest rate enhancement and non-perfect ester selectivity. Reactions conducted in neat epoxide showed pseudo zero-order kinetics, and thereby that epoxide opening was rate limiting. Across different substrates, the performance of each metal changed, with $[\text{Cp}_2\text{TiCl}_2]$ proving more effective for copolymerisations of CHO and PA, whilst $[\text{Cp}_2\text{ZrCl}_2]$ and $[\text{Cp}_2\text{HfCl}_2]$ were superior when TCPA was used in place of PA, likely due to the increased steric demand placed on a 1st row metal by a fully halogenated anhydride. Ether linkage formation occurred within polyester chains, rather than as a separate reaction, which was evidenced by MALDI-ToF mass spectrometry showing different levels of ether incorporation, and by DOSY NMR spectroscopy.

Mechanistic studies showed that $[\text{Cp}_2\text{ZrCl}_2]$ regioselectively ring-opened epichlorohydrin and propylene oxide when no-cocatalyst was present. Stoichiometric reactions when DMAP was present produced reaction mixtures containing oligomers, which were both chloride and DMAP initiated. DFT calculations allowed an energetically feasible catalytic cycle to be presented for simplified substrates and $[\text{Cp}_2\text{TiCl}_2]$. This cycle featured anhydride opening at an anhydride not directly bound to the metal centre, in contrast with the cycle reported in section 2.5 for aluminium. Added complications were encountered when real substrates in CHO and PA were modelled, with calculations suggesting that anhydride opening becomes rate-limiting. This re-ordering likely indicates that due to the hugely increased conformational space than must be explored by the calculations, that the transition state found is not the lowest energy transition state for anhydride opening.

The bio-derived limonene oxide was successfully copolymerised by the metallocene pre-catalysts, again providing significant rate enhancement compared to control reactions. Also, perfect ester selectivity was observed for LO, likely due to the unfavorability of LO homopolymerisation compared to CHO homopolymerisation. Over 200g of poly(LO-*alt*-PA) was synthesised in a single batch using

[Cp₂ZrCl₂], with only modest deterioration in molecular weight compared to small scale reactions, where more comprehensive monomer purification techniques are available.

Two *ansa*-zirconocene pre-catalysts were also tested for ROCOP, the polymerisation performance of which were largely similar to each other. Rates of conversion were comparable to those achieved with [Cp₂ZrCl₂], but molecular weights were far smaller. The *ansa*-zirconocenes were also able to produce oligomers of poly(LO-*alt*-PA) in the absence of co-catalyst.

3.10: References for Chapter 3

- 1 K. Ziegler, Nobel Lecture: Consequences and Development of an Invention - NobelPrize.org, <https://www.nobelprize.org/prizes/chemistry/1963/ziegler/lecture/>, (accessed 19 May 2020).
- 2 G. Natta, Nobel Lecture: From the Stereospecific Polymerization to the Asymmetric Autocatalytic Synthesis of Macromolecules, <https://www.nobelprize.org/prizes/chemistry/1963/natta/lecture/>, (accessed 19 May 2020).
- 3 G. J. P. Britovsek, V. C. Gibson and D. F. Wass, *Angew. Chemie - Int. Ed.*, 1999, **38**, 428–447.
- 4 M. Bochmann, *J. Chem. Soc. - Dalt. Trans.*, 1996, 255–270.
- 5 A. Andresen, H. -G Cordes, J. Herwig, W. Kaminsky, A. Merck, R. Mottweiler, J. Pein, H. Sinn and H. -J Vollmer, *Angew. Chemie Int. Ed. English*, 1976, **15**, 630–632.
- 6 H. Sinn, W. Kaminsky, H. -J Vollmer and R. Woldt, *Angew. Chemie Int. Ed. English*, 1980, **19**, 390–392.
- 7 L. Resconi, S. Bossi and L. Abis, *Macromolecules*, 1990, **23**, 4489–4491.
- 8 W. Kaminsky, *J. Chem. Soc. - Dalt. Trans.*, 1998, 1413–1418.
- 9 G. W. Coates, *Chem. Rev.*, 2000, **100**, 1223–1252.
- 10 B. D. Ward, O. G. Guppy and M. S. Shaw, in *Comprehensive Organometallic Chemistry IV*, Elsevier, 2022, pp. 85–162.
- 11 J. Chen, A. Motta, B. Wang, Y. Gao and T. J. Marks, *Angew. Chemie - Int. Ed.*, 2019, **58**, 7030–7034.
- 12 A. Rodriguez-Delgado, W. R. Mariott and E. Y. X. Chen, *Macromolecules*, 2004, **37**, 3092–3100.

- 13 S. Impemba, G. Roviello, S. Milione and C. Capacchione, *Inorg. Chem.*, 2021, **60**, 7561–7572.
- 14 Z. Sun, Y. Zhao, O. Santoro, M. R. J. Elsegood, E. V. Bedwell, K. Zahra, A. Walton and C. Redshaw, *Catal. Sci. Technol.*, 2020, **10**, 1619–1639.
- 15 A. G. Morozov, T. V. Martemyanova, V. A. Dodonov, O. V. Kazarina and I. L. Fedushkin, *Eur. J. Inorg. Chem.*, 2019, **2019**, 4198–4204.
- 16 M. D. Jones, L. Brady, P. McKeown, A. Buchard, P. M. Schäfer, L. H. Thomas, M. F. Mahon, T. J. Woodman and J. P. Lowe, *Chem. Sci.*, 2015, **6**, 5034–5039.
- 17 T. Xing, Z.-Y. Wang, Y.-C. Sun, Z.-H. He, K. Wang, Z.-T. Liu, M. R. J. Elsegood, E. V. Bedwell and C. Redshaw, *J. Appl. Polym. Sci.*, 2021, **138**, e50513.
- 18 S. K. Raman, A. C. Deacy, L. P. Carrodeguas, N. V. Reis, R. W. F. Kerr, A. Phanopoulos, S. Morton, M. G. Davidson and C. K. Williams, *Organometallics*, 2020, **39**, 1619–1627.
- 19 L. Suresh, R. Lalrempuia, J. B. Ekele, F. Gillis-D’Hamers, K. W. Törnroos, V. R. Jensen and E. Le Roux, *Molecules*, 2020, **25**, 4364.
- 20 R. Lalrempuia, J. Underhaug, K. W. Törnroos and E. Le Roux, *Chem. Commun.*, 2019, **55**, 7227–7230.
- 21 J. A. Garden, A. J. P. White and C. K. Williams, *Dalt. Trans.*, 2017, **46**, 2532–2541.
- 22 M. Mandal, D. Chakraborty and V. Ramkumar, *RSC Adv.*, 2015, **5**, 28536–28553.
- 23 M. Mandal, *J. Organomet. Chem.*, 2020, **907**, 121067.
- 24 S. Pappuru, D. Chakraborty, V. Ramkumar and D. K. Chand, *Polymer (Guildf.)*, 2017, **123**, 267–281.
- 25 R. W. F. Kerr and C. K. Williams, *J. Am. Chem. Soc.*, 2022, **144**, 6882–6893.
- 26 D. Takeuchi, T. Aida and T. Endo, *Macromol. Rapid Commun.*, 1999, **20**, 646–649.
- 27 Y. Jeong, M. K. Cho, S. Seo, H. Cho, K. Son and H. Kim, *ChemCatChem*, 2023, e202201086.
- 28 A. Meduri, M. Mazzeo, M. Lamberti, C. Capacchione and S. Milione, *Mol. Catal.*, 2019, **471**, 54–59.
- 29 T. Stößer, D. Mulryan and C. K. Williams, *Angew. Chemie - Int. Ed.*, 2018, **57**, 16893–16897.
- 30 M. E. Fieser, M. J. Sanford, L. A. Mitchell, C. R. Dunbar, M. Mandal, N. J. Van Zee, D. M. Urness, C. J. Cramer, G. W. Coates and W. B. Tolman, *J. Am. Chem. Soc.*, 2017, **139**, 15222–15231.

- 31 O. Shimomura, T. Nishisako, S. Yamaguchi, J. Ichihara, M. Kirino, A. Ohtaka and R. Nomura, *J. Mol. Catal. A Chem.*, 2016, **411**, 230–238.
- 32 O. Shimomura, K. Tokizane, T. Nishisako, S. Yamaguchi, J. Ichihara, M. Kirino, A. Ohtaka and R. Nomura, *Catalysts*, 2017, **7**, 172.
- 33 O. Shimomura, S. Sasaki, K. Kume, A. Ohtaka and R. Nomura, *J. Polym. Sci. Part A Polym. Chem.*, 2019, **57**, 2557–2561.
- 34 D. Bai, H. Jing, Q. Liu, Q. Zhu and X. Zhao, *Catal. Commun.*, 2009, **11**, 155–157.
- 35 D. Bai, G. Nian, G. Wang and Z. Wang, *Appl. Organomet. Chem.*, 2013, **27**, 184–187.
- 36 S. H. Kim, D. Ahn, Y. Y. Kang, M. Kim, K.-S. Lee, J. Lee, M. H. Park and Y. Kim, *Eur. J. Inorg. Chem.*, 2014, **2014**, 5107–5112.
- 37 M. S. Shaw, M. R. Bates, M. D. Jones and B. D. Ward, *Polym. Chem.*, 2022, **13**, 3315–3324.
- 38 N. Yi, T. T. D. Chen, J. Unruangsri, Y. Zhu and C. K. Williams, *Chem. Sci.*, 2019, **10**, 9974–9980.
- 39 G. Si, L. Zhang, B. Han, Z. Duan, B. Li, J. Dong, X. Li and B. Liu, *Polym. Chem.*, 2015, **6**, 6372–6377.
- 40 J. P. Agrawal and K. S. Kulkarni, *J. Appl. Polym. Sci.*, 1986, **32**, 5203–5214.
- 41 V. Shahedifar, A. Masoud Rezadoust and I. Amiri Amraei, *Propellants, Explos. Pyrotech.*, 2016, **41**, 321–326.
- 42 E. Hosseini Nejad, C. G. W. Van Melis, T. J. Vermeer, C. E. Koning and R. Duchateau, *Macromolecules*, 2012, **45**, 1770–1776.
- 43 N. J. Van Zee, M. J. Sanford and G. W. Coates, *J. Am. Chem. Soc.*, 2016, **138**, 2755–2761.
- 44 B. Liu, J. Chen, N. Liu, H. Ding, X. Wu, B. Dai and I. Kim, *Green Chem.*, 2020, **22**, 5742–5750.
- 45 J. M. Longo, M. J. Sanford and G. W. Coates, *Chem. Rev.*, 2016, **116**, 15167–15197.
- 46 F. Isnard, F. Santulli, M. Cozzolino, M. Lamberti, C. Pellicchia and M. Mazzeo, *Catal. Sci. Technol.*, 2019, **9**, 3090–3098.
- 47 T. Hofe and M. Susewind, *Column*, 2019, **15**, 14–19.
- 48 M. J. Frisch, G. W. Trucks, H. B. Schlegel, G. E. Scuseria, M. A. Robb, J. R. Cheeseman, G. Scalmani, V. Barone, G. Petersson, H. Nakatsuji, X. Li, M. Caricato, A. Marenich, J. Bloino, B. G. Janesko, R. Gomperts, B. Mennucci, H. P. Hratchian, J. V. Ortiz, A. F. Izmaylov, J. L. Sonnenberg,

- D. Williams-Young, F. Ding, F. Lipparini, F. Egidi, J. Goings, B. Peng, A. Petrone, T. Henderson, D. Ranasinghe, V. G. Zakrzewski, J. Gao, N. Rega, G. Zheng, W. Liang, M. Hada, M. Ehara, K. Toyota, R. Fukuda, J. Hasegawa, M. Ishida, T. Nakajima, Y. Honda, O. Kitao, H. Nakai, T. Vreven, K. Throssell, J. A. J. Montgomery, J. E. Peralta, F. Ogliaro, M. Bearpark, J. J. Heyd, E. Brothers, K. N. Kudin, V. N. Staroverov, T. Keith, R. Kobayashi, J. Normand, K. Raghavachari, A. Rendell, J. C. Burant, S. S. Iyengar, J. Tomasi, M. Cossi, J. M. Millam, M. Klene, C. Adamo, R. Cammi, J. W. Ochterski, R. L. Martin, K. Morokuma, O. Farkas, J. B. Foresman and D. J. Fox, *Gaussian 09, Revision D.01*, Gaussian Inc., Wallingford, CT, 2016.
- 49 Y. Zhao and D. G. Truhlar, *Theor. Chem. Acc.*, 2008, **120**, 215–241.
- 50 G. R. Fulmer, A. J. M. Miller, N. H. Sherden, H. E. Gottlieb, A. Nudelman, B. M. Stoltz, J. E. Bercaw and K. I. Goldberg, *Organometallics*, 2010, **29**, 2176–2179.
- 51 G. Luchini, J. Alegre-Requena, J. Rodriguez-Guerra, J. Chen and R. Paton, *Autom. Thermochem. Heterog. Comput. Chem. Data (v. 3.1.0). F1000Research*, 2020, **9**, 291.
- 52 H. E. Dyer, S. Huijser, N. Susperregui, F. Bonnet, A. D. Schwarz, R. Duchateau, L. Maron and P. Mountford, *Organometallics*, 2010, **29**, 3602–3621.
- 53 J. Wei, M. N. Riffel and P. L. Diaconescu, *Macromolecules*, 2017, **50**, 1847–1861.
- 54 C. Romain, Y. Zhu, P. Dingwall, S. Paul, H. S. Rzepa, A. Buchard and C. K. Williams, *J. Am. Chem. Soc.*, 2016, **138**, 4120–4131.
- 55 F. Weigend and R. Ahlrichs, *Phys. Chem. Chem. Phys.*, 2005, **7**, 3297–3305.
- 56 F. Weigend, *Phys. Chem. Chem. Phys.*, 2006, **8**, 1057–1065.
- 57 J. Tomasi, B. Mennucci and R. Cammi, *Chem. Rev.*, 2005, **105**, 2999–3094.
- 58 E. H. Nejad, A. Paoniasari, C. G. W. van Melis, C. E. Koning and R. Duchateau, *Macromolecules*, 2013, **46**, 631–637.
- 59 L. Peña Carrodegas, C. Martín and A. W. Kleij, *Macromolecules*, 2017, **50**, 5337–5345.
- 60 R. C. Jeske, A. M. DiCiccio and G. W. Coates, *J. Am. Chem. Soc.*, 2007, **129**, 11330–11331.
- 61 E. Mahmoud, D. A. Watson and R. F. Lobo, *Green Chem.*, 2014, **16**, 167–175.
- 62 M. J. Sanford, L. Peña Carrodegas, N. J. Van Zee, A. W. Kleij and G. W. Coates, *Macromolecules*, 2016, **49**, 6394–6400.
- 63 D. V. Uborsky, D. Y. Mladentsev, B. A. Guzeev, I. S. Borisov, A. Vittoria, C. Ehm, R. Cipullo, C.

- Hendriksen, N. Friederichs, V. Busico and A. Z. Voskoboynikov, *Dalt. Trans.*, 2020, **49**, 3015–3025.
- 64 J. H. Park, Y. E. Jang, J. Y. Jeon, M. J. Go, J. Lee, S. K. Kim, S. I. Lee and B. Y. Lee, *Dalt. Trans.*, 2014, **43**, 10132–10138.
- 65 H. Yuan, T. Kida, H. Kim, R. Tanaka, Z. Cai, Y. Nakayama and T. Shiono, *Macromolecules*, 2020, **53**, 4323–4329.
- 66 WO 2004/044018 A2, 2004.
- 67 K. A. Giffin, V. Cirriez, O. Santoro, A. Welle, E. Kirillov and J.-F. Carpentier, *Polymers (Basel)*, 2022, **14**, 2217.
- 68 J. W. Strauch, F. Jean-Luc, B. Stéphane, W. Cun, K. Gerald, F. Roland, H. Luftmann and G. Erker, *J. Am. Chem. Soc.*, 2004, **126**, 2089–2104.
- 69 S. Anga, K. Naktode, H. Adimulam and T. K. Panda, *Dalt. Trans.*, 2014, **43**, 14876–14888.
- 70 K. J. Blackmore, J. W. Ziller and A. F. Heyduk, *Inorg. Chem.*, 2008, **47**, 265–273.

Chapter 4: Post-Polymerisation Modification Reactions of Poly(LO-*alt*-PA) and Investigations into Polymer Flame Retardancy

4.1: Post-Polymerisation Modification Reactions

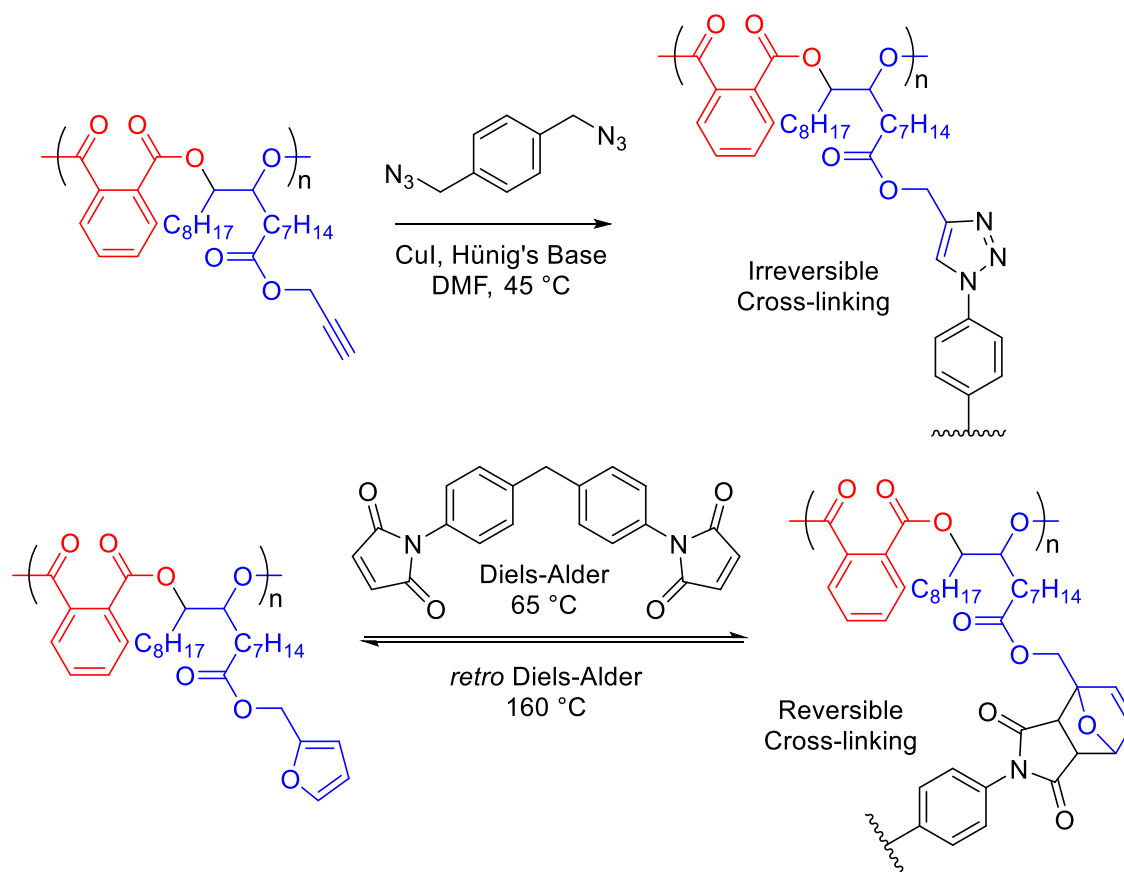
Reactively modifying polymers after their synthesis is a crucial strategy in preparing materials with specific and more desirable properties, and can trace its origins to the mid-19th Century and the vulcanisation of natural rubber with sulfur to increase its toughness.¹ Somewhat ironically, this predates the modern understanding of polymers as giant covalent macromolecules, yet the principle of modifying polymers in the same way one would small molecules has remains the same. Modern post-polymerisation modification (PPM) techniques are widely used if a certain functional group is desired in the final polymer, but is incompatible with the polymerisation reaction itself.² In place of this functionality, a (co-)monomer containing a different functional group, which is inert under polymerisation conditions, is used instead, before its subsequent reaction under different conditions to yield otherwise inaccessible chemical functionality. As well as the functional group tolerance of the monomer to the polymerisation conditions, the polymer must also be tolerant to the conditions required for the PPM reaction, which is particularly relevant for the hydrolysable polyesters produced by ROCOP that will be discussed in this chapter.

There is a huge diversity to PPM reactions, which include deprotections, simple addition reactions, Michael additions, isomerisation, oxidations or reductions, reversible and irreversible cross-linking, thermally induced curing, as well as transition metal catalysed cross-coupling chemistry.^{1,2} As well as modifying the chemistry of the polymer, PPM reactions may be aimed at manipulating the thermal properties of the material, such as the T_g , or the way the polymer self-assembles with a view to producing specific and highly controlled 3D architectures.^{3,4} In this section, PPM reactions including thiol-ene clicks, hydroboration-oxidation and phosphorylations will be performed on the poly(LO-*alt*-PA) copolymer produced on a large scale as described in section 3.7. The thermal properties of these polymers are also described, as are the flame retardant properties of the phosphorylated polymers.

4.2: Literature Modifications of ROCOP Polymers

Cross-linking is a common objective for PPM reactions, as a material's properties can be drastically changed, usually in the form of increased tensile strength and rigidity.⁵ This process is often irreversible, which is then termed "curing", and is commonly used to make thermoset materials, with these permanent cross-links precluding many thermal and solution processing techniques available to

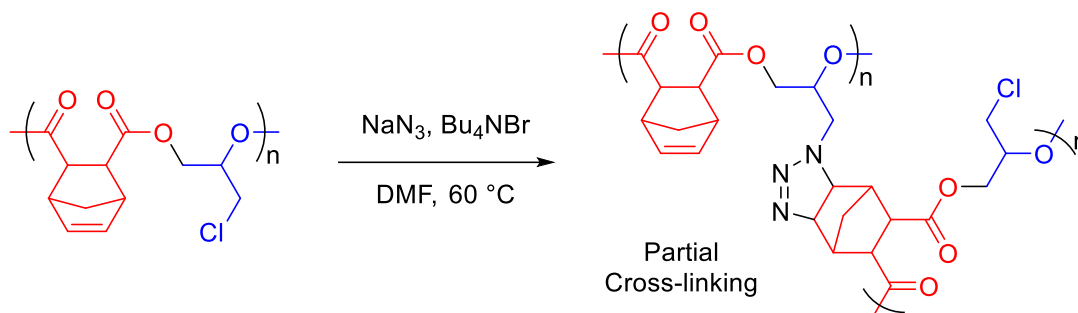
thermoplastics.⁶ However, cross-linking can also be reversible, with this allowing for easier reprocessing or recycling at a material's end of life stage.^{6,7} This concept has been neatly demonstrated on partially renewable ROCOP-made polyesters by Kleij and co-workers, who used a copper catalysed click reaction between an alkyne and a bis(azide) to form permanent cross-links, and a Diels-Alder reaction of a polymer containing pendant furan rings with a bis(maleimide) to form reversible cross-links (**Scheme 4.1**).⁸ As is common for thermosetting materials with high degrees of cross-linking, both cross-linked polymers were insoluble post-reaction, but, for the bis(maleimide) reversibly cross-linked polymer, the application of heat to shift the equilibrium towards the *retro* Diels-Alder pathway and the starting polymer allowed soluble material of identical molecular weight to be recovered. Furthermore, differential scanning calorimetry (DSC) traces of the Diels-Alder cross-linked polymers showed two endothermic transitions at 110 and 135 °C, indicating the different thermal stability of the *endo* and *exo* Diels-Alder adducts formed during the cross-linking process. Given the lack of solubility, cross-linked polymers of this type are often characterised by FT-IR spectroscopy.



Scheme 4.1: Formation of irreversible (top) and reversible (bottom) cross-links in a polyester made by the aluminium catalysed ROCOP of phthalic anhydride and biomass derived epoxides, as reported by Kleij *et al.*⁸

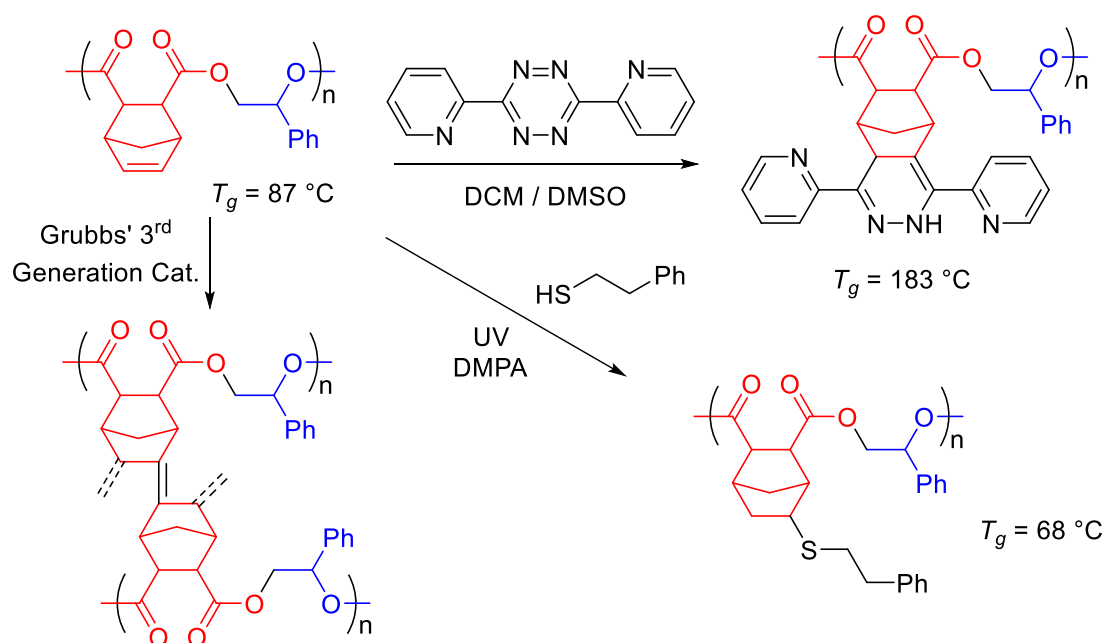
Another example of an azide-based cross-linking reaction was reported by Ding and colleagues, who showed that poly(ECH-*alt*-CA) would cross-link to form an insoluble material when reacted with NaN_3

(Scheme 4.2).⁹ This reaction was thought to process in two steps; first, the nucleophilic substitution of the chlorine atoms of the polymer with NaN₃, before cross-linking with the alkene groups of the anhydride. FT-IR analysis showed about 7% of the alkene groups had been cross-linked, with this small amount still sufficient to produce an insoluble polymer.



Scheme 4.2: Sodium azide mediated partial cross-linking on poly(ECH-*alt*-CA), as reported by Ding *et. al.*⁹

Alkene functionality is a widely used motif in PPM reactions given its highly versatile nature, which was demonstrated by Cheng and co-workers who performed three distinct PPM reactions of poly(SO-*alt*-CA) (SO = styrene oxide) (Scheme 4.3).¹⁰ This included a tetrazine click reaction, which introduced a high degree of aromaticity to the polymer and contributed to a near 100 °C increase in T_g compared to the unfunctionalised polymer, and cross-linking to form a gel with Grubbs' 3rd generation olefin metathesis catalyst.

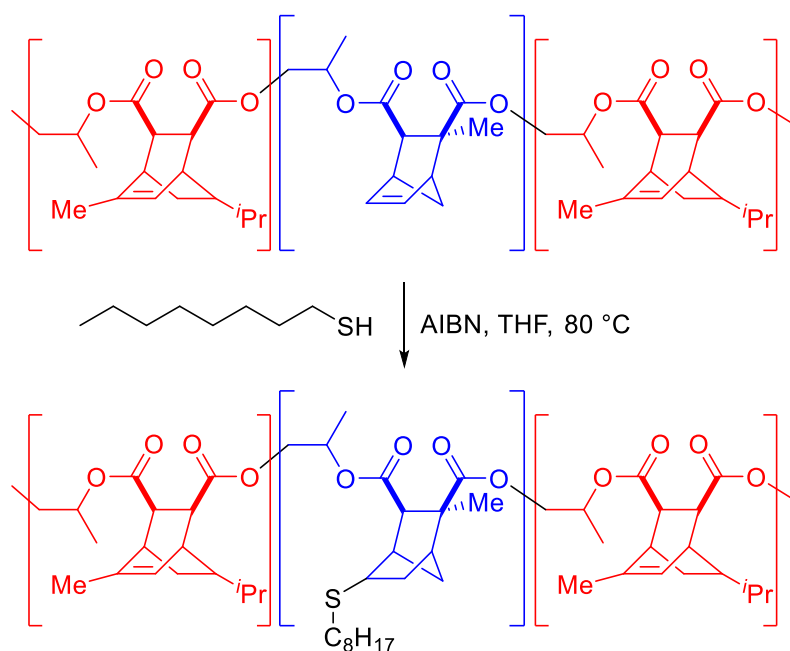


Scheme 4.3: Three PPM reactions performed on poly(SO-*alt*-CA), including a tetrazine click, olefin metathesis and a thiol-ene click. DMPA = 2,2-dimethoxy-2-phenylacetophenone. As reported by Cheng *et. al.*¹⁰

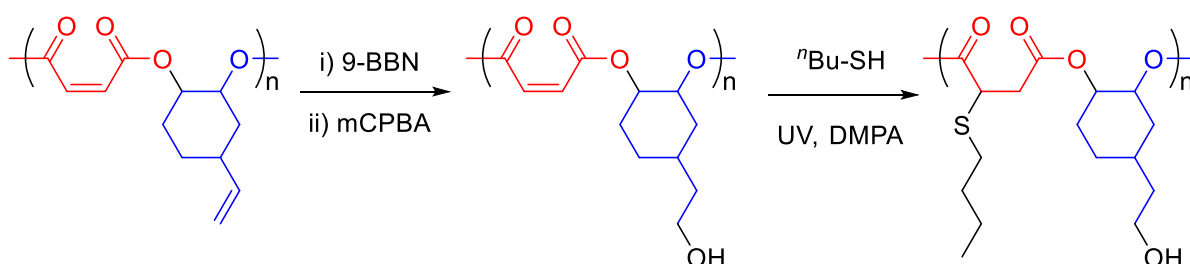
Thirdly, the authors utilised a thiol-ene click reaction, whereby thiols are added across a double bond to produce thioethers. This is perhaps the most commonly performed PPM reaction on ROCOP polymers, with its popularity due in large part to the mild conditions required and the vast array of thiols that can be added, each making their own distinct impact on the resulting polymer.^{11,12} Furthermore, thiols containing protic functionality such as carboxylic acids, amines or alcohols can be used, all of which can impart interesting properties to the polymer and provide scaffolds for further PPM reactions. This is highly advantageous, as protic groups act as chain transfer agents or catalyst poisons during ROCOP catalysis, meaning PPM is the only way to incorporate these groups.⁴ The thioether itself can be further modified, including by oxidation to sulfones.¹³

The thiol-ene reaction is generally (but not exclusively) radically initiated, either by UV light and a photochemical initiator (such as 2,2-dimethoxy-2-phenylacetophenone, DMPA) or a thermally initiated radical source (such as azobisisobutyronitrile, AIBN).¹⁴ Once initiated, these radicals react with thiols to form thiyl radicals, which subsequently add to alkenes in an *anti*-Markovnikov manner, forming the more substituted carbon radical, which in turn reacts with another molecule of thiol to add a hydrogen atom, and reforming a reactive thiyl radical.¹⁴ The rate of reaction is highly dependent on the substitution about the alkene group, with terminal alkenes far more reactive than internal ones, whilst *cis* alkenes can react reversibly with thiols and isomerise to their *trans* form.¹⁴ This difference in rate by alkene environment has been neatly demonstrated by the Coates group, who selectively performed a thiol-ene reaction on one block of a triblock ROCOP-made polyester, with reaction occurring at a doubly substituted alkene in one block, and not at the triply substituted alkenes in the other two blocks (**Scheme 4.4**).¹² The high selectivity of the PPM reaction was also reflected in the polydispersity of the modified polymer, which was unchanged from the precursor, at 1.04.

The Williams group have also harnessed the thiol-ene reaction in conducting two orthogonal PPM reactions on ROCOP-made polyesters containing both terminal (from VCHO) and internal double bonds (from MA).⁴ In this instance, the terminal double bond was first reacted with 9-BBN (9-borabicyclo(3.3.1)nonane) and mCPBA (*meta*-chloroperoxybenzoic acid) in a hydroboration-oxidation reaction to give a hydroxyl functionalised polymer, before a thiol-ene reaction at the unreacted internal double bond (**Scheme 4.5**). Interestingly, when butanethiol was used in the thiol-ene reaction, the resulting polymer contained alternating hydrophilic and hydrophobic substituents, which encouraged the self-assembly of nanostructures in water, as the polymer assembled in such a way to minimise interactions between the butanethiol groups and water.

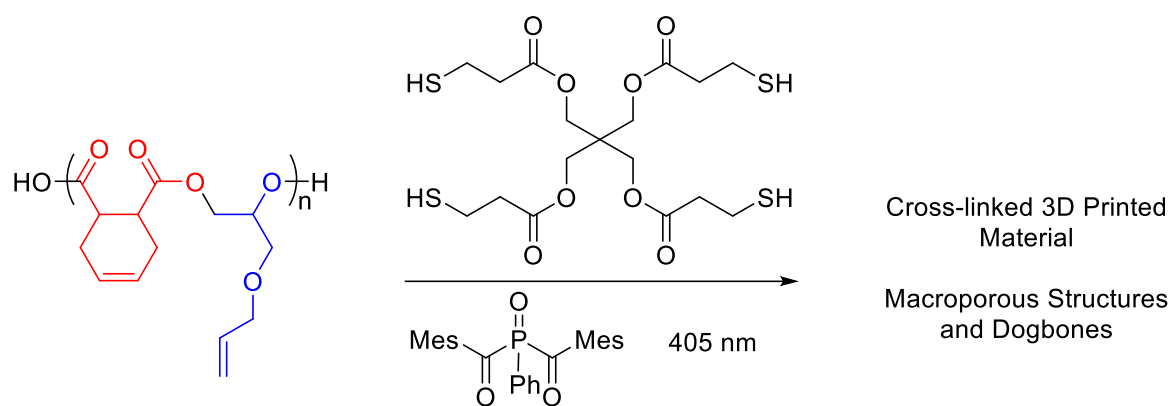


Scheme 4.4: Selective thiol-ene reaction of the middle block of a triblock polyester prepared *via* ROCOP, as reported by Sanford, Van Zee and Coates.¹² The middle block contains a less substituted double bond and so reacts preferentially with octanethiol.



Scheme 4.5: Orthogonal PPM reactions of poly(VCHO-*alt*-MA), with hydroboration-oxidation occurring selectively at the terminal alkene of VCHO, before thiol-ene click reaction at the unreacted internal double bond of MA. As reported by Williams and co-workers.⁴ 9-BBN = 9-borabicyclo(3.3.1)nonane), mCPBA = *meta*-chloroperoxybenzoic acid, DMPA = 2,2-dimethoxy-2-phenylacetophenone.

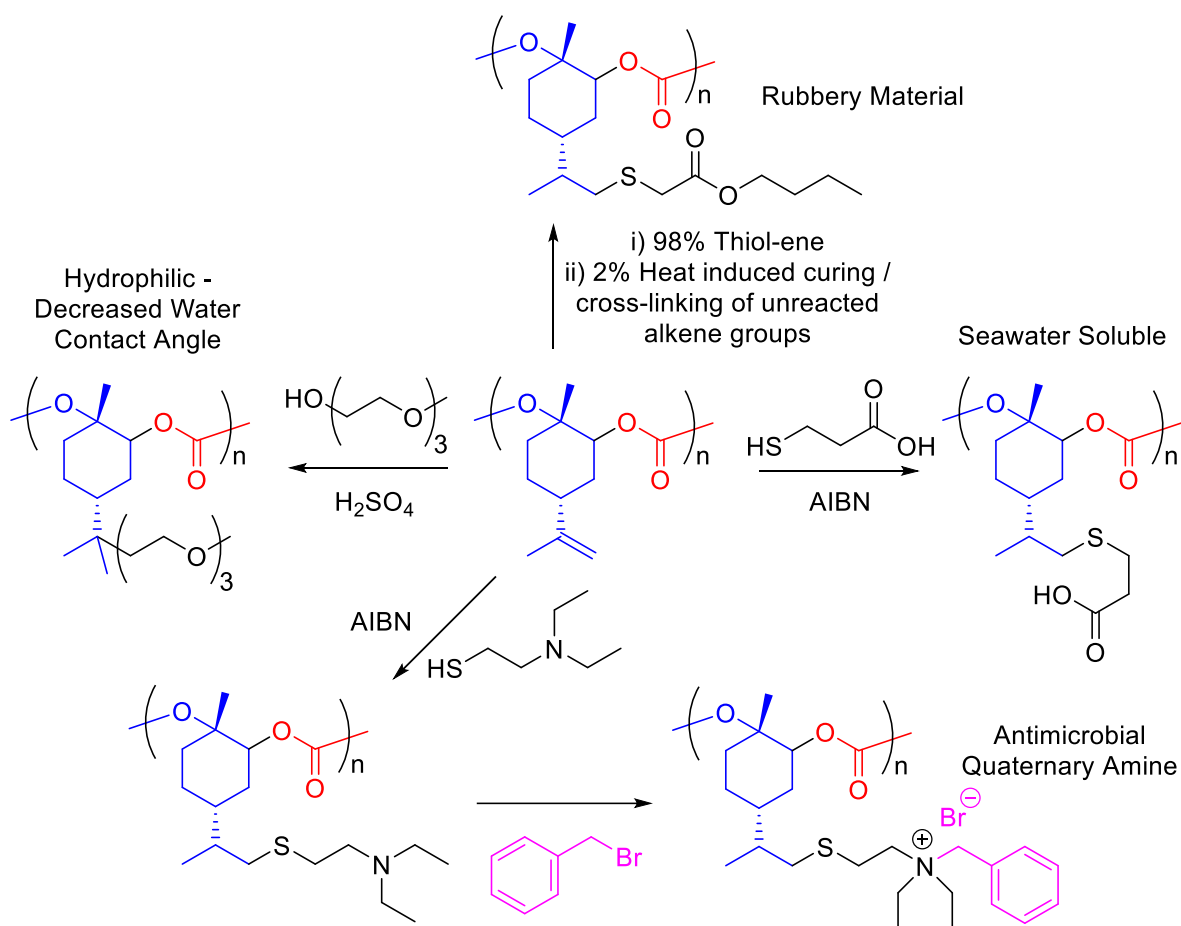
The thiol-ene click can also be used as a cross-linking reaction, as shown by Weems and colleagues, who used a tetrakis(thiol) in a photoinitiated thiol-ene reaction to rapidly cure a polyester resin prepared by ROCOP (**Scheme 4.6**).¹¹ The polyester contained both terminal and internal double bonds, both of which reacted rapidly (more than 60% conversion in 50 seconds) under these conditions, albeit the terminal group was marginally faster. In this case, the rapid rate of reaction was crucial, as the resin was being cured during a 3D printing process, in which complex microporous shapes were desired. If the curing process was too slow, these structures would not be able to support themselves. Also, the 3D printed polymers exhibited so-called “4D behaviour”, in that after stresses were applied, they would rebound to their original shape, with this ability attributed to the rigid cyclohexene moiety.



Scheme 4.6: Thiol-ene cured polyester resins used to make highly cross-linked polymers for 3D printing, using UV light and a phosphine oxide photoinitiator as detailed by Weems and co-workers.¹¹ Mes = 2,4,6-trimethylphenyl.

Polycarbonates made by the ROCOP of epoxides and CO₂ have also been subjected to PPM reactions, with one example being a series of transformations described for the partially bio-derived poly(LO-*alt*-CO₂).⁵ In this study, the authors performed several PPM reactions, which are shown in **Scheme 4.7**. Reactions investigated ranged from the thiol-ene addition of a carboxylic acid to give a salt-water soluble polycarbonate, to the acid-catalysed addition of hydrophilic side chains in trimethylene glycol methyl ether, which was seen to decrease its water contact angle significantly. The report also described the thiol-ene addition of a butyl ester to poly(LO-*alt*-CO₂), which left around 2% of the alkene groups untouched. However, this allowed the remaining alkenes to be thermally cured in thin films, producing a rubbery material with a T_g of 5 °C (*c.f.* 130 °C for unmodified poly(LO-*alt*-CO₂)) and a maximum elongation more than an order of magnitude higher than its precursor. Finally, a tertiary amine containing thiol was added to poly(LO-*alt*-CO₂), which could then be quaternarised by reaction with benzyl bromide, with this cationic polymer showing antimicrobial activity towards *E. coli*.

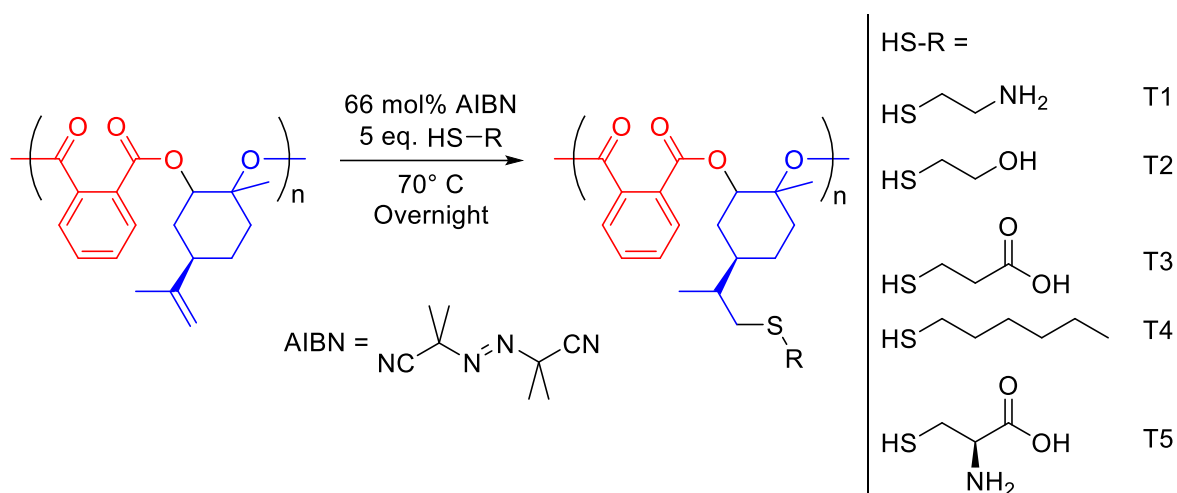
This report highlights the versatile and flexible nature of PPM, in that starting from a relatively unfunctionalised material in poly(LO-*alt*-CO₂), it is possible to produce materials with hugely different properties depending on what application the material is required for. Therefore, given that the same functionality is present in the poly(LO-*alt*-PA) produced on a large scale in section 3.7, there is clearly a large scope for further modification of these polymers. The subsequent investigations, including thiol-ene, oxidation and phosphorylation PPM reactions are detailed herein.



Scheme 4.7: Series of PPM reactions performed on poly(LO-*alt*-CO₂), as reported by Greiner *et. al.*⁵

4.3: Thiol-ene Click Modification of Poly(LO-*alt*-PA)

A series of thiol-ene reactions were performed on poly(LO-*alt*-PA) using AIBN as a thermally activated radical initiator. A summary of the conditions used is shown in **Scheme 4.8**, where the thiols T1-T5 were chosen to impart different properties onto the polymer. For example, thiols T1-T3 were chosen to impart protic functionality, specifically an amino, hydroxyl, or carboxylic acid groups respectively, into the polymer. Hexanethiol (T4) was selected as its long alkyl chain can strongly influence the packing of the polymer chains, which is often observed through a large decrease in T_g , whilst L-Cysteine introduces both protic functionality and has been seen to impart antimicrobial behaviour when appended to polymers.^{4,12,15} Dry THF was used as a solvent in each case, although the insolubility of cysteamine and L-cysteine meant reactions were also attempted in DMF and DMSO. The key parameters for each thiol are shown in **Table 4.1**, which details the conversion, molecular weight data and glass transition temperature for each polymer. The full ¹H and ¹³C{¹H} NMR spectra of the polymers are shown in section 7.5.2.



Scheme 4.8: Thiol-ene reactions of performed on poly(LO-*alt*-PA), as obtained in section 3.7, using thiols T1-T5. T1 = cysteamine, T2 = 2-mercaptoethanol, T3 = 3-mercaptopropionic acid, T4 = 1-hexanethiol, T5 = L-cysteine.

Table 4.1: Key parameters of the thiol-ene reactions of poly(LO-*alt*-PA), including conversions, molecular weight data and T_g s. The solvent used in each reaction is also listed. ^a

Thiol	Solvent ^b	Conversion C=CH ₂ / % ^c	M_n / kDa ^d	\bar{D} ^{d,e}	Expected M_n / kDa ^f	T_g / °C ^g
Unmodified poly(LO- <i>alt</i> -PA)			4.1	1.36	-	121
T1	THF or DMF	0	-	-	-	-
T2	THF	93	7.4	1.39	5.1	90
T3	THF	93	5.3	1.40	5.5	81
T4	THF	95	6.0	1.28	5.7	39
T5	THF or DMF	0	-	-	-	-
T5	DMSO	Insolubility precluded NMR, GPC and MALDI-ToF Analysis				102, 149 (weak)

^a Conditions: 1 mmol (1 eq., 300.3 mg) poly(LO-*alt*-PA), 5 eq. thiol, 5 mL solvent, 0.66 mmol AIBN, 70 °C, overnight. ^b THF was dried over potassium, degassed, and stabiliser free. DMF was dried over alumina and degassed. DMSO was degassed. ^c Determined by ¹H NMR of the polymers by the ratio of the reacted methylene peak and the unreacted ester peak. ^d Determined by viscometry detection GPC in THF against polystyrene standards. ^e $\bar{D} = M_w/M_n$. ^f = Expected M_n for the conversion observed experimentally (see equation 4.1). ^g Determined by Differential Scanning Colorimetry (DSC), on the third heating cycle ramping at 20 °C min⁻¹.

The extent of the functionalisation for each thiol was found by taking the ratio of the ester peak and methylene peak for poly(LO-*alt*-PA) post reaction. In the precursor polymer, this ratio is 1:2 (reflective of the number of protons in each environment), but upon reaction, the relative ratio of ester: methylene increases as the methylene peak is consumed. This is illustrated for T3, 3-

mercaptopropionic acid, in **Figure 4.1**, which shows a far smaller methylene peak in the product polymer. Given the high (but not complete) conversions for T2-T4, all spectra could be assigned fully by ^1H , $^{13}\text{C}\{^1\text{H}\}$, ^1H - ^1H COSY, HSQC and HMBC (see section 7.5), with these assignments for T3 shown in **Figure 4.1**. Interestingly, the new thioether peak (β to the cyclohexane ring, environment j) was split into two diastereotopic signals, with both signals corresponding to a single resonance in the $^{13}\text{C}\{^1\text{H}\}$ spectrum ($\delta_{\text{C}} = 36.5$). The identity of the acidic proton of the mercaptopropionic acid at $\delta_{\text{H}} 12.2$ was confirmed as such given its disappearance upon the addition of D_2O .

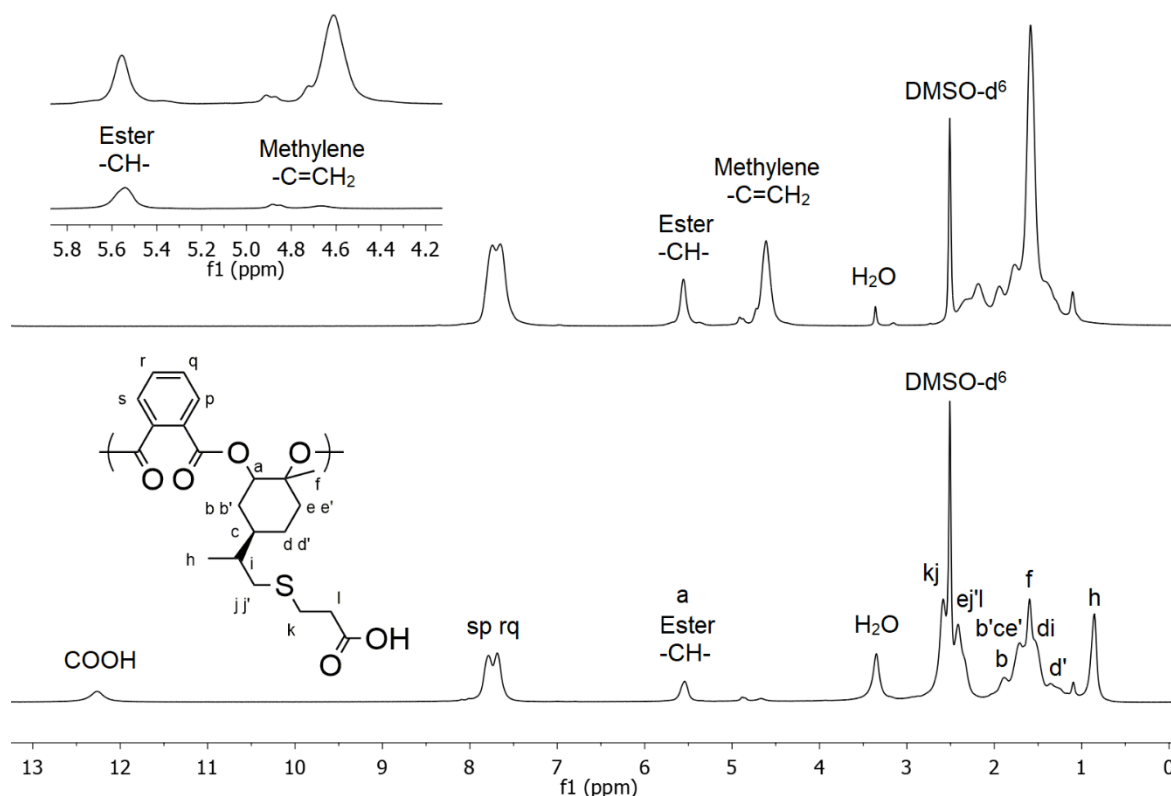


Figure 4.1: Stacked ^1H NMR spectra (500 MHz, DMSO-d_6) of top: unfunctionalised poly(LO-*alt*-PA) and bottom: after thiol-ene functionalisation with 3-mercaptopropionic acid, with assignments shown. Insert shows the near full consumption of the methylene peak of poly(LO-*alt*-PA), with the ratio indicating a conversion of 93%.

All the thiol-ene reactions which worked in THF (T2-T4) produced similar and high conversions. For cysteamine (T1), a lack of solubility in either THF or DMF was a likely reason for the failure of the reactions. Similar solubility problems were seen for L-cysteine (T5), where only in DMSO was there evidence of any reaction. The resultant polymer was insoluble in all solvents tested, which prevented its analysis by NMR and GPC. However, this insolubility is somewhat anecdotal evidence that a reaction has occurred, as this insolubility was not encountered with the known failed reactions in THF or DMF, which produced soluble, but unreacted, polymer. Therefore, only solid state analytical techniques, such as FT-IR, were available. The FT-IR spectra of poly(LO-*alt*-PA), the functionalised

polymer and L-cysteine are stacked in **Figure 4.2**, with the differences in the spectra particularly apparent in the 1200-2000 cm^{-1} range. Whilst the peak at $\approx 1700 \text{ cm}^{-1}$ remains after reaction, its intensity is diminished relative to other peaks in the spectrum, suggesting an incomplete reaction. Also, there are peaks in the modified polymer which do not appear in either the spectrum of poly(LO-*alt*-PA) or L-cysteine, such as the peak at $\approx 1480 \text{ cm}^{-1}$, with this peak therefore likely representing a modified polymer. Further to this, there are peaks in the spectrum of L-cysteine which do not appear in the modified polymer spectrum, such as those at $\approx 1530 \text{ cm}^{-1}$ and 1420 cm^{-1} , which have been attributed to CH_2 scissor and a NH_3 symmetric bend respectively.¹⁶ The absence of these peaks means there is unlikely to be large quantities of unreacted L-cysteine physically dispersed within an insoluble polymer. Although tentative, the FT-IR data and solubility observations suggest that some degree of functionalisation has occurred, although it is not certain to what extent the reaction has proceeded. As to why the functionalised polymer is insoluble, it is possible that as the zwitterionic nature of L-cysteine is highly hydrophilic, whilst the semi-aromatic polyester backbone is hydrophobic, that these two moieties cannot be solubilised simultaneously by any one solvent.

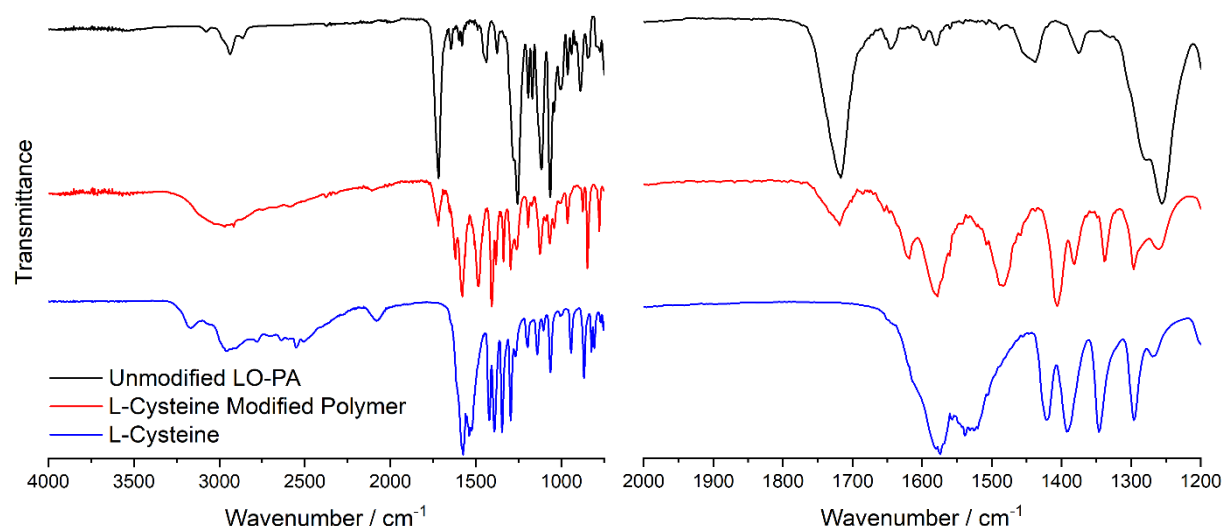


Figure 4.2: Stacked FT-IR spectra of poly(LO-*alt*-PA), L-cysteine and the insoluble polymer obtained post-functionalisation. The right hand spectrum is an expansion of the left, in the region 1200-1800 cm^{-1} .

As well as the diminished methylene peak in the ^1H NMR spectra of the soluble polymers, further evidence for successful reaction was seen in the increased molecular weights observed post modification. When considering the known extent of reaction from NMR analysis, the molecular weight one would expect to observe (when neglecting for the mass of end groups) can be calculated by **Equation 4.1**:

$$\text{Equation 4.1:} \quad \text{Expected } M_n = \frac{M_{n0}}{R_0} \times [RX + R_0(1 - X)]$$

Where M_{n0} is the number average molecular weight of the unfunctionalised polymer, R is the molar mass of the repeat unit of the product, R_0 is the molar mass of the repeat unit of the starting material, and X is the observed conversion of the reaction expressed as a fraction. This metric for a given conversion can then be compared to the observed value, which shows a close agreement for T3 and T4, and an underestimate of observed M_n for T2. As GPC measures polymer size rather than molecular weight directly, it is likely that the mercaptoethanol modified polymer (T2) folds in a significantly different way to the precursor in the THF eluent. This means its size can increase disproportionately with M_n , thereby leading to a larger than expected observed M_n .⁴ The high degree of conversion seen for T2-T4 is reflected in the polydispersities, which are similar to the unmodified polymer. As well as providing evidence for successful PPM, the increases in M_n and similarities in polydispersity also show that the conditions used for the thiol-ene reaction have not led to any detectable degradation of the polymer backbone. Pleasingly, this lack of degradation (at least in the short term) is even seen for T3, where there is potential for the carboxylic acid to promote ester hydrolysis.

Further qualitative evidence for successful PPM reaction is the changing solubility of the polymers. For example, both T2 and T3 introduce polar functionality into the polymer, meaning these polymers were no longer soluble in CDCl_3 (meaning DMSO-d_6 was used), whilst in contrast to poly(LO-*alt*-PA) they are soluble in isopropanol, and swell somewhat in water. Conversely, the addition of a hexyl chain in T4 meant the product polymer swelled in hexane, whilst poly(LO-*alt*-PA) does not. Likely because of the incomplete conversions, MALDI-ToF spectra did not show clean repeat units of the modified polymers. However, spectra were clearly different from the precursor, again showing there has been chemical modification of the polymer chains.

The DSC traces obtained on the third heating cycle for T2-T5 and the unmodified polymer are stacked in **Figure 4.3**, which also lists the T_g value observed. The modified polymers also showed different thermal behaviour than the precursor, with modification for T2-T4 leading to decreases in T_g . This decrease was most pronounced for T4, which is consistent with the appendage of a large alkyl chain disrupting the packing of the polymer in the solid state. Concordantly, the shorter chain thiols in T2 and T3 produced smaller decreases in T_g , despite their ability to hydrogen bond and thereby potentially limit the ability of the polymer chains to move past one another. Indeed, for T3, this hydrogen bonding could be the reason behind the relatively sharp endothermic transition observed at 128 °C (**Figure 4.3**). Interestingly T5 showed two very weak endothermic transitions in the DSC trace, one at higher temperature and one at lower temperature than the unmodified polymer. The reason

behind this cannot be readily explained, as one might expect one of the transitions to represent the unmodified polymer, and therefore be observed at a similar temperature, with the other representing the modified polymer at a different temperature. Despite this ambiguity, this change is more evidence that T5 has indeed been incorporated into the polymer.

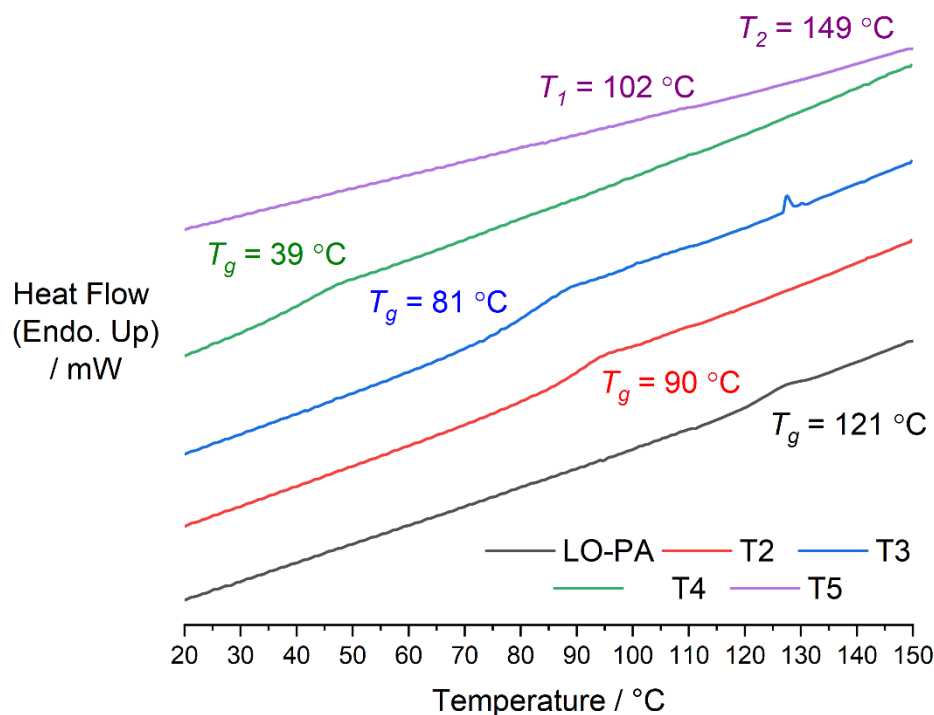


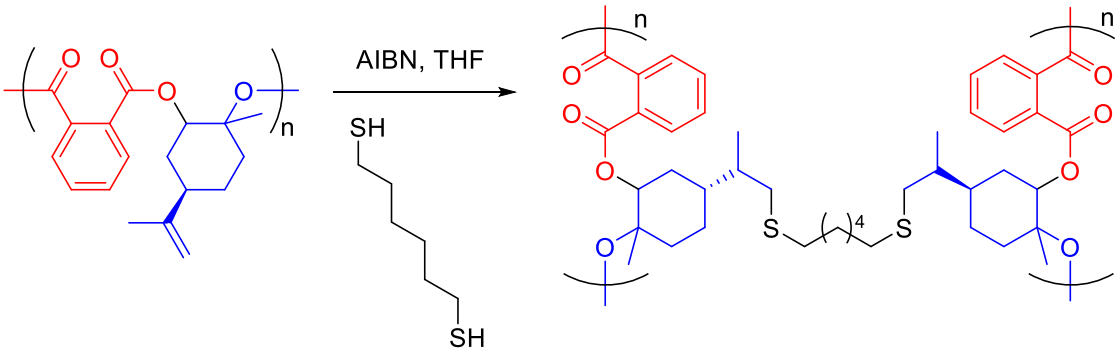
Figure 4.3: Stacked DSC traces (3rd heating cycle, 20 °C min⁻¹ ramp) for thiol-ene modified polymers, with transitions indicated. Vertical axis shows endothermic reactions pointing upwards.

4.4: 1,6-Hexanedithiol Crosslinking of Poly(LO-*alt*-PA)

As well as monothiol functionalisation, the thiol-ene reaction is a simple way of cross-linking polymers, with the stoichiometry of the thiol addition allowing for regulation of the degree of cross-linking. A series of cross-linking reactions were performed using 10, 20, 30 and 50 mol% 1,6-hexanedithiol, which if the reaction were to proceed with 100% efficiency, would produce degrees of cross-linking of 20, 40, 60 and 100% respectively. The results of these reactions are shown in **Table 4.2**, which show increasing levels of cross-linking with addition of hexanedithiol. Polymers up to the addition of 30 mol% hexanedithiol were soluble in CDCl₃ and THF, allowing their analysis by ¹H NMR spectroscopy and GPC. However, the use of 50 mol% (where in theory one would expect 100% of the alkene groups to react) produced an insoluble polymer which prevented solution phase analysis. This lack of solubility suggests the reaction has proceeded further than the 30 mol% reaction, forming a material more akin to a cured thermoset rather than a thermoplastic.⁸ This is reflected in its DSC trace, where no glass transition temperature could be observed. This contrasts to the soluble polymers, where a

similar temperature transition was seen regardless of degree of cross-linking, which is consistent with the presence of significant regions of non-cross-linked polymer. The similarity of the temperature to the unmodified T_g contrasts strongly with the T_g of the mono-hexanethiol polymer discussed previously, which was 39 °C. The fact that this large decrease is not observed for the hexanedithiol reactions is strong evidence that the hexanedithiol is indeed cross-linking the material, rather than reacting at only one thiol group and leaving a pendant hexanethiol chain intact.

Table 4.2: Key parameters of reactions of poly(LO-*alt*-PA) with 1,6-hexanedithiol, including conversions, molecular weight data and T_g s. ^a



1,6-Hexanedithiol / mol%	Conversion C=CH ₂ / % ^b	M_n / kDa ^c	M_w / kDa ^c	\bar{D} ^{c,d}	T_g / °C ^e
Unmodified poly(LO- <i>alt</i> -PA)		4.1	5.6	1.36	121
10	13	6.0	9.4	1.57	119
20	33	9.0	16.7	1.85	123
30	49	5.6	18.5	3.31	126
50	Insolubility precluded NMR and GPC Analysis				-

^a Conditions: 1 mmol (1 eq., 300.3 mg) poly(LO-*alt*-PA), x mol% 1,6-hexanedithiol, 5 mL dried, degassed, and stabiliser free THF, 0.66 mmol AIBN, 70 °C, overnight. ^b Determined by ¹H NMR of the polymers by the ratio of the reacted methylene peak and the unreacted ester peak. ^c Determined by viscometry detection GPC in THF against polystyrene standards. ^d $\bar{D} = M_w/M_n$. ^e Determined by Differential Scanning Colorimetry (DSC), on the third heating cycle ramping at 20 °C min⁻¹.

The M_n and polydispersity of the polymers increases with additional cross-linking up to the 30 mol% reaction, where M_n sharply decreases. However, this is accompanied by a large increase in polydispersity, with this consistent with the large degree of randomness introduced by have a polymer which is 49% reacted, and 51% unreacted. This however, does not explain the observed decrease in M_n . But, there is a consistent increase of M_w with the degree of cross-linking, with this depicted

graphically in **Figure 4.4**. For highly cross-linked materials, M_w may be a more appropriate measure of molecular weight because M_n is biased towards shorter chains, which do not necessarily best represent the properties of the polymer when there is a significant quantity of extremely high molecular weight chains caused by a large number of cross-links to other chains.¹⁷ The success of this reactions shows the versatility of the thiol-ene click, and shows that a relatively high degree of cross-linking can be achieved before the polymer becomes insoluble. This could well be due to the long length of the cross-linker, meaning a degree of structural flexibility is retained.

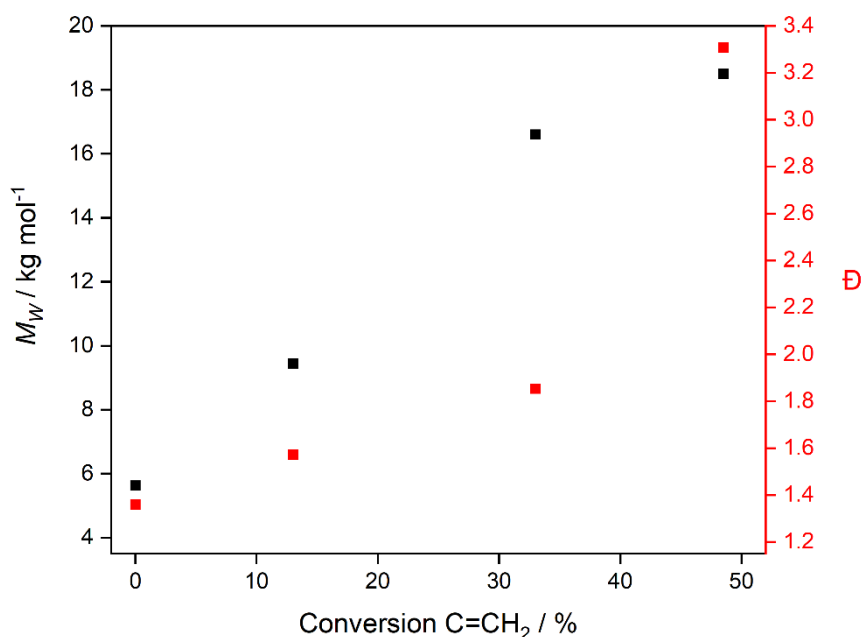


Figure 4.4: M_w and polydispersity (\bar{D} , M_w/M_n) against the degree of cross-linking for poly(LO-*alt*-PA), as determined by GPC in THF (viscometry detection against polystyrene standards).

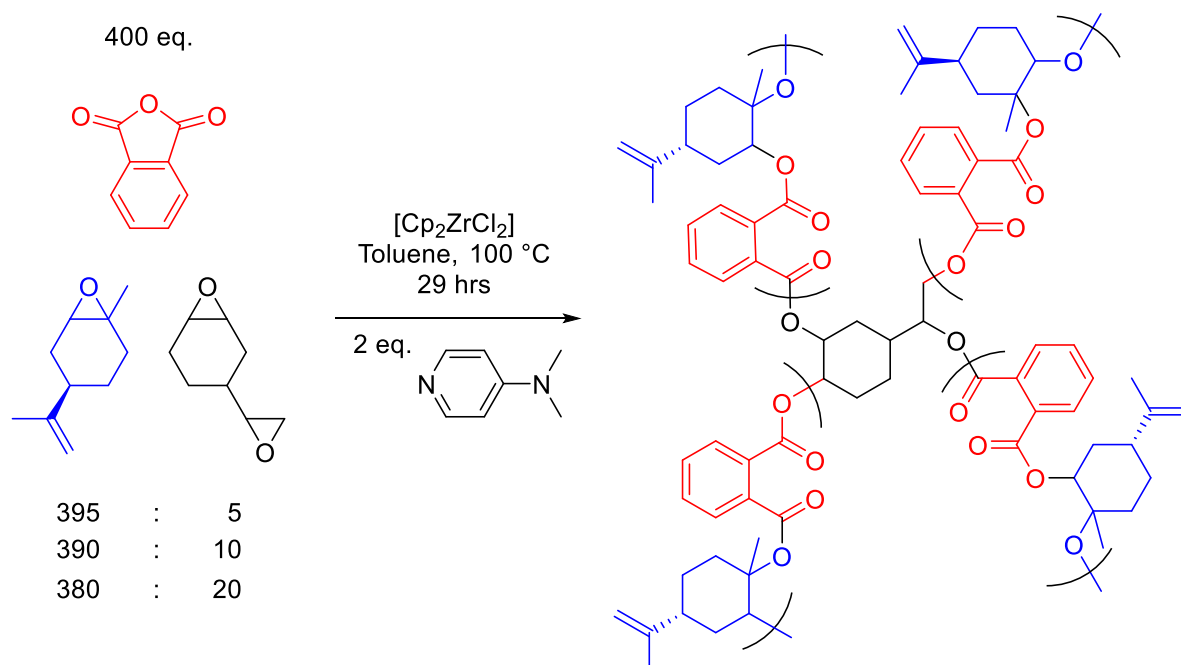
4.5: *In Situ* Diepoxide Cross-linking of Poly(LO-*alt*-PA)

As well as generating cross-links through PPM, it is possible to cross-link ROCOP polyesters during polymer synthesis. This was achieved by doping in vinyl cyclohexene dioxide*, VCHDO, into a $[\text{Cp}_2\text{ZrCl}_2]/\text{DMAP}$ -catalysed reaction of LO and PA, under identical conditions to those described in section 3.7. In this case, the two epoxide groups of VCHDO can both react with growing polymer chains, effectively coupling them together. In contrast to the hexanedithiol cross-links however, these cross-links are comprised of the same chemically recyclable ester bonds as the polymer backbone, and so should be degradable in the same way. This has the advantage of being an easy avenue for cross-linking, whilst avoiding an additional step in any subsequent depolymerisation process. Doping of VCHDO was done 24 hours into a 29 hour reaction, as when it was present from the start of the

* VCHDO was synthesised by epoxidation of VCHO with mCPBA. See section 7.1 for details.

reaction a highly insoluble viscous product formed immediately. This is highly likely to be cross-linked poly(VCHDO-*alt*-PA), which forms quickly given the expected fast rate of reaction of the relatively unhindered epoxide groups of VCHDO compared to LO. This solid precipitate also hampered further reaction of LO, as it is likely the catalyst and co-catalyst were largely encapsulated within the insoluble material, which severely limited further reaction of LO. However, when VCHDO was doped into an ongoing reaction, there was no such problem. A summary of VCHDO doping reactions is shown in **Table 4.3**, where 5, 10 and 20 equivalents of VCHDO were added to reactions after 24 hours against a flow of argon to make a total of 400 equivalents of epoxide in each reaction.

Table 4.3: Properties of polymers made by the *in situ* cross-linking of poly(LO-*alt*-PA) with VCHDO. ^a



Equivalents VCHDO	Conversion PA / % ^c	Ester / % ^d	M_n / kDa ^e	M_w / kDa ^e	\bar{D} ^{e,f}	T_g / °C ^g
0 ^b	75	> 95	5.8	8.8	1.52	114
5	65	> 95	4.3	7.7	1.81	105
10	66	> 95	4.7	10.4	2.23	120
20	67	> 95	4.5	13.2	2.94	124

^a Average of at least two runs. Conditions: 1 eq. = 6.4 μ mol (1 eq.) [Cp₂ZrCl₂], 2 eq. DMAP, 400 eq. PA, 400 eq. total epoxide, 1 mL toluene, 100 °C for 29 hours. VCHDO added against a flow of argon after 24 hours. ^b As reported in section 3.7. ^c Determined by ¹H NMR spectroscopy of reaction mixture. ^d Determined by ¹H NMR spectroscopy of the resultant polymer. ^e Determined by GPC (viscometry detection against polystyrene standards). ^f $\bar{D} = M_w / M_n$. ^g Determined by DSC on the third heating cycle.

Interestingly, all cross-linking experiments showed a slightly decrease conversion of PA. Even though one might expect to see a slightly reduced rate of reaction given the marginally smaller amounts of LO used (and hence lower concentration), this decrease is larger than this minor difference, and does not correlate between each run where different amounts of LO are used. This discrepancy is more likely due to a slower reaction after the addition of VCHDO, with the cross-linking perhaps leading to some degree of insolubility and coagulation as seen previously when VCHDO was added at the start of reactions. Addition of VCHDO did not affect the ester selectivity of the polymerisation.

In terms of molecular weight and polydispersity, even the relatively small ratios of VCHDO had a measurable impact on polymer properties. Despite a slight drop in M_w from 0 to 5 equivalents of VCHDO, the addition of 10 and 20 equivalents led to a significant increase in M_w , whilst polydispersity increased consistently with the relative amount of VCHDO used (**Figure 4.5**). In contrast to the hexanedithiol crosslinks, where T_g was largely insensitive to cross-linking up to 49%, the relatively small amount of cross-linking here did have a considerable effect on the T_g . This is likely due to the more rigid cross-links with VCHDO compared to hexanedithiol, which retains significant conformational freedom even when cross-linked. In fact, T_g is seen to positively correlate with M_w (**Figure 4.5**), with the formation of a higher number of rigid cross-links a likely cause of this. Although there was a clear difference in the physical properties of the polymers synthesised with VCHDO, given the small amounts used there were no clearly identifiable signals attributed to VCHDO cross-links in the ^1H NMR spectra of the polymers.

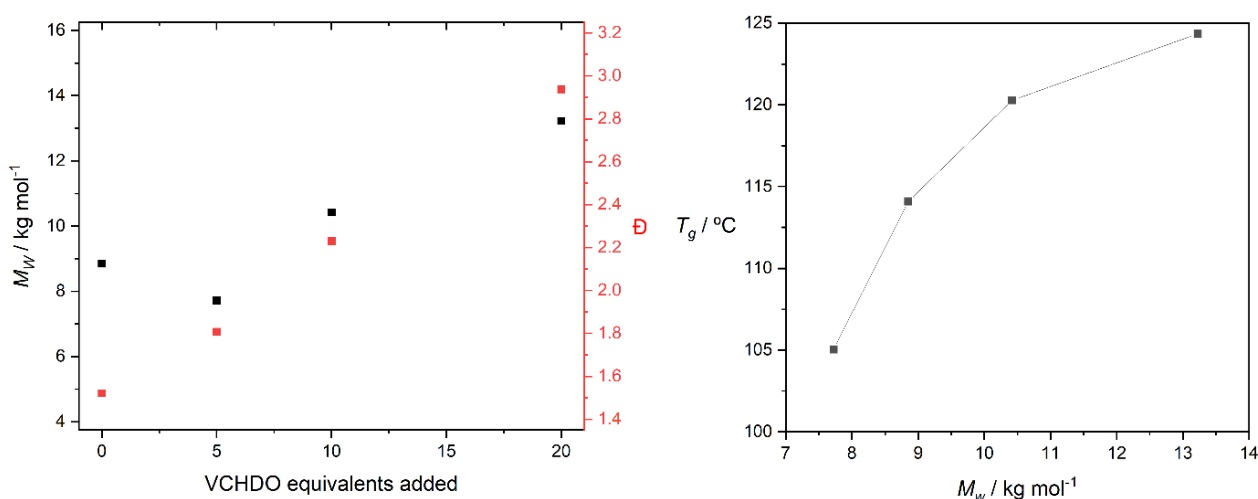


Figure 4.5: Left: M_w and polydispersity (\bar{M}_w/\bar{M}_n) against level of VCHDO doping, as determined by GPC against polystyrene standards (viscometry detection). Right: T_g (as determined by DSC, 3rd heating cycle) versus M_w .

This data and that reported in section 4.4 clearly show that properties of a polymer post cross-linking are highly dependant on the nature of the cross-links, as well as their relative abundance. Also highlighted is that significant changes can be made without much cross-linker, as for VCHDO the replacement of 5% of the LO with VCHDO (20 eq. VCHDO, 380 eq. of LO) increases M_w by 50%, and T_g by 10 °C (compared to 400 eq. LO).

4.6: Flame Retardant Behaviour of Polymers

Flame retardants are chemicals that are added to materials to both prevent burning and hinder the spread of fire once combustion has occurred.¹⁸ In terms of plastics specifically, flame retardants are often added to blends of polymers (as well as other components like plasticisers and dyes) during the manufacturing process.^{19,20} Until recently, a major class of flame retardants were fully or partially brominated compounds, most commonly polybrominated diphenyl ethers (PBDEs) (**Figure 4.6**).^{21,22} However, PBDEs are highly robust and persistent in the environment, and were designated as persistent organic pollutants under the Stockholm Convention in 2008.²³ Furthermore, PBDEs are known to bio-accumulate and present significant toxicity concerns, meaning their production has been banned in the EU since 2017.²⁴ This toxicity not only concerns exposure to PBDEs themselves, but brominated flame retardants typically work by supressing gas phase reactions crucial to combustion, with this producing highly toxic gases in the process.^{18,25} In spite of their efficiency in preventing and limiting fires, the use of brominated flame retardants is becoming increasingly limited in Europe and the US because of these environmental and toxicity concerns.^{26–28}

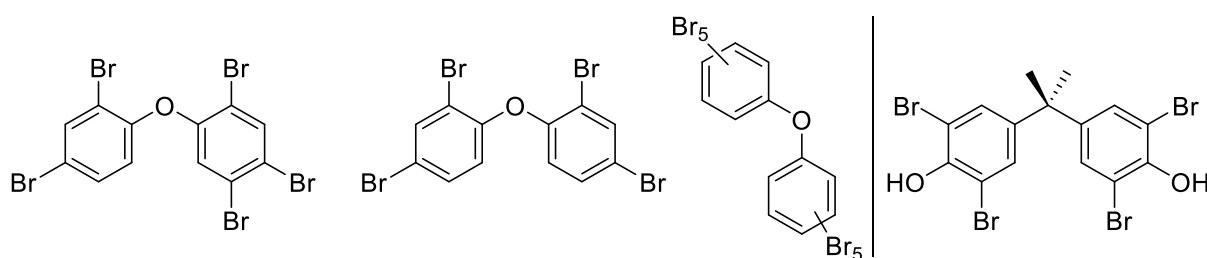


Figure 4.6: Selection of brominated flame retardants, including PBDEs (left), the production of which has been banned in the EU, and tetrabromobisphenol A (right), another brominated flame retardant.^{21,22}

As brominated flame retardants have been phased out, phosphorus-based flame retardants have increased in popularity.¹⁸ The flame retardancy of phosphorus compounds has long been harnessed, dating back to 1821 when theatre curtains were saturated with ammonium phosphate solution to limit their combustability.²⁹ The mechanism of action of phosphorus containing flame retardants is

complex, and is highly dependent not only on the specific compound used, but also the polymer it is blended with, as well as the presence of any further additives.²⁹ However, phosphorus-based flame retardants can impart flame retardancy in the gas phase and on the surface.^{29,30} Gas-phase activity is achieved through the formation of radicals (mainly PO•) which can combine with hydrocarbon radicals produced during combustion, which reduces the heat released during combustion and thereby limits flame propagation.³⁰ Surface activity arises as when exposed to flame, phosphorus compounds can encourage the formation of surface char which protects the underlying material and again limits the enthalpy of combustion.^{30,31} Several phosphorus flame retardants are active in both phases to some extent, although in many cases one mode of active is more significant than the other.¹⁸

Phosphorus containing flame retardants are typically phosphate esters, with a selection of commonly used examples shown in **Figure 4.7**.²¹ Both non-chlorinated and chlorinated compounds are shown, with the additional halogenation often enhancing the gas-phase activity of the flame retardants to contrast with the predominantly surface active phosphates.¹⁸ The non-halogenated compounds like TBP and TPP do not only show flame retardancy, but can also act as plasticisers and lubricants, and as a result are often found in hydraulic fluids and floor polishes.²¹ The chlorinated phosphates are commonly added to poly(urethane) and other polymers in the construction, electronics and furniture industries.²¹

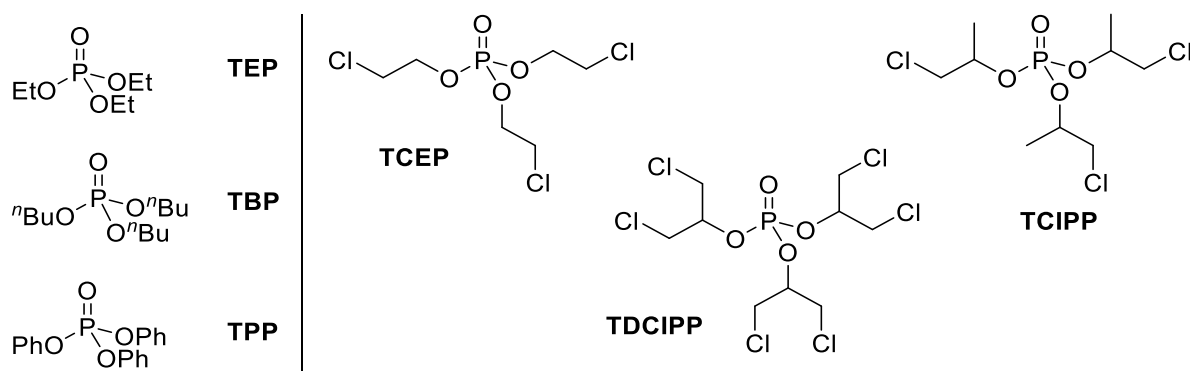


Figure 4.7: Selection of widely used non-chlorinated (left) and chlorinated (right) phosphorus flame retardants.¹⁸

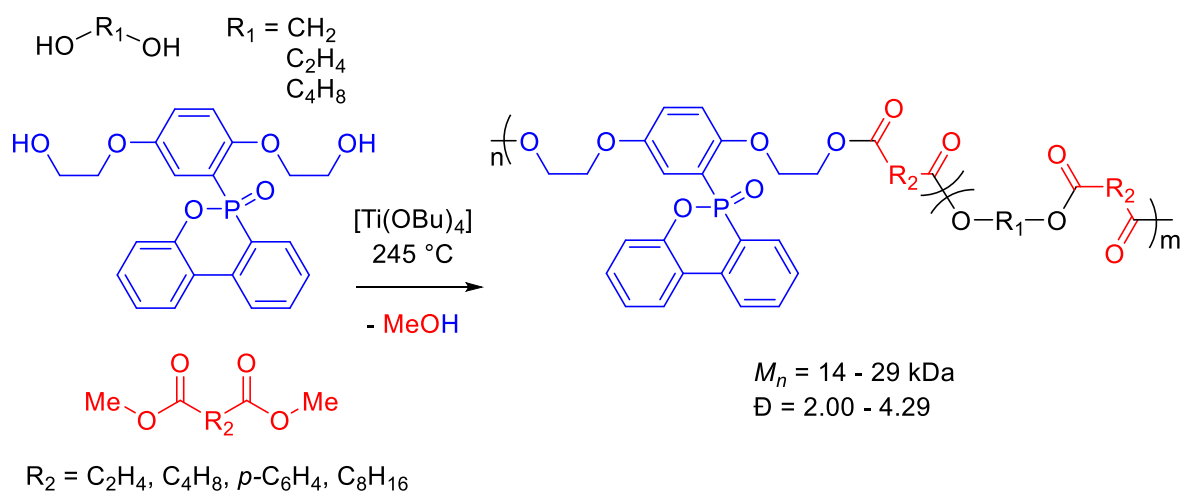
However, there are still problems associated with the use of these compounds, including toxicity concerns which plagued the use of brominated compounds.²¹ For example, TBP, TCIPP, TDCIPP and TPP have all shown agonistic activity towards various hormone receptors, whilst there is evidence that TCEP is a carcinogen.³² Taken as a whole, the selection of compounds in **Figure 4.7** have been linked to some extent to reproductive toxicity, developmental and birth defects, chromosomal abnormalities

and toxicity to aquatic life and humans.¹⁸ Whilst each individual compound is not a risk for all of these, the compounds are often used in blends with each other, and can be found in a wide variety of sources. This includes child car seats, where one study not only reported high levels of phosphorous flame retardants, but also the presence of legacy brominated flame retardants likely incorporated through the use of old recycled poly(urethane).³³ The concerns over the toxicity of flame retardants are particularly concerning considering that flame retardants are widespread in the environment, and have been detected in freshwater environments, seawater, sediments and even drinking water.²¹ Given the widespread use of plastics in furniture, it is also not surprising that over 96% of household dust samples taken in one study contained TPP and TDCIPP.³⁴ Furthermore, metabolites of TPP and TCEP have been detected in human urine.³²

One of the reasons why flame retardants are widespread in the environment is because over time, materials added as blends into plastics can leach out.^{35,36} Not only does this mean the flame retardancy of the material is lessened, but also that the additives are free to be transported away from their source and become environmental contaminants.^{35,37} One strategy to limit this leaching is to covalently tether the flame retardant to the polymer, rather than simply blending it into the product plastic.²⁸ This is termed reactive type flame retardancy, as opposed to additive type, and although it is generally seen as preferable given the diminished possibility of leaching, reactive type flame retardancy can have the added impact of influencing the mechanical properties of the polymer.³⁷

4.7: Reactive Type Phosphate Flame Retardants and Polyesters

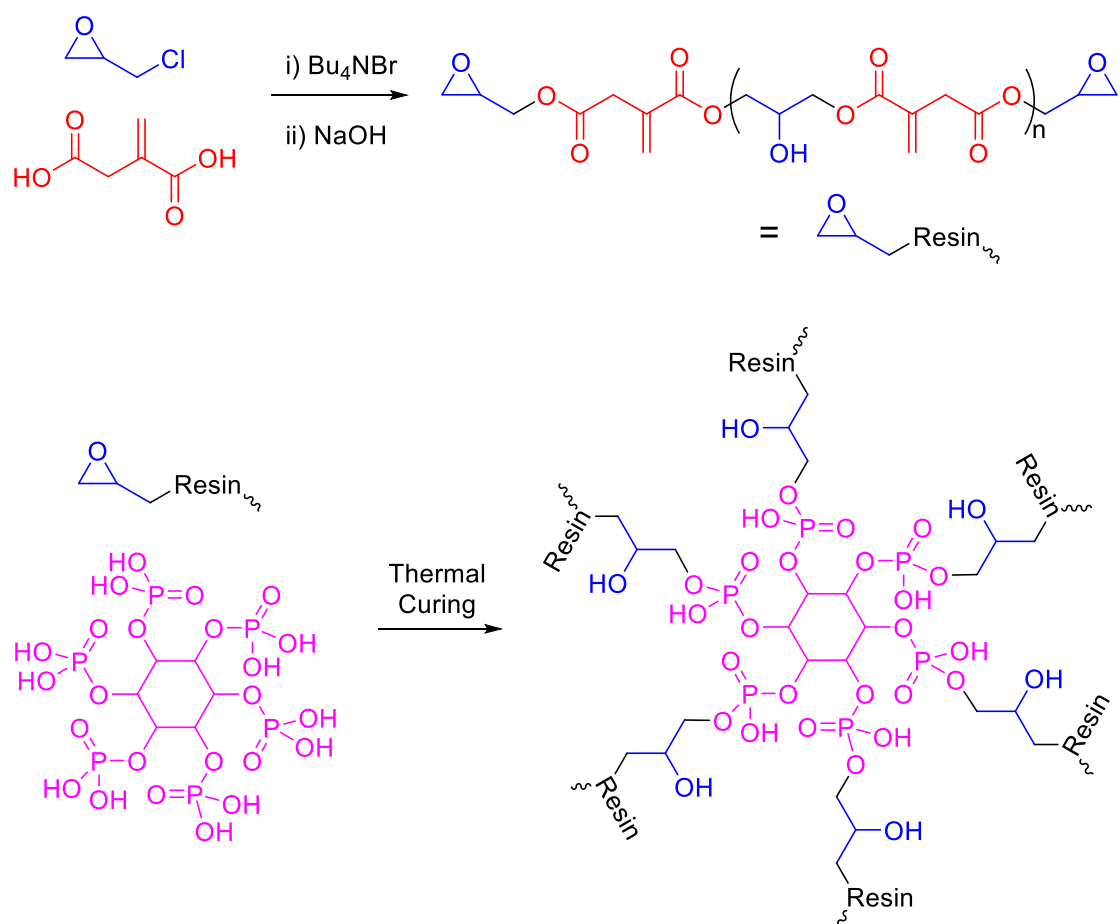
As well as investigating new additives, there are several reports of researchers attempting to modify polyesters to enhance their in-built flame retardancy. One simple way of achieving this is to change the monomers to those that already contain flame retardant groups, with this demonstrated by Pospiech *et. al.* in the synthesis of polyesters by polycondensation (**Scheme 4.9**).³⁸ In this study, the authors made a phosphorous containing diol and blended this into more conventional polymerisation mixtures of aliphatic diols and aliphatic or aromatic methyl esters. Although the polymers suffered from broad molecular weight distributions symptomatic of step-growth polymerisations, the introduction of the phosphorus significantly reduced the heat release of combustion and increased the limiting oxygen index (LOI), which is the minimum percentage oxygen that must be present in the atmosphere to maintain a flame.²⁹



Scheme 4.9: Polycondensation of various methyl esters (red) and blends of phosphorus-containing and simple aliphatic diols (black) to give polydisperse polyesters with diminished heat release of combustion values. As reported by Pospiech *et. al.*³⁸

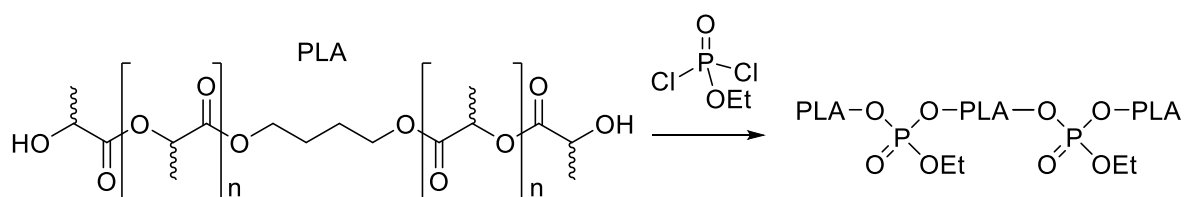
Phosphate flame retardants can also be introduced by PPM reactions, which are not necessarily limited in scope to simply adding phosphate groups into the polymer, in that more than one objective can be achieved in a single PPM reaction. An example of this was detailed by Ma and co-workers, who synthesised a polyester resin with terminal epoxy groups, which acted as scaffold for curing through reaction with phytic acid (**Scheme 4.10**).³⁹ This star-shaped, highly cross-linked thermosetting polymer has the added advantages of using a bio-based phosphate source in phytic acid, whilst its cross-links are readily degraded by mild base hydrolysis, aiding any potential recycling process. The phytic acid not only cross-linked the epoxy resin, but also significantly increased the LOI to between 31-33% depending on the stoichiometry of the polymer synthesis.

A key analytical technique used in assessing material behaviour as a function of heat is thermal gravimetric analysis (TGA), where mass loss of material is measured as a sample is heated.³⁹ The TGA of the cured epoxy thermoset showed that the cross-links were thermally stable to 250 °C, upon which the polymer itself began to degrade. This is crucial, as if the cross-links, or indeed any covalent tether between polymer and flame retardant is thermally sensitive, its performance may be severely hindered in a real-life fire. TGA experiments in air also showed that over 14% of the original mass remained at 800 °C, which represents a significant char mass, the formation of which is likely to be due to the high phosphorus content of phytic acid.



Scheme 4.10: Synthesis of an epoxy-terminated polyester resin, before curing with phytic acid to form a flame retardant thermoset material. As reported by Ma and co-workers.³⁹

Another example of end group reactivity was reported by Wang and colleagues, who synthesised poly(lactic acid) (PLA) by lactic acid polycondensation (rather than the ROP of lactide), whilst using butanediol as a bifunctional initiator.⁴⁰ This PLA was then chain-end coupled to other PLA chains through reaction with ethyl phosphorodichloridate, with this both introducing flame retardant phosphates and increasing molecular weight (**Scheme 4.11**). Although this approach led to significant increases in polydispersity, when a 10% blend of this modified PLA was mixed into conventional PLA the LOI of the material increased from 20 to 34%.



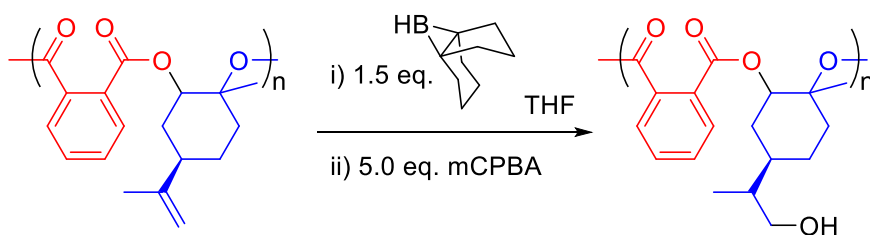
Scheme 4.11: Chain-end coupling of PLA with ethyl phosphorodichloridate to made a flame retardant PLA, as reported by Wang and colleagues.⁴⁰

In terms of polyesters made by ROCOP, there have only been limited studies into their flame retardant properties. One such study involved analysis of the thermal degradation properties of the polyesters made by the ROCOP of PA, CA or succinic anhydride (SA) with a sugar-derived oxetane.⁴¹ In this case TGA showed a good level of thermal stability, although there were no attempts made to increase the flame retardancy of the polymers by chemical modification. As well as this, there has been work within the Ward group investigating copolymers of tetrachlorophthalic anhydride (TCPA) and tetrabromophthalic anhydride (TBPA) with cyclohexene oxide, propylene oxide and epichlorhydrin.⁴² These halogenated polymers showed excellent flame retardancy as one would expect from polymers with high weight percentages of chlorine and bromine. Unfortunately, however, this high performance necessitated the use of halogenated substrates, which although part of the polymer structure rather than a blend represent a significant toxicity concern. In the following sections, the synthesis of phosphorylated poly(LO-*alt*-PA) will be described, with the phosphate groups introduced *via* a two step process. Firstly, the alkene group of poly(LO-*alt*-PA) will undergo hydroboration-oxidation to give a terminal hydroxyl group, before this substitutes at diphenyl phosphoryl chloride to append phosphate esters to the polymer to varying degrees of incorporation. The flame retardant properties of the polymers will then be assessed and compared to poly(CHO-*alt*-TCPA) and the unmodified polymers.

4.8: Synthesis and Characterisation of Phosphorylated Poly(LO-*alt*-PA)

4.8.1: Hydroboration-Oxidation of Poly(LO-*alt*-PA)

The first step to produce phosphorylated poly(LO-*alt*-PA) was to introduce nucleophilic character to the polymer, which was achieved through hydroboration-oxidation. This is shown in **Scheme 4.12**, with the synthetic procedure an adaptation of that reported by the Williams group.⁴ Hydroboration using 9-BBN (9-borabicyclo(3.3.1)nonane) was expected to occur with anti-Markovnikov selectivity, with oxidation to the hydroxyl group using the organic peroxide *meta*-chloroperoxybenzoic acid (mCPBA) performed without prior isolation of the intermediate borane.



Scheme 4.12: Hydroboration-oxidation of poly(LO-*alt*-PA), as adapted from a procedure reported by the Williams group.⁴ mCPBA = *meta*-chloroperoxybenzoic acid. The borane used is 9-BBN (9-borabicyclo(3.3.1)nonane). For full details see section 7.6.

Hydroboration-Oxidation occurred with quantitative conversion, as evidenced by the complete absence of the methylene peak of poly(LO-*alt*-PA) in the ^1H NMR spectrum of the product polymer (henceforth poly(OH), see section 7.6 for full ^1H and $^{13}\text{C}\{^1\text{H}\}$ spectral assignments). To help confirm the presence of a hydroxyl group in poly(OH), D_2O was added to a sample in DMSO-d_6 , which duly led to the disappearance of the OH peak identified at $\delta_{\text{H}} = 4.35$. The marginal increased mass of the hydroxyl group was not detected during GPC analysis, which returned an M_n of 4.1 kDa and a Đ of 1.53 (vs. 4.1 kDa and 1.36 for unmodified poly(LO-*alt*-PA)). However, the complete conversion of the polymer was evident in the MALDI-ToF mass spectrum of poly(OH), where the new repeat unit of 318 Da had replaced the repeat unit of 300 Da for poly(LO-*alt*-PA), with the m/z values consistent with the molecular weight data obtained by GPC (**Figure 4.8**). Similarly to the polymers containing polar functionality obtained by thiol-ene click reactions described previously, the solubility of poly(OH) was significantly different to its precursor. Poly(OH) was soluble in alcohols and only sparingly soluble in CDCl_3 , in direct contrast to poly(LO-*alt*-PA).

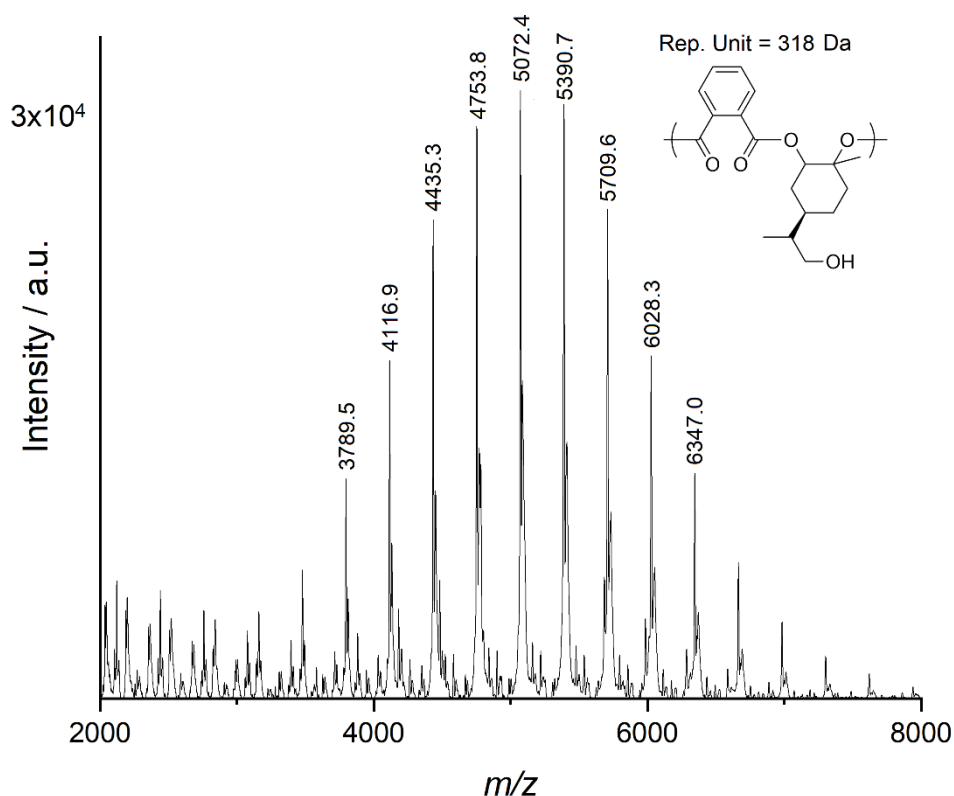
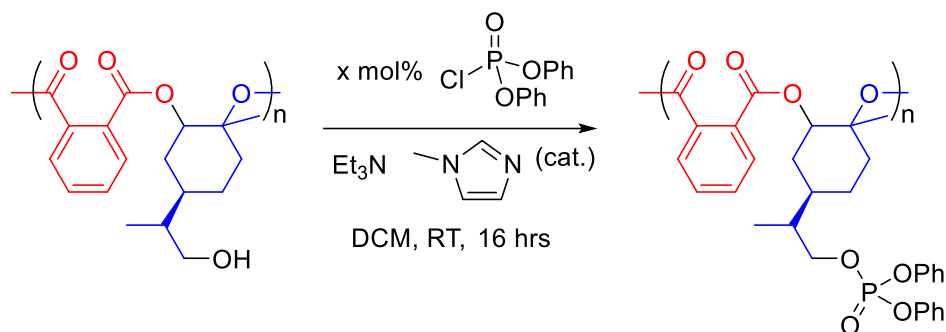


Figure 4.8: Positive mode MALDI-ToF spectrum of poly(OH), with the repeat unit of 318 Da indicated.

4.8.2: Phosphorylation of Poly(OH)

Now a hydroxyl group had been successfully introduced, this could be used as a scaffold to append a phosphate ester. A procedure based on one reported for the phosphorylation of secondary alcohols was used in this case, which required a nucleophilic catalyst (in this case *N*-methylimidazole), an

appropriate phosphoryl chloride reagent and a base in triethylamine to destroy the HCl by-product.⁴³ These reaction conditions are detailed in **Scheme 4.13**, where diphenyl phosphoryl chloride was used as a phosphate source given the widespread use of TPP in plastic blends as both a flame retardant and a plasticiser.²¹ Varying amounts of diphenyl phosphoryl chloride were used to synthesise an array of phosphorylated polymers, each with different degrees of phosphate incorporation.



Scheme 4.13: Synthesis of phosphorylated polyesters.

In total, four different phosphorylated polymers were prepared, with the aim to produce polymers with 25, 50, 75 and 100% phosphorylation. However, as can be seen in **Table 4.4**, which details the key characterising data for each polymer, the reaction did not proceed with 100% efficiency, and so in reality, the polymers were isolated with 12, 23, 41 and 83% phosphorylation (termed poly(OP_X) from herein). Polymers were purified by multiple reprecipitations until only a broad polymer-like resonance was observed in the ³¹P NMR spectrum at δ_P -11.8 (*c.f.* δ_P -5.2 (sharp) for OP(OPH)₂Cl).

Table 4.4: Characterisation data for poly(LO-*alt*-PA), poly(OH) and its phosphorylated derivatives.

Amount OP(OPH) ₂ Cl used / mol% ^a	Conversion poly(OH) / % ^b	M_n / kDa ^c	\bar{D} ^c	Expected M_n / kDa ^d	T_g / °C ^e
-	Poly(LO- <i>alt</i> -PA)	4.1	1.36	-	121
-	Poly(OH)	4.1	1.53	-	130
25	12	7.3	1.54	4.5	109
50	23	5.5	1.57	4.9	108
75	41	5.2	1.74	5.4	88
200	83	7.9	1.24	6.6	53

^a mol% relative to moles of poly(OH) used, see scheme 4.13. ^b Determined by the ratio of the CH₂OH peak of poly(OH) (δ_H = 3.25) to that of poly(OP_X) (δ_H = 4.25) in the ¹H NMR spectra of the polymers. ^c Determined by GPC in THF (viscometry detection against poly(styrene) standards). ^d Determined by equation 4.1 (section 4.3), using the repeat unit mass of poly(OH) as R_0 and its measured M_n as M_{n0} , and 550.5 g mol⁻¹ as R . ^e Determined by DSC on the third heating cycle, ramping at 20 °C min⁻¹.

All phosphorylated polymers showed an observable increase in M_n compared to poly(OH). However, the magnitude of this increase was not proportional to the expected M_n values for each degree of phosphorylation, with poly(OP_12) yielding a higher M_n value than poly(OP_41), despite its expected M_n being 900 Da lower. In fact, until the highly substituted poly(OP_83), M_n decreased with increasing substitution, likely as a result of the behaviour of the polymers in solution diverging from poly(OH) with increasing phosphorylation, meaning the measured molecular size does not scale proportionally with the true M_n . All GPC traces were monomodal, albeit with broader polydispersities at intermediate levels of phosphorylation given the increased randomness this would introduce to the polymer chains. Alongside the significantly altered ^1H , $^{13}\text{C}\{^1\text{H}\}$ and ^{31}P NMR spectra, this is good evidence that the phosphate has been covalently bound to the polymer, rather than simply dispersed in it. Further evidence for this comes in the MALDI-ToF spectrum of poly(OP_83), which shows the repeat unit of the phosphorylated polymer at 551 Da intervals. Although the mass spectrum is somewhat complicated due to the incomplete conversion of the phosphorylation producing many different signals from different ions, it presents clear evidence that phosphorylation has occurred. The concurrent mass increase seen in the m/z values is also consistent with the M_n observed by GPC and with the additional mass when compared to the MALDI-ToF spectrum of its precursor poly(OH), as seen in **Figure 4.8**.

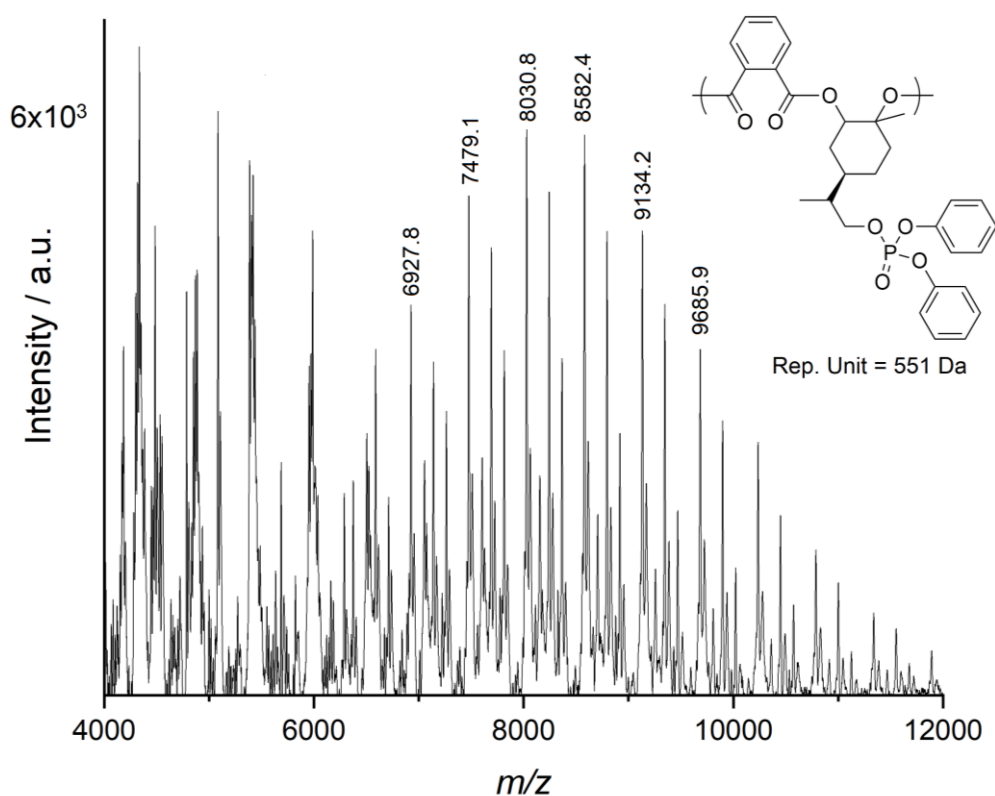


Figure 4.9: Positive mode MALDI-ToF mass spectrum of poly(OP_83), with the repeat unit of 551 Da identified.

The changing response of the polymers to temperature is also good evidence for successful reactions. This can be seen in the DSC traces and T_g values of the polymers, which are shown in **Figure 4.10**. Hydroboration-oxidation leads to a modest increase in T_g to 130 °C, which is then reduced by 21 °C at the lowest level of phosphorylation in poly(OP_12). The thermal behaviour of poly(OP_12) and poly(OP_23) are essentially identical, yet there are further significant decreases in T_g to poly(OP_41) and finally to poly(OP_83), with a T_g of 53 °C. Given that TPP is used as a plasticiser, this decrease in T_g with increasing phosphorylation is not surprising, as the bulky phosphate esters will be highly disruptive to the packing of polymer chains, hence lowering the energy required for the polymer chains to move past one another. Furthermore, the single, well-defined transitions were distinct from the precursor polymers, with no evidence of a residual transition relating to unreacted poly(OH). This is again consistent with the polymer having reacted, rather than having a material dispersed within it.

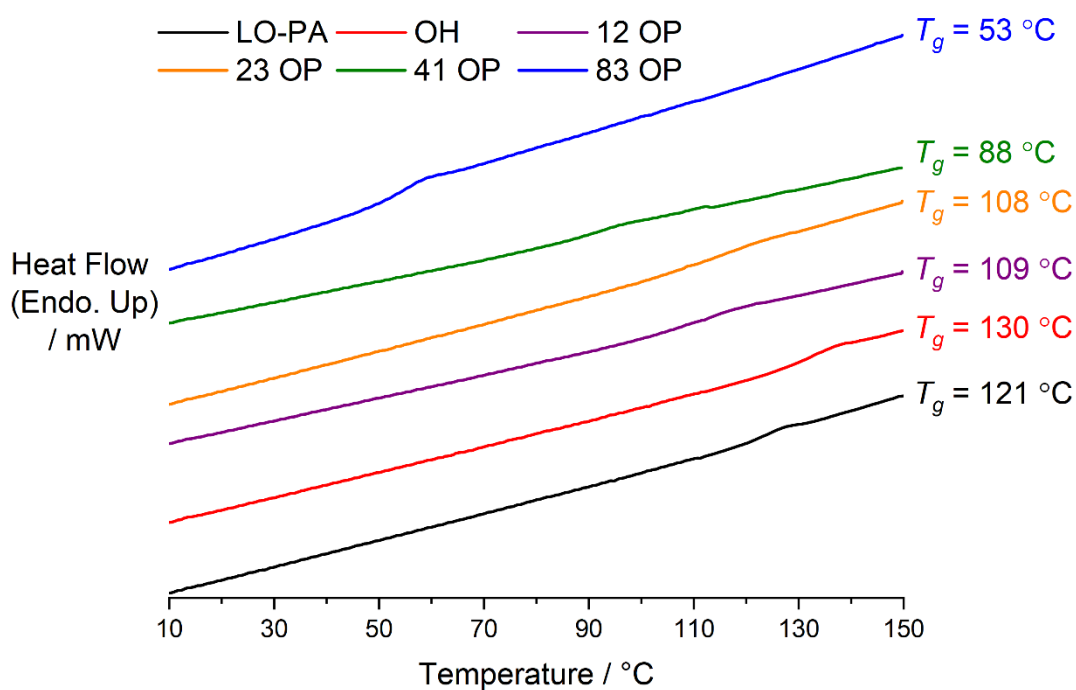


Figure 4.11: Stacked DSC thermographs (3rd heating cycle, 20 °C min⁻¹ ramp) of poly(LO-*alt*-PA), poly(OH) and the phosphorylated polymers. T_g values (right) generally decreases with increasing phosphorylation, consistent with both TPP's use as a plasticiser and chemical modification of the polymer.

4.9: Thermal Stability of the Phosphorylated Polymers

TGA and PCFC analysis performed by Dr. Malavika Arun (Victoria University, AU) in collaboration with Prof. Paul Joseph (Victoria University) and Dr. Svetlana Tretsiakova-McNally (Ulster University, UK).

To assess the thermal stability of the copolymers, TGA experiments were conducted on the phosphorylated polymers, in addition to their precursors and a sample of poly(CHO-*alt*-TCPA), as prepared on a large scale by Dr. Mark Sullivan.⁴² TGA measures weight loss due to degradation *versus* temperature, and can show how materials behave under extreme heat, as one might expect in a fire. The TGA curves are plotted in **Figure 4.12**, with these results obtained under a nitrogen atmosphere.

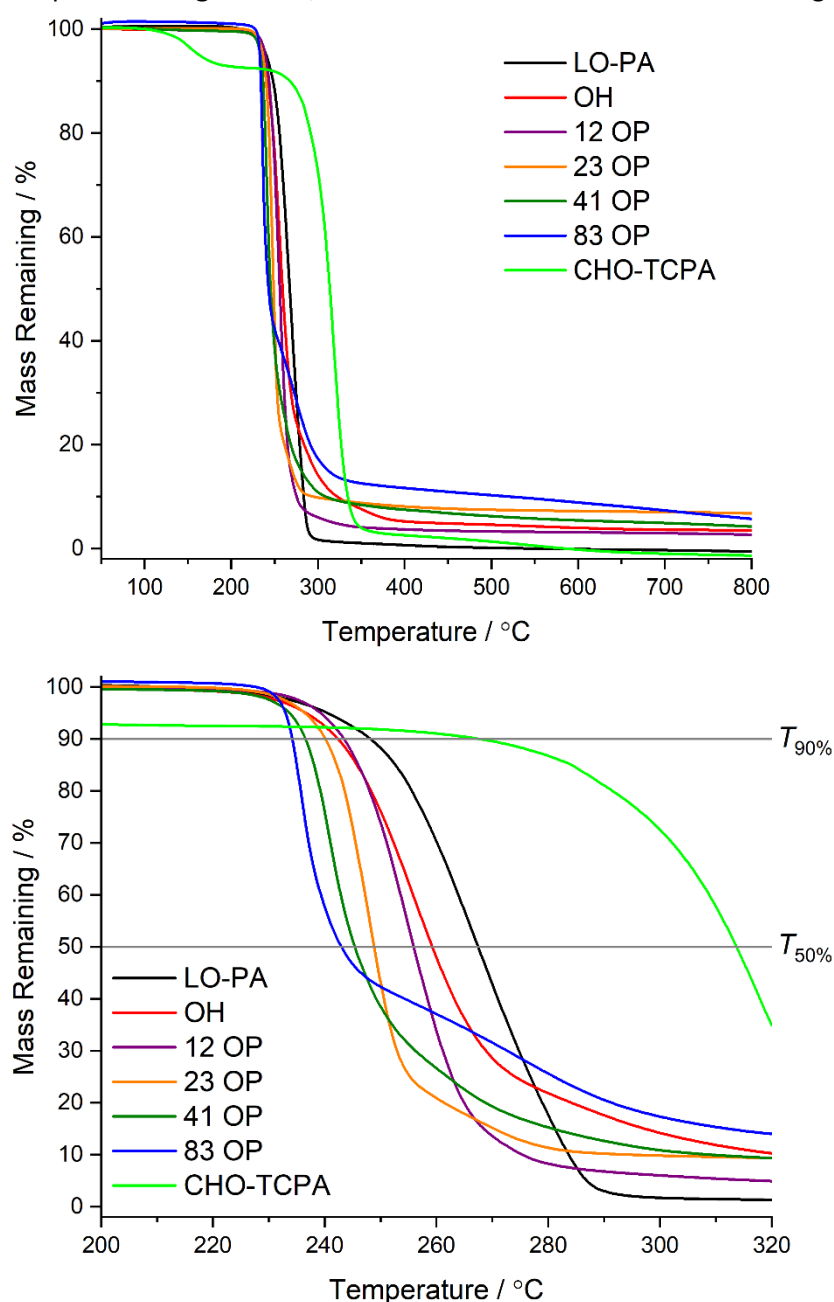


Figure 4.12: TGA curves of the copolymers in N₂ (10 °C min⁻¹, 30 °C to 800 °C, top), with the 200 °C to 320 °C temperature range expanded (bottom). Experiments performed by Dr. Malavika Alun (Victoria University).

All the TGA curves, aside from poly(CHO-*alt*-TCPA), show one major degradation event, meaning the phosphate linkages and the polymer itself are likely degrading simultaneously, rather than in sequence. This is important, as if the phosphate linkages were more thermally unstable than the polymer, the flame retardancy imparted by the phosphate may be significantly diminished when heated. There is an 8% mass loss in poly(CHO-*alt*-TCPA) between 100 and 200 °C, with this previously found to be caused by the mass loss of toluene solvent that is trapped in the polymer.⁴² Therefore, the temperature at 90% mass remaining ($T_{90\%}$) was taken for the onset of thermal degradation, whilst the temperature at 50% and 10% mass remaining ($T_{50\%}$ and $T_{10\%}$) were used as measures of the major degradation event and when degradation was largely complete, respectively. These measures, alongside the weight percentage of mass remaining, or char, at 700 °C, are listed in **Table 4.5**.

Table 4.5: TGA of the copolymers performed in N₂, at a heating rate of 10 °C min⁻¹. The temperature at 90, 50 and 10% of mass remaining are indicated, as well as the weight percentage remaining at 700 °C. Experiments performed by Dr. Malavika Alun (Victoria University).

Polymer	$T_{90\%}$ / °C	$T_{50\%}$ / °C	$T_{10\%}$ / °C	Residue at 700 °C / wt. %
LO- <i>alt</i> -PA	248	267	284	0.0
OH	242	259	322	3.7
OP_12	243	256	275	3.0
OP_23	240	249	294	7.1
OP_41	236	245	309	4.9
OP_83	234	243	521	7.4
CHO- <i>alt</i> -TCPA	268	314	334	0.0

The onset of the degradation was between 248 and 234 °C for all polymers based on poly(LO-*alt*-PA), with increasing levels of phosphorylation correlating with small decreases in $T_{90\%}$. Poly(CHO-*alt*-TCPA), with its different repeat unit, was more thermally stable, having a 20 °C higher onset of degradation and 47 °C higher $T_{50\%}$ than for poly(LO-*alt*-PA). The $T_{50\%}$ values follow a similar pattern to $T_{90\%}$ for the phosphorylated polymers, with increasing levels of phosphorus modestly decreasing the thermal stability. Interestingly however, the $T_{10\%}$ value for poly(OH) is 38 °C higher than poly(LO-*alt*-PA), whilst the highest degree of phosphorylation in poly(OP_83) led to a protracted degradation process, with mass loss from 50% to 10% occurring across a 278 °C range. This is in sharp contrast to poly(CHO-*alt*-

TCPA), where although the onset and main degradation temperature were higher, the equivalent 50% to 10% mass loss occurred over just 30 °C. This fast degradation is likely reflected in the residue at 700 °C, by which temperature all material had been volatilised. Unfunctionalised poly(LO-*alt*-PA) was also completely volatilised by 700 °C, meaning it is likely to be highly flammable, as it does not contain any gas-phase active flame retardant halogens (unlike poly(CHO-*alt*-TCPA) or produce any surface char to protect underlying material. Therefore, 100% of the material has been degraded into (presumably flammable) gaseous hydrocarbon fragments. All the modified polymers produced varying amounts of residue, albeit in an irregular manner, as poly(OP_23) produced significantly more char than poly(OP_41) and poly(OP_12), yet less than poly(OP_83).

4.10: Flame Retardancy (PCFC) of the Phosphorylated Polymers

TGA and PCFC analysis performed by Dr. Malavika Arun (Victoria University, AU) in collaboration with Prof. Paul Joseph (Victoria University) and Dr. Svetlana Tretsiakova-McNally (Ulster University, UK).

Pyrolysis Combustion Flow Calorimetry (PCFC) is an analytical technique which can provide a wealth of metrics to help assess flame retardant performance whilst only requiring small quantities of sample.⁴⁴ In essence, the method works in two stages; the firstly a sample is heated (and thereby volatilised and degraded) at a constant heating rate, in the same manner as in TGA. Secondly, the volatiles are mixed with air (while still at high temperature) and burned in a calorimeter, where oxygen consumption is measured. The amount of oxygen required to burn the sample can be related to the energy released during combustion, the heat release rate (HRR, measured in W g^{-1} material). This is often plotted as a function of temperature to examine a) how much energy is released upon combustion of a material, and b) at what temperature might one expect this energy to be released. The results of PCFC analysis are shown in **Figure 4.13**, which in terms of the temperatures where signal is observed correlate with the TGA results. This is not surprising given there is considerable overlap between the two methods, as rather than measuring mass loss from volatilisation in TGA, the HRR from the combustion of thermal degradation products is measured by PCFC, with this naturally overlapping with the material volatilising as seen by TGA. The height of the peak relates to more energy being released during combustion, with its maximum called the peak heat release rate (PHRR), whilst the temperature this is observed at is the T_{PHRR} . The total heat release (THR, kJ g^{-1} material combusted) during combustion can also be calculated, with flammable materials unsurprisingly showing higher THRs. The heat release capacity (HRC, $\text{J g}^{-1} \text{K}^{-1}$), is a measure of the maximum heat

release per unit mass per degree of a material, essentially the PHRR normalised for heating rate, meaning it a common metric when comparing flame retardant behaviour.⁴⁴ This is particularly pertinent when considering materials whose flame retardancy is derived from gas phase action, as the combustion aspect of PCFC is only applied to material which has been volatilised in the TGA-like aspect of the technique.

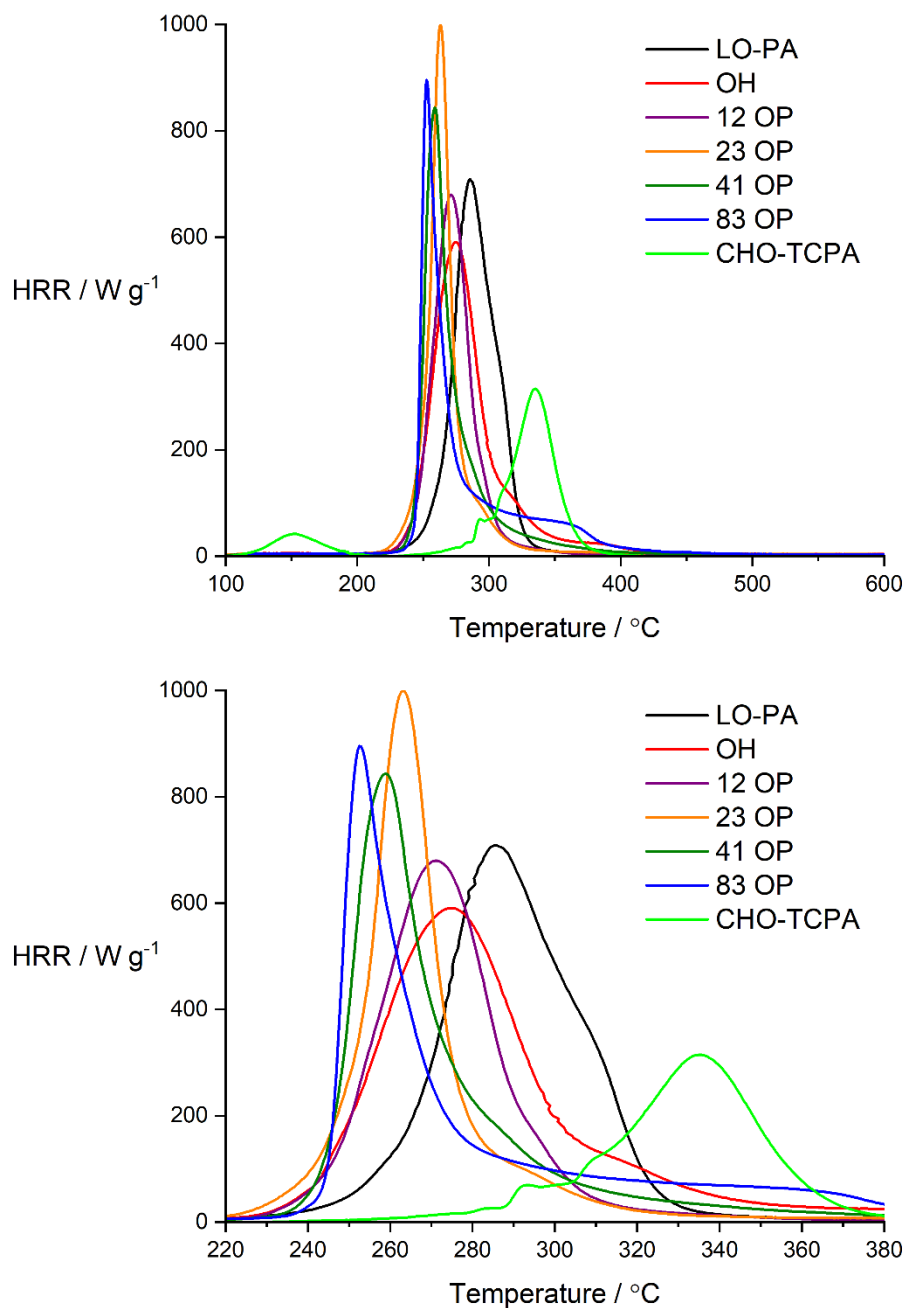


Figure 4.13: PCFC analysis of the copolymers, with heating at $1^{\circ}\text{C min}^{-1}$ in N_2 for the first stage of the analysis, before combustion in air at 900°C to measure the heat release rate (HRR). As performed by Dr. Malavika Alun (Victoria University). Bottom figure is identical to the top but focussed on the range $220\text{-}380^{\circ}\text{C}$.

Furthermore, the char residue (wt. %) can also be measured, which can be a good indicator of surface-derived flame retardancy. The more a substance chars at the surface, the more (potentially flammable) internal material can be protected. Another measure of flame retardancy which is informed by both gas phase and surface phase metrics is the effective heat of combustion (EHC, kJ g^{-1}), which is calculated according to **Equation 4.2**.

$$\text{Equation 4.2: } EHC = \frac{THR}{\left[1 - \frac{M_c}{M_s}\right]}$$

Where M_s is the starting mass of the sample, and M_c is the mass of char remaining after pyrolysis is complete. This means a sample with a higher char mass (and higher surface phase activity) will have a slightly elevated EHC, whilst a gas-phase active sample with a lower THR will lead to a decreased EHC. A complete set of measures obtained by PCFC are shown in **Table 4.6**, which also includes the weight percentage of the element responsible for flame retardancy (phosphorus or chlorine for poly(CHO-*alt*-TCPA)).

Table 4.6: PCFC data for the phosphorylated copolymers, poly(LO-*alt*-PA), poly(OH) and poly(CHO-*alt*-TCPA).^a

Polymer	P Loading / wt. % ^b	T_{PHRR} / °C	PHRR / W g^{-1}	HRC / $\text{kJ g}^{-1} \text{K}^{-1}$	THR / kJ g^{-1}	Char Residue / wt.%	EHC / kJ g^{-1}
LO- <i>alt</i> -PA	-	284	698	775	30.7	1.2	31.1
OH	-	275	574	640	30.0	2.8	30.4
OP_12	1.3	271	675	748	24.2	13.2	28.0
OP_23	1.9	264	897	992	24.5	11.8	27.8
OP_41	3.1	258	890	994	26.4	6.4	28.2
OP_83	4.8	251	953	1050	26.1	6.4	27.8
CHO- <i>alt</i> -TCPA	37.0 ^c	336	302	337	16.0	1.4	16.2

^a Testing performed in triplicate by Dr Malavika Arun (Victoria University). Heating at $1 \text{ }^\circ\text{C min}^{-1}$ in N_2 for the first stage of the analysis, before combustion in air at $900 \text{ }^\circ\text{C}$ for oxygen depletion colorimetry measurements. ^b Theoretically calculated from NMR conversion data, neglecting for the mass of end groups. ^c Weight percent of chlorine in the copolymer.

What is immediately obvious from **Table 4.6** is just how effective poly(CHO-*alt*-TCPA) is as a flame retardant, as its values for PHRR, HRC, THR and EHC are all far lower than the other samples. Given the incredibly high chlorine loading in the sample however, this is not particularly surprising. The

primarily gas-phase flame retardancy of chlorinated compounds is again demonstrated here, as poly(CHO-*alt*-TCPA) produces very little char, yet its HRC is less than half of poly(LO-*alt*-PA).

The introduction of hydroxyl groups produces a minor improvement in both char formation and HRC compared to unfunctionalised poly(LO-*alt*-PA). Increasing introduction of phosphate groups then actually leads to an increase in both PHRR and HRC, meaning the volatiles produced by thermal degradation produce more heat when burned post phosphorylation. This indicates that the phosphates do not lead to gas-phase suppression of combustion reactions, unlike poly(CHO-*alt*-TCPA). However, THR does decrease after the introduction of phosphate, with the lowest phosphorus loading in poly(OP_12) giving the largest drop. This is related to its ability to produce char, as the more char it produces, the less volatile material is burned, so less energy is produced overall. Indeed, the amount of char produced is again highest for poly(OP_12), whilst increasing the phosphorus loading decreases the char yield, although there is still significantly more char produced by poly(OP_83) than the non-phosphorylated polymers. Given the phosphorylated polymers have lower THR and EHC values and higher char yields, they can be considered somewhat flame retardant compared to their unmodified precursor.

The observation that higher phosphate loadings do not lead to increased char yields is not in itself unique, and has been previously observed for phosphate-appended epoxy resins and poly(acrylonitrile).^{31,45} Despite the diminishing returns in terms of char formation, the amount of char produced still exceeds the weight percentage of phosphorus added to each polymer, highlighting the role of phosphorus in promoting char formation, rather than simply being charred itself. This catalytic reaction is generally believed to be promoted by phosphoric acids produced on thermal degradation, which can encourage extensive cross-linking and aromatisation/graphitisation of the rest of the polymer.⁴⁶ Char formation was observed visually while exposing pellets of poly(OP_23) to flame from a cigarette lighter, whereas poly(LO-*alt*-PA) began to continuously burn after only a few seconds of exposure. This is demonstrated in **Figure 4.14**, which shows a partially charred pellet of poly(OP_23) obtained after 0, 10 and 25 seconds of exposure to flame, and the equivalent for poly(LO-*alt*-PA). After further exposure, the pellet of poly(OP_23) did eventually light, yet this qualitative test reinforces the quantitative findings from PCFC, that the introduction of covalently bound phosphate esters encourages the formation of surface char, which in turn contributes to a more flame retardant polymer. This flame retardancy has been achieved without any blended in additives to the polymer than can leach out and potentially cause environmental and toxicological damage.

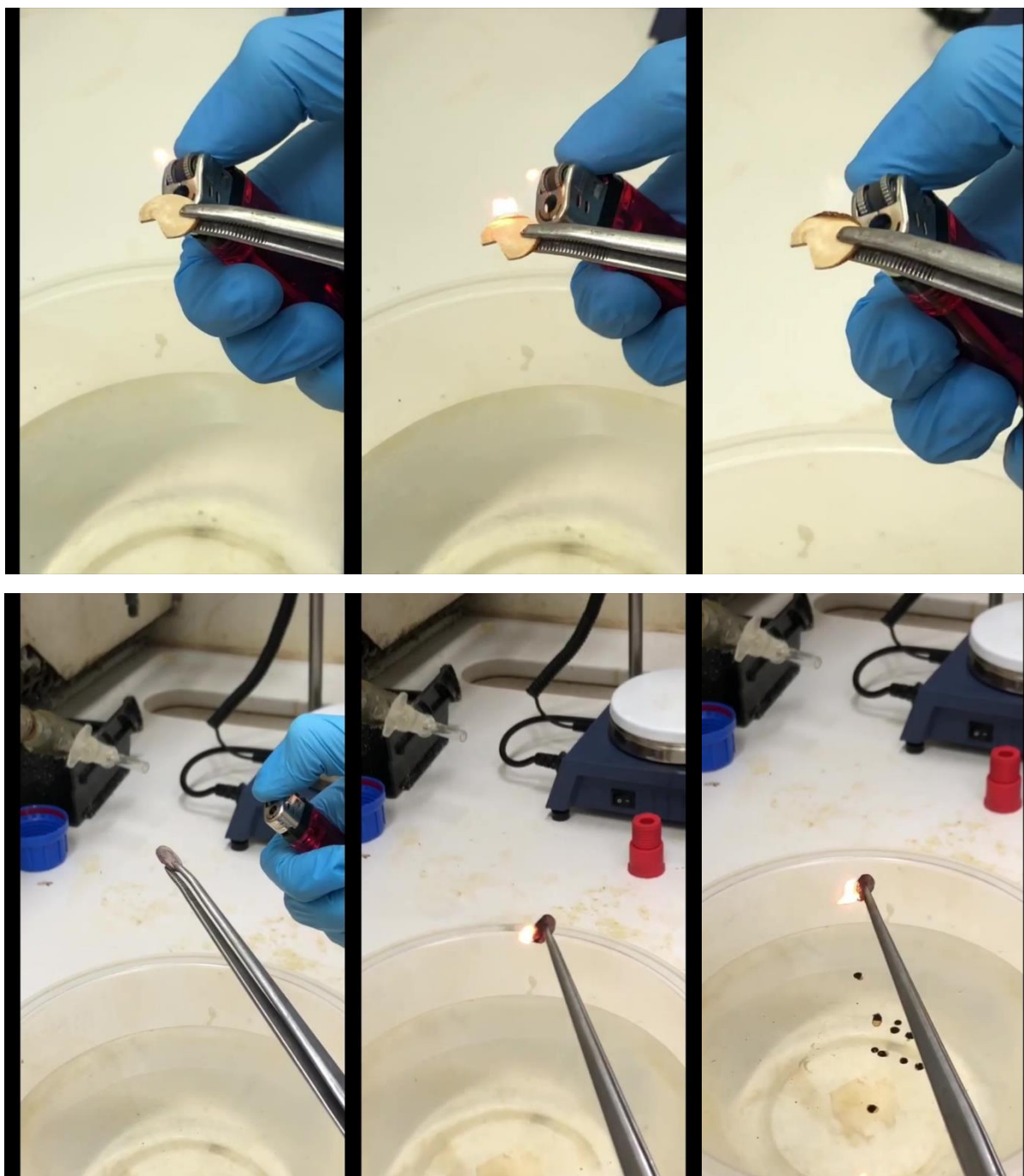


Figure 4.14: Still frames from a video of a pellet of top: poly(OP_23) being exposed to flame after 0 seconds (left), 10 seconds (middle) and 25 seconds (right). Note that rather than lead to propagating flame, the flame visible after 10 seconds led to the formation of a black char as seen after 25 seconds. The equivalent test with a pellet of poly(LO-*alt*-PA) is shown on the bottom, which led to self-sustained burning (and melting into the water bath below) after only a handful of seconds.

4.11: Summary

An array of PPM reactions were performed on material obtained from the large scale synthesis of poly(LO-*alt*-PA) described in section 3.7. This included thiol-ene click reactions, where 2-mercaptoethanol, 3-mercaptopropionic acid and 1-hexanethiol were efficiently added to poly(LO-*alt*-PA). These modifications had a significant effect on T_g , especially in the case of hexanethiol where an 82 °C reduction in T_g compared to poly(LO-*alt*-PA) was seen. Tentative FT-IR evidence, as well as qualitative observation of vastly reduced solubility suggested that modification by L-cysteine was at least partially successful.

1,6-hexanedithiol was used to cross-link poly(LO-*alt*-PA) to varying degrees. In contrast to reactions with (mono)hexanethiol, this produced little impact on T_g , suggesting cross-linking was indeed occurring. M_w did increase with the degree of cross-linking, as did polydispersity, whilst solubility in THF and CDCl₃ decreased, with the highest degree of cross-linking uncharacterisable by solution techniques. These cross-linked polymers were compared to poly(LO-*alt*-PA) cross-linked during its synthesis *in situ* through use of vinyl cyclohexene diepoxide (VCHDO). The more rigid cross-links here did have a discernible impact on T_g even at low cross-link densities, whilst also increasing M_w by 50% with only 5% replacement of LO for VCHDO.

Hydroboration-oxidation of poly(LO-*alt*-PA) led to quantitative conversion of the alkene group to give a hydroxyl-appended polyester, poly(OH), as evidenced by NMR, MALDI-ToF, and markedly different solubility. Poly(OH) was then reacted with diphenyl phosphoryl chloride in various stoichiometries to give a range of phosphorylated polyesters. These polymers possessed decreased T_g values with increasing phosphorylation, and increased molecular weights compared to their precursor.

The thermal degradation and flame retardant properties of the phosphorylated polymers were investigated by TGA and pyrolysis combustion flow colorimetry (PCFC), and compared to a halogenated flame retardant polymer in poly(CHO-*alt*-TCPA). TGA and PCFC both showed increased char formation upon heating with phosphorylation, suggesting a surface active form of flame retardancy. This is in keeping with literature reports of phosphorus-appended polymers, whilst the diminishing returns of char yield with increasing phosphorus loading is also a reported phenomenon. Despite higher heat release capacities of their volatilised products, the increased char formation led to lower total heat release, and therefore a degree of flame retardancy.

4.12: References for Chapter 4

- 1 K. A. Günay, P. Theato and H. A. Klok, *J. Polym. Sci. Part A Polym. Chem.*, 2013, **51**, 1–28.
- 2 M. A. Gauthier, M. I. Gibson and H. A. Klok, *Angew. Chemie Int. Ed.*, 2009, **48**, 48–58.
- 3 M. E. Lamm, P. Li, S. Hankinson, T. Zhu and C. Tang, *Polymer (Guildf.)*, 2019, **174**, 170–177.
- 4 N. Yi, T. T. D. Chen, J. Unruangsri, Y. Zhu and C. K. Williams, *Chem. Sci.*, 2019, **10**, 9974–9980.
- 5 O. Hauenstein, S. Agarwal and A. Greiner, *Nat. Commun.*, 2016, **7**, 1–7.
- 6 D. J. Fortman, J. P. Brutman, G. X. De Hoe, R. L. Snyder, W. R. Dichtel and M. A. Hillmyer, *ACS Sustain. Chem. Eng.*, 2018, **6**, 11145–11159.
- 7 A. Gandini, *Prog. Polym. Sci.*, 2013, **38**, 1–29.
- 8 A. Brandolese, F. Della Monica, M. À. Pericàs and A. W. Kleij, *Macromolecules*, 2022, **55**, 2566–2573.
- 9 H. Ding, X. Wu, B. Han, N. Liu, B. Liu and I. Kim, *Polymer (Guildf.)*, 2020, **213**, 123199.
- 10 R. Baumgartner, Z. Song, Y. Zhang and J. Cheng, *Polym. Chem.*, 2015, **6**, 3586–3590.
- 11 D. Merckle, E. Constant, Z. Cartwright and A. C. Weems, *Macromolecules*, 2021, **54**, 2681–2690.
- 12 M. J. Sanford, N. J. Van Zee and G. W. Coates, *Chem. Sci.*, 2018, **9**, 134–142.
- 13 L. Y. Wang, G. G. Gu, T. J. Yue, W. M. Ren and X. B. Lu, *Macromolecules*, 2019, **52**, 2439–2445.
- 14 A. B. Lowe, *Polym. Chem.*, 2010, **1**, 17–36.
- 15 S. Hafeez, J. Jaishankar, P. Srivastava and L. Nebhani, *Mater. Today Commun.*, 2021, **26**, 101813.
- 16 S. F. Parker, *Chem. Phys.*, 2013, **424**, 75–79.
- 17 S. Koltzenburg, M. Maskos and O. Nuyken, *Polymer Chemistry*, Springer, Berlin, English Ed., 2017.
- 18 I. van der Veen and J. de Boer, *Chemosphere*, 2012, **88**, 1119–1153.
- 19 Royal Society of Chemistry, *Polymers in liquid formulations Technical report: A landscape view of the global PLFs market*, 2021.
- 20 T. B. Young, O. G. Guppy, A. J. Draper, J. M. Whittington, B. M. Kariuki, A. Paul, M. Eaton, S. J. A. Pope and B. D. Ward, *Polym. Chem.*, 2023, **14**, 2478–2484.

- 21 I. Pantelaki and D. Voutsas, *Sci. Total Environ.*, 2019, **649**, 247–263.
- 22 A. Covaci, S. Voorspoels, M. A. E. Abdallah, T. Geens, S. Harrad and R. J. Law, *J. Chromatogr. A*, 2009, **1216**, 346–363.
- 23 Stockholm Convention, <http://chm.pops.int/>, (accessed 28 April 2023).
- 24 Commission Regulation (EU) 9 February 2017 Regulation (EC) No 1907/2006 of the European Parliament and of the Council concerning the Registration, Evaluation, Authorisation and Restriction of Chemicals (REACH) as regards to bis(pentabromophenyl)ether, <https://eur-lex.europa.eu/legal-content/EN/TXT/?uri=celex:32017R0227>, 2017.
- 25 Y. J. Chung, Y. Kim and S. Kim, *J. Ind. Eng. Chem.*, 2009, **15**, 888–893.
- 26 J. Feng, J. Hao and J. Du, in *Fires and Polymers VI: New Advances in Flame Retardant Chemistry and Science*, ACS, San Diego, Ch. 8., 2012, pp. 113–121.
- 27 A. Beard, The flame retardants market, <https://www.flameretardants-online.com/flame-retardants/market>, (accessed 27 April 2023).
- 28 A. B. Morgan, C. A. Wilkie and G. L. Nelson, in *Fires and Polymers VI: New Advances in Flame Retardant Chemistry and Science*, ACS, San Diego, Ch. 1., 2012, pp. 1–13.
- 29 P. Joseph and S. Tretsiakova-McNally, in *Fires and Polymers VI: New Advances in Flame Retardant Chemistry and Science*, ACS, San Diego, Ch. 3., 2012, pp. 37–50.
- 30 B. Scharte, *Materials (Basel)*, 2010, **3**, 4710–4745.
- 31 P. M. Hergenrother, C. M. Thompson, J. G. Smith, J. W. Connell, J. A. Hinkley, R. E. Lyon and R. Moulton, *Polymer (Guildf)*, 2005, **46**, 5012–5024.
- 32 B. K. Schindler, K. Förster and J. Angerer, *J. Chromatogr. B Anal. Technol. Biomed. Life Sci.*, 2009, **877**, 375–381.
- 33 Y. Wu, G. Z. Miller, J. Gearhart, K. Romanak, V. Lopez-Avila and M. Venier, *Environ. Sci. Technol. Lett.*, 2019, **6**, 14–20.
- 34 H. M. Stapleton, S. Klosterhaus, S. Eagle, J. Fuh, J. D. Meeker, A. Blum and T. F. Webster, *Environ. Sci. Technol.*, 2009, **43**, 7490–7495.
- 35 Y. J. Kim, M. Osako and S. ichi Sakai, *Chemosphere*, 2006, **65**, 506–513.
- 36 H. Guo, X. Zheng, S. Ru, X. Luo and B. Mai, *J. Environ. Sci. (China)*, 2019, **85**, 200–207.

- 37 M. A. Rashid, W. Liu, Y. Wei and Q. Jiang, *J. Appl. Polym. Sci.*, 2022, e52493.
- 38 D. Pospiech, A. Korwitz, H. Komber, D. Jehnichen, L. Häußler, H. Scheibner, M. Liebmann, K. Jähnichen and B. Voit, *Macromol. Chem. Phys.*, 2015, **216**, 1447–1461.
- 39 Y. Liu, B. Wang, S. Ma, X. Xu, J. Qiu, Q. Li, S. Wang, N. Lu, J. Ye and J. Zhu, *Eur. Polym. J.*, 2021, **144**, 110236.
- 40 D. Y. Wang, Y. P. Song, L. Lin, X. L. Wang and Y. Z. Wang, *Polymer (Guildf.)*, 2011, **52**, 233–238.
- 41 L. Zheng, J. Feng, H. Xie and Z. Xu, *J. Polym. Sci.*, 2023, **61**, 1–9.
- 42 M. Sullivan, PhD Thesis, Cardiff University, 2020.
- 43 B. R. Sculimbrene and S. J. Miller, *J. Am. Chem. Soc.*, 2001, **123**, 10125–10126.
- 44 S. Tretsiakova-McNally and P. Joseph, *Polymers (Basel)*, 2015, **7**, 453–467.
- 45 P. Joseph and S. Tretsiakova-McNally, *Polym. Degrad. Stab.*, 2012, **97**, 2531–2535.
- 46 M. Arun, S. Bigger, M. Guerrieri, P. Joseph and S. Tretsiakova-McNally, *Polymers (Basel)*, 2022, **14**, 1447.

Chapter 5: Metal Complex Incorporation into ROCOP Polyesters

5.1: Cyclometallated Iridium Complexes and their Luminescence

Cyclometallated iridium(III) complexes (**Figure 5.1**) have been widely investigated due to their photoluminescent properties, with a view to their potential applications as luminescent chemosensors¹⁻⁶, bioimaging agents⁷⁻¹², in photoredox catalysis¹³⁻¹⁵ and as the emissive component in light-emitting diodes.¹⁶⁻²⁰ The interesting photophysical properties of Ir(III) complexes are largely due to the significant spin-orbit coupling induced by the heavy iridium atom, with this in turn partially allowing the formally spin-forbidden process of intersystem crossing (ISC).^{21,22} This provides access to excited triplet states (typically ³MLCT states) with high emission quantum efficiencies, with the wavelength of subsequent phosphorescent emission readily tuneable through modification of the cyclometallating ligands.^{23,24}

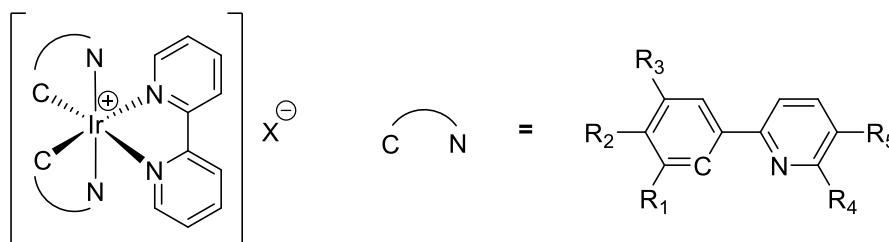
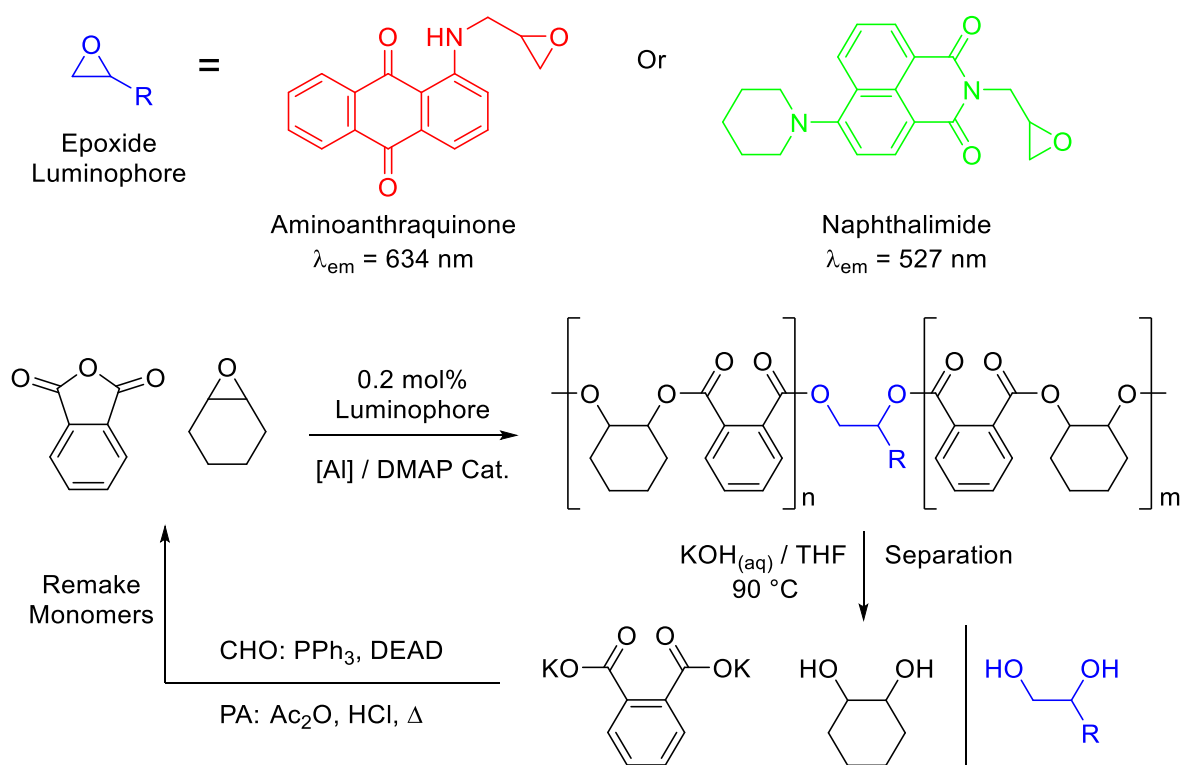


Figure 5.1: Generic cyclometallated cationic Ir(III) complex, featuring a 2,2'-bipyridine (bipy) ligand and two tuneable phenylpyridine (PhPy) based ligands. X typically equals Cl⁻ or PF₆⁻.²⁴

However, discreet iridium complexes present challenges for materials processing; aggregation and poor chemical stability can render any device less efficient, and so covalently tethering (and therefore segregating) the iridium centres to a polymer backbone is an enticing alternative.^{25,26} This allows for the use of solution-based processing techniques like ink-jet printing and spin-coating to manufacture films, displays and devices with potentially superior abilities to those based on molecular systems.^{23,27-29} Indeed, there are many examples of cyclometalated iridium complexes bound to polymers, either as part of the main chain or on side chains.^{2,23,26-32} Typically, these metallopolymers are comprised of chemically inert C-C bonds, with examples including poly(methyl methacrylate), poly(styrene) and poly(carbazole), with this presenting challenges in terms of degrading the material at end of life.^{25,33-35} Conversely, polyesters can be depolymerised into monomers or precursors to monomers in a chemical recycling process that is unavailable to polyolefins which rely on mechanical recycling.^{36,37} The challenge facing the polymer chemist is then how to go about introducing ligands, most probably bipyridine or phenanthroline based ligands, into a wider polyester microstructure.

On the one hand, this challenge could be solved by synthesising diacids, dimethyl esters or diols containing ligating groups for use in a step-growth polyester synthesis. However, step-growth approaches naturally lead to broader polydispersities and possibly less control of ligand incorporation. Conversely, given its versatility and chain-growth nature, ROCOP is an ideal candidate for the controlled introduction of functional monomers. This has been demonstrated recently in a collaboration involving the Ward group where organic luminophores were incorporated into poly(CHO-*alt*-PA) (**Scheme 5.1**).³⁸ In this case, the luminophores (both a red-emitting aminoanthraquinone and a green-emitting naphthalimide) were altered to introduce epoxide functionality, meaning they could be doped into in ROCOP reaction mixtures. This produced highly luminescent polymers with as little as 0.2 mol% of dopant epoxide added to the reaction mixture. Finally, the polyester linkages could be chemically recycled by base hydrolysis, where the coloured component was successfully separated from the other degradation products. Residual colour remaining when dyed plastics are mechanically recycled reduce their value and utility, and so the ability to remove colour upon chemical degradation is a key advantage of this method.^{39,40} The diacid and diol products of base hydrolysis were then converted to CHO and PA to remake new, uncoloured, polymer. Although in this case the polymers contained organic fluorophores, rather than iridium phosphors, the principle of functional monomer incorporation into polyesters remains the same.

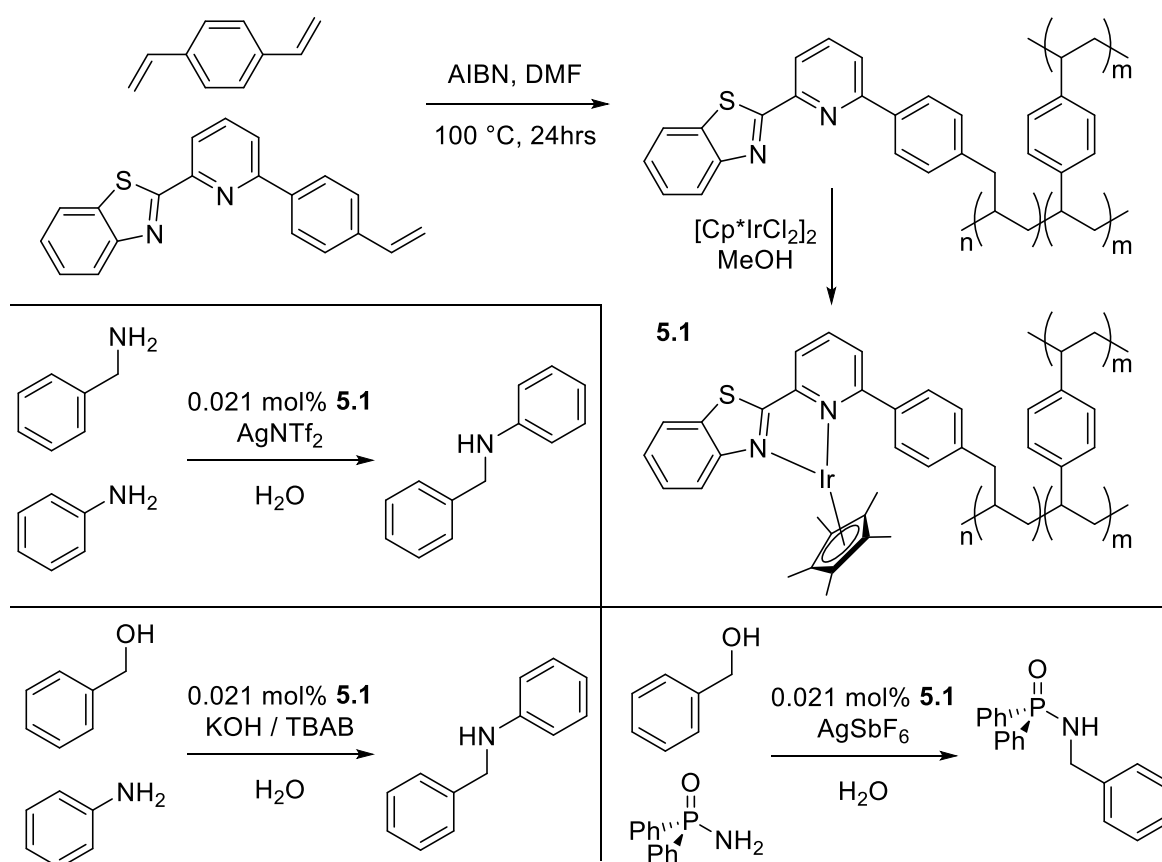


Scheme 5.1: Synthesis of luminophore-containing poly(CHO-*alt*-PA), using either a red (aminoanthraquinone) or green (naphthalimide) based epoxide as the emissive component, as reported by Ward, Pope and co-workers.³⁸ Chemical recycling by base hydrolysis and subsequent synthetic steps allowed for new, uncoloured, polymer to be produced from the reformed CHO and PA monomers. DEAD = diethyl azodicarboxylate.

In this section, the use of ROCOP to incorporate bipyridine-based ligands into a polyester backbone will be investigated, with a view to the binding of luminescent iridium complexes to a chemically recyclable material. The photophysical properties of the iridium polymers will be fully investigated, including theoretically by time-dependent (td)-DFT calculations. Further to this, several first row transition metals as well as ruthenium will be doped into ROCOP polyesters (in the former case into polymers produced from the bio-derived LO), with their properties fully analysed and characterised. This will include analysis of paramagnetic complexes, as well as the use of salt additives to GPC eluent to measure molecular weight of cationic polymers.

5.2: Iridium Doped Polymers

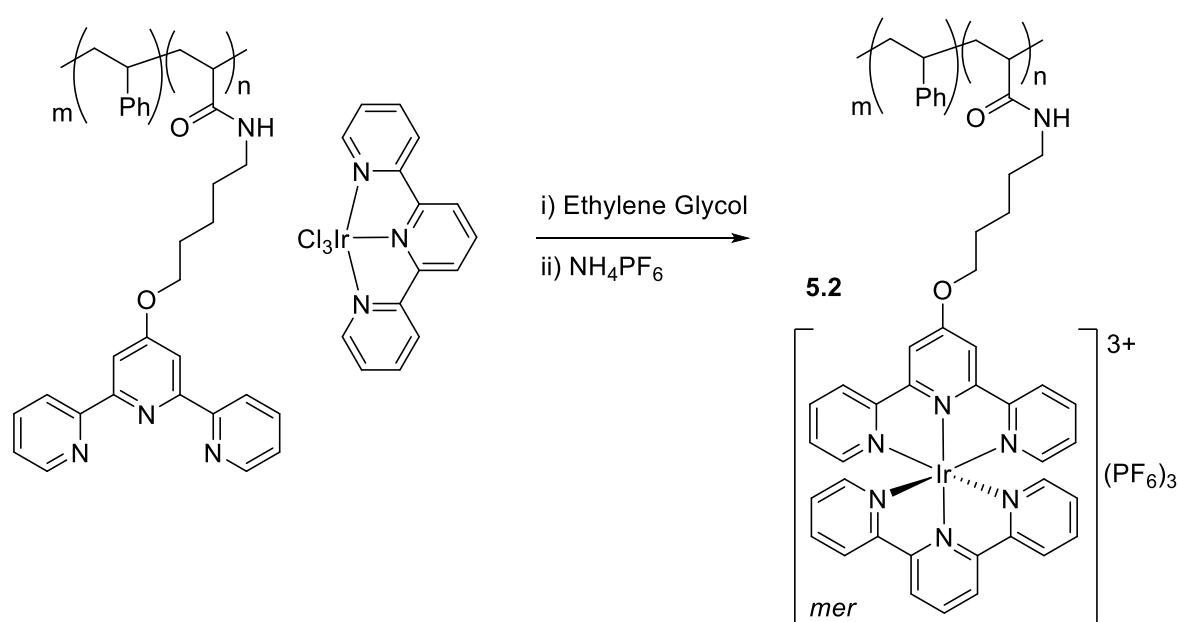
Iridium containing polymers have been synthesised for a variety of potential functions, including as a way of immobilising a catalyst onto a polymer support, allowing for a more efficient recovery of the expensive iridium component. This has been demonstrated by Wang and co-workers, who designed a monomer with a chelating component, before radically copolymerising with *p*-divinylbenzene and subsequent reacting with $[\text{Cp}^*\text{IrCl}_2]_2$ to give the Ir(I) complex **5.1** (Scheme 5.2).⁴¹



Scheme 5.2: Synthesis of a copolymer of *p*-divinylbenzene with an Ir(I) component, and some of its uses as a catalyst in water at low catalyst loadings. As reported by Wang and co-workers.⁴¹

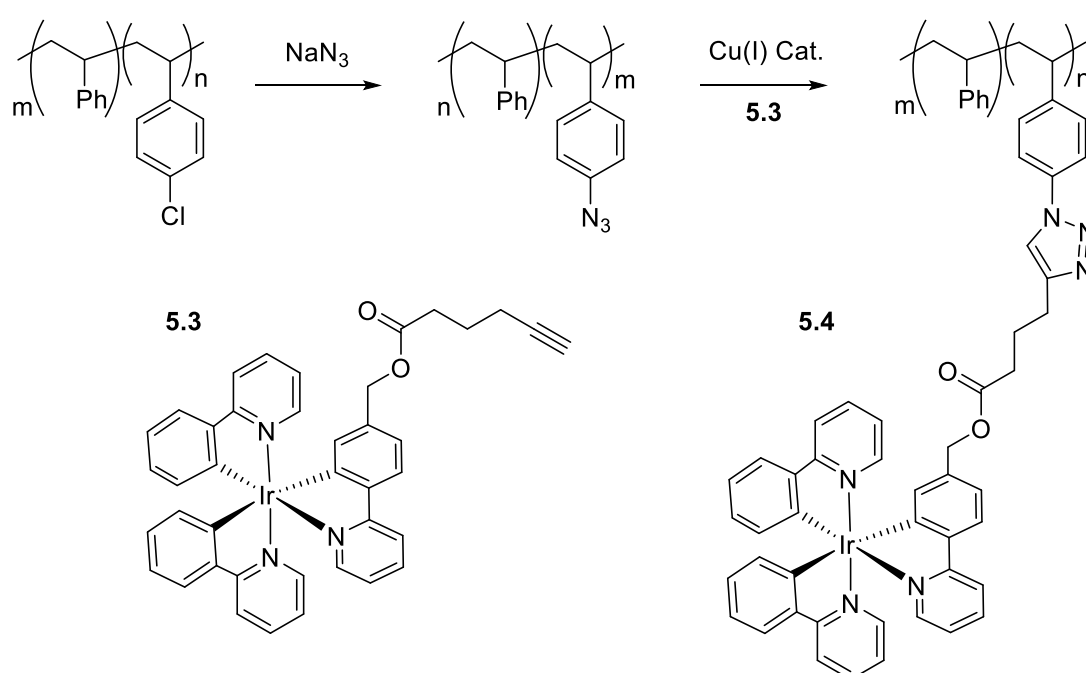
Polymer **5.1** was then shown to be an effective catalyst for ten different borrowing hydrogen reactions, including the coupling benzylamine or benzyl alcohol to aniline, as well as the coupling of diphenyl phosphinamide and benzyl alcohol. Importantly, all reactions only required very low catalyst loadings, and could be performed heterogeneously in water, meaning catalyst recovery and reuse was straightforward. This did not come at the expense of catalytic activity however, which remained competitive with iridium and ruthenium based molecular systems. In addition to this report and another by the same authors,⁴² polymer-immobilised iridium complexes have also been used as catalysts for methane borylation.⁴³

Despite their demonstrated utility as catalysts, polymer bound iridium complexes are primarily investigated for their luminescent properties, with the immobilisation of the polymer potentially allowing for more easily processable materials and devices. An early example of this was reported by Aamer and Tew, who synthesised a random copolymer of styrene and an acrylamide, which contained a pendant terpyridine ligand (**Scheme 5.3**).³⁵ This was then used to complex $[\text{Ir}(\text{terpy})\text{Cl}_3]$, giving polymer **5.2** as a trivalent PF_6 salt. Interestingly, the authors found that the absorbance properties of **5.2** were near identical to its non-polymer bound molecular analogue, yet the emissive properties were significantly different. The unchanging nature of the emission regardless of concentration of solvent led to the hypothesis that this contrast in photophysical behaviour was a direct result of polymer immobilisation, rather than from the formation of aggregates in solution.



Scheme 5.3: Reaction of a styrene/acrylamide-derived copolymer and $[\text{Ir}(\text{terpy})\text{Cl}_3]$ to give iridium-bound polymer **5.2**, as reported by Aamer and Tew.³⁵

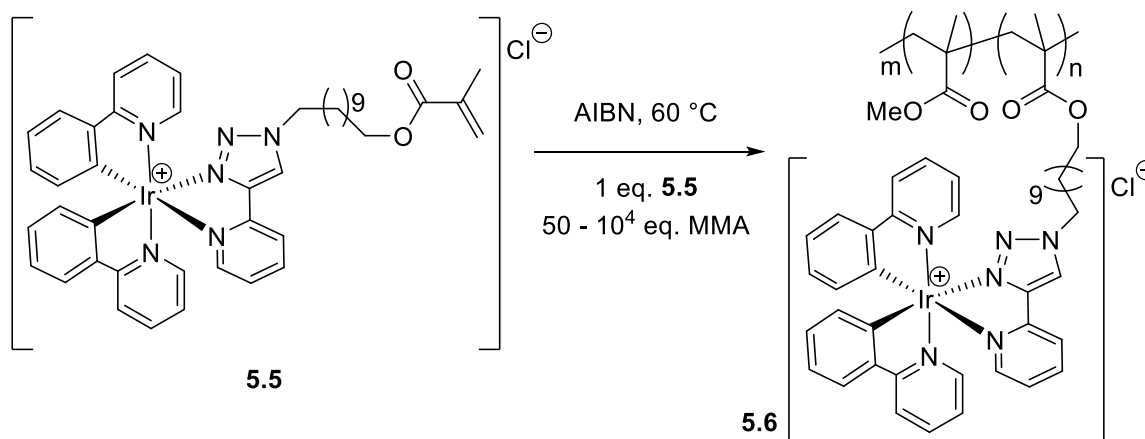
In contrast to the syntheses of **5.1** and **5.2**, where an iridium precursor is complexed to a polymer already containing ligands, an alternative approach is to use PPM reactions to incorporate a complex with all its ligands already in place, and harness separate reactivity to bind the complex and polymer together. An example of this is shown in **Scheme 5.4**, where the tris(phenylpyridine) complex **5.3** was designed to incorporate an alkyne into one of the ligands, allowing it to undergo a copper(I) catalysed addition across a pendant azide group in a styrene-like copolymer to give the iridium-bound polymer **5.4**.²⁶ Through modification of the ligands, the authors could tune the emissive properties of the iridium depending on the identity of the phenylpyridine ligands, and in another publication showed an alternative strategy to link complex and polymer using Schiff base condensation.²¹



Scheme 5.4: Radical copolymerisation of styrene and *p*-chlorostyrene, before its subsequent azidation and click reaction with **5.3** to give the iridium-bound polymer **5.4**. As reported by Weck *et. al.*²⁶

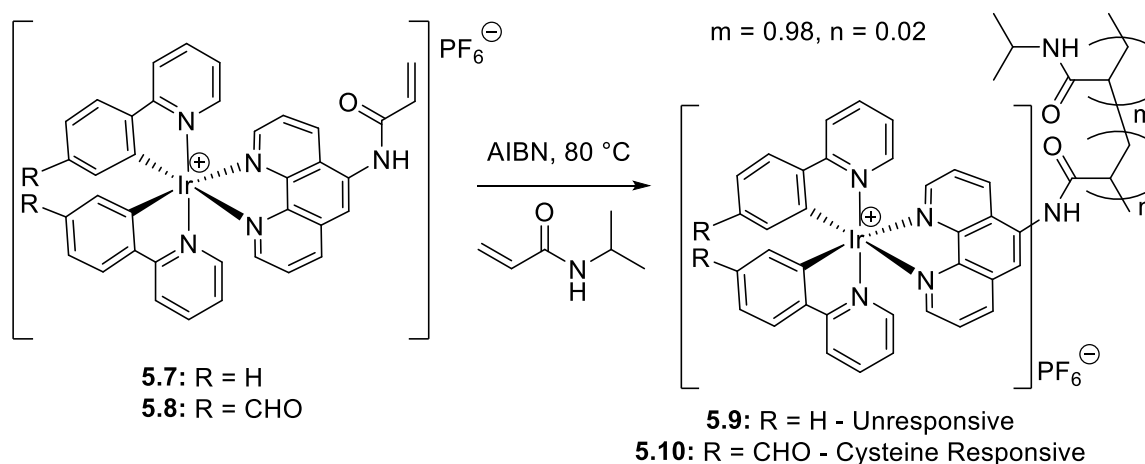
A third method of incorporating iridium into polymers is to synthesis an iridium-containing monomer, and then copolymerise with a major, non-iridium containing monomer. Naturally, this means any polymerisation strategy must be compatible with the iridium complex, yet in 2019 Baschieri *et. al.* demonstrated that complex **5.5** could undergo radical copolymerisation with methyl methacrylate (MMA) to form copolymers with stoichiometrically controlled degrees of incorporation (**Scheme 5.5**).³³ Importantly, the low (down to a 1:12100 ratio between n:m in **5.6**) iridium incorporation meant the physical properties of the polymer were dominated by poly(MMA), whilst the efficient luminescence of the iridium centre meant the photophysics were still controlled by **5.5**. Furthermore, the low oxygen diffusion through poly(MMA) contributed to enhanced luminescence by limiting

excited state quenching by oxygen, whilst the physical separation of luminophores hindered quenching by adjacent iridium centres, leading to exceptional performance far outstripping that (on a per mole basis) of unbound **5.5** in terms of excited state lifetime and photoluminescence quantum yield.



Scheme 5.5: Radical copolymerisation of the methacrylate-based iridium complex **5.5** and varying amounts of MMA to give the iridium-bound polymer **5.6**, as reported by Baschieri *et al.*³³

The luminescence properties of iridium complexes are sensitive to their ligand environments, meaning if the coordination sphere can be altered by the wider chemical environment, then the complex can serve as an effective chemical detector. This has been demonstrated in the context of iridium polymers by Zhao, Huang and colleagues who synthesised the acrylamide-based monomers **5.7** and **5.8**, before copolymerising with *N*-isopropylacrylamide to yield the water-soluble polymers **5.9** and **5.10** (Scheme 5.6).² The aldehyde group on the phenylpyridine ligands of **5.10** can undergo condensation reactions with cysteine, leading to visible enhancement of the luminescence, and thereby, a chemical sensor, whilst the protio-substituted **5.9** showed no such response.



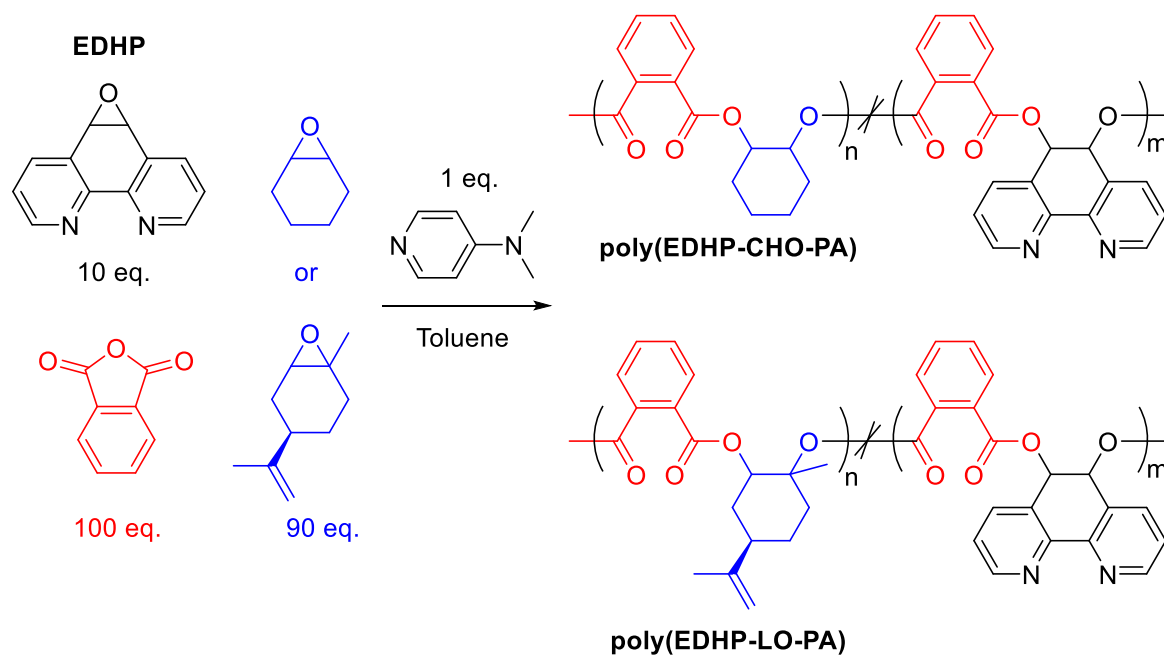
Scheme 5.6: Radical copolymerisation of two iridium acrylamide complexes with *N*-isopropylacrylamide, to give the cysteine responsive polymer **5.10**. As reported by Zhao, Huang and colleagues.²

Furthermore, **5.10** was cell membrane permeable, showed low toxicity and could selectively stain living cells, all meaning that the amount of cysteine in living cells could be determined spectroscopically. As well as cysteine, a report by Bochkarev *et. al.* has shown a red-emitting iridium polymer can be used as a detector for oxygen *in vivo*.⁴⁴ These are just a few examples of the array of potential applications luminescent iridium polymers can have, alongside previously discussed uses as catalysts, as components in light emitting devices, and as additives to solar cells to increase their efficiency.⁴⁵ Additional reports of iridium containing polymers are listed here.^{23,25,30–32,46–48}

However, all the cited examples have one common feature; that the polymers are based on kinetically and thermodynamically stable carbon-carbon bonds, which are not generally amenable to chemical recycling. Despite extensive searching, there is no evidence that an iridium polyester has ever been reported in the literature. Also, many of the polymers discussed previously require several steps to synthesise the highly bespoke ligand and/or monomer architectures required to incorporate the iridium complex. It was hypothesised that ROCOP may be an effective way to introduce an appropriate ligand environment in a one-pot reaction into a polyester, thereby allowing the complexation of a luminescent iridium complex in a relatively straightforward manner.

5.3: Incorporation of Bipyridine-like Units into Polyesters

A possible route to incorporating a chelating group into a ROCOP polyester is by using a ligand which also features epoxide functionality, in a similar way to that previously described for organic luminophores.³⁸ Therefore, 5,6-epoxy-5,6-dihydro-[1,10]-phenanthroline (EDHP) was investigated for use in ROCOP as a minor epoxide component, alongside major epoxide components in CHO or LO, and PA. DMAP was used by itself as an organocatalyst throughout this section so as to avoid potential occupation of the ligand sites by a metal derived from a catalyst, rather than iridium, whilst also eliminating the possibility that metal catalyst complexes could remain appended to the polymer chains and thereby effect the photophysical properties of the polymers.³⁸ A summary of this synthetic strategy is shown in **Scheme 5.7**, where a 9:1 ratio of major epoxide : EDHP was used. Although this visual representation of the polymers might suggest that a block copolymer has been synthesised, there was no evidence seen throughout this work to contradict the notion that the EDHP-PA units are statistically dispersed amongst a wider poly(epoxide-*alt*-PA) structure. Given its diminished reactivity compared to CHO (as seen in section 3.7), copolymerisations using LO were conducted at 100 °C (*vs.* 90 °C for CHO) for longer (47 hours *vs.* 24 hours for CHO).



Scheme 5.7: Synthesis of EDHP-doped polyesters, using CHO or LO and PA. 1 eq. = 25.6 μmol , 1 mL toluene. Conditions: CHO – 90 °C for 24 hours. LO – 100 °C for 47 hours. The crosses between the epoxide-*alt*-PA units and the EDHP-*alt*-PA units indicate that there is no evidence of block copolymer formation, and that a statistical copolymer has resulted. These markings are inferred throughout the rest of this section.

These reactions led to the formation of polyesters as expected, with their key parameters listed in **Table 5.1**. In accordance with the findings in chapter 3, the DMAP only reaction produced polyesters with no detectable ether linkages, whereas the longer reaction times and higher catalyst loadings (25.6 μmol vs. 12.8 μmol) led to high conversions of PA. Interestingly, CHO and LO produced identical EDHP incorporations with a 1: 8.2 ratio of EDHP : epoxide. This is slightly higher than the incorporation one would expect purely from the reaction stoichiometry of 1: 9, meaning EDHP incorporation is slightly favoured over CHO or LO under these conditions. Strictly speaking, this means that this is a statistical copolymer (as the reactivity of the epoxides differ, albeit marginally) rather than being truly random.

Table 5.1: Properties of the EDHP doped polymers. ^a

Major Epoxide	Conversion PA / % ^b	Selectivity Ester / % ^c	Ratio EDHP : Epoxide ^c	M_n / kDa ^d	\bar{D} ^{d,e}
CHO	89	> 95	1: 8.2	20.4	1.41
LO	78	> 95	1: 8.2	4.7	1.62

^a Conditions: 1 eq. (25.6 μmol) DMAP, 100 eq. PA, 10 eq. EDHP, 90 eq. either CHO or LO, 1 mL dry toluene. CHO – 90 °C for 24 hours. LO – 100 °C for 47 hours. ^b Determined by the ¹H NMR spectrum of the reaction mixture. ^c Determined by the ¹H NMR spectrum of the polymer. ^d Determined by GPC (viscometry detection against polystyrene standards). ^e $\bar{D} = M_w / M_n$.

The ratio of EDHP to major epoxide is readily calculable from the ^1H NMR spectra of the polymers. This was done by comparing the integration of the ester peak for CHO or LO to that of EDHP. EDHP contains four proton environments, with the most upfield signal at $\delta_{\text{H}} = 4.83$ (DMSO- d_6) in the monomer corresponding to the two protons about the epoxide group. Upon ring opening, this peak shifts downfield to $\delta_{\text{H}} 6.61$ (CDCl_3), and becomes highly broadened, characteristic of polymer peaks. ^1H - ^1H COSY experiments confirmed the identity of this peak given it does not couple to any other peaks in the spectrum, whilst three aromatic peaks do couple to one another (for full spectral assignment, see section 7.7). A representative spectrum for poly(EDHP-CHO-PA) is shown in **Figure 5.2**, with the peaks corresponding to the ester linkages in CHO shown at $\delta_{\text{H}} = 5.14$ and in EDHP at $\delta_{\text{H}} = 6.61$ ppm, with their ratio being 8.2 : 1. Ring-opened EDHP shows further resonances downfield of the residual solvent peak at $\delta_{\text{H}} = 8.81$, 7.97 and 7.35, the latter of which is obscured by the far more intense signals corresponding to ring-opened PA. Given the intensity and broadness of these PA signals, it was not possible to fully separate PA peaks which were adjacent to CHO or EDHP, and these peaks are not particularly sensitive to the identity of the epoxide in any case. The spectrum of poly(EDHP-LO-PA) was largely similar, and the degree of incorporation was calculated in the same way, aside from the integration of the LO ester peak being multiplied by 2 given there are half the number of protons in this environment as in the equivalent EDHP peak.

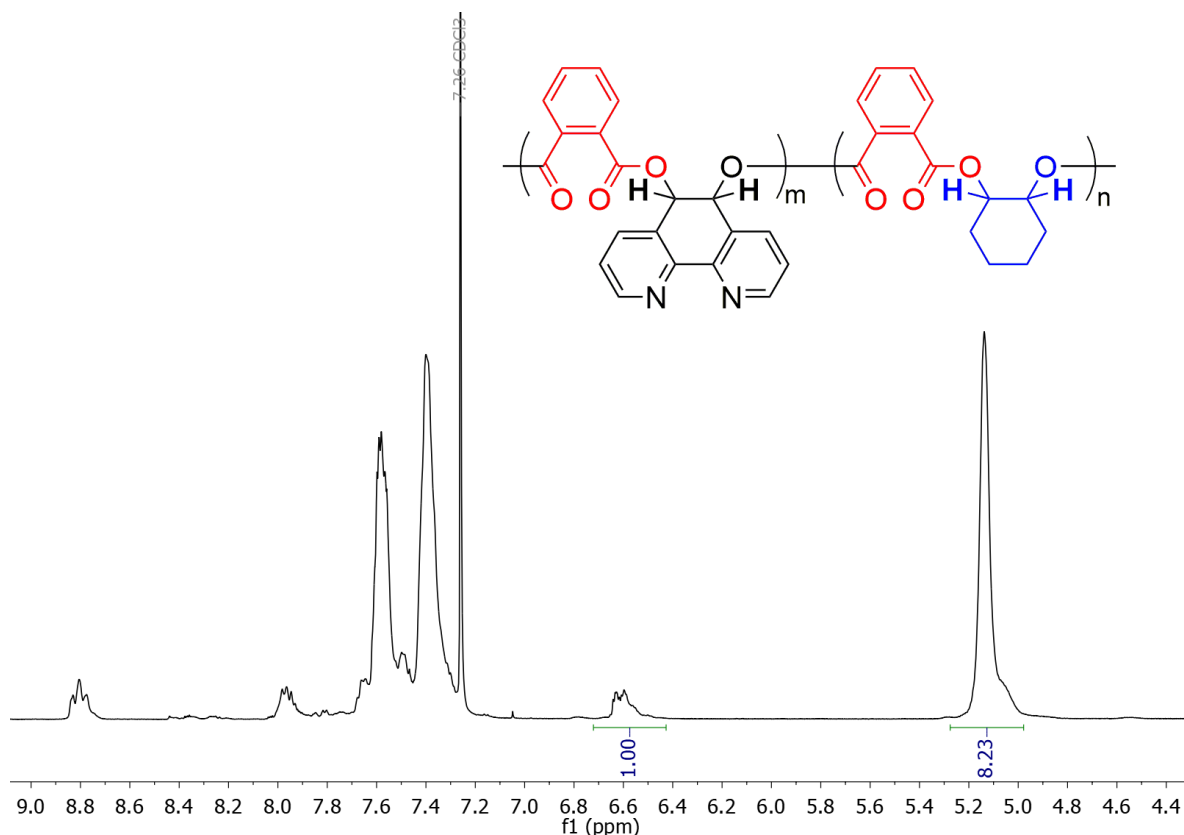


Figure 5.2: ^1H NMR spectrum (CDCl_3 , 500 MHz) of poly(EDHP-CHO-PA), with peaks corresponding to the ester units and their relative integrations indicated.

In terms of the polymer properties, the use of LO led to diminished molecular weights compared to CHO, whilst there is also a concurrent increase in polydispersity. This is consistent with the findings from the undoped reactions detailed in section 3.7, as it is likely that the harsher reaction conditions used to increase the rate of LO reaction also contribute to increased transesterification and thereby limit molecular weight and increase polydispersity. By using the molecular weight information in conjunction with the degree of EDHP incorporation from ^1H NMR data, it is possible to estimate both a) the average mass per single EDHP-PA unit and b) the average number of EDHP-PA units in each polymer chain. The average mass per single EDHP-PA unit (M_1) is a useful measure as it can be used to help determine the stoichiometry required for subsequent iridium complexation, and can be calculated using **Equation 5.1** for poly(EDHP-CHO-PA) as:

$$\text{Equation 5.1: } M_1 = [\delta_{EDHP}^H(M_{EDHP} + M_{PA})] + [\delta_{CHO}^H(M_{CHO} + M_{PA})]$$

Where M_{EDHP} , M_{PA} and M_{CHO} are the molar masses of EDHP, PA and CHO respectively, whilst δ_{EDHP} and δ_{CHO} represent the integrations of the ester resonances peaks in the ^1H NMR spectrum described in **Figure 5.2**. When δ_{EDHP} is set to unity, M_1 equals the average mass per EDHP-PA unit (assuming perfect ester selectivity and neglecting for the mass of end groups). For poly(EDHP-LO-PA), again, a factor of 2 is required to multiply δ_{LO} , and M_{CHO} is replaced by M_{LO} , but otherwise the relationship is the same. M_1 can then be used to calculate the average number of EDHP-PA units per polymer chain (N_{EDHP}) by **Equation 5.2** as:

$$\text{Equation 5.2: } N_{EDHP} = \frac{M_n}{M_1}$$

Table 5.2 lists the M_1 and N_{EDHP} values for poly(EDHP-CHO-PA) and poly(EDHP-LO-PA), showing that although the percentage incorporation of EDHP is identical in both polymers (from the ^1H NMR spectra), the number of units per polymer chain is significantly different an account of the far higher M_n of poly(EDHP-CHO-PA).

Table 5.2: M_1 and N_{EDHP} values for both doped polymers, as calculated by equations 5.1 and 5.2 using ^1H NMR and GPC data (Table 5.1)

Polymer	M_1 / kDa	N_{EDHP}
Poly(EDHP-CHO-PA)	2.4	8.6
Poly(EDHP-LO-PA)	2.8	1.7

Using different stoichiometries of EDHP, namely 15, 20 or 30 equivalents (out of a 100 total epoxide equivalents as before) in the polymerisation mixtures was also investigated for LO, with the properties of these polymers shown in **Table 5.3**. As expected, the amount of EDHP in the polymers increased with the amount of EDHP in the reaction mixture, whilst its increased prevalence also led to lower molecular weights and broadened molecular weight distributions. Interestingly, the amount of EDHP in the polymers was disproportionately elevated at higher doping concentrations. This is shown graphically in **Figure 5.3**, which shows that this increase was fairly linear, albeit at a steeper rate than expected, as at 30% inclusion in the reaction mixture, more than half (51%) of the repeat units were EDHP-PA.

Table 5.3: Effect of different EDHP concentrations in the polymerisation mixture on EDHP incorporation and molecular weight of the resultant polymers. ^a

EDHP Equivalents	LO Equivalents	Ratio EDHP : LO in Reaction Mixture	Ratio EDHP : LO in Polymer ^b	M_n / kDa ^c	\mathcal{D} ^{c,d}
10	90	1: 9	1: 8.2	4.7	1.62
15	85	1: 5.7	1: 3.0	1.6	2.56
20	80	1: 4	1: 1.8	1.3	2.97
30	70	1: 2.3	1: 0.9	1.3	2.44

^a Conditions: 1 eq. (25.6 μ mol) DMAP, 100 eq. PA, 100 total eq. of epoxide, 1 mL dry toluene, 100 °C for 47 hours.

^b Determined by the ¹H NMR spectrum of the polymer. ^c Determined by GPC (viscometry detection against polystyrene standards). ^d $\mathcal{D} = M_w / M_n$.

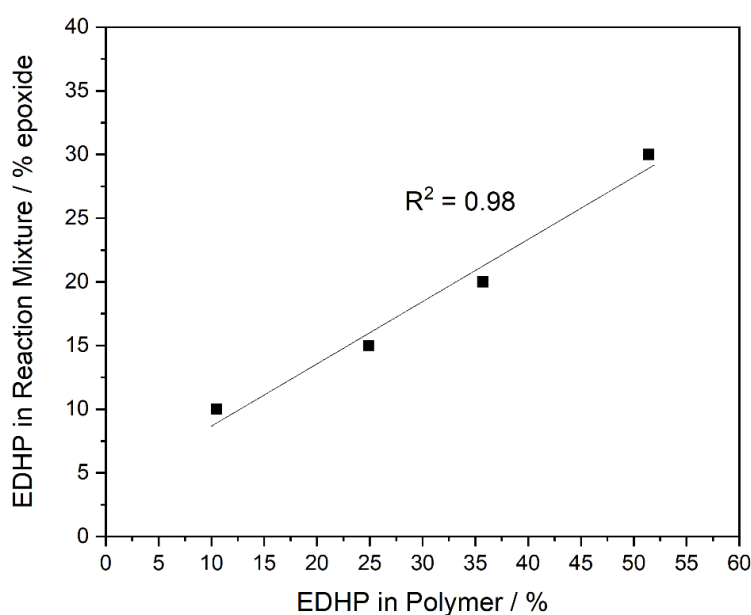


Figure 5.3: The percentage of EDHP used in the polymerisation mixture *versus* the percentage incorporated into the final polymer, indicating a broadly linear increase, albeit a shallower one than might be expected from the relative stoichiometries alone.

Despite the inferiority (from a molecular weight and polydispersity perspective) of the more highly doped EDHP poly(EDHP-LO-PA), the increased level of EDHP allowed for DOSY NMR experiments (**Figure 5.4**) to be performed. This showed that all peaks associated with ring-opened EDHP units had the same diffusion coefficient as peaks corresponding to ring-opened LO and PA. This is consistent with the EDHP-PA units and LO-PA being part of a copolymer, rather than a physical blend of two distinct polymers, given the relatively small probability that both poly(LO-*alt*-PA) and poly(EDHP-*alt*-PA) have identical diffusion coefficients.

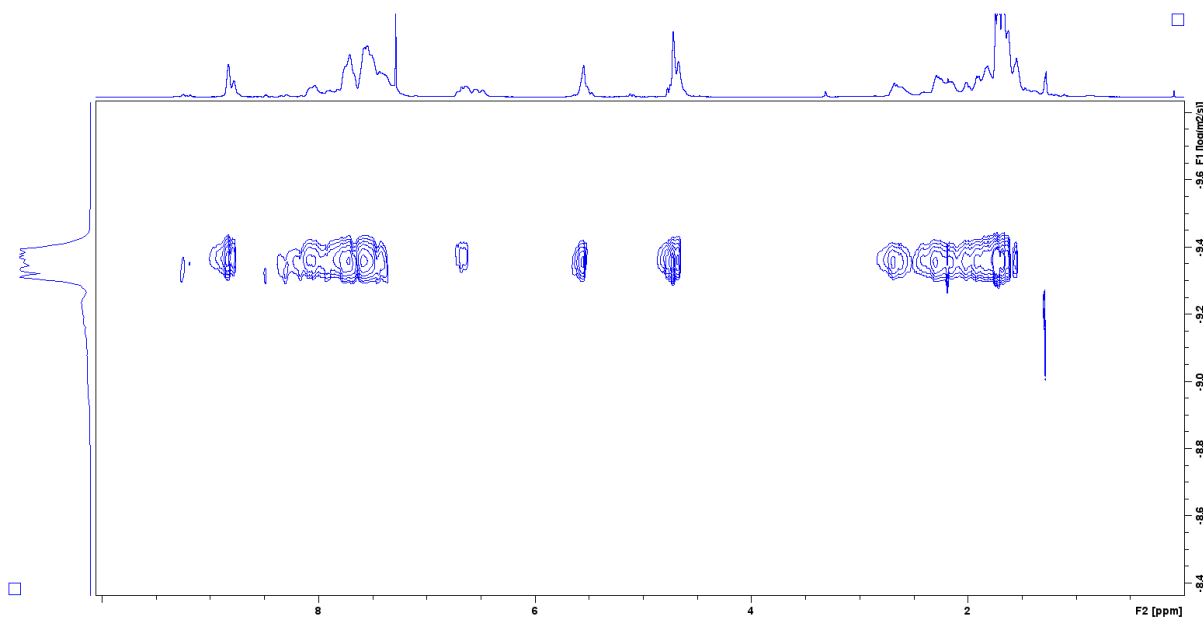
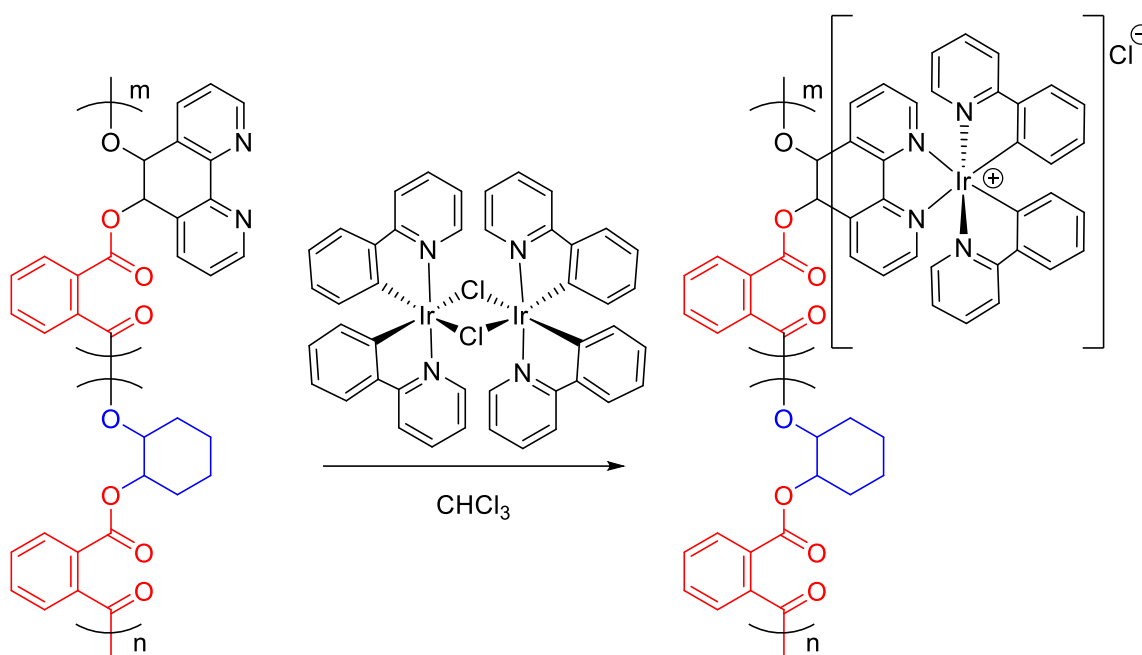


Figure 5.4: ^1H DOSY spectrum (600 MHz, CDCl_3) of a sample of poly(EDHP-LO-PA) prepared using a 1: 4 ratio of EDHP: LO in the reaction mixture (table 5.3). Each chemical shift associated with the ring-opened EDHP units ($\delta_{\text{H}} = 8.81, 7.97, 7.35$ and 6.61 ppm) correspond to the same diffusion coefficient (y-axis) as peaks associated with ring-opened LO (chiefly $\delta_{\text{H}} = 5.53, 4.67$ and $2.7 - 1.5$ ppm), consistent with a statistical copolymer of EDHP-PA and LO-PA units, rather than a physical dispersion of two distinct polymers.

5.4: Synthesis and Characterisation of Iridium Containing Polyesters

Iridium complexations were performed in collaboration with Sophie Fitzgerald and Prof. Simon Pope (both Cardiff University)

With the EDHP containing polymers in hand, complexation to iridium was performed using a well-established synthetic methodology, involving the “cracking” of a cyclometallated phenylpyridine (PhPy) iridium complex in $[\{\text{Ir}(\text{PhPy})_2\mu\text{-Cl}\}_2]$ (**Scheme 5.8**). A 2:1 reaction of both polymers (M_1 was used as a surrogate for formula mass) and iridium dimer in chloroform instantly led to a bright orange colour, suggestive of complexation (**Figure 5.5**). Although no other iridium precursors were investigated throughout this work, the synthesis of $[\{\text{Ir}(\text{PhPy})_2\mu\text{-Cl}\}_2]$ proceeds in a single step from $[\text{IrCl}_3] \cdot x\text{H}_2\text{O}$, and so the cyclometallating ligands could be readily altered in future studies.⁴⁹



Scheme 5.8: Synthesis of iridium-doped polyesters, as shown for poly(EDHP-CHO-PA).



Figure 5.5: Photograph of poly(EDHP-CHO-PA) after its complexation to in $[\{\text{Ir}(\text{PhPy})_2\mu\text{-Cl}\}_2]$, taken during its exposure to UV light. The orange/yellow glow is indicative of iridium, and contrasts strongly to the off-white polymer seen pre-complexation and the pale yellow colour of the iridium precursor.

As well as instant colour change, further evidence for complexation was seen in the ^1H NMR spectrum of the resultant polymers, with both the pre- and post-complexation spectra shown in **Figure 5.6**. The region highlighted in red shows a clear shift in the protons about the ring-opened epoxide of EDHP post-complexation, with this shift concurrent with the observance of new aromatic resonances belonging to the PhPy ligands. Indeed, there are no discernible resonances in the region representing the epoxide-EDHP protons of the precursor polymer, and the ratio of this shifted peak to the CHO ester peak at δ_{H} at 5.14 ppm is unchanged from the precursor. Taken together, this means it the vast majority, if not all, of the available EDHP sites have been occupied by iridium.

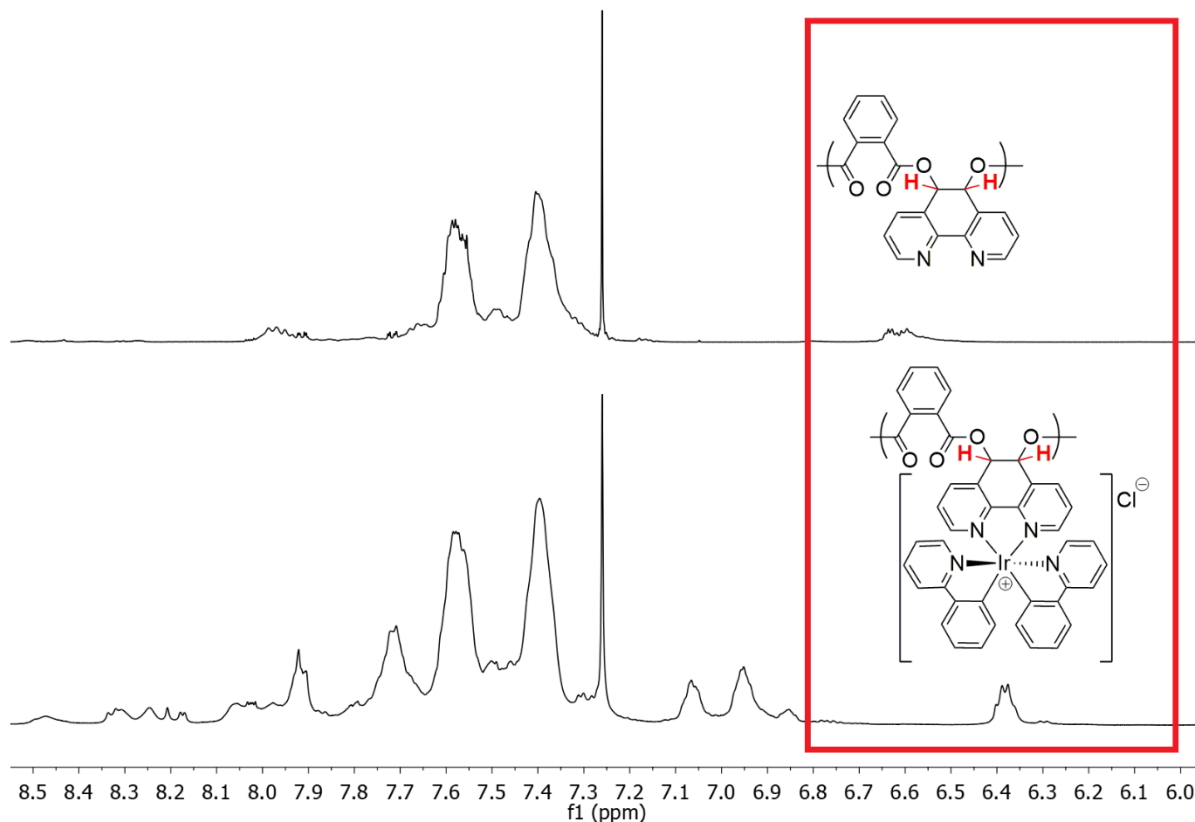


Figure 5.6: ¹H NMR spectra (CDCl₃, 500 MHz) of top: poly(EDHP-CHO-PA) and bottom: after its complexation with $[\{\text{Ir}(\text{PhPy})_2\mu\text{-Cl}\}_2]$, with a clear shift in the protons about the ring-opened epoxide shown in red.

The molecular weight data for both iridium polymers is presented in **Table 5.4** and compared to that of their precursors. Interestingly, a significant decrease in M_n and polydispersity is seen for the CHO-based polymer post-complexation. Whilst this could be attributed to partial degradation of the polymer chain, this would not explain either why the polydispersity decreases, or why no such decrease in M_n is seen for the LO-based polymer, which would be expected to also undergo degradation under identical reaction conditions. An alternative explanation is that this is caused by the higher number of EDHP units in a polymer chain (N_{EDHP}) for poly(EDHP-CHO-PA), which in turn means each polymer chain would average, contain approximately 8.6 (or 9.6 for α -DMAP, ω -H chains) positive charges post-complexation. This would change both the way the polymer folds and aggregates in the non-polar GPC eluent (THF), whilst also potentially changing the nature of the interaction with the stationary phase. Both these factors would influence the retention time in GPC analysis, yet are largely independent of molecular weight. This is significant as during instrument calibration, retention time is the principal parameter used to calculate molecular weight. Conversely, the lower charge density (on a per molecule basis) for poly(EDHP-LO-PA) may be the reason a small increase and consistent polydispersity is seen, which is one would expect to see for the additional

mass of the iridium and the PhPy ligands. In short, the more cationic a polymer is, the more challenging routine GPC analysis can be, as the relationship between the molecular weight and retention time can differ significantly in charged polymers compared to the polystyrene standards often used in calibration.^{50,51} However, the changing molecular weight properties of poly(EDHP-CHO-PA) post-complexation is somewhat anecdotal evidence for complexation, as clearly the polymer has been modified in some capacity: if the iridium complex was simply physically bound into the polymer then one would expect the same molecular weight characteristics to be seen post-complexation. Another impact of the introduction of positive charges from iridium complexes was the low-quality MALDI-ToF spectra seen for both polymers, as the multiply charged polymer chains would either appear at lower m/z than expected, or not be sufficiently vaporised and deflected to even reach the detector. Again, a physical dispersion of iridium in polymer would give an unchanged MALDI-ToF spectrum, yet this was not observed. Although attempts to observe iridium complexes directly bound to EDHP in the mass spectrum of a sample of base-hydrolysed poly(EDHP-CHO-PA) were unsuccessful, the changing ^1H NMR and GPC data previously discussed is highly suggestive of efficient iridium complexation.

Table 5.4: Molecular weight characteristics for poly(EDHP-CHO-PA) and poly(EDHP-LO-PA) pre- and post-complexation to iridium. ^a

Major Epoxide	N_{EDHP} ^b	Pre/Post Complexation	M_n / kDa ^c	\bar{D} ^{c,d}
CHO	8.6	Pre-Complexation	20.4	1.41
	-	Ir	12.0	1.17
LO	1.7	Pre-Complexation	4.7	1.62
	-	Ir	5.6	1.60

^a Polymers produced by 9: 1 reaction of epoxide and EDHP (as detailed in table 5.1) were used. ^b As calculated in table 5.2. ^c Determined by GPC (viscometry detection against polystyrene standards). ^d $\bar{D} = M_w / M_n$.

5.5: Photophysical Properties of the Iridium Containing Polyesters

Further characterisation of the iridium-doped polymers was performed using UV-Vis Spectroscopy, with the absorbance spectra of both the pre- and post-complexation polymers for (a) poly(EDHP-CHO-PA) and b) poly(EDHP-LO-PA) shown in **Figure 5.7**. By plotting the residual (*i.e.* the iridium doped spectrum minus the undoped precursor), it is clear that post-complexation there is a significant increase in the absorbance above 250 nm, with both polymers showing a broad absorbance feature until around 450 nm. This wavelength absorption is consistent with the inclusion of a cyclometallated iridium complex, with similar absorption energies and line shapes reported in the UV-Vis spectrum of

the closely related molecular complex $[\text{Ir}(\text{PhPy})_2(\text{bipy})]^+$.^{52,53} Specifically, $[\text{Ir}(\text{PhPy})_2(\text{bipy})]^+$ contains an absorption feature at 419 nm (in CHCl_3), which has been attributed to a $^1\text{MLCT}$ -like transition, and it is likely that absorption seen for the iridium polymers also represents this transition. Access to $^1\text{MLCT}$ excited states is important as from these states, ISC can give access to the triplet manifold and therefore phosphorescence back to the singlet ground state. The increased absorbance between 250 – 300 nm is consistent with reported values for $\pi - \pi^*$ transitions of the PhPy ligands.^{52,53}

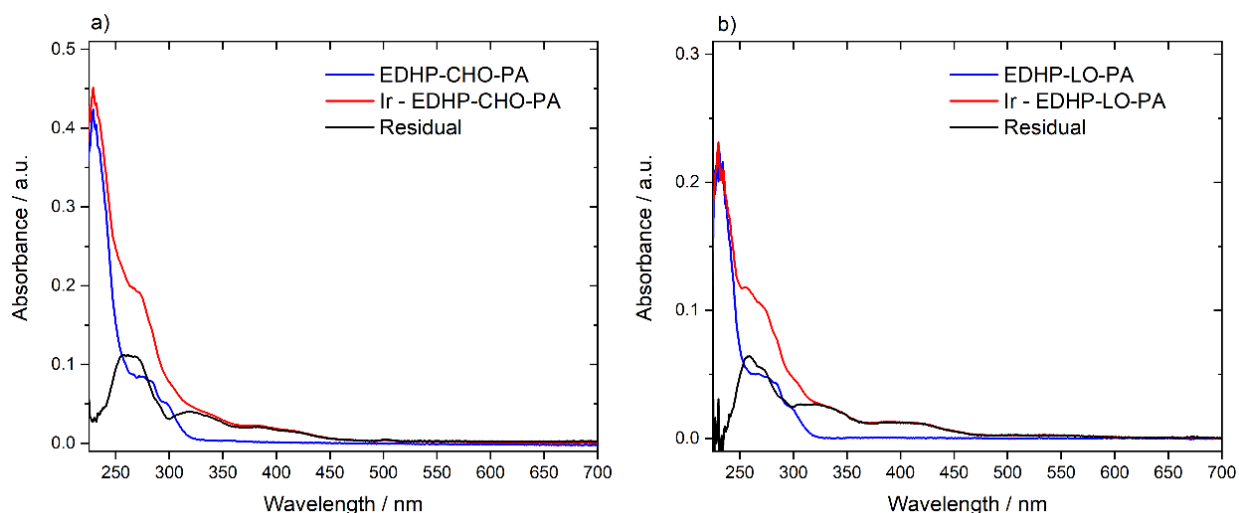


Figure 5.7: UV-Vis absorbance spectra ($10 \mu\text{g mL}^{-1}$ in THF) of (left, a) poly(EDHP-CHO-PA) before and after complexation and (right, b) the equivalent for poly(EDHP-LO-PA). Also shown is the residual spectrum when the undoped polymer spectrum is subtracted from the iridium-doped spectrum.

Solution phase luminescence spectroscopy measurements were also used to probe the photophysical properties of the polymers, with the normalised emission spectra for both poly(EDHP-CHO-PA) and poly(EDHP-LO-PA) displayed in **Figure 5.8** ($\lambda_{\text{ex}} = 255, 410, 450 \text{ nm}$, in acetonitrile).

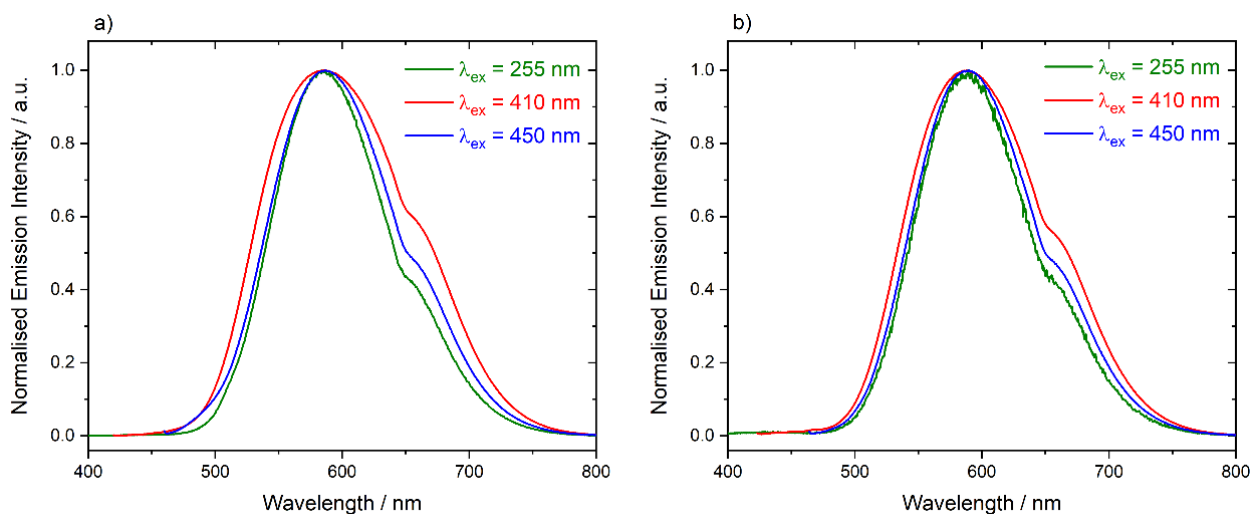


Figure 5.8: Normalised luminescence emission spectra (acetonitrile) of the iridium-doped polymers across three excitation wavelengths (255, 410 and 450 nm) of (left, a) poly(EDHP-CHO-PA) and (right, b) poly(EDHP-LO-PA). As measured by Sophie Fitzgerald (Cardiff University).

The λ_{max} for emission is 588 nm in all cases (both polymers across the 3 excitation wavelengths), with this nearly identical to the reported luminescence properties of $[\text{Ir}(\text{PhPy})_2(\text{bipy})]^+$, which displays a λ_{max} for emission at 590 nm in acetonitrile.⁵³ In addition, an extra shoulder at 660 nm was consistently observed, meaning the polymers have a highly characteristic emission profile. Furthermore, the consistency of the photophysical properties across the two polymers, as well as the close agreement to the molecular analogue $[\text{Ir}(\text{PhPy})_2(\text{bipy})]^+$, is highly indicative of the expected iridium complexation.

The photophysical properties of the polymers were also examined computationally by employing td-DFT calculations in the Gaussian 09 suite.⁵⁴ Throughout this work, $[\text{Ir}(\text{PhPy})_2(\text{DBDHP})]^+$ (DBDHP = *trans*-5,6-dibenzoatedihydrophenantholine (**Figure 5.9**), henceforth referred to as ***Ir-1***) was used to model the polymer-bound luminophore, with the LANL2DZ basis set used for the iridium atom and 6-31G** basis set for all non-Ir atoms.^{55–58} To provide a close as possible match to the experimental conditions where the absorbance behaviour was examined, implicit THF solvent was used in all calculations.⁵⁹

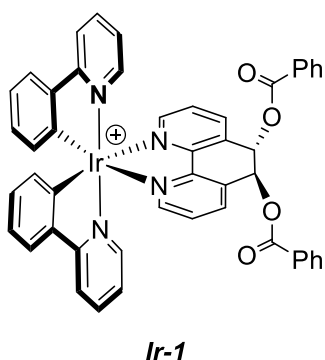


Figure 5.9: Structure of $[\text{Ir}(\text{PhPy})_2(\text{DBDHP})]^+$ (***Ir-1***) (DBDHP = *trans*-5,6-dibenzoatedihydrophenantholine), the iridium complex used to model the polymer bound luminophore in this study.

Four density functionals were originally tested to find the most appropriate method for td-DFT full modelling of ***Ir-1***; B3LYP, CAM-B3LYP, m06 and m11.^{60–64} This benchmarking was done by simulating the UV-Vis absorption spectrum of ¹***Ir-1*** (superscript 1 is used to distinguish between calculations performed in the singlet and triplet manifold) for each functional, up to an including excitation to the first 60 excited states (from longest to shortest wavelengths). Although computationally costly, this high number of N_{states} was required to fully simulate the absorption features to wavelengths approaching the solvent front. The simulated (line widths use the Gaussian default standard deviation of 0.4 eV) absorption spectra across the four density functionals are overlain in **Figure 5.10**.

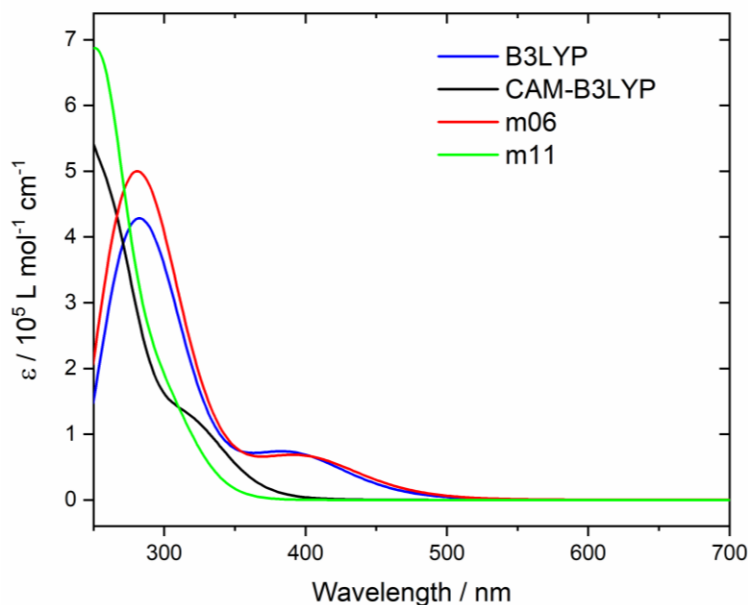


Figure 5.10: Simulated UV-Vis absorption spectra of ${}^1Ir-1$ using four different density functionals (Gaussian 09, LANL2DZ basis set for Ir, 6-31G** for all other atoms, $N_{States} = 60$, line widths are generated by fitting to a Gaussian curve with standard deviation = 0.4 eV, THF implicit solvent).

Of the four functionals, only B3LYP and m06 feature significant absorbance above 400 nm, with both methods producing two main peaks of similar λ_{max} of ≈ 300 and 400 nm. Interestingly, this correlates more closely to the observed λ_{max} of 419 nm for $[Ir(PhPy)_2(bipy)]^+$ for the primary 1MLCT transition.⁵² For this reason, and for alignment with methods employed across the literature, the nature of the simulated transitions were fully investigated and visualised from calculations employing B3LYP.^{7,49,53}

As well as simulating the entire spectrum, td-DFT calculations allow for analysis of specific transitions to excited states. Not only is the energy of each individual transition computed, but the specific orbitals involved can be visualised to inspect what the nature of the transition is (*i.e.* MLCT, $\pi - \pi^*$ etc.). Further still, each ground and excited state for a given transition will be comprised of contributions from several MOs, with the magnitude of each individual contribution a given MO makes to a ground or excited state also tabulated. A summary of the more intense (*i.e.* high oscillator strength, $f > 0.03$) transitions, along with the assignment of the orbitals primarily involved, is shown in **Table 5.5**. Also shown is the relative contribution (above one fifth) each MO makes to a given electronic state. All the transitions show varying degrees of $\pi - \pi^*$ character, however excited state 6 also shows significant MLCT character, arising from the highest orbital contribution (HOMO-3 to LUMO) to this transition, which is visualised in **Figure 5.11**.

Table 5.5: Summary of simulated high oscillator strength ($f > 0.03$) absorptions of $^1Ir-1$ (B3LYP/LANL2DZ (Ir) 6-31G** (C, H, N, O), Gaussian 09, THF implicit solvent), with the orbital contributions giving rise to the transitions, as well as the nature and the location of the major orbitals involved indicated.

Excited State No. ^a	Energy / nm	f	Orbital Contributions (Fractional Contribution) ^b	Assignment (Location)	
5	394	0.057	HOMO \rightarrow LUMO+3 (0.69)	$\pi - \pi^*$ (PhPy)	
6	386	0.069	HOMO-3 \rightarrow LUMO (0.57)	Mix MLCT (DBDHP) /	
			HOMO \rightarrow LUMO+4 (0.30)	LLCT (PhPy-DBDHP)	
			HOMO-5 \rightarrow LUMO (0.24)	/ $\pi - \pi^*$ (PhPy)	
18	317	0.034	HOMO-2 \rightarrow LUMO+3 (0.54)	$\pi - \pi^*$ (PhPy)	
			HOMO-4 \rightarrow LUMO+3 (0.32)		
19	312	0.037	HOMO-1 \rightarrow LUMO+4 (0.47)	Mix $\pi - \pi^*$ (PhPy) /	
			HOMO-1 \rightarrow LUMO+2 (0.39)		LLCT (PhPy-DBDHP)
			HOMO-2 \rightarrow LUMO+3 (0.21)		
26	299	0.059	HOMO-3 \rightarrow LUMO+4 (0.47)	Mix MLCT (DBDHP) /	
			HOMO-3 \rightarrow LUMO+2 (0.30)		$\pi - \pi^*$ (PhPy)

^a $N_{\text{States}} = 60$, first five transitions with $f > 0.03$ shown. HOMO = MO number 199. ^b Only fractional orbital contributions > 0.2 are shown.

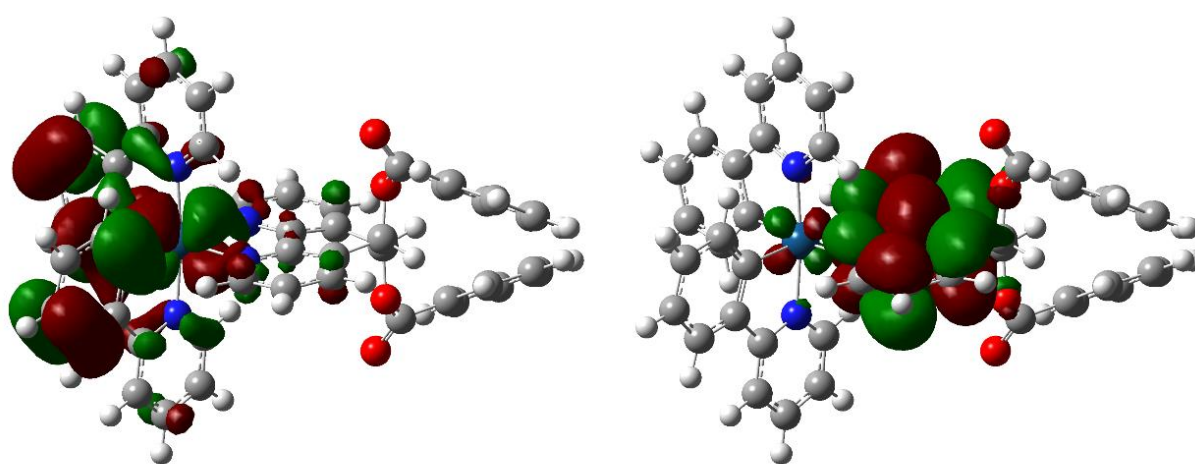


Figure 5.11: Visualised (GaussView, Isovalue = 0.02) HOMO-3 (left) and LUMO (right) of $^1Ir-1$, with these orbitals being the major contributors (0.57) to excited state 6 in Table 5.5, reflecting its significant MLCT character, as well as LLCT character.

As seen in **Figure 5.11**, the HOMO-3 of $^1Ir-1$ contains significant electron density in an iridium d orbital, whilst the LUMO has almost all its electron density centred upon the DBDHP ligand, indicative of an MLCT-like transition, with some LLCT-like character given the π orbital contributions from the PhPy ligands in the HOMO-3. Also noteworthy is the extra node separating aromatic π orbitals in the LUMO compared to the HOMO-3, highlighting the contribution of anti-bonding π^* orbitals to excited state 6. The wavelength of this MLCT-like absorbance of 386 nm is consistent with both the experimental absorbance spectrum, and the reported 1MLCT absorbance of $[Ir(PhPy)_2(bipy)]^+$ at 419 nm.⁵² Considering this, as well as the agreement in spectral line shapes and energies when comparing the simulated and experimental absorbance spectra, this td-DFT model can be considered an appropriate method for the study of the photophysics of this system.

Excited state 26 also has significant MLCT character, albeit to the LUMO+4 (centred on PhPy) and the LUMO+2 (centred on the phenyl rings of DBDHP). In both cases, the primary orbital contribution towards the ground state was from the HOMO-3, which is comprised of both an Ir d -orbital and π -orbitals on the PhPy ligands. The other three transitions shown (excited states 6, 18, 19) can all be characterised as being largely π - π^* transitions centred on the PhPy ligands, and do not feature significant contributions from the iridium centre.

As well as absorbance, DFT calculations were used to examine emission from the ground triplet state ($^3Ir-1$) in both an adiabatic (emission to the singlet ground state, allowing for relaxation) and non-adiabatic (emission to a singlet state with no relaxation permitted, using a single point energy calculation) fashion. Both these values across the four functionals previously discussed are displayed in **Table 5.6**. The experimental λ_{max} (**Figure 5.8**) of 588 nm is also shown, with this in close agreement to the calculated adiabatic emission using B3LYP, further emphasising its utility in modelling the system of choice. Also of interest is the close agreement between the weaker longer wavelength (660 nm) feature of the luminescence spectra and the non-adiabatic emission. Simulating the emission both adiabatically and non-adiabatically using m06 and m11 respectively also give reasonable (≤ 30 nm) agreements to experiment, whilst CAM-B3LYP shows a generally poor match to the observed luminescence. Using the methodology outlined here, it may be possible to readily predict the influence of cyclometallating ligand upon the luminescence properties of its analogous iridium polymer, thereby allowing for rational design to reliably produce luminescence of tuneable wavelengths.

Table 5.6: Summary of simulated adiabatic (relaxation allowed) and non-adiabatic (relaxation forbidden) phosphorescence wavelengths of $^3Ir-1$ to $^1Ir-1$ (B3LYP/LANL2DZ (Ir) 6-31G** (C, H, N, O), Gaussian 09, THF implicit solvent) for B3LYP, CAM-B3LYP, m06 and m11. Also shown is the experimental λ_{max} from the luminescence spectra of the iridium-doped polymers (Figure 5.8).

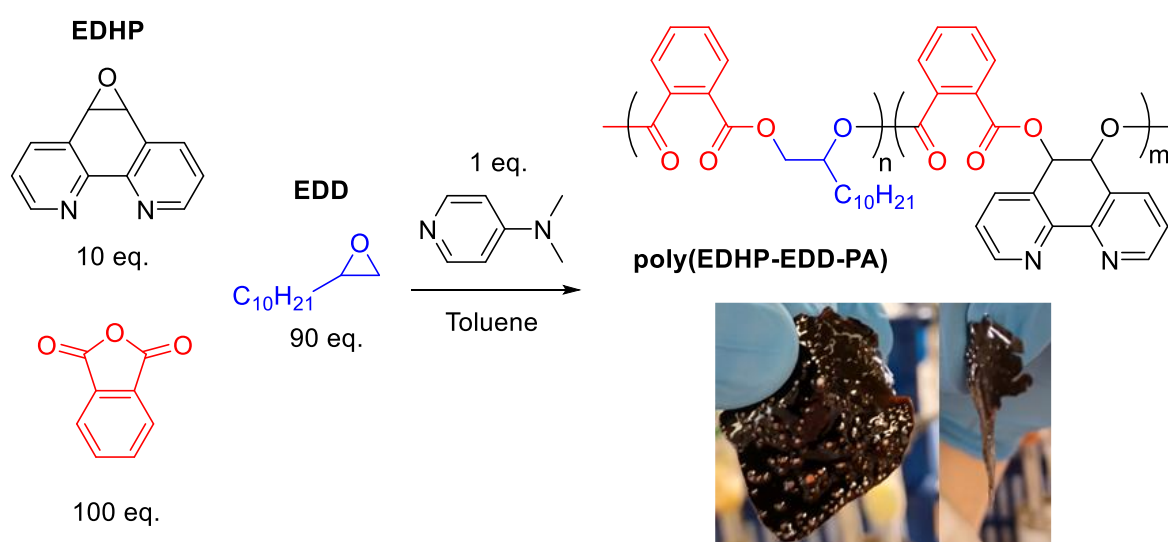
Functional	Adiabatic $^3Ir-1 - ^1Ir-1$ Wavelength / nm	Non-adiabatic $^3Ir-1 - ^1Ir-1$ Wavelength / nm
B3LYP	585	667
CAM-B3LYP	534	663
m06	615	688
m11	511	566
Experimental Luminescence		
λ_{max} / nm	588, 660 (shoulder)	

To summarise sections 5.3 – 5.5, the doping of EDHP into ROCOP reaction mixtures has proved a simple and atom-economical method to produce a scaffold for iridium incorporation into a polyester. This is (to the best of our knowledge), the first example of an iridium polyester, presenting a major advantage over poly(olefin) systems from a chemical recyclability standpoint. An additional advantage of this method is the diminished number of synthetic steps to go from commercial starting materials to an iridium polymer. In this case, only three reactions are required: the synthesis of the iridium dimer from $[IrCl_3].xH_2O$; the synthesis of the polymer; and the reaction of dimer and polymer. These reactions are straightforward and efficient, use a relatively cheap iridium source, and also allows for facile modification of the cyclometallating ligands during dimer synthesis.²⁴ This contrasts to some of the methods described in section 5.2, where up to 7 steps are required. For example, the syntheses of **5.2** and **5.4 (Scheme 5.3, 5.4)** both involve 7 steps from commercial starting materials,^{26,35} whilst **5.6 (Scheme 5.5)** needs 5 steps,³³ and **5.1 (Scheme 5.2), 5.9 and 5.10 (Scheme 5.6)** all require 4 steps, including a palladium cross coupling step for **5.1**.^{2,41} There is (to our knowledge) only one example of an iridium polymer synthesis in 3 steps, a highly cross-linked thermosetting poly(carbazole) where one of the three steps requires to use of a precious metal palladium catalyst.⁴³ As much as modification of the PhPy ligands in the ROCOP-based method may add to the number of synthetic steps, the relative simplicity of this process is clear to see, and therefore represents a significant enhancement on many previously reported examples. Also noteworthy is the relatively high level of iridium doping used in this study compared to previous examples. Whilst this helped produce unambiguous NMR data, it is likely that superior molecular weights and narrower molecular weight distributions would arise from using smaller quantities of EDHP. This would produce potentially more useful polymers, whilst retaining the desired photophysical properties imparted by the iridium complexation.

5.6: Synthesis of Low T_g Bipyridine-containing Polyesters

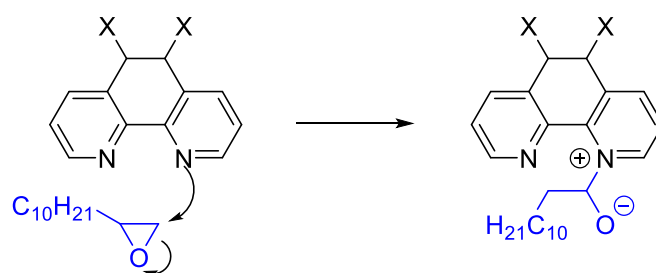
To increase the scope of potential applications for any luminescent iridium-based polyester, potential methods to synthesise low T_g polyester through use of major epoxide monomers with long alkyl substituents were investigated. By introduction of these bulky side groups, the polymer chains cannot stack as efficiently, and so the energy required for them to move past each other (*i.e.* achieve a rubbery state) is reduced, lowering the T_g .⁶⁵

Initially, 1,2-epoxydodecane (EDD) was examined, although the polymers produced (before iridium complexation) were black, despite appearing pure by ^1H NMR spectroscopy and possessing the desired rubbery texture (**Scheme 5.9**). This dark colouration represents a major problem when the main objective of synthesising the material relates to its optical properties. Several attempts to produce less strongly coloured (and thereby not interfering with the optical properties of the iridium) polymers were ultimately unsuccessful, with these including using repeatedly recrystallised EDHP, the use of different (non-conjugated) anhydrides such as succinic and glutaric anhydride, using benzyl glycidyl ether in place of EDD, using diglyme or 1,4-dioxane in place of toluene as solvents, and adding EDHP in small portions to the reaction mixture over time. Given the fact that all these measures were unsuccessful, and that there was no evidence of any significant impurities in the ^1H NMR spectra of the polymers, it seemed likely that the black colour was not down to an impurity in the starting materials, but is due to an as yet unknown side reaction.



Scheme 5.9: Synthesis of poly(EDHP-EDD-PA), with photographs showing the stretchy rubbery texture of the black polymer produced, which appeared pure by ^1H NMR spectrometry. Note that poly(EDD-*alt*-PA) with no EDHP added is colourless.

As EDHP is nucleophilic and can thereby yield cationic quaternary nitrogen centres, it was hypothesised that EDHP could itself ring open EDD (**Scheme 5.10**), with this reaction particularly prevalent for EDD at the sterically unhindered CH₂-O face of the molecule. These conjugated quaternary centres may be highly coloured, as so could represent to cause of the polymers going black, even if it only occurs in trace amounts. This terminal epoxide functionality is not present in CHO and LO, and so one might expect this reaction pathway to be vastly diminished for these substrates, hence the off-white polymers produced.



Scheme 5.10: Potential ring-opening of EDD at its sterically unhindered methylene position by EDHP, or one of its derivatives, to give a potentially highly coloured quaternary ammonium centre. X = any initiating group, a polyester chain, or an epoxide group of unreacted EDHP.

To test this hypothesis, a 10:1 reaction of various epoxides with 2,2'-bipyridine (50.0 mg) in 1 mL of toluene at 80 °C for 24 hours were undertaken. Images of the reaction products (**Figure 5.12**) show that for the three non-terminal epoxides screened, no colour change is observed. Conversely, both terminal epoxides showed colouration. Despite the colouration of the EDD reaction, ¹H NMR spectroscopy of the reaction mixture contained only resonances corresponding to bipyridine and EDD.

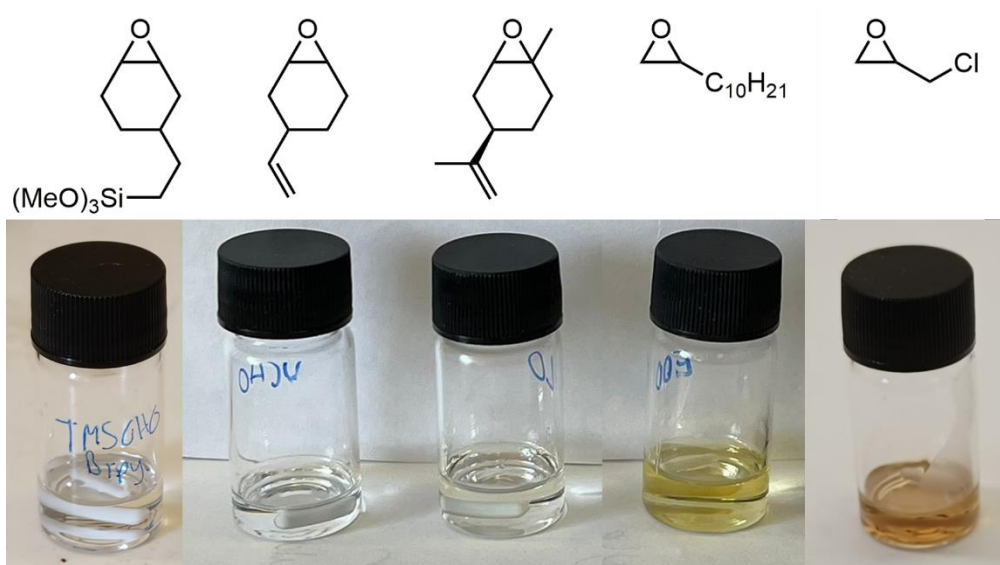


Figure 5.12: Images of vials after 24 hours (80 °C) of 10:1 reactions of epoxides (labelled at top) to 2,2'-bipyridine (50.0 mg) in 1 mL toluene. Note the colouration of the reactions containing terminal epoxide functionality.

More precisely, the electrospray ionisation mass spectrum of the EDD reaction mixture (**Figure 5.13**) showed two peaks, one for protonated bipyridine, and another with a mass matching to ring-opened EDD by bipyridine. This observation is consistent with the hypothesis that bipyridine (and likely by extension EDHP) can ring-open sterically unhindered epoxides like EDD, producing coloured quaternary nitrogen centres in the process, and is likely the cause of the black colour seen when synthesising poly(EDHP-EDD-PA). The ring-opened species in the mass spectrum was not observed by ^1H NMR spectroscopy, meaning it is likely to be only present in small quantities, which is consistent with the apparently pure ^1H NMR spectrum of poly(EDHP-EDD-PA).

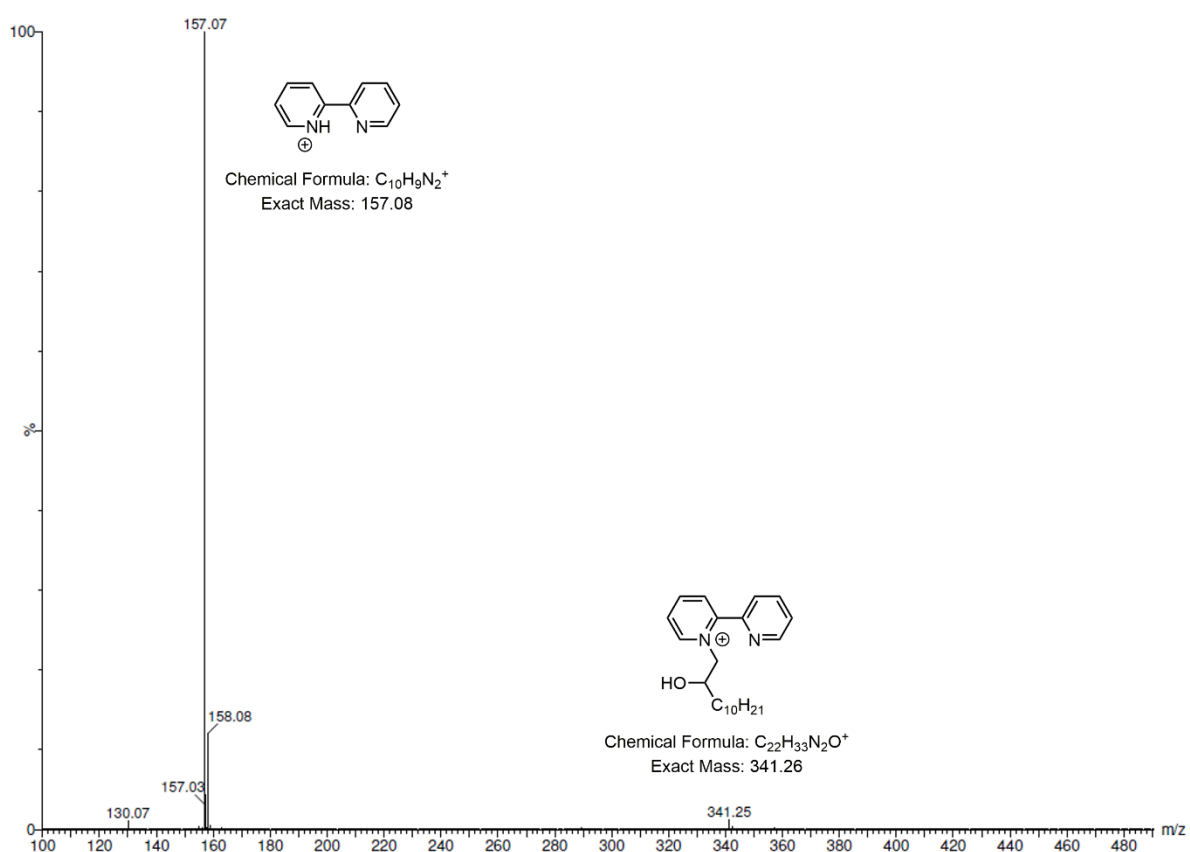
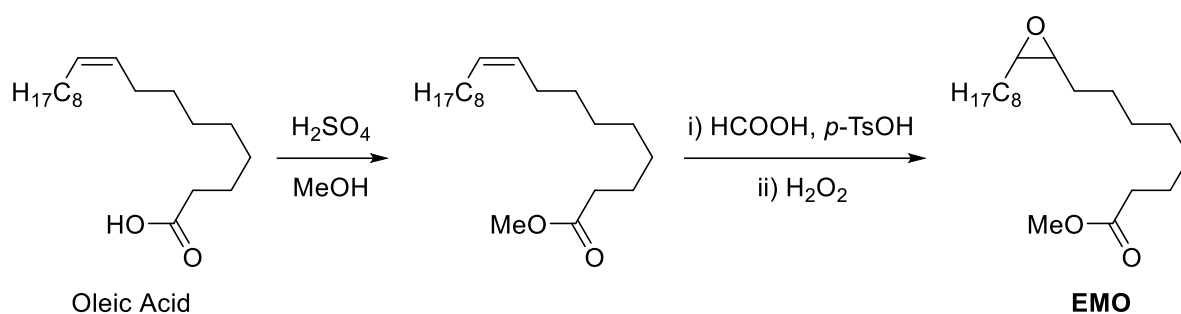


Figure 5.13: Positive mode electrospray ionisation mass spectrum of a 10:1 reaction of EDD and bipyridine, showing the trace presence of a ring-opened EDD unit, hypothesised to be the source of the colour observed by eye.

After establishing that the black colour of poly(EDHP-EDD-PA) is intrinsic to this combination of monomers (rather than a result of the reaction conditions), an alternative, non-terminal epoxide was targeted. Epoxy-methyl oleate (EMO), an oleic acid derivative which can be found in duck fat and olive oil, was chosen given its known ability to produce polyesters of low T_g whilst possessing an internal epoxide group.^{65,66} The synthesis of EMO is shown in **Scheme 5.11**.



Scheme 5.11: Synthesis of epoxy methyl oleate (EMO) from bio-derived oleic acid, as reported by Kleij *et. al.*^{65,66}

The copolymerisation of EMO with EDHP and PA was performed both in toluene solution (as was done for CHO, LO and EDD), and in neat excess EMO (as for the [Al(Salpy)Cl] complexes in chapter 2). In both cases however, only low conversions of PA were seen, meaning workable quantities of pure polymer were not isolatable. However, the relative incorporation of EDHP: EMO could be determined, with these values listed in **Table 5.7**. Interestingly, neat polymerisation produced a polymer overwhelmingly comprising of poly(EDHP-*alt*-PA), whilst the incorporation of EDHP in the solution produced polymer was also higher than one might expect solely from the reaction stoichiometry. At first glance, the decreased EMO content when using neat EMO may appear puzzling, yet in this case, the concentration of EDHP is also increased, and so the rate of its polymerisation would be expected to increase also. The significantly decreased rate of reaction of EMO (as seen through the low EMO content of the polymer) means an alternative, more active catalyst system may be more appropriate to counteract its elevated activation energy. This could include replacing DMAP with [PPN]Cl, or the use of a metal catalyst. Quantities of EDHP would likely have to be reduced in the reaction mixture, as any effort to increase the rate of EMO ring-opening would also increase the rate of EDHP ring-opening, meaning polymers with excessive EDHP content would likely still result. However, the polymers did have the desired rubbery texture, validating the approach taken, despite its present limitations.

Table 5.7: Polymerisation of EDHP, EMO and PA, in both toluene solution and neat excess EMO.^a

Solution / Neat	Eq. EDHP	Eq. EMO	Conversion PA / % ^b	Ratio EDHP : EMO in Polymer ^c
Solution	10	90	38	1: 3.7
Neat	25	375	42	1: 0.2

^a Conditions: 1 eq. (25.6 μmol) DMAP, 100 eq. PA, 80 °C. Solution – 100 eq. total epoxide, 1 mL toluene for 24 hours. Neat – 400 eq. total epoxide for 5 hours. ^b Determined from ¹H NMR spectroscopy of the reaction mixture.

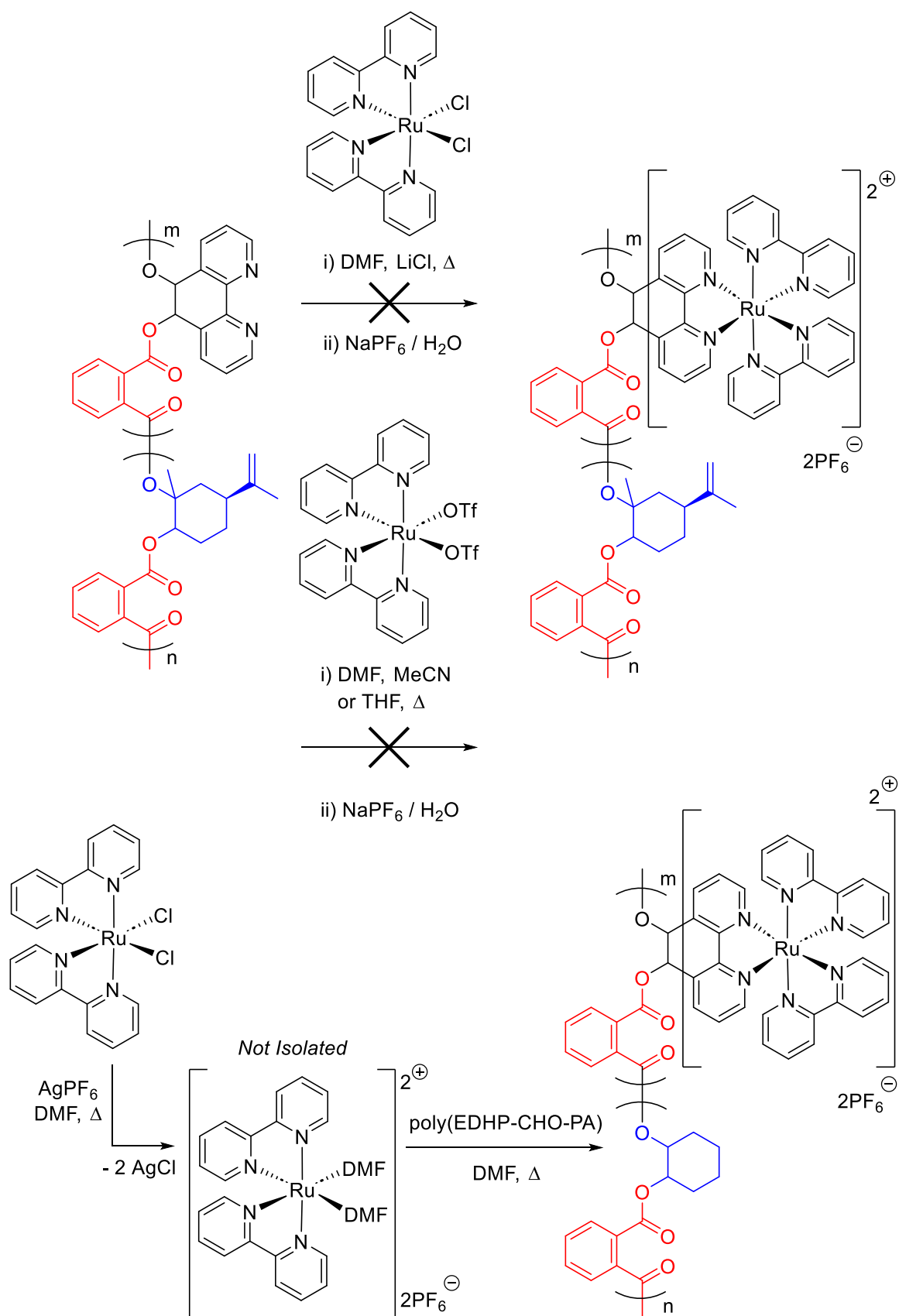
^c Determined by ¹H NMR spectroscopy of the polymeric product.

5.7: Ruthenium Doped Polyesters

Ruthenium, particularly its bipyridine complexes and derivatives, is another metal commonly investigated for its photophysical properties, as its electronically excited MLCT states can also undergo ICS to give rise to phosphorescence.^{67,68} This ability to efficiently absorb light has been harnessed in photoredox catalysis⁶⁹, most commonly as photosensitisers for the catalytic generation of singlet oxygen.⁷⁰⁻⁷² Singlet oxygen is a highly reactive species that can be used to destroy persistent environmental pollutants such as bisphenol A.⁷³ Further to their photophysical properties, ruthenium complexes have been investigated for medicinal applications, including in anti-cancer therapies⁷⁴, and as catalysts more generally.⁷⁵

In terms of their use in polymers,^{68,76} ruthenium complexes are primarily investigated for their photophysics, including in one example where a cooperativity between ruthenium complexes and organic electron acceptors allowed for upconversion of photon energy through a triplet-triplet annihilation process.⁷⁷ However, many of these polymers are again based on chemically resistant carbon-carbon bonds. Therefore, using the same EDHP-based polymers described previously, it was hypothesised that ruthenium could also be incorporated into a polyester.

Originally, a simple ligand displacement synthesis was devised using *cis*-[RuCl₂(bipy)₂],⁷⁴ with the EDHP of poly(EDHP-LO-PA) replacing the chloride ligands to give a dicationic ruthenium complex, before final addition of NaPF₆ to yield a potentially more organic soluble ruthenium complex (**Scheme 5.12**). However, this proved unsuccessful, even under the relatively forcing conditions involved and using a two-fold excess of ruthenium. Therefore, *cis*-[Ru(OTf)₂(bipy)₂] was prepared instead (see section 7.8), to try to take advantage of the weaker bound triflate ligands. However, this too failed to cleanly produce the desired polymer when using THF, MeCN or DMF as reaction solvents. As a final attempt, *cis*-[RuCl₂(bipy)₂] was stirred with AgPF₆ in a DMF solution, until there was visible precipitate (AgCl) in the reaction flask. A sample of poly(EDHP-CHO-PA) with high EDHP content (1: 3.9 ratio of EDHP: CHO) was then added, and the mixture was heated to reflux in DMF (**Scheme 5.12**). The addition of AgPF₆ was an attempt to break the highly stable and kinetically inert d⁶ low spin configuration of the Ru(II) complex. After addition of a vast excess of water, a fine orange precipitate was isolated.



Scheme 5.12: Attempted syntheses of an EDHP-based ruthenium polymer. Simple substitution of either chloride or triflate ligands proved ineffective, but the addition of AgPF₆ prior to polymer addition proved somewhat successful.

The ^1H NMR spectrum of the isolated orange polymer (DMSO- d_6) is shown in **Figure 5.14**, and compared to that of the poly(EDHP-CHO-PA) used in its synthesis. There are clear differences between the spectra, perhaps most noticeably the disappearance of the EDHP peaks at $\delta_{\text{H}} = 6.50, 7.99$ and 8.72 ppm, suggesting complexation has occurred. However, the new aromatic peaks in the ruthenium-doped spectrum (red) are far lower in intensity when compared to the phthalate or ester peak (not shown here), meaning there are fewer EDHP sites in the polymer post-complexation. This could be caused by degradation during the harsh reaction conditions leading to the cleavage of ester linkages. Furthermore, the sample of poly(EDHP-CHO-PA) had a high EDHP content (1: 3.9 ratio of EDHP: CHO in the polymer), and so if all EDHP sites were to react, each hosting a dicationic complex, then the resultant polymer would become highly charged. With precipitation occurring in water, it is possible that the material that immediately precipitated was biased towards polymer chains which happened to have a lower density of positive charges on account of their relatively low EDHP content. This would explain the diminished dopant peaks relative to other peaks in the spectrum post-complexation. The supernatant from water precipitation was bright orange, and so almost certainly contained significant amounts of ruthenium complex, possibly with some bound to polymer chains. Sadly, concentration of the supernatant gave a DMF solution from which polymeric material could not be isolated.

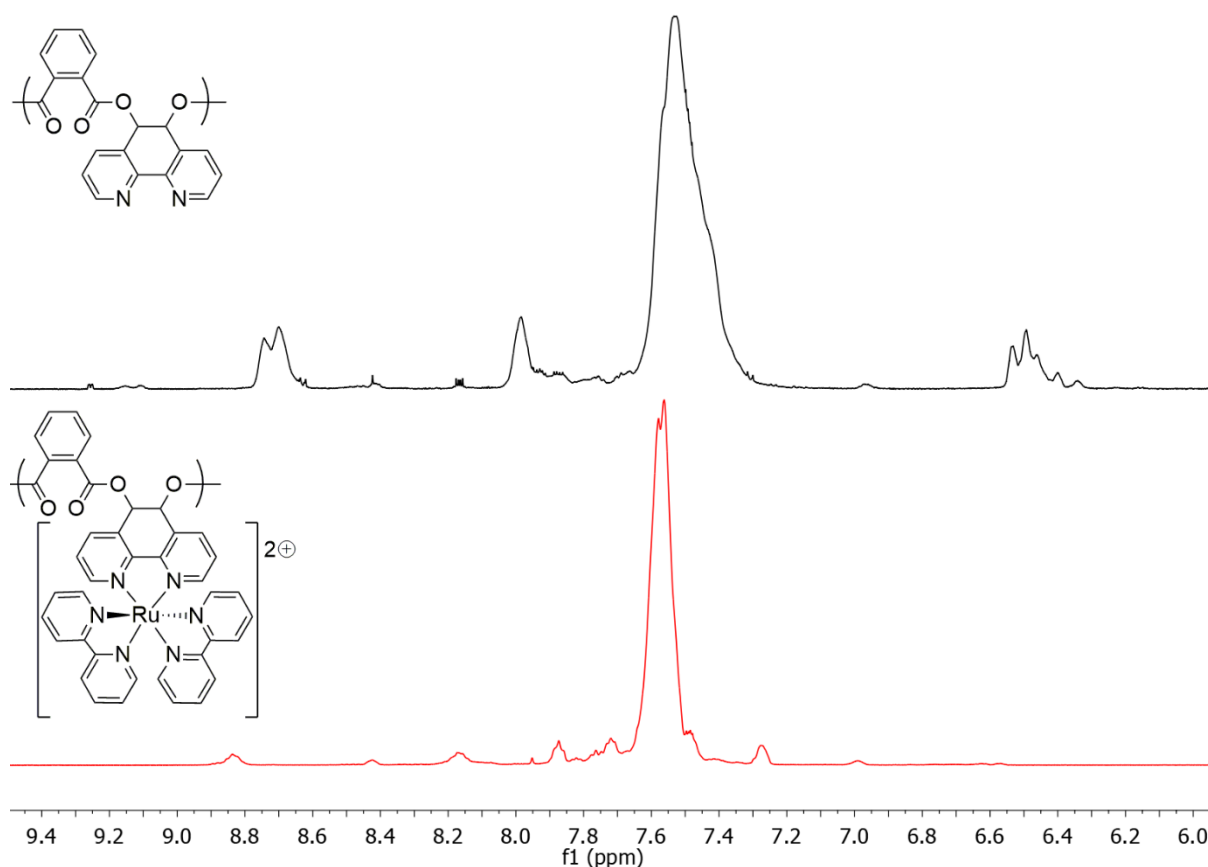


Figure 5.14: Stacked ^1H NMR spectra (DMSO- d_6 , 500 MHz) of top (black): poly(EDHP-CHO-PA) and bottom (red): the water-insoluble orange polymer produced after its complexation to ruthenium.

Upon complexation, there was a decrease in molecular weight and polydispersity, with the ruthenium polymer possessing a M_n of 2.1 kDa and polydispersity index of 1.50 (*c.f.* the precursor polymer, $M_n = 3.7$ kDa, $\mathcal{D} = 2.36$). Although the decreased M_n might be indicative of degradation, this would not explain the narrowing polydispersity, and the now cationic polymer may exhibit significantly different behaviour in THF than its neutral precursor, as discussed in the context of the iridium doped polymers in section 5.4. Although ambiguous, the GPC data does confirm that the isolated product was polymeric, and, given its significantly different properties from the precursor, that ruthenium complexation has most likely occurred, at least in part. Furthermore, unlike the precursor polymer, the polymer post-complexation exhibited a light scattering trace in-keeping with the refractive index and viscometry traces, again suggesting that the properties of the polymer itself have been modified to affect its interaction with light, *i.e.*, that the ruthenium complexes are truly polymer bound.

The ruthenium polymer was also investigated with UV-Vis spectroscopy, with its absorbance spectrum, and that of its precursor polymer, shown in **Figure 5.15**. The absorbance spectrum of the ruthenium polymer shows two main peaks, at 284 nm and a broader, less intense absorbance at 454 nm. This mirrors the absorbance spectrum of $[\text{Ru}(\text{bipy})_3]\text{Cl}_2$ incredibly closely ($\lambda_{\text{max}} = 289, 451$ nm (MeCN)), which is consistent with the coordination environment expected in the polymer, and further supports that ruthenium complexation has occurred.⁷⁸ Specifically, the transition at 289 nm has been characterised as a ligand centred $\pi - \pi^*$ transition, whilst absorbance at 451 nm is the MLCT transition.

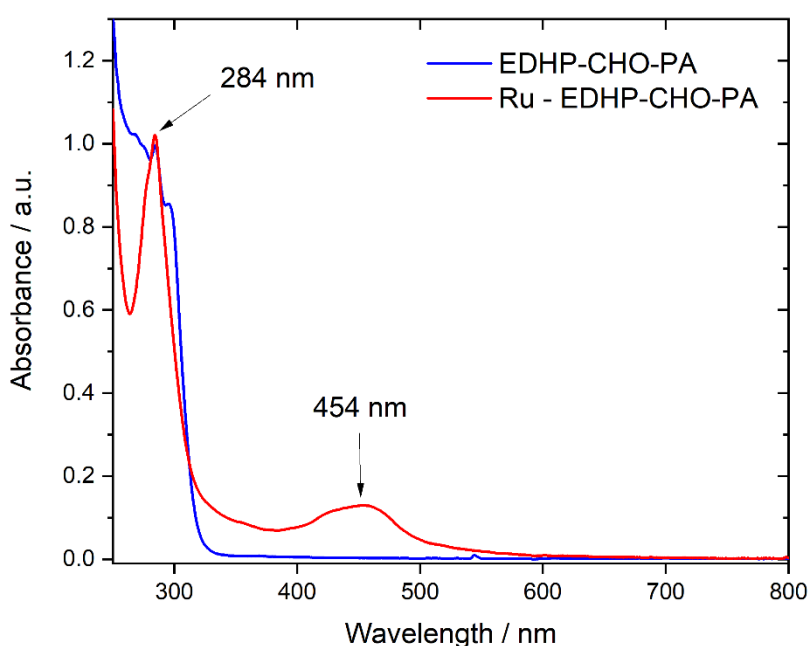
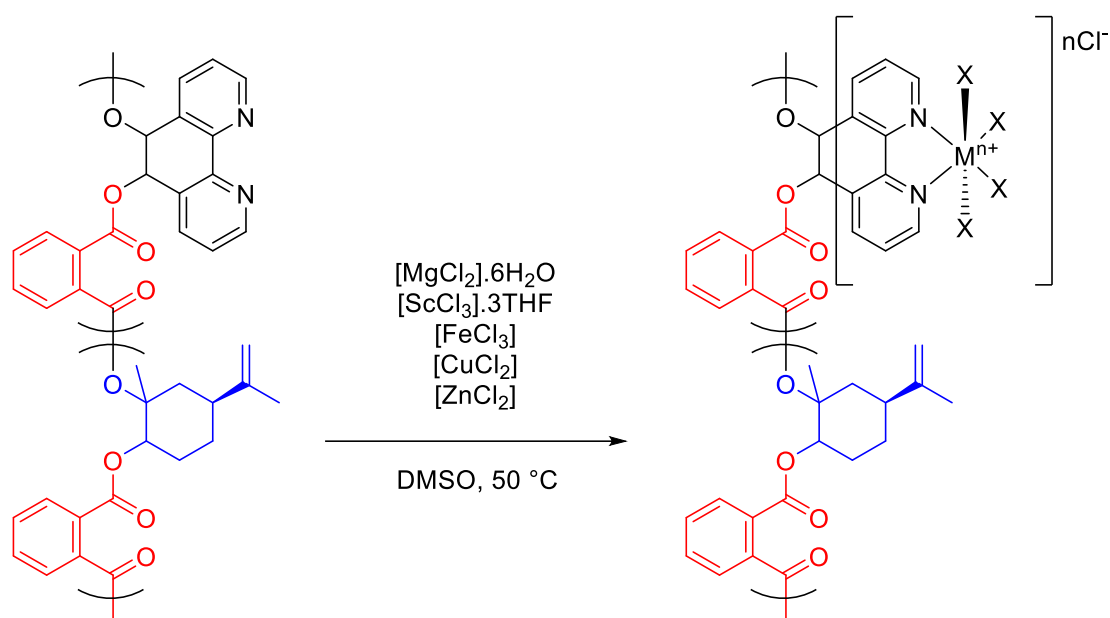


Figure 5.15: UV-Vis absorbance spectrum (THF, $100 \mu\text{g mL}^{-1}$) of poly(EDHP-CHO-PA) both pre- (blue) and post-complexation (red), showing absorbances resembling ligand centred $\pi - \pi^*$ transitions (284 nm) and an MLCT transition (454 nm).

5.8: Synthesis and Characterisation of 1st Row Transition Metal Containing Polyesters

Further to the introduction of heavy metals to polyesters, the bipy-like framework of poly(EDHP-LO-PA) was investigated for the complexation of some 1st row metals. In this case, five 1:1 reactions of simple chloride metal salts across the period table were studied; [MgCl₂].6H₂O, [ScCl₃].3THF, [FeCl₃], [CuCl₂] and [ZnCl₂] (**Scheme 5.13**). Complexation was performed in DMSO at 50 °C for 2 hours, albeit in the case of [CuCl₂] there was an immediate colour change to bright green upon mixing. The polymers were precipitated into an excess of methyl *tert*-butyl ether, before purification by repeated reprecipitations from THF/water mixtures to ensure the removal of any excess metals. Photographs of the isolated polymers are shown in **Figure 5.16**, where the green and rusty orange colours of the copper and iron-doped polymers respectively can be seen.



Scheme 5.13: Syntheses of 1st row metal-doped poly(EDHP-LO-PA).

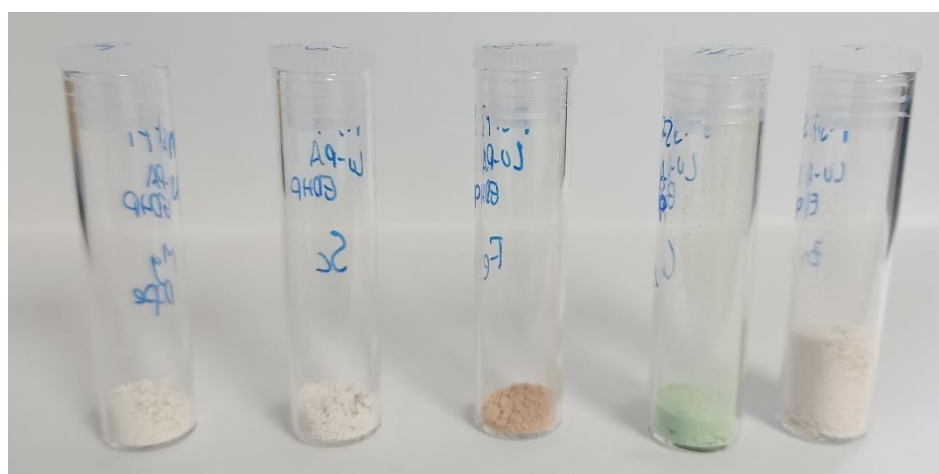


Figure 5.16: Photographs of the isolated metal doped polymers, from left to right; Mg, Sc, Fe, Cu, Zn.

The ^1H NMR spectra of the polymers showed contrasting behaviour depending on which metal was used. For both Mg and Sc, there was no change seen post-complexation, suggesting that complexation was unsuccessful. However, for Fe and Cu, the resonances associated with EDHP were no longer observable, yet the peaks associated with ring-opened LO and PA appeared unchanged. This is consistent with complexation, as in both cases one would expect a paramagnetic complex to result; Fe(III) is d^5 , and is paramagnetic regardless of its spin state, whilst Cu(II) is d^9 , and features a single unpaired electron. This explains the apparent disappearance of the EDHP protons, as their proximity to Cu or Fe leads to paramagnetic broadening, in this case to the extent that the resonances are spread across a wide enough portion of the spectrum to be unobservable. Extending the chemical shift range from +200 to -200 ppm did not show any paramagnetic peaks for the Cu or Fe polymers. For Zn, there were observable shifts in the EDHP protons of the polymer, with the diamagnetic complex of Zn(II) (d^{10}) in this case meaning the EDHP protons are still visible, albeit shifted from their positions in the unmodified spectrum (**Figure 5.17**). Given the use of DMSO (itself a coordinating solvent), the presence of water in the DMSO and use in work up (and likely presence in the precursors), the specific makeup of the coordination environment is not known for certain, or indeed, whether a charged or neutral complex forms.

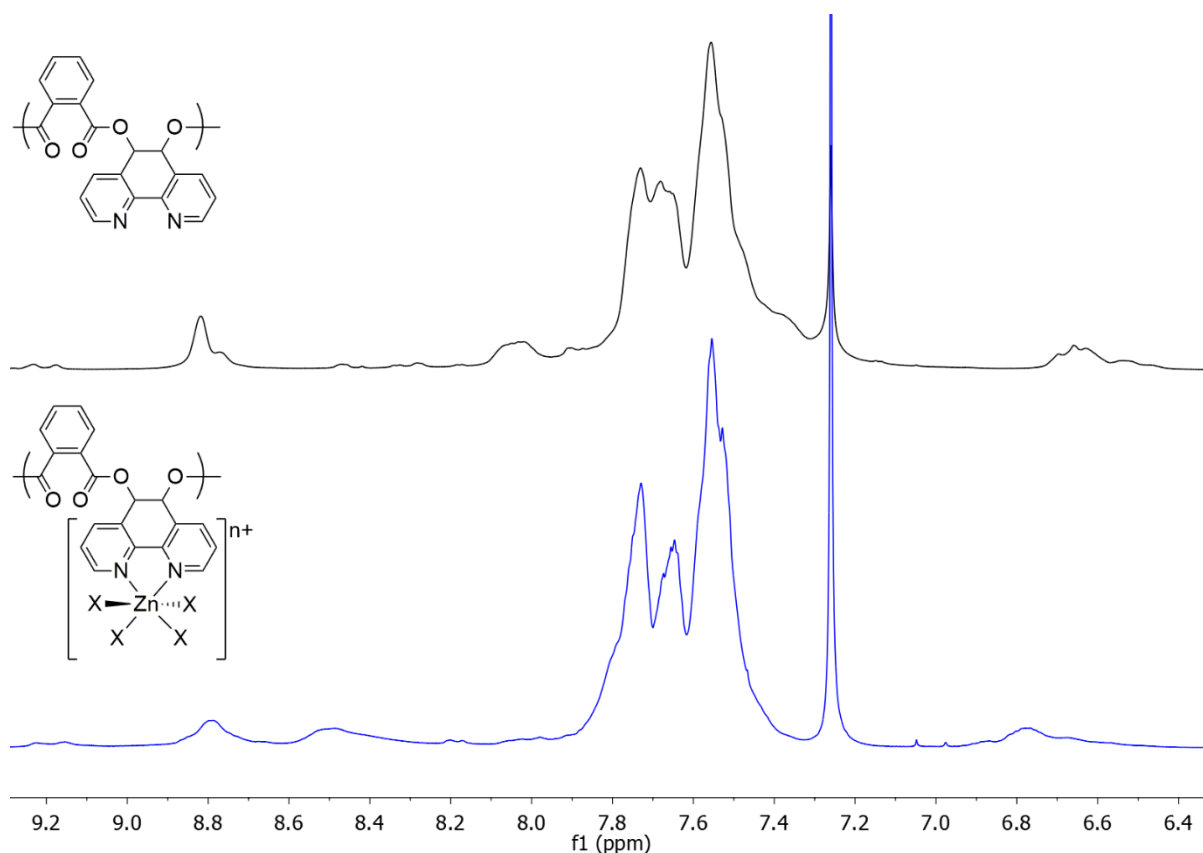


Figure 5.17: Stacked ^1H NMR spectra (CDCl_3 , 500 MHz) of top (black); unmodified poly(EDHP-LO-PA) and bottom (blue); after its complexation to $[\text{ZnCl}_2]$, showing clear differences. X = H_2O , Cl or DMSO, $n = 2, 1$ or 0 , depending on the as yet unknown number of chloride ligands in the complex's coordination sphere.

To try to differentiate between charged or neutral metal complex formation, the conductivity of 1 mg mL⁻¹ solutions of each polymer in THF were measured. The conductivity measurements are shown in **Table 5.8**, and show that for Fe, Cu and Zn, there is a large increase in conductivity compared to Mg and Sc, where the complexation failed. This increase in conductivity is consistent with the formation of charged complexes, as the free chloride ions would allow for increased ionic conductivity in this case. In a neutral complex however, there would be no increase in the ionic strength of the solution and therefore little change in the conductivity. The increase in conductivity is weakest for Cu, and far higher for Fe, which is perhaps due to the increased charge of Fe(III) meaning a higher number of free chloride ions are present in solution. However, there could be a mixture of neutral and charged coordination environments, and so it is impossible to say what the exact nature of the coordination sphere is. The small increases for Mg and Sc compared to blank THF is likely as a result of the positive charge provided by the DMAP initiated chains, as discussed in detail in section 3.4.

Table 5.8: Conductivity measurements (1 mg mL⁻¹ solutions in HPLC grade THF) of poly(EDHP-LO-PA) doped with each metal.

Doping Metal	Conductivity / $\mu\text{S cm}^{-1}$
None – Blank THF	0.01
Mg	0.08
Sc	0.05
Fe	1.31
Cu	0.23
Zn	0.87

MALDI-ToF mass spectrometry was also used to characterise the polymers. In accord with the NMR and conductivity measurements, the MALDI-ToF mass spectra of the Mg and Sc doped polymers were identical to the precursor, again highlighting the lack of coordination. The MALDI-ToF spectra of the Fe, Cu and Zn doped polymers all showed differences however, although no specific peaks corresponding to metal complexed to polymers could be identified. **Figure 5.18** shows the MALDI-ToF spectra of the Zn and Cu doped polymers, the polymer obtained after the failed Sc complexation and the unmodified precursor polymer. There are clear shifts in the *m/z* of the repeat units for the Zn polymer consistent with complexation. Both Fe and Cu exhibited poor quality MALDI-ToF spectra, yet this difference in of itself is evidence for the polymer being modified, and contrasts to the identical spectra obtained for the failed Mg and Sc complexations.

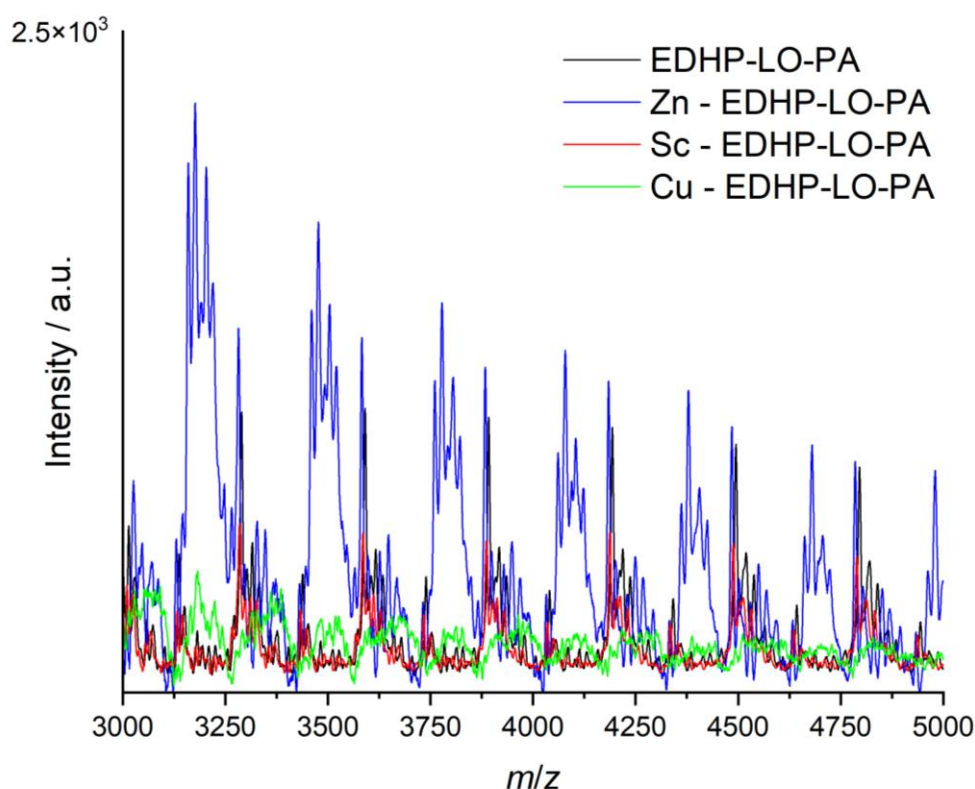


Figure 5.18: Overlain MALDI-ToF spectra (positive mode) of the Zn, Cu and failed Sc doped polymers, and the unmodified precursor. Note the close match between the unmodified (black) and Sc (red) spectra, and the differences to the Zn (blue) spectrum and the poor quality Cu (green) spectrum.

The UV-Vis absorbance spectra of the Fe, Cu and Zn polymers also showed distinct differences from the precursor, with these overlain and displayed in **Figure 5.19**. The Mg and Sc complexations led to no change in the absorbance properties, again highlighting the lack of reaction. The Zn doped polymer shows little absorbance in the visible region of the spectrum, consistent with both its fully occupied *d*-orbitals preventing *d-d* transitions, and its lack of colour seen by eye. The absorbance seen in the UV region of the spectrum is comparable to that of $[\text{Zn}(\text{bipy})\text{Cl}_2]$, which shows absorbances attributable to MLCT transitions, with the luminescence from these states studied in an analogous way to previously discussed iridium and ruthenium.⁷⁹ Conversely, both the coloured polymers containing Fe or Cu do show absorbance in the visible region; the Fe doped polymer contains a broad absorbance centred on 360 nm, and non-zero absorbance until 550 nm, whilst the Cu-doped polymer shows a weaker absorbance at 410 nm. This absorbance is somewhat different from the reported λ_{max} of $[\text{Cu}(\text{bipy})\text{Cl}_2]$ in MeCN of 370 nm, although this is likely due to the potentially charged nature of the coordination sphere in this case, as evidenced by the previously discussed conductivity measurements.⁸⁰ All three metal doped polymers show addition absorbance at ≈ 320 nm when compared to poly(EDHP-LO-PA). No absorbance could be seen for any of the polymers above 600 nm at this concentration ($100 \mu\text{g mL}^{-1}$).

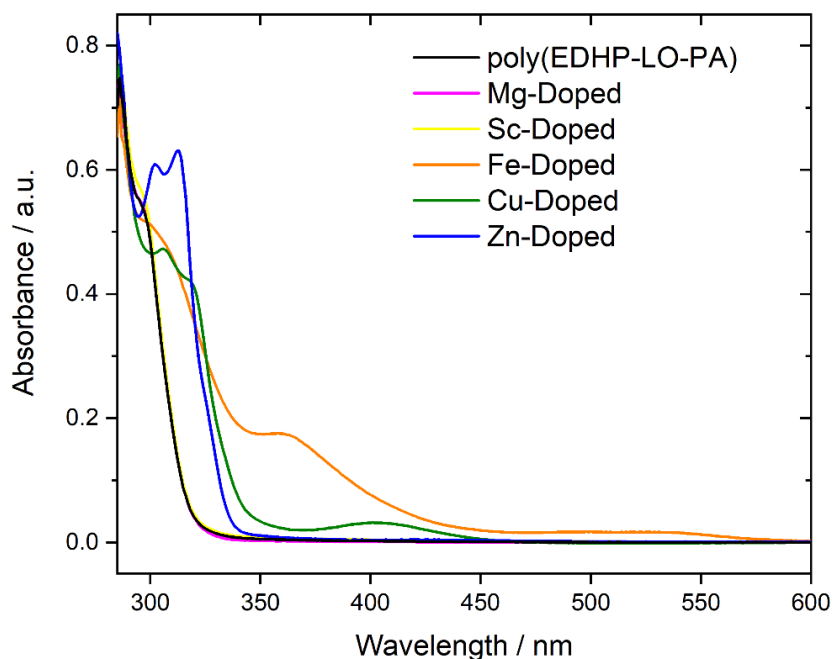


Figure 5.19: UV-Vis absorbance spectra ($100 \mu\text{g mL}^{-1}$, THF) of the polymers obtained after doping with the 5 metals and the precursor, poly(EDHP-LO-PA).

The FT-IR spectra of the polymers (**Figure 5.20**) showed little difference upon doping, presumably due to the dominance of the unchanging poly(LO-*alt*-PA) units (*c.f.* ester stretch of poly(LO-*alt*-PA) at $\approx 1700\text{cm}^{-1}$). Even in the region where one might expect the CN stretches of the bipyridine units (**Figure 5.20**, right), there are no significant or characterisable changes.⁸⁰

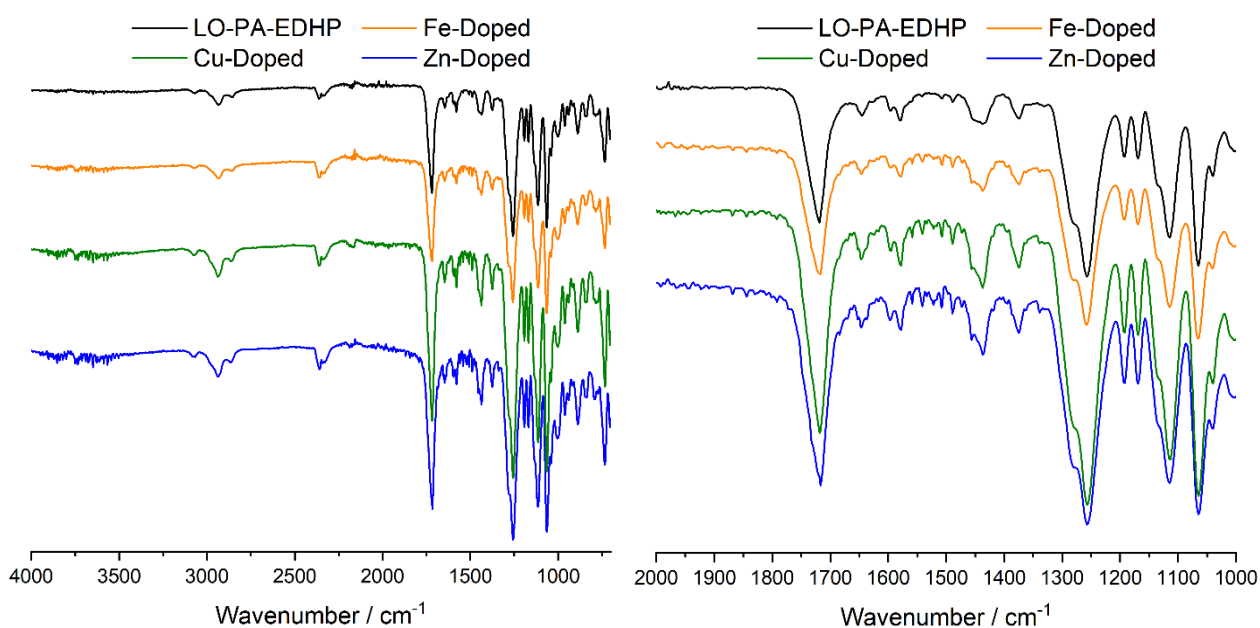


Figure 5.20: Stacked FT-IT spectra of poly(EDHP-LO-PA) and the Fe, Cu, and Zn modified polymers, showing little change across $4000 - 700 \text{ cm}^{-1}$ (left), or upon closer inspection between $2000 - 1000 \text{ cm}^{-1}$ (right).

The paramagnetism of the Fe and Cu doped polymers was investigated by Evans method NMR spectroscopy, whereby a CDCl₃ solution of known concentration of both polymers were made into an NMR tube insert, which itself contained CDCl₃. Both tubes contained the same concentration of ^tBuOH, which typically displays a shift at δ_H = 1.25 ppm. However, the presence of a paramagnetic species causes this peak to shift, with this shift proportional to both the concentration and magnetic susceptibility of the sample. The molar susceptibility (χ_{mol}) of the samples are given by **Equation 5.3**.⁸¹

$$\text{Equation 5.3:} \quad \chi_{mol} = \frac{3\Delta_F}{4\pi Fc}$$

Where Δ_F is the shift in the ^tBuOH peak in Hz, F is the field strength of the magnet in Hz, and c is the concentration in mol mL⁻¹. The molar susceptibility can then be converted to magnetic moment, μ_{exp} (measured in Bohr Magnetons, BM) by **Equation 5.4**, where T is the temperature in Kelvin.⁸¹

$$\text{Equation 5.4:} \quad \mu_{exp} = 2.828\sqrt{\chi_{mol}T}$$

For first row metals, the contribution spin-orbit coupling makes to the total magnetic moment is small, and so the number of unpaired electrons, n, is related to the theoretical magnetic moment, μ_{theo}, by the spin-only formula, **Equation 5.5**, which can be rearranged to give **Equation 5.6**, where only the positive solution represents a physically meaningful result.⁸¹

$$\text{Equation 5.5:} \quad \mu_{theo} = \sqrt{n(n+2)}$$

$$\text{Equation 5.6:} \quad n = -1 \pm \sqrt{1 - \mu^2}$$

Therefore, measuring the shift in the ^tBuOH peak when it is dissolved in a paramagnetic or diamagnetic medium can allow one to estimate the number of unpaired electrons in the complex. In this case, solvent and diamagnetic ligand corrections were neglected, and the molar concentration of each polymer was calculated by taking the M₁ (**Equation 5.1**) value as the molar mass. **Table 5.9** shows the key parameters measured for the Fe and Cu polymers, alongside the number of unpaired electrons each magnetic moment would predict, although, naturally, decimal values are unphysical, and so are only included as an estimate. In theory, as a d⁹ metal, Cu(II) complexes would be expected to have one unpaired electron. In practice, a smaller than expected magnetic moment is observed, possibly due to the lack of sensitivity in calculating the concentration of the polymer, or that the concentration of paramagnetic species in the polymer (as governed by the EDHP incorporation) is generally low, hence giving only a small shift in Δ_F. However, the calculated value is not altogether inconsistent with the expected value, and as a minimum is confirmation that the Cu-doped polymer exhibits paramagnetism.

Table 5.9: Evans method NMR predictions of the number of unpaired electrons in the coordination environments of each polymer. ^a

Polymer	$c / \text{mol mL}^{-1}$	$\Delta_F \text{ } ^t\text{BuOH} / \text{Hz}$	$X_{\text{mol}} / \text{mL mol}^{-1}$	$\mu_{\text{exp}} / \text{BM}$	n_{exp}
Fe	6.60×10^{-6}	35.3	2.55×10^{-3}	2.45	1.6
Cu	6.42×10^{-6}	7.6	5.66×10^{-4}	1.15	0.5

^a $F = 500173000 \text{ Hz}$, $T = 293 \text{ K}$.

For Fe, the analysis is somewhat more complex, as there is a choice of high spin or low spin configurations. For low spin, one would expect to see one unpaired electron, and for high spin, five unpaired electrons. Whilst a n_{exp} value of 1.6 is more closely aligned to a low spin complex, it is peculiar that the Fe polymer would give a far larger shift in the ^tBuOH peak (at comparable concentrations) yet have the same number of unpaired electrons. It is possible that given there is a significant underestimate in n for Cu, that this is this case for Fe too, meaning it could well contain high spin Fe complexes. Although the data is ambiguous, again there is clear paramagnetism in the sample, which supports the NMR interpretation that the EDHP peaks disappear due to paramagnetic broadening, and is also further evidence for metal complex incorporation in the sample.

Another technique used to analyse paramagnetic compounds is electron paramagnetic resonance (EPR) spectroscopy. Frozen glasses (77 K) of 1:1 mixtures of DMSO and DMF were used for all experiments, which were performed by Dr. Emma Richards (Cardiff University). Mixtures of solvent systems are often used in EPR to minimise any solvent crystallisation upon freezing, which can introduce directionality into the analysis, rather than the desired time-average signal analogous to those seen in liquid state techniques like NMR, whilst colder temperatures increase the sensitivity of the analysis by increasing the population of the ground spin state of the unpaired electron.⁸² This particular mixture was chosen as the Cu polymer, the unmodified polymer, CuCl₂, and bipyridine are all soluble in it, allowing direct comparison between four EPR experiments: a) a 7.5 mM solution of CuCl₂, b) a 1:1 mixture of 7.5 mM solutions of bipyridine and CuCl₂, c) a 1:1 mixture of 7.5 mM solutions of CuCl₂ and undoped poly(EDHP-LO-PA) and d) a 7.5 mM solution of the isolated and purified Cu-doped polymer. The spectra resulting from experiments a), b) and d) are shown stacked from top to bottom in **Figure 5.21** (the inverse peaks are cropped for clarity). The EPR spectrum of CuCl₂ is highly amorphous, and does not feature the characteristic line shapes seen for Cu. Both major isotopes of Cu have a spin of $I = 3/2$, meaning one would expect $2nI+1 = 4$ peaks in its EPR spectrum. Depending on the ligand environment, different signals can be seen whether the unpaired electron is in the $d_{x^2-y^2}$

(perpendicular) or d_{z^2} (parallel) orbitals, and this effect is exacerbated by Jahn-Teller distortion of Cu(II) complexes, which generally (but not always) have lengthened axial bonds, meaning the unpaired electron resides in the $d_{x^2-y^2}$ orbital.^{82,83} None of this spectral information is seen for CuCl₂, meaning it likely exists as a complex mixture of different coordination environments. Furthermore, there is no evidence for the presence of free CuCl₂ in the EPR spectrum of the Cu-doped polymer, highlighting that the paramagnetism observed by NMR is due to the presence of copper bound to the polymer, and not residual CuCl₂ that has not been removed.

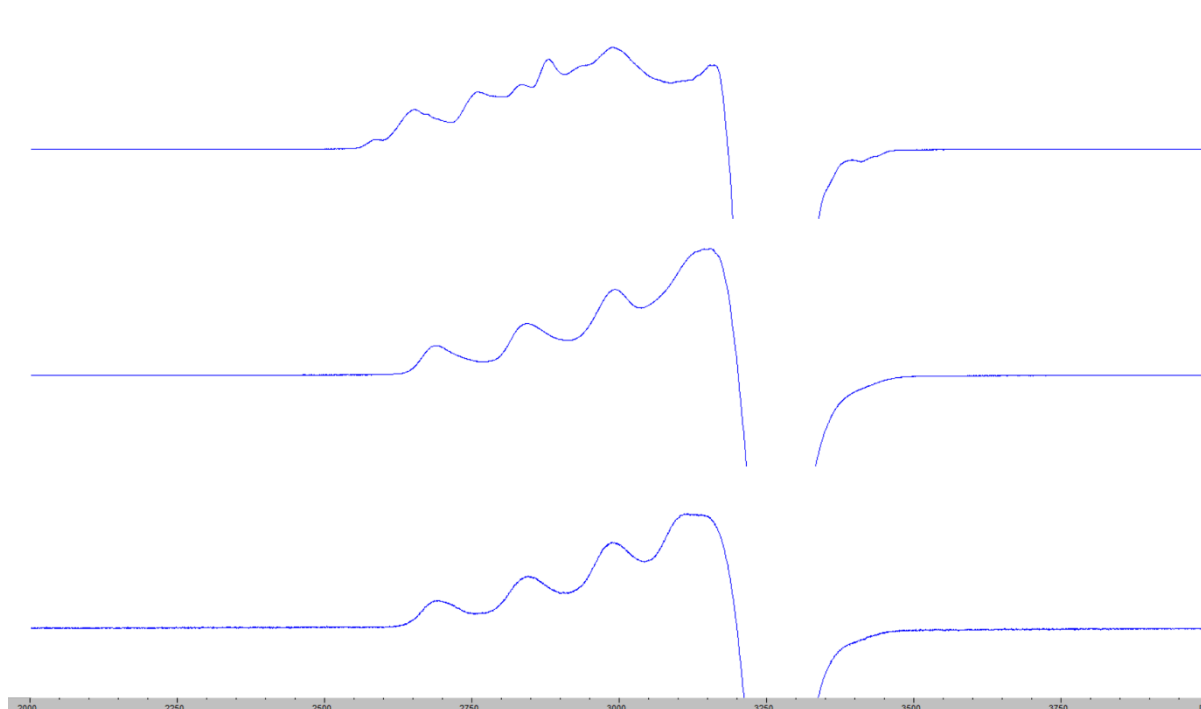


Figure 5.21: Stacked EPR spectra (77K, 1:1 DMSO, DMF) of top: CuCl₂ (7.5 mM), middle: a 1:1 mixture of 7.5 mM solutions of CuCl₂ and bipyridine, bottom: the Cu doped polymer (7.5 mM). Note the similarity of the middle and bottom spectra. The inverse section of the parallel peak is cropped for clarity.

For both the 1:1 mixture of CuCl₂ and bipyridine and the Cu-doped polymer, the perpendicular and parallel signals are overlapping, meaning only four peaks are seen in the spectra. This overlap has been observed for analogous molecular complexes, and the multiplicity of four is expected to arise from coupling to a single $I = 3/2$ nucleus.^{83,84} Indeed, the similarity between these two spectra is indicative that complexation has occurred as expected, which is further reinforced by the colour change to pale green seen immediately once CuCl₂ and bipyridine, with this colour matching that of the polymer. This colour change was also seen when combining undoped poly(EDHP-LO-PA) and CuCl₂ in a 1:1 ratio, with this mixture producing a highly similar spectrum to both the mixture of CuCl₂ and bipyridine and the isolated Cu polymer. This similarity is strong evidence for complexation at the bipyridine-like groups

of EDHP in the polymer. Unfortunately, no hyperfine couplings to ^{14}N ($l = 1$, two equivalent nuclei, $2nI+1 =$ further splitting into a quintet) were observed, although this is likely due to the relatively low concentrations and the use of an unoptimised solvent system, where solubility of a wide range of substrates was prioritised over resultant spectral quality. In any case, the absence of the hyperfine couplings does not preclude bonding to nitrogen. This bonding could be observed directly using advanced EPR techniques like ENDOR, but this was not done here.⁸²

Finally, in terms of molecular weight, the results of GPC analysis for the Fe, Cu and Zn doped polymers, as well as the precursor are shown in **Table 5.10** (the data for Mg and Sc was similar to the undoped polymer, as expected given the lack of complexation).

Table 5.10: Molecular weight characteristics of the metal doped polymers. ^a

Polymer	Ratio EDHP: LO Polymer ^b	M_n / kDa ^c	\bar{D} ^{c,d}
EDHP-LO-PA	1: 6.6	2.0	3.48
Fe	-	22.1	1.66
Cu	-	16.5	2.26
Zn	-	11.6	1.97

^a Sample of EDHP-LO-PA made as in Table 5.1 by with all amounts multiplied by 5. ^b Determined by ^1H NMR spectroscopy of the polymer. ^c Determined by GPC (viscometry detection in THF), against polystyrene standards. ^d $\bar{D} = M_w / M_n$.

All doped polymers showed a peculiar increased in M_n and decrease in polydispersity. As discussed previously for the iridium and ruthenium polymers, the introduction of cationic metal complexes can complicate GPC analysis, producing the anomalous molecular weight data in **Table 5.10**. To try to correct for this, the same molecular weights were measured in THF where 0.1 and 0.2 wt.% tetrabutylammonium bromide (TBAB) was added to the mobile phase. The increase of the ionic strength by adding TBAB was hypothesised to better solubilise to charged groups of the polymer, thereby allowing them to fold in THF solution in a manner more analogous to the undoped polymer, and thereby provide a more realistic estimate of molecular weight. Indeed, this method has been used for the characterisation of poly(ionic liquids) in DMF or THF eluent, where the salt additive was chosen so as to match the anion to the anion of the polymer.⁵¹ In this case however, TBAB was chosen over TBA-chloride due to its improved solubility in THF and more limited hygroscopicity. The results of the GPC analysis in both concentrations of TBAB are shown in **Table 5.11**.

Table 5.11: GPC data for the doped polymers at various TBAB concentrations.^a

Polymer	THF		0.1 wt.% TBAB in THF		0.2 wt.% TBAB in THF	
	M_n / kDa	\bar{D}	M_n / kDa	\bar{D}	M_n / kDa	\bar{D}
Unmodified	2.0	3.48	1.8	3.44	1.3	3.92
Fe	22.1	1.66	2.5	3.94	2.9	3.25
Cu	16.5	2.26	2.1	3.55	2.4	3.23
Zn	11.6	1.97	2.7	2.85	2.8	2.89

^a Determined by viscometry detection against polystyrene standards, $\bar{D} = M_w / M_n$. The same calibration was used in all cases.

Interestingly, there is a vast decrease in observed molecular weight with only a relatively low TBAB concentration in the GPC eluent for the doped polymers. However, this decrease is relatively small for the undoped polymer. This highlights the huge difference in the solution phase behaviour of the metal polymers depending on the ionic strength of the solution, and again supports the notion that the metal complexes are predominantly charged, rather than neutral. The magnitude of the decrease is large enough that the doped polymers have a higher molecular weight than the precursor, which is what one would expect after the addition of mass during the doping reaction.

Taken together, the characterisation data support successful complexation of the chloride salts of Fe, Cu and Zn to poly(EDHP-LO-PA). Although specific information about the exact nature of the coordination sphere(s) is not forthcoming, evidence from conductivity measurements and GPC with TBAB additives is suggestive of at least some charged complexes being present. This method therefore represents a simple and versatile way of metal complex incorporation into polymers. These polymers are potentially an efficient way to support metal complexes for use as catalysts, whilst copper's antimicrobial properties mean a copper doped polyester may be an effective way of producing an antimicrobial surface.⁸⁵

5.9: Summary

In this section, 5,6-epoxy-5,6-dihydrophenanthroline (EDHP) was successfully doped into ROCOP reaction mixtures of PA and either CHO or the bio-derived LO to make polymers with the ability to bind metals. Firstly, iridium was investigated as its luminescent properties are highly desirable and have potential applications in making electronic devices, with its immobilisation on a polymer potentially allowing for a higher efficiency and easier material processing. A cyclometallating iridium complex with phenylpyridine ligands was successfully reacted with the EDHP containing polymers, and the absorbance and emission properties of the resulting polymers were consistent with the formation of a cationic Ir(III) complex. The observed photophysics were supported by theoretical td-DFT calculations, and allowed the MLCT-like transitions leading to charge separated (and thereby susceptible to ICS and later phosphorescence) excited states to be visualised. This method represents a simple method of preparing an as of yet unreported chemically recyclable iridium doped polymer.

The attempted synthesis of a low T_g analogue using 1,2-epoxydodecane was successful, but a black colour likely caused by the ring-opening of terminal epoxides by EDHP limited the utility of the material. An alternative monomer featuring an internal epoxide group, epoxy methyl oleate (EMO), was synthesised from oleic acid. However, the slow rate of the DMAP only catalysis employed so far led to low conversions and only small amounts of isolate polymer, albeit polymer which possessed the desired rubbery texture. After several attempts, ruthenium was successfully complexed, as evidenced by distinct shifts in the ^1H NMR chemical shifts of the EDHP protons pre- and post-complexation, as well an absorbance spectrum in close agreement to the molecular analogue $[\text{Ru}(\text{bipy})_3]^{2+}$.

A series of 1st row metals (Fe, Cu, Zn) were successfully complexed to poly(EDHP-LO-PA) using simple chloride salts, although Mg and Sc proved unsuccessful. The polymers were extensively characterised by NMR, MALDI-ToF, FT-IR, UV-Vis and by taking conductivity measurements of their THF solutions. This supported the formation of at least some charged metal complexes at the EDHP sites. The paramagnetism of both the Cu and Fe polymers was investigated by Evans method NMR, which confirmed the paramagnetic broadening (and apparent disappearance) of the EDH peaks in the ^1H NMR spectra. EPR experiments were also performed on the Cu polymer, where a close match between the polymer spectrum and that of a 1:1 mixture of CuCl_2 and bipyridine was seen, supported the expected complexation. The addition of tetrabutylammonium bromide to the THF eluent in GPC analysis allowed for a more realistic estimate of molecular weight for the metal doped polymers.

5.10: References for Chapter 5

- 1 S. A. Rommel, D. Sorsche and S. Rau, *Dalt. Trans.*, 2015, **45**, 74–77.
- 2 Y. Ma, S. Liu, H. Yang, Y. Wu, H. Sun, J. Wang, Q. Zhao, F. Li and W. Huang, *J. Mater. Chem. B*, 2013, **1**, 319–329.
- 3 K. Huang, I. W. Bulik and A. A. Martí, *Chem. Commun.*, 2012, **48**, 11760–11762.
- 4 P. Alam, G. Kaur, C. Climent, S. Pasha, D. Casanova, P. Alemany, A. R. Choudhury and I. R. Laskar, *Dalt. Trans.*, 2014, **43**, 16431–16440.
- 5 D.-L. Ma, S. Lin, W. Wang, C. Yang and C.-H. Leung, *Chem. Sci.*, 2017, **8**, 878–889.
- 6 S. K. Sheet, B. Sen and S. Khatua, *Inorg. Chem.*, 2019, **58**, 3635–3645.
- 7 A. Nakagawa, Y. Hisamatsu, S. Moromizato, M. Kohno and S. Aoki, *Inorg. Chem.*, 2013, **53**, 409–422.
- 8 P. Steunenbergh, A. Ruggi, N. S. van den Berg, T. Buckle, J. Kuil, F. W. B. van Leeuwen and A. H. Velders, *Inorg. Chem.*, 2012, **51**, 2105–2114.
- 9 C. Li, M. Yu, Y. Sun, Y. Wu, C. Huang and F. Li, *J. Am. Chem. Soc.*, 2011, **133**, 11231–11239.
- 10 M. Yu, Q. Zhao, L. Shi, F. Li, Z. Zhou, H. Yang, T. Yi and C. Huang, *Chem. Commun.*, 2008, 2115–2117.
- 11 Q. Zhao, C. Huang and F. Li, *Chem. Soc. Rev.*, 2011, **40**, 2508–2524.
- 12 C. Caporale and M. Massi, *Coord. Chem. Rev.*, 2018, **363**, 71–91.
- 13 A. J. Hallett, N. White, W. Wu, X. Cui, P. N. Horton, S. J. Coles, J. Zhao and S. J. A. Pope, *Chem. Commun.*, 2012, **48**, 10838–10840.
- 14 C. K. Prier, D. A. Rankic and D. W. C. MacMillan, *Chem. Rev.*, 2013, **113**, 5322–5363.
- 15 D. T. Ahneman and A. G. Doyle, *Chem. Sci.*, 2016, **7**, 7002–7006.
- 16 S. Lamansky, P. Djurovich, D. Murphy, F. Abdel-Razzaq, H.-E. Lee, C. Adachi, P. E. Burrows, S. R. Forrest and M. E. Thompson, *J. Am. Chem. Soc.*, 2001, **123**, 4304–4312.
- 17 G. Li, D. Zhu, T. Peng, Y. Liu, Y. Wang and M. R. Bryce, *Adv. Funct. Mater.*, 2014, **24**, 7420–7426.
- 18 Z. Hao, K. Zhang, P. Wang, X. Lu, Z. Lu, W. Zhu and Y. Liu, *Inorg. Chem.*, 2019, **59**, 332–342.
- 19 T. M. Stonelake, K. A. Phillips, H. Y. Otaif, Z. C. Edwardson, P. N. Horton, S. J. Coles, J. M. Beames

- and S. J. A. Pope, *Inorg. Chem.*, 2020, **25**, 30.
- 20 J. Zhou, G. Fu, Y. He, L. Ma, W. Li, W. Feng and X. Lü, *J. Lumin.*, 2019, **209**, 427–434.
- 21 X. Y. Wang, R. N. Prabhu, R. H. Schmehl and M. Weck, *Macromolecules*, 2006, **39**, 3140–3146.
- 22 K. P. S. Zanoni, R. L. Coppo, R. C. Amaral and N. Y. M. Iha, *Dalt. Trans.*, 2015, **44**, 14559–14573.
- 23 F. Xu, H. U. Kim, J. H. Kim, B. J. Jung, A. C. Grimsdale and D. H. Hwang, *Prog. Polym. Sci.*, 2015, **47**, 92–121.
- 24 S. A. Fitzgerald, H. Y. Otaif, C. E. Elgar, N. Sawicka, P. N. Horton, S. J. Coles, J. M. Beames and S. J. A. Pope, *Inorg. Chem.*, 2021, **60**, 15467–15484.
- 25 F. Xu, H. U. Kim, D. Mi, J. M. Lim, J. H. Hwang, N. S. Cho, J. I. Lee and D. H. Hwang, *Bull. Korean Chem. Soc.*, 2013, **34**, 399–405.
- 26 X. Y. Wang, A. Kimyonok and M. Weck, *Chem. Commun.*, 2006, 3933–3935.
- 27 S. Tokito, M. Suzuki and F. Sato, in *Thin Solid Films*, Elsevier, 2003, vol. 445, pp. 353–357.
- 28 E. Holder, V. Marin, D. Kozodaev, M. A. R. Meier, B. G. G. Lohmeijer and U. S. Schubert, *Macromol. Chem. Phys.*, 2005, **206**, 989–997.
- 29 A. C. Grimsdale, K. L. Chan, R. E. Martin, P. G. Jokisz and A. B. Holmes, *Chem. Rev.*, 2009, **109**, 897–1091.
- 30 E. O. Platonova, A. P. Pushkarev, V. A. Ilichev, E. V. Baranov, T. A. Kovylina and L. N. Bochkarev, *Russ. J. Coord. Chem. Khimiya*, 2017, **43**, 491–499.
- 31 Y. E. Begantsova, L. N. Bochkarev, E. V. Baranov and V. A. Ilichev, *Russ. J. Coord. Chem. Khimiya*, 2019, **45**, 856–866.
- 32 C. Ulbricht, C. R. Becer, A. Winter and U. S. Schubert, *Macromol. Rapid Commun.*, 2010, **31**, 827–833.
- 33 A. Baschieri, F. Monti, N. Armaroli, G. Mazzotti, L. Giorgini, L. Sambri and T. Benelli, *Dye. Pigment.*, 2019, **160**, 188–197.
- 34 V. Fiorini, N. Monti, G. Vigarani, G. Santi, F. Fasulo, M. Massi, L. Giorgini, A. B. Muñoz-García, M. Pavone, A. Pucci and S. Stagni, *Dye. Pigment.*, 2021, **193**, 109532.
- 35 K. A. Aamer and G. N. Tew, *J. Polym. Sci. Part A Polym. Chem.*, 2007, **45**, 1109–1121.
- 36 M. Hong and E. Y. X. Chen, *Green Chem.*, 2017, **19**, 3692–3706.

- 37 M. Häußler, M. Eck, D. Rothauer and S. Mecking, *Nature*, 2021, **590**, 423–427.
- 38 T. B. Young, O. G. Guppy, A. J. Draper, J. M. Whittington, B. M. Kariuki, A. Paul, M. Eaton, S. J. A. Pope and B. D. Ward, *Polym. Chem.*, , DOI:10.1039/D3PY00209H.
- 39 G. Faraca and T. Astrup, *Waste Manag.*, 2019, **95**, 388–398.
- 40 Z. O. G Schyns and M. P. Shaver, *Macromol. Rapid Commun.*, 2021, **42**, 2000415.
- 41 J. Li, H. Liu, H. Zhu, W. Yao and D. Wang, *ChemCatChem*, 2021, **13**, 4751–4758.
- 42 W. Yao, Z. Duan, Y. Zhang, X. Sang, X. Xia and D. Wang, *Adv. Synth. Catal.*, 2019, **361**, 5695–5703.
- 43 Q. Chen, A. Dong, D. Wang, L. Qiu, C. Ma, Y. Yuan, Y. Zhao, N. Jia, Z. Guo and N. Wang, *Angew. Chemie Int. Ed.*, 2019, **58**, 10671–10676.
- 44 L. N. Bochkarev, Y. P. Parshina, Y. V. Gracheva, T. A. Kovylnina, S. A. Lermontova, L. G. Klapshina, A. N. Konev, M. A. Lopatin, M. M. Lukina, A. D. Komarova, V. I. Shcheslavskiy and M. V. Shirmanova, *Molecules*, 2021, **26**, 6349.
- 45 T. Wang, R. Sun, M. Shi, F. Pan, Z. Hu, F. Huang, Y. Li, J. Min, T. Wang, R. Sun, M. M. Shi, J. Min, F. Pan, Y. F. Li, Z. C. Hu and F. Huang, *Adv. Energy Mater.*, 2020, **10**, 2000590.
- 46 Q. Chen, N. Liu, L. Ying, W. Yang, H. Wu, W. Xu and Y. Cao, *Polymer (Guildf.)*, 2009, **50**, 1430–1437.
- 47 J. Sun, H. Wang, H. Xu, T. Zhang, L. Li, J. Li, Y. Wu, B. Xu, X. Zhang and W. Lai, *Dye. Pigment.*, 2016, **130**, 191–201.
- 48 Y. Koga and K. Matsubara, *J. Polym. Sci. Part A Polym. Chem.*, 2009, **47**, 4358–4365.
- 49 C. E. Elgar, H. Y. Otaif, X. Zhang, J. Zhao, P. N. Horton, S. J. Coles, J. M. Beames and S. J. A. Pope, *Chem. - A Eur. J.*, 2021, **27**, 3427–3439.
- 50 R. Roemling, K. Tokunaga and H. Moriyama, *Analysis of cationic polymers by Size Exclusion Chromatography (SEC)*, Tosoh Bioscience, Technical Report, 2008.
- 51 H. He, M. Zhong, B. Adzima, D. Luebke, H. Nulwala and K. Matyjaszewski, *J. Am. Chem. Soc.*, 2013, **135**, 4227–4230.
- 52 S. Horiuchi, H. Tanaka, E. Sakuda, Y. Arikawa and K. Umakoshi, *Chem. – A Eur. J.*, 2016, **22**, 17533–17537.

- 53 J. Sun, F. Zhong, X. Yi and J. Zhao, *Inorg. Chem.*, 2013, **52**, 6299–6310.
- 54 M. J. Frisch, G. W. Trucks, H. B. Schlegel, G. E. Scuseria, M. A. Robb, J. R. Cheeseman, G. Scalmani, V. Barone, G. Petersson, H. Nakatsuji, X. Li, M. Caricato, A. Marenich, J. Bloino, B. G. Janesko, R. Gomperts, B. Mennucci, H. P. Hratchian, J. V. Ortiz, A. F. Izmaylov, J. L. Sonnenberg, D. Williams-Young, F. Ding, F. Lipparini, F. Egidi, J. Goings, B. Peng, A. Petrone, T. Henderson, D. Ranasinghe, V. G. Zakrzewski, J. Gao, N. Rega, G. Zheng, W. Liang, M. Hada, M. Ehara, K. Toyota, R. Fukuda, J. Hasegawa, M. Ishida, T. Nakajima, Y. Honda, O. Kitao, H. Nakai, T. Vreven, K. Throssell, J. A. J. Montgomery, J. E. Peralta, F. Ogliaro, M. Bearpark, J. J. Heyd, E. Brothers, K. N. Kudin, V. N. Staroverov, T. Keith, R. Kobayashi, J. Normand, K. Raghavachari, A. Rendell, J. C. Burant, S. S. Iyengar, J. Tomasi, M. Cossi, J. M. Millam, M. Klene, C. Adamo, R. Cammi, J. W. Ochterski, R. L. Martin, K. Morokuma, O. Farkas, J. B. Foresman and D. J. Fox, *Gaussian 09, Revision D.01*, Gaussian Inc., Wallingford, CT, 2016.
- 55 P. J. Hay and W. R. Wadt, *J. Chem. Phys.*, 1985, **82**, 270.
- 56 P. J. Hay and W. R. Wadt, *J. Chem. Phys.*, 1985, **82**, 29F9.
- 57 W. R. Wadt and P. J. Hay, *J. Chem. Phys.*, 1985, **82**, 284.
- 58 G. A. Petersson and M. A. Al-Laham, *J. Chem. Phys.*, 1991, **94**, 6081.
- 59 J. Tomasi, B. Mennucci and R. Cammi, *Chem. Rev.*, 2005, **105**, 2999–3094.
- 60 A. D. Becke, *Phys. Rev. A*, 1988, **38**, 3098.
- 61 A. D. Becke, *J. Chem. Phys.*, 1993, **98**, 5648.
- 62 T. Yanai, D. P. Tew and N. C. Handy, *Chem. Phys. Lett.*, 2004, **393**, 51–57.
- 63 Y. Zhao and D. G. Truhlar, *Theor. Chem. Acc.*, 2008, **120**, 215–241.
- 64 R. Peverati and D. G. Truhlar, *J. Phys. Chem. Lett.*, 2011, **2**, 2810–2817.
- 65 A. Brandolese, F. Della Monica, M. À. Pericàs and A. W. Kleij, *Macromolecules*, 2022, **55**, 2566–2573.
- 66 M. Decostanzi, J. Lomège, Y. Ecochard, A. S. Mora, C. Negrell and S. Caillol, *Prog. Org. Coatings*, 2018, **124**, 147–157.
- 67 C. E. McCusker and J. K. McCusker, *Inorg. Chem.*, 2011, **50**, 1656–1669.
- 68 A. J. Tilley, M. J. Kim, M. Chen and K. P. Ghiggino, *Polymer (Guildf.)*, 2013, **54**, 2865–2872.

- 69 S. Cerfontaine, S. A. M. Wehlin, B. Elias and L. Troian-Gautier, *J. Am. Chem. Soc.*, 2020, **142**, 5549–5555.
- 70 J. L. Bourdelande, J. Font, G. Marques, A. A. Abdel-Shafi, F. Wilkinson and D. R. Worrall, *J. Photochem. Photobiol. A Chem.*, 2001, **138**, 65–68.
- 71 A. Gellé, G. D. Price, F. Voisard, N. Brodusch, R. Gauvin, Z. Amara and A. Moores, *ACS Appl. Mater. Interfaces*, 2021, **13**, 35606–35616.
- 72 A. A. Abdel-Shafi, D. R. Worrall and A. Y. Ershov, *Dalt. Trans.*, 2004, 30–36.
- 73 R. Luo, M. Li, C. Wang, M. Zhang, M. A. Nasir Khan, X. Sun, J. Shen, W. Han, L. Wang and J. Li, *Water Res.*, 2019, **148**, 416–424.
- 74 O. A. Lenis-Rojas, C. Roma-Rodrigues, A. R. Fernandes, F. Marques, D. Pérez-Fernández, J. Guerra-Varela, L. Sánchez, D. Vázquez-García, M. López-Torres, A. Fernández and J. J. Fernández, *Inorg. Chem.*, 2017, **56**, 7127–7144.
- 75 M. Zeng, L. Li and S. B. Herzon, *J. Am. Chem. Soc.*, 2014, **136**, 7058–7067.
- 76 G. Zhou, J. He, I. I. Harruna and K. E. Geckeler, *J. Mater. Chem.*, 2008, **18**, 5492–5501.
- 77 P. C. Boutin, K. P. Ghiggino, T. L. Kelly and R. P. Steer, *J. Phys. Chem. Lett.*, 2013, **4**, 4113–4118.
- 78 T. N. Kropacheva, V. I. Kornev, D. A. Loginov, V. I. Meshcheryakov, E. V. Mutseneck, D. V. Muratov, D. S. Perekalin, L. S. Shul'pina and A. R. Kudinov, *Russ. Chem. Bull.*, 2005, **54**, 2354–2358.
- 79 G. H. Eom, H. M. Park, M. Y. Hyun, S. P. Jang, C. Kim, J. H. Lee, S. J. Lee, S.-J. Kim and Y. Kim, *Polyhedron*, 2011, **30**, 1555–1564.
- 80 P. Majumdar, A. K. Ghosh, L. R. Falvello, S. M. Peng and S. Goswami, *Inorg. Chem.*, 1998, **37**, 1651–1654.
- 81 C. G. Lin, M. Hutin, C. Busche, N. L. Bell, D. L. Long and L. Cronin, *Dalt. Trans.*, 2021, **50**, 2350–2353.
- 82 M. M. Roessler and E. Salvadori, *Chem. Soc. Rev.*, 2018, **47**, 2534–2553.
- 83 F. A. Walker and H. Sigel, *Inorg. Chem.*, 1972, **11**, 1162–1164.
- 84 M. Noack and G. Gordon, *J. Chem. Phys.*, 1968, **48**, 2689.
- 85 D. Mitra, E.-T. Kang and K. G. Neoh, *ACS Appl. Mater. Interfaces*, 2020, **12**, 21159–21182.

Chapter 6: Conclusions and Future Work

6.1: Summary of Completed Work

In summary of the previous chapters, the ROCOP of cyclic epoxides and anhydrides has been investigated from a wide array of perspectives including pre-catalyst synthesis and characterisation, catalytic performance, mechanistic investigations, the use of bio-derived monomer at a large scale, the analysis and modification of the resultant polymers, the investigation of polymer flame retardancy, and the incorporation of metal complexes into the polymers with a view to applications in functional materials such as in LEDs.

Chapter 1 highlighted the potential utility of ROCOP in synthesising a wide array of chemically recyclable polyesters in a well-controlled chain growth manner, and some of the key breakthroughs in terms of the development of metal complexes for use as ROCOP catalysts. Chapter 2 detailed the synthesis and characterisation of hemi-labile $[\text{Al}(\text{Salpy})\text{Cl}]$ complexes, with the hypothesis that the coordination and de-coordination of a pyridyl donor may assist with the de-coordination of polymer chains necessary for propagation. Unfortunately, however, there was no discernible rate enhancement compared to co-catalyst only control reactions, and no improvement of molecular weights or in substrate scope. This was in spite of the fact that stoichiometric reactions showed that $[\text{Al}(\text{Salpy})\text{Cl}]$ complexes can ring-open epoxides, and that the DFT-calculated energies for the catalytic cycle were feasible.

Chapter 3 focussed on using simple Group 4 $[\text{Cp}_2\text{MCl}_2]$ pre-catalysts in ROCOP, all of which ($\text{M} = \text{Ti}, \text{Zr}, \text{Hf}$) showed significant rate enhancements compared to control reactions. Although these complexes were not fully ester selective (apart from when LO was used), it is clear that the Group 4 metals are under-investigated in the field, and that further catalyst development beyond the use of simple, commercially available pre-catalysts may yield improved performance. Pleasingly, over 200 g of poly(LO-*alt*-PA) was synthesised in one batch using $[\text{Cp}_2\text{ZrCl}_2]$, with the properties of this polymer fully investigated in Chapter 4. PPM reactions also showed the versatility of ROCOP and the advantage of using a monomer containing pendant alkene functionality, which included the two-step synthesis of phosphorylated polymers. These polymers contained varying amounts of phosphates chemically bound to the polymer chain, rather than simply being added in a blend as is typically done for modern plastics. This chemical tethering may reduce the risk of leaching and thereby ameliorate the toxicity concerns associated with phosphate flame retardants. PCFC measurements showed enhanced char

formation, and indication of surface derived flame retardancy upon addition of phosphate, albeit with reduced returns of char upon further addition of phosphate.

Chapter 5 showed how EDHP, a bipyridine-like monomer, could be doped into ROCOP reaction mixtures and thereby provide a scaffold for metal complex incorporation. This included cyclometallated Ir(III) complexes, whose photophysical properties are of wide interest and could have potential applications in LEDs or as photoredox catalysts. The absorbance and luminescence of the iridium-doped polymers was investigated both experimentally and theoretically, all of which was consistent with MLCT-like absorbance giving rise to ICS and subsequently phosphorescent emission. Ruthenium doping was less straightforward and characterisation more ambiguous, yet again there was features in the absorbance spectrum of the polymer consistent with MLCT-like absorbances arising from a $[\text{Ru}(\text{bipy})_2\text{EDHP}]^{2+}$ unit. A series of first row metals were also trialled for polymer doping, which proved unsuccessful for Mg and Sc, yet successfully for mid and late transition metals in Fe, Cu and Zn. These polymers were extensively characterised, including by techniques bespoke to paramagnetic materials such as EPR spectroscopy in the case of the Cu-doped polymer.

6.2: Future Work

In terms of avenues for further investigation, there is clearly scope for further catalyst development in order to synthesise ROCOP polyesters faster and with greater control of molecular weight. This is perhaps most pertinent to the Group 4 metals given that there are relatively few reports into their use, and that the aluminium catalysis in this work was underwhelming in comparison. Naturally, and as touched upon lightly in section 3.8, there are a large array of metallocene and half-metallocene complexes which may be suitable for further study. However, there are also wider possibilities, including the use of Salph or related Schiff base ligands which have proved so popular in the field, or heteroaryl-amido Zr or Hf which have been developed for olefin polymerisation (**Figure 6.1**).¹ As well as catalyst development, and with it the enormous chemical space of potential catalysts, the use of the Group 4 elements and the availability of its organometallic (*i.e.* methyl or benzyl) complexes means there is scope for investigation into non-initiating complexes. This was discussed in section 1.5, where addition of CTAs such as diacids or diols could lead to monomodal molecular weight distributions and potentially elevated molecular weights.^{2,3} Although this would lead to pre-catalysts that are more air and moisture sensitive than non-organometallic complexes, it allows a far broader range of complexes to be studied for the first time in the context of ROCOP.

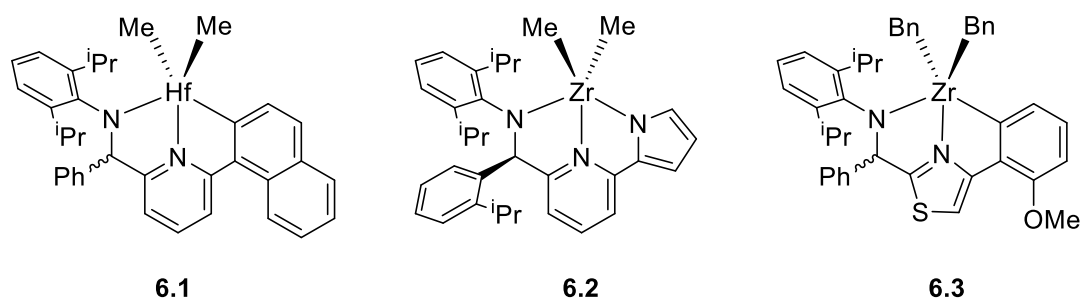


Figure 6.1: Series of Zr and Hf heteroaryl-amido complexes feature organometallic co-ligands, as developed by researchers from Symyx and Dow. Complexes of this type may be particularly amenable to ROCOP experiments featuring the use of CTAs given the presence of non-initiating alkyl ligands.¹

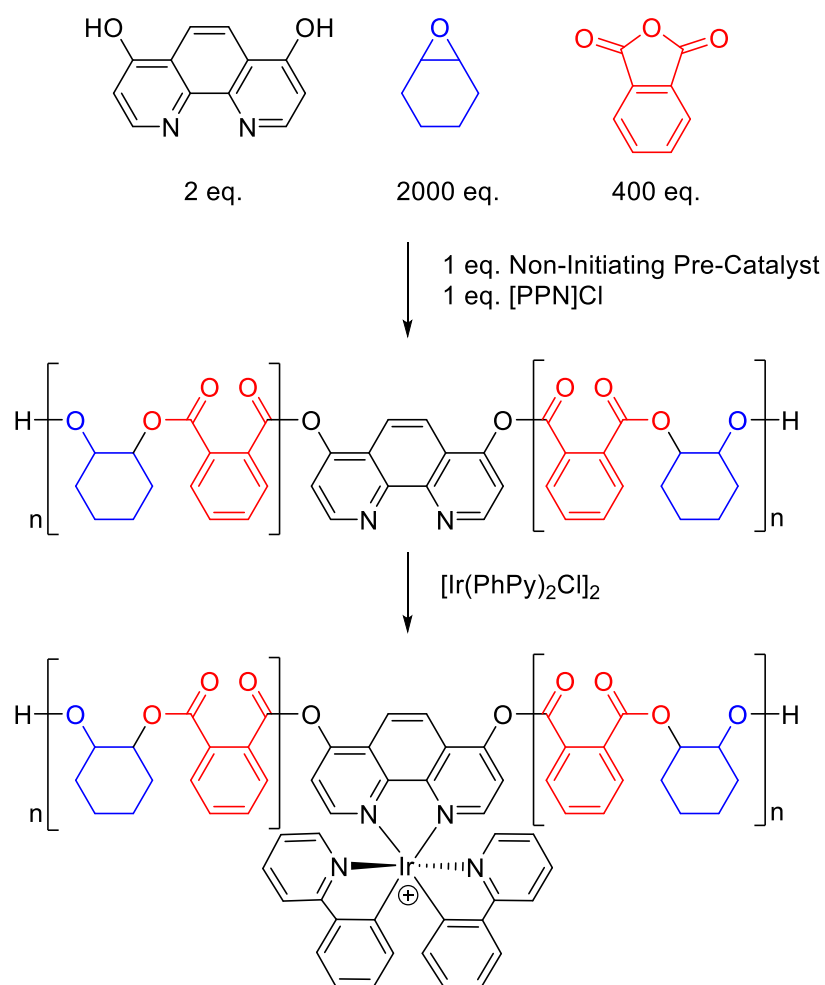
In addition to catalyst development, it is important to further tune the properties of the resultant polyesters to better suit real world usage, and thereby displace some petroleum-derived polymers from certain applications. This includes further development of the phosphorylation chemistry used to introduce flame retardancy into the polymers. A simple avenue for further exploration would be the modification of the chlorophosphate used, as in this work on diphenyl phosphoryl chloride was studied. However, this could be modified to diethyl phosphoryl chloride, in order to investigate how reducing the mass percentage of carbon in the sample may impact flame retardancy, or the use of chlorophosphates with additional halogenation, meaning the materials may have gas phase activity in addition to surface activity in char formation. Furthermore, in this work, phosphorylation required two synthetic steps, and the development of a one-step reaction akin to phosphorylation across a double bond may provide a simpler route. This could have the additional advantage in modifying the bond linking polymer and phosphate from an O-P bond to a C-P bond, with the latter less prone to hydrolysis and thereby potential leaching out of the plastic.

The synthesis of higher molecular weight analogues of the phosphorylated polymers described in this study would also be a valid research objective, as this would potentially allow for increased processability and reduced brittleness, as has been reported for polymers made *via* ROCOP.³ Although achieving this objective may necessitate the move away from using LO as a monomer, analogous chemistry could be investigated for VCHO. Another interesting feature of the phosphorylated polymers investigated so far is that triphenyl phosphate is a commonly used plasticiser⁴, meaning that the brittleness of molecular weight polymers could be further reduced by the presence of the flame retardant, again helping to limit the amount of additives required. Investigations into the degradation behaviour of the phosphorylated polymers would also prove useful, as chemical recycling would lead

an additional hydroxyl group in the diol, meaning the ability to re-make the starting epoxide is more complicated than for the unmodified polymer.

In terms of the work detailed in Chapter 5, a relatively simple avenue for future work is to modify the cyclometallating ligands of the iridium dimer precursor to modify the luminescence behaviour of the polymer. As described in section 5.5, the simple approach employed here means modification of the precursor can be done independently of the polymer synthesis, meaning a large array of different complexes could be immobilised onto poly(EDHP-CHO-PA). In addition, throughout this work a relatively high doping percentage of EDHP (and thereby iridium) has been used, mostly to aid with the characterisation of the resultant polymers. However, to maximise the benefit of binding iridium complexes to the polymer, a lower incorporation percentage may be more applicable. This could be quantified by solid state luminescence measurements, and metrics such as emission wavelength, excited state lifetime and quantum yields could be measured and compared to those seen in solution. Again, higher molecular weight doped polymers could be beneficial, and decreasing the EDHP loading may help to increase molecular weight and narrow molecular weight distributions. An interesting experiment could be to use the commercially available 4,7-dihydroxy-1,10-phenanthroline as a CTA for a ROCOP reaction, meaning each polymer chain would contain precisely one bipyridine-like unit (**Scheme 6.1**). This small loading would be comparable to the 0.2 mol% of organic luminophores doped into ROCOP reactions as described previously,⁵ and could lead to a more controlled polymerisation whilst still allowing for iridium complexation and thereby luminescence. Also, this approach is compatible with conducting reactions in neat excess epoxide, although may require the addition of a non-initiating metal complex, which could complicate the luminescence profile of the material if it remains trapped within the polymer post work-up. However, if residual metal could be removed prior to addition of iridium, or if an organocatalytic method could be used, then this could be a simple method to produce iridium doped polymers in a highly controlled manner.

As well as iridium complexes based upon cyclometallating ligands, the incorporation of different scaffolds would again be independent of the polymer synthesis, in that the iridium precursor would simply be exchanged for another. This would then allow for investigation into the immobilisation of iridium catalysts, with the advantage of easier material recovery at the end of the reaction.



Scheme 6.1: Potential use of 4,7-dihydroxy-1,10-phenanthroline as a CTA to increase the control of its incorporation during polymer synthesis. This could lead to doped polymers with higher molecular weights and lower polydispersities, whilst still allowing for easy incorporation of the luminophore.

6.3: References for Chapter 6

- 1 G. M. Diamond, K. A. Hall, A. M. Lapointe, M. K. Leclerc, J. Longmire, J. A. W. Shoemaker and P. Sun, *ACS Catal.*, 2011, **1**, 887–900.
- 2 M. J. Sanford, N. J. Van Zee and G. W. Coates, *Chem. Sci.*, 2018, **9**, 134–142.
- 3 W. T. Diment and C. K. Williams, *Chem. Sci.*, 2022, **13**, 8543–8549.
- 4 I. Pantelaki and D. Voutsas, *Sci. Total Environ.*, 2019, 649, 247–263.
- 5 T. B. Young, O. G. Guppy, A. J. Draper, J. M. Whittington, B. M. Kariuki, A. Paul, M. Eaton, S. J. A. Pope and B. D. Ward, *Polym. Chem.*, 2023, **14**, 2478–2484.

Chapter 7: Experimental

7.1: Instrumentation, General Considerations and Polymerisations

NMR experiments were performed on Bruker Fourier 300, Avance III HD 400 or 500 spectrometers, with the chemical shifts (δ) referenced to residual solvent resonances (δ^H , $\delta^C = 0$ for $\text{Si}(\text{CH}_3)_4$). Electrospray ionisation mass spectrometry analyses were performed by analytical services, Cardiff University School of Chemistry. Polymers were characterised using an Agilent 1260 Infinity II Multi Detector GPC/SEC fitted with a 5 μm Mixed-D PLgel column and calibrated by polystyrene standards. Analysis was performed using THF as an eluent (1 mL min^{-1} flow rate), with samples made up to 3 mg mL^{-1} before auto injection unless otherwise stated. MALDI-ToF experiments were performed in positive mode on a Bruker AutoFlex speed MALDI-ToF mass spectrometer, with samples prepared by vortex mixing DCTB (50 μL of 20 mg mL^{-1} in THF), polymer sample (10 μL of 10 mg mL^{-1} in THF) and NaOAc (5 μL of 50 mg mL^{-1} in THF). Glass transition temperatures were measured using a double furnace, power compensation Perkin Elmer Differential Scanning Calorimeter 8000. The DSC was calibrated using indium and an empty sealed sample pan was used as a reference. DSC experiments involved the heating of the reference and the sample from -50°C to 180°C at a rate of $20^\circ\text{C min}^{-1}$ under nitrogen flow, with a hold at 150°C for 1 minute, before cooling to -50°C at the same gradient and a further 1 minute hold. This cycle was repeated two more times, with the T_g taken from the third cycle. PCFC measurements were performed using a Fire Testing Technology Ltd. (Gosport, UK) micro-scale combustion calorimeter, at Victoria University by Prof. Paul Joseph and Dr. Malavika Arun, using a heating rate of 1°C min^{-1} in N_2 to 900°C . All computational experiments were performed in the Gaussian 09 suite, with specific methods given in each section.

Manipulations involving air or moisture sensitive reagents were performed using nitrogen dry-boxes and standard double manifold Schlenk techniques under an argon atmosphere. Dichloromethane, toluene, dimethyl formamide, acetonitrile, hexanes and pentane were dried by passing through an alumina column fitted to a MBraun SPS800 solvent purification system, with hexanes, pentane and toluene then stored over potassium mirrors. Diethyl ether and tetrahydrofuran were pre-dried over vacuum-dried molecular sieves, before being refluxed in an argon atmosphere over sodium wire/benzophenone or potassium respectively. Dimethoxyethane and deuterated solvents (C_6D_6 , $\text{THF-}d^8$, CDCl_3 , CD_2Cl_2 and $\text{C}_2\text{D}_2\text{Cl}_4$) were dried over freshly ground CaH_2 for a minimum of 48 hours, degassed by at least three freeze-pump-thaw cycles, and distilled under reduced pressure. Except for epoxydodecane (EDD), epoxy methyl oleate (EMO) and 5,6-epoxy-5,6-dihydro-1,10-phenanthroline, all epoxides and citraconic anhydride used in standard scale ROCOP reactions were dried in the same

way as deuterated solvents. Phthalic anhydride, tetrachlorophthalic anhydride, maleic anhydride and succinic anhydride were extracted into hot chloroform, concentrated, dried, and then sublimed under vacuum. Carbic anhydride (cis-5-Norbornene-endo-2,3-dicarboxylic anhydride) was repeatedly recrystallised in ethyl acetate before sublimation. DMAP was sublimed under vacuum and used to prepare stock solutions (78 mg mL⁻¹ in dry THF) which were remade regularly. VCHDO was synthesised according to a modification of a literature method, where vinyl cyclohexene oxide was used in place of 4-vinyl cyclohex-1-ene.¹ EMO was made according to a published method.² All reactants used in small scale polymerisations were stored in a nitrogen glovebox. For every small scale ROCOP reaction, oven-dried 7 mL screw cap vials were changed with reagents inside a nitrogen glovebox (amounts detailed in each section) and an oven-dried magnetic stirrer bar which had been cleaned using aqua regia. The vials were sealed within the glovebox and heated for a given time in an aluminium heating block containing a vial with *c.a.* 1.5 mL of paraffin oil, into which the thermocouple was placed.

For the large scale synthesis of poly(LO-*alt*-PA), PA was used as received, toluene and limonene oxide ((+)-Limonene 1,2-epoxide, mixture of *cis/trans* isomers) were dried over molecular sieves, and DMAP was sublimed under vacuum. Phthalic anhydride (190 g, 1280 mmol, 400 eq.), limonene oxide (195 g, 210 mL, 1280 mmol, 400 eq.), zirconocene dichloride (935 mg, 3.2 mmol, 1 eq.), DMAP (782 mg, 6.4 mmol, 2 eq.) and toluene (500 mL) were charged into an argon-purged Radleys Reactor Ready 2 L reactor. The reactor was fitted with an oil bubbler and heated to 100 °C with mechanical stirring. During this time, aliquots were taken *via* syringe against a flow of argon to monitor conversion, and extra toluene was added as the solvent level reduced. After 3 days, the reaction mixture was poured onto isopropanol, where after settling the supernatant was decanted. The polymer was then washed with isopropanol, before filtering and drying *in vacuo*.

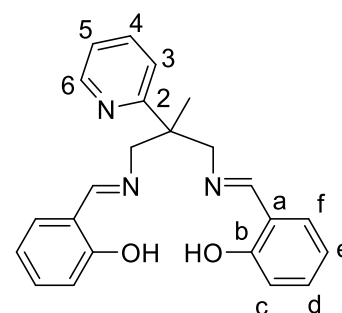
7.2: Synthesis and Characterisation of Salpy Ligands

2-methyl-2-(pyridin-2-yl)propane-1,3-diamine (ppda) and 1,3-Diamino-*N,N'*-bis(3,5-di-*tert*-butylsalicylidene)-2,2-dimethylpropane were prepared according to published procedures.^{3,4} Salpy ligands were synthesised *via* a Schiff base condensation of ppda and two equivalents of aldehyde as detailed in the generic experimental description below. Yields and characterising data are then tabulated individually for each ligand variant.

A methanolic (40 mL) solution of salicylaldehyde derivative (2.0 eq., *ca.* 3 mmol) was magnetically stirred and heated to reflux, before dropwise addition of a solution of ppda (1.0 eq. *ca.* 6 mmol, 1.0 g) in methanol (20 mL). The resulting solution was then refluxed for three hours, after which the cooled precipitate was isolated by Büchner filtration, washed with ice-cold methanol, and dried *in vacuo* to give the corresponding Salpy ligand. Crystals of sufficient quality for X-Ray diffraction studies were grown by anti-solvent addition of hexanes to concentrated methanol solutions. All solvent quantities were scaled in accordance with the amount of ppda used.

7.2.1: Salpy (L-1). Yield = 78%

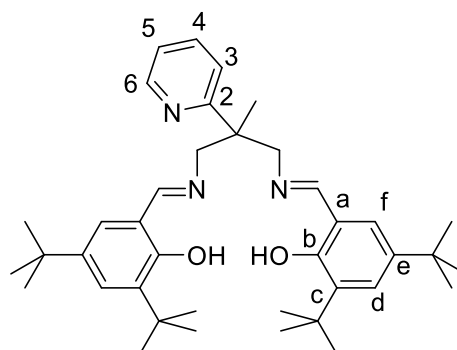
^1H NMR (CDCl_3 , 500 MHz, 298 K): δ 1.53 (3H, s, CH_3), 4.01 (2H, dd, $J = 12.3$ Hz, $J' = 1.2$ Hz, $2\text{CHH}'$), 4.13 (2H, dd, $J = 12.3$ Hz, $J' = 1.2$ Hz, $2\text{CHH}'$), 6.85 (2H, dt, $J = 7.4$ Hz, $J' = 1.1$ Hz, H^e), 6.90 (2H, ddd, $J = 8.3$ Hz, $J' = 1.0$ Hz, $J'' = 0.5$ Hz, H^f), 7.14 (1H, ddd, $J = 7.6$ Hz, $J' = 4.8$ Hz, $J'' = 1.1$ Hz, H^5), 7.20 (2H, dd, $J = 7.6$ Hz, $J' = 1.7$ Hz, H^c), 7.28 (2H, ddd, $J = 8.4$ Hz, $J' = 7.3$ Hz, $J'' = 1.8$ Hz, H^d), 7.34 (1H, dt, $J = 8.0$ Hz, $J' = 1.0$ Hz, H^3), 7.66 (1H, td, $J = 7.7$ Hz, $J' = 1.9$ Hz, H^4), 8.31 (2H, s, $2\text{N}=\text{CH}$), 8.63 (1H, ddd, $J = 4.8$ Hz, $J' = 1.9$ Hz, $J'' = 0.9$ Hz, H^6), 13.19 (2H, s, OH).



$^{13}\text{C}\{^1\text{H}\}$ NMR (CDCl_3 , 126 MHz, 298 K): δ 21.8 (CH_3), 46.3 (CCH_3), 67.2 (CH_2), 117.1 (C^f), 118.7 (C^e), 118.8 (C^a), 121.3 (C^3), 121.8 (C^5), 131.5 (C^c), 132.4 (C^d), 136.6 (C^4), 149.2 (C^6), 161.2 (C^b), 163.4 (C^2), 166.2 ($\text{N}=\text{CH}$).

7.2.2: 3,5-di-tert-butylsalpy (L-2). Yield = 79%

^1H NMR (CDCl_3 , 400 MHz, 298 K): δ 1.29 (18H, s, $2\text{C}(\text{CH}_3)_3$), 1.43 (18H, s, $2\text{C}'(\text{CH}_3)_3$), 1.57 (3H, s, CH_3), 4.06 (4H, s, 2CH_2), 7.05 (2H, d, $J = 2.5$ Hz, H^f), 7.15 (1H, ddd, $J = 7.6$ Hz, $J' = 4.8$ Hz, $J'' = 0.9$ Hz, H^5), 7.34-7.38 (3H, overlapping m, H^dH^3), 7.65 (1H, td, $J = 7.6$ Hz, $J' = 1.9$ Hz, H^4), 8.35 (2H, s, $2\text{N}=\text{CH}$), 8.63 (1H, ddd, $J = 4.8$ Hz, $J' = 1.9$ Hz, $J'' = 0.8$ Hz, H^6), 13.55 (2H, s, OH).



$^{13}\text{C}\{^1\text{H}\}$ NMR (CDCl_3 , 101 MHz, 298 K) δ 22.4 (CH_3), 29.5 ($\text{C}^e\text{C}(\text{CH}_3)_3$), 31.6 ($(\text{C}^c\text{C}(\text{CH}_3)_3)$), 34.2 ($\text{C}^c\text{C}(\text{CH}_3)_3$), 35.2 ($\text{C}^e\text{C}(\text{CH}_3)_3$), 46.3 ($\text{C}(\text{CH}_3)$), 67.0 (2CH_2), 118.0 (C^b), 121.4 (C^3), 121.6 (C^5), 126.1 (C^f), 127.0 (C^d), 136.5 (C^4), 136.7 (C^e), 140.0 (C^c), 149.1 (C^6), 158.2 (C^a), 163.8 (C^2), 167.3 ($\text{C}=\text{N}$).

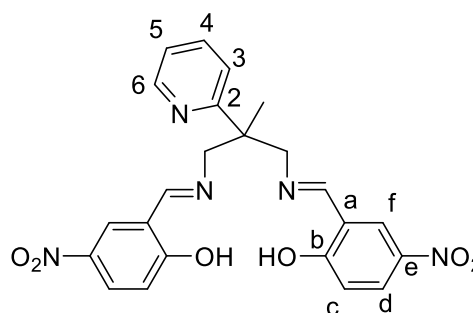
FT-IR ν_{max} / cm^{-1} 2954, 2906, 2870, 2357, 1624, 1590, 1470, 1439, 1433, 1389, 1362, 1335, 1269, 1251, 1234, 1202, 1173, 1033, 881, 855, 829, 791, 774, 752, 652.

ES-MS m/z : 598.44 ($[\text{M}+\text{H}]^+$, 100%), 299.72 ($[\text{M}+2\text{H}]^{2+}$, 21).

X-ray crystal structure and refinement data in Appendix.

7.2.3: 5-nitrosalpy (L-3). Yield = 42%

^1H NMR (CDCl_3 , 500 MHz, 298 K): δ 1.57 (3H, s, CH_3), 4.04 (2H, dd, $J = 12.4$ Hz, $J' = 0.9$ Hz, $2\text{CHH}'$), 4.22 (2H, dd, $J = 12.4$ Hz, $J' = 0.9$ Hz, $2\text{CHH}'$), 6.91 (2H, d, $J = 9.1$ Hz, H^c), 7.21 (1H, ddd, $J = 7.5$ Hz, $J' = 4.8$ Hz, $J'' = 1.0$ Hz, H^5), 7.32 (1H, dt, $J = 8.1$ Hz, $J' = 1.0$ Hz, H^3), 7.69 (1H, td, $J = 7.8$ Hz, $J' = 1.9$ Hz, H^4), 8.15 (2H, dd, $J = 9.1$ Hz, $J' = 2.8$ Hz, H^d), 8.17 (2H, d, $J = 2.6$ Hz, H^f), 8.32 (2H, s, $2\text{N}=\text{CH}$), 8.66 (1H, ddd, $J = 4.8$ Hz, $J' = 1.8$ Hz, $J'' = 0.9$ Hz, H^6), 14.35 (2H, s, 2OH).



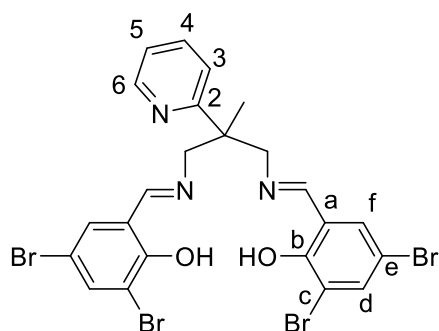
$^{13}\text{C}\{^1\text{H}\}$ NMR (CDCl_3 , 126 MHz, 298 K): δ 21.5 (CH_3), 46.3 ($\text{C}(\text{Me})$), 65.9 (CH_2), 116.8 (C^a), 119.1 (C^f), 121.3 (C^3), 122.4 (C^5), 128.4 (C^c/C^d), 128.5 (C^c/C^d), 137.1 (C^4), 139.1 (C^b), 149.5 (C^6), 161.7 (C^2), 165.5 ($\text{C}=\text{N}$), 169.0 (C^e).

FT-IR ν_{max} / cm^{-1} 3061, 2365, 1635, 1610, 1538, 1524, 1473, 1446, 1318, 1216, 1173, 1094, 1049, 938, 907, 833, 782, 754, 728, 701, 631.

ES-HRMS m/z : 464.1575 ($[\text{M}+\text{H}]^+$, 100%, Calc. 464.1570), 315.1465 ($[\text{M}-(\text{C}_6\text{H}_3(\text{OH})(\text{NO}_2)-\text{CH})+3\text{H}]^+$, 78).

3.1.7: 3,5-di-bromosalpy (L-4). Yield = 44%

^1H NMR (CDCl_3 , 500 MHz, 298 K): δ 1.54 (3H, s, CH_3), 4.02 (2H, dd, $J = 12.4$ Hz, $J' = 1.2$ Hz, $2\text{CHH}'$), 4.12 (2H, dd, $J = 12.4$ Hz, $J' = 1.2$ Hz, $2\text{CHH}'$), 7.14 (1H, ddd, $J = 7.5$ Hz, $J' = 4.8$ Hz, $J'' = 1.0$ Hz, H^5), 7.23 (2H, d, $J = 2.4$ Hz, H^f), 7.27 (1H, dt, $J = 8.0$ Hz, $J' = 1.0$ Hz, H^3), 7.63 (1H, td, $J = 7.8$ Hz, $J' = 1.9$ Hz, H^4), 7.64 (2H, d, $J = 2.4$ Hz, H^d), 8.12 (2H, s, $2\text{N}=\text{CH}$), 8.59 (1H, ddd, $J = 4.8$ Hz, $J' = 1.9$ Hz, $J'' = 0.9$ Hz, H^6), 14.2 (2H, s, 2OH).



$^{13}\text{C}\{^1\text{H}\}$ NMR (CDCl_3 , 126 MHz, 298 K): δ 21.6 (CH_3), 46.2 (CMe), 66.2 (CH_2), 109.4 (C^c), 112.6 (C^e), 119.8 (C^a), 121.2 (C^3), 122.1 (C^5), 132.9 (C^f), 137.0 (C^b), 137.9 (C^d), 149.3 (C^6), 158.5 (C^4), 161.9 (C^2), 164.8 ($\text{C}=\text{N}$).

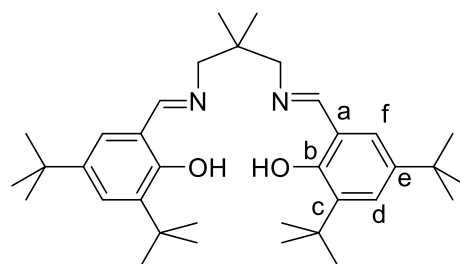
FT-IR ν_{max} / cm^{-1} 3744 (br), 2966, 2366, 2360, 2343, 1647, 1633, 1589, 1529, 1522, 1496, 1490, 1454, 1431, 1208, 1172, 1134, 1049, 984, 862, 852, 826, 748.

ES-HRMS m/z : 693.8226 ($[\text{M}(^{81}\text{Br}_4)+\text{H}]^+$, 17 %), 691.8240 ($[\text{M}(^{81}\text{Br}_3^{79}\text{Br})+\text{H}]^+$, 67), 689.8257 ($[\text{M}(^{81}\text{Br}_2^{79}\text{Br}_2)+\text{H}]^+$, 100), 687.8276 ($[\text{M}(^{81}\text{Br}^{79}\text{Br}_3)+\text{H}]^+$, 68), 685.8297 ($[\text{M}(^{79}\text{Br}_4)+\text{H}]^+$, 17, Calc. 685.8289), 429.9782 ($[\text{M}(^{81}\text{Br}_2)-(\text{C}_6\text{H}_2(\text{OH})\text{Br}_2)-\text{CH}]+3\text{H}]^+$, 18), 427.9801 ($[\text{M}(^{81}\text{Br}^{79}\text{Br})-(\text{C}_6\text{H}_2(\text{OH})\text{Br}_2)-\text{CH}]+3\text{H}]^+$, 35), 425.9821 ($[\text{M}(^{79}\text{Br}_2)-(\text{C}_6\text{H}_2(\text{OH})\text{Br}_2)-\text{CH}]+3\text{H}]^+$, 19).

X-ray crystal structure and refinement data in Appendix.

7.2.5: 1,3-Diamino-*N,N'*-bis(3,5-di-tert-butylsalicylidene)-2,2-dimethylpropane (L-5). Yield = 86%

^1H NMR (CDCl_3 , 400 MHz, 298 K): δ 1.10 (6H, s, 2CH_3), 1.31 (18H, s, $2\text{C}(\text{CH}_3)_3$), 1.47 (18H, s, $2\text{C}'(\text{CH}_3)_3$), 3.48 (4H, s, 2CH_2), 7.11 (2H, d, $J = 2.4$ Hz, $\text{H}^{d/f}$), 7.39 (2H, d, $J = 2.4$ Hz, $\text{H}^{d/f}$), 8.37 (2H, s, $2\text{N}=\text{CH}$), 13.86 (2H, s, OH).



$^{13}\text{C}\{^1\text{H}\}$ NMR (CDCl_3 , 101 MHz, 298 K): δ 24.7 (2CH_3), 29.6 ($2\text{C}'(\text{CH}_3)_3$), 31.6 ($2\text{C}(\text{CH}_3)_3$), 34.3 ($2\text{C}(\text{CH}_3)_3$), 35.2 ($2\text{C}'(\text{CH}_3)_3$), 36.5 (CMe_2), 68.2 (2CH_2), 118.0 ($\text{C}^{a/b}$), 126.1 ($\text{C}^{d/f}$), 127.4 ($\text{C}^{d/f}$), 137.0 (ArC^tBu), 140.3 (ArC^tBu), 158.4 ($\text{C}^{a/b}$), 167.0 ($\text{N}=\text{CH}$).

FT-IR ν_{max} / cm^{-1} 2954, 2903, 2867, 2360, 1631, 1609, 1466, 1439, 1387, 1378, 1361, 1355, 1345, 1274, 1251, 1208, 1201, 1173, 1081, 895, 879, 827, 801, 773, 730, 715, 644.

ES-MS m/z : 535.43 ($[\text{M}+\text{H}]^+$, 100 %), 268.22 ($[\text{M}+2\text{H}]^{2+}$, 8).

7.3: Synthesis and Characterisation of [Al(Salpy)Cl] Complexes

General procedure: Under an argon atmosphere, a solution of diethylaluminium chloride (1.0 eq., *ca.* 2.5 mmol) in hexanes (1M, *ca.* 2.5 mL) was added dropwise to an oven-dried Schlenk flask containing a stirring solution of salpy ligand (1.0 eq., *ca.* 2.5 mmol) in dry toluene (30 mL). The solution was stirred for 2 hours, after which the solvent was removed *in vacuo* to produce a yellow solid. This solid was reprecipitated by dissolution in the minimum amount of dry dichloromethane, before addition of dry hexanes. The product was then washed three times with dry hexanes (3 x *ca.* 15 mL) and dried to give a [Salpy-Al-Cl] complex. Crystals of sufficient quality for X-Ray Diffraction studies were grown by slow diffusion of hexanes into a concentrated dichloromethane solution. All solvent quantities were scaled in accordance with the amount of ligand used. Analytical data and yields for the prepared complexes are tabulated below.

7.3.1: [Salpy-Al-Cl] (**Al-1**). Yield = 86%

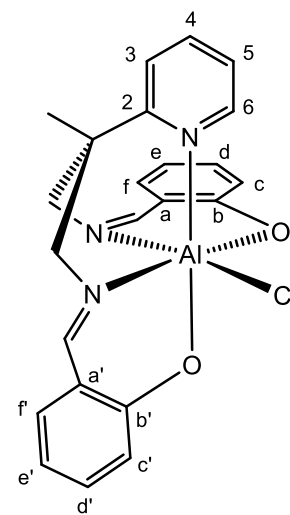
^1H NMR (500 MHz, CD_2Cl_2 , 298 K): δ 1.61 (3H, s, CH_3), 3.35-3.79 (2H, br s, CH_2), 3.94-4.45 (2H, br s, CH_2), 6.64 (2H, t, $J = 7.3$ Hz, Ar), 6.69-6.92 (2H, br s, Ar), 7.32 (2H, t, $J = 7.8$ Hz, Ar), 7.44 (2H, m, Ar), 7.28-7.58 (1H, br s, Ar), 7.65 – 8.25 (3H, br s, Ar), 7.88 (1H, td, $J = 7.8$ Hz, $J' = 1.8$ Hz, Ar), 9.32 (1H, dd, $J = 5.5$ Hz, $J' = 1.7$ Hz, H^6).

$^{13}\text{C}\{^1\text{H}\}$ NMR (298K): Limited solubility in a range of solvents precluded sensitive measurement of peaks.

IR: FT-IR ν_{max} / cm^{-1} 1637, 1620, 1609, 1546, 1473, 1449, 144, 1409, 1398, 1325, 1302, 1262, 1205, 1150, 1061, 1047, 897, 882, 778, 758, 760, 745, 724, 697, 648, 627, 590, 534, 483, 474, 466, 444, 431, 428, 420, 416, 409, 404.

MS: ES-HRMS m/z : 398.1452 ($[\text{M-Cl}]^+$, Calc. 398.1449 (0.8 PPM))

This data is consistent with that previously found within the group, where X-ray diffraction has confirmed the above structure.⁵



7.3.2: [3,5-di-tert-butylsalpy-Al-Cl] (**AI-2**). Yield = 87%

^1H NMR (500 MHz, CDCl_3 , 298 K): δ 0.96-1.59 (39H, br m, $4\times\text{C}(\text{CH}_3)_3$, CH_3), 3.09-3.69 (2H, br s, CH_2), 3.84-4.57 (2H, br s, CH_2), 6.87 (2H, br s, Ar), 7.34-7.43 (4H, br m, Ar, Py), 7.79 (1H, td, $J = 7.8$ Hz, $J' = 1.8$ Hz, H^4), 7.56-8.16 (2H, br s, $\text{N}=\text{CH}$), 9.68 (1H, ddd, $J = 5.5$ Hz, $J' = 1.8$ Hz, $J'' = 0.6$ Hz, H^6).

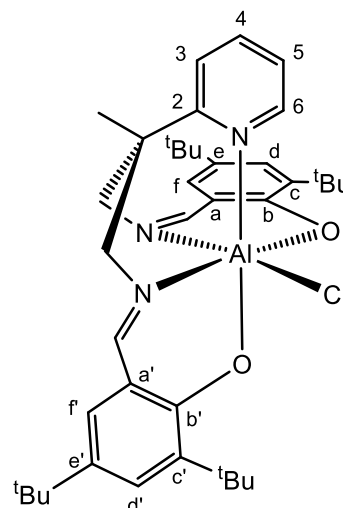
$^{13}\text{C}\{^1\text{H}\}$ NMR (126 MHz, CDCl_3 , 298 K): δ 22.2 (CH_3), 31.5 ($\text{C}(\text{CH}_3)_3$), 34.0 ($\text{C}(\text{CH}_3)_3$), 40.3 ($\underline{\text{C}}\text{CH}_3$), 119.1 (Ar), 122.9 (Ar), 126.7 (Ar), 136.8 (Ar), 139.3 (C^4), 152.3 (C^6), 161.1 (Ar), 163.9 (Ar).

FT-IR ν_{max} / cm^{-1} 2949, 1636, 1622, 1609, 1551, 1462, 1439, 1418, 1389, 1360, 1323, 1279, 1260, 1236, 1202, 1175, 1065, 1055, 1024, 843, 785, 752, 631, 579, 556, 511, 471, 444, 422.

Elemental Analysis Found: C, 70.5; H, 8.3; N, 6.0. Calc. for $\text{C}_{39}\text{H}_{53}\text{AlClN}_3\text{O}_2$: C, 71.2; H, 8.1; N, 6.4%.

ES-HRMS m/z : 622.3961 ($[\text{M}-\text{Cl}]^+$, Calc. 622.3953 (1.3 PPM))

X-ray crystal structure and refinement data in Appendix.

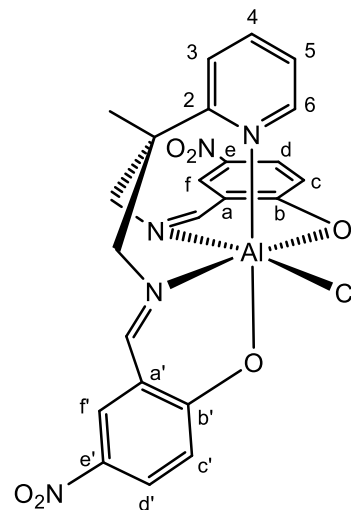


7.3.3: [5-nitrosalpy-Al-Cl] (**AI-3**). Yield = 83%

^1H NMR (500 MHz, CD_2Cl_2 , 298 K): δ 1.66 (3H, s, CH_3), 3.48 (1H, d, $J = 14.4$ Hz, $\underline{\text{C}}\text{HH}'$), 3.69 (1H, d, $J = 14.1$ Hz, $\text{C}^*\underline{\text{H}}\text{H}'$), 4.30 (1H, d, $J = 14.4$ Hz, CHH') 4.37 (1H, d, $J = 14.1$ Hz, $\text{C}^*\underline{\text{H}}\text{H}'$), 6.62 (1H, d, $J = 9.4$ Hz, H^c), 7.00 (1H, d, $J = 9.3$ Hz, $\text{H}^{c'}$), 7.51-7.55 (2H, m, H^3H^5), 7.88 (1H, br s, $\text{N}=\text{CH}$), 7.98 (1H, td, $J = 7.9$ Hz, $J' = 1.8$ Hz, H^4), 8.14 (2H, m, $\text{H}^{f'}$, H^d), 8.20 (1H, dd, $J = 9.3$ Hz, $J' = 2.8$ Hz, $\text{H}^{d'}$), 8.25-8.28 (2H, m, $\text{N}=\text{C}^*\text{H}$, H^f), 9.30 (1H, ddd, $J = 5.6$ Hz, $J' = 1.7$ Hz, $J'' = 0.6$ Hz, H^6).

$^{13}\text{C}\{^1\text{H}\}$ NMR (126 MHz, CD_2Cl_2 , 298 K): δ 22.2 (CH_3), 40.6 ($\underline{\text{C}}\text{Me}$), 64.6 (CH_2), 69.0 (C^*H_2), 119.0 (Ar-C), 120.8 (C^3/C^5), 122.9 (C^c), 123.2 ($\text{C}^{c'}$) 124.3 (C^3/C^5), 130.5 (Ar-C), 130.7 (Ar-C), 130.8 (Ar-C), 131.0 (Ar-C), 137.8 (Ar-C), 141.1 (C^4), 151.6 (C^6), 160.7 (Ar-C), 166.7 ($\text{N}=\text{C}$), 167.2 ($\text{N}=\text{C}^*$), 169.6 (Ar-C), 171.6 (Ar-C), 171.7 (Ar-C), 179.5 (Ar-C).

FT-IR ν_{max} / cm^{-1} 2922 (br), 1632, 1607, 1558, 1490, 1472, 1398, 1313, 1245, 1098, 946, 841, 811, 787, 758, 709, 661.



ES-HRMS m/z : 524.0916 ($[M+H]^+$, Calc. 524.0917, 12 %), 488.1173 ($[M-Cl]^-$, 100), 398.1451 (49).

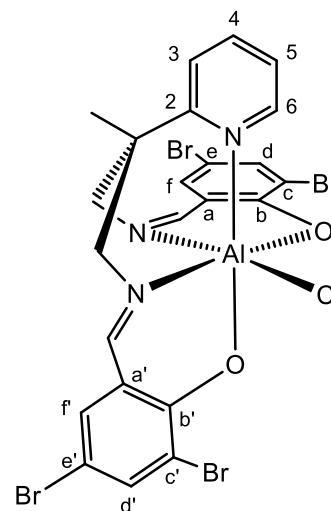
Elemental Analysis Found: C, 51.5; H, 4.6; N, 11.7. Calc. for $C_{23}H_{19}AlClN_5O_6$: C, 52.7; H, 3.7; N, 13.4%.

X-ray crystal structure and refinement data in Appendix.

7.3.4: [3,5-dibromosalpy-Al-Cl] (**AI-4**). Yield = 58%

1H NMR (500 MHz, DMSO- d_6 , 298 K): δ 8.65 (1H, d, $J = 5.3$ Hz, H^6), 8.61 (1H, s, N=CH'), 8.22 (1H, app t, $J = 7.8$ Hz, H^4), 8.19 (1H, s, N=CH), 7.86 (2H, m, H^dH^d'), 7.79 (1H, d, $J = 8.1$ Hz, H^3), 7.77 (1H, d, $J = 2.1$ Hz, $H^{b'}$), 7.74 (1H, app t, $J = 6.6$ Hz, H^5), 7.56 (1H, d, $J = 2.2$ Hz, H^b), 4.42 (1H, d, $J = 14.9$ Hz, C^dH), 4.07 (1H, d, $J = 14.7$ Hz, C^eH), 3.94 (1H, d, $J = 14.9$ Hz, C^fH), 3.70 (1H, d, $J = 14.9$ Hz, CHH), 1.58 (3H, s, CH_3).

$^{13}C\{^1H\}$ NMR (126 MHz, DMSO- d_6 , 298 K) δ 170.5 (N=C'H), 167.5 (N=CH), 161.4 (C^2), 159.9 (C^3), 159.0 ($C^{3'}$), 148.1 (C^6), 141.6 (C^4), 139.0 ($C^{d'}$), 138.4 (C^d), 134.8 ($C^{b'}$), 134.5 (C^b), 124.1 (C^5), 122.0 (C^f), 121.8 (C^3), 121.4 ($C^{f'}$), 116.4 (C^e), 116.3 ($C^{e'}$), 106.1 ($C^{c'}$), 105.7 (C^c), 66.5 (C^fH_2), 61.8 (CH_2), 39.4 (CMe), 20.7 (Me).



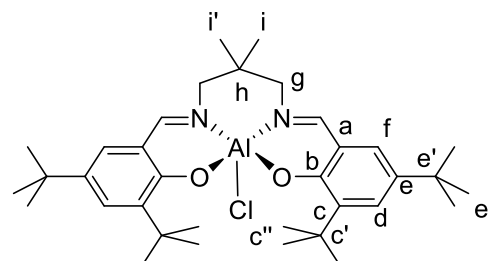
FT-IR ν_{max} / cm^{-1} 1641, 1626, 1609, 1520, 1482, 1467, 1450, 1362, 1319, 1216, 1164, 1062, 1049, 991, 862, 787, 752, 718, 700, 649, 600, 564, 540, 521, 487, 475, 455, 445, 422, 418, 412, 408, 403.

ES-HRMS m/z : 713.7830 ($[M(^{79}Br_2^{81}Br_2) - Cl]^+$, Calc. 713.7829 (0.1 PPM))

7.3.5: [3,5-di-tert-butylsalpn-Al-Cl] (**AI-5**). Yield = 86%

1H NMR ($CDCl_3$, 500 MHz, 298 K): δ 8.19 (2H, s, N=CH), 7.57 (2H, d, $J = 2.6$ Hz, H^d), 7.09 (2H, d, $J = 2.6$ Hz, H^f), 3.68 (2H, d, $J = 12.5$ Hz, H^g), 3.31 (2H, d, $J = 12.5$ Hz, $H^{g'}$), 1.53 (18H, s, $H^{c''}$), 1.31 (18H, s, $H^{e''}$), 1.18 (3H, s, H^i), 1.07 (3H, s, $H^{i'}$).

^{13}C NMR ($CDCl_3$, 126 MHz, 298 K): δ 171.6 (N=CH), 162.8 (C^b), 141.2 (C^c), 139.0 (C^e), 131.4 (C^d), 127.4 (C^f), 118.3 (C^a), 67.4 (C^g), 36.5 (C^h), 35.7 ($C^{c'}$), 34.2 ($C^{e'}$), 31.5 ($C^{e''}$), 29.8 ($C^{c''}$), 26.4 ($C^{i'}$), 25.7 (C^i).



FT-IR ν_{max} / cm^{-1} 2954, 1620, 1544, 1417, 1345, 1314, 1257, 1238, 1179, 1086, 878, 864, 842, 786, 752, 640, 627, 601, 570, 532, 503, 477, 448, 429, 419, 413, 409, 402.

ES-MS m/z : 559.3842 ($[M-Cl]^+$, Calc. 559.3844 (0.4 PPM))

X-ray crystal structure confirmed connectivity but was highly disordered.

7.4: Synthesis and Characterisation of *ansa*-Zirconocene Complexes

7.4.1: $[Cp_2SiMe_2]Li_2$

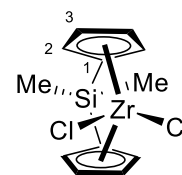
Lithium cyclopentadienide (1 eq., 13.9 mmol, 1.00 g) was added to an oven dried Schlenk flask fitted with a magnetic stirrer bar and cooled to $-78\text{ }^\circ\text{C}$. Anhydrous THF (15 mL) was then added to give a brown solution, before Cl_2SiMe_2 (0.5 eq., 6.9 mmol, 0.84 mL) was added. The reaction was maintained at $-78\text{ }^\circ\text{C}$ for 1 hour, before slow warming to room temperature and eventual concentration *in vacuo* to a volume of *c.a.* 5 mL. Dry hexanes (*c.a.* 50 mL) were then added to precipitate a large volume of colourless solid, and the flask was the frozen to ensue full precipitation. The mixture was the filtered, and the dark solution was concentrated once more, before addition of a further 10 mL of dry THF and cooling to $-78\text{ }^\circ\text{C}$. $^n\text{BuLi}$ (2.5 M solution in hexanes, 1.1 eq., 15.3 mmol, 6.1 mL) was then added dropwise, which led to solid precipitation. The suspension was stirred at $-78\text{ }^\circ\text{C}$ for one hour before being allowed to warm to room temperature. Once warmed, the suspension was filtered, and the solid washed with 3 x 15 mL dry hexane. The brown solid was then dried *in vacuo* to give a powder (847 mg, 70%). Due to the insolubility of the lithiated product in non-halogenated solvents (C_6D_6 , THF- d^8) no NMR analysis was possible, which is typical for the nature of the product.

7.4.2: $[Cp_2SiMe_2ZrCl_2]$ (**Zr-1**)

$[Cp_2SiMe_2]Li_2$ (1 eq., 4.19 mmol, 839 mg) was added to an oven dried Schlenk flask fitted with a magnetic stirrer bar alongside $[ZrCl_4(THF)_2]$ (0.95 eq., 3.98 mmol, 1.501 g) and cooled to $-78\text{ }^\circ\text{C}$. Dry dimethoxyethane (25 mL) was then slowly added to give a muddy brown suspension, and after one hour the reaction mixture was allowed to warm to room temperature. The reaction flask was then placed under static vacuum and heated to $70\text{ }^\circ\text{C}$ in an oil bath and left overnight. The resulting reaction mixture was concentrated and then extracted with three 5 mL portions of dry dichloromethane. Addition of 15 mL hexanes led to the formation of a dark sticky precipitate and a yellow supernatant, which was collected and stored at $-18\text{ }^\circ\text{C}$ overnight, at which point a pale precipitate had formed. This was isolated by filtration, washed with $-9\text{ }^\circ\text{C}$ (ice/brine) pentane, and dried *in vacuo*. The title compound was isolated as a pale yellow solid (124 mg, 9%).

^1H NMR (500 MHz, CDCl_3 , 298 K): δ 0.76 (6H, s, SiMe_2), 5.98 (t, 4H, $J = 2.4$ Hz, H^2), 6.97 (t, 4H, $J = 2.4$ Hz, H^3).

$^{13}\text{C}\{^1\text{H}\}$ NMR (126 MHz, CDCl_3 , 298 K): δ 128.7 (C^3), 114.4 (C^2), 109.3 (C^1), -5.0 (SiMe_2).



7.4.3: $[\text{Ind}_2\text{SiMe}_2]\text{Li}_2$

Indene (1 eq., 22.7 mmol, 2.64 g, 2.65 mL) was added to an oven dried Schlenk flask fitted with a magnetic stirrer bar and cooled to -78 °C. Anhydrous THF (40 mL) was then added, before $^n\text{BuLi}$ (2.5 M solution in hexanes, 1.1 eq., 25.0 mmol, 10.0 mL) was added dropwise. The reaction was maintained at -78 °C for 1 hour, before warming to room temperature to give a deep red/purple solution which was stirred overnight. The reaction was then again cooled to -78 °C before Cl_2SiMe_2 (0.5 eq., 12.5 mmol, 1.50 mL) was added, and was maintained at -78 °C for 1 hour, before slow warming to room temperature and eventual concentration *in vacuo* to a volume of *c.a.* 5 mL. Dry hexanes (*c.a.* 50 mL) were then added to precipitate a large volume of colourless solid, and the flask was the frozen to ensue full precipitation. The mixture was the filtered, and the solid washed with two portions of hexanes (10 mL). The solution was concentrated to *c.a.* 10 mL, before addition of a further 10 mL of dry THF and cooling to -78 °C. $^n\text{BuLi}$ (2.5 M solution in hexanes, 1.1 eq., 15.3 mmol, 6.1 mL) was then added dropwise, which led to solid precipitation. The suspension was stirred at -78 °C for one hour before being allowed to warm to room temperature. Once warmed, the suspension was concentrated, and further precipitation was induced by the addition of hexanes (*c.a.* 50 mL), with the solid then washed with 3 x 15 mL dry hexane. The solid was then stored at -18 °C overnight, and then dried *in vacuo* to give a dark purple powder (2.542g, 74%). Due to the insolubility of the lithiated product in non-halogenated solvents (C_6D_6 , THF-d^8) no NMR analysis was possible.

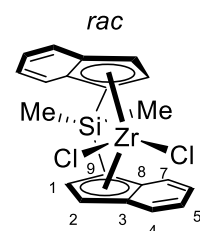
7.4.4: *rac*- $[\text{Ind}_2\text{SiMe}_2\text{ZrCl}_2]$ (**Zr-2**)

$[\text{Ind}_2\text{SiMe}_2]\text{Li}_2$ (0.95 eq., 3.03 mmol, 1.000 g) was added to an oven dried Schlenk flask fitted with a magnetic stirrer bar alongside $[\text{ZrCl}_4(\text{THF})_2]$ (1 eq., 3.19 mmol, 1.202 g) and cooled to -78 °C. Dry dimethoxyethane (25 mL) was then slowly added to give a muddy brown suspension, and after one hour the reaction mixture was allowed to warm to room temperature. The reaction flask was then placed under static vacuum, and heated to 70 °C in an oil bath, and left overnight. The resulting reaction mixture was concentrated and then extracted with three 5 mL portions of dry dichloromethane, with the combined extracts dried *in vacuo* to give an orange solid. This solid was extracted with 3x10 mL portions of hot toluene, which was then cooled to -18 °C, and the solid

precipitate isolated and washed with -78 °C pentane, before being dried *in vacuo* and isolated as a bright orange solid (29 mg, 3 %) as the *rac* isomer.

^1H NMR (500 MHz, CDCl_3 , 298 K): δ 1.14 (6H, s, SiMe_2), 6.11 (2H, d, $J = 3.3$ Hz, H^1), 6.93 (2H, dd, $J = 3.3$ Hz, $J' = 0.9$ Hz, H^2), 7.10 (2H, ddd, $J = 8.7$ Hz, $J' = 6.7$ Hz, $J'' = 1.0$ Hz, H^5), 7.37 (2H, ddd, $J = 8.6$ Hz, $J' = 6.7$ Hz, $J'' = 0.9$ Hz, H^6), 7.51 (2H, ddd, $J = 8.7$ Hz, $J' = 1.9$ Hz, $J'' = 0.9$ Hz, H^4), 7.60 (2H, dt, $J = 8.6$ Hz, $J' = 1.0$ Hz, H^7).

$^{13}\text{C}\{^1\text{H}\}$ NMR (126 MHz, CDCl_3 , 298 K): δ 133.7 (C^3), 127.7 (C^6), 127.1 (C^5), 126.4 (C^8), 126.3 (C^7), 124.4 (C^4), 118.1 (C^2), 117.6 (C^1), 89.6 (C^9), -1.4 (SiMe_2).



7.5: Thiol-ene Click Post-Polymerisation Modification

7.5.1: Synthetic Procedure for Thiol-ene Click Modification

For each thiol (T1-T5) poly(LO-*alt*-PA) (300.4 mg, 1 mmol) and azobisisobutyronitrile (AIBN, 108.4 mg, 0.66 mmol) were added to an oven-dried Schlenk flask fitted with a magnetic stirrer bar, placed under an argon atmosphere, and filled with dry THF, dry DMF, or DMSO (5 mL). Thiol (5 mmol) was then added, before the Schlenk flask was placed under a static vacuum. The reaction was heated to 70 °C overnight, with the product precipitated into water. The polymeric material was then washed with water, a reprecipitated from THF/ H_2O , DCM/hexanes, or DCM/isopropanol as appropriate. The polymers were dried in a vacuum oven, with isolated yields listed below. For 1,6-hexanedithiol reactions, the amount of polymer and AIBN remained the same as for the monothiols.

Isolated Yields of Successfully Modified Polymers:

T2 – 2-Mercaptoethanol – 30%

T3 – 3-mercaptopropionic acid – 65%

T4 – 1-hexanethiol – 35%

10% Hexanedithiol – 79%

20% Hexanedithiol – 60%

30% Hexanedithiol – 69%

50% Hexanedithiol – 59% - Purity could not be assessed by ^1H NMR Spectroscopy

7.5.2: NMR Spectra of Thiol-ene Click Modified Polymers

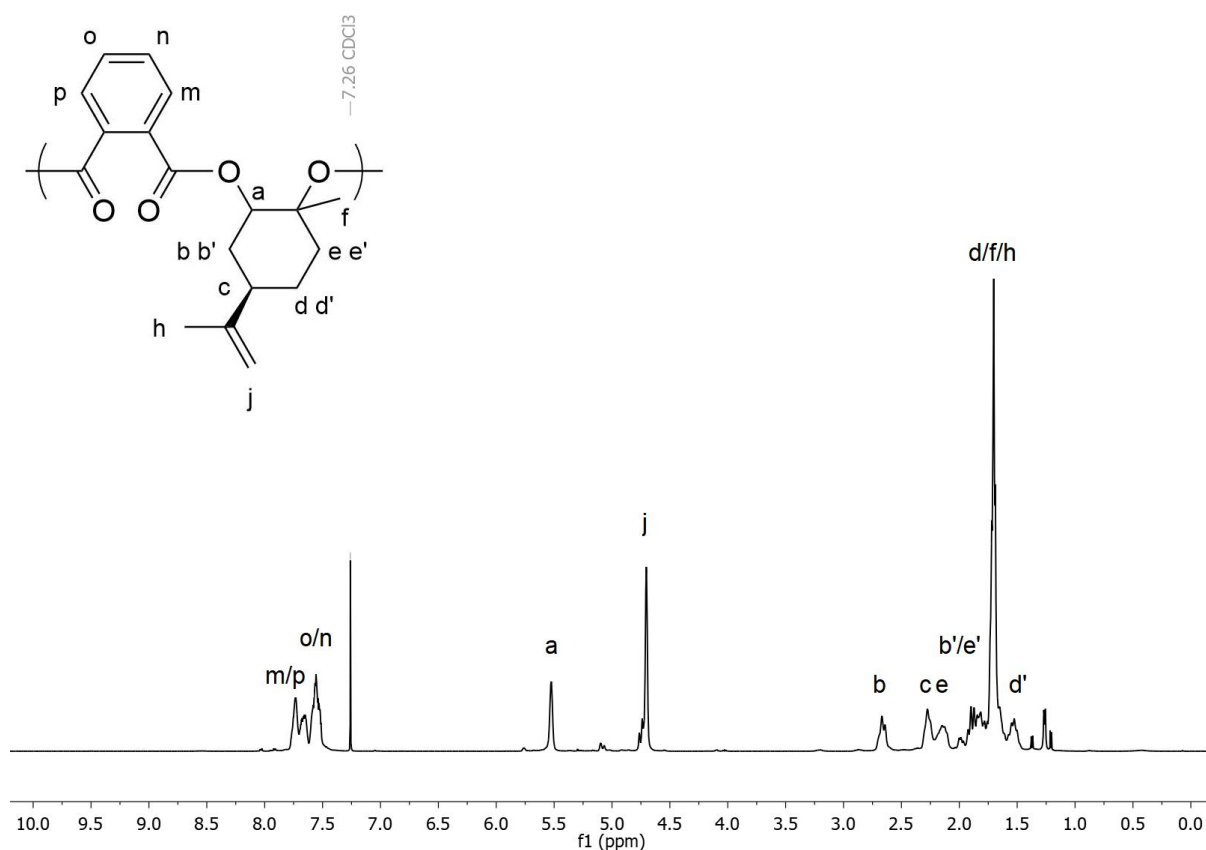


Figure 7.1: ^1H NMR spectrum (CDCl₃, 500 MHz) of unmodified poly(LO-*alt*-PA).

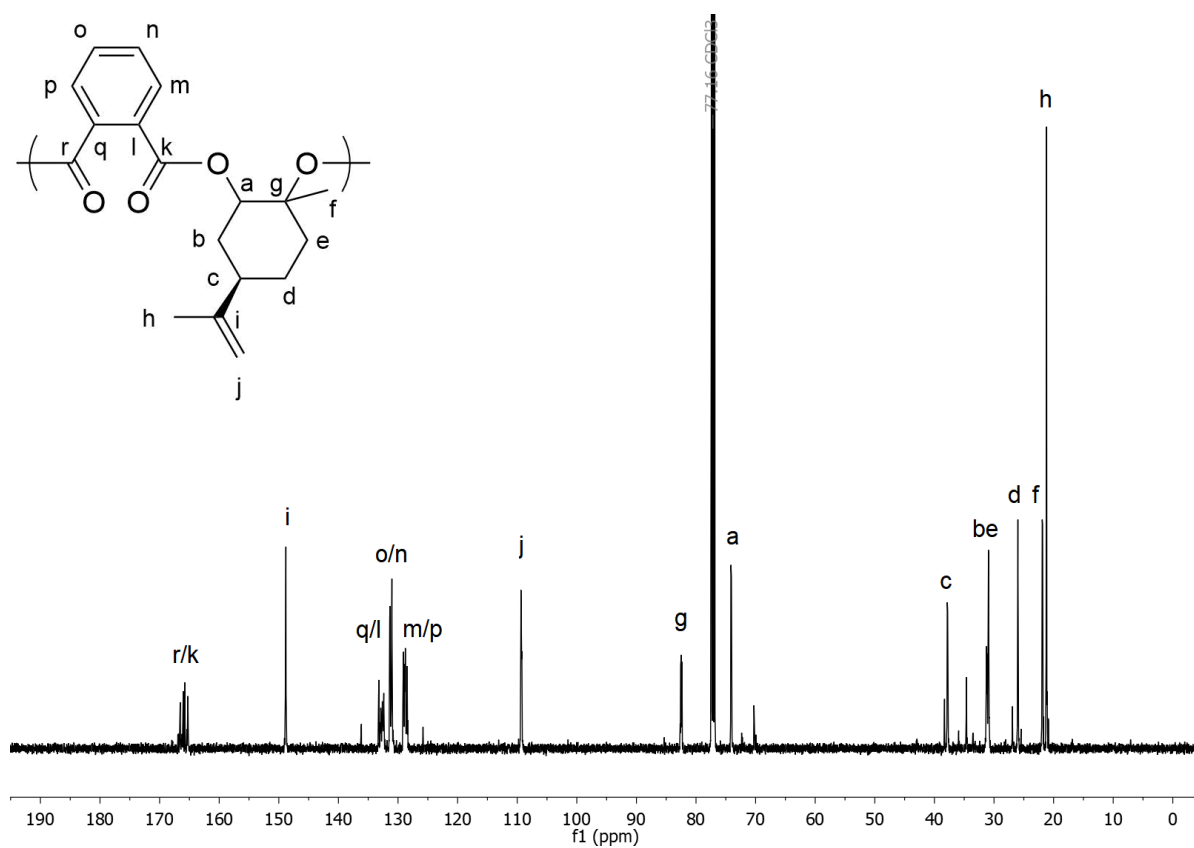


Figure 7.2: $^{13}\text{C}\{^1\text{H}\}$ NMR spectrum (CDCl₃, 126 MHz) of unmodified poly(LO-*alt*-PA).

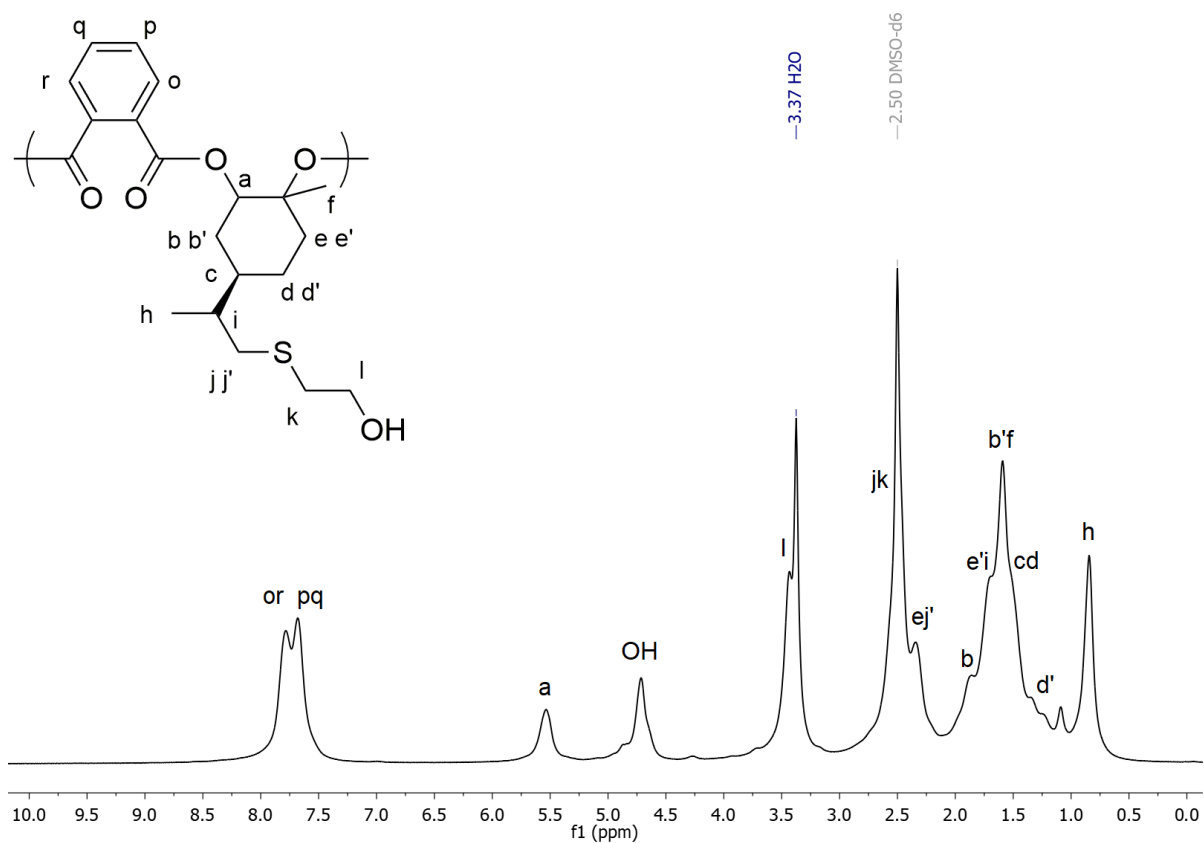


Figure 7.3: ^1H NMR spectrum (DMSO- d_6 , 500 MHz) of 2-mercaptoethanol (T2) modified poly(LO-*alt*-PA).

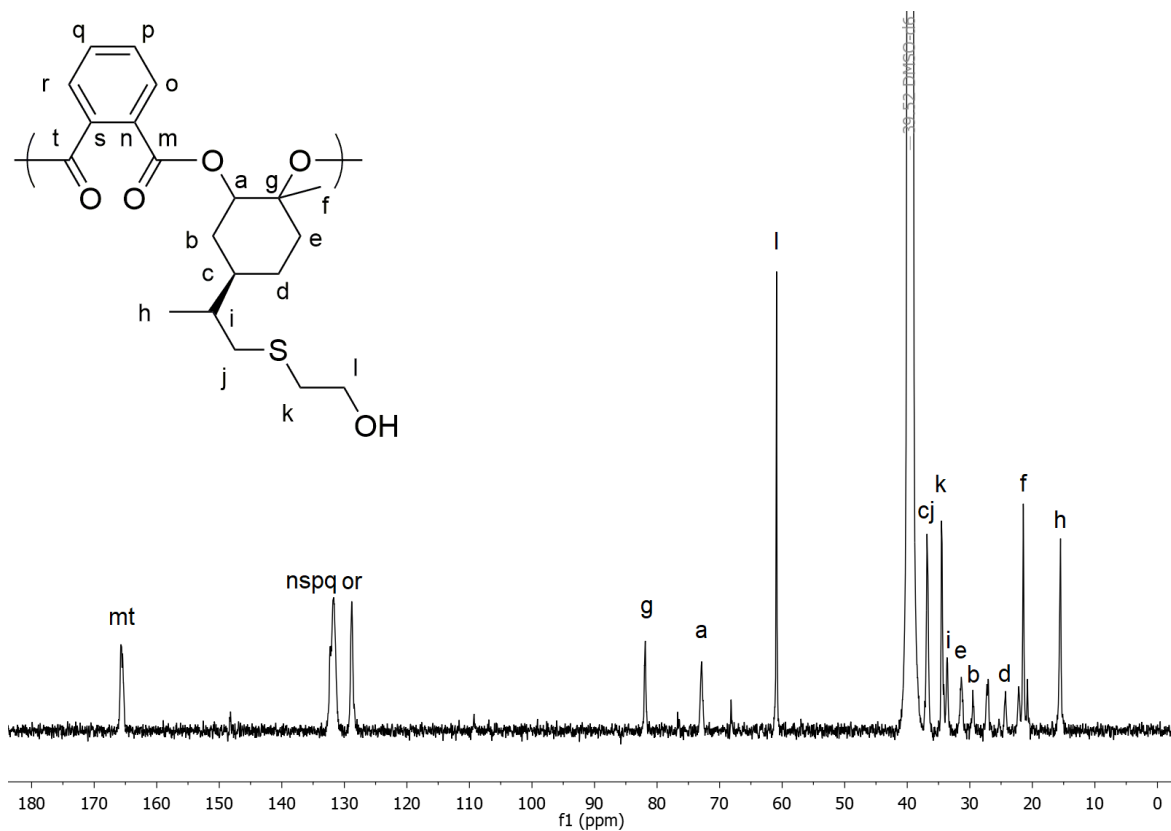


Figure 7.4: $^{13}\text{C}\{^1\text{H}\}$ NMR spectrum (DMSO- d_6 , 126 MHz) of 2-mercaptoethanol (T2) modified poly(LO-*alt*-PA).

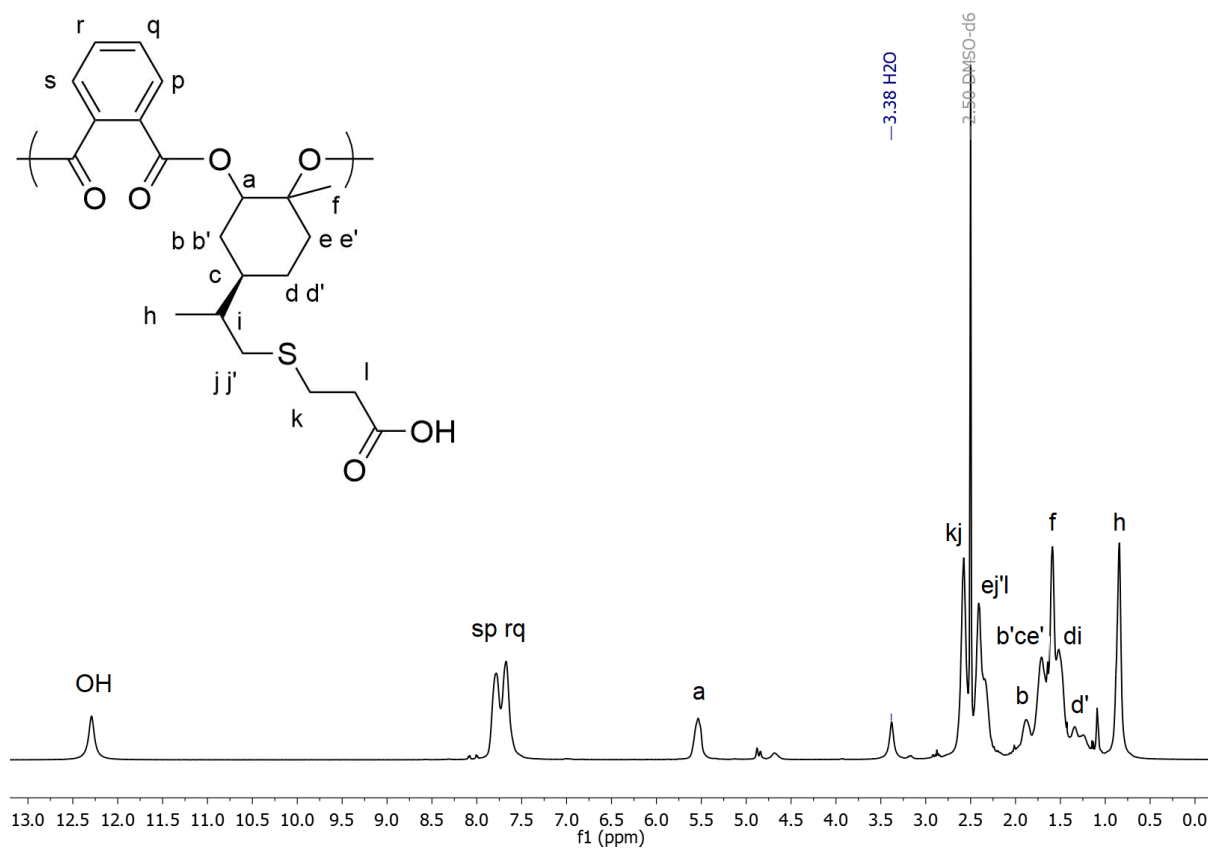


Figure 7.5: ^1H NMR spectrum (DMSO-d_6 , 500 MHz) of 3-mercaptopropionic acid (T3) modified poly(LO-*alt*-PA).

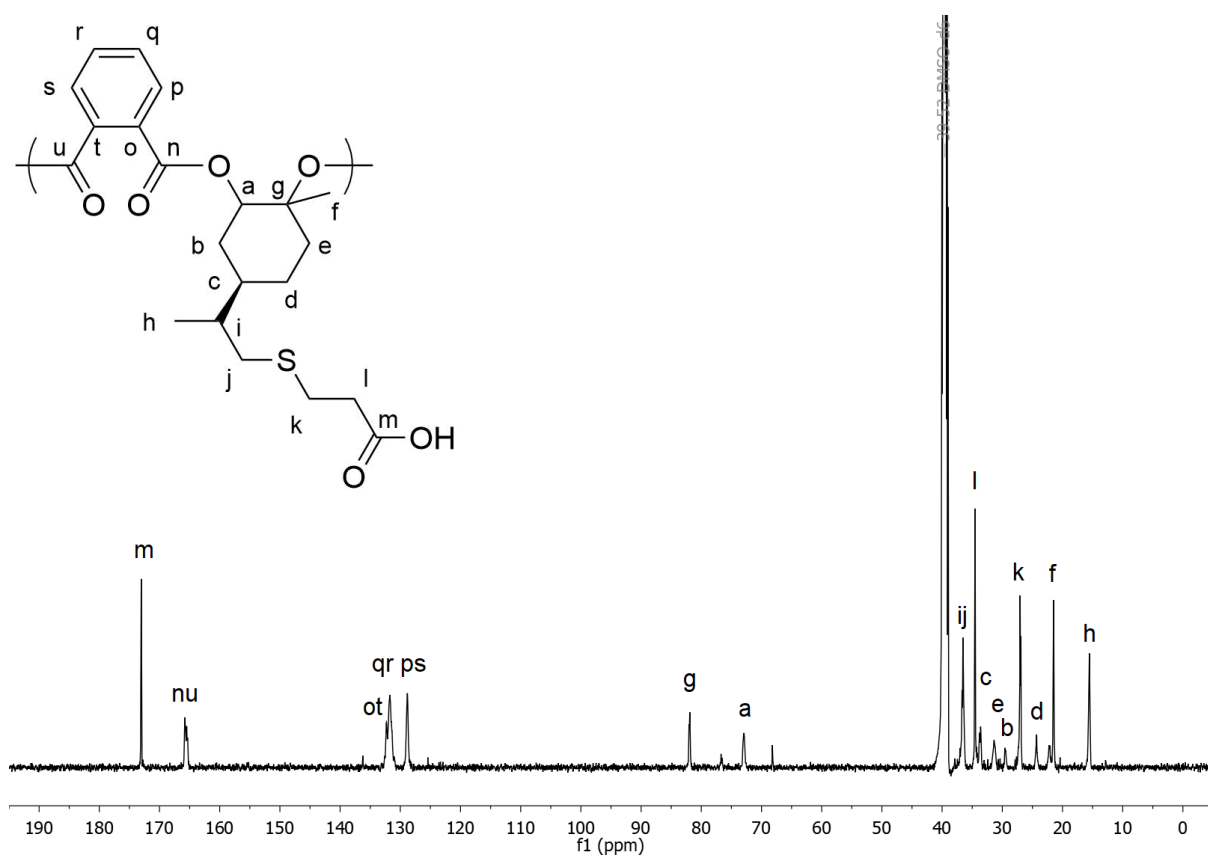


Figure 7.6: $^{13}\text{C}\{^1\text{H}\}$ NMR spectrum (DMSO-d_6 , 126 MHz) of 3-mercaptopropionic acid modified poly(LO-*alt*-PA).

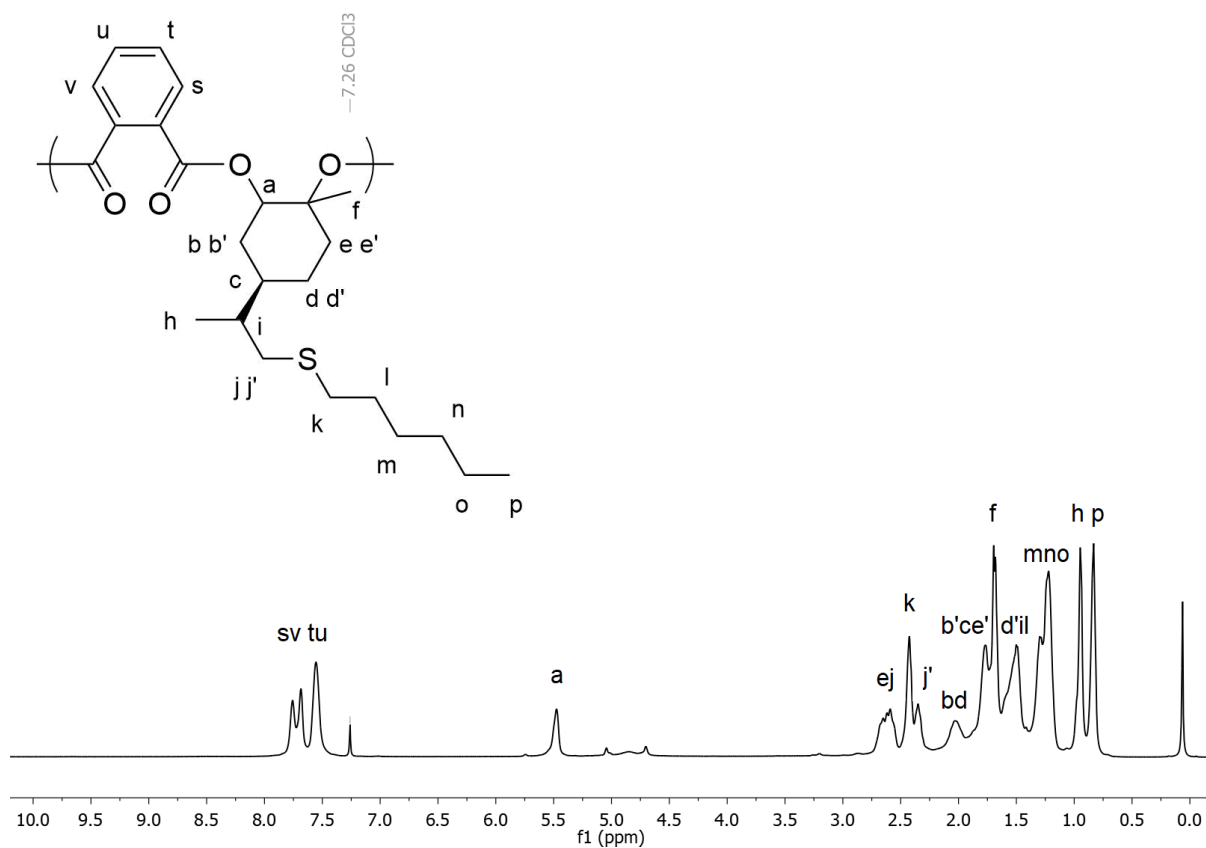


Figure 7.7: ^1H NMR spectrum (CDCl₃, 500 MHz) of 1-hexanethiol (T4) modified poly(LO-*alt*-PA).

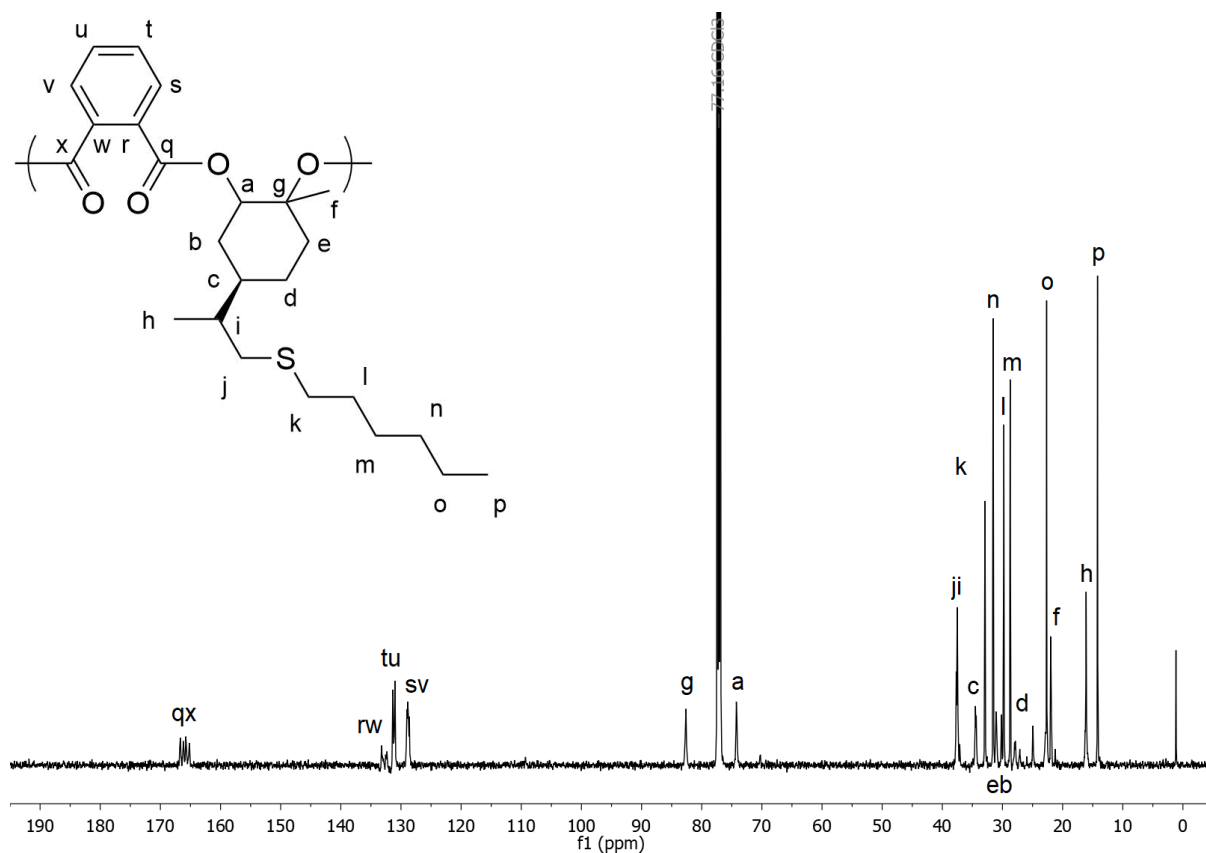


Figure 7.8: $^{13}\text{C}\{^1\text{H}\}$ NMR spectrum (CDCl₃, 126 MHz) of 1-hexanethiol (T4) modified poly(LO-*alt*-PA).

7.6: Hydroboration-Oxidation and Phosphorylation of poly(LO-*alt*-PA)

Hydroboration-Oxidation

Hydroboration-Oxidation of poly(LO-*alt*-PA) was performed as described using a procedure reported by Williams and co-workers.⁶ In an argon atmosphere, poly(LO-*alt*-PA) (1 eq., 10 mmol, 3.004 g) was dissolved in anhydrous THF (30 mL) in a Schlenk flask. A solution of 9-Borabicyclo[3.3.1]nonane (9-BBN, 0.5 M in THF, 1.5 eq., 15 mmol) was then added, and the reaction was stirred at room temperature for 2 hours. After this time, methanol (0.2 mL) was added, before the solution was cooled in an ice bath and *meta*-chloroperoxybenzoic acid (mCPBA 75% by mass, 5.0 eq., 50 mmol, 11.5 g) added, leading to effervescence. The solution was maintained at 0 °C for 15 minutes, before further stirring at room temperature for 2 hours. A 10:1 v/v methanol: water mixture (10 mL) was then added dropwise, and the reaction mixture concentrated to *c.a.* 10 mL. Polymer was then precipitated by adding the reaction mixture (in air) to saturated NaHCO₃ (150 mL) solution. The polymer was washed with further NaHCO₃ solution and sodium metabisulfite solution, before drying *in vacuo*. Yield = 84%.

Phosphorylation – for 100% attempted conversion. For 75, 50 and 25% attempted conversions, all quantities except polymer and solvent were scaled accordingly.

Poly(OH) (210.1 mg, 0.66 mmol, 1 eq.) was dissolved in dichloromethane (25 mL), before addition of a dichloromethane solution of *N*-methylimidazole (2.5 mol%, 50 μL of a solution comprising 13.2 μL *N*-methylimidazole in 500 μL DCM) triethylamine (184.0 μL, 1.32 mmol, 2 eq.) and diphenyl phosphoryl chloride (273.6 μL, 1.32 mmol, 2 eq.), and left to stir at room temperature overnight. Methanol (2 mL) was added to quench the reaction, which was then dried *in vacuo* before repeated reprecipitations from saturated solutions of dichloromethane and tetrahydrofuran into hexanes and water respectively. This was repeated until there was only one major resonance in the ³¹P{¹H} NMR spectrum ($\delta^P = -11.8$).

Isolated Yields of Phosphorylated Polymers:

Poly(OP_83) – 39%

Poly(OP_41) – 62%

Poly(OP_23) – 66%

Poly(OP_12) – 53%

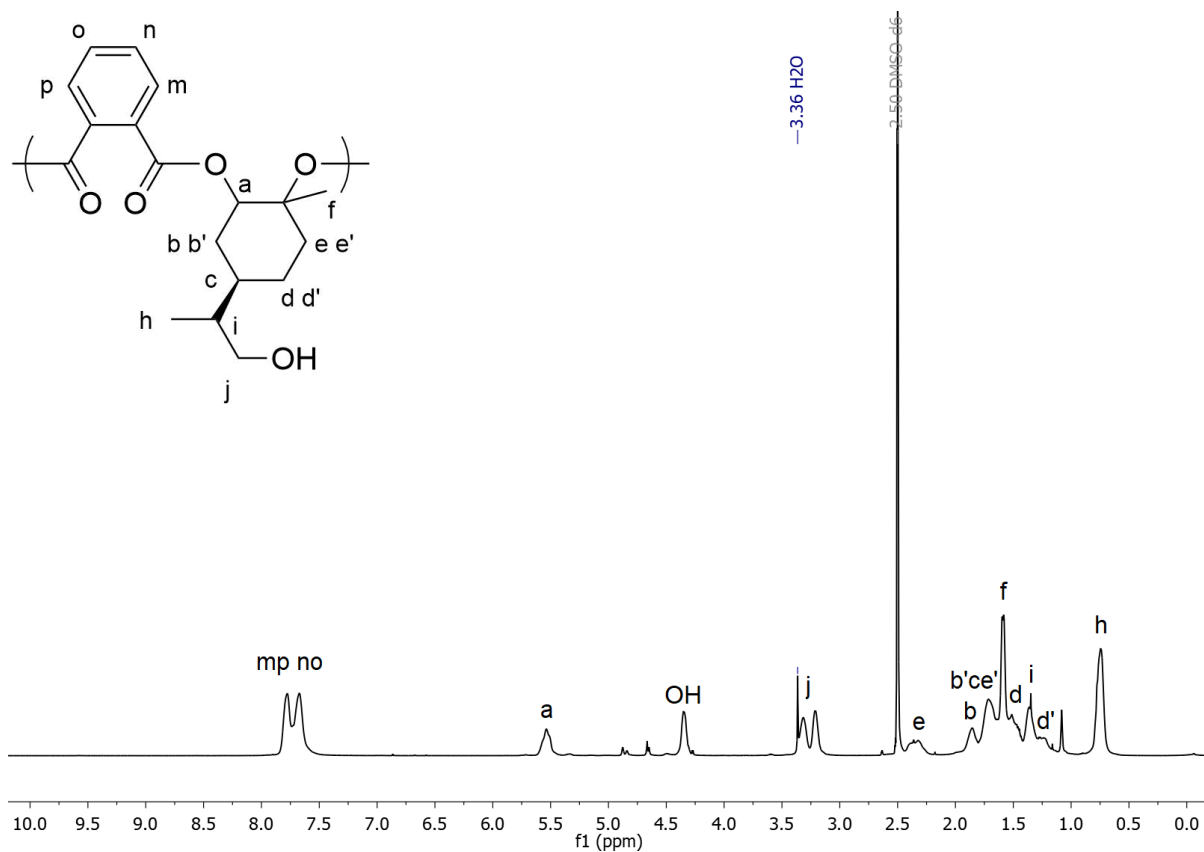


Figure 7.9: ^1H NMR spectrum (DMSO-d_6 , 500 MHz) of poly(OH).

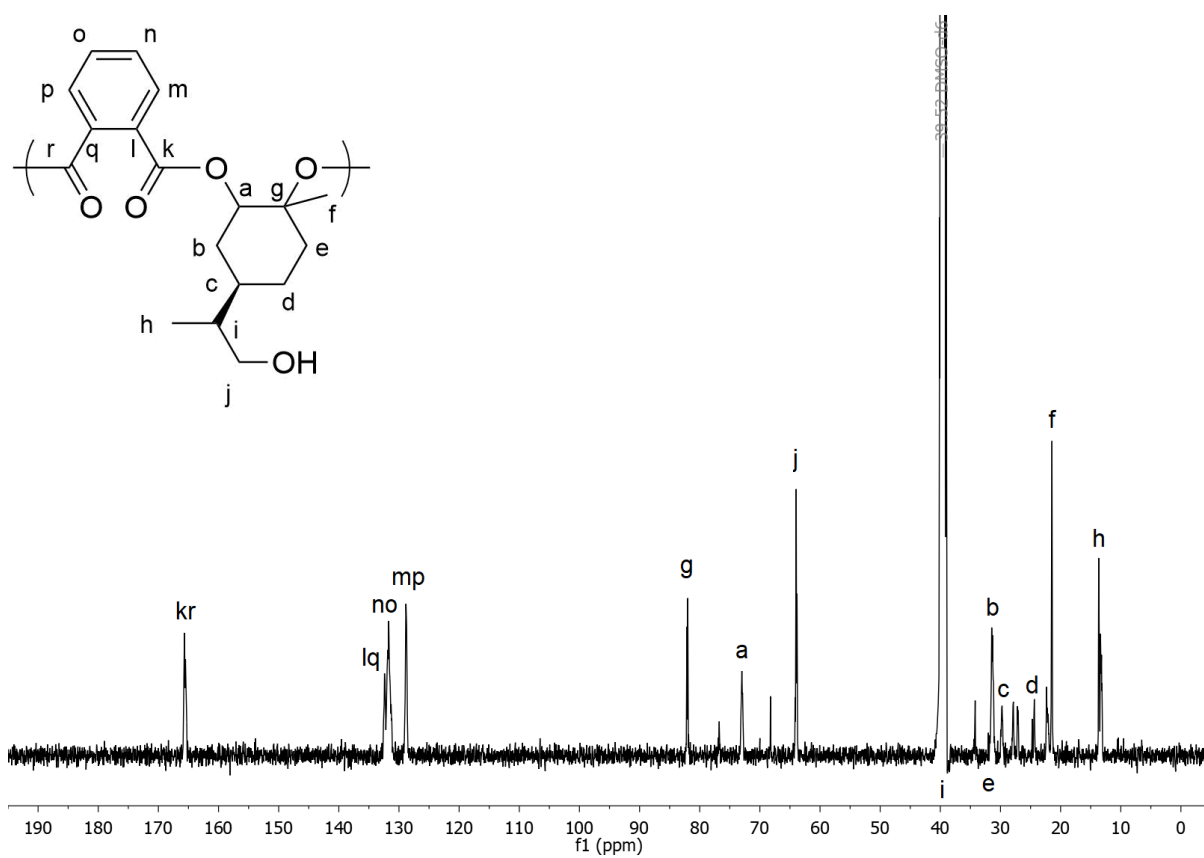


Figure 7.10: $^{13}\text{C}\{^1\text{H}\}$ NMR spectrum (DMSO-d_6 , 126 MHz) of poly(OH).

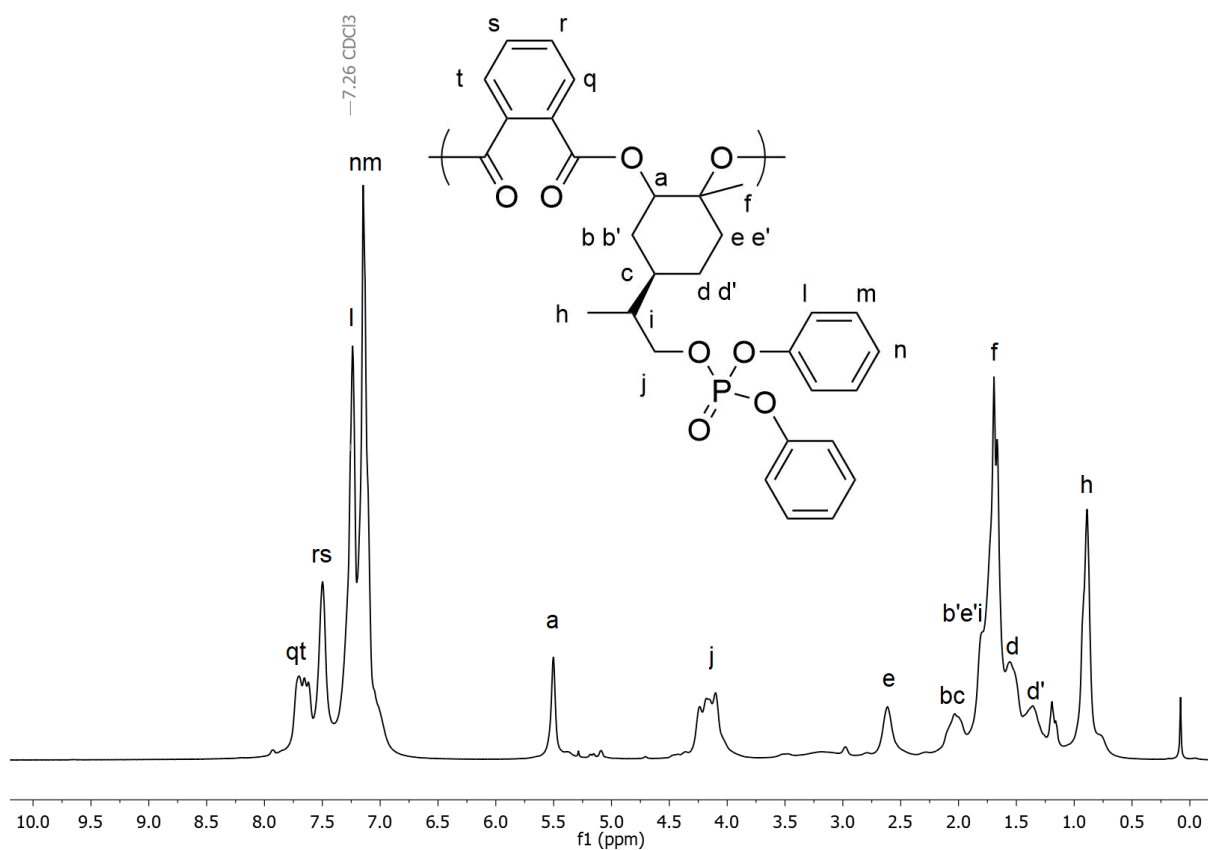


Figure 7.11: ^1H NMR spectrum (CDCl_3 , 500 MHz) of poly(OP-83).

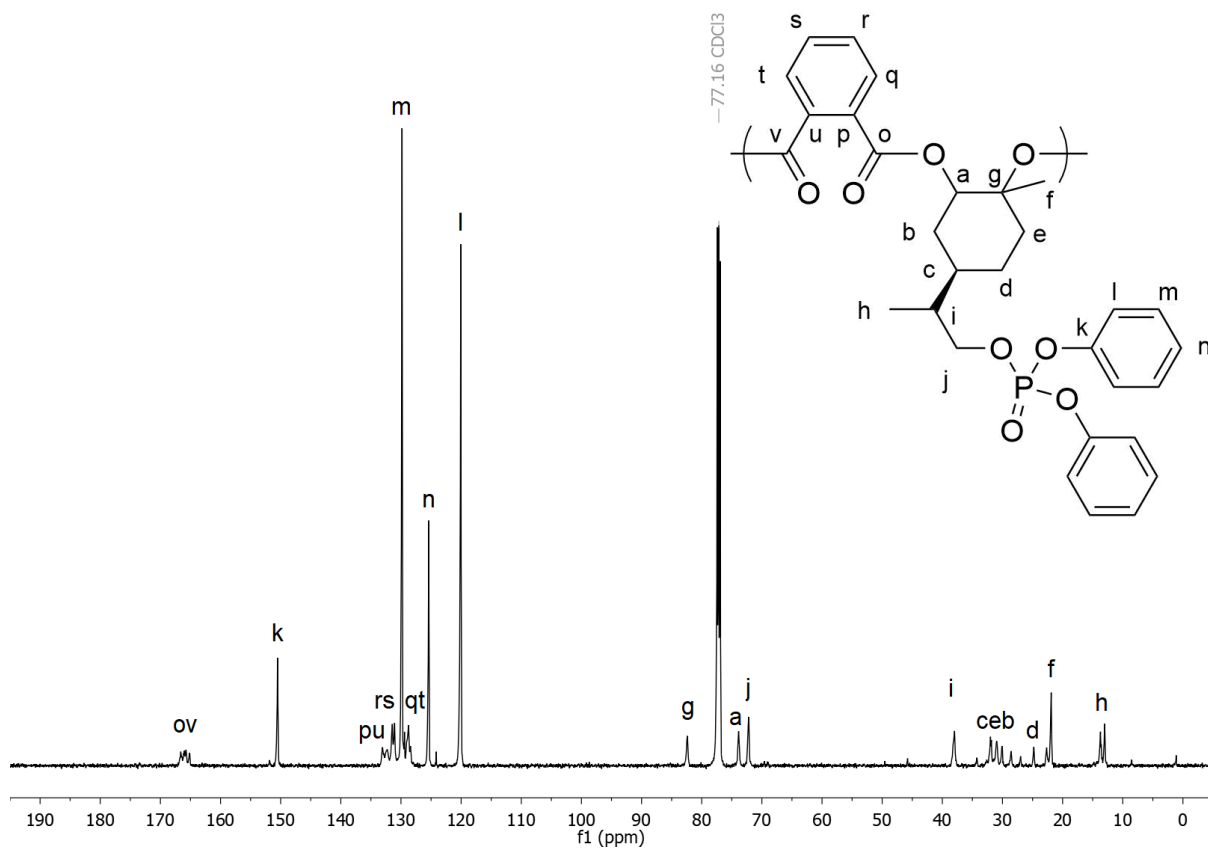


Figure 7.12: $^{13}\text{C}\{^1\text{H}\}$ NMR spectrum (CDCl_3 , 126 MHz) of poly(OP-83).

7.7: NMR Spectra of EDHP-doped Polymers

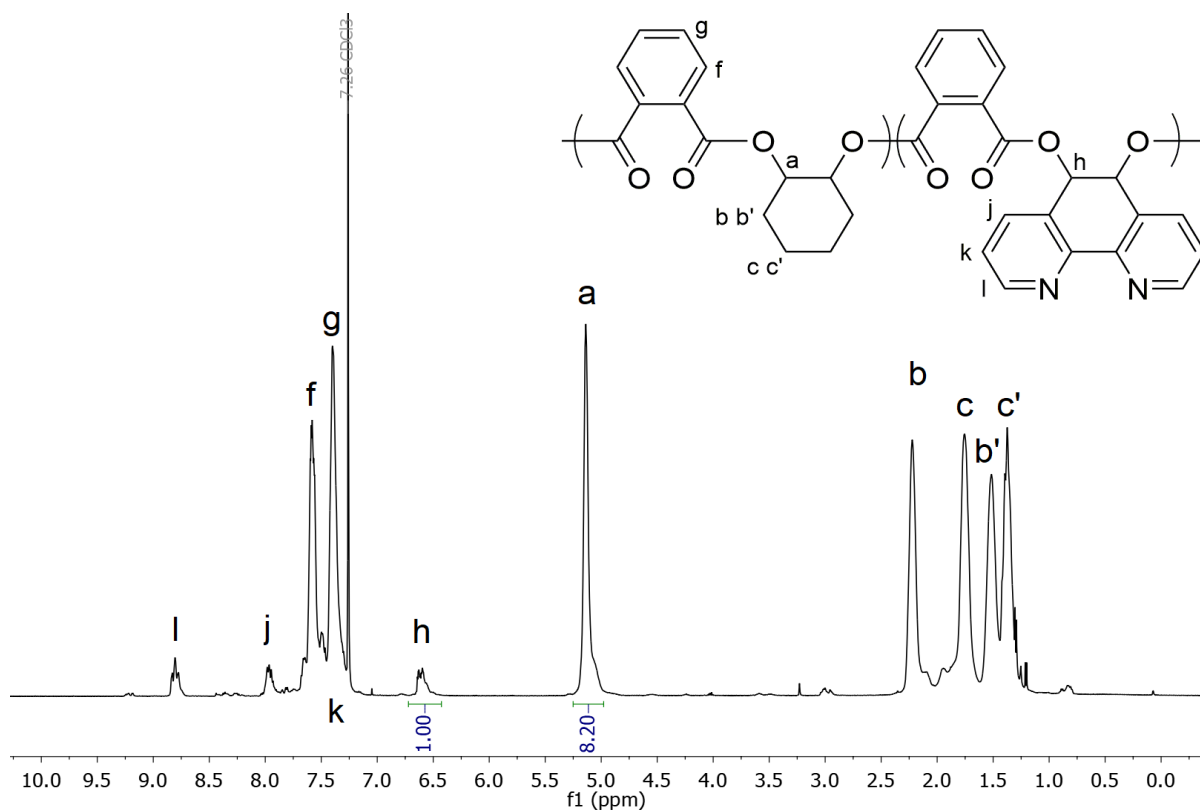


Figure 7.13: ^1H NMR spectrum (CDCl_3 , 500 MHz) of poly(EDHP-CHO-PA), with the ratio of a:h of 8.2: 1.0 indicative of the degree of EDHP incorporation.

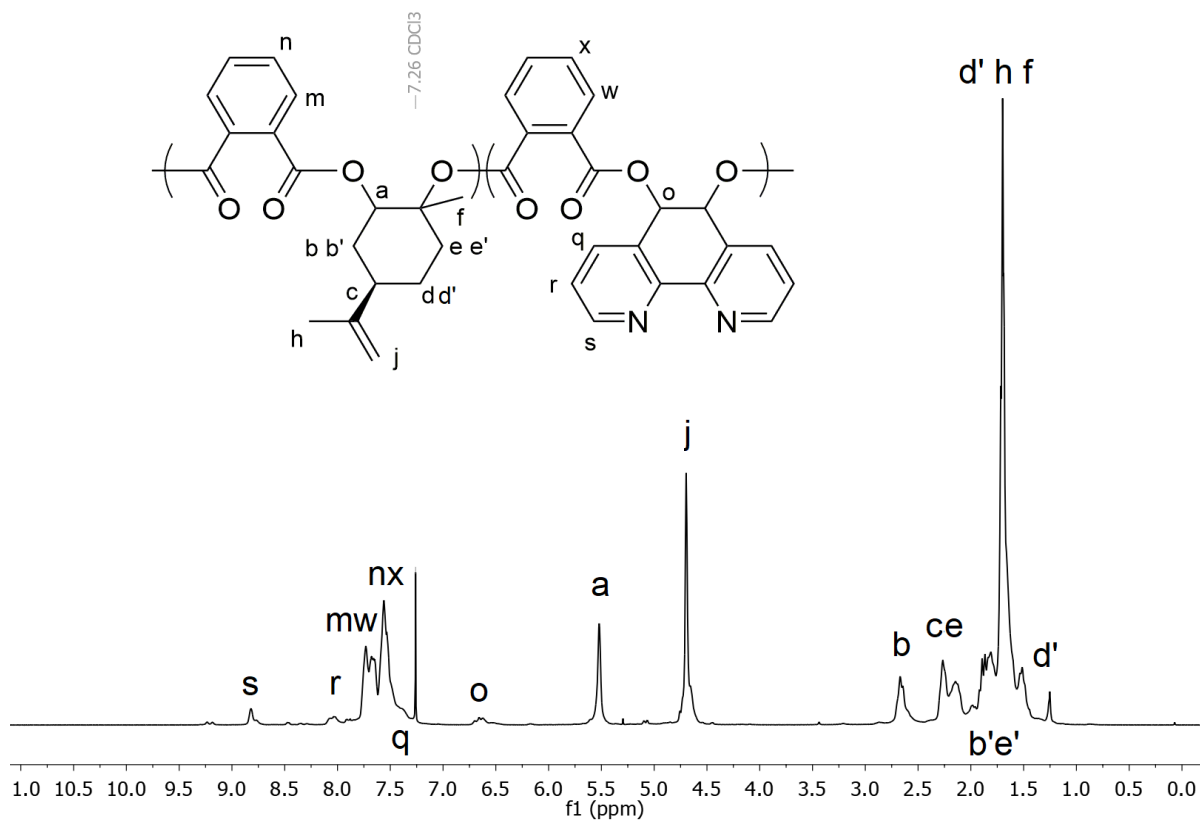


Figure 7.14: ^1H NMR spectrum (CDCl_3 , 500 MHz) of poly(EDHP-LO-PA).

7.8: Synthesis of Ruthenium Doped poly(EDHP-CHO-PA)

cis-[RuCl₂(bipy)₂] was synthesised according to a reported procedure.⁷ Under an argon atmosphere in a shaded vessel, *cis*-[RuCl₂(bipy)₂] (1 eq., 0.192 mmol, 92.8 mg) and AgPF₆ (2 eq., 0.383 mmol, 96.9 mg) were dissolved in dry dimethylformamide (5 mL), and heated to 150 °C for 30 minutes before being allowed to cool, with a precipitate visible. Poly(EDHP-CHO-PA) (1 eq., 0.192 mmol EDHP units, 250.0 mg) was dissolved in dry dimethylformamide and added to the cooled reaction flask. This was then heated to reflux for 4 hours, where an orange suspension could be seen, which was allowed to cool, exposed to air, and poured into 150 mL swirling diethyl ether. The filtrate was concentrated, and added to an excess of cold deionised water. The resulting precipitate was dissolved into dichloromethane and precipitated in diethyl ether to give an orange solid. Yield = 12%. ³¹P{¹H} NMR (202 MHz, DMSO-d₆, 298 K): δ -144.2 (app quintet, *J*^{P-F} = 711 Hz, lack of sensitivity precludes observation of expected septet arising from coupling to 6 fluorine atoms of the PF₆ anion) ¹⁹F{¹H} NMR (471 MHz, DMSO-d₆, 298 K): δ -70.2 (d, *J*^{P-F} = 711 Hz).

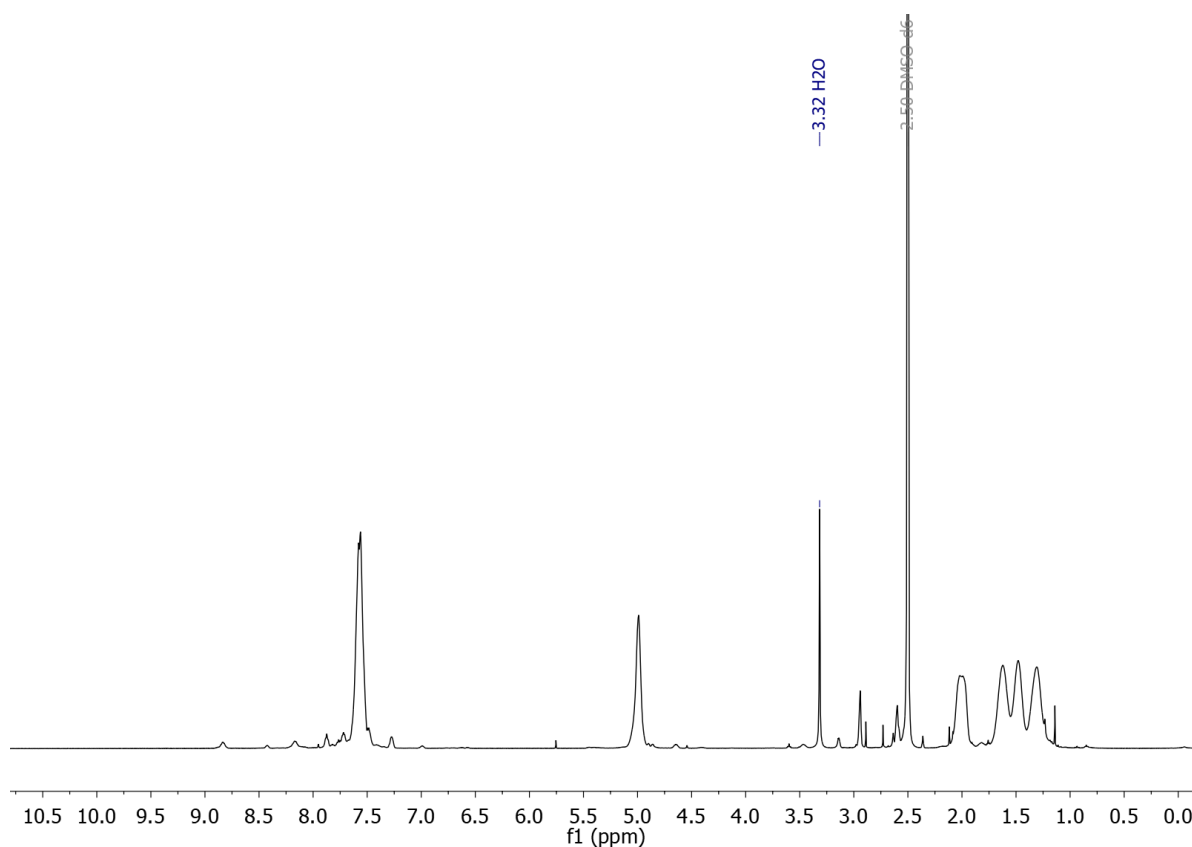


Figure 7.15: ¹H NMR spectrum (DMSO-d₆, 500 MHz) of ruthenium doped poly(CHO-PA-EDHP).

7.9: Synthesis of 1st Row Transition Metal Doped Polyesters

Poly(EDHP-LO-PA) (1 eq., 86 μmol EDHP units, 200.0 mg) was combined with metal chloride salts ($\text{MgCl}_2 \cdot 6\text{H}_2\text{O}$, $\text{ScCl}_3 \cdot (\text{THF})_3$, FeCl_3 , CuCl_2 , ZnCl_2 , 2 eq.) and dissolved in dimethyl sulfoxide (3 mL). The solutions were stirred for 50 °C for 18 hours, before the reaction mixtures were added to methyl tertbutyl ether (MTBE, 50 mL) to precipitate polymers. Multiple reprecipitations from DCM/MTBE and THF/ H_2O and drying *in vacuo* allowed polymers to be recovered in the following yields: Mg – reaction unsuccessful, Sc – reaction unsuccessful, Fe – 58 mg, Cu – 97 mg, Zn – 180 mg. The characterising data for each of the metal-doped polymers are presented and discussed in section 5.8.

7.10: References for Chapter 7

- 1 E. R. Baral, D. Kim, S. Lee, M. H. Park and J. G. Kim, *Catalysts*, 2019, **9**, 311.
- 2 M. Decostanzi, J. Lomège, Y. Ecochard, A. S. Mora, C. Negrell and S. Caillol, *Prog. Org. Coatings*, 2018, **124**, 147–157.
- 3 S. Friedrich, M. Schubart, L. H. Gade, I. J. Scowen, A. J. Edwards and M. McPartlin, *Chem. Ber./Recueil*, 1997, **130**, 1751–1759.
- 4 M. Zendejdel, H. Khanmohamadi and M. Mokhtari, *J. Chinese Chem. Soc.*, 2010, **57**, 205–212.
- 5 M. A. Bahili, PhD Thesis, Cardiff University, 2017.
- 6 N. Yi, T. T. D. Chen, J. Unruangsri, Y. Zhu and C. K. Williams, *Chem. Sci.*, 2019, **10**, 9974–9980.
- 7 O. A. Lenis-Rojas, C. Roma-Rodrigues, A. R. Fernandes, F. Marques, D. Pérez-Fernández, J. Guerra-Varela, L. Sánchez, D. Vázquez-García, M. López-Torres, A. Fernández and J. J. Fernández, *Inorg. Chem.*, 2017, **56**, 7127–7144.

Appendix: X-Ray Crystallographic Data of [Salpy-Al-Cl] Complexes

Diffraction data from single-crystal X-ray crystallography was obtained at either the National Crystallographic Centre, University of Southampton or by Dr. Benson M. Kariuki, Cardiff University, with structures solved and refined by Dr. Benjamin Ward.

A.1: [3,5-di-tert-butylsalpy-Al-Cl] (Al-2).

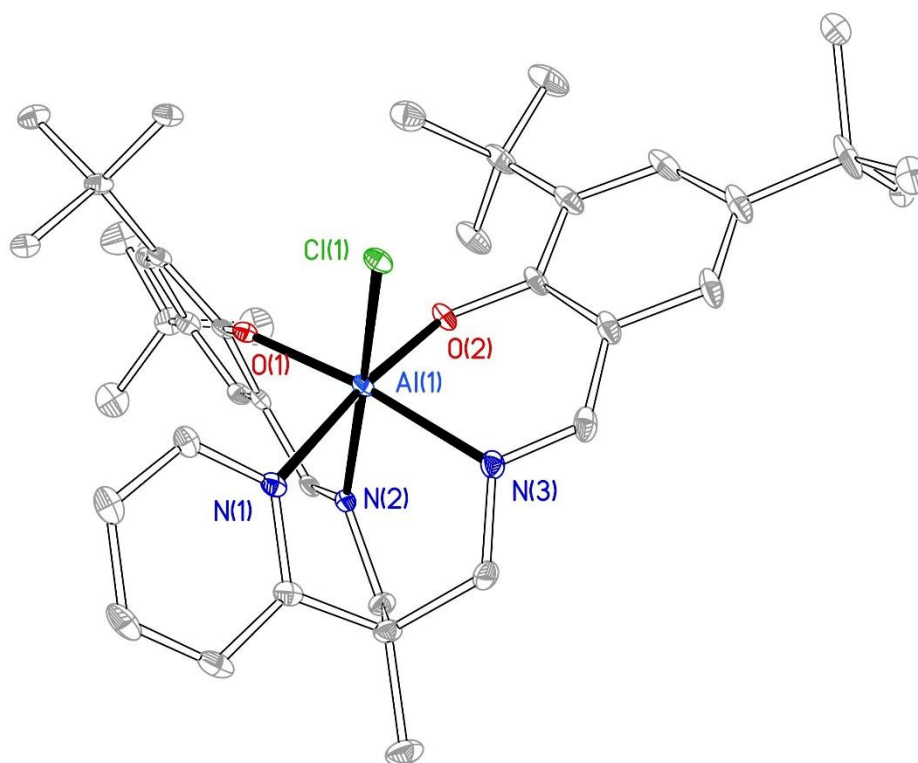


Figure A.1: X-Ray crystal structure of Al-2, with hydrogen atoms omitted for clarity, and ellipsoids drawn at 30% probability.

Table A.1. Crystal data and structure refinement for Al-2

Identification code	Al-2
Empirical formula	C ₈₅ H ₁₂₂ Al ₂ Cl ₄ N ₆ O ₄
Formula weight	1487.64
Temperature	100(2) K
Wavelength	0.71073 Å
Crystal system	Triclinic

Space group	$P\bar{1}$	
Unit cell dimensions	$a = 13.4170(3) \text{ \AA}$	$\alpha = 72.638(3)^\circ$
	$b = 16.1417(5) \text{ \AA}$	$\beta = 73.441(2)^\circ$
	$c = 21.6082(7) \text{ \AA}$	$\gamma = 89.969(2)^\circ$
Volume	$4263.0(2) \text{ \AA}^3$	
Z	2	
Density (calculated)	1.159 Mg/m^3	
Absorption coefficient	0.210 mm^{-1}	
F(000)	1600	
Crystal size	$0.400 \times 0.040 \times 0.010 \text{ mm}^3$	
θ range for data collection	2.082 to 27.485°	
Index ranges	$-17 \leq h \leq 17, -20 \leq k \leq 20, -28 \leq l \leq 28$	
Reflections collected	90334	
Independent reflections	19535 [R(int) = 0.0901]	
Completeness to $\theta = 25.242^\circ$	99.9%	
Absorption correction	Semi-empirical from equivalents	
Max. and min. transmission	1.00000 and 0.27520	
Refinement method	Full-matrix least-squares on F^2	
Data / restraints / parameters	19535 / 286 / 1026	
Goodness-of-fit on F^2	1.092	
Final R indices [$I > 2\sigma(I)$]	$R_1 = 0.0828, wR_2 = 0.1656$	
R indices (all data)	$R_1 = 0.1176, wR_2 = 0.1795$	
Extinction coefficient	n/a	
Largest diff. peak and hole	0.825 and $-0.787 \text{ e.\AA}^{-3}$	

Table A.2. Atomic coordinates ($\times 10^4$) and equivalent isotropic displacement parameters ($\text{\AA}^2 \times 10^3$)**for Al-2. $U(\text{eq})$ is defined as one third of the trace of the orthogonalized U^i tensor.**

	x	y	z	$U(\text{eq})$
Cl(1)	6291(1)	2653(1)	3633(1)	18(1)
Cl(2)	3593(1)	2085(1)	6817(1)	18(1)
Cl(3)	1319(1)	1534(1)	5658(1)	44(1)
Cl(4)	1156(1)	3340(1)	5615(1)	60(1)
Al(1)	6247(1)	4142(1)	3222(1)	13(1)
Al(2)	3814(1)	625(1)	7132(1)	14(1)
O(1)	7315(2)	4412(1)	3514(1)	14(1)
O(2)	7071(2)	4244(1)	2368(1)	18(1)
O(3)	5201(2)	779(1)	6672(1)	16(1)
O(4)	4039(2)	604(1)	7924(1)	18(1)
N(1)	5190(2)	4099(2)	4145(1)	15(1)
N(2)	5989(2)	5405(2)	2986(1)	15(1)
N(3)	4996(2)	3986(2)	2907(1)	19(1)
N(4)	3467(2)	559(2)	6244(1)	16(1)
N(5)	3809(2)	-671(2)	7260(1)	15(1)
N(6)	2273(2)	352(2)	7626(1)	15(1)
C(1)	3041(3)	5384(2)	3648(2)	31(1)
C(2)	4079(2)	4967(2)	3534(2)	20(1)
C(3)	4335(2)	4550(2)	4195(2)	18(1)
C(4)	3707(3)	4565(2)	4825(2)	25(1)
C(5)	3949(3)	4113(2)	5407(2)	28(1)
C(6)	4824(3)	3655(2)	5352(2)	23(1)

C(7)	5423(2)	3671(2)	4715(2)	18(1)
C(8)	4931(2)	5678(2)	3020(2)	19(1)
C(9)	6747(2)	6016(2)	2755(2)	16(1)
C(10)	7800(2)	5874(2)	2781(2)	15(1)
C(11)	8557(2)	6588(2)	2444(2)	18(1)
C(12)	9558(2)	6542(2)	2493(2)	19(1)
C(13)	9757(2)	5771(2)	2936(2)	19(1)
C(14)	9031(2)	5058(2)	3308(2)	16(1)
C(15)	8030(2)	5085(2)	3200(2)	14(1)
C(16)	10375(3)	7331(2)	2116(2)	27(1)
C(17)	10449(3)	7628(3)	1362(2)	41(1)
C(18)	10036(3)	8073(2)	2418(2)	36(1)
C(19)	11462(3)	7120(3)	2179(3)	46(1)
C(20)	9267(2)	4286(2)	3851(2)	18(1)
C(21)	10376(2)	4402(2)	3892(2)	25(1)
C(22)	8521(2)	4254(2)	4542(2)	20(1)
C(23)	9141(3)	3409(2)	3720(2)	22(1)
C(24)	3966(2)	4228(2)	3236(2)	23(1)
C(25)	5054(3)	3673(2)	2416(2)	24(1)
C(26)	5990(3)	3479(2)	1985(2)	24(1)
C(27)	5881(3)	3000(2)	1552(2)	30(1)
C(28)	6735(3)	2842(2)	1092(2)	33(1)
C(29)	7708(3)	3211(2)	1047(2)	31(1)
C(30)	7871(3)	3698(2)	1447(2)	25(1)
C(31)	6978(3)	3807(2)	1957(2)	20(1)
C(32)	6654(4)	2310(2)	620(2)	41(1)
C(33)	5762(10)	1741(8)	847(6)	36(3)

C(34)	6764(11)	2927(8)	-96(6)	24(3)
C(35)	7682(10)	1713(7)	548(6)	29(3)
C(33A)	5423(7)	1935(5)	808(4)	31(2)
C(34A)	7028(8)	2921(6)	-118(4)	29(2)
C(35A)	7219(8)	1538(5)	721(4)	33(2)
C(36)	8948(3)	4118(2)	1351(2)	29(1)
C(37)	9796(3)	3932(3)	769(2)	43(1)
C(38)	8928(3)	5116(2)	1173(2)	34(1)
C(39)	9272(3)	3770(3)	1998(2)	34(1)
C(40)	1328(3)	-1262(2)	6935(2)	23(1)
C(41)	2155(2)	-635(2)	6963(2)	17(1)
C(42)	2854(2)	-119(2)	6258(2)	17(1)
C(43)	2858(3)	-290(2)	5668(2)	24(1)
C(44)	3477(3)	244(2)	5048(2)	29(1)
C(45)	4085(3)	956(2)	5027(2)	24(1)
C(46)	4057(2)	1080(2)	5636(2)	19(1)
C(47)	2816(2)	-1175(2)	7394(2)	16(1)
C(48)	4635(2)	-1066(2)	7108(2)	16(1)
C(49)	5695(2)	-672(2)	6866(2)	17(1)
C(50)	6475(3)	-1248(2)	6812(2)	23(1)
C(51)	7517(3)	-946(2)	6546(2)	27(1)
C(52)	7746(3)	-40(2)	6328(2)	26(1)
C(53)	7011(2)	560(2)	6352(2)	18(1)
C(54)	5933(2)	238(2)	6645(2)	15(1)
C(55)	8381(3)	-1567(2)	6515(2)	35(1)
C(56)	8023(3)	-2398(3)	6392(3)	62(2)
C(57)	9369(3)	-1154(3)	5936(2)	38(1)

C(58)	8618(3)	-1806(3)	7190(2)	48(1)
C(59)	7355(2)	1541(2)	6062(2)	20(1)
C(60)	8545(3)	1731(2)	5804(2)	31(1)
C(61)	6924(3)	1955(3)	5470(2)	37(1)
C(62)	6957(3)	1978(2)	6613(2)	38(1)
C(63)	1597(2)	18(2)	7314(2)	17(1)
C(64)	1837(2)	434(2)	8217(2)	18(1)
C(65)	2357(2)	694(2)	8635(2)	18(1)
C(66)	1726(3)	822(2)	9241(2)	25(1)
C(67)	2161(3)	1026(2)	9687(2)	29(1)
C(68)	3255(3)	1098(2)	9512(2)	30(1)
C(69)	3918(3)	992(2)	8926(2)	23(1)
C(70)	3456(3)	763(2)	8471(2)	20(1)
C(71)	1501(3)	1157(3)	10358(2)	38(1)
C(72)	1512(5)	356(4)	10938(2)	75(2)
C(73)	356(4)	1278(3)	10370(2)	54(1)
C(74)	1901(5)	2003(4)	10426(3)	87(2)
C(75)	5097(3)	1219(2)	8720(2)	27(1)
C(76)	5442(3)	1369(3)	9306(2)	40(1)
C(77)	5348(3)	2085(2)	8140(2)	29(1)
C(78)	5743(3)	507(2)	8504(2)	32(1)
C(79)	1942(4)	2470(3)	5690(3)	46(1)
C(80)	5973(9)	5908(6)	1021(5)	54(2)
C(81)	6397(9)	5459(7)	488(5)	64(2)
C(82)	6569(8)	5866(7)	-211(5)	58(2)
C(83)	6952(7)	5387(5)	-664(4)	61(2)
C(84)	7494(10)	5780(9)	-1304(6)	92(3)

C(85)	7738(14)	5387(10)	-1879(7)	71(3)
C(80A)	5464(16)	5829(14)	1050(10)	42(4)
C(81A)	6020(17)	5359(14)	540(10)	59(3)
C(82A)	6205(17)	5952(15)	-204(9)	57(3)
C(83A)	6387(16)	5644(13)	-818(9)	70(3)
C(84A)	7214(17)	5923(15)	-1479(10)	74(3)
C(85A)	7670(40)	5146(19)	-1717(17)	78(6)

Table A.3. Bond lengths [Å] and angles [°] for Al-2.

Cl(1)-Al(1)	2.3068(11)
Cl(2)-Al(2)	2.2932(11)
Cl(3)-C(79)	1.755(4)
Cl(4)-C(79)	1.753(4)
Al(1)-O(2)	1.819(2)
Al(1)-O(1)	1.822(2)
Al(1)-N(2)	2.004(3)
Al(1)-N(3)	2.025(3)
Al(1)-N(1)	2.072(3)
Al(2)-O(4)	1.812(2)
Al(2)-O(3)	1.820(2)
Al(2)-N(6)	2.018(3)
Al(2)-N(5)	2.026(3)
Al(2)-N(4)	2.131(3)
O(1)-C(15)	1.324(3)
O(2)-C(31)	1.319(4)

O(3)-C(54)	1.315(3)
O(4)-C(70)	1.315(4)
N(1)-C(7)	1.343(4)
N(1)-C(3)	1.354(4)
N(2)-C(9)	1.294(4)
N(2)-C(8)	1.474(4)
N(3)-C(25)	1.288(4)
N(3)-C(24)	1.474(4)
N(4)-C(46)	1.345(4)
N(4)-C(42)	1.356(4)
N(5)-C(48)	1.288(4)
N(5)-C(47)	1.470(4)
N(6)-C(64)	1.290(4)
N(6)-C(63)	1.460(4)
C(1)-C(2)	1.534(4)
C(2)-C(3)	1.522(5)
C(2)-C(24)	1.540(4)
C(2)-C(8)	1.541(4)
C(3)-C(4)	1.389(5)
C(4)-C(5)	1.379(5)
C(5)-C(6)	1.382(5)
C(6)-C(7)	1.374(4)
C(9)-C(10)	1.445(4)
C(10)-C(11)	1.403(4)
C(10)-C(15)	1.416(4)
C(11)-C(12)	1.377(4)
C(12)-C(13)	1.404(5)

C(12)-C(16)	1.536(4)
C(13)-C(14)	1.386(4)
C(14)-C(15)	1.425(4)
C(14)-C(20)	1.540(4)
C(16)-C(17)	1.526(5)
C(16)-C(19)	1.533(5)
C(16)-C(18)	1.538(5)
C(20)-C(22)	1.529(4)
C(20)-C(21)	1.531(4)
C(20)-C(23)	1.543(4)
C(25)-C(26)	1.433(5)
C(26)-C(31)	1.406(5)
C(26)-C(27)	1.416(4)
C(27)-C(28)	1.368(6)
C(28)-C(29)	1.401(6)
C(28)-C(32)	1.539(5)
C(29)-C(30)	1.387(5)
C(30)-C(31)	1.430(5)
C(30)-C(36)	1.529(5)
C(32)-C(33)	1.383(10)
C(32)-C(35A)	1.450(7)
C(32)-C(34)	1.536(11)
C(32)-C(34A)	1.541(9)
C(32)-C(33A)	1.652(9)
C(32)-C(35)	1.680(10)
C(36)-C(39)	1.530(5)
C(36)-C(37)	1.541(5)

C(36)-C(38)	1.543(5)
C(40)-C(41)	1.527(4)
C(41)-C(42)	1.524(4)
C(41)-C(63)	1.550(4)
C(41)-C(47)	1.550(4)
C(42)-C(43)	1.382(4)
C(43)-C(44)	1.380(5)
C(44)-C(45)	1.392(5)
C(45)-C(46)	1.378(4)
C(48)-C(49)	1.441(4)
C(49)-C(50)	1.404(4)
C(49)-C(54)	1.408(4)
C(50)-C(51)	1.378(5)
C(51)-C(52)	1.400(5)
C(51)-C(55)	1.532(5)
C(52)-C(53)	1.384(4)
C(53)-C(54)	1.430(4)
C(53)-C(59)	1.535(4)
C(55)-C(58)	1.519(6)
C(55)-C(57)	1.525(6)
C(55)-C(56)	1.544(5)
C(59)-C(61)	1.526(5)
C(59)-C(62)	1.527(5)
C(59)-C(60)	1.531(4)
C(64)-C(65)	1.438(4)
C(65)-C(70)	1.411(5)
C(65)-C(66)	1.415(4)

C(66)-C(67)	1.374(5)
C(67)-C(68)	1.403(5)
C(67)-C(71)	1.542(5)
C(68)-C(69)	1.384(5)
C(69)-C(70)	1.432(4)
C(69)-C(75)	1.529(5)
C(71)-C(72)	1.512(7)
C(71)-C(74)	1.531(6)
C(71)-C(73)	1.542(7)
C(75)-C(77)	1.533(5)
C(75)-C(78)	1.541(5)
C(75)-C(76)	1.546(5)
C(80)-C(81)	1.515(11)
C(81)-C(82)	1.405(11)
C(82)-C(83)	1.410(11)
C(83)-C(84)	1.322(11)
C(84)-C(85)	1.515(13)
C(80A)-C(81A)	1.540(17)
C(81A)-C(82A)	1.555(17)
C(82A)-C(83A)	1.508(17)
C(83A)-C(84A)	1.479(17)
C(84A)-C(85A)	1.556(19)
O(2)-Al(1)-O(1)	94.69(10)
O(2)-Al(1)-N(2)	93.64(10)
O(1)-Al(1)-N(2)	88.08(10)
O(2)-Al(1)-N(3)	87.95(11)

O(1)-Al(1)-N(3)	172.81(11)
N(2)-Al(1)-N(3)	85.07(11)
O(2)-Al(1)-N(1)	173.64(11)
O(1)-Al(1)-N(1)	89.99(10)
N(2)-Al(1)-N(1)	82.19(10)
N(3)-Al(1)-N(1)	86.90(11)
O(2)-Al(1)-Cl(1)	94.86(8)
O(1)-Al(1)-Cl(1)	95.04(7)
N(2)-Al(1)-Cl(1)	170.67(9)
N(3)-Al(1)-Cl(1)	91.40(8)
N(1)-Al(1)-Cl(1)	89.00(8)
O(4)-Al(2)-O(3)	93.25(10)
O(4)-Al(2)-N(6)	88.97(10)
O(3)-Al(2)-N(6)	174.93(10)
O(4)-Al(2)-N(5)	97.96(10)
O(3)-Al(2)-N(5)	90.28(10)
N(6)-Al(2)-N(5)	84.89(10)
O(4)-Al(2)-N(4)	175.48(11)
O(3)-Al(2)-N(4)	89.73(10)
N(6)-Al(2)-N(4)	87.79(10)
N(5)-Al(2)-N(4)	78.62(10)
O(4)-Al(2)-Cl(2)	94.52(8)
O(3)-Al(2)-Cl(2)	94.30(7)
N(6)-Al(2)-Cl(2)	90.06(8)
N(5)-Al(2)-Cl(2)	166.43(9)
N(4)-Al(2)-Cl(2)	88.63(8)
C(15)-O(1)-Al(1)	126.6(2)

C(31)-O(2)-Al(1)	129.1(2)
C(54)-O(3)-Al(2)	132.44(19)
C(70)-O(4)-Al(2)	132.7(2)
C(7)-N(1)-C(3)	118.7(3)
C(7)-N(1)-Al(1)	118.0(2)
C(3)-N(1)-Al(1)	123.0(2)
C(9)-N(2)-C(8)	117.1(2)
C(9)-N(2)-Al(1)	121.7(2)
C(8)-N(2)-Al(1)	121.11(19)
C(25)-N(3)-C(24)	116.8(3)
C(25)-N(3)-Al(1)	122.3(2)
C(24)-N(3)-Al(1)	120.9(2)
C(46)-N(4)-C(42)	118.2(3)
C(46)-N(4)-Al(2)	118.4(2)
C(42)-N(4)-Al(2)	121.5(2)
C(48)-N(5)-C(47)	115.4(2)
C(48)-N(5)-Al(2)	124.4(2)
C(47)-N(5)-Al(2)	118.88(19)
C(64)-N(6)-C(63)	116.9(3)
C(64)-N(6)-Al(2)	124.1(2)
C(63)-N(6)-Al(2)	119.02(19)
C(3)-C(2)-C(1)	112.2(3)
C(3)-C(2)-C(24)	106.7(3)
C(1)-C(2)-C(24)	107.8(3)
C(3)-C(2)-C(8)	112.5(3)
C(1)-C(2)-C(8)	107.5(3)
C(24)-C(2)-C(8)	110.1(3)

N(1)-C(3)-C(4)	120.6(3)
N(1)-C(3)-C(2)	115.7(3)
C(4)-C(3)-C(2)	123.5(3)
C(5)-C(4)-C(3)	120.0(3)
C(4)-C(5)-C(6)	119.1(3)
C(7)-C(6)-C(5)	118.4(3)
N(1)-C(7)-C(6)	123.2(3)
N(2)-C(8)-C(2)	111.9(2)
N(2)-C(9)-C(10)	124.1(3)
C(11)-C(10)-C(15)	121.1(3)
C(11)-C(10)-C(9)	117.0(3)
C(15)-C(10)-C(9)	121.3(3)
C(12)-C(11)-C(10)	121.4(3)
C(11)-C(12)-C(13)	116.6(3)
C(11)-C(12)-C(16)	120.4(3)
C(13)-C(12)-C(16)	122.8(3)
C(14)-C(13)-C(12)	124.8(3)
C(13)-C(14)-C(15)	117.7(3)
C(13)-C(14)-C(20)	121.4(3)
C(15)-C(14)-C(20)	120.7(3)
O(1)-C(15)-C(10)	120.8(3)
O(1)-C(15)-C(14)	121.1(3)
C(10)-C(15)-C(14)	118.0(3)
C(17)-C(16)-C(19)	108.1(3)
C(17)-C(16)-C(12)	109.5(3)
C(19)-C(16)-C(12)	112.3(3)
C(17)-C(16)-C(18)	109.7(3)

C(19)-C(16)-C(18)	108.4(3)
C(12)-C(16)-C(18)	108.8(3)
C(22)-C(20)-C(21)	106.8(3)
C(22)-C(20)-C(14)	108.0(2)
C(21)-C(20)-C(14)	111.9(3)
C(22)-C(20)-C(23)	109.8(3)
C(21)-C(20)-C(23)	107.8(3)
C(14)-C(20)-C(23)	112.4(3)
N(3)-C(24)-C(2)	111.2(2)
N(3)-C(25)-C(26)	125.9(3)
C(31)-C(26)-C(27)	121.3(3)
C(31)-C(26)-C(25)	121.1(3)
C(27)-C(26)-C(25)	117.5(3)
C(28)-C(27)-C(26)	121.0(4)
C(27)-C(28)-C(29)	116.9(3)
C(27)-C(28)-C(32)	122.7(4)
C(29)-C(28)-C(32)	120.4(4)
C(30)-C(29)-C(28)	125.2(3)
C(29)-C(30)-C(31)	117.2(3)
C(29)-C(30)-C(36)	122.5(3)
C(31)-C(30)-C(36)	120.3(3)
O(2)-C(31)-C(26)	120.7(3)
O(2)-C(31)-C(30)	120.9(3)
C(26)-C(31)-C(30)	118.3(3)
C(33)-C(32)-C(34)	110.1(8)
C(33)-C(32)-C(28)	115.2(6)
C(35A)-C(32)-C(28)	112.7(4)

C(34)-C(32)-C(28)	109.8(6)
C(35A)-C(32)-C(34A)	112.4(5)
C(28)-C(32)-C(34A)	108.0(5)
C(35A)-C(32)-C(33A)	104.8(5)
C(28)-C(32)-C(33A)	109.1(4)
C(34A)-C(32)-C(33A)	109.7(5)
C(33)-C(32)-C(35)	107.4(7)
C(34)-C(32)-C(35)	106.5(7)
C(28)-C(32)-C(35)	107.4(5)
C(30)-C(36)-C(39)	110.7(3)
C(30)-C(36)-C(37)	112.0(3)
C(39)-C(36)-C(37)	107.5(3)
C(30)-C(36)-C(38)	109.9(3)
C(39)-C(36)-C(38)	109.1(3)
C(37)-C(36)-C(38)	107.5(3)
C(42)-C(41)-C(40)	112.4(3)
C(42)-C(41)-C(63)	108.3(2)
C(40)-C(41)-C(63)	108.7(2)
C(42)-C(41)-C(47)	110.3(2)
C(40)-C(41)-C(47)	108.1(3)
C(63)-C(41)-C(47)	109.0(2)
N(4)-C(42)-C(43)	121.2(3)
N(4)-C(42)-C(41)	114.7(3)
C(43)-C(42)-C(41)	124.1(3)
C(44)-C(43)-C(42)	120.0(3)
C(43)-C(44)-C(45)	119.2(3)
C(46)-C(45)-C(44)	117.8(3)

N(4)-C(46)-C(45)	123.6(3)
N(5)-C(47)-C(41)	110.1(2)
N(5)-C(48)-C(49)	125.6(3)
C(50)-C(49)-C(54)	122.0(3)
C(50)-C(49)-C(48)	115.7(3)
C(54)-C(49)-C(48)	122.1(3)
C(51)-C(50)-C(49)	121.2(3)
C(50)-C(51)-C(52)	116.4(3)
C(50)-C(51)-C(55)	121.9(3)
C(52)-C(51)-C(55)	121.7(3)
C(53)-C(52)-C(51)	125.0(3)
C(52)-C(53)-C(54)	118.1(3)
C(52)-C(53)-C(59)	120.3(3)
C(54)-C(53)-C(59)	121.6(3)
O(3)-C(54)-C(49)	122.0(3)
O(3)-C(54)-C(53)	120.7(3)
C(49)-C(54)-C(53)	117.3(3)
C(58)-C(55)-C(57)	109.9(3)
C(58)-C(55)-C(51)	107.6(3)
C(57)-C(55)-C(51)	111.9(3)
C(58)-C(55)-C(56)	109.9(4)
C(57)-C(55)-C(56)	106.8(4)
C(51)-C(55)-C(56)	110.6(3)
C(61)-C(59)-C(62)	109.5(3)
C(61)-C(59)-C(60)	107.9(3)
C(62)-C(59)-C(60)	106.9(3)
C(61)-C(59)-C(53)	109.8(3)

C(62)-C(59)-C(53)	110.2(3)
C(60)-C(59)-C(53)	112.4(3)
N(6)-C(63)-C(41)	110.5(2)
N(6)-C(64)-C(65)	126.4(3)
C(70)-C(65)-C(66)	121.2(3)
C(70)-C(65)-C(64)	121.2(3)
C(66)-C(65)-C(64)	117.5(3)
C(67)-C(66)-C(65)	121.2(3)
C(66)-C(67)-C(68)	116.8(3)
C(66)-C(67)-C(71)	122.8(3)
C(68)-C(67)-C(71)	120.4(3)
C(69)-C(68)-C(67)	125.0(3)
C(68)-C(69)-C(70)	117.8(3)
C(68)-C(69)-C(75)	121.6(3)
C(70)-C(69)-C(75)	120.3(3)
O(4)-C(70)-C(65)	121.0(3)
O(4)-C(70)-C(69)	120.9(3)
C(65)-C(70)-C(69)	118.0(3)
C(72)-C(71)-C(74)	113.6(5)
C(72)-C(71)-C(67)	108.5(4)
C(74)-C(71)-C(67)	110.1(3)
C(72)-C(71)-C(73)	108.1(4)
C(74)-C(71)-C(73)	104.5(4)
C(67)-C(71)-C(73)	111.9(3)
C(69)-C(75)-C(77)	106.6(3)
C(69)-C(75)-C(78)	113.4(3)
C(77)-C(75)-C(78)	111.1(3)

C(69)-C(75)-C(76)	111.8(3)
C(77)-C(75)-C(76)	107.1(3)
C(78)-C(75)-C(76)	106.7(3)
Cl(4)-C(79)-Cl(3)	111.5(2)
C(82)-C(81)-C(80)	123.4(9)
C(81)-C(82)-C(83)	119.0(9)
C(84)-C(83)-C(82)	121.2(9)
C(83)-C(84)-C(85)	126.6(11)
C(80A)-C(81A)-C(82A)	111.0(16)
C(83A)-C(82A)-C(81A)	125.8(18)
C(84A)-C(83A)-C(82A)	130.8(18)
C(83A)-C(84A)-C(85A)	113(2)

A.2: [5-nitrosalpy-Al-Cl] (Al-3).

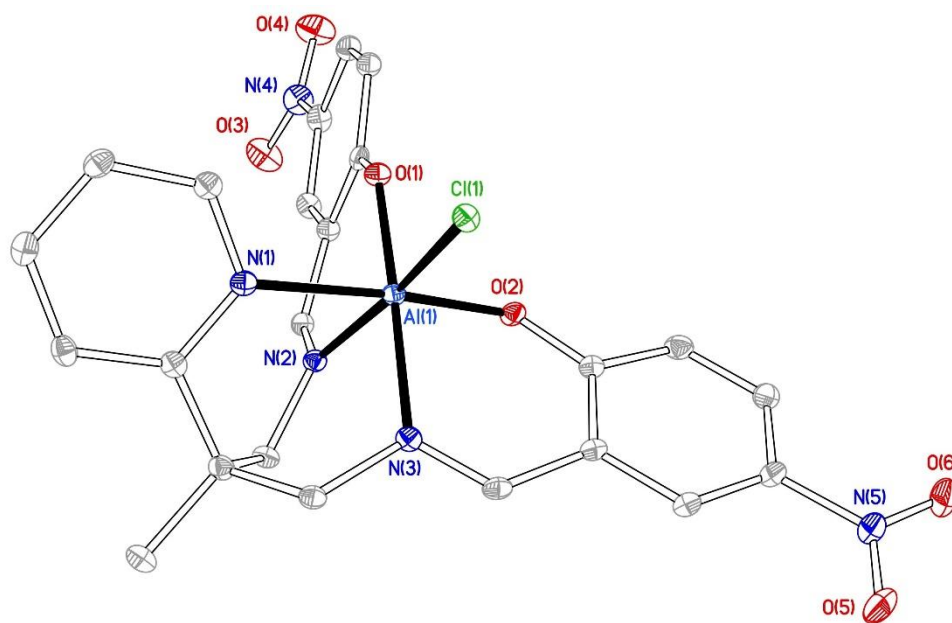


Figure A.2: X-Ray crystal structure of Al-3, with hydrogen atoms omitted for clarity, and ellipsoids drawn at 30% probability.

Note: Partially occupied solvent (dichloromethane was disordered and spread over several locations) sites were modelled by SQUEEZE to improve refinement.

Table A.4. Crystal data and structure refinement for Al-3.

Identification code	Al-3	
Empirical formula	C _{24.73} H _{22.46} AlCl _{4.46} N ₅ O ₆	
Formula weight	670.61	
Temperature	293(2) K	
Wavelength	0.71073 Å	
Crystal system	Monoclinic	
Space group	P2 ₁ /c	
Unit cell dimensions	$a = 11.1638(3)$ Å	$a = 90^\circ$
	$b = 13.2412(3)$ Å	$b = 104.717(3)^\circ$
	$c = 20.1988(5)$ Å	$g = 90^\circ$

Volume	2887.87(13) Å ³
Z	4
Density (calculated)	1.542 Mg/m ³
Absorption coefficient	0.532 mm ⁻¹
F(000)	1370
Crystal size	0.400 × 0.080 × 0.050 mm ³
θ range for data collection	2.430 to 27.480 °
Index ranges	-14 ≤ h ≤ 14, -17 ≤ k ≤ 16, -26 ≤ l ≤ 26
Reflections collected	65413
Independent reflections	6630 [R(int) = 0.0536]
Completeness to θ = 25.242 °	99.9%
Absorption correction	Semi-empirical from equivalents
Max. and min. transmission	1.00000 and 0.69696
Refinement method	Full-matrix least-squares on F ²
Data / restraints / parameters	6630 / 40 / 437
Goodness-of-fit on F ²	1.143
Final R indices [I > 2σ(I)]	R ₁ = 0.0535, wR ₂ = 0.1431
R indices (all data)	R ₁ = 0.0608, wR ₂ = 0.1469
Extinction coefficient	n/a
Largest diff. peak and hole	1.121 and -0.494 e.Å ⁻³

Table A.5. Atomic coordinates ($\times 10^4$) and equivalent isotropic displacement parameters ($\text{\AA}^2 \times 10^3$)

for Al-3. $U(\text{eq})$ is defined as one third of the trace of the orthogonalized U^{ij} tensor.

	x	y	z	U(eq)
Cl(1)	5428(1)	2861(1)	8972(1)	19(1)
Al(1)	5081(1)	4211(1)	8252(1)	15(1)
O(1)	6492(2)	4000(1)	7973(1)	18(1)
O(2)	4157(2)	3530(1)	7498(1)	18(1)
O(3)	7870(2)	6437(2)	5636(1)	43(1)
O(4)	9084(2)	5159(2)	5694(1)	44(1)
O(5)	-823(2)	1408(2)	7511(1)	46(1)
O(6)	-322(2)	623(2)	6683(1)	39(1)
N(1)	6042(2)	5131(2)	9044(1)	17(1)
N(2)	4844(2)	5561(2)	7778(1)	17(1)
N(3)	3503(2)	4520(2)	8528(1)	17(1)
N(4)	8272(2)	5619(2)	5878(1)	32(1)
N(5)	-129(2)	1270(2)	7138(1)	31(1)
C(1)	3791(3)	7255(2)	9041(1)	24(1)
C(2)	4270(2)	6265(2)	8807(1)	19(1)
C(3)	5606(2)	6044(2)	9180(1)	18(1)
C(4)	6345(2)	6696(2)	9651(1)	21(1)
C(5)	7556(2)	6428(2)	9965(1)	23(1)
C(6)	7998(2)	5495(2)	9823(1)	22(1)
C(7)	7211(2)	4868(2)	9364(1)	20(1)
C(8)	4090(2)	6328(2)	8016(1)	18(1)
C(9)	5346(2)	5825(2)	7296(1)	18(1)

C(10)	6286(2)	5238(2)	7086(1)	19(1)
C(11)	6760(2)	5636(2)	6564(1)	22(1)
C(12)	7773(3)	5182(2)	6411(1)	24(1)
C(13)	8345(2)	4335(2)	6767(1)	23(1)
C(14)	7894(2)	3942(2)	7286(1)	20(1)
C(15)	6859(2)	4379(2)	7462(1)	17(1)
C(16)	3477(2)	5388(2)	8974(1)	18(1)
C(17)	2498(2)	4003(2)	8337(1)	19(1)
C(18)	2299(2)	3192(2)	7842(1)	18(1)
C(19)	1222(2)	2610(2)	7742(1)	22(1)
C(20)	963(2)	1898(2)	7228(1)	24(1)
C(21)	1725(2)	1769(2)	6784(1)	26(1)
C(22)	2767(2)	2346(2)	6870(1)	24(1)
C(23)	3121(2)	3044(2)	7414(1)	18(1)
C(24)	-1077(15)	2966(10)	4708(6)	39(2)
CI(2)	-756(2)	2203(4)	5442(1)	34(1)
CI(3)	-763(8)	2219(5)	4032(4)	50(1)
C(24A)	-1090(20)	2789(15)	4548(9)	41(4)
CI(2A)	-644(10)	2477(14)	5418(4)	92(3)
CI(3A)	-632(11)	1929(17)	4007(6)	73(3)
CI(4)	6250(3)	4756(2)	4509(1)	40(1)
CI(5)	7887(3)	4861(2)	3575(2)	41(1)
C(25)	7000(6)	5524(4)	4049(3)	33(1)
CI(4A)	6540(10)	5022(19)	4307(9)	79(7)
CI(5A)	8193(16)	4827(11)	3399(7)	48(3)
C(25A)	7830(20)	5477(16)	4090(11)	37(4)

Table A.6. Bond lengths [Å] and angles [°] for Al-3.

Cl(1)-Al(1)	2.2751(9)
Al(1)-O(1)	1.8229(17)
Al(1)-O(2)	1.8437(19)
Al(1)-N(2)	2.012(2)
Al(1)-N(3)	2.020(2)
Al(1)-N(1)	2.080(2)
O(1)-C(15)	1.304(3)
O(2)-C(23)	1.297(3)
O(3)-N(4)	1.226(3)
O(4)-N(4)	1.224(3)
O(5)-N(5)	1.223(3)
O(6)-N(5)	1.235(3)
N(1)-C(7)	1.346(3)
N(1)-C(3)	1.358(3)
N(2)-C(9)	1.289(3)
N(2)-C(8)	1.476(3)
N(3)-C(17)	1.287(3)
N(3)-C(16)	1.465(3)
N(4)-C(12)	1.453(3)
N(5)-C(20)	1.449(3)
C(1)-C(2)	1.535(3)
C(2)-C(3)	1.519(3)
C(2)-C(16)	1.548(3)
C(2)-C(8)	1.560(3)
C(3)-C(4)	1.390(4)

C(4)-C(5)	1.386(4)
C(5)-C(6)	1.387(4)
C(6)-C(7)	1.380(4)
C(9)-C(10)	1.453(3)
C(10)-C(11)	1.399(3)
C(10)-C(15)	1.425(3)
C(11)-C(12)	1.382(4)
C(12)-C(13)	1.396(4)
C(13)-C(14)	1.375(3)
C(14)-C(15)	1.416(3)
C(17)-C(18)	1.445(3)
C(18)-C(19)	1.398(3)
C(18)-C(23)	1.425(3)
C(19)-C(20)	1.377(4)
C(20)-C(21)	1.395(4)
C(21)-C(22)	1.365(4)
C(22)-C(23)	1.414(4)
C(24)-Cl(2)	1.753(12)
C(24)-Cl(3)	1.792(12)
C(24A)-Cl(3A)	1.742(15)
C(24A)-Cl(2A)	1.750(14)
Cl(4)-C(25)	1.730(7)
Cl(5)-C(25)	1.776(7)
Cl(4A)-C(25A)	1.719(17)
Cl(5A)-C(25A)	1.771(16)
O(1)-Al(1)-O(2)	90.92(8)

O(1)-Al(1)-N(2)	90.52(8)
O(2)-Al(1)-N(2)	93.65(9)
O(1)-Al(1)-N(3)	176.67(9)
O(2)-Al(1)-N(3)	89.01(8)
N(2)-Al(1)-N(3)	86.16(8)
O(1)-Al(1)-N(1)	90.58(8)
O(2)-Al(1)-N(1)	173.46(9)
N(2)-Al(1)-N(1)	79.97(8)
N(3)-Al(1)-N(1)	89.13(8)
O(1)-Al(1)-Cl(1)	93.25(6)
O(2)-Al(1)-Cl(1)	96.44(6)
N(2)-Al(1)-Cl(1)	169.17(7)
N(3)-Al(1)-Cl(1)	90.07(6)
N(1)-Al(1)-Cl(1)	89.83(6)
C(15)-O(1)-Al(1)	130.92(16)
C(23)-O(2)-Al(1)	130.04(15)
C(7)-N(1)-C(3)	119.1(2)
C(7)-N(1)-Al(1)	117.79(16)
C(3)-N(1)-Al(1)	122.36(17)
C(9)-N(2)-C(8)	117.0(2)
C(9)-N(2)-Al(1)	124.76(17)
C(8)-N(2)-Al(1)	118.22(15)
C(17)-N(3)-C(16)	116.7(2)
C(17)-N(3)-Al(1)	124.41(17)
C(16)-N(3)-Al(1)	118.90(15)
O(4)-N(4)-O(3)	122.9(2)
O(4)-N(4)-C(12)	118.6(2)

O(3)-N(4)-C(12)	118.5(2)
O(5)-N(5)-O(6)	123.0(2)
O(5)-N(5)-C(20)	118.8(2)
O(6)-N(5)-C(20)	118.2(2)
C(3)-C(2)-C(1)	112.8(2)
C(3)-C(2)-C(16)	106.9(2)
C(1)-C(2)-C(16)	108.09(19)
C(3)-C(2)-C(8)	111.87(19)
C(1)-C(2)-C(8)	107.8(2)
C(16)-C(2)-C(8)	109.3(2)
N(1)-C(3)-C(4)	120.7(2)
N(1)-C(3)-C(2)	115.4(2)
C(4)-C(3)-C(2)	123.9(2)
C(5)-C(4)-C(3)	119.7(2)
C(4)-C(5)-C(6)	119.3(2)
C(7)-C(6)-C(5)	118.4(2)
N(1)-C(7)-C(6)	122.7(2)
N(2)-C(8)-C(2)	111.20(19)
N(2)-C(9)-C(10)	124.0(2)
C(11)-C(10)-C(15)	119.9(2)
C(11)-C(10)-C(9)	117.2(2)
C(15)-C(10)-C(9)	122.1(2)
C(12)-C(11)-C(10)	119.4(2)
C(11)-C(12)-C(13)	121.9(2)
C(11)-C(12)-N(4)	118.7(2)
C(13)-C(12)-N(4)	119.4(2)
C(14)-C(13)-C(12)	119.2(2)

C(13)-C(14)-C(15)	121.1(2)
O(1)-C(15)-C(14)	118.8(2)
O(1)-C(15)-C(10)	122.7(2)
C(14)-C(15)-C(10)	118.5(2)
N(3)-C(16)-C(2)	110.68(18)
N(3)-C(17)-C(18)	124.8(2)
C(19)-C(18)-C(23)	119.9(2)
C(19)-C(18)-C(17)	119.0(2)
C(23)-C(18)-C(17)	120.8(2)
C(20)-C(19)-C(18)	119.7(2)
C(19)-C(20)-C(21)	121.5(2)
C(19)-C(20)-N(5)	119.8(2)
C(21)-C(20)-N(5)	118.7(2)
C(22)-C(21)-C(20)	119.3(2)
C(21)-C(22)-C(23)	121.7(2)
O(2)-C(23)-C(22)	119.3(2)
O(2)-C(23)-C(18)	122.9(2)
C(22)-C(23)-C(18)	117.8(2)
Cl(2)-C(24)-Cl(3)	106.8(7)
Cl(3A)-C(24A)-Cl(2A)	114.9(11)
Cl(4)-C(25)-Cl(5)	114.3(3)
Cl(4A)-C(25A)-Cl(5A)	113.9(12)
